

# **BULGARIAN CHEMICAL COMMUNICATIONS**

**2017** Volume 49 / Special Issue C

Dedicated to Prof. Zdravko Stoyanov on the occasion of his 80<sup>th</sup> anniversary in appreciation of his enormous contributions to the development of electrochemical science and electrochemical impedance spectroscopy in particular and in recognition of his exceptional service in favor of the Bulgarian Academy of Sciences as an outstanding national research center

*Journal of the Chemical Institutes  
of the Bulgarian Academy of Sciences  
and of the Union of Chemists in Bulgaria*



## Preface

It is a great pleasure for the Bulgarian Electrochemical Society to present this special issue of Bulgarian Chemical Communications in honor of Prof. Zdravko Stoynov in appreciation for his enormous contributions to the development of the Electrochemical science and Electrochemical Impedance Spectroscopy in particular. On the occasion of Prof. Stoynov's 80th anniversary, we celebrate his brilliant academic career, which has lit over half a century with the sparks of innovation.

The cross-disciplinary expertise of Prof. Zdravko Stoynov covers a vast area of scientific fields and disciplines. For his original experiments and findings he develops non-standard and unique equipment, writes specialized software and applies sophisticated mathematical and statistical tools. He introduced the application of digital frequency response analyzers in electrochemistry and pioneered the idea of impedance measurements out of equilibrium. Together with the team of Prof. Epelboin, he measured impedance of batteries for the first time in the world and continued with the development of the now widely applied 4D non-stationary impedance analysis. Two of the papers in this issue exploit this advanced technique, which vastly increases the information capability of impedance spectroscopy. Stoynov's Differential Impedance Analysis ensures both structural and parametric identification without the need of preliminary working hypothesis. His Differential Coulometry Spectroscopy method for kinetic studies of batteries entered in the newest equipment of Bio-Logics (Fr). The Rotating Fourier Transforms, cited in this issue by Boris Grafov and co-workers, are already entering in huge application area. In the moment, Prof. Zdravko Stoynov is still hard at work, is developing new tools for evaluation of state of health and lifetime of batteries and fuel cells.

Prof. Stoynov's activities are part of the joint efforts of a unique generation of original scientists from many countries, who established and developed impedance society into an integral part of the electrochemical society. Through the Electrochemical Impedance Spectroscopy Symposia and the European Electrochemical Impedance Analysis Symposia, they have put EIS on the map and have nurtured a community of

scientists in the field for the past 30 years. To this day, Zdravko Stoynov's voice is highly regarded during those meetings as an insightful guide for the next generation of scientists.

Prof. Stoynov has insightfully played an integral role in the development of regional and national electrochemical science during the last decades. He has strongly been supporting the electrochemists from South-East Europe in the establishment of the Regional Symposium on Electrochemistry – South East Europe (RSE-SEE). He chaired the Bulgarian Electrochemical Society with its biannual symposium Sofia Electrochemical Days, focusing on the representation and growth of the next generation of Bulgarian electrochemists. He has also focused on the integration of Bulgaria into the International Electrochemical Society through the establishment of the Bulgarian Section of IES. We are happy to mark the strong contribution of many scientists from these organizations in this special issue of Bulgarian Chemical Communications, which comprises 31 papers with the participation of researchers from 12 countries from Europe, Asia and America (Bulgaria, Croatia, Czech Republic, France, Hungary, Italy, Korea, Rumania, Russia, Serbia, Slovenia, USA).

Our intention as editors was to design a non-standard and original issue, to reflect as much as possible the unique person to whom it was dedicated. We think that we succeeded thanks to all the contributors who offered original papers both as form and as content. The book was designed to comprise several parts:

- "Stories" about electrochemistry in the second part of the 20th century and the people behind it, about the spirit and atmosphere created by the "fathers" that developed the fundamentals on which today's electrochemistry germinated and flourished. We are happy to announce that this part, named "The Fathers", came into being with the strong contribution of Prof. Stoynov who wrote about his teacher in electrochemistry – Acad. Evgeni Budevski.

- Review papers in Electrochemistry. For the realization of this part we would like to thank another pioneer in impedance and in electrochemistry – Prof. Digby Macdonald, as well as to his younger colleagues Roxana Apetrei

from Rumania, Zoran Mandi from Croatia and Marin Pandev from Bulgaria.

- Scientific contributions in the field of Electrochemistry - original results, not published in other journals. We are happy to present 22 scientific contributions, which demonstrate the vast application areas of electrochemistry, as well as its continuing development.

- Letters to the editor – one classical dissemination form applied strongly in scientific journals in the last century, ensuring a platform for discussions on some challenging and/or contradictory topics. After consultation with Prof. Stoynov, we are offering one topic in which the question starts from the title.

In addition to those parts of the special issue, you can find a review of Prof. Stoynov's multidisciplinary activities. The Bulgarian Academy of Sciences awarded Prof. Zdravko Stoynov with the special medal of the President of BAS in recognition of his entire scientific and academic activities: outstanding contributions to

electrochemical impedance science and its applications in electrochemical power sources and recognized exceptional service in favour to the Bulgarian Academy of Sciences as an outstanding national research center.

With this special issue including reviews and latest achievements, the international electrochemical community thanks Prof. Zdravko Stoynov for his enormous contributions in the development of the electrochemical science and its scientific society.

For us as guest editors it was a great honor and pleasure to coordinate the activities of the international electrochemical community. We would like to thank them for the enthusiasm, efforts and dedication in the preparation of the papers. We would also like to thank the reviewers for the precise and accurate work. We wish to express our gratitude to Dr. Gergana Raikova, Mr. Georgi Pchelarov, Dr. Milena Krapchanska and Mr. Marin Pandev for devoting their energy and time for the preparation of this issue.

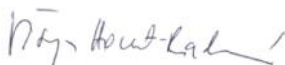
Finally, we all join the wishes of Prof. Michel Keddam for Zdravko Stoynov's 80<sup>th</sup> anniversary, saying together:

*"Please, keep on working hard...so many discoveries are still ahead".*

Guest Editors:



Daria Vladikova



Višnja Horvat-Radoševi



Tamás Pajkossy

April, 2017

## Zdravko Stoynov - the scientist who turns curiosity into multidisciplinary

D. Vladikova

*Acad. E. Budevski Institute of Electrochemistry and Energy Systems, Bulgarian Academy of Sciences, 10 Acad. G. Bonchev St., Sofia 1113, Bulgaria*

It is not easy to write about the scientist Zdravko Stoynov, about his achievements and contributions, which stem from his vivid and unconventional personality, about his original way of thinking – sometimes too avant-garde for its time, or as they say today – innovative, and thus not at all easy to understand and accept. It is not easy, however, it is downright challenging.

While trying to systemize his activities, I realized that nearly everything Zdravko Stoynov has set his mind on doing has turned into an achievement on the cutting edge of science.... since the beginning of his career at the age of 25, i.e. 55 years ago, when he developed the first analog computer to calculate systems of differential equations to the twelfth order after the decimal point for his thesis at the Technical University of Sofia. That took place in 1960 and now – 56 years later he continues to introduce new methodological algorithms and solutions which, when integrated into his nonstandard equipment, register significant unexplored phenomena in electrochemical power sources – the latest area of his professional interests.

Prof. Stoynov's scientific achievements are not only numerous and significant, but also cross between different disciplines to redefine problems outside normal boundaries and reach solutions based on a new understanding of complex processes - a novel approach in modern science which usually involves different teams of scientists from diverse backgrounds and fields. Zdravko Stoynov's research marries electrochemistry with engineering, mathematics, computer sciences... he suits the equipment he creates to his experimental goals – from the development of unique hardware and software to original methods for data analysis. For example, he measured the underpotential pre-nucleation of Ag on dislocation free surface of single crystal face by constructing an ultra-sensitive potentiostat with a voltage range of 10 mV and sensitive current measurements. His precision equipment and methodology registered impedance

on a single dislocation. His extensive interdisciplinary knowledge and skills reflect in his academic degrees: Ph.D. in engineering (automatization of the experiment) from the Bulgarian Academy of Sciences (BAS); Doctor of Technical Sciences (technical cybernetics) from Zurich Polytechnical University, and Doctor of Chemical Sciences from BAS.

I had been wondering for many years about the source of Prof. Stoynov's limitless scientific curiosity and inexhaustible constructive energy to define new topics and undertake seemingly insoluble problems, transforming them into fertile and attractive research fields. Finally, I found the answer. While preparing my presentation for the official 80<sup>th</sup> anniversary ceremony, I asked Prof. Stoynov for some childhood photos... and there it was... I saw the same expression, the curiously-mischievous same smile - as open and playful at the age of 3-4 as it was at the age of 70-80 (Fig. 1). Throughout all this time, he has preserved and developed this childish curiosity and disregard for limits and taboos which, combined with extraordinary intelligence and the multidisciplinary knowledge accumulated during the years, makes him an extraordinary scientist, just as it is in the words of the renowned physical chemist Ivan Stransky: "*A scientist must possess the capability to wonder. A scientist has to see voids where others see nothing.*"

Born in Kardjali on May 16, 1936, Zdravko Stoynov spent his childhood in Stara Zagora, in the family of his maternal grandfather Stefan juharov, the headmaster of the regional girls' high school, founded in 1863 and famous for its educational traditions since the time of the Bulgarian cultural revival. Stefan juharov's daughters were enthralled by literature – Zdravko's mother was a teacher, while her sister became a poetess in the literary circle of Georgi Bakalov, a famous Bulgarian literary critic and publisher from the beginning of the 20<sup>th</sup> century. His father, Boris Stoynov, was a lawyer, but both sons, Stefan and Zdravko himself cut ties with the social science family tradition and became engineers. Their professional orientation took such a sharp turn

---

To whom all correspondence should be sent:  
E-mail: d.vladikova@bas.bg

thanks to... a matador!... a children's game, which became their game in life. After completing all levels of the "Matador" game, Stefan and Zdravko began to ask questions themselves, solve puzzles and complete tasks. When Zdravko Stoynov constructed his first battery (the Volta

battery) at the age of 8, he didn't have inkling that batteries would become an integral part of his professional destiny. This is how the "Matador" technical construction game completely changed Zdravko's childhood and determined his professional life - the life of an inventor.



**Fig. 1.** Zdravko Stoynov in: early 1940's (left); 2010's (right).

Hence, in 1960 Zdravko Stoynov graduated from the Technical University of Sofia by constructing the first in Bulgaria analog computer to calculate differential equations to the 12<sup>th</sup> order after the decimal point. In the next 2 years, he established the "Computing and Modeling Laboratory" at the Technical University and

constructed a large analog computer to calculate non-linear differential equations up to the 120<sup>th</sup> order. At the same time, he developed non-standard equipment for researchers at the Bulgarian Academy of Sciences. As a result, in 1963 Prof. Todor Vitanov (a research fellow then), introduced him to the team of Academician Evgeni Budevski,

who was feverishly working on creating a dislocation-free crystal. If successful, they would create the first in the world “perfect crystal” and confirm the Stransky-Kaischew theory of two-dimensional nucleation.

Thus, in 1963 Zdravko Stoynov became part not just of the Bulgarian Academy of Sciences, but also of a talented world-renowned research team on the verge of a significant discovery. In a matter of months, he considerably increased the sensitivity, precision and stability of the measuring equipment and, albeit coming from a completely different scientific field, started to actively participate in the scientific work of the team. Zdravko Stoynov himself enthusiastically described the atmosphere, emotions, and dedication of the entire team during those exiting times in his contribution for Academician Evgeni Budevski in this special issue of Bulgarian Chemical Communications.

In 1965, 33 years after the publication of the Stransky-Kaischew theory, came its experimental proof – the Budevski team successfully grew the first in the world dislocation-free single crystal. This accomplishment sparked extensive research of electrochemical behavior in a new, experimentally unexplored system with completely different behavior from systems with dislocations in the

crystal lattice. Zdravko Stoynov actively participated in the novel research by developing models for surface diffusion and monoatomic layer growth [1,2].

With such a strong scientific beginning, what to do next?! By participating in the development of ultra-sensitive equipment for a unique experiment, Zdravko Stoynov fell within the orbit of Academicians Rostislav Kaischew and Evgeni Budevski – an orbit which determined to a great extent his professional path. His exceptional engineering and mathematical background gave him the unique independence to develop targeted task-specific equipment. From then on, he had freedom to choose what scientific peak to overcome next. He selected to go into electrochemical impedance spectroscopy (EIS) - a difficult and little exploited at the time, yet exciting field full of potential and enormous opportunities. In parallel, he continued to work in a pure engineering field - automatization of the scientific experiment, developing a series of automated battery testing equipment for the newly established Central Laboratory of Electrochemical Power Sources with Director Evgeni Budevski, founded in 1967 (Figs. 2-4).



**Fig. 2.** The nucleus of the newly founded Central Laboratory of Electrochemical Power Sources (from left to right): Veselin Bostanov, Dechko Pavlov, Jordan Geronov, Evgeni Budevski (standing), Todor Vitanov, Georgi Staykov (standing), Zdravko Stoynov, Ilia Iliev.



**Fig. 3.** The Electrochemical Methods Department, founded by Zdravko Stoynov: 1976 (left); 2016 (right).

That equipment was implemented in the Bulgarian lead acid batteries plants (in Dobrich, Targovishte, Pazardjik). Prof. Stoynov's power potentiostats were introduced in the Laboratories of the German and Czech Academies of Sciences. During his specialization in Case Western Reserve University in Cleveland, he developed a new-generation ultra-fast power potentiostat (BC 6000), which was put into production in Stonehard Ass. (USA) - the company owned by the inventor of the fuel cell for the American lunar rover.

Zdravko Stoynov never ceases to develop unique non-standard equipment (Figs. 5,6), but it serves as a means to a greater end as the focus of his work shifts to experimental methodologies.

Despite his interest and work in various scientific fields, his greatest and undying love remains electrochemical impedance. He is irresistibly drawn to this method by its exceptional informative capabilities and numerous exciting challenges. Electrochemical impedance has the unique advantage of separating the kinetics of the different steps describing the phenomenon or process under investigation. However, there are serious hurdles in the analysis of the experimental data, which need a statistical approach. The challenge is two-fold and consists in both the method and the system under investigation... and Zdravko Stoynov has been "digging" in both directions – for already more than 40 years.

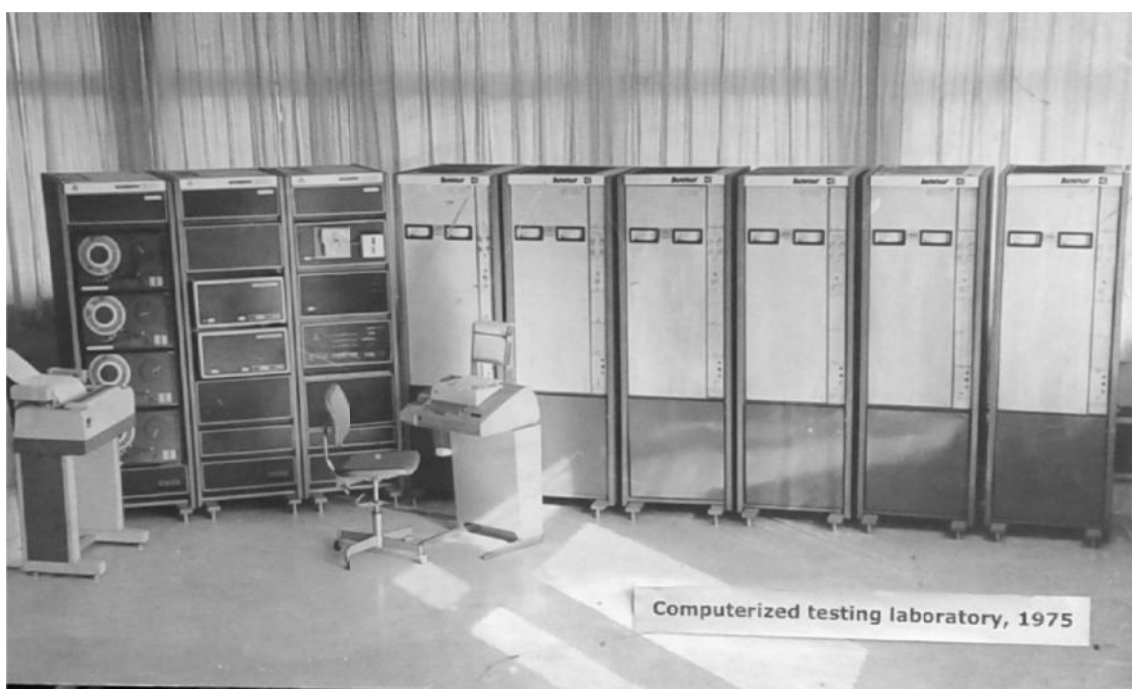


**Fig. 4.** Zdravko Stoynov's computerized testing laboratory in CLEPS (1975)





**Fig. 5.** Zdravko Stoynov's "Hydrogen Laboratory" in IEES (2015).



**Fig. 6.** Zdravko Stoynov and Massimo Schiavetti in front of Stoynov's equipment for impedance testing of large batteries for accumulation of energy from solar cells (ENEL- Pisa, 2014).

Nowadays, measuring electrochemical impedance with frequency response analyzers is a mainstream method used by all. However, few know that they have to thank Zdravko Stoynov for this; he implemented this equipment into electrochemical measurements after a visit to the Solartron company in 1968. The first two frequency response analyzers were implemented by Prof. Epelboin in his laboratory in Paris (CNRS-UPMC, Université Pierre et Marie Curie) and by Prof. Stoynov himself in CLEPS (Bulgarian Academy of Sciences) – both in 1968.

Working in a "battery institute", Zdravko Stoynov decided to investigate the impedance of batteries – an object whose impedance was considered impossible to measure at the time. Under these circumstances, he started to systematically chisel away at the scientific taboos... and continues to do so to this day. For a start, he introduced measurements outside the point of chemical balance. Today, this is customary;

however, it was out of the question of about 40 years ago. Prof. Stoynov developed specialized equipment and with his colleagues at CNRS in Paris measured, for the first time in the world, impedance of batteries – galvanostatically and quasistationary [3] (Fig. 7). A year later, he measured the impedance of large-scale batteries. He promoted the introduction of this method in laboratories and practices of the European Space Agency, the Soviet space program, as well as, in the Lewis Center at NASA.

JOURNAL OF APPLIED ELECTROCHEMISTRY 7 (1977) 539–544

SHORT COMMUNICATION

### *Impedance measurement on Pb/H<sub>2</sub>SO<sub>4</sub> batteries*

M. KEDDAM, Z. STOYNOV,\* H. TAKENOUTI

Groupe de Recherche no. 4 du C.N.R.S. 'Physique des Liquides et Electrochimie', associé à l'Université P. et M. Curie, 4 place Jussieu, 75230 Paris Cedex 05, France

Received 4 March 1977

#### I. Introduction

Relatively few works have been carried out on Pb/H<sub>2</sub>SO<sub>4</sub> batteries from an electrochemical kinetics point of view. This is partly due to the

The purpose of this note is to demonstrate that it is technically possible to measure the impedance of electrochemical generators by means of a transfer function analyser over a very wide frequency range. The impedance measurements are

**Fig. 7.** The first publication for impedance on batteries.

What would be the next challenge? Delving deeper into the impedance of batteries, Prof. Stoynov focused on the non-steady state of batteries during the measurement process.

#### *Non-stationary (4-D) impedance analysis*

Based on the classical method of the Transfer Function (TF), Electrochemical Impedance Spectroscopy gives a local, linearized and full (in a frequency aspect) description of the investigated electrochemical system, which is assumed to be a steady-state one. However, batteries behave as big statistical systems with distributed parameters on a macro and micro scale. During cycling, processes of mass and energy transfer take place. They change the object's structure and parameters. Thus, batteries show non-steady state behavior, which is a restriction for correct impedance studies. For further development of impedance of batteries, a liberation from the restriction of steady state conditions was needed and thus Zdravko Stoynov developed non-stationary (4-D) impedance analysis – a procedure which eliminates the delay errors [4-8]. This approach is based on the assumption that the state and the parameter space of the system is a continuum. It corrects the errors arising from the measurement delay during the frequency sweep. In contrast to classical electrochemical impedance spectroscopy, which works with a 3-dimensional (3D) set of data, Zdravko Stoynov formulated a 4-dimensional initial set of experimental data, including the time of measurement. He approximated every iso-frequency dependence with

a formal model and applied two orthogonal iso-frequency cubic splines respectively for the real and the imaginary components. The interpolation (and extrapolation) for a given time  $t_j$  and a set of frequencies  $\omega_j$  gives the corresponding estimates of the real and imaginary parts. Thus, the data of each evolving diagram are reconstructed and the corresponding impedance diagrams already represent the impedances measured virtually at one and the same time for all frequencies which, as it can be seen in Fig. 8, in practice, corrects the deformations due to the non-steady state evolution.

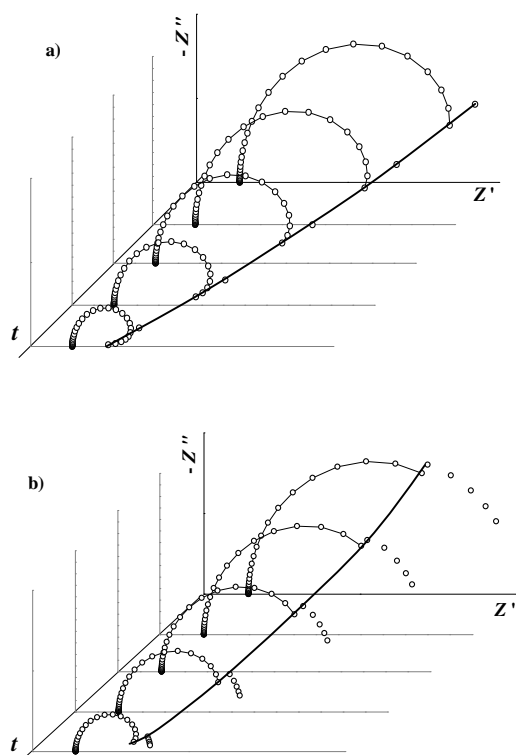


**Fig. 8.** Simulated impedance diagrams of evolving simple Faradaic reaction deformed by measurement delay errors: a) iso-frequency dependence for the lowest frequency; b) fifth iso-frequency dependence (starting from the lowest frequency). *Reproduced with permission from Z. Stoynov and D. Vladikova (2006) Nonstationary differential impedance spectroscopy in energy sources. In: Stoynov Z and Vladikova D (eds.) Portable and Emergency Energy Sources, pp. 411–436. Sofia: Marin Drinov Academic Publishing House.*

The developed 4-D approach improved significantly the impedance studies of batteries [8-12]. It has also been introduced in the battery testing software of Zahner Elektrik GmbH & Co. KG and successfully applied by Mitsubishi in Li-ion batteries research [13,14], as well as, for studies of other time-evolving systems. Two of the papers in this issue apply the 4D analysis and contribute to further development of its application window [15,16].

### Rotating Fourier Transform (RFT)

The non-steady state conditions of the electrochemical system during impedance measurements penetrate deeper, affecting the Fourier Transform (FT) which is the mathematical kernel of every impedance analyzer of our days. The FT is the best estimator of sinusoidal signals in steady-state conditions. However, out of those conditions, the FT produces specific errors dependent on the frequency. After a profound analysis of those errors, Stoynov succeeded to develop theoretically an advanced generalized form of this transform – the Rotating Fourier Transform. This was the subject of his doctoral dissertation in the Federal Institute of Technology – Zurich [17,18]. The RFT was proved both in simulations and in practice. The implementation of the RFT in impedance spectroscopy provides for precise measurements of time-evolving systems out of the steady-state conditions. It opens a new horizon for studies of batteries and fuel cells, corrosion and many other systems. Although created 30 years ago, in our days, the Rotating Fourier Transforms are entering in their application area, exploring the infra-low frequency range (down to the  $\mu\text{Hz}$  region), where many important phenomena take place.

### Differential Coulometry Spectroscopy

Battery testing is an important application-oriented tool for evaluation of their operational capability and performance as sources of energy and power. The typical testing results give general information that represents the overall behavior and thus does not support the analytical understanding of the processes taking place. To fill this gap, Zdravko Stoynov developed the Differential Coulometry Spectroscopy (DCS) which extracts valuable information about the batteries' internal kinetics, electrochemical design and life degradation. This technique requires measurements of the voltage changes with the time followed by precise aperiodic function Spectral Transform analysis. [18,19]. In order to separate the thermodynamic kinetics from the masking dynamic effect of the intrinsically connected transport limitations, very slow rate galvanostatic testing (charge/discharge) is required. In principle, the galvanostatic mode of testing is a sweep coulometry and provides for the evaluation of the quantity of electricity necessary for the propagation of the investigated process or its steps. DCS was found to be a useful tool for investigation of the electrochemical behavior and performance of rechargeable batteries based on intercalation materials (Fig. 9). Recently, it was included in the

analysis package of BioLogic Science Instruments latest EC-Lab software version V11.01 [20].

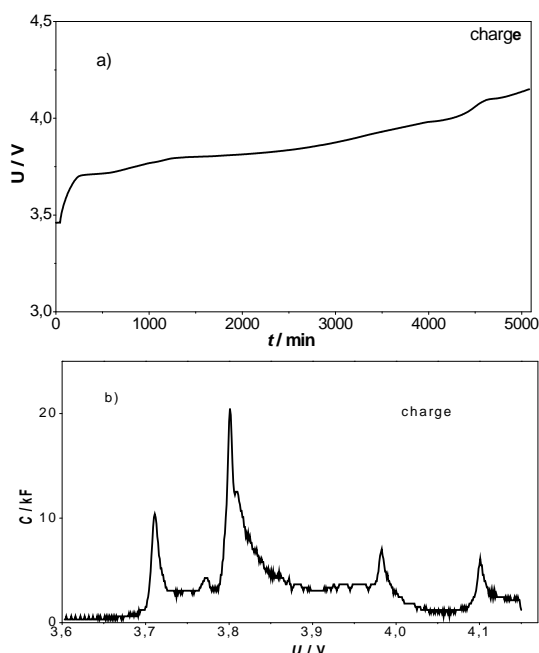


**Fig. 9.** Four volts Li-ion sample with nominal capacity of 2200 mAh: (a) Slow sweep voltage–time charge curve ( $h = 100$  hours); (b) Capacity spectrum of the slow sweep voltage–time charge and discharge curves ( $h = 100$  hours). *Reproduced with permission from Z. Stoynov and D. Vladikova (2006) Differential Coulometry spectroscopy In: Stoynov Z. and Vladikova D. (eds.) Portable and Emergency Energy Sources, pp. 411–436. Sofia: Marin Drinov Academic Publishing House.*

#### Differential Impedance Analysis (DIA)

Although electrochemical impedance as a TF gives a local, linear and full description of the system under study, this information has to be extracted from the experimental data, since impedance does not directly measure the processes caused by the perturbation signal, i.e. it is not a physical reality, but an information property of the object. The commonly applied approach for the interpretation of the experimental data is the construction and confirmation of a preliminarily derived hypothetical model. The model structure is chosen a priori, and thus the identification procedure is only parametric.

The main efforts towards the improvement of the impedance data analysis are focused on the advancements of the identification procedure. In this direction, Zdravko Stoynov's achievements concern the development of the original Model Reduction Method [20]. However, the data analysis advancements by improvements in the parametric identification did not satisfy him because of the principle discrepancy between the power of the

impedance measurement technique, which ensures a large volume of precise data, and their analysis, based on the formulation of hypotheses, often built on subjective or oversimplified assumptions.

In Technical Cybernetics the Structural Identification approach is applied for data analysis. It does not require an initial working hypothesis and provides both structural and parametric identification. However, the application of this procedure to electrochemistry creates a multitude of problems, which for a long time had been accepted as insoluble. This challenge attracted Zdravko Stoynov and to overcome it, he developed the technique of Differential Impedance Analysis (DIA), introducing the Structural Identification approach in the frequency domain [21-28].

The DIA procedure starts with the initial set of experimental data (angular frequency, real and imaginary components of the impedance), and thus can be applied to previously measured data. The kernel is the local scanning analysis, performed with the so-called local operating model (LOM) with a simple structure consisting of a resistance  $R_1$  in series with parallel connection of capacitance  $C$  and resistance  $R_2$ . The effective time-constant  $T = RC$  is also introduced as a LOM parameter. In contrast to the classical parametric identification, which is performed over the entire frequency range and estimates the parameters' vector as a preliminarily chosen model structure, the identification of the LOM parameters' vector by local analysis is carried out within a narrow frequency range, regarded as an operating window. When the window width is a single frequency point, the solution is purely deterministic. The procedure of the structural and parametric identification can be described by the following steps:

- Scanning with the LOM throughout the whole frequency range with a scanning window of a single frequency point;
- Parametric identification of the LOM at every working frequency. Since the number of the independent data available inside the observation window is smaller than the number of the unknown parameters, the initial set of impedance data is extended with two additional terms - the derivatives of the real and imaginary components of the impedance with respect to the frequency. Thus, the set of equations for determination of the LOM parameters estimation becomes solvable;
- Frequency analysis of the LOM parameters' estimates. The results are presented in the so-called temporal plots, which give the frequency dependence of the LOM parameters' estimates (Fig.10). If the LOM parameters estimates are

frequency-independent in a given frequency region, the sub-model corresponding to this frequency segment follows the LOM structure, i.e. it is described with a parallel combination of capacitance and resistance, which determine a time-constant. Thus, the number of the plateaus gives the number of the time-constants in the model (Fig. 10b). The results may be transformed in spectra, where the plateaus are depicted as spectral lines (Fig. 10c, d) [25-28].

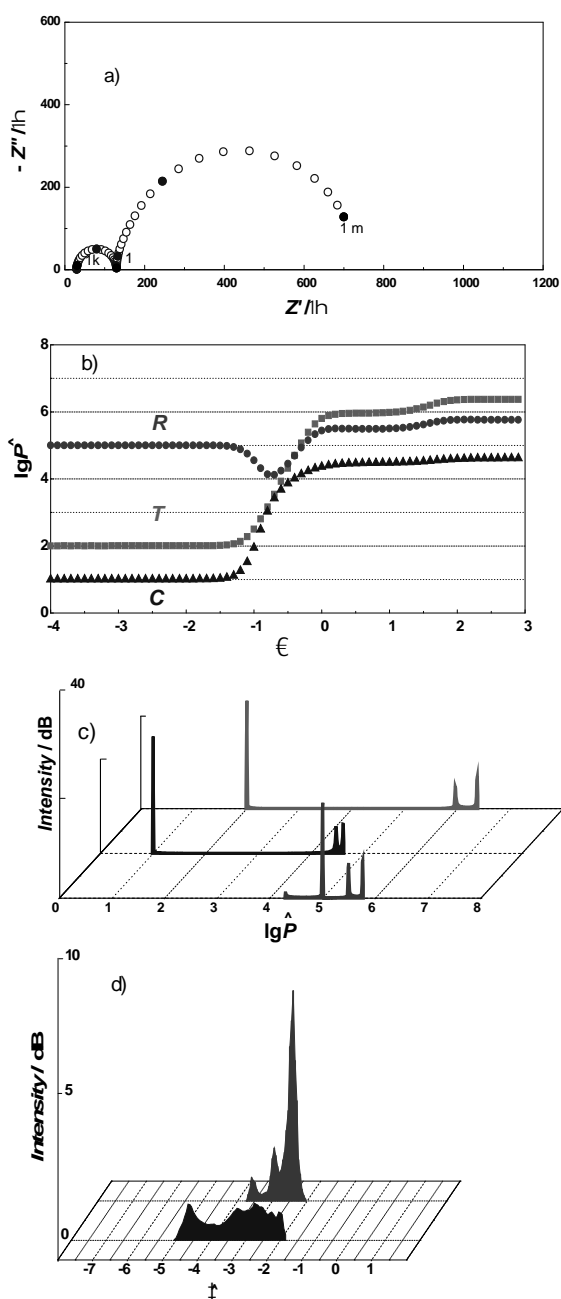


**Fig. 10.** DIA of three step reaction: (a) equivalent circuit and complex-plane impedance diagram; (b) temporal plots (c) spectral plots; (d) time-constant spectra of motor oil Mobil Delvac MX 15W40: new (■); after 10000 km. (■). Reproduced with permission from Z. Stoynov and D. Vladikova (2005) *Differential Impedance Analysis*. Sofia: Marin Drinov Academic Publishing House.

The presence of frequency dependence in the temporal plots marks either the regions of mixing between two phenomena or frequency dependent behavior. Those segments are additionally examined by Secondary DIA [25,27,28]. The procedure, known as differential temporal analysis, includes the differentiation of the LOM parameters' estimates with respect to the log frequency. It recognizes frequency-dependent elements (CPE, Warburg, Bounded Warburg etc.), as well as, their presence in more complicated models. DIA opens new horizons for EIS by increasing its information capability. It is successfully applied in electrochemical power source studies and other systems [28-37].

### Today's Challenges

In the last 15 years Zdravko Stoynov is "divided" between batteries and fuel cells. Water behavior in solid oxide fuel cells (SOFC) is as much important, as difficult. By performing precise impedance measurements with high accuracy at low frequencies (down to 1 mHz) he could monitor the formation, transport and evacuation of water in a new SOFC design [37]. In the moment he is developing new tools with increased sensitivity and enhanced information capability for "zoomed" monitoring and more accurate diagnostics of state of health of batteries and fuel cells (Fig. 11).

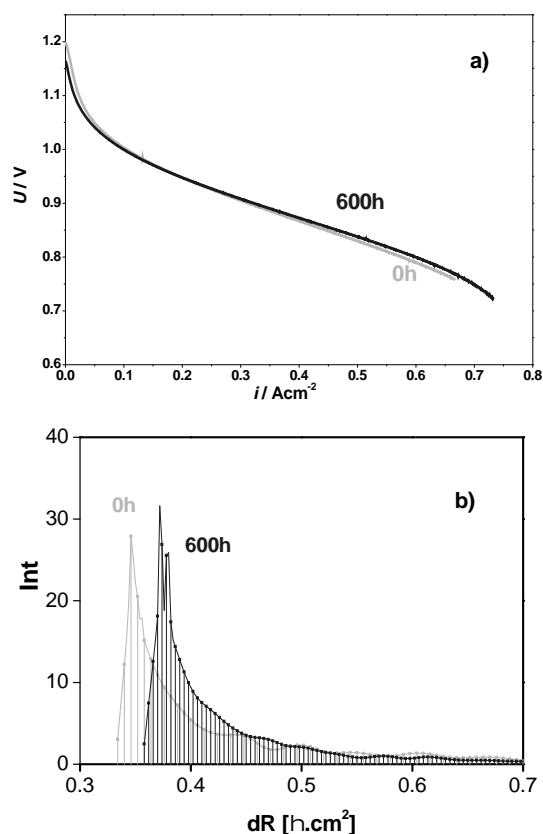


**Fig. 11.** DIVA of SOFC: (a)  $I-V$  curves; (b) spectral transform of the Differential Resistance  $dR$  ( $dU/dI$ ).

The new analysis (DIVA) is based on the classical current-voltage (I-V) characteristics and surprises with its simplicity and originality. It works with the derivative of the voltage in respect to the current, which is more sensitive to small deviations and thus ensures increased sensitivity and noise immunity. The method can give information about the origin of the degrading phenomena via combination with impedance measurements in selected characteristic working points and numerical modeling. The analysis is about 10 times more sensitive than the classical evaluation of fuel cells degradation based on voltage decrease measurements at constant current.

#### International Activities

Although engulfed in practical and applied research, Zdravko Stoykov is no less valued as a "social scientist" with an acute sense of establishment, with excellent teaching skills and an unwithering enthusiasm to educate and pass on his

knowledge and skills. He is one of founders - a similarly minded enthusiastic group of colleagues fascinated by the potential of electrochemical impedance, who established an international impedance society. For over 30 years, it has been gathering within the framework of two international conference chains:

- The International Electrochemical Impedance Spectroscopy Symposia, dating from 1989 (Fig. 12);

- The International Electrochemical Impedance Analysis Symposia, dating from 1988 (organized in Bulgaria in 1991, 1994, 2014, Fig. 13).

On a regional level, he strongly supported and aided in the establishment of the Regional Symposium of Electrochemistry – South-East Europe (RSE-SEE) and acted as its co-organizer in 2015 (Fig. 14). Starting in 1996, Zdravko Stoykov established the national electrochemical event with international participation "Sofia Electrochemical Days" (Fig. 15).

Dear Zdravko,

A best friendly message from the ancients of LISE

Chantal & Hubert Cachet, Claude Gabrielli, Georges Maurin, Robert Wiart,...

We remember all the good time we had together.

We are sharing this happy day with you.

*Please keep on working hard...*

*so many discoveries are still ahead*



*Bien amicalement*  
*Zdravko Stoykov*  
*M. Cachet*



Bombannes, 1<sup>st</sup> EIS Symposium, 1989

Souvenirs of formal and less formal instants at two memorable EIS Symposia



Tasting the Italian "Grappa", Val de Sole Marilleva, 5<sup>th</sup> EIS Symposium, 2001

Fig. 12. (a) International Symposium on Electrochemical Impedance Spectroscopy



**Fig. 12.** (b) Official Dinner, Algarve, Portugal, 8<sup>th</sup> EIS Symposium, 2010; (c) Lecture, A Toxa, Galicia, Spain, 10<sup>th</sup> EIS Symposium, 2016.

To this day, Prof. Stoynov continues to invigorate these scientific forums with his innovative and avant-garde ideas.

#### *Scientific management*

In the first difficult years after the changes in Bulgaria, the Central Laboratory of Electrochemical Power Sources, as well as the Bulgarian Academy of Sciences as a whole were functioning under the impending doom of being closed down and a great number of researchers left Bulgaria to seek professional realization in Western Europe and the Americas. However, during those troubling times, Prof. Stoynov's sense of duty towards Bulgarian science and his remaining colleagues did not let him emigrate. Instead of packing his suitcases for California, where he was expected to join Stanford University, he undertook the responsibility to preserve and develop the scientific legacy of his greatest teachers, Rostislav Kaischew and Evgeni Budevski, accepting the position of Director of CLEPS in 1992. Four years later, he was elected as Chairman of the General Assembly (GA) of the Bulgarian Academy of Sciences - the executive body which needed to reform the Academy in order to preserve its existence.

Prof. Stoynov once again united seemingly disparate fields such as electrochemistry, management, economics, and policy-making.



**Fig. 13.** International Symposium on Electrochemical Impedance Analysis (EIA) (a) Castle Trest, Moravia, Czech Republic, 5<sup>th</sup> EIA Symposium, 2008; (b) Welcome party, Red Island, Croatia 9<sup>th</sup> EIA Symposium, 2011; (c) Opening session, Borovetz, Bulgaria, 10<sup>th</sup> EIA Symposium, 2014.



**Fig. 14.** 5<sup>th</sup> Regional Symposium on Electrochemistry- South East Europe (RSE-SEE5), Pravets, Bulgaria, 2015.



**Fig. 15.** Opening of Sofia Electrochemical Days, 2012.

He applied his rich experience from impedance studies of energy systems, knowing that they behave like large statistical systems with distributed parameters on a micro and macro scale, that due to mass and energy transfer, those systems change their structures and show non-steady state behavior. In spite of these severe restrictions, he saw great potential and developed new and more sophisticated tools. Well, the scientific infrastructure, being a large statistical system of similar behavior, could be described in a similar way. The tool he offered for this system on a micro and macro scale (IEES and BAS) was a new type of scientific management based on: (i) microeconomic reforms; (ii) stable project financing; (iii) global scientific market participation; (iv) high-quality and high-level scientific products with a new positive emphasis on applied research still adequately balanced with fundamental studies.

Now, 25 years later, this socio-economic experiment which Prof. Stoynov took an active leading role in, has been proven successful. Not only did the Central Laboratory of Electrochemical

Power Sources grow into the Institute of Electrochemistry and Energy Systems - one of the most successful BAS institutes with strong participation in the European Research Area, but also the Bulgarian Academy of Sciences withstood the turmoil of the post-communist transition period and strengthened its position as a national research center with 150-year history and a bright future ahead.

Here are some facts to illustrate this point: in comparison with 1996 – the starting year of Stoynov's chairing of the GA in 2008 (his 3rd mandate), BAS' self-funding increased about 30 times. In a few short years, IEES also attained a balanced income with about 50% self-funding.

Zdravko Stoynov established the Innovation Centre at BAS, which has been a long-term partner in Enterprise Europe Network. He initialized the establishment of BAS Education Center, through which the Bulgarian Academy of Sciences obtained its accreditation for training and education. Noting the weakening of the BAS institutes in terms of the most valuable resource of any effective scientific infrastructure - the expert human resource, Prof. Stoynov implemented pro-active policies for career advancement and maintenance of the scientific staff above critical levels. While such policies sound trivial today, they were almost unheard of in Bulgaria during the 90's and the beginning of the 21<sup>st</sup> century.

It is a quite rewarding experience to be able to reap what you have sown. Today Zdravko Stoynov reaps the respect and appreciation of his friends and colleagues from IEES, BAS, and all over the world, who joined together physically and virtually to celebrate his 80's birthday, turning it into a joyous and heartwarming event (Fig. 16). The Bulgarian Academy of Sciences honored his exceptional service with the special medal of the President of BAS (Fig. 16).

The international electrochemical community and Bulgarian colleagues express their gratitude to Prof. Zdravko Stoynov for his avant-garde, and insightful contributions to the development of electrochemical science and its applications with this special issue of Bulgarian Chemical Communications.

Wishing Prof. Stoynov good health and high spirits, I would like to conclude with the greeting from Digby Macdonald, one of his closest friends from the circle of EIS pioneers:

*"Zdravko Stoynov has been a giant in electrochemical impedance spectroscopy and we look forward to his future contributions".*



**Fig. 16.** Celebration of Zdravko Stoynov's 80<sup>th</sup> Anniversary (16.05.2016): the official part and award (pictures 1,2); with the group (picture 3); dancing at the party (picture 4)

## REFERENCES

1. E. Budevski, W. Bostanov, T. Vitanov, Z. Stoynov, A. Kotzewa, R. Kaischew, Keimbildungserscheinung an versetzungsfreien (100) Flächen von Silbereinkristallen, *Electrochimica Acta*, **11**, 1697 (1966).
2. E. Budevski, W. Bostanov, Z. Stoynov, A. Kotzewa, R. Kaischew, Zweidimensionale Keimbildung und Ausbreitung von monoatomaren Silbereinkristallen, *Phys. Stat. Sol.*, **13**, 577 (1966).
3. M. Keddama, Z. Stoynov, H. Takenouti, Impedance Measurement on PB-H<sub>2</sub>SO<sub>4</sub> Batteries, *Journal of Applied Electrochemistry*, **7(6)**, 539 (1977).
4. Z. Stoynov, B. Savova Stoynov, Impedance Study of Non-Stationary Systems - 4-Dimensional Analysis, *Journal of Electroanalytical Chemistry*, **183(1-2)**, 133 (1985).
5. B. Savova Stoynov, Z. Stoynov, 4-Dimensional Estimation of the Instantaneous Impedance, *Electrochimica Acta*, **37(12)**, 2353 (1992).
6. Z. Stoynov, "Nonstationary Impedance Spectroscopy", *Electrochimica Acta*, **38(14)**, 1919 (1993).
7. Z. Stoynov, B. Savova Stoynov, Instrumental Error in Impedance Measurements of Non Steady-State Systems, *Journal of Electroanalytical Chemistry*, **112(1)**, 157 (1980).
8. Z. Stoynov, Advanced Impedance Techniques for Lithium Batteries Study - Four Dimensional Analysis, *Materials for Lithium-Ion Batteries*, Ed. C. Julien and Z. Stoynov, NATO Science Series, 3. High Technology, 85, p. 359, Kluwer Academic Publishers (2000).
9. Z. Stoynov, B. Savova-Stoynov, T. Kossev, Nonstationary Impedance Analysis of Lead-Acid-Batteries, *Journal of Power Sources*, **30(1-4)**, 275 (1990).
10. Z. Stoynov, T. Nishev, V. Vacheva, et al., Nonstationary analysis and modelling of battery load performance, *Journal of Power Sources*, **64(1-2)**, 189 (1997).
11. Z. Stoynov, D. Vladikova, Non-stationary differential impedance spectroscopy in energy systems in: Z. Stoynov, D. Vladikova (Eds.), "Portable and Emergency Energy Sources", Marin Drinov Academic Publishing House, Sofia, p. 411, 2006.
12. M. Itagaki, A. Taya, K. Watanabe, *Electrochemistry*, **68**, 596 (2000).
13. M. Itagaki, S. Yotsuda, N. Kobari, K. Watanabe, S. Kinoshita, M. Ue, *Electrochim. Acta*, **51**, 1629 (2006).
14. M. Ujvári, D. Zalka, S. Vesztegom, S. Eliseeva, V. Kondratiev, G. Láng, Electrochemical impedance measurements in non-stationary systems- Application of the 4-dimensional analysis method for the impedance analysis of overoxidized poly(3,4-ethylenedioxythiophene)-modified electrodes (*in this issue*)
15. V. Horvat-Radošević, K. Kvastek, K. Magdi Košićek, Application of Stoynov's 4-D analysis for nonstationary impedance spectra corrections of thin



- poly(o-ethoxyaniline) modified Pt electrode (*in this issue*)
16. Z. Stoynov, Fourier Analysis in the Presence of Nonstationary Periodic Noise, Dissertation No 1839, Swiss Federal Institute of Technology, Zurich, 1985.
  17. Z. Stoynov, *Electrochimica Acta*, **37(12)**, 2357 (1992).
  18. Z. Stoynov, D. Vladikova, Differential Coulometry spectroscopy in: Z. Stoynov, D. Vladikova (Eds.), Portable and Emergency Energy Sources, Marin Drinov Academic Publishing House, Sofia, 2006 p. 437.
  19. <http://www.bio-logic.net/wp-content/uploads/EC-BT-Lab-AN57.pdf>
  20. Z. Stoynov, B. SavovaStoynov, *Journal of Electroanalytical Chemistry*, **170(1-2)**, 63 (1984).
  21. Z. Stoynov, *Electrochimica Acta*, **34**, 1187 (1989).
  22. Z. Stoynov, *Polish J. Chem.*, **71**, 1204 (1997).
  23. Z. Stoynov, Advanced Impedance Techniques for Lithium Batteries Study - Differential Impedance Analysis, Materials for Lithium-Ion Batteries, Ed. C. Julien and Z. Stoynov, NATO Science Series, 3. High Technology, 85, p. 371, Kluwer Academic Publishers (2000).
  24. D. Vladikova, Z. Stoynov, *J. Electroanal. Chem.*, **572**, 377 (2004).
  25. D. Vladikova, P. Zoltowski, E. Makowska, Z. Stoynov, *Electrochimica Acta*, **47**, 2943 (2002).
  26. Z. Stoynov, D. Vladikova, "Differential Impedance Analysis", Marin Drinov Publ. House, Sofia, 2005.
  27. Z. Stoynov, D. Vladikova, Impedance Spectroscopy of Electrochemical Power Sources in: U. Garche (Ed.) Encyclopedia of Electrochemical Power Sources, Elsevier, p. 632, 2009.
  28. M. Viviani, M. Buscaglia, L. Mitoseru, A. Testino, P. Nani, D. Vladikova, *J. Europ. Ceram. Soc.*, **24**, 1221 (2004).
  29. D. Vladikova, A. Kilner, S. J. Skinner, G. Raikova, Z. Stoynov, *Electrochim. Acta*, **51**, 1611 (2006).
  30. D. Vladikova, G. Raikova, Z. Stoynov, H. Takenouti, J. Kilner, St. Skinner, *Solid State Ionics*, **176**, 2005 (2005).
  31. A. Barbucci, M. Viviani, P. Carpanese, D. Vladikova, Z. Stoynov, *Electrochim. Acta*, **51**, 1641 (2006).
  32. D. Vladikova, Z. Stoynov, A. Barbucci, M. Viviani, P. Carpanese, G. Raikova, The Technique of the Differential Impedance Analysis - Applications for SOFC studies" in: L. Mitoseriu (Ed.), New Developments in Advanced Functional Ceramics, Transworld Research Network, Kerala, India, Ch. 16, p. 457, 2007.
  33. A. Kirchev, *J. Power Sources*, **170(2)**, 495 (2007).
  34. A. Kirchev, *J. of Power Sources*, **191(1)**, 82 (2009).
  35. A. Kirchev, *J. of Power Sources*, **179(2)**, 808 (2008).
  36. D. Vladikova, Z. Stoynov, G. Raikova, A. Thorel, A. Chesnaud, J. Abreu, M. Viviani, A. Barbucci, S. Presto, P. Carpanese, *Electrochimica Acta*, **56**, 7955 (2011).
  37. D. Vladikova, Z. Stoynov, A. Chesnaud, A. Thorel, M. Vivianu, A. Barbucci, G. Raikova, P. Carpanese, M. Krapchanska, E. Mladenova, *International Journal of Hydrogen Energy*, **39(36)**, 21561 (2014).



# The Fathers



## Rostislaw Kaischew and his trace in the fundamental science. A brief historical overview of the genesis and rise of Sofia School of crystal growth

M. Michailov

Rostislaw Kaischew Institute of Physical Chemistry, Bulgarian Academy of Science, cad. G. Bonchev Str., bl. 11, 1113 Sofia, Bulgaria

The process of nucleation and growth of crystals is one of the most exotic phenomena in nature. Starting from disordered ensembles and small clusters of single atoms and molecules, matter organizes itself in beautiful figures and shapes with immaculate symmetry and ordering, ideal cubes, pyramids, needles, dendrites. These ensembles of crystal shapes and their divine beauty attend our entire being and consciousness, our entire life, they are everywhere around us. This incredible art of nature is generated spontaneously, without any influence of human mind, thinking, desire or action. Why is this occurring and how? Where the science meets the unfathomable loveliness and marvelous aesthetics of the art of crystal growth? A substantial contribution in answering these fundamental questions of condensed matter physics is given by a very bright generation of Bulgarian scientists in the last century [1-8].

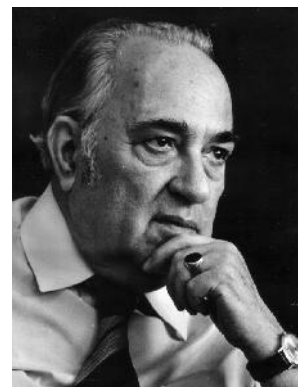
In the 1930s in Bulgaria originated the famous Sofia School of Crystal Growth, founded by the Bulgarian scholars prof. Iwan Nikolow (Nicola) Stranski and prof. Rostislaw Atanasov Kaischew. Brilliantly developed later, it is among the few internationally known substantial Bulgarian contributions in the world's scientific history. How this school has been established? How an internationally acknowledged scientific team, setting up the fundamentals of a novel theory in the field of solid state physics, phase formation and crystal growth is affirmed in times of wars, communist regimes and Berlin wall? How do the names of its founders Iwan Stranski and Rostislaw Kaischew manage to stand abreast with the names of Josiah W. Gibbs, Walther Kossel, Yakov I. Frenkel, Max Volmer and Frederick C. Frank? Exploring these questions and primarily unriddling the genesis of the scientific schools by the psychological and personal image of their founders

has great educational, historical and moral standing. This is because the birth and rise of the scientific schools and their ideas mirror the noetic values of mankind at the actual historical time [9-12].

Prof. Iwan Stranski and prof. Rostislaw Kaischew, the founders of the most famous Bulgarian scientific school have a dramatic personal and scientific destiny. Their illustrious academic and research activity plays a key role in Bulgarian science as well as in the development of the most important scientific institutions – the „St. Kliment Ohridski“ University of Sofia and the Bulgarian Academy of Sciences [2,4,5].



Iwan Nikolow (Nicola)  
Stranski



Rostislaw Atanasov  
Kaischew

Prof. Rostislaw Atanasov Kaischew was born on February 29th 1908 . In Sankt Petersburg in the family of captain Atanas Kaischew and Mrs. Anastassia Hadjimarinoва. Both the genealogical lines of the Kaischew's and the Hadjimarinov's families are rather interesting. The roots of the Kaischew's ancestry have a history time line of more than 250 years in the Rhodope's village of Chokmanovo, near Smolyan – a calm, peculiarly picturesque site in the Rhodope mountain, beyond the vanity and temptation of the modern world, urging the human mind to thoughtfulness, contemplation and existentialism, exciting curiosity and cognition [13,14].

This small mountain village with almost 100 inhabitants (94 in 2011, but 941 in 1934), placed on

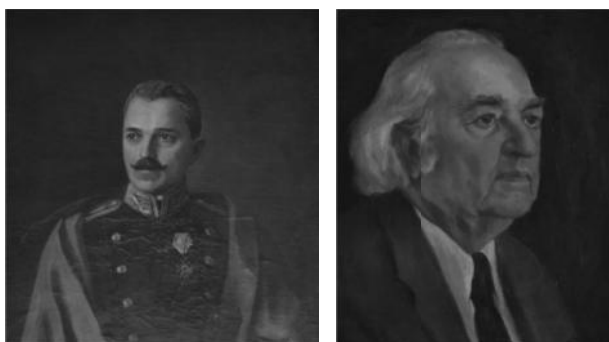
---

To whom all correspondence should be sent:  
E-mail: mike@ipc.bas.bg

sunny hills around green meadows and with several small churches, has given birth to a remarkable number of scientists, writers, art directors, physicians, musicians, artists. The Chokmanovo village manifests specific intellectual singularity with all the gifted persons born there. Only the people with academic rank and degree, originated from this very small village, are more than 20 [14]. The Kaischew's family also belongs to this unique ensemble of remarkable personalities.



Chokmanovo village and the Kaischew's family house, 2014 .



Portraits of general Atanas Kaischew and prof. Rostislaw Kaischew in the municipality of Chokmanovo village.

In 1905, the father of prof. Kaischew, Captain Atanas Kaischew is recruited to Sankt Petersburg, where he graduates with excellence „summa cum laude“ from the General Staff Military Academy. A few months after Rostislaw was born in 1908, the family returns to Bulgaria. General Atanas

Kaischew takes part in the first and second Balkan wars and World War 1, later he is promoted as a Chief of the Military Academy in Sofia, professor in the General Staff Academy and one of the most prominent Bulgarian military experts. The mother, Mrs. Anastassia Hadjimarinoва also originates from a famed Bulgarian family of large landowners and merchants from the region of Stara Zagora. In 1913 the family moves to Sofia. Their son Rostislaw graduates from high school in Sofia and matriculates at the Department of Physics and Mathematics of Sofia University. In his third years he attends the lectures in physical chemistry of Iwan Stranski, recently appointed as a professor at the University.



Iwan Stranski



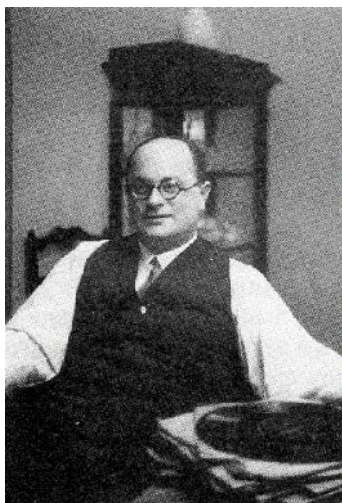
Rostislaw Kaischew, 1939

At that time, Stranski involves Kaischew in scientific activity and between them grows a tight collaboration and, later, an amity. Their first joint paper, entitled “On the equilibrium shapes of homopolar crystals”, initiated already in the time of the student years of Kaischew, is published in 1931 [15]. After his graduation from Sofia University, Kaischew accepts a Humboldt scholarship, recommended by Stranski, and in 1930 leaves for Berlin to the famous scholar and keen connoisseur of thermodynamics, Francis Simon.

Simon is a person with exceptional individuality and flavor, disciple of Walther Nernst, the founder of the Third Law of Thermodynamics. In 1931 Simon becomes a professor of physical chemistry at the Laboratory of Low Temperatures at the University of Breslau (presently, Wroclaw, Poland). Two years later, in 1933, he moves to the famous Clarendon Laboratory at the University of Oxford, invited personally by Frederic Lindemann. Later, in 1956, he becomes head of the Laboratory. Simon performs extraordinary, pioneering research in the field of low temperature physics. He succeeds to liquefy helium for the first time in the world by means of a system of magnetic cooling, based on adiabatic demagnetizing. Together with his assistant, Nicolas Kurti, he attains

experimentally a temperature of  $1\mu\text{K}$  (one micro kelvin), which is considered as a feat of the experimental physics at the time. Simon investigates and introduces the basic method for

separation of uranium isotopes via gaseous diffusion and production of uranium-235. He is one of the principal scientists, taking part in the physical design and creation of the nuclear bomb with the so-called „Manhattan Project“ [16].



Sir Francis Simon (the man with the hat at the second row) at the annual meeting of the Bunsen Gesellschaft, May 1928 in Munich, accompanied by Walther Kossel, Kazimierz Fajans, Peter Debye, Fritz London. (G.F.Hund, <https://commons.wikimedia.org>).

As a disciple of Francis Simon, Kaischew lands in the surroundings of notable researchers and gains a great opportunity for academic development and scientific life. In Berlin he attends lectures by Nernst, London, Simon and Bodenstein. In March 1931 Francis Simon is invited to head the Institute of Physical Chemistry at the University of Breslau and his entire research group, including the assistants Nicolas Kurti and Kurt Mendelson as well as the doctoral students Heinz London (brother of the famous Fritz London who introduced London's forces) and Rostislaw Kaischew, moves there.



Rostislaw Kaischew at the University of Breslau, 1931.

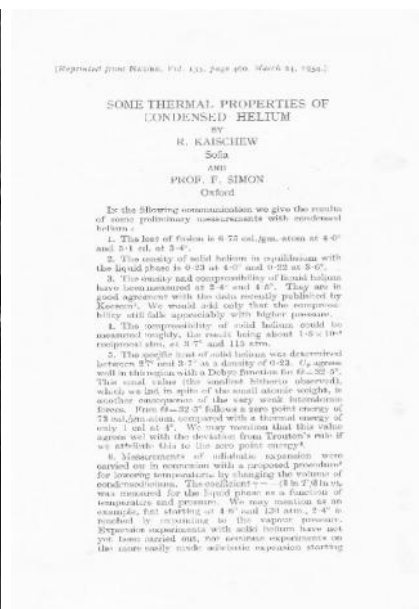
Reining in that group are excellent scientific ambience and sincere, artistic relations. There, Kaischew starts for the first time in the world the study of the basic thermodynamic properties of liquid and solid helium. In these pioneering studies, he determines experimentally the density and the heat of fusion of solid helium in equilibrium with the liquid phase, its specific thermal capacity, compressibility and other fundamental physical quantities. These experiments open up a way to estimate the so-called „zero entropy“ in the Nernst' theorem – a subject of a large discussion at that time. Kaischew's results will be used later in the interpretation of the Nernst-Simon formulation of the Third Law of Thermodynamics, in the form that a thermodynamic process, bringing a system to the absolute zero temperature by means of a finite number of steps, is impossible [16].

Kaischew defends his doctoral thesis on November 7<sup>th</sup>, 1932 with excellence „summa cum laude“ and becomes the first doctor of the Institute of Physical Chemistry at the University of Breslau. The results of his dissertation are published in the famous journal „Nature“ in 1934 in collaboration with Francis Simon - „Some thermal properties of condensed helium“. Let us point out that it has been possible to publish even preliminary results in „Nature“ in these years [17].

During his stay in Breslau, Kaischew maintains active correspondence with Stranski, who is in Berlin at that time. In this way is completed their first theoretical study. The paper „On the

equilibrium shapes of homopolar crystals”, published in “Zeitschrift für Physikalische Chemie” in 1931, marks the beginning of the theory of mean separation works [6, 15]. It is shown for the first time in this paper, that only atoms or molecules bound stronger than in the site of half-crystal position (kink), can belong to an equilibrium crystal

shape. This definition of equilibrium formulated in a completely new way, different from that of the classical thermodynamics of Gibbs, i.e. by the binding energy of a separate single element of the crystal lattice (atom or molecule) will lay the cornerstone of the entire construction of the new molecular theory of crystal growth.



The doctoral thesis of Kaischew, Breslau, 1932 (left), Kaischew at the Low Temperatures Laboratory, Breslau, 1931, (middle), the publication of Kaischew and Simon in Nature, 1934 (right).

The time spent in Breslau, in Simon's group, shapes the basic path of scientific evolution of Kaischew's life characterised by deep involvement in the world of scientific thought. Being a part of a research team in which many of its members Heinz London, Nicolas Kurti and Kurt Mendelson will become Fellows of the British Royal Society, and Nicolas Kurti its vice-president (1965-1967), Kaischew gains a remarkable start for scientific activity and career. Furthermore, he shapes his personality in environment of extremely variegated and often exotic cultural interests. Besides his achievements in the field of low temperature experimental physics, Nicolas Kurti becomes one of the founders of the so-called "molecular cuisine", moderates a number of cooking shows on BBC and organizes the first colloquium on "Molecular and Physical Gastronomy", held in Erice, Italy in 1992 [18]. Kurt Mendelson becomes famous with his treatise on the origination and construction of the Egypt Pyramids, too [19].

Already affiliated intellectually to the cultural and scientific values of the Western world, Kaischew returns to Bulgaria and enters the Department of Physical Chemistry of Sofia University, headed by prof. Iwan Stranski. Kaischew starts his career as a volunteering

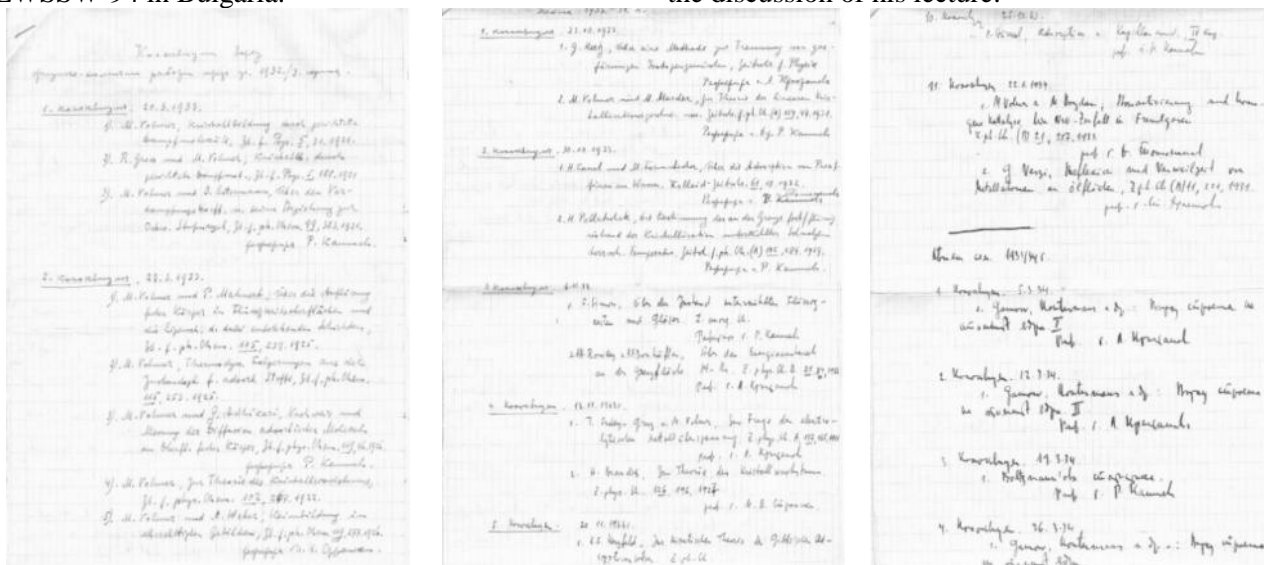
assistant, without any emolument. Only six months later, the efforts of Stranski with the Ministry of Education succeed and Kaischew is inaugurated as a full-time assistant at the Department. At that time, the oldest scientific colloquium in Bulgaria is instituted, still existing today as the „Stranski-Kaischew Colloquium on phase formation and crystal growth". This informal forum of discussions, with its first members Iwan Stranski, Rostislav Kaischew, Stefan Christov, Lubomir Krastanov, Dimitar Totomanow, will play later a key role in the creation of entire generation of researchers. The topics of the discussions are not restricted to phase formation and crystal growth, but cover a broad range of contemporary, cutting-edge problems of condensed matter physics and physical chemistry.

The time between 1933 and 1936 is the most valuable period of the research collaboration between Kaischew and Stranski. This remarkable scientific communion and empathy result in a ceaseless friendship. Thus, in a sequence of five papers in 1934, are presented the basic ideas and models of the theory of mean separation work [6, 20-24]. The new theoretical model of Stranski and Kaischew considers for the first time the equilibrium and the growth of the new phase at the



molecular level, from the viewpoint of the kinetics of elementary steps in phase formation and crystal growth. Furthermore, it complements in a perfect way the classical Gibbs thermodynamic model of phase formation, demonstrates the identity of the two models and thus attains a great physical importance. 60 years later these envisaged model concepts will be visualized at the atomic level by the brilliant Scanning Tunneling Microscopy experiments of Joost Frenken, presented at the first “East-West Surface Science Workshop”, EWSSW’94 in Bulgaria.

In 1935 Kaischew leaves for three months to Kharkiv, to the Physical and Technical Institute of Ukraine, recommended by Martin Rueman, senior assistant of Simon. There Kaischew works on the adiabatic effect of nitrogen expansion at liquid helium temperatures. During his stay in Kharkiv, he gives a lecture on the method of mean separation work, presenting the results obtained under the guidance of Iwan Stranski. There he meets for the first time the famous theoretical physicists Lev D. Landau and Evgeni M. Lifshitz, who take part in the discussion of his lecture.



The original record and part of the lectures presented at the Colloquium of Physical Chemistry in 1932/1933 at the Department of Physics and Mathematics of Sofia University.

After five years career as a full-time assistant at Sofia University, Kaischew attains the possibility for a sabbatical year abroad. So, he leaves for Germany in 1937 with a Humboldt scholarship to prof. Klaus Clusius at the Institute of Physical Chemistry of Munich University. Clusius is a student of Arnold Eucken of Göttingen, and later is the leading scientist and the head of the German experiments on the production of heavy water. Together with his assistant Gerhard Dickel he develops the method of separating isotopes by means of thermal diffusion. In the Clusius group, Kaischew retains his interest in the field of low temperature physics and investigates the crystallization of carbon monoxide by slow condensation from the gaseous phase and the conversions of condensed hydrogen halides by means of polarization microscopy. These studies are published in the “Zeitschrift für Physikalische Chemie” in 1938 and 1939. This sabbatical year in Munich spent in the bachelor company of two other scholarship fellows and his friends Sazdo Ivanov and Georgi Bradistilov is one of the happiest periods in the life of Kaischew. With his return to

Sofia at the end of September 1938, comes the end of his romantic student’s life. From now on, he starts his own, individual way, the most important and most interesting part of his life leading to the creation of the Sofia School of crystal growth.

Looking into Kaischew’s life in science, it is important to consider the more general question, that of the birth and rise of scientific schools. Is it an individual feat and goal of a single highly erudite person, just a prodigy, or a natural, synergetic process of self-organization of highly capable and motivated team of researchers following the same scientific ideas in the presence of a distinguished leader with strong personality and character? How does the generation, development and recognition of a scientific society which designates the tracks of scientific vogue in a given field depend on the environment in which it exists? A retrospective survey on the Sofia School of crystal growth would throw a light on these heuristic questions.

Science is a luxury exercise of the human soul, set up with time, assiduity, curiosity and moral. It is a state of constant dreaming. Allegiance to science

and the affiliation to the academic world is, in itself, a great human privilege, based on the desire and ability to study oneself in relation to the structure, logic and aesthetics of the world outside. It is a far, long-distance mental horizon overreaching the everyday existence and the personal life. However, the individual ability of contemplation and reasoning is not sufficient for the construction of cognitive image of the nature. The retrospection shows that fundamental human knowledge is often formed not by individual achievements and discoveries, but by scientific schools that provide direction, style and meaning of the scientific research. The formation and development of these schools determines the understanding of fundamental laws of the ambient world for prolonged periods of time. This process of self-organization of knowledge is an archetype of the human soul, occurring as a result of the capability of thought to arrange and construct various logical and physical models and to project their evolution in different temporary and spatial directions. Therefrom stems the essence of the scientific schools, namely heuristic classification of knowledge in a particular scientific field, creation of highly competent scientific environment, setting the direction and dynamics of the discussions in the field, and formulation of the scientific paradigms at a particular historical moment. In this way the scientific schools outline and decorate the ranges of human knowledge in historical context [9-12].

A basic feature of every scientific school is its ability to attract and educate young researchers. It should be emphasized that the scientific schools do not represent simply an aggregation or a team of gifted researchers. Teams of scientists exist in many research laboratories around the world. The presence of various scientific ideas, theoretical models, experimental observations and experienced researchers is by far not a sufficient condition for genesis of a scientific school. Going back in the history of human knowledge, we observe that the formation of scientific school is a rather complex phenomenon, grounded on an ensemble of scientific paradigms, competence, imagination, academic freedom and particular taste for research. These characteristics, however, are still not enough. The presence of a glamorous, authoritative and influential personality is compulsory to attract researchers, to focus scientific curiosity and most of all to guarantee academic freedom and unrestricted discussions for all researchers. This excites a strong synergetic behavior along with cognitive and mental processes leading to a very distinctive heuristic state of the scientific school. In that state, as a result of interaction and integration between

knowledge and intuition of separate investigators, the specific scientific school has the opportunity to create a more general (to some extent) picture and scenario of the phenomena in a given field, to depict the outlines of the future scientific research and finally to rationalize the scientific curiosity.

Let us point out that the outstanding feature of such ensemble of synergy-associated scholars cannot be obtained by simple gathering or just assembling of well-known theoretical and experimental models, all created by individual skilled researchers. The only real recognition of any scientific school is its influence on the international scientific community and the worldwide credit for its achievements. Furthermore, the great scientific schools are distinguished not only by their contribution to specific field of knowledge, but also by their impact on the entire human knowledge and human values [9-12].

In line with the above psychological path of the genesis of scientific schools, the birth and evolution of the Sofia School of crystal growth could be classified scientifically, thematically and historically in three time periods, each of them having its specific scientific achievements and own research glory and drama. It is important to stress, however, that Kaischew's great supervisory power and style are natively governing the scientific ambience in all these periods. In some cases his attendance is a strong motivation for the researchers, in others it is a wall against mediocrity, speculation and conjecture, and in others it is just a great emotional reminiscence of the old times of nascence of the School.

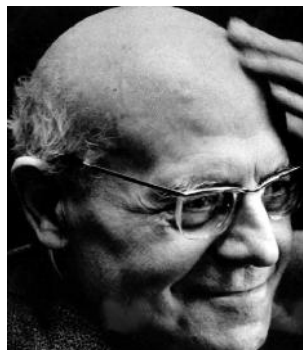
The first period (1927 – 1944), marked by the initial development of the molecular theory of crystal growth, has a remarkable pre-history. The time when Kossel and Stranski introduced the concept of 'kink' or 'half-crystal position' that would play a fundamental role in the study of the nucleation and growth of crystals, is a time of impetuous rise of new ideas and discoveries in the physical sciences.

In 1927 the Belgian Jesuit cleric Georges Lemaître creates the Big Bang theory for the birth of the Universe. The principles of the quantum theory are formulated in 1925 - 1927 and accepted by the international physical community, after dramatic discussion, at the 5<sup>th</sup> Solvay Conference in 1927. The electron microscope is invented by Ernst Ruska in 1933, Paul Dirac predicts the existence of antimatter in 1928. Entirely new model concepts about the crystal structure are developed by the solid state physics. In 1918 Erwin Madelung studies the interactions in the crystal lattice of sodium chloride and defines the "Madelung

constant”, relating the electrostatic potential of interaction to the parameters of the crystal lattice. Max Born and Otto Stern introduce in 1919 the definition of surface energy by means of the energy of creation of new surface at splitting the crystal along a certain, well-defined crystallographic plane.



Walther Kossel



Iwan Stranski

The Wulff theorem for the polar diagram of the specific surface energy of a crystal is introduced in 1901 (it has been proved much later by Herring, 1956) [7,8,25,26]. All these impressive scientific discoveries prepare the creation and development of a new molecular-kinetic theory of crystal growth as one fundamental theoretical model in the solid state physics. The introduction of this theory is not an accidental phenomenon. It follows however the heuristic logic and appears as a part of the whole remarkable ensemble of scientific achievements generated during the thirties and forties.

Such is the dynamics of the physical research in the world, when the Department of Physics and Mathematics of Sofia University becomes one of the international scientific centers, where the molecular-kinetic theory of crystal growth emerges and develops (1927 – 1941). At that time Kossel and Stranski introduce the separation work of the crystal building units as a measure of the crystal lattice energy and determine the separation work for an individual structural element in the special, “kink” position on the crystal surface. These quantities are crucial for understanding the proposed new model of crystal growth at the molecular level. They form the basis of the theory of mean separation works, developed later in the thirties, which demonstrates the first kinetic treatment of the equilibrium and growth of crystals. A remarkable advantage of this theory is that it gives for the first time a clear notion of the basic phenomena in crystal growth at the molecular level by considering a maximally simplified model crystal, namely the Kossel crystal. Furthermore, the new theory opens the way to estimate the interaction energies between the particles setting up the crystal lattice. One of the most beautiful

outcomes of the theory of Stranski and Kaischew is that it reveals and proves the identity of the classical Gibbs thermodynamic approach with the kinetic treatment of phase formation. On that background, the most fundamental and intriguing problems in nucleation, equilibrium shape and growth of crystals, thin film formation and epitaxy may be studied in great detail.

Stranski and Kaischew publish their great theoretical papers in the field of phase formation and crystal growth during the period 1931 – 1936. As already mentioned, in their first joint paper, published 1931 in *Zeitschrift für Kristallographie*, „On the equilibrium shape of homopolar crystals“, they show that only atoms, bound more strongly than those in the kink position, can belong to the equilibrium shape [15]. On the basis of these calculations, the method of mean separation works is introduced, which reveals a remarkable agreement of the theoretical with the experimentally observed shapes of various metal crystals, grown via condensation from the gas phase. The introduced mean separation work, a quantity determined from the disassembling of the outermost rows of growth units at the periphery of a two-dimensional crystal, provides the possibility to formulate, by means of kinetic reasoning, the Gibbs-Thomson equation for the equilibrium of small, finite-size crystals, as well as the Gibbs-Wulff theorem for the equilibrium shape of crystals. With the mean separation works, it becomes possible to determine the supersaturation dependence of the energy barriers for attachment or detachment of growth units (atoms or molecules) at various positions on the crystal surface. In this way, the probabilities of nucleation and dissolution of arbitrarily sized two-dimensional and three-dimensional nuclei on a crystal surface can be calculated. Thus, the crystal nucleation and growth rates are determined for the first time from kinetic point of view. Kaischew publishes the first papers on the kinetic treatment of the nucleation of crystals and gaseous bubbles together with Stranski in 1934 [6].

One of the most famous and striking achievements of the Sofia School of crystal growth during this period is the unveiling of one of the basic mechanisms of nucleation and growth of thin epitaxial films. The mechanism of layer-by-layer growth of ionic crystals of NaCl is unravelled in detail in an original paper of 1939, summarizing the PhD thesis of Lubomir Krastanov, done under the supervision of Iwan Stranski. Although the phenomena of epitaxial growth are not directly discussed in a proper way in the paper, the mechanism of nucleation and growth of lattice

planes of heteropolar ionic crystals, proposed therein, represents a realistic physical model of heteroepitaxial growth. This gives a reason to Ernst Bauer in 1958, in his classification of the basic growth modes of thin epitaxial films grounded on the subtle competition between the surface energy of the substrate, the film, and the interface between them, to name the Stranski-Krastanov growth mechanism this extremely frequently occurring mechanism of heteroepitaxial film formation [27-29].

This mechanism explains the initial stages of transition from two-dimensional, layer-by-layer

growth mode (Frank-Van der Merve) to three-dimensional (Volmer-Weber) mechanism of heteroepitaxial films formation. Thus, depending on the ratio of cohesion and adsorption energies of the atoms of the crystalline phase and on the misfit between the lattices of substrate and film, one or several two-dimensional, entirely completed monolayers are formed at the epitaxial interface, followed by the nucleation of three-dimensional clusters. This very frequently encountered mechanism of growth of thin epitaxial films follows directly from the remarkable paper of Stranski and Krastanov in 1939.



The “great trinity” – Rostislav Kaischew (left), Iwan Stranski (middle) and Lubomir Krastanov, the dissertation of Krastanov (middle), and the original Stranski-Krastanov paper of 1939 (right).

The achievements of Stranski, Kaischew and Krastanov, the “great trinity” (see the picture) in the field of phase formation, presented so far, mark the beginning of the Sofia School of crystal growth. Kaischew is appointed as a private docent (associate professor) at Sofia University in 1941, regular docent in 1944, and professor in 1947. During that time, as well as for a long time after, he is involved in extensive teaching and university activity. In the period 1944 - 1962 he is head of the Department of Physical Chemistry at Sofia University. His lectures on physical chemistry, delivered many years keep on being a basic source for the education of young researchers and doctoral students in this field. It can be stated that at the end of the 1930s, having published the main papers on the model of mean separation work, Kaischew is a well-established scientist already. From this time on begins the second period in the rise of the Sofia School of crystal growth, covering the time from 1944 to 1990.

The endowment of Kaischew to organize scientific investigations, to formulate problems, to introduce significant topics, to assess and involve gifted people in research teams around himself and most of all to make science according to West European standards develops and expands in

admirable way when the Department of Physical Chemistry is constituted at the Institute of Physics of the Bulgarian Academy of Sciences (BAS) in 1947. As head and founder of the Department, he appoints his first collaborators: Jordan Malinovski, Boyan Mutaftchiev and Dimitar Nenov, as well as the laboratory assistant Valentin Hitov. Later, Alexey Scheludko, Georgi Bliznakov and Evgeni Budevski join them. These Kaischew’s disciples become the core of the established later, in 1958, Institute of Physical Chemistry of BAS. In the following years some of them, doing pioneering research, succeed to launch brand new directions in the physical chemistry of surface phenomena (A. Scheludko), photographic processes (J. Malinovski), electrochemical kinetics (E. Budevski), quantum theory of electrode processes (S. Christov). These new research lines comprise the image of the Bulgarian physical chemistry during the twentieth century. As mentioned, the Department of Physical Chemistry of the Institute of Physics has been transformed in the autonomous Institute of Physical Chemistry in 1958, and prof. Rostislav Kaischew is appointed as its first Director. Herewith begins the best organized, scientifically and thematically structured period in

the development of the already existing Sofia School of crystal growth.

The foundation of the Institute of Physical Chemistry follows the line of natural expansion of successful scientific investigations. The aim was to concentrate and motivate tightly the research in the fields of thermodynamics and kinetics of phase formation and crystal growth on the ground of already well-established scientific teams and their proven achievements. Five departments are formed under the leadership of prof. Kaischew: Department of Phase Formation and Crystal Growth, Department of Surface Phenomena and Dispersion Systems, Department of Physical Chemistry of Photographic Processes, Department of Electrochemistry, and Department of Kinetics and Catalysis. The initial subject line of the Institute follows the development of the existing theory of phase formation and the model experiments planned to prove the fundamental concepts in the field of crystal growth. Leading role at this stage of the history of the Institute plays the remarkable and versatile scientific erudition of Kaischew, allowing infallible and intuitive treatment of the core of scientific problems. His direction follows the sense and the clear formulation of the problems, the collaborators are always included in the process of discussion and decision making – a feature, which is often lacking in the scientific management of researcher teams.

Kaischew's scientific and administrative management transform the Institute of Physical Chemistry into a leading scientific structure in Bulgaria, where the development of the school of crystal growth founded by Stranski and himself is maintained. How should an internationally respected scientific institution be constructed to become an academic standard in the Bulgarian science? As already mentioned, two basic prerequisites are necessary for that – availability of a competent and leading personality and capable assistants. Kaischew owns both. His talent and willingness to fascinate young people for research is remarkable. Kaischew lures his collaborators not with rapid career or monetary promises, but with the sense of what they are doing. The strength of this talent is revealed not only by his purely personal qualities, but most of all by his ability to point out and demonstrate the horizon of any scientific research. The particular problems are turned to merely steps towards the main task of the scientific study. This feature of Kaischew's scientific style is a strong motivation for his collaborators. Kaischew does not allow for mediocrity and sets extremely high scientific criteria at the Institute of Physical Chemistry. This

large-scale scientific style would be impossible without another feature, which is ever less frequently encountered in our time. This is his uncompromising honest attitude towards the results of any research. His erudition does not allow scientific dodging. But maybe most impressive is his aptitude to acknowledge his own fault, when something turned to be different from his ideas. Kaischew never published incomplete results or results without clear physical interpretation. Furthermore, Kaischew requires himself to be deeply and tightly convinced in the physical rationality of the models providing the results. A good example of this attitude is the so-called "rebellion of the young". At the end of the 1950s part of the young collaborators - Malinovski, Scheludko, Budevski, Bliznakov - express their discontent, because they have worked hard and accumulated a huge amount of experimental results, which however are not published, because not everything has been explained and interpreted. Kaischew reacts emphatically: "Out of question, you may publish! I do not object. But without me!" [4]. It is difficult to find a better proof of scientific style and honourability. This is the ambiance, in which begin the most important years in the development of the Sofia school of crystal growth.

The scientific style of Kaischew, built up in Europe and directed towards fundamental scientific problems, is in clear conflict with the formal scientific policy of the communist regime in Bulgaria in the 1960s, known as "science for the people". Kaischew succeeds to find a compromise and to preserve the fundamental studies at the Institute. In a very clever way, he constitutes a special department for applied research, thus formally consenting with the required public image of "studies for the practice and for the national economy". In this way his collaborators doing fundamental research are not compelled to deal with, often preposterous, applied and industrial problems. However, the most important achievement and great benefit of this fine and complicated process of juggling are the very good relations between the collaborators dealing with fundamental and applied research. He persuaded all scientists in the institute that the applied studies can be successfully performed only in close relation and interaction with the fundamental investigations. This was also proven by a number of excellent works done by the Department of Electrochemistry that solved in spectacular way many technologically essential problems. Possessing a good understanding about the significance and the long distance horizon of fundamental science, Kaischew succeeded to keep it at the Institute and

to ensure calm and comfortable environment for research. In this environment, his most gifted disciples Evgeni Budevski, Jordan Malinovski, Boyan Mutaftchiev, Ivan Gutzow, Svetoslav Toshev, Dimitar Nenov and later on Dimo Kashchiev, Ivan Markov, Stoyan Stoyanov, Alexander Milchev, Christo Nanev form their own research style and notable scientific achievements. In this way, a remarkable reputation for the Institute is built up in the country and internationally, too. One of the most distinguished students and a coworker of Kaischew, Boyan Mutaftchiev after emigration in France conducts in the 1980-90s a number of Laboratories and research teams in the field of phase formation and crystal growth at the French National Center for Scientific Research, CNRS, (Centre National de la Recherche Scientifique) in Marseille, Nancy and Paris. The raising of collaborators with their own scientific face and profile is a particularly important quality of Kaischew style, which proves to be very significant for the creation of scientific school.

In this atmosphere at the end of the 1950s and the beginning of the 1960s starts up the development of unique experimental methods for studying morphological changes of crystal surfaces and determining their growth rate, the double-pulse method for kinetic investigations of electrochemical nucleation, the capillary technique for electrochemical growth of single crystals. All these novel methods play a key role in the later long-time experimental investigations of various aspects of the nucleation and crystal growth phenomena. New studies are initiated revealing the impact of adsorption of foreign particles during the growth of crystals and the role of the active centers for condensation in the formation of crystal nuclei.

One of the most remarkable achievements of the Kaischew School in the 1960s are, however, the brilliant experiments on electrocrystallization, revealing the mechanisms of crystal growth by two-dimensional nucleation and spiral growth. The capillary method of growth of silver single crystals with separate dislocation-free crystal faces, created by Kaischew, Budevski and their collaborators, as well as the obtaining of crystal faces intersected by a single screw dislocation allow to demonstrate, study and prove in a spectacular way the two basic mechanisms of crystal growth, namely, the layer-by-layer growth by two-dimensional nucleation and the screw dislocation growth [6,30-33]. These experiments settle one of the most famous scientific discussions open by Sir Charles Frank during the Bristol conference of the British Royal Society in 1949 about the role and significance of these two fundamental mechanisms of crystal growth. These

experiments of the Sofia School are presented today in every textbook on crystal growth.

In the middle of the 1960s, Jordan Malinovski and Ivan Konstantinov started new exciting investigations of the mechanism of the photographic processes in silver bromide single crystals. They made a notable contribution in the study of the "latent image" in the photographic processes, i.e. the invisible image, formed by irradiation of photosensitive materials, which is visualized later by means of chemical or physical development. The unique results demonstrate the essential role of the so-called photo-holes generated by light irradiation modification of silver halides. The formulated new theory is acknowledged in the photographic science as the "Malinovski symmetric scheme", which accounts for the contribution of both electrons and photo-holes.

This impressive development of the studies in the field of phase formation and crystal growth at the Institute of Physical Chemistry gives birth in 1967 of two new, separate Laboratories – the Central Laboratory of Electrochemical Power Sources and the Central Laboratory of Photographic Processes. Founders and leaders of these laboratories are the most brilliant disciples of Kaischew – Evgeni Budevski and Jordan Malinovski. These two internationally recognised scientists initiate entirely new directions in the fields of electrocrystallization and photographic processes. It has to be noted however, that the new scientific organizations appear undoubtedly as a result of Kaischew's scientific role and style, academic spirit and uncompromising, tight scientific criteria. These laboratories, graduated from the Kaischew School with "summa cum laude", turn to be the prodigy of the Institute of Physical Chemistry. Another of the most promising collaborators, Georgi Bliznakov, heads the Institute of General and Inorganic Chemistry in 1960, and the Department of Kinetics and Catalysis moves there. Later, in 1983, this Department is transformed into a separate Institute at the Academy of Sciences. With the creation of these individual scientific institutions begins the time of expansion of the Sofia School of crystal growth.

In the 1960-70s the closest collaborators of Kaischew succeeded to attract young physicists and chemists, talented and well-motivated, just graduated students, to the Department of Phase Formation and Crystal Growth. They join the Kaischew team with a great ardor and eagerness to grow up in knowledge. The Kaischew team of this Department is called by their colleagues from other academic institutions "the Kaischew gang". They

have the attitude that they belong to a different scientific environment, maintaining high scientific criteria, free communication, good-humored curiosity and profound knowledge. A particular role plays the still active Colloquium on Phase Formation and Crystal Growth founded by Stranski, as mentioned, as far back as in the 1930s. This Colloquium keeps on being the academic location for specialized discussions of a broad range of ideas not merely from the field of crystal growth, but also from materials science, soft matter physics, biophysics and computer modelling.

Entirely new leading lines of investigations are formed in the following years at the Institute of Physical Chemistry. Studies on formation and development of morphological instability of the growing crystals, the atomistic theory of nucleation in electrocrystallization, theoretical and experimental studies of non-stationary effects in nucleation, the mechanisms of epitaxial growth, atomic structure and properties of epitaxial interfaces, surface diffusion phenomena turn to be dominant accents. An expression for the non-stationary nucleation rate is derived, which is widely used in the understanding of the results on crystallization kinetics. A general theorem of nucleation is proven, connecting the nucleation work, supersaturation and nucleus size. Being generally accepted in the literature and it is used in studying the formation of bubbles, droplets and crystals, since it does not involve any theory to determine the nucleus size. Studies are initiated in the field of glassy state, crystallization of glass and new materials of glassy ceramics.

Investigations of the processes of phase formation by means of computer modelling start at the Institute of Physical Chemistry in the 1980-90s. For the first time it is possible to solve exactly a number of "insolvable" problems that could not be approached theoretically due to the unavoidable approximations needed for the formulation of the theory. With this novel and powerful method, complex phenomena in thermodynamics and kinetics of crystal growth are studied, such as two-dimensional phase transitions, atomic surface roughness, growth of epitaxial films, two-dimensional surface alloying at epitaxial interfaces, thermodynamic properties of atomic clusters, nanocrystals, structure and properties of quantum nanowires and nanocomposite materials, diffusion transport phenomena, structure of interfaces, macromolecular and biological systems.

The third period in the development of the Sofia School of crystal growth starts in the 1990s, coinciding with the withdrawal of prof. Kaischew

from active scientific work and administration as a Head of the Institute in 1989.

Still, the large-scale way of thinking inherited from Kaischew, leads and motivates his collaborators in the establishment of new interdisciplinary topics that expand the scientific activity of the Institute of Physical Chemistry. Several research teams are formed dealing with the crystallization of proteins, electrochemical formation of conductive polymer films and metal-polymer nanocomposites, atomistic simulations of diffusion phenomena at epitaxial interfaces, modelling the structure and thermodynamic properties of nano-sized atomic clusters, quantum nanowires and polymer systems. Applying basic thermodynamic and kinetic models of the classical theory to new objects, such as protein crystals or thin conductive polymer films, quantum atomic nanowires, biopolymers and biological systems, results in revealing new important regularities in Nature.

The scientific ideas and results of the scientists belonging to the Sofia school of crystal growth are presented in thousands of publications in renowned international journals, book chapters, monographs and review papers. Since the formation of the Institute of Physical Chemistry in 1958, its members have published over 3 400 scientific papers in specialized and referred scientific editions, cited over 35 000 times by other authors. Distinguished disciples of prof. Kaischew, including Evgeni Budevski, Boyan Mutaftchiev, Ivan Gutzow, Ivan Markov, Dimo Kashchiev, Alexander Milchev, Georgi Staikov, issued in most renowned scientific publishers their monographs as originating from the Department of Phase Formation and Crystal growth at the Institute of Physical Chemistry [34-40]. Collaborators and disciples of Kaischew in the Department of Crystal Growth, including Andrey Milchev, Stoyan Stoyanov, Christo Nanev, Isak Avramov, Vessela Tsakova, Michail Michailov, have been invited to write book chapters and reviews, devoted to modern fields in surface physics, crystal growth, electrocrystallization, computer modelling of interfaces, crystallization of proteins, etc., based on the investigations in the Institute of Physical Chemistry [41-52]. The inherited scientific style motivates the members of the Kaischew School to keep this publication activity, despite of the grave financial pressure and the public contempt felt by the scientific community in Bulgaria during the last twenty years.

The story of creation and raising the Institute of Physical Chemistry and particularly the Department of Phase Formation and Crystal Growth has one

extra dimension besides the purely scientific features. It is due to the remarkable charm and strong personality of Rostislav Kaischew. Without taking into account this dimension, the narrative of the general development of the Sofia School of crystal growth and the Institute of Physical Chemistry would have an ordinary, commonplace and maybe even trite, character. Following this psychological line, it is worth noting one of the most striking features of prof. Kaischew's character. This is his fine ability to mix the academic discussions with human sentimentality. On the face of it, this sentimentality seems to be in conflict with the exacting academic view of Kaischew, his strong physical and psychological presence, the scientific erudition and strong, tight physical argumentation during the discussions. Simultaneously, Kaischew possessed a very emotional nature and this was by far not pretended. Being immanent to his inner world, this extraordinary sentimentality was aroused from his attitude toward music, mountains, skiing, nature and the personal life of his collaborators. The mixture of academic rigor and fine, delicately discernible emotion turns Kaischew into a fascinating example for all his collaborators. His presence in the soul and being of the collaborators was evident in the everyday meetings and conversations, but exclusively in the time of the unforgettable workshops and symposia in Varna, Gyulechitsa and Pamporovo, organized enthusiastically by all collaborators of the Institute. Kaischew could narrate unobtrusive and captivating interesting stories about his life as young man, his mentors and meetings with celebrated scientists, his travels and wanderings in Rila or Pirin mountains, the musical analysis on Bach, Schubert, Brahms and Chopin, the interpretations of Glenn Gould and Dinu Lipatti. The haughtiness of sagacity, usually emitted by the elderly was lacking in these narrations.

The scientific conversations with him have always been exceptionally interesting. During the discussion of a particular problem, Kaischew was able intuitively to create a specific dramaturgy and to incite curiosity, invoked by philosophical, historical and moral topics parallel with the research problem. He was able to dominate, even to obsess the scientific imagination of the audience. His presence in the Institute created in everybody confidence and feeling of affiliation to a unique research team, an ambiance not existing in the other academic institutions. The members of the Department of Phase Formation and Crystal Growth were dubbed among the colleagues "the classicists" or "the Kaischew gang". Kaischew

demonstrated that for him happiness and gladness are a question of character, but the sense lies in the seeking. There were, of course, such people who could not accept his academic enchantment, intellectual power and scientific erudition. Most of all, those were people far below his class, who were simply envious.

The discussions in the Colloquium of Phase Formation and Crystal Growth presented an emanation of Kaischew's criteria and style in science. His comments on the reports and lectures always touched the physical core of the problem and demonstrated a remarkable insight into the scientific value and the limits of validity of the problem discussed. Even without entering into the details of some model investigation with more complex mathematics, Kaischew succeeded to find its place in the general physical image of the phenomenon and, before all, whether the results of the study are in conflict with the physical reality or the scientific paradigm. As a result of this enormous erudition, he was capable of formulating the scale of the investigation. In this way, the researchers could build a notion about the horizon of their particular tasks and thus to find and enhance their own motivation.

The formulation of the molecular theory of crystal growth and the following dynamic developments at the Institute of Physical Chemistry have created a great reputation for Kaischew abroad. In 1992 on the occasion of the EWSSW international conference on surface physics, organized by the Department in Pamporovo Ski Center, I received a letter from Sir Charles Frank (FRS), the famous Frank who created the theory of dislocation growth of crystals, where he writes: "It would give me great pleasure to participate in an event, celebrating the 85<sup>th</sup> birthday of my old friend, Professor Kaischew".

The respect of Frank was not only expressed in the words "my old friend", it has been a respect to Kaischew's work together with Stranski. It can be seen in the original edition of the British Royal Society „The Growth of Crystals and the Equilibrium Structure of their Surfaces“, by W. K. Burton, N. Cabrera, F. C. Frank [7].

In this remarkable survey on more than 60 pages, cited more than 5000 times in the scientific literature, published in 1951 in Philosophical Transactions, only 34 fundamental studies in the field of crystal growth are referenced. Among these carefully selected papers, next to the names of Gibbs, Kossel, Bethe, Volmer, Onsager, Frenkel, Kramers, Knudsen and Max von Laue are the names of Kaischew and Stranski with



their papers, published in Z. Phys. Chem. 136, 259 (1928) and Z. Phys. Chem. (B) 26, 31, (1934). With these papers, Kaischew and Stranski

were already a part of the world history of phase formation and crystal growth.

From Sir Charles Frank  
Orchard College  
Fane Road  
Cambridge  
England CB3 9EJ  
19 Sept 1992

Dear Dr. Michailov  
It would give me great pleasure to participate in an event celebrating the 85th birthday of my old friend Professor Kaischew, and I would expect to find matters of interest to me presented in the program. However, though I am ten years younger than Kaischew, I am ten months older than he is, I believe, and I am less than I used to be. Consequently, I can only give you a provisional indication of my desire to attend EWSSW 94. The facilities of the Stei Centre will be of no benefit to me.

If I were to attend, I would offer a paper on 'Crystal Growth by Nucleation at Corners'. I would not call it a review paper, since I am quite likely to fail to give credit to significant contributions to the subject by others. I think there are few, but I may be wrong.

I will consent to be a member of the International Advisory Board for the

P.F.O.

conference, though my advice may not be very useful with regard to the most recent generation of scientists. Of the 11 names you list, I know the first 6, and confirm that they are persons worth listening to, but the last 5 are unknown to me.

Yours sincerely  
F.C. Frank



Sir Frederick Charles Frank, RSF

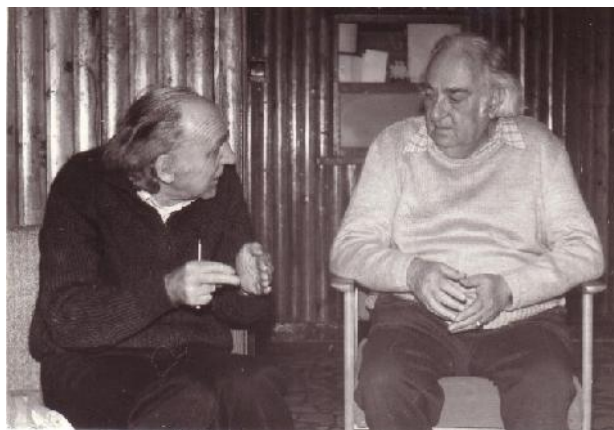
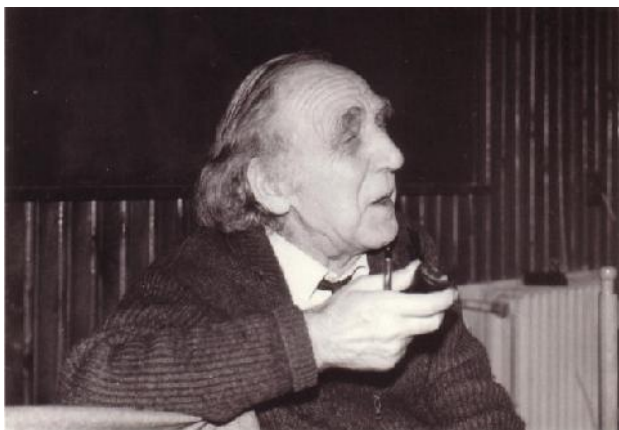
A letter of Sir Charles Frank to Michail Michailov on the occasion of the 85<sup>th</sup> birthday of prof. Kaischew and his participation in the „First East-West Surface Science Workshop“, EWSSW 1994, in Pamporovo, Bulgaria, organized by the Department of Phase Formation and Crystal Growth.

Between many foreign scientists and friends such as the notable Max Volmer, the great electrochemist Alexander Frumkin, the Nobel Prize holder Jaroslav Heyrovsky, Peter Rebinder, the encyclopedic Yakov Zeldovich, there were two who have a special place in Kaischew's heart and played significant role in his life – Heinz Bethge and Alexander Chernov.

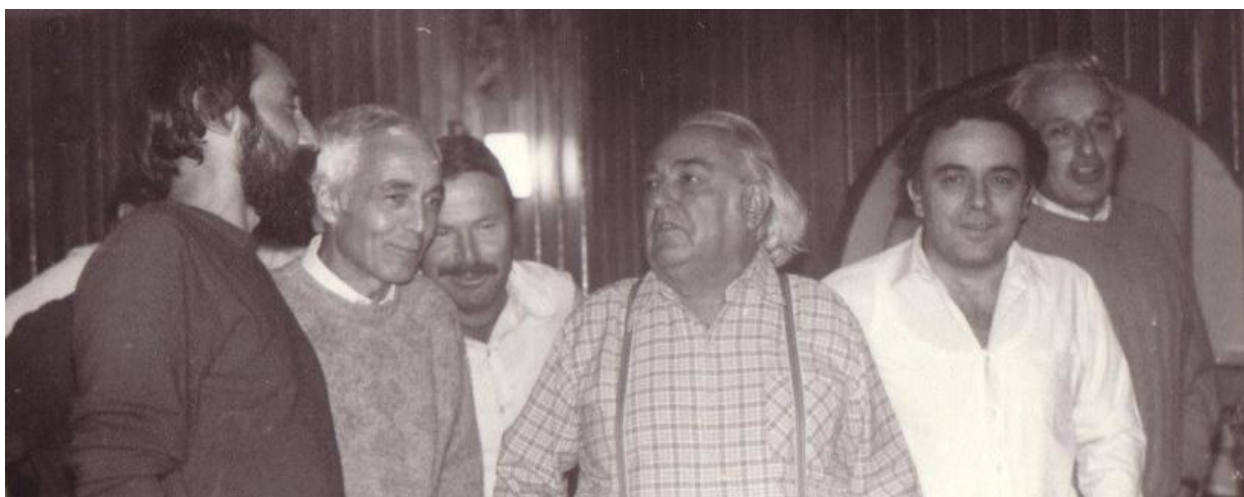
Kaischew and Bethge proved to be persons of similar size and spirit as people and scientists. In the 1980s, Heinz Bethge studies experimentally in great detail and visualizes a number of basic phenomena in crystal growth, including model concepts of the molecular theory, by means of scanning, reflection and transmission electron microscopy, (SEM and TEM) in Halle, East Germany. Particularly, the decoration with gold atoms at monoatomic steps and screw dislocation on the surface of sodium chloride crystals was of great importance. The relation between Kaischew and Bethge was particularly strong and was based not only on their personalities, but also on significant scientific interest. Heinz Bethge was President of the famous German National Academy

of Sciences „Leopoldina“ from 1974 till 1990. Kaischew was a member of that academy since 1968 and was awarded with the prestigious „Cothenius“ medal. The Academy „Leopoldina“ was founded in 1652 and its members were Albert Einstein, Charles Darwin, Otto Hahn, Ernst Rutherford, Max Planck, etc. It was the only scientific institution, common for East and West Germany at the Communism times.

The scientific interests and the close amity between Kaischew and Bethge were the background of the joint seminars, organized by the Institute of Physical Chemistry, Sofia and the Institute of Electron Microscopy, Halle. These scientific workshops organized ardently by the collaborators of both Institutes were held regularly, every three years in Halle and Gyulechitsa. Besides the intimate friendship between the coworkers of Kaischew and Bethge, the seminars ensured a wonderful ambiance for social life and scientific discussions. Always at these meetings, the favorite song of Kaischew „I'm a pirate, I'm a pirate...“ was sung traditionally by him in the company of his coworkers.



Prof. Heinz Bethge and prof. Rostislaw Kaischew. Joint seminary of the Institute of Physical Chemistry, Sofia and the Institute of Electron Microscopy, Halle, GDR in Gyulechitsa, 1987.

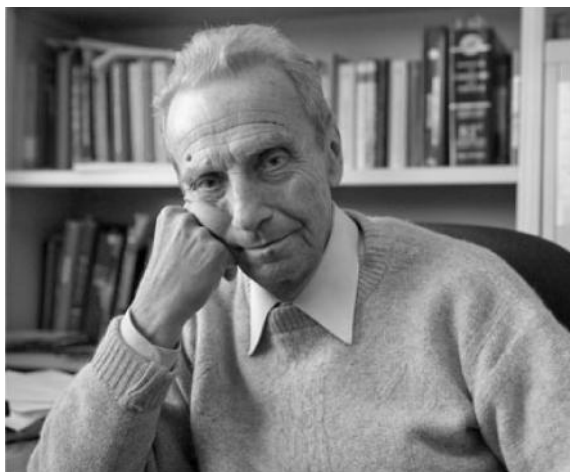


German-Bulgarian seminar, Gyulechitsa, 1987. The favorite song of prof. Kaischew “I’m a pirate, I’m a pirate...” From left to right: M. Michailov, S. Stoyanov, E. Mihaylov, R. Kaischew, A. Milchev, Chr. Nanev.

Remarkably close were his relations with another great name in the field of nucleation and crystal growth – Alexander A. Chernov. As a brilliant and encyclopedic scientist, Chernov originates from the most rigorous school in theoretical physics, the school of Landau and Lifshitz. Kaischew considered him as his disciple, since he had directed Chernov to join the Institute of Crystallography at the Russian Academy of Sciences and had recommended him to prof. Shubnikov who headed the Institute at that time. In the following years, Chernov achieved an outstanding scientific career in the fields of thermodynamics and kinetics of nucleation, morphological instability and kinetic coefficients in crystal growth, computer modelling, crystallization of proteins and biological minerals. An exceptional quality of prof. Chernov was his capability

during discussions on specific problem, even without knowing the answer, to turn the discourse in a direction that would get closer to that answer. In fact this is an element of the Kaischew School and it is not incidentally that Chernov referred to Kaischew as the “Patriarch”. Since 1992 Alexander Chernov works in the USA as a research director at the most renowned American research centers as NASA; George C. Marshall Space Flight Center, Huntsville, Alabama; Lawrence Livermore and Lawrence Berkeley National Laboratories, California.

In the 1990s and the beginning of the new century, Kaischew is the main person that attracts a number of renowned scientists in condensed matter physics to influential international scientific forums, organized by the Institute of Physical Chemistry.



Prof. Alexander Chernov and prof. Rostislaw Kaischew.

The so-called “Stranski-Kaischew” conferences in Bulgaria bring together leading world scientists in the field of surface physics and crystal growth. Among the regular lecturers and participants are David Landau (Georgia, USA), Kurt Binder (Mainz, Germany), Robert Sekerka (Carnegie Melon, Pittsburg, USA), Boyan Mutaftchiev (Paris, France), Kenneth Jackson (Arizona, USA), Joost Frenken (Leiden, Holland), Theodor Einstein

(Maryland, USA), Doon Gibbs (Berkley, USA), Alexander Chernov (NASA; George C. Marshall Space Flight Center, Alabama, USA), Raymond Kern (Marseille, France), Matias Scheffler (Max Planck Institute, Berlin, Germany), Martin Henzler (Hanover, Germany), Ellen Williams (Maryland, USA), Erio Tosatti (Trieste, Italy), Harald Ibach (Jülich, Germany), Harald Brune (Lausanne, Switzerland).



Prof. David Landau, Georgia University and prof. Theodor Einstein, Maryland University at the third „Stranski-Kaischew” Workshop in Surface Science, SKSSW 2005, Pamporovo, Bulgaria..

Particularly impressive was the scientific workshop “EWSSW 94” in Bulgaria, at which Joost Frenken from Leiden University in Holland demonstrated for the first time the diffusion dynamics of individual metal atoms in the vicinity of monoatomic steps on crystal surfaces. The brilliant experiment performed by high temperature scanning tunneling microscopy (STM) revealed that growth and dissolution of crystals is indeed accomplished by attachment and detachment of individual atoms at the theoretically predicted kink

positions in the monoatomic steps. Kaischew, who was 86 at the time, deeply moved during the lecture said: “I have never imagined that in my live I would see with my eyes a direct experimental proof of our notion with Stranski about the mechanism of crystal growth. Despite of its simplicity, our model created in 1934 seems to be true”. Here, a general distinctive characteristic of the scientific ideas of Stranski and Kaischew, developed in the classical molecular theory of phase formation and crystal growth, is emphasized. It is their simplicity.



Prof. Kaischew at the Workshop in Pamporovo, 1994, devoted to his 85 anniversary (left). Prof. Robert F. Sekerka (left), Carnegie Mellon University and prof. Kenneth A. Jackson, University of Arizona, lecturers at the same conference (right).

These notions follow elegantly the concept of Karl Popper about the substance of science and scientific theories stating that “The methods of scientific knowledge are related to our attempts to describe the world by means of simple theories. The complex theories may fail to be proved even when they turn to be true. The science itself may be described as the art of systematic simplification – the art to discern what can be initially excluded“.

To the end of his life, Kaischew remained a classical university professor and scientist, keeping the academic tradition in its genuine style, namely searching and trying to understand the general regularities and the fundamental reasons for the processes and phenomena in Nature. He succeeded throughout the years to avoid vanity and popularity of speculative, unprincipled attractive study that brings fast but evanescent fame just because of the lack of scientific depth and meaning. For Kaischew the understanding, assembling and spreading fundamental scientific knowledge was much more significant than the loud engagement in modern, technologically oriented projects which bring attractive financing. He had no taste for monetary success and luxury, lived modestly and did not care for the banal socialists’ living standards – lodging, car, country house. He was probably the only Member of the Academy who did not possess a summerhouse. The personal life of Kaischew followed largely the excellent verse by Pasternak - „ , „ (it is not lovely to

be famous). He used to say to his collaborators and students that “science is made with worn out pants” and that was no airs and graces. The ambiance of his home was build up by the music of Bach, Brahms and Schubert, Vihren mountain peak and Vasilashki lakes in Pirin, the beautiful Chokmanovo in Rhodope, the moderate sadness and nostalgia for the old Europe, the restrained, self-controlled indignation to the communist regime. This way of life was amazingly shared by the qualities and values of his wife, Milka Kaischewa, an extremely cordial, fine and highly educated woman, daughter of the famous Bulgarian mathematician, Lubomir Chakalov, Member of the Academy. Mrs. Kaischewa dedicated her entire life wholeheartedly and delicately to create calmness, placidity, silence and warmth for her husband, consecrated and ardent to science.

Rostislaw Kaischew was the last person of the outstanding generation of the „Great Masters“ W. Kossel, I. Stranski, M. Volmer and F. Frank who laid the foundations of the modern theory of crystal growth. He knew to the end of his life what he leaves behind, and this was not only the contribution to the theory of phase formation and crystal growth. Kaischew left a scientific school and through it – respect, disciples, friendship, devotion, scientific standards, style of research and academic dignity. All of this under the rule of a communist regime, at a time inauspicious for the footloose investigating spirit. Nevertheless, he

succeeded to conserve the meaningful and to decline cleverly the commonplace and mediocre. Kaischew was not merely a scientist, he was an institution. Together with Iwan Stranski, he left one of the few uncontested, substantial Bulgarian contributions to the world scientific history of mankind.

Each scientific school has its own glorious rise and inevitable fall. The dynamics of these rises and falls is determined not only by the unavoidable drama of the particular scientific paradigm, but also by the dominating values of the time of its existence. During the last two decades, the science and research in Bulgaria are rather subject to Caesar's rules (*Matthew 22:15-22*), than to the classical genuine moral, ethic and academic values. Nowadays, the dominating aims of knowledge are cynically utilitarian, technologically oriented and directed toward consumerist society. The science increasingly serves technologies of wealth and pleasure. This is a metaphysical, fundamental contradiction with the genuine meaning of the human knowledge, trying to find the place of man in the architecture and ordering of the world, in its wonderful structure, logic and aesthetics. Possibly, because of that the contemporary scientific schools cannot exist in their classical form anymore. They are rather high-tech engineering centers, founded and developed by economic and financial reasons and interests. At the present time, science and research are motivated by the usefulness and not by knowledge. „*Gaudeamus igitur, vivat academia, vivant professores*“ turn to emotional, historical mental impressions, memories, retrospections carrying the nucleus of knowledge, but ineligible and eliminated in the name of the benefit. This is the fate of the famous Stranski-Kaischew Sofia School of crystal growth, too. It was however, a remarkable intellectual phenomenon during the twentieth century and its existence, success and resplendency give moral and cognitive sense to many people, particularly to that not tempted by vanity, lucre and riches, sentimental and worthy research academic community in Bulgaria, for which, as stated in the widely held Bulgarian anthem of knowledge, „science is a sun shining within the souls“ or, as it sounds in Bulgarian, „

**Acknowledgment:** *The present paper is a modified translated edition of the review chapter devoted to prof. Rostislav Kaischew and Sofia school of crystal growth in the forthcoming book celebrating 90 years of the Physical Chemistry science in Bulgaria; Prof. M. Drinov Publishing House, Sofia (in press).*

*The author is thankful to Willy Obretenov for valuable help throughout the preparation of the English version of the manuscript.*

-----  
*Academic ranks and grades of prof. Rostislav Kaischew*

Doctor, 1932, Breslau University, Germany.  
Assistant, 1933, Department of Physics and Mathematics, University of Sofia.  
Docent, 1944, (private docent since 1941), Department of Physics and Mathematics, University of Sofia.  
Professor, 1947, Department of Physics and Mathematics, University of Sofia  
Corresponding Member of BAS, 1947.  
Full Member (Academician) of the Bulgarian Academy of Sciences, 1961.

*Leading positions of prof. Rostislav Kaischew*

Head of Chair “Physical Chemistry”, University of Sofia, 1944-1966.  
Dean of the Department of Physics and Mathematics, University of Sofia, 1955-1956.  
Director of the Institute of Physical Chemistry, BAS, 1958-1989.  
Secretary to the Section of Chemical Sciences of BAS, 1961.  
Vice-President of the Bulgarian Academy of Sciences, 1961-1968.

*Membership of prof. Rostislav Kaischew in international scientific institutions*

Member of the German Academy of Sciences, 1957.  
Member of the Czech Academy of Sciences, 1966.  
Member of the Saxon Academy of Sciences, 1968.  
Member of the German National Academy of Sciences “Leopoldina”, 1968.  
Vice-President of the International Union of Pure and Applied Physics, 1975-1980.

*Government and academic awards of prof. Rostislav Kaischew*

Grand gold sign of honor for merits to Austrian Republic, 1983.  
“Cothenius” gold medal of the German National Academy of Sciences “Leopoldina”, 1987.  
Order “Cyril and Methodius” – I grade, 1958, 1963.  
Sign of honor from the city of Sofia, 1978.  
Sign of honor from the University of Sofia, 1988, 1998.  
Sign of honor “Marin Drinov” from the Bulgarian Academy of Sciences, 1999.





## Academician Evgeni Budevski

Z. Stoynov\*, W. Obretenov

Acad. E. Budevski Institute of Electrochemistry and Energy Systems, Bulgarian Academy of Sciences, 10 Acad. G. Bonchev St., Sofia 1113, Bulgaria

*In Memoriam to my brother,  
Academician Evgeni Budevski (1922-2008)*



“I would like to start with the deepest roots, because the roots shape the personality afterwards. The start will be with the Evgeni’s grandfather, Gancho Budevski, brother of Adriana Budevka. Following the Liberation of Bulgaria in 1878, many young passionate Bulgarians look for education abroad, everyone according to his interests and the possibilities to acquire free education.



Gancho and Gergana Budevski (seated) and their children Bogdan (Evgeni’s father), Galina, Stephen, Peter and Karan sometimes at the beginning of the XX. Century.

---

To whom all correspondence should be sent:  
E-mail: zistoynov@gmail.com

Gancho studies in Sankt Peterburg, attending a military school of explosives. When returned, he loses interest in the army and starts his own business with signaling flares. He wins all auctions with his ingenuity. Maybe that is the first contact of the family with chemistry eventually better defined as solid state chemistry. Barium blazes in green, strontium in red and so on.

This is the beginning of the XX century. Gancho Budevski makes friends with Kemal Ataturk, by this time a military attache of Turkey in Burgas. The two are passionate backgammon players. Then the World War I breaks, after which Ataturk seizes power in Turkey in the lead of the so called “young turks”, and makes Turkey a secular state – forbids the burkas and replaces the arab script with latin. Kemal remembers Gancho and summons him to Istanbul to establish an explosive materials plant for the needs of the new Turkish state. Gancho develops a grand facility together with his sons Karan, Bogdan and Peter. Tens of turning machines are belt-driven by a common steam machine, bombs and shells are produced.

After the death of Kemal and also of Gancho (in 1932), there is no place for Bulgarians in the turkish military industry anymore. Bogdan and his brothers return to Bulgaria, well compensated with money. Bogdan makes one plant, then second. Very enterprising and skilled. Here a diversion about Evgeni’s mother – Dima. First in mathematics in the Lovech College, she is sent to study architecture in Belgium. However, the World War returns her to Bulgaria and her education remains uncompleted after her marriage to Bogdan. Bogdan himself suffers the same destiny – he studies math for a few semesters, but is sent to the front and he fights at all fronts. Herewith, I would like to emphasize the inclination of both parents of Eugenii towards mathematics.

Besides, Bogdan is very good in chemistry. His chemical articles are widely scientifically backgrounded. He introduces for the first time in Bulgaria a potentiometric pH-meter with a platinum quinhydrone electrode (1937-1939).





The parents of Evgeni Budevski – Dima and Bogdan Budevski.



Dima and the children: Eugeni, Nadja and Omurtag (in the Thirties).

By this time Evgeni attends the Deutsche Schule and helps his father in the understanding the device's handbook, which is in German. This is maybe the first contact of Evgeni with electrochemistry. It's a pity for this historical appliance that has been derelicted to some attic. It could be an excellent showpiece now at the Institute of Electrochemistry.

Deutsche Schule is a corner stone for the development not only of Evgeni, but also of a number of his classmates – all of them future engineers, doctors, professors. The basic requirement there is to think independently and the second – strong mathematics. After graduating (1943) straight to the military – The academy for reserve officers in Bankja, faculty of artillery.

Mathematics should have been strong there too - to calculate the ballistics. The raving World War II involves Evgeni in both of its phases. He guides the shooting of the Bulgarian artillery being located before the front line –under the fire of the German machine guns. Unfortunately, the communication with the monitoring point is broken and the monitoring officer cannot execute his functions. He sends one effective, second effective – nobody wants to try. Crawling between the two front lines, under the muzzles of the German machine guns, Evgeni finds the broken cable. He returns to the point and takes the monitoring over. For this he is awarded military cross and a St George cross.

Thanks God he returns from the front safe and sound with the first group of soldiers to his father's house in Midjur street, met with the happy tears of all of us and mostly of our dear mother Dima. The stay at the front helps for his admittance to study chemistry at the Sofia University. There he wins the admiration of prof. Kaischew, who invites him to start as an assistant at his chair. However the bourgeois origin is an impediment. Fortunately right then Adriana Budevaska returns from exile in Argentine on the invitation of Georgi Dimitrov himself. Things are arranged simultaneously for two future academicians – Evgeni Budevski and Jordan Malinovski.



Adriana Budevaska (1878-1955), sister of Gancho Budevski.

Further on, the carrier of Evgeni follows the predestined path – Ph. D, professor, Dimitrov's award for achievements in the fields of

electrochemistry, corresponding member of BAS and academician. He puts enormous organizational and creative power in the formation of the Central Lab of Electrochemical Power Sources. I would skip the details of this part, because they are well-known.

Another feature of Evgeni is his devotion to sports. He was an excellent skier, summoned to the national team by the Austrian coach Peter Radecher. Only the War prevent his participation at the Olympics. He also revealed great capabilities in organizing both the summer and the winter holidays of his friends. And not only of his friends – later he organized the holidays of all fellows of the CLEPS in a tent lager at Gradina Beach. It all started with the famous „Lawless camp” at the Alepu Beach, where about 15 – 20 admirers of the wild nature had wonderful adventures for more than 20 years with spearfishing (he was the best), water ski, yachting, surfing. He was my greatest supporter in my efforts to build a self-made windsurf and to impress the entire coast with flying over the waves with it.”

*Omurtag Budevski, 13 October 2007*

Biographical notes about acad. Evgeni Budevski by his brother, prof. Omurtag Budevski.

## THE BEGINNING

Passed through the check of manhood of the World War, young Evgeni enrolled to study chemistry at Sofia University. Still in his second year, he chooses the specialization of physical chemistry, led by professor Kaischew himself. During his study Evgeni Budevski enhances his knowledge and develops excellent capability of scientific reasoning. After graduating from the Faculty of Chemistry, he is selected by prof. Kaischew as his assistant. And when Kaischew establishes the Institute of Physical Chemistry in 1958, he invites Evgeni Budevski as an Associate professor and head of the section Electrochemistry at the new Institute.

25 years have already passed since the formulation of the two-dimensional nucleation theory by Stanski and Kaischew. All this time Rostislav Kaischew urges his assistants and collaborators to prove the theory experimentally. After many trials and small, step-by-step successes it becomes clear that electrochemistry should be most appropriate for experimental proof of the theory, due to the most precise control of the experiments. Thus the recently formed section of Electrochemistry under the management of Evgeni

Budevski had one primary goal – experimental proof of the theory of two-dimensional nucleation.

## THE CRYSTAL

Understanding the problem to attack and knowing the previous achievements, Budevski acknowledges that the task is multidisciplinary. An intimate and new fundamental mechanism of crystal growth must be studied in an electrochemical environment. The potential of the growing crystal, used as one of the electrodes of the electrochemical cell should be controlled precisely and very low values of electrochemical current should be measured at high rates.

Evgeni Budenski affronts these problems directly. First of all he expands the section of electrochemistry with specialists from other fields – one metallurgist - Vesselin Bostanov, one experienced electrochemist - Todor Vitanov and, a little bit later, one electrical engineer - Zdravko Stoynov. On the other hand, Budevski personally takes the task to find and purchase top-level (for the time) instrumentation – the best quality optical microscopes, high resolution recording galvanometer, state-of-the-art oscilloscope. What cannot be purchased is created and built in the laboratory – specialized appliance for zone melting of single crystals, device for precise optical orientation of the single crystal according to the main crystallographic axes, electronic circuit for controlling the cell potentials with very high precision. The use of triple distilled water is introduced. These all lead to detailed mastering of the capillary method of growing silver single crystals decisively improved by these enhancements.

Strenuous work begins. Working time is often not enough – experiments are done until late in the evening. Soon a technology for decoration the existing dislocations, intersecting the crystal face observed in the microscope is developed. This allows the dislocations to be registered with the optical microscope and their coordinates to be determined. A method for removing the existing dislocations is also found. By a purposeful modification of the growing potential the Burgers vector of the dislocation may be reoriented and the dislocation intersection point starts moving across the crystal face with successive growth. Finally, it can reach the periphery and thus leave the crystal face observed.

The method is operative, the number of dislocation can be reduced. However their initial concentration is too high and an absolutely dislocation-free crystal face cannot be produced.

Then Budevski starts from the beginning again. Everything must be extremely clean and more precise. Each step of the experimental technology is assessed and perfected. A new furnace for preparation of the initial single crystals, a new device for orientation of the crystal and processing with a watchmaker's precision turning machine. A more elaborated glass capillary with careful finishing of the front edge. A new electronic circuit with enhanced precision and stability. Electronic pulse generator, synchronized with the oscilloscope. And many experiments. Up to 10-15 hours per day. In shifts. Refinement of the optical microscope, allowing observation in polarized light, providing an extreme resolution of the optics.

Gradually, the experiment turns to a laboratory technology, purposely elaborated with a number of technological appliances and measurement technique. This creates the possibility to make many experiments quickly. The investigators are learning quickly from the results and understand what is there to improve even more. And another set of experiments...

And so, in one wonderful autumn late afternoon comes the success.

When observed with the microscope, the crystal is grey, growth layers and spirals are constantly moving – the crystal lives. But in this afternoon the miracle occurs. In an instance a glittering golden mirror flashes in the microscope. No layers, no movement. As if that's another crystal. A frozen golden mirror. And then comes the understanding that this is what is ever looked for. Predicted by Stranski and Kaischew 33 years ago. One gets the creeps.

## THE SUCCESS

The dislocation-free face of the silver single crystal is an extremely delicate object. Each casual slip, an unintended pulse or an intrinsic contamination can become the source of a new dislocation. With careful treatment, however, the dislocation-free face can persist for days and allows unique experiments.

Before all the Stranski-Kaischew theory of two-dimensional nucleation must be checked. With a suitable potential pulse, a two-dimensional nucleus should be formed and should propagate to form a monoatomic layer. The experiment reveals an initial linear increase of the current through the electrolytic cell (of the order of nanoamperes) and after reaching a maximum, the current decreases, describing a specific curve. These decreasing curves are different and this induces a suspicion about the precision of recording the current. It turns

out, however, that independently of the shape of the curve, the integration of the current transient yields an amount of electricity, exactly equal to the calculated value for one single monoatomic layer. The theory of two-dimensional growth of a perfect crystal is verified. After 33 years.

Budevski suggests that the different shapes of the curves are due to the formation of the nucleus at different places on the crystal face. The equations are derived and solved for a single evening. The experimental curves follow the numerical solutions. This indicates further that there are no preferred locations for the nucleation process and the nuclei are formed at arbitrary places. Therefore the crystal surface is homogeneous, there are no atomic-scale defects and it is atomically smooth. In this sense the crystal surface is perfect.

The electrochemical behavior of dislocation-free crystal faces can now be investigated. The double layer capacity, the adsorbed silver atoms capacity and the zero charge potential are estimated. The experimental data do not correspond with the literature data, but the previous studies are carried out in the presence of dislocations and other rough defects. This finding provokes a great interest in the international electrochemical community. And simultaneously initiate a whole series of investigations by Budevski and his coworkers.

It is established already with the initial experiments that the exchange current is concentrated around the growth mono-atomic steps (more exactly in a small area around them) and the hypothesis of surface diffusion controlled growth is disproved.

Studies of the structure of the double electrical layer, the growth rate of monoatomic steps, the impedance of single screw dislocations and of pre-nucleation states on the crystal face set up the carriers and the habilitations of many members of the team and their pupils further on. And acad. R. Kaischew with prof. E. Budevski are awarded with the highest governmental prize for science in Bulgaria.

The creation of a dislocation-free single crystal face arises a great scientific and technological interest. Leading electrochemists from Moscow, Berlin, Prague, Paris, London etc. visited the Institute to take a look in the microscope and to see this "marvelous" crystal. Just a year after the first success, Budevski was invited to give lectures in a number of American universities. He visited 15 different universities in various cities in just 14 days. Meeting an extraordinary interest and full halls. At that time (1966-1967) the influence of dislocations in the crystal structure was a red-hot problem for the electronics and critical factor for

the miniaturization of transistors and other electronic elements. The production of transistors in Botevgrad according to a French license dealt with up to 10 000 dislocations per square centimeter, while the Americans from Texas Instruments have reduced this number to 600 on a silicon wafer. Only a single year after the Budevski's lectures this company started the production of dislocation-free silicon single crystals, by modifying our electrochemical method into a thermal one. The door for the development of the microelectronics is open. A typical example of scientific interrelations.

### CLEPS – THE YOUNG DIRECTOR

The second half of the sixties is marked by a new stage in the development of the Bulgarian industry – the creation of Bulgarian computing industry. The mastermind basis for this development is a report of the Institute of Economics by the Bulgarian Academy of Sciences which stated that part of the investments in heavy industry must be redirected towards intellectual products, where the percentage of highly qualified labour is high and where the profitability is enhanced. The mega-project ISOT was created – a big industrial complex of over 30 plants for production and export of computers and elements.

Leader of this development became prof. Ivan Popov – a man with two university educations (Germany and France), improbable working capacity and a broad managing experience. By this time the first Bulgarian computers have already been constructed (both analogous and digital), the first computing center has been established, the first digital computer has been imported from the Soviet Union.

Parallel to this development started a process of reorientation of the available scientific potential towards R&D activities – the university personal as well as the scientists from the Academy of Sciences. Branch scientific institutes and R&D laboratories were formed with purely applied orientation, their number gradually reached 600.

In the frames of the valid international agreements (*COMECON -The Council for Mutual Economic Assistance*), Bulgaria has already been specialized in the field of gross production of lead acid batteries and electric fork lifts. The industrial complex of Balkancar with its 36 plants became the largest world producers of electric fork lifts – the production of 1 000 000 electrical fork-lifts was achieved for the first time. Bulgaria was fourth in the list of world producer of lead acid batteries.

One of the first newly established units at the Academy (altogether more than 10) was the Central Laboratory of Electrochemical Power sources. The new Laboratory had to support scientifically Balkancar and the battery industry – by improving the production of lead acid batteries and by creating novel, non-lead batteries for electric traction. Prof. Evgeni Budevski was appointed director of the new Laboratory.

In this way, two years after the great success of producing the dislocation-free crystal and verification of a brilliant Bulgarian theory, Evgeni Budevski was entitled to build up a practically applied institution and in a brand new field. There were no specialists in this area by that time. The young Director started to build his Laboratory with enthusiasm and great assiduity, involving his whole enormous intellect. He had to switch from a small scientific section with 7-8 coworkers to an Institute with planned personal of 240 employees.

Using his experience about the advantages of a multidisciplinary team during the studies of the single crystal, Budevski enhanced this concept for the formation of the CLEPS – he needed chemists (from the University) as well as chemical engineers, physicists, mechanical and electrical engineers. Even two mathematicians were drawn in. For a couple of years CLEPS swelled to 60, later to 80 employees. Dozens of young specialists found their realization in the new Laboratory. Experienced middle level staff was attracted from the battery industry and engineers for the mechanical department were recruited.

For the successful work of all those people, specialized machines and devices are needed. At that time the purchase of facilities had to be planned – preparation and acceptance of proposals and delivery two years later. A set of mechanical machines, electronic measuring devices and analytical apparatus were acquired. Construction and production of specialized test benches for starter and traction batteries was initiated.

It was decided that a new building will be constructed for CLEPS. A number of set-backs are surmounted – location, specific design, enhanced construction. The building is finished in about two years and the machines start arriving.

The most important question, however, is the subject. Subject is of a strategical importance in creating a novel establishment. In the novel establishment there is no experience, no tradition, no assignment of the leading specialists. Everything is new.

The first new mission was the creation of an iron-air battery. Budevski imported the technological concept from Germany. A broad

working group of about 80 people was formed, external collaborators were also involved. A classical version was employed for the iron electrode, (from the iron-nickel batteries), but the air electrode was new. After sedulous work came the first success – in about 18 months an iron-air traction battery of 6 kW power was created and tested on a real electrical fork-lift. The idea of building a large plant for the production of iron-air traction batteries started to hover.

Meanwhile, another applied job was assigned to CLEPS – a technology for the production of tube-shaped separators for the novel type of tubular traction batteries, which had to be mastered by the industry. Budevski accepted the assignment, formed a small, but strong team and the development was finished within a year. The technology was successfully implemented by the industry. This was the first gross contribution of CLEPS to the Bulgarian industry.

Later, experimental investigations have shown that the iron-air batteries are not suitable for traction purposes due to their low energy efficiency. The projects for a new plant were discarded.



Stephan Rashkov, Rostislav Kaischew, Evgeni Budevski, Jordan Malinovski, Sofia, 1978.

The idea of another novel type of batteries pop up – zinc-air. This mission was connected to a larger task at a national level – the creation of an electrical car with a zinc-air battery. Several other applied institutes took part in the project – The Institute of Electrical Industry, the Institute of Motors and Automobiles, and others. The elaboration is made for a single year – an original electrical automobile was created with a novel battery and a novel type of engine – a “statorless” electrical motor by which both rotor and stator rotate. This makes the mechanical differential unnecessary. The battery was new, elaborated by CLEPS – zinc-air with 25 kW power. The electrical automobile covered 240 km in spite of its large

weight. This was a new success of CLEPS and it found a response in the whole world. It is to be noted, that General Motors created its electrical automobile with a zinc-air battery six months later.

### THE INTERNATIONAL SCIENTIST

Budevski had a sort of natural gift to create friendly relations. He had a command of three languages – perfect English and German and a little French. His command of the German language was especially profound – he could give nuances to the sentences in his letters to emphasize his respect or his friendliness to his correspondent. This allowed him easily to turn new acquaintances to friendship and eventually to collaboration.

He learned English for two years. Before our eyes. The dictionaries were always on the shelf behind his back. In only two years he could advance so much, that he could maintain his correspondence and write his scientific publications. Afterwards he continued to improve his English language.

Still later he loved to play with us a game, he called “buzzy word”. He chose a relevant new word (or rather a term) and challenged us to learn it and to use it in our presentations and publications. Then we regularly exchanged our experience with the application of the term in different context. And afterwards – another “buzzy word”.

He spoke French too – although difficult, but clean. And he loved to switch languages in the middle of the conversation – English, German, English again... and when he switched to French his interlocutor was compelled to admit his outstanding intelligence.

Well, his Russian was rather bulgarian-church-slavonic. But he was always so enthusiastic, that our Russian colleagues, who understood the general sense of his talks, decided that the Bulgarian language is too close to the Russian...

These achievements seem to be almost fantastic from the outside, but behind them lurks enormous labour and much attention.

Budevski maintained contacts with an extraordinary large number of foreign scientists. From Tokyo through Novosibirsk, Moscow and Kiev, Riga, Vilnius, Bucharest and Istanbul, Belgrade, Zagreb, Graz, Budapest and Vienna, the entire Germany, the entire France, Geneva, Bern, England, USA and as far as Argentina. I have tried to count these scientists, but after reaching 100 I have always given up. But Budevski knew everyone of them personally and was informed about their welfare. Frequently, after my travel abroad he questioned me if I met someone “new”

and what is my opinion about his intellect, field of interest and professional activity. Those conversations enriched us both.

Budevski paid special attention to his letters to his new acquaintances. Sometimes he labored all day long on a particular nuance. And finally wrote down the elaborated variant. Thus Prof. Evgeni Budevski was well-known to his colleagues in the world.

I have also taken advantage of this huge human capital. Only his name and that I am his long-time coworker have opened for me the doors of many Laboratories and Universities. And even of Embassies...

Budevski participated actively in the international living of the physical chemistry and electrochemical society. He was member of International Society of Electrochemistry (ISE) and fellow of the American Electrochemical Society, member of the "Leopoldina" and "Surface" Academies... He attended more than 200 international congresses and workshops, mostly with plenary lectures. He was invited to give three-monthly cycles of lectures in Tokyo, Japan, Lausanne, Switzerland and Cleveland, USA.

He was good in organizing international events too. The German-Bulgarian "Fischer" Symposium lasted for more than 30 years, the XX ISE Congress, held in Bulgaria, and many others. He was elected Vice-president of ISE.

Budevski loved his foreign friends and always invited them to his home, when they visited Sofia. Although not big, his quarters have been illuminated by his vivid intellect and his spouse, Lilly enchanted the guests with her flawless English, exquisite food and broad culture.

#### THE MATURE SCIENTIST

There is a period of maturing in the carrier of the scientist, when his interests and possibilities are balanced. After a decade of intensive activity, switching the hot topics and achieving goals, CLEPS was already an established scientific institution, worldwide known. And Prof. Budevski was already a distinguished Director and one of the best electrochemists in the world.

Various applied tasks are solved by the CLEPS and the Director is responsible for the successful completion. During all this time, however, parallel to all his engagements, Budevski does not forget his first and favorite topic – electrocrystallization. In the continuing efforts, different faces of silver and cadmium single crystals are grown to be dislocation-free. It is established that the parameters of the double electric layer and the zero charge

potential are different at the different crystal faces. This explains the observed differences on non-perfect metal electrodes. Especially interesting were the investigations of the adsorption of foreign atoms on atomically smooth crystal faces, carried out with our crystals.

These investigations gave rise to the development of a new subject, that later becomes especially actual in the electrochemistry – the underpotential deposition of structured monoatomic layers. However, this process can be investigated precisely only on a crystal face with exactly defined structure, such as our crystal faces. A particular role in these investigations played the long-term collaboration with the Laboratories of prof. Wolfgang Lorenz in Karlsruhe, Germany and prof. Eberhard Schmidt in Bern, Switzerland.

A little bit later this collaboration gave rise to a novel and innovative subject – Scanning Tunneling Microscopy of the perfect single crystal faces. Prof. Schmidt and prof. Siegenthaler had collaboration with the creator of the Scanning Tunneling Microscope, the Nobel prize winner, prof. Rohrer in Switzerland. This tripartite collaboration with the participation of other our colleagues resulted in the successful application of STM *in-situ*, in the electrolytic environment, for the first time in the world. The investigations indicated that the monoatomic steps of growth are not smooth. Studies on a copper single crystal, carried out in Argentina showed a high degree of fractality of the monoatomic growth steps. This explains the results about the exchange current on monoatomic growth steps, obtained in the first year after obtaining the dislocation-free face.

These studies laid the foundations of an entirely new field, which is actual today as well – local surface electrochemistry. They have also another importance, creating a positive feedback with the method of scanning microscopy, enhancing the perfection of this technique.

So the general topics of Budevski and his team changed, each one creating the background for the next. The results of this topic chain were generalized in a monograph by Budevski, Lorez and Staikov [11]. It was highly appreciated and is still actual today. The chain of topics, reflecting the scientific interests of Budevski rolled on. When the nanotechnologies became extremely actual in the world, he was not late to switch to this field. There he showed an intense activity on national level. He initiated the creation of Center for Nanotechnologies, consolidating Bulgarian scientists from different fields. Budevski was its chairman and CLEPS was the first basic organization of this 'virtual' structure. This

scientific and coordination council involved more than 50 scientific and industry structures of the country as members and organized annual conferences, this tradition continued even today. This was the foundation for one of the basic scientific directions of the Bulgarian Academy of Sciences, unifying a number of Institutes in the field of materials science.

And this was not all. In a next and unfortunately last phase of his activity he turned his unappeasable interest towards the hydrogen energy and fuel cells. Maybe he was prepared for this change, since he was long time counselor of UNESCO on this topic. As a top rated electrochemist he quickly made his way in the field of fuel cells and suggested a unique model cell, combining the properties of a fuel cell and an electrolyzer. This cell, called „Easy test” is patented and produced by a small firm and is applied by several foreigner Laboratories. Another idea of his was the so-called “green house”, an energy independent household, combining renewable energy with fuel cells. Today such projects are funded by a number of investors abroad.

Together with Budevski matured his Institute also. And the people of the Institute. The initial coworkers, then their follower and the new disciples. Some of them worked on the basic topics, others organized the branching, ensuring the necessary synergy. Budevski worked together with everybody. More intensively with the younger ones – he spared more time for them. For the more experienced he cared in other way – tried to stimulate them to attend international congresses, to prepare and give lectures, he was always interested in their successes.

He had worked out a special technology for assessment. When a distinguished scientist visited the Institute for a week for instance, Budevski prepared him a program for the first two days only. The guest visited each of the departments for two hours. In the next couple of days the guest was free to choose the laboratories, where he wanted to spend more time. And in the end of the week Budevski invited him to dinner in an exquisite restaurant, where, in a friendly atmosphere, the impressions of the guest were discussed. A wonderful form of assessments – objective estimates by specially selected referees – leading scientist in the field of electrochemistry. I would like to emphasize that these guests were about a dozen annually. A system of mutual enrichment and mutual assessment. Without special effort and useless written reports. In this way we learned the international relations and collaboration.

Then the Berlin wall fell, the democracy came and the borders were wiped out. And many of our coworkers emigrated. The young ones emigrated, just getting their Ph.D., some experienced emigrated – habilitated or ready to habilitate. More than 60 scientists – a ready set for a separate new Institute... This bleeding created many difficulties for the CLEPS, now Institute of Electrochemistry and Energy Systems. But it has a positive side too. Everyone of our coworkers abroad carried with him the lessons of Budevski and maybe because of that he usually found a warm reception. And gave these lessons further. In this way the Budevski school disseminated to Germany, Switzerland, USA and Japan. As Plamen Atanasov says (our alumnus, long ago a professor in the USA and Vice president of the World Electrochemical Society): “Here (in the USA) each Bulgarian electrochemist, disciple of prof. Budevski is estimated as a nugget of gold.”

That is why all of us, who were lucky to work together with academician Budevski are favoured by the fate that we could touch the reef of gold called Evgeni Budevski.

#### SCIENTIFIC PAPERS ABOUT THE INITIAL PHASE OF INVESTIGATIONS ON ELECTROCRYSTALLIZATION

- 1.E. Budevski, W. Bostanov, T. Vitanov, Z. Stoynov, A. Kotzewa, R. Kaischew, Keimbildungse-rscheinung an versetzungsfreien (100) Flächen von Silbereinkristallen, *Electrochimica Acta*, **11**, 1697 (1966).
- 2.E. Budevski, W. Bostanov, Z. Stoynov, A. Kotzewa, R.Kaischew, Zweidimensionale Keimbildung und Ausbreitung von monoatomaren Silbereinkristallen, *Phys. Stat. Sol.* **13**, 577 (1966).
3. . . . .  
 . . . . .  
(100)  
 . . . . .  
, **6**, 43 (1967).
4. . . . .  
 . . . . .  
(100)  
 . . . . .  
, **3**(7), 856 (1967).
- 5.R. Kaischew, E. Budevski, Surface Processes in Electrocrystallization, *Contemp. Phys.*, **8**, 489 (1967).





# Review Papers



## Review of the extraction of electrochemical kinetic data from electrochemical impedance data using genetic algorithm optimization

D. Macdonald<sup>1\*</sup>, S. Sharifi-Asl<sup>1</sup>, G. Engelhardt<sup>2</sup>

<sup>1</sup>Department of Materials Science and Engineering University of California at Berkeley, Berkeley, CA 94720, USA

<sup>2</sup>OLI Systems, Inc., 240 Cedar Knolls Road, Cedar Knolls, NJ 07927, USA

Received December 26, 2016      Revised January 15, 2016

This present paper was prepared in honor of the contributions of Dr. Zdravko Stoyanov to electrochemical impedance spectroscopy (EIS) on the occasion of his eightieth birthday. Recognizing the seminal contributions that Prof. Stoyanov has made to EIS, in this paper, we illustrate the application of EIS in the analysis of impedance data for passive metal systems; in particular, the impedance of copper in sulfide-containing granitic rock ground water that will exist in the repository for High Level Nuclear Waste (HLNW) in Sweden and Finland. We demonstrate the feasibility of optimizing the Point Defect Model (PDM) upon experimental impedance data to extract values for important model parameters, which in turn can be used to calculate the steady state barrier layer thickness and passive current density as a function of voltage. These quantities are required for determining the corrosion rate of copper in contact with the repository sulfide-containing ground water and hence in estimating canister life-time, which is designed to be of the order of 100,000 years.

**Key words:** electrochemical impedance spectroscopy, copper, point defect model, optimization.

### INTRODUCTION

Professor Zdravko Stoyanov was one of the early pioneers of the modern form of electrochemical impedance spectroscopy (EIS) and has contributed greatly to the rich fabric of this important subject. His many, impressive accomplishments are cataloged in the scientific literature, including this Special Issue commemorating his 80<sup>th</sup> birthday, and serve as a beacon for those who follow in his footsteps. In this paper, we review how EIS is now used to define the mechanism of the formation of a passive film on a metal surface; in this case, the formation of Cu<sub>2</sub>S on Cu in sulfide-containing brine. The present work was performed to provide a scientific basis for estimating the lifetimes of copper canisters in crystalline rock repositories in Sweden that are used for the disposal of high level nuclear waste (HLNW). The paper is presented in honor of the many profound contributions that Professor Zdravko Stoyanov has made to electrochemical impedance spectroscopy.

### THEORY

The Point Defect Model was developed over the past thirty-five years by Macdonald and coworkers as a mechanistically-based model that could be tested analytically against experiment [1-3]. The

PDM is now highly developed and, to our knowledge, there are no known conflicts with experiment, where confluence between theory and experiment has been first demonstrated. Indeed, the model has predicted new phenomena that have subsequently been observed, including the photo-inhibition of passivity breakdown (PIPB) [4-7], and has provided a theoretical basis for designing new alloys from first principles [8, 9]. The PDM has been previously used to interpret electrochemical impedance data by optimizing the model on the experimentally-determined real and imaginary components of the interphasial (metal/passive film/solution) impedance, with considerable success [10-14]. An earlier version of the model has been extensively used to analyze data obtained in this laboratory on a program defining the electrochemistry and corrosion behavior of carbon steel in simulated concrete pore water. Our early work [13,15,16], used the commercial DataFit software [16] for optimization, which employs the Levenberg-Marquardt [17] method of minimization, in order to estimate values for various model parameters. The optimization work described in the present paper was performed using the much the same physico-electrochemical model derived from the PDM as in our previous work, with the exception that the model describes a bi-layer film. However, the optimization itself is performed using the newer, more powerful method of optimization; Differential Evolution (DE), using custom software [18]. This algorithm resolves many of the issues

---

To whom all correspondence should be sent:  
E-mail: macdonald@berkeley.edu

associated with parameter optimization of functions of this type, including being less susceptible to being “hung-up” on minima other than the global minimum. Consequently, the quality of solution is vastly improved (several orders of magnitude reduction in the chi-squared error over gradient-based methods). The mechanics of the Evolutionary Algorithm methods are presented in Ref. [19]. Although gradient-based methods are computationally much faster than evolutionary methods, such as DE, without operator experience and the requirement for non-intuitive knowledge

about a highly dimensional system, they are not operationally more efficient. The man-hours saved more than makes up for any shortcomings in terms of computational speed.

### THE POINT DEFECT MODEL

As noted above, the PDM was developed to provide an atomic-scale description of the formation and breakdown of passive films [1-5]. The physico-chemical basis of the PDM is shown in Figure 1.

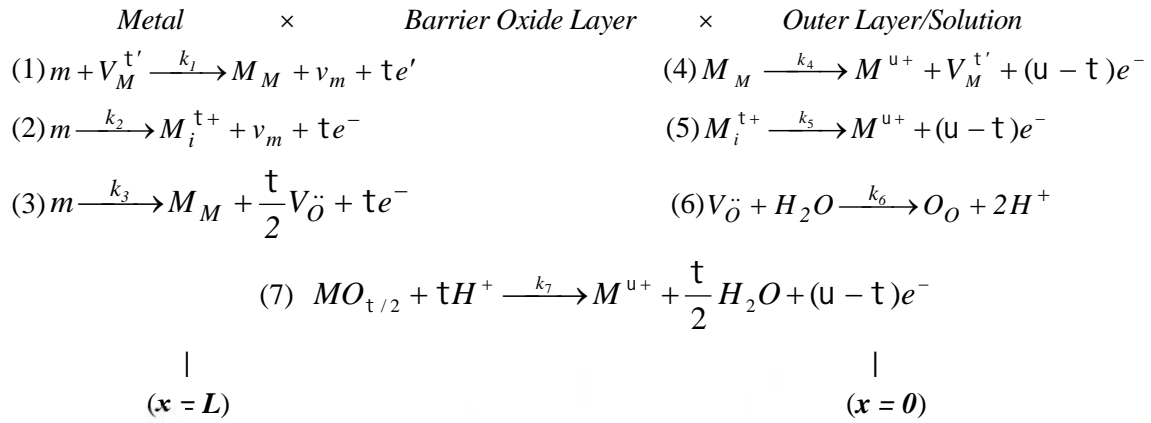


**Fig. 1.** Interfacial defect generation/annihilation reactions that are postulated to occur in the growth of anodic barrier oxide films according to the Point Defect Model.  $m \equiv$  metal atom,  $V_M^{X'}$   $\equiv$  cation vacancy on the metal sublattice of the barrier layer,  $M_i^{X+}$   $\equiv$  interstitial cation,  $M_M \equiv$  metal cation on the metal sublattice of the barrier layer,  $V_{\ddot{O}} \equiv$  oxygen vacancy on the oxygen sublattice of the barrier layer,  $O_O \equiv$  oxygen anion on the oxygen sublattice of the barrier layer,  $M^{\delta+} \equiv$  metal cation in solution.

Briefly, the model postulates that defect generation and annihilation reactions occur at the metal/barrier layer (m/bl) and the barrier layer/outer layer (bl/ol) interfaces, which are separated by a few nano-meters, and that these reactions, as depicted in Figure 1, establish the point defect concentrations within the barrier layer. The charged point defects are envisioned to migrate across the film in a direction that is consistent with their charge and the sign of the electric field. Thus, positively-charged oxygen vacancies and metal interstitials migrate from the m/bl interface, where they are generated by Reactions (2) and (3), respectively, to the bl/s interface, where they are annihilated by Reactions (5) and (6), while negatively-charged cation vacancies migrate in the reverse direction. The electric field strength for oxides is  $= 1.5 \times 10^6$  V/cm, but is lower by about an order of magnitude for the more polarizable sulfides. In both cases, the field strength is such that the defects move by migration, not by diffusion. The field strength is postulated to be buffered by Esaki, band-to-band tunneling, possibly via inter band-gap states, and hence is insensitive to the applied voltage and the thickness of the barrier

layer. Finally, it is assumed that the potential drop across the bl/s interface ( $\Phi_{f/s}$ ) is a linear function of the applied voltage and pH

$$\Phi_{f/s} = \alpha V + \beta pH + \Phi_{f/s}^0 \quad (1)$$

such that the potential drop across the m/bl interface is given as

$$\Phi_{m/bl} = (1 - \alpha)V - \beta pH - \epsilon L - \Phi_{f/s}^0 \quad (2)$$

where  $L$  is the thickness of the barrier layer and  $\Phi_{f/s}^0$  is a constant. The form of Equation (1) is dictated by electrical double layer theory for oxide/solution interfaces. Other assumptions and postulates are contained in the original publications [4,5].

The electron current density,  $I$ , which is sensed as an electron current in the external circuit, is expressed in terms of the kinetics of all reactions that produce or consume electrons and, hence, is written as:

$$I = F \left\{ \chi k_1 C_v^L + \chi k_2 + \chi k_3 + (\delta - \chi)k_4 + (\delta - \chi)k_5 C_i^0 + (\delta - \chi)k_7 \right\} \quad (3)$$

where  $C_{\epsilon}^L$  is the concentration of cation vacancies at the m/bl interface and  $C_i^0$  is the concentration of cation interstitials at the bl/ol (bl/s) interface. Note that Equation 3 does not depend upon the concentration of oxygen vacancies or upon the rate constant for Reaction (6), Figure 1. Thus, no relaxations in the impedance response involving oxygen vacancies is predicted, but this is essentially an artifact of considering Reactions (3) and (6), Figure 1, to be irreversible. If this reaction was assumed to be reversible, then a relaxation involving oxygen vacancies would be present. Furthermore, the concentration of  $H^+$  is considered to be constant, corresponding to a well-buffered solution, and is included in the definition of  $k_7$ , as indicated in Equation 6, below. Parenthetically, we note that the inclusion of reversible reactions would allow the PDM to also account for the reduction of passive films, albeit at a considerable cost in mathematical complexity.

Using the method of partial charges, the rate constants for the reactions in the presence of a porous, resistive outer layer are found to be of the form [20]:

**Table 1.** Coefficients for the rate constants for the reactions that generate and annihilate point defects at the m/bl interface [Reactions (1) – (3)] and at the bl/s interface [Reactions (4) – (6)], Figure 1, and for dissolution of the film [3–5].  $k_i = k_i^0 e^{a_i V} e^{b_i L} e^{c_i pH}$

Reaction	$a_i (V^{-1})$	$b_i (cm^{-1})$	$C_i$	Units of $k_i^0$
(1) $m + V_M^{t'} \xrightarrow{k_1} M_M + v_m + te'$	1(1- )	- 1	- 1	$\frac{1}{s}$
(2) $m \xrightarrow{k_2} M_i^{t+} + v_m + te^-$	2(1- )	- 2	- 2	$\frac{mol}{cm^2 s}$
(3) $m \xrightarrow{k_3} M_M + \frac{t}{2} V_{\ddot{O}} + te^-$	3(1- )	- 3	- 3	$\frac{mol}{cm^2 s}$
(4) $M_M \xrightarrow{k_4} M^{u+} + V_M^{t'} + (u - t)e^-$	4		4	$\frac{mol}{cm^2 s}$
(5) $M_i^{t+} \xrightarrow{k_5} M^{u+} + (u - t)e^-$	5		5	$\frac{cm}{s}$
(6) $V_{\ddot{O}} + H_2O \xrightarrow{k_6} O_O + 2H^+$	2 6		6	$\frac{cm}{s}$
(7) $MO_{t/2} + tH^+ \xrightarrow{k_7} M^{u+} + \frac{t}{2} H_2O + (u - t)e^-$	7 ( - )		7 ( - )	$\frac{mol}{cm^2 s}$

Let us assume that the applied potential changes sinusoidally around some mean value ( $\bar{V}$ ) in accordance with Equation (7):

$$V = \bar{V} + uV = \bar{V} + \Delta V e^{jSt} \quad (7)$$

$$k_i = k_i^0 \exp[a_i(V - R_{ol}I) - b_iL], i = 1, 2, 3 \quad (4)$$

$$k_i = k_i^0 \exp[a_i(V - R_{ol}I)], i = 4, 5 \quad (5)$$

and

$$k_7 = k_7^0 \exp[a_7(V - R_{ol}I)] \left( \frac{C_{H^+}}{C_{H^+}^0} \right)^n \quad (6)$$

where  $n$  is the kinetic order of barrier layer dissolution with respect to  $H^+$ . In deriving these expressions theoretically, it is assumed that a resistive outer layer,  $R_{ol}$ , exists on the surface of the barrier layer and that the passive current flows through the outer layer to a remote cathode, which is the normal experimental configuration. Because of this, the potential that exists at the bl/ol interface must be corrected from that applied at the reference electrode located at the outer layer/solution interface by the potential drop across the outer layer, where  $R_{ol}$  ( $cm^2$ ) is the specific resistance of the outer layer. The coefficients in the rate constant expressions are summarized in Table 1.

where  $\omega$  is the angular frequency and  $\Delta V$  is the amplitude. The bar over a letter refers to the corresponding value under steady-state conditions. Accordingly, in the linear approximation the independent variables have the following response  $f = \bar{f} + \Delta f e^{jSt}$ , where  $f$  represents current density,

$I$ , and values on which  $I$  depends, namely,  $L$ ,  $C_i^0$ ,  $C_\epsilon^L$ , and the various rate constants.

Our task, then, is to calculate the faradic admittance,  $Y_F$ , which is defined as:

$$Y_F = \frac{1}{Z_F} = \frac{uI}{uV} = \frac{\Delta I}{\Delta V} \quad (8)$$

where  $Z_F$  is the faradic impedance. Note that  $I$ , is a function of the potential at the bl/ol interface ( $U$ ), but the potential that is modulated is that at the outer layer/solution (ol/s) interface ( $V$ ), or close to it, depending upon the exact placement of the tip of the Luggin probe. The two potentials are related by

$$U = V - R_{ol}I \quad (9)$$

It is evident, then, that,

$$\frac{1}{Y_F} = \frac{1}{Y_F^0} + \frac{1}{R_{ol}} \text{ or } Y_F = \frac{Y_F^0}{1 + R_{ol}Y_F^0} \quad (10)$$

where  $Y_F^0$  is the admittance calculated in the absence of the outer layer, assuming that the potential at the bl/ol interface is  $\bar{U}$  under steady-state conditions. We see that  $Y_F \rightarrow Y_F^0$  as  $R_{ol} \rightarrow 0$  and  $Y_F \rightarrow 1/R_{ol}$  for  $Y_F^0 \rightarrow \infty$ ; that is, the interphasial impedance becomes controlled by the outer layer in the limit of an infinitely large outer layer specific resistance or infinitely small barrier. The values of  $\bar{U}$  and other steady state values can be easily calculated. Assuming some arbitrary value of  $\bar{U}$ , we can immediately calculate  $\bar{k}_i$ ,  $i = 4, 5, 7$  from Equations (5) and (6). From the rate equation for the change in thickness of the barrier layer, which is written as

$$\frac{dL}{dt} = \Omega k_3 - \Omega k_7 \quad (11)$$

we have  $\bar{k}_3 = \bar{k}_7$ , i.e.

$$L_{ss} = \left( \frac{a_7 - a_3}{b_3} \right) U + \left( \frac{C_7 - C_3}{b_3} \right) pH + \frac{1}{b_3} \ln \left[ \left( \frac{k_7^0}{k_3^0} \right) \left( \frac{C_H}{C_H^0} \right)^n \right] \quad (12)$$

After that, the values  $\bar{k}_i$  ( $i = 1, 2$ ) can be calculated by using Equations (4).

The values of the steady-state concentrations  $\bar{C}_\epsilon^L$ ,  $\bar{C}_i^0$  and  $\bar{C}_o^0$  (concentrations of metal vacancies at the m/bl interface and of oxygen vacancies and metal interstitials at the bl/ol interface, respectively) can be found by equating the rates of formation and annihilation at the two interfaces to yield:

$$\bar{C}_v^L = \frac{\bar{k}_4}{k_1} \quad (13)$$

$$\bar{C}_i^0 = \frac{\bar{k}_2}{k_5} \quad (14)$$

and

$$\bar{C}_o^0 = \frac{\bar{k}_3}{k_6} \quad (15)$$

Equations (13) to (15) follow from the condition that steady state fluxes of cation vacancies, cation interstitials, and oxygen vacancies, are the same at the two interfaces; otherwise time-dependent defect accumulations would occur.

Finally, we calculate the values of

$$\bar{I} = F \left\{ \begin{array}{l} t \bar{k}_1 \bar{C}_v^L + t \bar{k}_2 + t \bar{k}_3 + (u - t) \bar{k}_4 \\ +(u - t) \bar{k}_5 \bar{C}_i^0 + (u - t) \bar{k}_7 \end{array} \right\} \quad (16)$$

and

$$\bar{V} = \bar{U} + R_{ol} \bar{I} \quad (17)$$

i.e. we calculate the polarization behavior as the dependence  $\bar{I}(\bar{V})$ . As the actual value of  $\bar{U}$ , we will choose the value at which  $\bar{V}$  equals the prescribed value, because no outer layer is assumed in defining the impedance of the barrier layer, in this analysis. Practically, the task is reduced to the solution of the single equation  $\bar{V} = \bar{U} + R_{ol} \bar{I}(\bar{U})$  relative to the unknown value  $\bar{U}$  (the voltage at the bl/ol interface).

It is important to recognize that, if we have a code for calculating the admittance of the system in the absence of the outer layer,  $Y_F^0$ , we can derive the admittance in the presence of the outer layer,  $Y_F$ , by using Equation (10), assuming that  $Y_F^0$  is calculated at the steady state applied potential that equals  $\bar{U}$  (but not  $\bar{V}$ ).

#### Derivation of $Y_F^0$

From Equation (3) we can write, in the linear form:

$$Y_F^0 = \frac{uI}{uU} = \frac{\Delta I}{\Delta U} = I_U + I_L \frac{\Delta L}{\Delta U} + I_v^L \frac{\Delta C_v^L}{\Delta U} + I_i^0 \frac{\Delta C_i^0}{\Delta U} \quad (18)$$

where

$$I_U = F \left\{ \begin{array}{l} t a_1 \bar{k}_1 \bar{C}_v^L + t \bar{k}_2 a_2 + t \bar{k}_3 a_3 + (u - t) \bar{k}_4 a_4 \\ +(u - t) \bar{k}_5 a_5 \bar{C}_i^0 + (u - t) \bar{k}_7 a_7 \end{array} \right\} \quad (19)$$

$$I_L = -F \left\{ t \bar{k}_1 \bar{C}_e^L + t \bar{k}_2 b_2 + t \bar{k}_3 b_3 \right\} \quad (20)$$

$$I_v^L = F t \bar{k}_1 \quad (21)$$

$$I_i^0 = F(u - t) \bar{k}_5 \quad (22)$$

Here, it is assumed that the imposed voltage varies sinusoidally,  $U = \bar{U} + uU = \bar{U} + \Delta U e^{j\check{S}t}$  and the four terms on the right side can be attributed to relaxations with respect to the applied potential  $V$ , the thickness of the barrier layer with respect to the voltage at the bl/ol interface,  $U$ , cation vacancies,  $\bar{C}_e^L$ , and cation interstitials,  $\bar{C}_i^0$ , respectively. Note the absence of a term for the relaxation of oxygen vacancies, because, again, the concentration of oxygen vacancies does not appear in the current [Equation (3)], because of assuming that Reaction (3), Figure 1, is irreversible. Physically, though, the oxygen vacancies carry at least part of the current, so that the concomitant transport impedance must be accounted for. This is done by adding a Warburg impedance ( $Z_w$ ) element in series with the Faradaic impedance ( $Z_F$ ) as explained later in the paper. Thus, the Faradaic impedance is redefined as being  $Z_F + Z_w$ .

Let us now derive expressions for  $\frac{\Delta L}{\Delta U}$ ,  $\frac{\Delta C_v^L}{\Delta U}$  and  $\frac{\Delta C_i^0}{\Delta U}$ . For reasons that will become apparent below, it is convenient to start with  $\frac{\Delta L}{\Delta U}$ .

The rate of change of the thickness of the barrier layer is described by Equation (11). Thus, by taking the total differential of Equation (11), we obtain

$$\frac{duL}{dt} = j\check{S}\Delta L e^{j\check{S}t} = \Omega u k_3 - \Omega u k_7 = \Omega (\bar{k}_3 a_3 u U - \bar{k}_3 b_3 u L) - \Omega \bar{k}_7 a_7 u V \quad (23)$$

or

$$L_U \equiv \frac{\Delta L}{\Delta U} = \frac{\Omega (\bar{k}_3 a_3 - \bar{k}_7 a_7)}{j\check{S} + \Omega \bar{k}_3 b_3} \quad (24)$$

which is the desired result.

*Derivation of  $\Delta C_i^0 / \Delta U$*

The flux density of interstitials is

$$J_i = -D_i \frac{\partial C_i}{\partial x} - t D_i K C_i \quad (25)$$

In this expression,  $D_i$  is the diffusion coefficient of the cation interstitials,  $K = F/RT$ , where is the electric field strength of the barrier layer, and  $T$  is

the temperature. The continuity equation is then written as:

$$\frac{\partial C_i}{\partial t} = D_i \frac{\partial^2 C_i}{\partial x^2} + t D_i K \frac{\partial C_i}{\partial x} \quad (26)$$

which must be solved subject to the boundary conditions

$$-k_5 C_i = -D_i \frac{\partial C_i}{\partial x} - t D_i K C_i \text{ at } x = 0 \quad (27)$$

Substitution  $C_i = \bar{C}_i + \Delta C_i e^{j\check{S}t}$  into Equations (25) to (27) and linearization of the boundary conditions relative to  $U$  and  $L$  yields:

$$j\check{S}U C_i = \frac{\partial^2 U C_i}{\partial x^2} + t D_i K \frac{\partial U C_i}{\partial x} \quad (28)$$

or

$$-\bar{k}_5 (\bar{C}_i^0 a_5 \Delta U + \Delta \bar{C}_i^0) = -D_i \left( \frac{\partial \Delta C_i}{\partial x} \right)_{x=0} - t D_i K \Delta C_i^0 \text{ at } x = 0 \quad (29)$$

$$-\bar{k}_2 (a_2 \Delta U - b_2 \Delta L) = -D_i \left( \frac{\partial \Delta C_i}{\partial x} \right)_{x=L} - t D_i K \Delta C_i^L \text{ at } x = L \quad (30)$$

Analytical solution of the linear boundary problem (28) – (30) is easily obtained and the sought value  $\Delta C_i^0 / \Delta U$  can be presented in the following form:

$$\frac{U C_i^0}{U U} = \frac{A + B}{U U} = U C_{iU}^0 + U C_{iL}^0 \frac{U L}{U U} \quad (31)$$

where

$$\Delta C_{iU}^0 = \frac{b_{1U} (a_{22} - a_{21}) + b_{2U} (a_{11} - a_{12})}{a_{11} a_{22} - a_{12} a_{21}} \quad (32)$$

$$\Delta C_{iL}^0 = \frac{b_{2L} (a_{11} - a_{12})}{a_{11} a_{22} - a_{12} a_{21}} \quad (33)$$

$$r_{1,2} = \frac{-tK \pm \sqrt{t^2 K^2 + 4j\check{S} / D_i}}{2} \quad (34)$$

$$a_{11} = (r_1 + tK) D_i - \bar{k}_5, \quad a_{12} = (r_2 + tK) D_i - \bar{k}_5, \quad a_{21} = (r_1 + tK) D_i e^{r_1 L}, \quad a_{22} = (r_2 + tK) D_i e^{r_2 L} \quad (35)$$

$$b_{1U} = \bar{k}_5 a_5 \bar{C}_i^0, \quad b_{2U} = \bar{k}_2 a_2, \quad b_{2L} = -\bar{k}_2 b_2 \quad (36)$$

and  $\frac{U L}{U U}$  is given by Equation (24).

The reader should note that the expressions given above for cation interstitials can be shown to be the same as those for oxygen vacancies, with the oxidation number,  $t$ , being replaced by 2, Subscript 2 being replaced by Subscript 3, and Subscript 5 being replaced by Subscript 6, so as to identify the correct reactions in Figure 1.

#### Derivation of $\Delta C_v^L / \Delta U$

By analogy with the above it can be shown that:

$$\frac{\Delta C_\epsilon^L}{\Delta U} = \frac{Ae^{r_1L} + Be^{r_2L}}{\Delta U} = \Delta C_{vV}^L + \Delta C_{vL}^L \frac{\Delta L}{\Delta U} \quad (37)$$

where

$$\Delta C_{vU}^L = \frac{(b_{1U}a_{22} - b_{2U}a_{12})e^{r_1L} + (b_{2U}a_{11} - b_{1U}a_{21})e^{r_2L}}{a_{11}a_{22} - a_{12}a_{21}} \quad (38)$$

$$\Delta C_{vL}^L = \frac{b_{2L}a_{11}e^{r_2L} - b_{2L}a_{12}e^{r_1L}}{a_{11}a_{22} - a_{12}a_{21}} \quad (39)$$

$$r_{1,2} = \frac{tK \pm \sqrt{t^2K^2 + 4j\bar{S}/D_v}}{2} \quad (40)$$

where

$$\begin{aligned} a_{11} &= (r_1 - tK)D_v, & a_{12} &= (r_2 - tK)D_v, \\ a_{21} &= [(r_1 - tK)D_v + \bar{k}_1]Je^{r_1L}, \\ a_{22} &= [(r_2 - tK)D_v + \bar{k}_1]Je^{r_2L} \end{aligned} \quad (41)$$

$$\begin{aligned} b_{1U} &= -\bar{k}_4a_4, \\ b_{2U} &= -\bar{k}_1a_1\bar{C}_v^L, \\ b_{2L} &= \bar{k}_1\bar{C}_v^Lb_1 \end{aligned} \quad (42)$$

and, again,  $\frac{UL}{UU}$  is given by Equation (24).

By substituting Equations (24), (31) and Equation (37) into Equation (18) we have the result:

$$Y_F^0 = I_U + I_L L_U + I_v^L (\Delta C_{vU}^L + \Delta C_{vL}^L L_U) + I_i^0 (\Delta C_{iU}^0 + \Delta C_{iL}^0 L_U) \quad (43)$$

The Swedish plan for the isolation of high-level nuclear waste (HLNW) calls for encapsulation of spent nuclear fuel in a copper canister located within bore holes within a crystalline bedrock repository at a depth of about 500 m. The groundwater is a brine containing bi-sulfide ion ( $HS^-$ ), which is known to activate the corrosion of copper [21]. The current plan calls for emplacement of spent fuel in an inner cast iron canister shielded

with a 50 mm thick outer layer of metallic copper [22–24], which, in turn, is surrounded by a layer of compacted bentonite. After emplacement of the canisters in the boreholes in the floors of the drifts (tunnels), the remaining space will be backfilled with a compacted bentonite clay buffer [22]. The role of the inner cast iron layer is to provide mechanical strength as well as radiation shielding, while the copper outer layer provides corrosion protection. Hydration of the bentonite layer produces a highly impervious barrier to the transport of deleterious species, such as  $HS^-$ , to the copper surface, representing one barrier in the multi-barrier concept for HLNW disposal. Thus, in the anoxic groundwater environment, corrosion mechanisms involving sulfides have been identified by SKB (the Swedish vendor of the disposal technology) to be important in controlling canister lifetime [24]. Sulfide species, such as bisulfide ion ( $HS^-$ ), are present in groundwater in the near-field environment and hence in the vicinity of the copper canisters. As noted above, these species are powerful activators of copper corrosion [21] by inducing a partial anodic reaction ( $2Cu + HS^- \rightarrow Cu_2S + H^+ + 2e^-$ ) at a potential that is about 600 mV more negative than that for the formation of the oxide ( $2Cu + H_2O \rightarrow Cu_2O + 2H^+ + 2e^-$ ) in the absence of sulfide. Thus, in the presence of sulfide species, copper is converted from being a semi-noble metal to an active metal [21], resulting in corrosion and hence in a reduction of the canister lifetime.

Figure 2 displays the potentiodynamic polarization of copper in a deaerated 0.1 M  $NaCl + 2 \times 10^{-4}$  M  $Na_2S \cdot 9H_2O$  solution at 25 °C, as measured in our previous work [25,26].

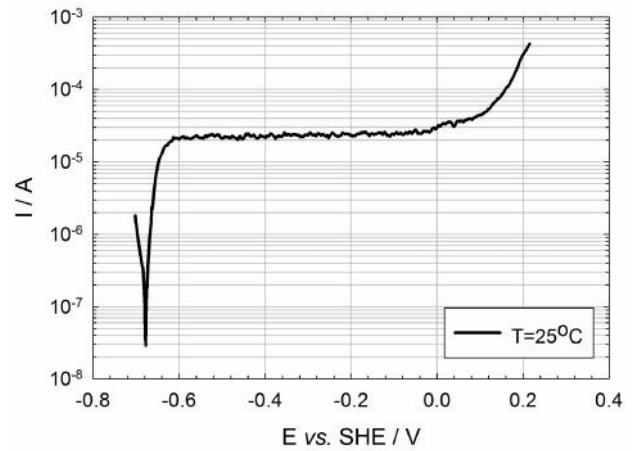


**Fig. 2.** Potentiodynamic polarization curves of  $Cu$  in a deaerated 0.1 M  $NaCl + 2 \times 10^{-4}$  M  $Na_2S \cdot 9H_2O$  solution at 25 °C. (Scan rate = 1 mV s<sup>-1</sup>).



A broad passive range of potential is observed, starting from about -0.7 (potential which is related to the formation of copper sulfide) and extending up to +0.15 V vs. SHE. Four potentials within the passive region were selected for the impedance analysis, -0.495 V, -0.395 V, -0.295 V and -0.195 V vs. SHE, with the electrode at these potentials being controlled potentiostatically for the entire time of the experiments.

A modified point defect model (PDM) for the formation of the bi-layer  $Cu/Cu_2S/CuS$  passive films on copper in the sulfide-containing solutions was proposed [26]. The physico-chemical basis of the modified PDM is shown in Figure 3. In this study, we propose a PDM specifically for the growth and dissolution of the passive sulfide films on copper.

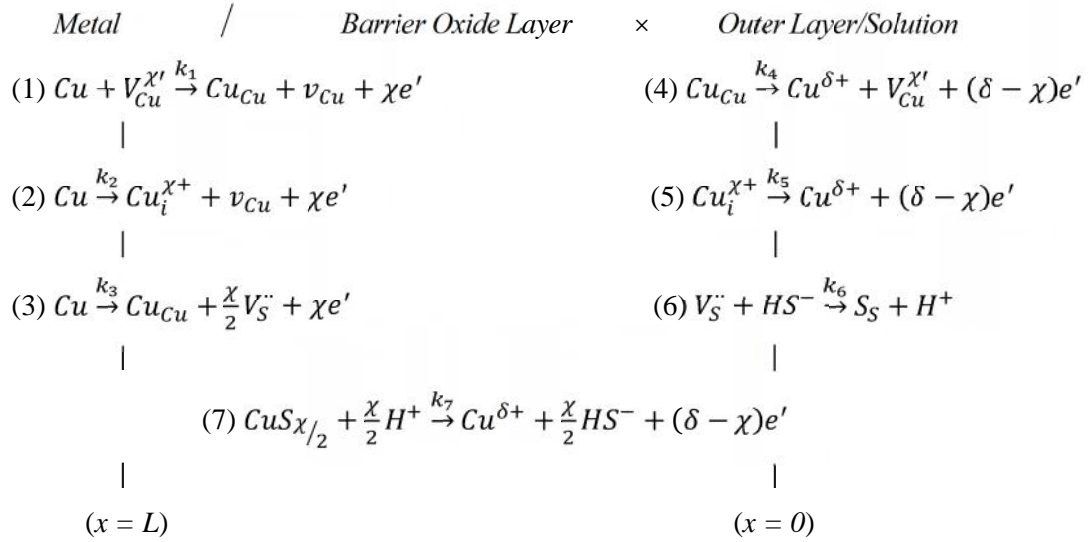


**Fig. 3.** Interfacial defect generation/annihilation reactions that are postulated to occur in the growth of anodic barrier sulfide films ( $\chi = 1$  for both  $Cu_2S$  and  $CuS$ , where the latter is the Cu(I) salt of the disulfide ion,  $S_2^{2-}$ ) according to the Point Defect Model.  $V_{Cu}^{\chi'}$   $\equiv$  cation vacancy on the metal sublattice of the barrier layer,  $Cu_i^{\chi+}$   $\equiv$  cuprous cation interstitial,  $Cu_{Cu}$   $\equiv$  cuprous cation in cation site on the metal sublattice of the  $Cu_2S$  barrier layer  $V_S^{\cdot\cdot}$   $\equiv$  sulfur vacancy on the anion sublattice of the barrier layer,  $S_S$   $\equiv$  sulfur anion on the anion sublattice of the barrier layer,  $Cu^{u+}$   $\equiv$  cuprous cation in solution.

Note that the model is written in general form; being capable of describing the formation of both  $Cu_2S$  and  $CuS$  barrier layers.

Figures 4 and 5 display typical experimental electrochemical impedance spectra (Nyquist and Bode plots) for the passive sulfide film formed on copper in a deaerated 0.1 M  $NaCl + 2 \times 10^{-4}$  M  $Na_2S \cdot 9H_2O$  solution at 25°C. The best fit results, calculated from the parameters obtained from optimization of the proposed mechanism (Figure 3) on the experimental EIS data are listed in Tables 2 and 3, and the impedance calculated from those parameters are also included in Figures 4 and 5 as solid lines. One will note that the correlation between experiment and the model is very good, indicating that the proposed model (Figure 3) provides an excellent account of the observed experimental data.

**Table 2.** Averaged Kinetic parameters obtained from the PDM optimization of copper in a deaerated 0.1 M  $NaCl + 2 \times 10^{-4}$  M  $Na_2S \cdot 9H_2O$ , at 25°C.

Parameter	Value	Dimensions
	0.26	-
1	0.44	-
3	0.21	-
4	0.07	-
n	-0.15	-
$k_1$	$3.52 \times 10^{-07}$	( $s^{-1}$ )
$k_2$	$1.85 \times 10^{-16}$	( $mol\ cm^2\ s^{-1}$ )
$k_3$	$2.46 \times 10^{-11}$	( $mol\ cm^2\ s^{-1}$ )
$k_4$	$7.85 \times 10^{-13}$	( $mol\ cm^2\ s^{-1}$ )
$k_7$	$7.31 \times 10^{-13}$	( $mol\ cm^2\ s^{-1}$ )

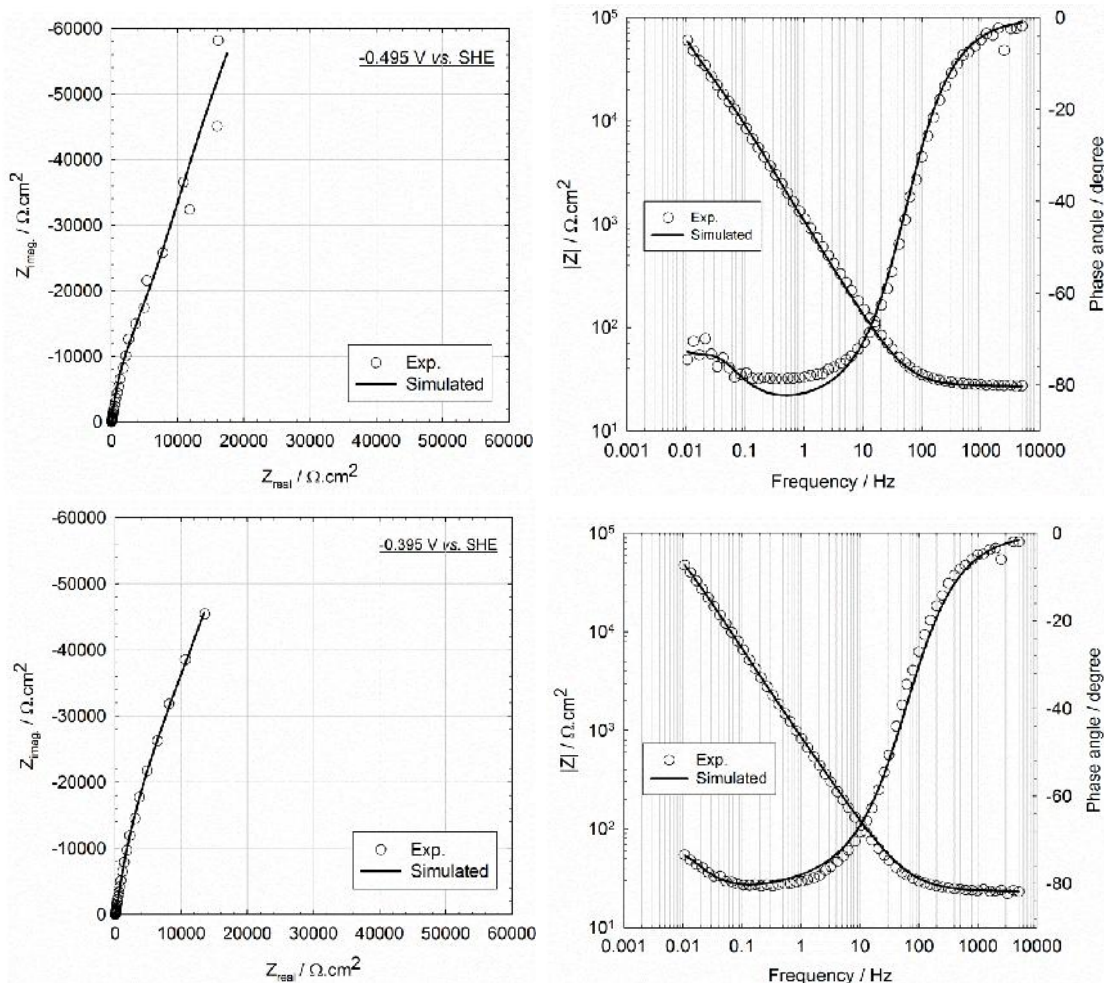


**Fig. 4.** Experimental and simulated Nyquist and Bode plots for copper in a deaerated 0.1 M  $NaCl + 2 \times 10^{-4}$  M  $Na_2S \cdot 9H_2O$ ,  $T = 25^\circ C$  as a function of applied potential, solid lines show the best fit calculation of the PDM using the optimized parameter values

It is important to note that the obtained parameters should not only reproduce the experimental impedance spectra, but should also deliver values of various properties that are physically reasonable. Thus, the obtained kinetic parameters, such as the standard rate constants, transfer coefficients, and defect diffusivities listed in Tables 2 and 3, show no systematic dependency on the applied potential as required by the fundamental electrochemical kinetic theory. This is a good test of viability of the proposed model. Of particular interest is the value of the electric field strength as a function of voltage. It is seen that the value ( $2.1 \times 10^5$  V/cm) is about an order of magnitude lower than that typically found for oxide barrier layers [14], corresponding with the greater polarizability of the sulfide compared with the oxide ion. Furthermore, within experimental accuracy, the electric field strength is independent of the applied voltage, confirming one of the important postulates upon which the PDM is based.

Cuprous sulfide,  $Cu_2S$ , is a p-type semiconductor, indicating that the dominant point defect

in the lattice is the cation vacancy. The value of the cation vacancy diffusivity is quite high [ $(1.0 \pm 0.7) \times 10^{-13}$   $cm^2/s$ ] and appears to display some voltage-dependence, although the experimental uncertainty is difficult to judge accurately. Also, the diffusivity is a “deeply buried” parameter in the model, so that its value is possibly only semi-quantitative in nature. Nevertheless, it is in reasonably good agreement with the value of  $10^{-15}$  to  $10^{-14}$   $cm^2/s$  that is predicted theoretically using Density Functional Theory (DFT) [27]. As mentioned in the previous section, the rate of change of the barrier layer thickness that forms on a metal surface can be expressed as:

$$\frac{dL}{dt} = k_3^0 e^{a_3 V} e^{b_3 L} e^{c_3 pH} - k_7^0 \left( \frac{C_{H^+}}{C_{H^+}^0} \right)^n e^{a_7 V} e^{c_7 pH} \quad (44)$$

where  $\Omega$  is the molar volume of the barrier layer per cation,  $C_{H^+}$  is the concentration of hydrogen ion,  $C_{H^+}^0$  is the standard state concentration, and “ $n$ ” is the kinetic order of the barrier layer dissolution reaction with respect to  $H^+$ .

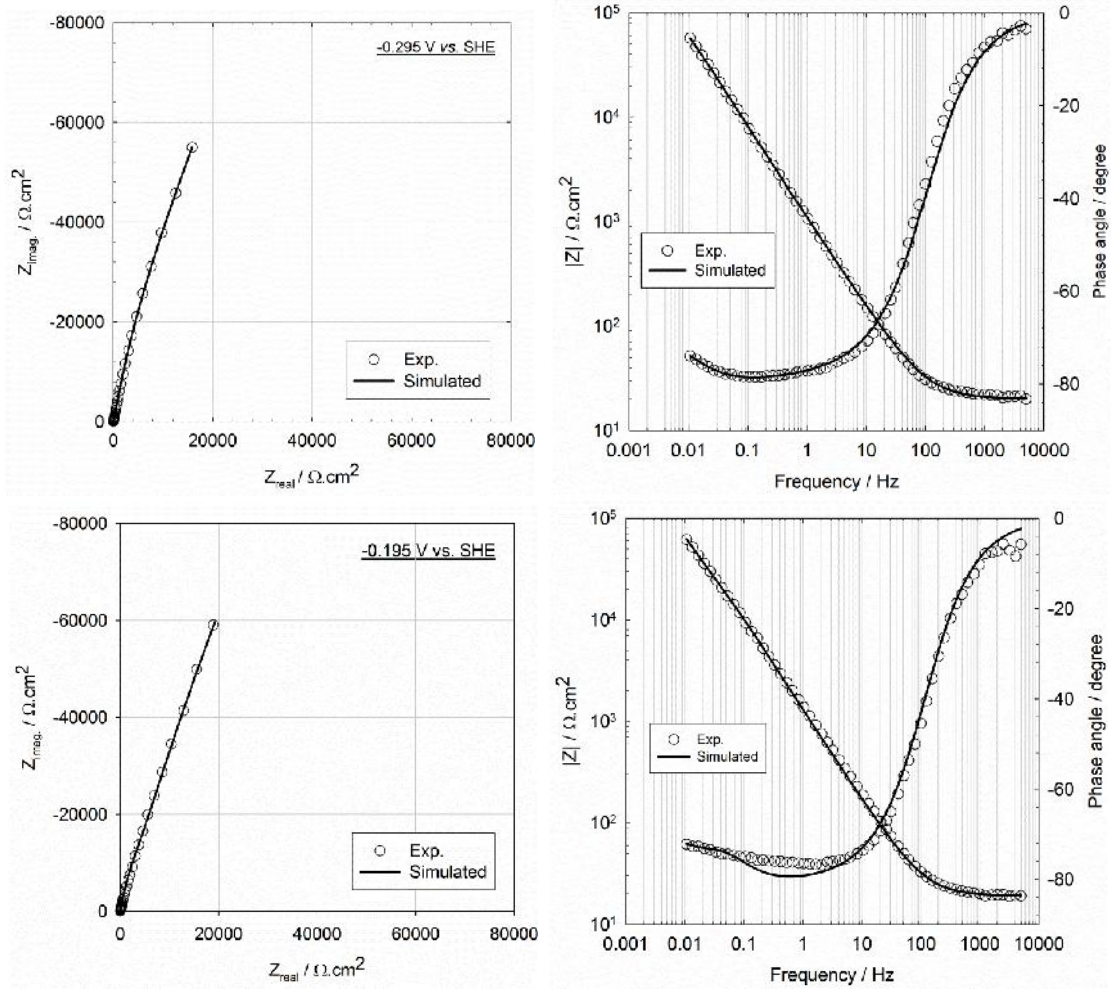


**Fig. 5.** Experimental and simulated Nyquist and Bode plots for copper in a deaerated 0.1 M  $NaCl + 2 \times 10^{-4}$  M  $Na_2S \cdot 9H_2O$ ,  $T = 25^\circ C$  as a function of applied potential, solid lines show the best fit calculation of the PDM using the optimized parameter values

Definitions of the other parameters are listed in Table 2. It should be mentioned that, since the pH of the solution was higher than the pH of zero charge for  $Cu_2S$  and  $CuS$  dissolution ( $PZC < 3.5$  [28]), “ $n$ ” should be a negative value as is obtained from the optimization. Another point to be noted is that the rate of the dissolution reaction is potential dependent if the oxidation state of copper in the barrier layer is different from its oxidation state in the solution. However, under an anoxic condition, the oxidation state of copper in both phases is +1, in that  $CuS$  is the  $Cu(I)$  salt of the disulfide ( $S_2^{2-}$ ) and should be written as  $Cu_2S_2$ . Therefore, the rate of film dissolution is considered to be potential-independent.

Under steady-state conditions  $\frac{dL}{dt} = 0$  and the steady-state thickness of the barrier layer can be derived as:

$$L_{SS} = \left[ \frac{1-\alpha}{\varepsilon} \right] V + \left[ \frac{2.303n}{\alpha_3 \varepsilon_{XY}} - \frac{\beta}{\varepsilon} \right] pH + \frac{1}{\alpha_3 \varepsilon_{XY}} \ln \left( \frac{k_3^0}{k_7^0} \right) \quad (45)$$

Figure 6(a) shows a comparison of the calculated steady-state thickness of the barrier layer with the experimental results as a function of applied potential, while the steady-state current for passive copper in sulfide-containing sodium chloride solution calculated from the parameters obtained from the PDM optimization is shown in Figures 6(b). As seen from these figures, there is a linear dependence of  $\log(I_{ss})$  on the applied potential, which is consistent with the PDM diagnostic criteria for p-type passive films. The parameters obtained from the PDM optimization listed in Tables 2 and 3 were used to calculate theoretically the steady-state properties (thickness and passive current density) of the barrier layer using Equations.16 and 45.

**Table 3.** Other parameters obtained from the Simulation of the proposed model for copper in a deaerated 0.1 M NaCl+2×10<sup>-4</sup> M Na<sub>2</sub>S.9H<sub>2</sub>O, at 25°C .

E <sub>app.</sub> (V vs. SHE)	-0.495	-0.395	-0.295	-0.195	Origin
	1	1	1	1	Assumed
	1	1	1	1	Assumed
CPE-g (S s cm <sup>-2</sup> )	5.31×10 <sup>-04</sup>	4.90×10 <sup>-04</sup>	2.93×10 <sup>-04</sup>	2.71×10 <sup>-04</sup>	2 <sup>nd</sup> stage optim
CPE-	0.82	0.78	0.81	0.83	2 <sup>nd</sup> stage optim
pH	10.18	10.18	10.18	10.18	Measured
(V cm <sup>-1</sup> )	1.94×10 <sup>+05</sup>	2.10×10 <sup>+05</sup>	2.10×10 <sup>+05</sup>	2.20×10 <sup>+05</sup>	1 <sup>st</sup> stage optim
C <sub>dl</sub> (F cm <sup>-2</sup> )	1.60×10 <sup>-04</sup>	2.22×10 <sup>-04</sup>	1.43×10 <sup>-04</sup>	1.38×10 <sup>-04</sup>	2 <sup>nd</sup> stage optim
R <sub>ct</sub> ( cm <sup>2</sup> )	2.80×10 <sup>+05</sup>	9.99×10 <sup>+10</sup>	9.98×10 <sup>+10</sup>	9.99×10 <sup>+10</sup>	2 <sup>nd</sup> stage optim
R <sub>s</sub> ( cm <sup>2</sup> )	27	23	19	18	Estimated
D <sub>v</sub> (cm <sup>2</sup> s <sup>-1</sup> )	7.44×10 <sup>-14</sup>	1.00×10 <sup>-13</sup>	1.00×10 <sup>-13</sup>	7.45×10 <sup>-13</sup>	2 <sup>nd</sup> stage optim
R <sub>ol</sub> ( cm <sup>2</sup> )	4.27×10 <sup>+04</sup>	1.03×10 <sup>+05</sup>	1.48×10 <sup>+05</sup>	2.78×10 <sup>+04</sup>	2 <sup>nd</sup> stage optim
C <sub>ol</sub> (F cm <sup>-2</sup> )	2.35×10 <sup>-04</sup>	4.01×10 <sup>-04</sup>	4.66×10 <sup>-04</sup>	3.04×10 <sup>-04</sup>	2 <sup>nd</sup> stage optim
( cm <sup>2</sup> s <sup>-0.5</sup> )	10	10	11	12	2 <sup>nd</sup> stage optim
R <sub>e,h</sub> ( cm <sup>2</sup> )	9.11×10 <sup>+10</sup>	9.94×10 <sup>+10</sup>	1.00×10 <sup>+07</sup>	1.00×10 <sup>+07</sup>	2 <sup>nd</sup> stage optim
L <sub>SS</sub> (cm)	3.86×10 <sup>-07</sup>	7.65×10 <sup>-07</sup>	1.14×10 <sup>-06</sup>	1.42×10 <sup>-06</sup>	Calculated
I <sub>SS</sub> (A cm <sup>-2</sup> )	2.43×10 <sup>-06</sup>	2.44×10 <sup>-06</sup>	2.45×10 <sup>-06</sup>	2.46×10 <sup>-06</sup>	Calculated

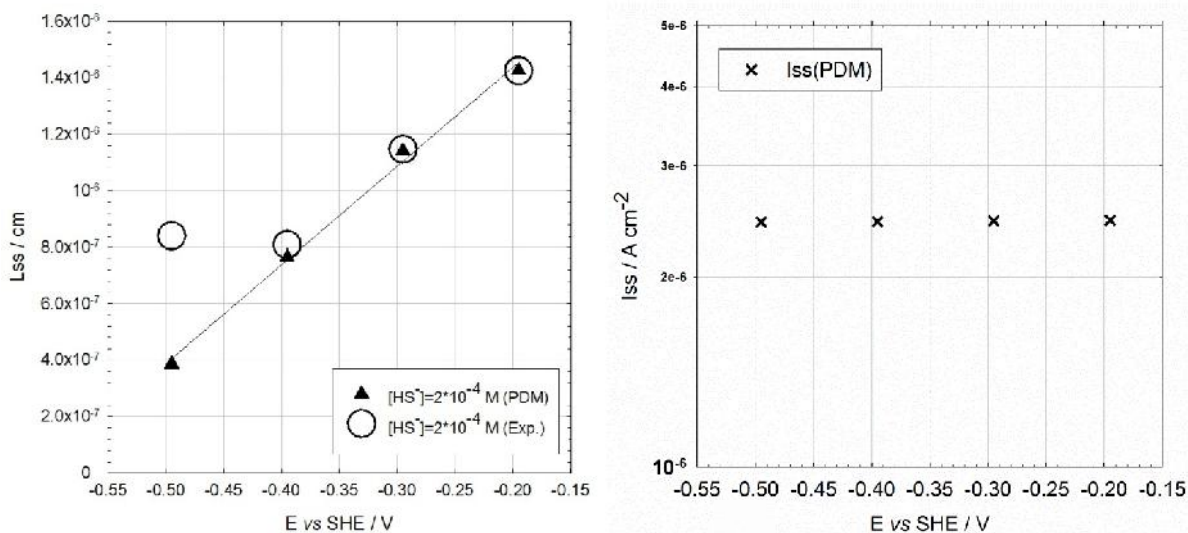


**Fig. 6.** Plots of the calculated and experimental steady-state barrier layer thickness as a function of potentials for copper in a deaerated 0.1 M NaCl+2×10<sup>-4</sup> M Na<sub>2</sub>S.9H<sub>2</sub>O at 25°C.

In order to obtain the experimental steady-state thickness, we used the well-known parallel plate capacitance formula (Eq.46) assuming a value of the capacitance from the high frequency (1 kHz) imaginary part of the experimental impedance data.

$$C = \frac{\tilde{\epsilon}\epsilon^0}{d} \quad (46)$$

where  $\tilde{\epsilon}$  is the dielectric constant (calibrated based on the obtained thickness,  $\tilde{\epsilon} = 724$ ),  $\epsilon^0 = 8.85 \times 10^{-14}$  (F cm<sup>-1</sup>) is the vacuum permittivity,  $d$  is the thickness of the film (cm), and  $C$  is the capacitance (F cm<sup>-2</sup>). As can be seen, the thickness of the barrier layer increases with applied potential as predicted by the PDM [1-5]. Good agreement is obtained

between the calculated and experimental thickness except at the lowest potential, which is closest to the active-to-passive transition (Fig. 2) and it is possible that the barrier layer had not fully developed at that potential. This postulate is somewhat supported by the fact that instabilities were observed in the impedance measurements at that potential.

## SUMMARY AND CONCLUSIONS

In this paper, we illustrate the application of electrochemical impedance spectroscopy (EIS) in analyzing impedance data for passive metal systems. We demonstrate the feasibility of deriving an impedance version of the Point Defect Model (PDM) and of optimizing the model upon experimental impedance data to extract values for important model parameters. These, in turn, are used to calculate the steady state barrier layer thickness and passive current density as a function of voltage. This work provides a scientific basis for estimating the lifetimes of copper canisters in crystalline rock repositories in Sweden for the disposal of high level nuclear waste (HLNW).

**Acknowledgements:** *The authors gratefully acknowledge the support of this work by Strålsäkerhets myndigheten (SSM) of Sweden.*

## REFERENCES

1. C. Y. Chao, L. F. Lin, and D. D. Macdonald, "A Point Defect Model for Anodic Passive Films I. Film Growth Kinetics," *J. Electrochem. Soc.*, **128**, 1187 (1981).
2. L. F. Lin, C. Y. Chao, and D. D. Macdonald, "A point defect model for anodic passive films II. Chemical breakdown and pit initiation," *J. Electrochem. Soc.*, **128**, 1194 (1981).
3. C. Y. Chao, L. F. Lin, D. D. Macdonald, "A Point Defect Model for Anodic Passive Films III. Impedance Response," *J. Electrochem. Soc.*, **129**, 1874–1879 (1982).
4. D. D. Macdonald, "Passivity-the key to our metals-based civilization," *Pure Appl. Chem.*, **71**, 951 (1999).
5. D. D. Macdonald, "On the Existence of Our Metals-Based Civilization," *J. Electrochem. Soc.*, **153**, B213 (2006).
6. H. Song, D. D. Macdonald, "Photoelectrochemical Impedance Spectroscopy I. Validation of the Transfer Function by Kramers-Kronig Transformation," *J. Electrochem. Soc.*, **138**, 1408 (1991).
7. D. D. Macdonald, E. Sikora, M. W. Balmas, R. C. Alkire, "The photo-inhibition of localized corrosion on stainless steel in neutral chloride solution," *Corros. Sci.*, **38**, 97 (1996).
8. M. Urquidi, D. D. Macdonald, "Solute-Vacancy Interaction Model and the Effect of Minor Alloying Elements on the Initiation of Pitting Corrosion," *J. Electrochem. Soc.*, **132**, 555 (1985).
9. L. Zhang, D. D. Macdonald, "Segregation of alloying elements in passive systems—I. XPS studies on the Ni–W system," *Electrochim. acta*, **43**, 2661 (1998).
10. D. D. Macdonald and S. I. Smedley, "An electrochemical impedance analysis of passive films on nickel (111) in phosphate buffer solutions," *Electrochim. Acta*, **35**, 1949 (1990).
11. D. D. Macdonald, M. Urquidi-Macdonald, "Application of Kramers-Kronig Transforms in the Analysis of Electrochemical Systems I. Polarization Resistance," *J. Electrochem. Soc.*, **132**, 2316 (1985).
12. M. Urquidi-Macdonald, S. Real, and D. D. Macdonald, "Application of Kramers-Kronig Transforms in the Analysis of Electrochemical Impedance Data II. Transformations in the Complex Plane," *J. Electrochem. Soc.*, **133**, 2018 (1986).
13. J. Ai, Y. Chen, M. Urquidi-Macdonald, D. D. Macdonald, "Electrochemical Impedance Spectroscopic Study of Passive Zirconium," *J. Electrochem. Soc.*, **154**, C52 (2007).
14. D. D. Macdonald, A. Sun, "An electrochemical impedance spectroscopic study of the passive state on Alloy-22," *Electrochim. Acta*, **51**, 1767 (2006).
15. J. Geringer, M. L. Taylor, D. D. Macdonald, "Predicting the steady state thickness of passive films with the point defect model in fretting corrosion experiments," Proceedings of PRIME 2012 (22nd Electrochemical Society Meeting, Pacific Rim Meeting on Electrochemical and Solid State Science), 2012.
16. DataFit, Oakdale Engineering, [www.oakdale engr.com](http://www.oakdale engr.com).
17. K. Levenberg, "A method for the solution of certain problems in least squares", *The Quart. Appl. Math.*, **2**, 164 (1944).
18. "Ellis 2: Complex curve fitting for one independent variable | IgorExchange.", 2012.
19. T. Bäck, H.-P. Schwefel, "An Overview of Evolutionary Algorithms for Parameter Optimization," *Evolutionary computation*, **1**, 1 (1993).
20. [D. D. Macdonald, and G. R. Engelhardt, "The Point Defect Model for Bi-Layer Passive Films", *ECS Trans*, **28**(24), 123 (2010).
21. S. Sharifi-Asl and D. D. Macdonald. "Corrosion domain analysis of copper corrosion in aqueous media", *Corr. Eng. Sci. Tech.*, **50**, 467-470 (2015).
22. F. King, L. Ahonen, C. Taxén, U. Vuorinen, and L. Werme, "Copper corrosion under expected conditions in a deep geologic repository," Swedish Nuclear Fuel and Waste Management Company Report, SKB TR 01-23, 2001 and Posiva Oy Report POSIVA 2002-01, 2002.
23. F. King, "Container Materials for the Storage and Disposal of Nuclear Waste," *Corrosion*, **69**, 986 (2013).
24. King, C. Lilja, M. Vähänen, "Progress in the understanding of the long-term corrosion behaviour of copper canisters," *Journal of Nuclear Materials*, **438**, 228 (2013).

25. S. Sharifi-Asl, "Corrosion issues in high-level nuclear waste containers", Diss. The Pennsylvania State University, 2013.
26. C-F. Dong, F. Mao, S. Gao, S. Sharifi-Asl, P. Lu, D. D. Macdonald, Passivity Breakdown on Copper: Influence of Temperature, *Journal of The Electrochemical Society*, **163(13)**, C707 (2016).
27. M. Kosmulski, Surface charging and points of zero charge, Surfactant Science Series, Vol. **145**, CRC Press, Boca Raton, FL 2010, p. 1696.

1

2

26 2016 .; 15 2016 .

( )

( )

( )

( )

100000

## Electrochemical methods in drug discovery and development

Z. Mandi

Faculty of Chemical Engineering and Technology, University of Zagreb, HR-10000 Zagreb, Croatia

Received December 12, 2016      Revised January 16, 2016

A brief outline of the applications of electrochemical methods in pharmaceutical research was given. The aim of the review was not exhaustive since it would not be possible to cover such a diverse field in one review paper. Rather, several examples from the author's experience were given which demonstrate the applicability and usefulness of electrochemistry in the improving and accelerating drug design and development. The applications covered in this paper include electrochemical synthesis, electroanalytics and drug transfer across liquid/liquid interface.

**Key words:** electrochemical synthesis, ion transfer at liquid/liquid interface, ADME, DMPK, macrolide, azithromycin, electroanalytics.

### INTRODUCTION

The main goal of pharmaceutical research revolves around design of a new drug or improving the properties or bioavailability of drugs already existing on the market. Drug discovery is a time and money consuming process which involves complex interactions among scientists of different profiles including medicinal chemists, pharmacologists, pharmaceutical scientists, biochemists, biotechnologists and physicians. Traditional trial-and-error approaches to drug discovery are nowadays increasingly replaced with modern paradigms of rational drug design such as structure-based and ligand-based drug design. Both approaches rely on the knowledge of the biological target either as its 3D structure or the interactions it elicits in the presence of other drug-like molecules. As the result of combined efforts of X-ray spectroscopy and NMR labs with molecular modelling and high-throughput screening, usually the "lead" compound(s) possessing suitable pharmacological responses are identified and isolated. Due to very high attrition rates of drugs which reached the costly clinical phases, a care is taken to optimize lead compounds in order to improve their Absorption, Distribution, Metabolism, Excretion and Toxicology (ADMET) properties as well as to assess their Drug Metabolism and Pharmacokinetics (DMPK).

Main cause of the failure of drugs in clinical phases is their adverse unfavourable biological effects or their poor absorption mostly due to the inability of drug substance to cross biological

membranes and other barriers. Even if the substances possessed high affinity toward designated biological targets and had high therapeutic potential they would still be useless in case they would not be able to reach targeted biomolecule. The importance of drug absorption was thus recognized long time ago and its concept has progressed into a scientific discipline without which no contemporary pharmaceutical research could be considered. This is especially important for orally formulated drugs as the most convenient dosage forms since these drugs undergo gut and hepatic first-pass metabolism.

Among a vast variety of disciplines involved in the successful bringing the substance from the discovery of its potential therapeutic effect to the market, physical chemistry occupies a special place. Physico-chemical properties of substances are key factors determining the fate of the drug in the organism from its administration and absorption to its excretion. Not only they are responsible for successful ligand-target interactions through hydrogen bonding and hydrophobic interactions, but also four physico-chemical processes, *i.e.* ionization, solubility, lipophilicity and permeability, are of high relevance to the absorption of most orally administered drugs [1].

These processes are commonly expressed through the quantities such as ionization constant,  $pK_a$ , intrinsic solubility,  $\log S_0$ , partition coefficient,  $\log P$  and permeability coefficient,  $P_e$ , respectively. Careful evaluation of these parameters has led to the development of Biopharmaceutical classification system (BCS) [2], which provides a framework for the division of substances according to their aqueous solubility and intestinal permeability. There were also several empirical rules of thumb developed for the prediction of

---

To whom all correspondence should be sent:  
E-mail: zmandic@fkit.hr

the extent of passive permeation of drug molecules through cell membranes. The example is famous Lipinski "rule of five" [3] which identified several criteria any molecule should match to increase the chances to be absorbed by the body. Nowadays, physico-chemical parameters such as  $pK_a$ ,  $\log P$  or  $\log S$  are no longer perceived by medicinal chemists or formulation and pre-formulation engineers as "good" or "bad" numbers, but provide valuable prediction about the behaviour of active drug substance upon administration. Measurement of physico-chemical properties of potentially active substances has become a routine practice in the pharmaceutical research and many methods were developed for their accurate determination and prediction.

Electrochemical methods are widely used in almost all fields of pharmaceutical research. Their applications penetrate almost all labs and phases of drug development. The aim of this paper is to give an overview of the potential of electrochemistry and electrochemical methods in the synthesis and analysis of drugs. However, the subject is so broad that it would be impossible to address all the issues and applications in one review. Instead, this review is based on the author's decade experience in dealing with electrochemistry field in pharmaceutical research and development.

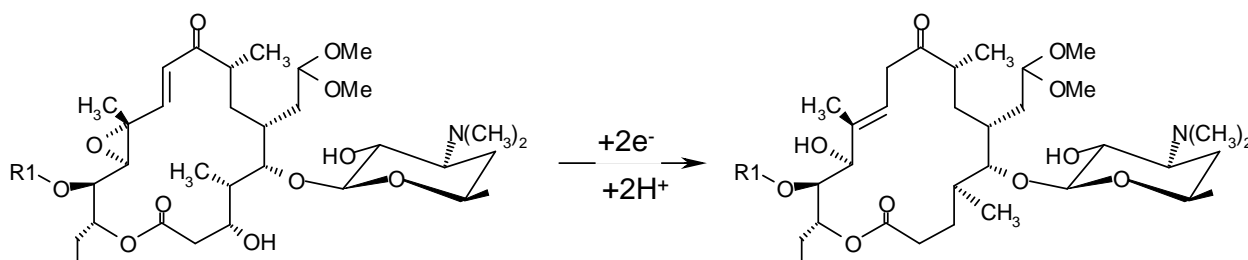
### ELECTROCHEMICAL SYNTHESIS OF BIOLOGICALLY ACTIVE COMPOUNDS

Electrochemical synthetic procedures are valuable tool for the synthesis and modifications of a large group of biologically active molecules and functional groups and as such are unavoidable techniques in medicinal and organic chemistry labs. They have proven useful not only because some products and intermediates could be obtained more easily by electrochemical means than by conventional chemical routes but also because some molecules could be synthesized almost exclusively electrochemically [4-23]. Large variety

of direct and indirect electrochemical transformations of organic compounds is available to the skilful organic electrochemists which can be utilized to carry out desired chemical transformation hopefully leading to the active compounds with high biological activities. In direct electrochemical reactions, the product or reacting intermediate is formed by the electron transfer from the electrode to the reactant or vice versa, while in the indirect electrochemical reactions mediators and/or reagents are electrochemically generated to initiate the desired reaction. With the existence of a wide range of electron transfer mediators, the scope of the useful electrochemical synthetic reactions is largely extended to involve many reactions which otherwise would not be able to proceed by direct electrochemistry.

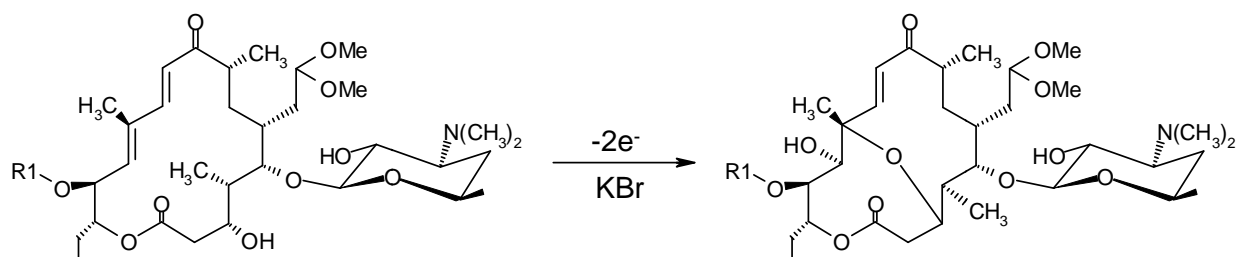
The usefulness of direct and indirect electrochemical reactions can be demonstrated with the examples of electrochemical functionalization of tylozin/desmycosin antibiotics: electrochemical opening of 12,13-oxirane desmycosin (Scheme 1) [6] and electrochemical oxidation of desmycosin (Scheme 2) [7], respectively. Electrochemical methodology can be also utilized in chiral electrosynthesis which is of high importance for pharmaceutical companies since many drugs are marketed in the enantiomerically pure forms.

Heterogeneous nature of the electrode processes with highly structured solvent and electrolyte molecules at interphase region favours enantioselective electrochemical reactions. Relatively recent example demonstrated that exocyclic double bond of 8-methylene oleandomycin (**1**) can be reduced at mercury electrode with 67 % enantiomeric excess resulting in (*R*)-8-methyl oleandomycin (**2**) as the main product (Scheme 3) [11]. Stereoselectivity of electroreduction was explained by the approaching of the 8-methylene-oleandomycin "bottom side" at the electrode surface and exposing "top" side for the proton transfer from solution upon electron transfer.

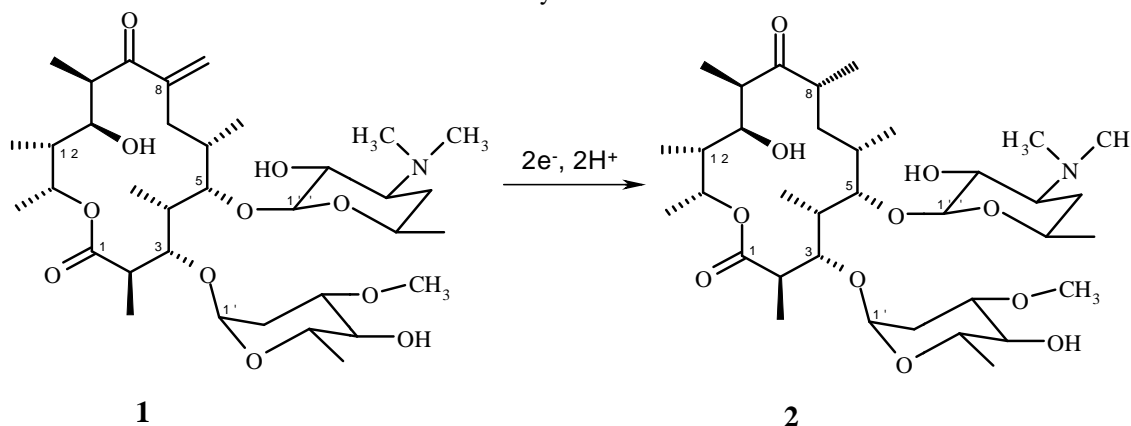


Scheme 1. Electrochemical opening of 12,13-oxirane ring of desmycosin.





Scheme 2. Indirect electrochemical oxidation of desmycosin.



Scheme 3. Electrochemical reduction of 8-methylene oleandomycin at mercury electrode.

There are also other approaches for the electrochemical synthesis of chiral compounds. Electroenzymatic reactions belong to the realm of indirect electrochemical chiral transformations. They got into the focus of pharmaceutical research and development due to widespread applications of high enantio- and regioselectivity of the enzyme catalysed reactions. Electroenzymatic reactions open a route to the design of commercially attractive and environmentally friendly reactors and chemical plants. The function of redox enzymes such as, for example, dehydrogenases, oxygenases, reductases and oxidases, are dependent on either bound (flavin adenine dinucleotide (FAD), flavin mononucleotide (FMN), pyrroloquinoline quinone (PQQ)... ) or freely dissolved cofactors (nicotinamide adenine dinucleotide (NAD(P)H) redox cofactors. The use of redox enzymes suffers from several intrinsic problems which limit their widespread applications in carrying out efficient and selective chemical transformations. The most important issue is a high cost associated with the cofactors so that their use in stoichiometric amounts is not economically feasible. The solution is to use small quantities of cofactors in the reaction mixture and to apply simple and efficient methods for their regeneration. Common method is to couple another enzyme in the reaction mixture which is called regeneration enzyme in order to convert reacted cofactor back to its initial state. The complications which arise in this case are mostly connected with

the complexity of reaction mixture and the necessity of subsequent separation and isolation of the product. To circumvent this problem there have been many efforts to design an electrochemical system with the suitable mediator which would be able to transfer the electrons from the electrode to cofactor with the regeneration efficiency close to 100 % (Figure 1).

The real life application of the above procedure can be demonstrated in the synthesis of antidepressant (*R*)-fluoxetine where one of the steps could be the enantiometric conversion of aromatic ketone to the corresponding alcohol using alcohol dehydrogenase and NADH as a redox system (Scheme 4).

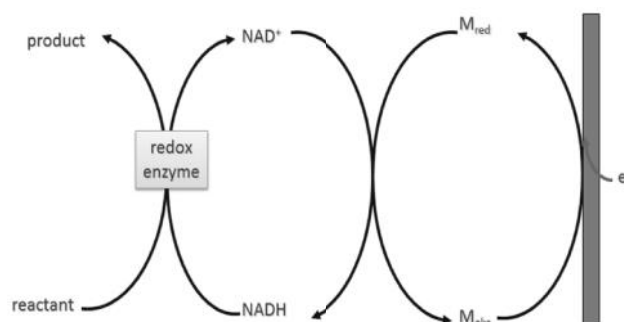
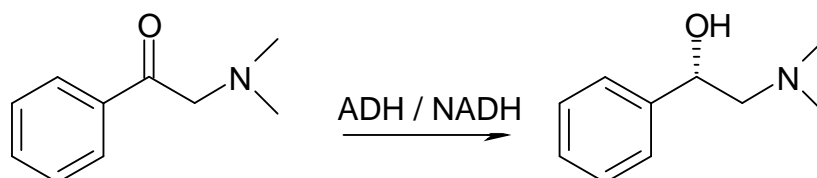


Fig. 1. The principle of indirect electrochemical regeneration system for the enzymatic reduction process.



Scheme 4. Alcohol dehydrogenase and NADH redox system have a potential to be used in the synthesis of antidepressant drug fluoxetine.

## ELECTROANALYTICAL CHEMISTRY IN THE DRUG ANALYSIS

The applications of electroanalytical methods in pharmaceutical industry are so broad that it would be very difficult, if not impossible, to address them all in this review. Maybe most neglected in scientific literature are potentiometric methods of analysis. Besides their utilization for purity determination of pharmaceutical active ingredients in routine quality control laboratories [24-35], potentiometric titrations have been developed as fast and accurate methods of choice for physico-chemical profiling of drug substances. Except in the cases when the analyte is sparingly soluble or is available in limited quantities when either Yasuda-Shedlovsky cosolvent [36-40], or spectrophotometric titrations could be ordinarily used, ionization macro- and microconstants are readily determined by potentiometric titrations [1 and references therein]. Even in the cases when  $pK_a$ s of the analyte fall in the water buffering range ( $pH < 3$  or  $pH > 11$ ), the ionization constants could be accurately determined if the glass electrode is appropriately calibrated and standardized in this region [1, 41, 42].

Partition coefficient  $\log P$  as a parameter which describes affinity of neutral substance toward lipophilic environment, as well as lipophilicity profile representing a distribution coefficient, and  $\log D$  as a function of  $pH$ , are nowadays determined more accurately and more quickly by two-phase octanol/water potentiometric titration in comparison to the traditional "shake-flask" procedures [1 and references therein]. In a typical experiment, titration curve from the two-phase octanol/water system yields  $pK_a^{oct}$ , which is compared to the  $pK_a$  of the substance obtained in aqueous solution. From the known octanol/water ratio,  $\log P$  could be calculated. Other methods of  $\log P$  determination include HPLC [43-51], capillary electrophoresis [43,52,53] and centrifugal partition chromatography [54].

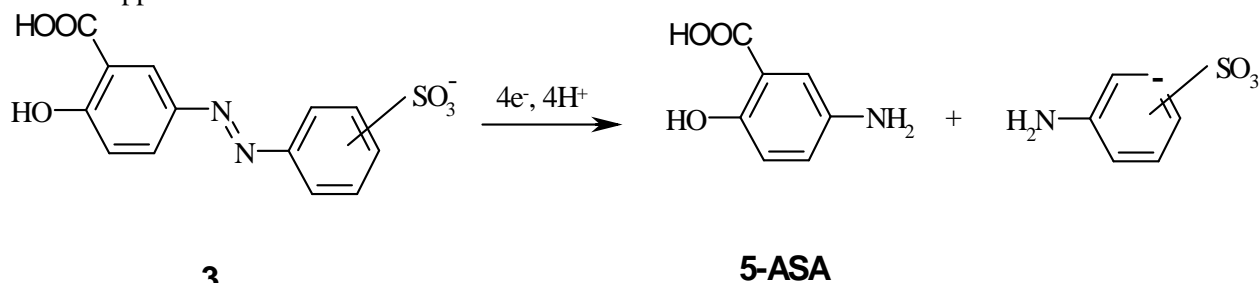
Potentiometric titrations are very frequently used for the determination of intrinsic solubility.

Solubility determination by potentiometric titration was introduced by A. Avdeef [55-57]. The intrinsic solubility is calculated from the difference of the substance  $pK_a$  and the apparent  $pK_a^{app}$  in the presence of the precipitate. Relatively recently faster potentiometric approach was introduced and developed by Sirius Analytical Ltd. [58-60]. The method is called Chasing equilibrium method (Cheqsol) and it is based on the back and forth titrations around equilibrium  $pH$  of the solution.

Despite the fact that polarographic and voltammetric methods of analysis provide several advantages over traditional spectrophotometric techniques such as high sensitivity, low limit of detection and reduction in cost and time of analysis, their real world applications for the qualitative and quantitative analysis of pharmaceuticals are very scarce. Up to the author's knowledge only the pulse polarographic determination of iron sucrose in injections is listed in US Pharmacopeia [61]. The main reason for the lack of electrochemical methods broader application in analytical determinations and validations of drugs is the popularity of combined separation/detection techniques such as HPLC/UV and HPLC/mass spectrometry. Only in the cases where the active substance does not possess a chromophore, but can undergo electrochemical reaction, the HPLC with the coulometric or amperometric detection could be employed. The striking example of this case is the determination of macrolide antibiotics such as erythromycin and azithromycin [62-64] with their tertiary amine groups which can undergo one- or two-electron oxidation reactions. Nevertheless, many research efforts have been made to develop and validate electroanalytical methods for almost all drug substances which can be directly oxidized or reduced at electrodes, especially for the determination of active substances in pharmaceutical formulations such as tablets [65-68.] or in bodily fluids [69 and references within].

On the other hand, electrochemical methods were widely employed for the in-vitro investigations of drug metabolism [64,70-75], ligand-protein binding interactions [76-80], drug-

DNA interactions [81-89] and anti-oxidative potential of certain compounds [90-95]. The mechanism and kinetics of the electrochemical reduction of four derivatives of 2-hydroxy-5-[(sulfophenyl)azo]benzoic acids (**3**) were investigated by cyclic voltammetry and chronoamperometry with the view on their potential application in the treatment of



Scheme 5. Azo bond reduction follows DISP2 mechanism. The first stage in the reaction is the reduction of hydrazone tautomer giving corresponding hydrazo intermediate. The hydrazo bond cleavage is an acid catalyzed reaction and is followed by homogenous redox reaction between 5-ASA quinoneimine and parent hydrazo compound [71].

Cyclic voltammograms of these compounds are rather complex and strongly pH-dependent. On the basis of the experimental results, 2-hydroxy-5-[(2-sulfophenyl)azo]benzoic acid having sulfo group in ortho position was identified as the compound subject to the slowest rate of azo bond cleavage which in turn enables the highest efficiency to pass upper gastrointestinal tract and consequently higher biological potency for the treatment of Ulcerative colitis and Chron's disease.

#### THE TRANSFER OF IONISABLE DRUGS ACROSS LIQUID/LIQUID INTERFACE

It was estimated that more than 60 % of drugs on the market exist in ionic forms in the physiological pH ranges [96]. If ionic forms are sufficiently lipophilic overall membrane transport properties of ionisable drug compounds depend not only on lipophilicity and permeability, but also on the difference between the actual membrane potential and their standard transfer potential. In order to probe the possibility of the transfer of ionisable drug compounds through the membrane, it was recognized that the liquid/liquid interface (LLI) between two immiscible solvents, one usually being water and another providing lipophilic environment, can practically mimic a biological membrane. The transfer of ionisable drug compounds through such an interface can be conveniently studied by electrochemical methods in a four-electrode electrochemical cell [97-105]. Most frequently used solvents having acceptable dielectric constants for dissolving electrolytes suitable for electrochemical measurements at their

inflammatory bowel diseases [71]. Similarly to market medicines sulfasalazine and olsalazine, the mechanism of biological action of these compounds includes the bacterial reduction of azo bond in the gastrointestinal tract liberating active compound 5-aminosalicylic acid (5-ASA) (Scheme 5).

interface with water are nitrobenzene and 1,2-dichloroethane.

The electrochemical measurements at LLI can provide information about partitioning of all species present in aqueous phase. While the partitioning of neutral species does not depend on pH or Galvani potentials at LLI, ionised forms are susceptible to both quantities. The dependence of ionic partition can conveniently be represented by ionic partition diagram, i.e. plots of dependence of equilibrium Galvani potential difference between two phases on pH, which resembles well known Pourbaix diagram [106-108]. From ionic partition diagrams the predominance of species in each phase can be deduced, but also a mechanism of ionic transfer such as simple ionic transfer or proton coupled transfer can be revealed [106,109].

The establishment of correlation between electrochemical data obtain on either LLI interface or on supported liquid membranes (SLM) and pharmacological profiling of drugs has been attempted several times [110-114].

It has recently been demonstrated that cyclic voltammetry at water/nitrobenzene interface can be used as a fast in vitro method for the pharmacokinetic screening of macrolide compounds [110]. Macrolides' ability to pass through biological membranes and to accumulate in high concentrations intracellularly are of paramount importance for their pharmacokinetics, as proven by the significant amount of in vivo and in vitro data accumulated on the subject over the years [115].

Although all macrolides show similar ADME properties and pharmacokinetics, azithromycin (**4**) (Figure 2) stands out due to its ability to accumulate in 200-fold excess intracellularly than extracellularly [115]. Cyclic voltammogram of

doubly protonated azithromycin taken at water/nitrobenzene interface at pHs of aqueous phase below 6 and compared to single protonated erythromycin is shown in Figure 3.

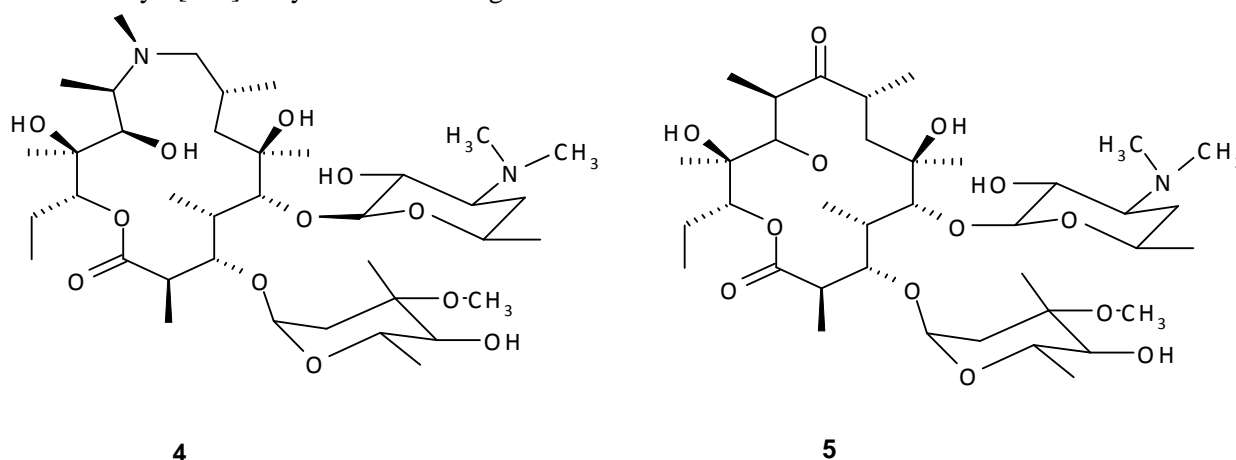


Fig. 2. Chemical structures of azithromycin (**4**) and erythromycin (**5**).

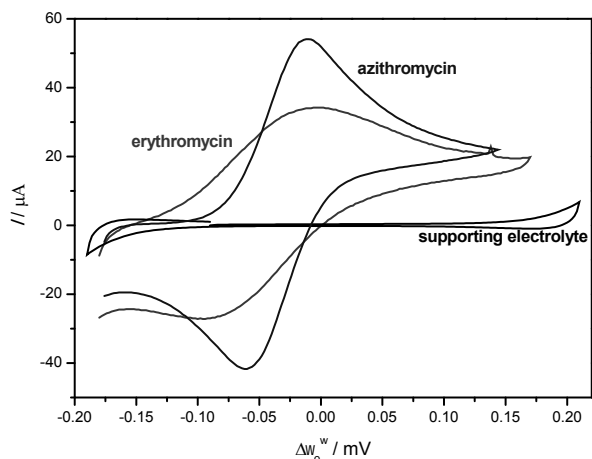


Fig. 3. Cyclic voltammograms of erythromycin and azithromycin at pH of aqueous phase 5.8 and  $C=0.2$  M. Scan rate: 20 mV/s. Plot taken from [110].

While the increase of pH of aqueous phase above 6 induces only the shift of the cyclic voltammogram of erythromycin toward more positive potential, the electrochemical behaviour of azithromycin is more complex (Figure 4). Its transfer mechanism changes from simple ionic transfer of doubly protonated species at acidic pHs to the facilitated proton transfer in basic aqueous solutions [110]. The formal transfer potentials of all investigated macrolide compounds were tabulated revealing a significant difference in their values and consequently in the values of transfer free energy. Azithromycin, having the lowest standard transfer potential at water/nitrobenzene interface, stands out among investigated compounds and proves that membrane permeation of macrolide compounds influences their overall pharmacokinetics. What is more, the results showed that cyclic voltammetry

can be used in pharmaceutical research and development as a fast and simple method for screening out macrolide compounds with potentially good ADME properties.

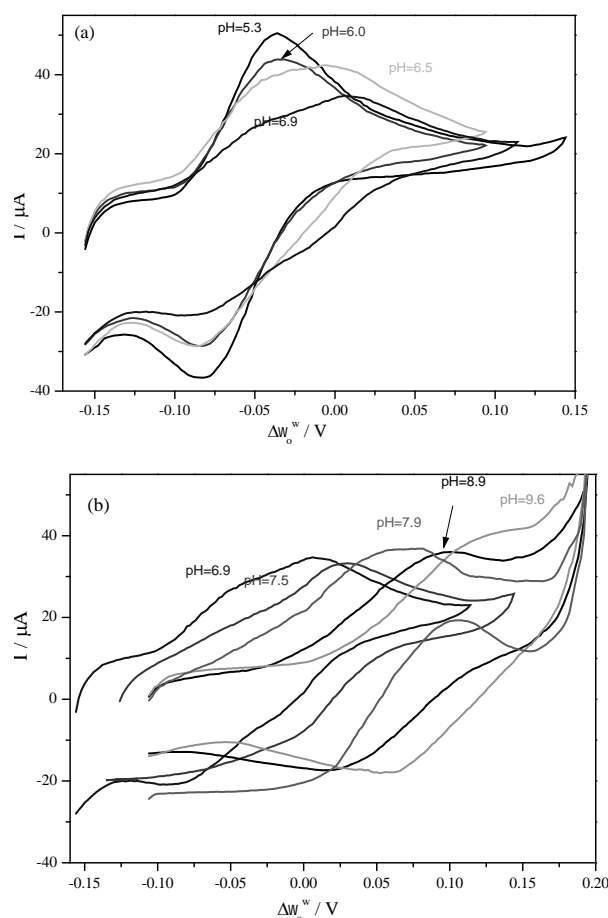


Fig. 4. Cyclic voltammograms of azithromycin at various aqueous phase pH and  $C=0.2$  M. Actual pHs indicated on the graphs. Scan rate = 20 mV/s. Plots taken from [24].

## REFERENCES

1. A. Avdeef, Absorption and Drug Development, John Wiley & Sons, NJ, 2012.
2. G. Amidon, H. Lennernas, V. Shah, J. Crison, *Pharm. Res.*, **12**, 413 (1995).
3. C.A. Lipinski, F. Lombardo, B.W. Dominy, P.J. Feeney, *Adv. Drug Delivery Rev.*, **23**, 3 (1997).
4. Z. Mandi, N. Lopotar, *Electrochem. Comm.*, **7**, 45 (2005).
5. D. Ivekovi, N. Lopotar, K. Brajša, Z. Mandi, *Eur. J. Pharm. Sci.*, **18**, 323 (2003).
6. Z. Mandi, A. Naran a, N. Lopotar, Lj. Dui, D. Ivekovi, M. Tkal ec, *J. Antibiot.*, **52**, 1143 (1999).
7. Z. Mandi, A. Naran a, P. Novak, K. Brajša, M. erek, D. Ivekovi, *J. Antibiot.*, **55**, 807 (2002).
8. Zoran Mandi, Gorjana Lazarevski, Zlatko Weitner, Predrag Novak, Nataša Marši, Ana Budimir, *ADMET DMPK* **2**, 179 (2014).
9. Z. Mandi, S. Tomši, I. Bratoš, *Sulf. Lett.*, **24**, 229 (2001).
10. M. Ochiai, O. Aki, A. Morimoto, T. Okada, K. Shinozaki, Y. Asaki, *J. Chem. Soc. Perkin Trans.*, **1**, 258 (1974).
11. Z. Mandi, M. Ilijaš, G. Turkalj, *Electrochem. Solid State Lett.*, **13**, E5 (2010).
12. H. Ding, P.L. Deroy, C. Perreault, A. Larivée, A. Siddiqui, C.G. Caldwell, S. Harran, P.G. Harran, *Angew. Chem.*, **54**, 4818 (2015).
13. D.S. Dayama, P.N. Khatale, S.A. Khedkar, S.R. Nazarkar, P.A. Vedpathak, *Pharma Chem.*, **6**, 123 (2014).
14. D. Chai, D. Genders, N. Weinberg, G. Zappi, E. Bernasconi, J. Lee, J. Roletto, L. Sogli, D. Walker, C.R. Martin, V. Menon, P. Zelenay, H. Zhang, *Org. Proc. Res. Dev.*, **6**, 178 (2002).
15. C. Hughes, A. Miller, D. Trauner, *Org. Lett.*, **7**, 3425 (2005).
16. H. Ding, P.L. DeRoy, C. Perreault, A. Larivée, A. Siddiqui, C.G. Caldwell, S. Harran, P.G. Harran, *Angew. Chem.*, **54**, 4818 (2015).
17. C. Gütz, M. Selt, M. Bänziger, C. Bucher, C. Römelt, N. Hecken, F. Gallou, T.R. Galvão, S.R. Waldvogel, *Chem. Eur. J.*, **21**, 13878 (2015).
18. H. Tanaka, H. Ogawa, H. Suga, S. Torii, A. Jutand, S. Aziz, A.G. Suarez, C. Amatore, *J. Org. Chem.*, **61**, 9402 (1966).
19. M. Tokuda, H. Fujita, T. Miyamoto, H. Suginome, *Tetrahedron*, **49**, 2413 (1993).
20. E. Guni, I. Tabakovi, M.J. Gaši, *J. Chem. Soc. Chem. Comm.*, 1496 (1993).
21. K. Oda, T. Ohnuma, Y. Ban, *J. Org. Chem.*, **49**, 953 (1984).
22. H. Tanaka, Y. Kameyama, S. Sumida, S. Torii, *Tetrahedron Lett.*, **33**, 7029 (1992).
23. D. Anderson, D. Coburn, A. Haag, *Tetrahedron Lett.*, **24**, 1329 (1983).
24. S.F. Rassi, *J. Electrochem. Sci. Eng.*, **6**, 187 (2016).
25. D. Patel, S. Patel, Y. Parmar, K. Chauhan, P. Sannigrahi, A.S. Rawat, A. Vardhan, *Int. J. Pharma Res. Rev.*, **2**, 10 (2013).
26. P. Ribeiro, A. Santini, H. Pezza, L. Pezza, *Ecl. Quím.*, **28**, 39 (2003).
27. E.Y.Z. Frag, G.G. Mohamed, M.M. Khalil, M.M.A. Hwehy, *Int. J. Anal. Chem.*, 604, (2011).
28. N. Aslan, P. Erden, E. Canel, E. Kilic, *Bulg. Chem. Comm.*, **46**, 497 (2014).
29. R. Rele, R. Terse, *J. Chem. Pharm. Res.*, **3**, 1 (2011).
30. M. Hefnawy, A. Homoda, M. Abounassif, A. Alanazi, A. Al-Majed, G. Mostafa, *Chem. Cent. J.*, **8**, 59 (2014).
31. S. Richheimerx, M. Schachet, *J. Pharm. Sci.*, **72**, 822 (1983).
32. V. Maslarska, *Int. J. Pharm. Pharm. Sci.*, **6**, 538 (2014).
33. V.K. Gupta, S. Agarwal, B. Singhal, *Int. J. Electrochem. Sci.*, **6**, 3036 (2011).
34. M. Ardeshiri, F. Jalali, *Mat. Sci. Eng. C*, **63**, 30 (2016).
35. A. Ensafi, A. Allafchian, B. Rezaei, *Anal. Bioanal. Electrochem.*, **7**, 569 (2015).
36. K. Takács-Novák, K. Box, A. Avdeef, *Int. J. Pharm.*, **151**, 235 (1997).
37. G. Volgyi, R. Ruiz, K. Box, J. Comer, E. Bosch, K. Takács-Novák, *Anal. Chim. Acta*, **583**, 418 (2007).
38. A. Avdeef, K.J. Box, J.E.A. Comer, M. Gilges, M. Hadley, C. Hibbert, W. Paterson, K.Y. Tam, *J. Pharm. Biomed. Anal.*, **20**, 621 (1999).
39. N. Sun, A. Avdeef, *J. Pharm. Biomed. Anal.*, **56**, 173 (2011).
40. Krisztina Takács-Novák, Katalin Deák, Szabolcs Béni, Gergely Völgyi, *ADMET DMPK*, **1**, 6 (2013).
41. A. Avdeef, J. Bucher, *Anal. Chem.*, **50**, 2137 (1978).
42. A. Avdeef, J. Comer, S. Thomson, *Anal. Chem.*, **65**, 42 (1993).
43. J. Cabot, X. Subirats, E. Fuguet, M. Rosés, *ADMET DMPK*, **2**, 98 (2014).
44. K. Valkó, P. Slegel, *J. Chromatogr.*, **631**, 49 (1993).
45. K. Valkó, C. Bevan, D. Reynolds, *Anal. Chem.*, **69**, 2022 (1997).
46. L. Hitzel, A.P. Watt, K.L. Locker, *Pharm. Res.*, **17**, 1389 (2000).
47. K. Valkó, C. Du, C. Bevan, D. Reynolds, M. Abraham, *Curr. Med. Chem.*, **8**, 1137 (2001).
48. K. Valkó, C.M. Du, C.D. Bevan, D.P. Reynolds, M.H. Abraham, *J. Pharm. Sci.*, **89**, 1085 (2000).
49. W. Schrader, J. Andersson, *J. Pharm. Sci.*, **90**, 1948 (2001).
50. F. Lombardo, M.Y. Shalaeva, K.A. Tupper, F. Gao, M.H. Abraham, *J. Med. Chem.*, **43**, 2922 (2000).
51. K. Valkó, Measurements of physical properties for drug design in industry, in K. Valkó, (ed.), *Separation Methods in Drug Synthesis and Purification*, Elsevier, Amsterdam, 2001, Ch. 12.
52. Y. Ishihama, Y. Oda, K. Uchikawa, N. Asakawa, *Anal. Chem.*, **67**, 1588 (1995).
53. J. Razak, B. Cutak, C. Larive, C. Lunte, *Pharm. Res.*, **18**, 104 (2001).
54. N. El Tayar, R. Tsai, P. Vallat, C. Altomare, B. Testa, *J. Chromatogr.*, **556**, 184 (1991).
55. A. Avdeef, *Pharm. Pharmacol. Commun.*, **4**, 165 (1998).

56. A. Avdeef, E. Fuguet, A. Llinàs, C. Ràfols, E. Bosch, G. Völgyi, T. Verbi, E. Boldyreva, K. Takács-Novák, *ADMET DMPK*, **4**, 117 (2016).
57. A. Avdeef, *ADMET DMPK*, **3**, 84 (2015).
58. M. Stuart, K. Box, *Anal. Chem.*, **77**, 983 (2005).
59. K. Box, G. Völgyi, E. Baka, M. Stuart, K. Takács-Novák, J. Comer, *J. Pharm. Sci.*, **95**, 1298 (2006).
60. J. Comer, S. Judge, D. Matthews, L. Towes, B. Falcone, J. Goodman, J. Dearden, *ADMET DMPK*, **2**, 18 (2014).
61. U.S. Food and Drug Administration Iron sucrose injection, official monograph. United States Pharmacopeial Convention, Rockville, 3564, (2012).
62. R.M. Shepard, G.S. Duthu, R.A. Ferraina, M.A. Mullins, *J. Chromatogr.*, **565**, 321 (1991).
63. R. Gandhi, C.L. Kaul, R. Panchangula, *J. Pharm. Biomed. Anal.*, **23**, 1073 (2000).
64. Z. Mandi, Z. Weitner, M. Ilijaš, *J. Pharm. Biomed. Anal.*, **33**, 647 (2003).
65. S. Patil, V. Pattar, S. Nandibewoor, *J. Electrochem. Sci. Eng.*, **6**, 265 (2016).
66. A.E. Esteva, E. Blanco, J.J. Piña, A.I. Balbin, C. Quintana, P. Hernández, *J. Electrochem. Sci. Eng.*, **4**, 37(2014).
67. P.A.M. Farias, A.A. Castro, A.P. Cordoves, *J. Electrochem. Sci. Eng.*, **2**, 133 (2012).
68. N. Teradal, S. Prashanth, J. Seetharamappa, *J. Electrochem. Sci. Eng.*, **2**, 67 (2012).
69. M. Gumustas, S.A. Ozkan, *Open Anal. Chem. J.*, **5**, 1 (2011).
70. E. Nigjeh, *ADMET DMPK*, **2**, 157 (2014).
71. Z. Mandi, B. Nigovi, B. Šimuni, *Electrochim. Acta*, **49**, 607 (2004).
72. A. Alvarez-Lueje, S. Bollo, *Comb. Chem. High Throughput Screen.*, **13**, 712 (2010).
73. W. Lohmann, R. Dötzer, G. Gütter, S.M. van Leeuwen, U. Karst, *J. Am. Soc. Mass. Spec.*, **20**, 138 (2009).
74. S. Leeuwen, B. Blankert, J. Kauffmann, U. Karst, *Anal. Bioanal. Chem.*, **382**, 742 (2005).
75. K. Madsen, C. Skonberg, U. Jurva, C. Cornett, S. Hansen, T. Johansen, J. Olsen, *Chem. Res. Tox.*, **21**, 1107 (2008).
76. M. Mahanthappa, B. Gowda, J. Gowda, R. Rengaswamy, *J. Electrochem. Sci. Eng.*, **6**, 155 (2016).
77. A. Menzela, A.T.-H. Lina, P. Estrela, P. Li, A.A. Seshi, *Sensors Actuators B: Chemical*, **160**, 301 (2011).
78. M. Ho, S. Goodchild, P. Estrela, D. Chua, P. Migliorato, *Analyst.*, **139**, 6118 (2014).
79. C. Altay, E. Eksin, G. Congur, A. Erdem, *Talanta*, **144**, 809 (2015).
80. J. Molinari, C. Moina, G. Ybarra, *J. Electrochem. Sci. Eng.*, **5**, 9 (2015).
81. A. Shah, A. Rauf, A. Ullah, A. Munir, R. Qureshi, I. Ahmad, M.T. Soomro, Z.-U. Rehman, *J. Electrochem. Sci. Eng.*, **3**, 19 (2013).
82. S. Raufa, J.J. Goodingb, K. Akhtara, M.A. Ghauria, M. Rahmana, M.A. Anwara, A.M. Khalid, *J. Pharm. Biomed. Anal.*, **37**, 205 (2005).
83. M. Hasanzadeh, N. Shadjou, *Mater. Sci. Eng. C. Mater. Biol. Appl.*, **61**, 1002 (2016).
84. A. Erdem, M. Ozsoz, *Electroanalysis*, **14**, 965 (2002).
85. M. Mallappa, B Gowda, R. Mahesh, *Pharma Chem.*, **6**, 398 (2014).
86. D. Šimkova, J. Labuda, *Curr. Anal. Chem.*, **7**, 2 (2011).
87. R. Ovádeková, J. Labuda, *Curr. Top. Electrochem.*, **11**, 21 (2006).
88. J. Labuda, A. Oliveira-Brett, G. Evtugyn, M. Fojta, M. Mascini, M. Ozsoz, I. Palchetti, E. Pale ek, J. Wang, *Pure Appl. Chem.*, **82**, 1161 (2010).
89. M.M. Aleksić, M. Kapetanović, *Acta Chim. Slov.*, **61**, 555 (2014).
90. T. Weitner, I. Batini -Haberle, *ADMET DMPK*, **2**, 185 (2014).
91. T. Weitner, I. Kos, Z. Mandic, I. Batinic-Haberle, M. Biruš, *Dalton Trans.*, **42**, 14757 (2013).
92. A. Budimir, T. Šmuc, T. Weitner, I. Batinic-Haberle and M. Biruš, *J. Coord. Chem.*, **63**, 2750 (2010).
93. T. Weitner, A. Budimir, I. Kos, I. Batinic-Haberle, M. Biruš, *Dalton Trans.*, **39**, 11568 (2010).
94. S. Plattner, R. Erb, J. Chervet, H. Oberacher, *Anal. Bioanal. Chem.*, **406**, 213 (2014).
95. J. Sochor, J. Dobes, O. Krystofova, B. Ruttkay-Nedecky, P. Babula, M. Pohanka, T. Jurikova, O. Zitka, V. Adam, B. Klejdus, R. Kizek, *Int. J. Electrochem.Sci.*, **8**, 8464 (2013).
96. J. Comer and K.Y. Tam, in *Pharmacokinetic Optimization in Drug Research: Biological, Physicochemical and Computational Strategies* (B. Testa, H. Van De Waterbeemd, G. Folkers, and R. Guy, eds.), Verlag Helvetica Chimica cta, Zürich, 2 1, p. 275.
97. M. Velický, A.N.J. Rodgers, R.A.W. Dryfe, K. Tam, *ADMET DMPK*, **2**, 143-156 (2014).
98. G. Bouchard, A. Pagliara, G. P. Van Balen, P. A. Carrupt, B. Testa, V. Gobry, H. H. Girault, G. Caron, G. Ermondi, R. Fruttero, *Helv. Chim. Acta*, **84**, 375 (2001).
99. S. M. Ulmeanu, H. Jensen, G. Bouchard, P.A. Carrupt, H. Girault, *Pharm. Res.*, **20**, 1317 (2003).
100. R. Gulaboski, F. Borges, C. Pereira, M. Cordeiro, J. Garrido, A. Silva, *Comb. Chem. High Throughput Screen.*, **10**, 514 (2007).
101. L. Yudi, A. Baruzzi, V. Solis, *J. Electroanal. Chem.*, **360**, 211 (1993).
102. K. Kontturi, L. Murtomaki, *J. Pharm. Sci.*, **81**, 970 (1992).
103. M. Velický, K. Tam, R. Dryfe, *J. Electroanal. Chem.*, **683**, 94 (2012).
104. R.A. Fernandez, M.I. Velasco, L.I. Rossi, S.A. Dassie, *J. Electroanal. Chem.*, **650**, 47 (2010).
105. L.M. Yudi, E. Santos, A.M. Baruzzi, V.M. Solis, *J. Electroanal. Chem.*, **379**, 151 (1994).
106. G. Bouchard, A. Pagliara, G.P. Van Balen, P.A. Carrupt, B. Testa, V. Gobry, H.H. Girault, G. Caron, G. Ermondi, R. Fruttero, *Helv. Chim. Acta*, **84**, 375 (2001).

107. F. Reymond, G. Steyaert, P.A. Carrupt, D. Morin, J.P. Tillement, H.H. Girault, B. Testa, *Pharm. Res.*, **16**, 616 (1999).
108. R.P. Nia, B. Su, M.A. Mendez, J.M. Barbe, Z. Samec, H.H. Girault, *J. Electroanal. Chem.*, **656**, 147 (2011).
109. F. Reymond, V. Chopineaux-Courtois, G. Steyaert, G. Bouchard, P. A. Carrupt, B. Testa, and H.H. Girault, *J. Electroanal. Chem.*, **462**, 235 (1999).
110. Z. Mandi , *ADMET DMPK*, **2**, 168-178 (2014).
111. L.M. Hondeghem, R.D. Miller, in *Basic and Clinical Pharmacology* (B. G. Katzung, ed.), Prentice-Hall Int. Inc., New York, 1992, p. 363.
112. E. McNeal, G. Lewandowski, J. Daly, C. Creveling, *J. Med. Chem.*, **28**, 381 (1985).
113. Z. Samec, A. Trojáněk, J. Langmaier, E. Samcová, J. Málek, *Electroanalysis*, **12**, 901 (2000).
114. K. Arai, M. Ohsawa, F. Kusu, K. Takamura, *Bioelectrochem. Bioenerg.*, **31**, 65 (1993).
115. W. Schönfeld, H.A. Kirst (Eds.), *Macrolide Antibiotics*, Birkhäuser Verlag, Basel-Boston Berlin, 2002.

.  
,  
, *HR-10000* ,  
12                    2016 .;                    16                    2016 .  
(                    )

## Spectroelectrochemical characteristics of Polypyrrole synthesized by different methods

R.-M. Apetrei<sup>1\*</sup>, G.-E. Bahrim<sup>1</sup>, G. Cârâc<sup>2</sup>

<sup>1</sup>"Dun rea de Jos" University of Galati, Faculty of Food Science and Engineering, Domneasc Street, 47, RO-800008, Galati, Romania

<sup>2</sup>"Dun rea de Jos" University of Galati, Faculty of Science and Environment, Domneasc Street, 47, RO-800008, Galati, Romania

Received October 15, 2016

Revised January 10, 2017

The present review summarizes several studies performed on polypyrrole (PPy) in order to emphasize the paramount importance of characterizing the conductive polymer both by electrochemical and spectroscopic techniques. The investigations take into account one or more of the following factors: type of polymerisation, temperature and pH during synthesis, dopant of choice etc. Initially, fundamental concepts concerning the charge transport within conductive polymers are presented, followed by recent developments both in PPy synthesis and PPy composites for various applications.

**Key words:** conductive polymers, polypyrrole, spectroscopy, electrochemistry

### INTRODUCTION

The flexibility of electric character in conductive polymers (CPs) initiated substantial perspectives for their use in a variety of applications. Since the discovery of CPs [1, 2], they have been of academic and technological interest representing a significant scientific challenge for chemists, physicists and material science researchers [3].

The main objective has been achieving a thorough understanding of their electrochemical properties as derived from their chemical structure. Besides traditional electrochemical and chemical methods of synthesis, many polymerization techniques are available including but not limited at: photochemistry, metathesis, chemical vapor deposition, UV-induced polymerisation, concentrated emulsion synthesis, plasma polymerisation etc. [4]. In addition, in pursuit of an economical and environmentally benign pathway, enzymatic synthesis was extensively researched [5].

Therefore, an overview of different characterization techniques for conductive polymers along with the similarities and discrepancies observed in these materials related to their synthesis method is proposed. The main focus will be on polypyrrole as it is representative to the field and its simplicity of synthesis and adherence

to many types of surfaces as well as stability and conductivity render it an illustrative model of analysis.

### FUNDAMENTAL CONCEPTS IN THE CHARACTERIZATION OF POLYPYRROLE

The elementary theoretical models and experimental data which were to later become the fundamentals in the characterization of conducting polymers will be assessed in this section. The first investigations of the charge mechanism in CPs were performed on electrochemically synthesized films due to simplistic and controllable deposition manner along with ability for adequate parameter setting. Factors such as: potential or current applied, solvent and supporting electrolyte are of significance affecting the structure, electrochemical and mechanical properties of the resulting polymer. The nature of the counterion, in particular, was of extended interest because the electrochemical synthesis does not render a neutral polymer in insulating state, rather it is tailoring it with conductivity and charge according to synthesis conditions [6, 7].

Yakushi et al. [8] performed an optical study on perchlorate doped PPy (33 mol %) at various stages of reduction. The as-grown PPy film was already in oxidized form as it is the case in electrochemical synthesis and applying progressive reduction potentials rendered the opportunity to analyze the polymer at intermediate oxidation stages between the conductive and the insulating form. The as-

---

To whom all correspondence should be sent:  
E-mail: roxana.apetrei@ugal.ro



grown film (highly oxidized form) revealed absorption peaks at 1.0 eV (1240 nm) and 2.7 eV (460 nm) while the highly reduced form absorbed mainly at 4.5 eV (275 nm) and 3.2 eV (387 nm). It was noticed that as the reduction increases, the absorbance bands decrease in intensity and shift to higher wavelengths, however several weak bands are common for most films. The absorption peaks at most oxidized state, were still present in the most reduced films as weak bands and vice-versa. Thus, a coexistence of the oxidized and neutral forms of PPy within the same film was considered. Therefore, it must be that the polymer chain is composed of several neutral and cationic segments of different lengths, randomly distributed within the film and that the electron hopping between segments is imparting electrical conductivity. Thereupon, Bredas et al. [9, 10] developed a theoretical model involving the concept of polarons and bipolarons in conductive polymers intrigued by the fact that electron hopping within the highly conductive films did not exhibit paramagnetic behaviour. They stated that the oxidation of the conjugated polymer leads to a localized deformation associated with charge carriers which means lengthening of double bonds and shortening of single ones along the polymer chain and upon analyzing the spectra obtained for 33% perchlorate doped PPy at intermediate states of reduction, they introduced the concepts of polaron and bipolaron charge carriers. Therefore, polarons are radical cations formed within CPs at low levels of oxidations that, upon further oxidation, pair up into double charged radical dicationic or bipolarons. Electron spin resonance (ESR) studies revealed a spin of  $\frac{1}{2}$  for cationic units while for dicationic species there was no paramagnetic signal. The high conductivity in the absence of paramagnetism was thus, to be related to double charged spinless bipolarons. The theoretical model was supported by optical, magnetic and structural data.

Albeit the resemblance of electric nature between conductive polymers and semiconductors, the two systems are elementary different. Conventional semiconductors display three-dimensional structures while conductive polymers consist of conjugated one-dimensional chains. Accordingly, they do not obey semiconductor type of behaviour, their conductivity being an intrinsic property upon exposing them (e.g. polyacetylene) to oxidation or reduction. This process was referred to as doping analogous with the doping of inorganic semiconductors, however it is an oxidoreduction reaction [11]. The facility of oxidation/reduction is related to the conjugated character of the polymer

which renders a facile removal or inclusion of electrons into the chain with little disruption of bonds. The electrical susceptibility of the material is given by the width of the bandgap, the gap between the highest occupied molecular orbitals (HOMO) or valence band and the lowest unoccupied molecular orbitals (LUMO) or the conduction band. The movement of charges between these two bands leads to conductive behaviour. Taking for instance, the oxidation i.e. expulsion of an electron from the conjugated chain will lead to the appearance of localized electronic states inside the gap [12] such as two polaron levels: the lower polaron level represented by the bonding cation level (BCL) and the upper polaron level or the antibonding cation level (ACL). Removal of a second electron would generate two bonding and antibonding dication levels (BDL/ADL) [13]. Thus, the dication state is not to occur at low levels of oxidation yet predominant at high doping levels. Still, the question remained, whether if bipolaron formation is thermodynamically favorable i.e. the energy required to form a dication is less than that of generating two radical cations as well as the stability of this state. Worth noting is that polyacetylene possesses a degenerate ground state which accounts for two structures with the same energy allowing alternation of single and double bonds within the chain, while heterocycles have a nondegenerate ground state i.e. a single possible geometric structure. The polaron formation within aromatic CPs corresponds to soliton carriers in polyacetylene [3].

Genies and Pernaut [14] undertook an optical study of polypyrrole in order to characterize the kinetics of the radical cation and dication charges in correlation with the redox properties of the polymer by recording the species equilibrium during potential cycling. The electrochemical cycling of the PPy films describe a typical redox system around  $-0.2$  V. Extra oxidation peak is assigned to leftover monomer in the film, consequently polymerized as it is catalytically favorable at low scan speed while an extra reduction peak proves a two-step electron transfer. Extended cycling leads to polymer degradation with consequences such as electroactivity loss. In terms of optical spectroscopy, PPy exhibits absorption peaks according to its redox state, as expected. The absorbance band at 3.4 eV (370 nm) due to  $\pi \rightarrow \pi^*$  or valence band (VB) conduction band (CB) transition is specific to the reduced state of the polymer. The oxidized state corresponds to several peaks: 2.8 eV (440 nm) related to valence band

(VB) antibonding cation/dication level (ACL/ADL); 2.3 eV (540 nm) due to bonding cation level (BCL) antibonding cation level (ACL). The transition from valence band to bonding cation/dication level (BCL/BDL) was not recorded. The experiment consisted of plotting the absorbance areas described previously against the oxidation level.

The peak at 3.4 eV (interband transition) fades as the oxidation increases probably due to the appearance of intermediate gap states. The absorption peaks at 2.8 eV and 2.3 eV are increasing as the oxidation increases as long because charge is distributed along polaron species. Decreasing of these two absorption peaks leads to the belief that radical cations are starting to pair forming dications. The results are consistent with the transition from neutral PPy to the formation of cationic (PPy<sup>+</sup>) and dicationic (PPy<sup>2+</sup>) as molecular orbitals move closer to each other within the gap corresponding to the structure modification from non-conjugated to conjugated aromatic and to quinoid type units, respectively [15]. Nechtschein et al. [16] varied the redox properties of a polypyrrole film by applying different voltages and assessed the doping level by ESR and optical analysis stating that the bipolaron species is more difficult to characterize due to lack of paramagnetic signal. However, for CPs with a non-degenerate ground state it has been of essential importance. Patil et al. [17] published an extensive review regarding optical properties of conductive polymers assigning the 1.4 eV absorption band recorded previously [8, 10] in the spectra of mildly oxidized PPy as polaronic peak seeing how it fades at higher oxidation state, while the absorption at 1 eV and 2.7 eV was correspondent to bipolaronic charges. A discussion on solitons versus polarons and bipolarons is presented by constructing an analogy between polyacetylene and polythiophene. It is also disclosed that charged species are not confined to a solid state of the material they are present in liquid solution as well, owing to their intrinsic molecular nature.

A multitude of parameters can affect the mobility and distribution of charge carriers thus optical spectroscopy is not to be solely relied upon but further investigations through electrochemical and structural techniques are to be performed. Furukawa et al. [18] correlated Raman and optical absorption spectroscopy to distinguish the vibrational signals correspondent to charge carriers in polypyrrole at intermediate oxidation stages. Their study indicated that radical cations and dications coexist in highly oxidized form of PPy

and as the polymer is reduced, dications turn into cations, which are further converted in neutral species. Zhong et al. [19] performed a comparison between theoretic kinetic predictions based on the polaron/bipolaron model and experimental in situ ESR data. As seen from an electrochemical perspective, the formation of the polaron state and evolution to bipolaron is a function of the potential applied. Different investigation had led to contradicting theories about the species accountable for the charge transfer in PPy chain. While Bredas et al. [10] stated that bipolaron formation is thermodynamically more favorable than formation of two different polarons, Nechtschein et al. [16] estimated that the energy necessary for both processes is similar which is why the bipolaron state is questionable. Since the electric properties of PPy do not rely only on bipolaron formation and proof of polaron state was attained at least at low doping levels, determining the stability of the charge carriers was demanded. Raman spectroscopy was employed in order to observe the structural changes of the polymer chain simultaneously with charge carrier detection by ESR. Charge injections onto a reduced film of PPy led to following observations at intermediate oxidation stages: paramagnetic signal increases until a certain point after which it decreases; C=C backbone stretching vibration band is blue shifted upon applied potential as double conjugated bonds are lengthened and the polymer chain is transitioning from benzenoid to quinoid structure.

John et al. [20] employed resistometry in analogy with voltammetry for the characterization of redox properties for PPy-nitrate films. The insights gained were related to the kinetics of the switching mechanism in conductivity such as the degree of change in resistance, the potential at which it occurs and the rate versus applied potential. Both voltammetry and resistometry revealed how the intrinsic conductivity of CPs varies with potential and provided information about the charge required to trigger this mechanism. Kaplin and Qutubuddin [21, 22] tested five different potentials for synthesizing PPy for two different electrolyte systems: sodium perchlorate and p-toluenesulfonate. The redox behaviour of polypyrrole consists of electron transfer either to or from PPy along with counterion insertion or repulsion from polymer matrix for reaching charge neutrality. In this sense the polymer exhibits switching ability from conductor to insulator. Upon voltammetric cycling, it was observed that the films prepared at potential of 1.0 V display one redox exchange with oxidation-

reduction peaks positioned symmetrically, while the films prepared at lower potentials such as 0.6 or 0.75V reveal an oxidation yet two reduction peaks.

Films obtained at potentials higher than 1.0 V such as 1.5 V or 2 V do not display symmetrical peaks. It was determined that two reduction peaks are proof of the presence of both polarons and bipolarons within the polymer chain. Bipolarons are attained in this case due to the perchlorate ion, such behaviour not being observed for the toluenesulfonate-doped PPy. In addition, by analysis of the chronoamperometric response to the applied potential during electrosynthesis, the incorporation of hydroxyl or carbonyl groups into the polymeric chain can be detected by distinctive ceasing of the process. Lower potential leads to a polymer film less susceptible for overoxidation because the oxidation of the electrode occurs slowly, while for higher potentials the electrode oxidizes faster contributing to adhesion of termination groups to the electrode surface blocking pyrrole. Thus, overoxidation of the polymer starts after 1.0 V and can be considered independent on the electrolyte. However, structural properties are subordinate to the dopant of choice. ESR spectroscopy was employed for studying the polaron:bipolaron ratio in the polymer film according to applied potential and results showed that films prepared at lower potentials had lower spin concentration i.e. preponderance of bipolaron states while in films prepared at 1.0 V, cationic species prevailed rendering higher paramagnetic signal.

Lee et al. [23] synthesized PPy in a chemical manner using dodecylbenzenesulfonic acid (DBSA) as dopant and ammonium persulfate (APS) as oxidant. The polymer was soluble in m-cresol and mildly soluble in other solvents. Even though PPy is usually hard to process due to strong intra and interchain crosslinking, doping a large molecule able to reduce such interactions as well as the monomer:oxidant ratio made it accessible. The PPy obtained was slightly overoxidized as shown by elemental analysis and had low molecular weight, yet exhibited prolonged reactivity during CV. Demoustier-Champagne and Stavaux [24] synthesized PPy in an electrochemical manner in polycarbonate membranes with different pore sizes using four different dopants discussing the consequences on the morphology and conductivity of the polymer.

Aguiar-Hernandez and Potje-Kamloth [25] performed a spectroelectrochemical study on a polypyrrole – polyoxyphenylene composite prepared by potentiostatic technique at alkaline pH

using 4-hydroxybenzenesulfonate (4HBS) as dopant. A slight overoxidation of the composite film was observed, however, the polymer retained a conductive character. It was stated that an increased polymerisation potential led to the evolution of polypyrrole from a quinoid to a benzenoid type structure as observed from infrared spectra which is generally associated with intrusion of carbonyl groups within the polymer's backbone which can terminate the conjugated length and affect the conductivity. C=O groups disrupt the delocalization of electrons along the polymer creating defects in the - conjugated chain. Their presence is regarded as imparted by the high deposition potential and high pH. Zhou and Heinze [26-28] defined three types of structural PPy entities differentiated by the degree of conjugation and conductivity focusing on the analysis of the electrolyte used in the electrosynthesis. Hence, pure conductive PPy or PPy (I) can be obtained in non-acidic media, even low acidity leads to PPy (II) while high acidity passivates the electrode due to formation of nonconductive low conjugated PPy (III). Elemental analysis can provide an approximation of the doping content by the ratio between different nitrogens. Three types of N atoms were identified in oxidized PPy while in neutral form only one type of nitrogen was detected. Further Raman spectroscopy connected with cyclic voltammetry was employed for studying the charging/discharging mechanism of a nitrate PPy film upon doping as reported by Liu et al. [29]. The structural change in PPy during redox switching was examined by in situ cyclic voltammetry - surface enhanced Raman spectroscopy (CV-SERS). SERS measurements were performed while the film was being cycled and for each potential the corresponding Raman peaks were identified. Thus, the peak corresponding to C-H in plane deformation did not shift either in the anodic or cathodic scan, the peak assigned to C=C backbone, correspondent to reduced form of PPy in cathodic scan, shifted toward higher frequency during anodic scan as expected [19] and the peaks assigned to ring deformation and N-H in-plane deformation transited to lower and higher wavenumbers with anodic and respectively, cathodic scan. It can be assessed that the C-H in plane deformation is autonomous of the PPy redox behaviour, the conjugated lengthening occurs during oxidation while the nitrate counterions are incorporated into the cationic polymer to neutralize the charge. Joo et al. [30] reported a comparison between charge transport and structural properties of three differently synthesized pyrrole polymers. While the

electrochemically prepared PPy was doped with hexafluorophosphate (PF<sub>6</sub>) the chemical ones included dodecylbenzenesulfonic acid (DBSA) or naphthalenesulfonic acid (NSA). The comparison concluded that the PPy-DBSA and PPy-NSA displayed the insulating soluble polymer state due to the large size dopants which reduced interchain links, while PPy-PF<sub>6</sub> had a high concentration of interchain links contributing to charge hopping and conductive behaviour. Density of states was higher in electrochemically prepared polymer rather than in chemical ones. However, neither the effects of large dopants within electrosynthesized polymer films nor the influence of highly mobile species in chemically prepared polymer were evaluated.

Upon attaining these fundamental concepts, innovation in the field of conductive polymers was impeding. For further inquiry in the elementary mechanisms of pyrrole synthesis either by chemical or electrochemical means and the resulting properties, the reader is referred to Sadki et al. [31] and Ansari [32] for comprehensive reviews.

#### ADVANCES IN THE PREPARATION AND CHARACTERIZATION OF POLYPYRROLE

Having established the basic redox processes as well as structural modifications occurring within PPy when switching between its conducting and insulating state, a series of modifications were proposed for tailoring the polymer for specific applications. Continuous involvement in the characterization of polypyrrole is imperative in order to find an equilibrium between functionality and processability. Several pathways for modification are available either by functionalization of the monomer with functional groups preceding the polymerisation or by in situ inclusion of counterions and/or template molecules [33].

Liu et al. [34] synthesized PPy by chemical vapor deposition on metallized Nafion® electrodes for diminishing the aging issue encountered in hydrogen sensors. The results were adequate for anti-aging properties, however a loss in sensitivity emerged. Heinze and co-workers [35] have made further progress in preparing different entities of polypyrrole providing new insights in the structural diversity of the polymer. Two types of transporters within different PPy variants, mobile and immobile charge carriers are considered, the former contributing to polymer conductivity and the latter to the formation of a crosslinked network. PPy (I) and PPy (III) are able to transfer only anionic compounds, while PPy (II) is capable of motioning both anions and cations. Morphological and mass

changes within the polymer on this basis were addresses by Cohen et al. [36]. Masuda and Asano [37] provided a short note consisting of the spectroelectrochemical characterization of PPy synthesized galvanostatically with sodium alkylbenzenesulfonate dopants. The UV-Vis-NIR spectra were fairly independent of the chosen dopant molecule while in voltammetric cycling just the cathodic peak, otherwise associated with removal of counterions from the polymer matrix, was distinct dopant-wise.

Omastova et al. [38] employed chemical synthesis of pyrrole in aqueous media in the presence of different types of surfactants (anionic, cationic, neutral) in an attempt to identify the nature of the interaction between them. Conclusions were that anionic surfactants develop an ionic bond with the polymer adding to the process as dopants, increasing the polymerisation rate, while cationic ones have the reverse effect. The surfactant addition to polypyrrole led to good conductivity as well as stability towards deprotonation due to the hydrophobic nature of the surfactant. He et al. [39] synthesized novel structures of PPy so-called "coral-like nanowires" in a ferric chloride – based aqueous chemical polymerisation with the addition of dodecyl-benzene sulfonic acid (DBSA) and poly(vinyl-alcohol) (PVA). The improved structural morphologies increased the electrochemical properties of PPy as assessed by temperature-dependent conductivity measurements.

Can et al. [40] investigated the interactions between protons or Lewis acids and pyrrole from both theoretical and experimental perspectives. It was ascertained that both proton and Lewis acids act through similar mechanisms leading to pyrrole oligomers and possible addition to the polymer's backbone. Pokrop et al. [41] reported the preparation of processable PPy by using ammonium peroxydisulfate as oxidant and salts of sulfosuccinic acid diesters as dopants attempting a counter-ion provided processability [42]. A highly conductive polymer is known to be intractable due to its ionic nature, so hardly solvable, while a certain degree of processability leads to a decrease in conductivity. A compromise between the two is to be attained. Spectroelectrochemical properties of the obtained PPy were assessed with UV-Vis-NIR and cyclic voltammetry techniques.

Benabderrahmane et al. [43] functionalized pyrrole with N-succinimidyl ester and performed in situ copolymerization in presence of polystyrene latex particles using FeCl<sub>3</sub> as oxidizer. Spectroscopy and elemental analysis of the composite particles were performed pursuing

reactivity towards amine and thiol groups for further attachment of proteins in biomedical applications. Hien et al. [44] tested a double layer of PPy for protection against iron corrosion. They manipulated the PPy by doping the outer film with dodecyl sulfate anions and the inner one with tetraoxalate anions in order to modify the permselectivity of the film from anion to cation exchanger impeding the intrusion of chloride anions. Xu et al. [45] took advantage of the redox switching mechanism of PPy and explored the hydrophobic – hydrophilic switch, the wettability of solid surfaces being of increased interest. Certainly, the dopant of choice has prevalent influence upon water contact behaviour and the switchable wettability resulted to be a function of applied potential.

Cong et al. [46] developed multi-composite electrodes consisting of polypyrrole and mixed oxides on a glassy carbon electrode: GC/PPy/PPy(Ox)/PPy. The electrocatalytic activity towards oxygen reduction (orr) was found to be highly dependent on the electrochemical properties of PPy. The oxygen reduction reaction proceeds at the oxide layer while the polymer is accounted for charge transportation. As electrochemical behaviour is highly susceptible to the anionic dopant used, samples doped with different small size anions (Cl<sup>-</sup>, ClO<sub>4</sub><sup>-</sup>, PF<sub>6</sub><sup>-</sup>, NO<sub>3</sub><sup>-</sup>, SO<sub>4</sub><sup>2-</sup>) were analyzed by cyclic voltammetry. Highest redox activity was registered by chlorate doped PPy in agreement with conductivity measurements and absorption spectra which showed the effect of the doping agent by a hypsochromic shift of  $\lambda_{max}$  from 419 nm (Cl<sup>-</sup>) to 404 nm (SO<sub>4</sub><sup>2-</sup>). Similar composite type of electrodes was developed by Singh et al. [47] using CoFe<sub>2</sub>O<sub>4</sub> nanoparticles resulting in a desirable electrocatalytic response.

Bufon et al. [48] undertook the study of voltammetric cycling in relation to the polymeric chain length and conductivity. Two different PPy entities are identified as a function of temperature and applied potential. Shorter chains and higher conductivity are assigned to PPy II in accordance with disorder dominated transport i.e. delocalization of charge with an increased localization length occurring in shorter chains. Thus, chain length is not considered primarily relevant for assessing CPs conductivity. PPy II it is the species produced when lower temperature or potential are employed during polymerization and it readily transforms into PPy I during CV. The two types of PPy were clearly distinguished both in cyclic voltammetry and optical absorption analysis. In voltammetric cycling, an oxidation peak at -0.12 V

is assigned to PPy II, while the peak at +0.1 V relates to PPy I oxidation. Similarly, an absorption band at 386 nm corresponds to PPy II, while absorption between 450 and 470 nm is caused by PPy I owing to the significantly longer polymer chain which has higher extinction coefficient. Previously, the fact that the wavenumbers of CPs are scaling linearly to the reverse of the polymerisation degree was determined. Thereby, the longest the polymer chain is, the higher the wavelength at which will absorb light [49].

Hwang et al. [50] investigated the changes in mass and volume of PPy doped with perchlorate upon pH variation. The paramount redox switching property can be not only a measure of applied potential, but also adjustable through pH manipulation. In contact with basic solutions, PPy experiences deterioration due to the attack of hydroxyl ions on the  $\alpha$ -carbons along with anion expulsion leading to neutral and insulating forms. Contrary, immersion in acidic media recovers, at least partially, the former electric properties of PPy. Quantification of mass and volume changes in the polymer chain when varying the pH was performed using atomic force microscopy and quartz crystal nanobalance. With increasing pH, the mass of the polymer was found to decrease as anion expulsion occurs, while an increasing mass during anion incorporation due to protonation of nitrogen sites within the polymer is noticed during the pH drop. Anion incursion is a slower mechanism than anion discharge.

Kim et al. [51] prepared carbon nanotube/polypyrrole composites with controlled pore size using nanosized silica embedded into CNT during electrodeposition. The composites contained around 80% nanosized polymer and provided facile ion transport at electrode level along with conductivity and higher surface area. Ayad et al. [52] employed PPy as host for entrapping noble metals by chemical synthesis using hydrochloride and ferric chloride. Subsequently, the polymer was de-doped using ammonia and exposed to silver nitrate for reduction of the Ag ions. The silver-PPy composite can be applied for silver detection. Parakhonskiy et al. [53] developed PPy microcontainers by electrochemical synthesis in the presence of a surfactant (*n*-naphthalene sulfonic acid) for obtaining polypyrrole shells at the surface of the oxygen bubbles generated during the monomer oxidation. The resulted polymer shells exhibited high redox activity and controllable permeability.

Sharifirad et al. [54] probed PPy as coating against copper corrosion and estimated the

efficacy with potentiodynamic polarization and electrochemical impedance techniques. Three different dopants were tested for the electrodeposition of polypyrrole on copper from aqueous media and the final polymer provided efficient corrosion protection despite being slightly overoxidized as observed from FTIR spectroscopy. Cui et al. [55] devised nanowires consisting of polypyrrole and SnO<sub>2</sub> nanoparticles by one-pot chemical oxidation. The SnO<sub>2</sub>-PPy composites showed high potential for anode materials for lithium-ion batteries due to good electrochemical properties. Madani et al. [56] prepared polypyrrole/cadmium sulfide composites by electropolymerisation in presence of CdS nanoparticles for applications in optoelectronics. Even though a high concentration of nanoparticles leads to increased resistance, electroactivity is still remnant as displayed by cyclic voltammetry. Moreover, electrical impedance indicates increased capacitance and photoconductivity. Arjomandi et al. [57] prepared and characterized polypyrrole and poly(pyrrole-2,6-dimethyl- $\beta$ -cyclodextrin) [P(Py-DMCD)]. Differences between the two polymers are discussed in respect to their structural and electrochemical properties.

Zhang et al. [58] developed polypyrrole/graphene nanosheets (PPy/GNS) composite electrodes by in situ chemical polymerisation to obtain higher specific capacitance for supercapacitors. Graphene represents a single atomic plane of graphite and the association with polypyrrole leads to high conductivity within a single layer network. FTIR spectroscopy reveals a shift in main peaks upon addition of graphene which is associated with so-called graphene doping of PPy i.e. introduction of GNS groups into the PPy backbone. Concerning the electrochemical properties, cyclic voltammetry and charge-discharge measurements proved good capacitive behaviour. Konwer et al. [59] studied the influence of graphene oxide (GO) in association with polypyrrole for electrode applications. Subsequently, the composites were investigated by UV-Vis and FTIR spectroscopy for identification of structural changes while conductivity and CV attested to enhanced electrochemical characteristics most probably due to extension of conjugated segments within PPy owing to the interaction with GO.

Wang and Yu [60] analyzed the dopant influence on the polaron:bipolaron ratio in PPy synthesized chemically with three different anions: chloride (Cl<sup>-</sup>), p-toulensulfonate (p-TS<sup>-</sup>) and anthraquinone-2-sulfonate (AQS<sup>-</sup>). While the

conductivity of CPs is commonly determined by resistance measurements, more insights into their electrical behaviour is to be acquired by analyzing the origin of it i.e. the charged species within the polymer chain. Thus, the present study aims to prove the charge-carrier distribution dependency on the chosen dopant molecule. ESR and Raman spectroscopy techniques were employed for gathering information about paramagnetic and structural behaviour of the samples along with UV-Vis-NIR, FTIR. NIR absorption assigned higher charge mobility according to chosen dopant in the following order Cl<sup>-</sup> < p-TS<sup>-</sup> < AQS<sup>-</sup> in agreement with conductivity measurements. Raman spectra displayed both radical cation and dication bands attesting that bipolarons are prevalent in PPy: AQS<sup>-</sup> and polarons in PPy: Cl<sup>-</sup> and PPy: p-TS<sup>-</sup> which leads to adequate correlation between charge distribution and electrical properties.

Functionalization of PPy was thoroughly addressed by Singh et al. [61] in a review on the characterization and synthesis of polypyrrole composites.

#### CHARACTERIZATION OF BIOSYNTHESIZED POLYPYRROLE

The current requirement for environmentally friendly pathways towards obtaining technologically important polymers has been widely documented. Though not the scope of the present review, enzymatic or otherwise greener methods for the polymerisation of PPy cannot be overlooked in an attempt gain understanding on spectral and electrochemical properties of the polymer.

Nabid and Entezami [62] synthesized a water-soluble polypyrrole in the presence of horseradish peroxidase (HRP) using sulfonated polystyrene (SPS) as counterion at pH 2. The use of templates in this process was crucial for attaining chain alignment and low pH, both imperative for a qualitative final product. UV-Vis analysis was used for proving a certain redox reversibility of the polymer during adjustment of pH. Adsorption peaks at 440 and 600 nm were used as reference points. Song and Palmore [63] attempted the polymerisation of pyrrole using laccase. The investigation is significant due to its environmental benign character however the process was rather slow in the absence of a redox mediator. They employed 2,2'-azino-bis-(3-ethylbenzthiazoline-6-sulfonic acid) (ABTS) diammonium salt as mediating molecule, which is easily oxidized by laccase being able, in turn, to oxidize the pyrrole monomer. In this sense, the synthesis does not take

place through an enzymatic mechanism, but rather through a biocatalytic mediated chemical one. ABTS was incorporated in the polymeric chain as a counterion, found to be in ratio of one to each 5 pyrrole units regardless of its concentration and improved charge transport and mechanical properties of PPy. The use of an enzyme for ABTS regeneration made continuous reaction possible as opposite to electrochemical generation of ABTS cations. Additionally, as the potential necessary for lengthening the polymeric chain decreases, the reaction between laccase and pyrrole multimers becomes thermodynamically more favorable. Cui et al. [64] prepared polypyrrole through a biocatalytic route assembling composites consisting of lactate oxidase – PPy – CNT. UV-Vis spectroscopy revealed the level of oxidation of the polymeric chain according to the polaron/bipolaron model. Absorbance bands at 460 nm and subsequently, at 570 nm are considered proof of polaron charge formation, however the mild oxidation did not lead to the development of bipolaron states. The length of the polymeric chain was considered high according to reported investigations [48]. The hybrid nanocomposites were tested for biosensors for lactate detection. Ramanavicius et al. [65] realized a spectrophotometric study of pyrrole polymerisation oxidized by hydrogen peroxide produced from glucose oxidase (GOx) - glucose reaction and further on, employed the mechanism for detecting the adhesion of oxidoreductases at the electrode surface [66].

Cruz-Silva et al. [67] employed horseradish peroxidase for pyrrole oxidation, but since the monomer is not a usual substrate for the enzyme, a redox mediator was necessary. Elemental and thermogravimetric analysis revealed high similarities with chemically synthesized PPy. Kupriyanovich et al. [68] adopted a similar system and reported an increased conductivity upon addition of sodium polystyrene-4-sulfonate among other dopants. Certainly, under synthesis conditions, infrared spectroscopy displayed vibration band corresponding to carbonyl group i.e. overoxidation of the polymer, which is the case with most enzymatic pathways of polymerisation. Further on, encapsulation of laccase in PPy shells was reported by Mazur et al. [69] by droplet/solution interface synthesis. The microcontainers as studied by visible spectroscopy, revealed increasing absorption peak at 480 nm corresponding to low level of doping. FTIR spectra displayed proof of laccase encapsulation within PPy shells while cyclic voltammetry showed a typical redox system. Bouldin et al. [70] considered

soybean peroxidase (SBP) a more suitable enzyme for pyrrole oxidation and without using a redox mediator, generated a conductive polymer as revealed from conductivity and UV-Vis absorption spectra. However, various template-dopants were tested for improving final properties. Junker et al. [71] performed a study on laccase-induced polymerisation of pyrrole using sodium bis-(2-ethylhexyl) sulfosuccinate anionic vesicles as templates. The process was optimized and the final products characterized by optical, EPR and FTIR spectroscopy indicating a conductive form of PPy. Moreover, MD simulations were performed in order to investigate the regulatory influence of the template within the synthesis.

Regarding environmentally benign routes for pyrrole polymerisation it can be concluded that the genuine enzymatic pathways proceed slowly and they must be improved by addition of redox mediators, oxidative compounds and/or templates. The aqueous media and neutral pH, while suitable for enzymes, promotes the production of low molecular weight oligomers due to the nucleophilic attack of water on the polymer. In turn, a branched structure of the polymer is consistent with loss in electric properties. Nevertheless, most enzymes are not stable at highly acidic pH. However the potential for biomedical applications is indisputable, thus intensive research is being progressively conducted [5].

## CONCLUSIONS

By attempting to determine the parameters that govern the equilibrium of charged species within the redox polymers, the aforementioned researchers set the basis for the characterization of conductive polymers. Following their breakthrough, extensive research and improvement has been made. However, the significance of the fundamental concepts is not to be disregarded.

Certainly, the present review could not comprise the amplitude of research conducted within the field, but the main purpose of displaying the evolution in the characterization and application of polypyrrole was fulfilled. Even after decades of investigating conducting polymeric materials, inquiries related to synthesis, reaction mechanisms and dopant influence are still valid. Nevertheless, innovative and promising applications are widely researched.

## REFERENCES

1. A. Diaz, K. K. Kanazawa, G. P. Gardini, *J. Chem. Soc. Chem. Commun.*, 635 (1979).

2. H. Shirakawa, E. J. Louis, A. G. MacDiarmid, C. K. Chiang, A. J. Heeger, *J. Chem. Soc. Chem. Commun.*, **578** (1977).
3. J.-L. Bredas, G. B. Street, *Accounts Chem. Res. Am. Chem. S.*, **18**, 309 (1985).
4. D. Kumar, R. C. Sharma, *Eur. Polym. J.*, **34**, 1053 (1998).
5. R. Cruz-Silva, P. Roman, J. Romero, in: *Biocatalysis in polymer chemistry*, K. Loos (ed.), Wiley-VCH Verlag GmbH & Co., 2010, p. 187.
6. P. S. Tóth, B. Endr di, C. Janáky, C. Visy, *J. Solid State Electrochem.*, **19**, 2891 (2015).
7. C. Visy, J. Lukkari, T. Pajunen, J. Kankare, *Synth. Met.*, **33**, 289 (1989).
8. K. Yakushi, L. J. Lauchlan, T. C. Clarke, G. B. Street, *J. Chem. Phys.*, **79**, 4774 (1983).
9. J.-L. Bredas, R. Silbey, D. S. Boudreaux, R. R. Chance, *J. Am. Chem. S.*, **105**, 6555 (1983).
10. J.-L. Bredas, J. C. Scott, K. Yakushi, G. B. Street, *Phys. Rev. B.*, **30**, 1023 (1984).
11. A. Gregušová, Š. Varga, I. ernušák, J. Noga, *J. Phys. Chem. B.*, **106**, 10523 (2002).
12. R. G. Pearson, in: *Chemical reactivity theory. A density functional view*, P. K. Chattaraj (ed.), vol. 11, CRC Press, 2009.
13. J.-M. Andre, J. Delhalle, J.-L. Bredas, in *Quantum Chemistry Aided Design of Organic Polymers*, World Scientific, 2012, p. 163.
14. E. M. Genies, J. M. Pernaut, *J. Electroanal. Chem. Interfac.*, **191**, 111 (1985).
15. B. Tian, G. Zerbi, *J. Chem. Phys.*, **92**, 3892 (1990).
16. M. Nechtschein, F. Devreux, F. Genoud, E. Vieil, J. M. Pernaut, E. Genies, *Synth. Met.*, **15**, 59 (1986).
17. A. O. Patil, A. J. Heeger, F. Wudl, *Chem. Rev.*, **88**, 183 (1988).
18. Y. Furukawa, S. Tazawa, Y. Fujii, I. Harada, *Synth. Met.*, **24**, 329 (1988).
19. C. J. Zhong, Z. Q. Tian, Z. W. Tian, *J. Phys. Chem. Am. Chem. S.*, **94**, 2171 (1990).
20. R. John, A. Talaie, G. G. Wallace, S. Fletcher, *J. Electroanal. Chem. Interfac.*, **319**, 365 (1991).
21. D. A. Kaplin, S. Qutubuddin, *Polymer*, **36**, 1275 (1995).
22. D. A. Kaplin, S. Qutubuddin, *J. Electrochem. Soc.*, **140**, 3185 (1993).
23. J. Lee, D. Kim, C. Kim, *Synth. Met.*, **74**, 103 (1995).
24. S. Demoustier-Champagne, P.-Y. Stavaux, *Chem. Mater.*, **11**, 829 (1999).
25. J. Aguilar-Hernández, K. Potje-Kamloth, *PCCP*, **1**, 1735 (1999).
26. M. Zhou, J. Heinze, *Electrochim. Acta*, **44**, 1733 (1999).
27. M. Zhou, J. Heinze, *J. Phys. Chem. B.*, **103**, 8443 (1999).
28. M. Zhou, J. Heinze, *J. Phys. Chem. B.*, **103**, 8451 (1999).
29. Y.-C. Liu, B.-J. Hwang, W.-J. Jian, R. Santhanam, *Thin Solid Films*, **374**, 85 (2000).
30. J. Joo, J. K. Lee, S. Y. Lee, K. S. Jang, E. J. Oh, A. J. Epstein, *Macromolecules*, **33**, 5131 (2000).
31. S. Sadki, P. Schottland, N. Brodie, G. Sabouraud, *Chem. Soc. Rev.*, **29**, 283 (2000).
32. R. Ansari, *E- J. Chem.*, **3**, 186 (2006).
33. K. Jüttner, K.-M. Mangold, M. Lange, K. Bouzek, *Russ. J. Electrochem.*, **40**, 317 (2004).
34. Y.-C. Liu, B.-J. Hwang, W.-C. Hsu, *Sens. Actuator B-Chem.*, **87**, 304 (2002).
35. M. Zhou, M. Pagels, B. Geschke, J. Heinze, *J. Phys. Chem. B.*, **106**, 10065 (2002).
36. Y. S. Cohen, M. D. Levi, D. Aurbach, *Langmuir*, **19**, 9804 (2003).
37. H. Masuda, D. K. Asano, *Synth. Met.*, **135**, 43 (2003).
38. M. Omastova, M. Trchova, J. Ková ová, J. Stejskal, *Synth. Met.*, **138**, 447 (2003).
39. C. He, C. Yang, Y. Li, *Synth. Met.*, **139**, 539 (2003).
40. M. Can, H. Özaslan, N. Ö. Pekmez, A. Yıldız, *Polymer*, **45**, 7011 (2004).
41. R. Pokrop, M. Zagórska, M. Kulik, I. Kulszewicz-Bajer, B. Dufour, P. Rannou, A. Pron, E. Gondek, J. Sanetra, *Mol. Cryst. Liq. Cryst.*, **415**, 93 (2004).
42. Y. Cao, P. Smith, A. J. Heeger, *Synth. Met.*, **48**, 91 (1992).
43. S. Benabderrahmane, S. Bousalem, C. Mangeney, A. Azioune, M.-J. Vaulay, M. M. Chehimi, *Polymer*, **46**, 1339 (2005).
44. N. T. Hien, B. Garcia, A. Pailleret, C. Deslouis, *Electrochim. Acta*, **50**, 1747 (2005).
45. L. Xu, W. Chen, A. Mulchandani, Y. Yan, *Angew. Chem. Int. Ed.*, **44**, 6009 (2005).
46. H. N. Cong, K. El Abbassi, J. L. Gautier, P. Chartier, *Electrochim. Acta*, **50**, 1369 (2005).
47. R. N. Singh, B. Lal, M. Malviya, *Electrochim. Acta*, **49**, 4605 (2004).
48. C. C. Bof Bufon, J. Vollmer, T. Heinzl, P. Espindola, H. John, J. Heinze, *J. Phys. Chem. B.*, **109**, 19191 (2005).
49. G. Zotti, S. Martina, G. Wegner, A.-D. Schlüter, *Adv. Mater.*, **4**, 798 (1992).
50. J.-H. Hwang, M. Pyo, *Synth. Met.*, **157**, 155 (2007).
51. J.-Y. Kim, K. H. Kim, K. B. Kim, *J. Power Sources*, **176**, 396 (2008).
52. M. M. Ayad, E. Zaki, *Appl. Surf. Sci.*, **256**, 787 (2009).
53. B. Parakhonskiy, D. Andreeva, H. Möhwald, D. G. Shchukin, *Langmuir*, **25**, 4780 (2009).
54. M. Sharifirad, A. Omrani, A. A. Rostami, M. Khoshroo, *J. Electroanal. Chem.*, **645**, 149 (2010).
55. L. Cui, J. Shen, F. Cheng, Z. Tao, J. Chen, *J. Power Sources*, **196**, 2195 (2011).
56. A. Madani, B. Nessark, R. Boukherroub, M. M. Chehimi, *J. Electroanal. Chem.*, **650**, 176 (2011).
57. J. Arjomandi, S. Bilal, H. Van Hoang, R. Holze, *Spectrochim. Acta Mol. Biomol. Spectrosc.*, **78**, 1 (2011).
58. D. Zhang, X. Zhang, Y. Chen, P. Yu, C. Wang, Y. Ma, *J. Power Sources*, **196**, 5990 (2011).
59. S. Konwer, R. Boruah, S. K. Dolui, *J. Electron. Mater.*, **40**, 2248 (2011).
60. P.-C. Wang, J.-Y. Yu, *React. Funct. Polym.*, **72**, 311 (2012).



61. <http://www.intechopen.com/books/electropolymerization/polypyrrole-composites-electrochemical-synthesis-characterizations-and-applications>
62. M. R. Nabid, A. A. Entezami, *J. Appl. Polym. Sci.*, **94**, 254 (2004).
63. H.-K. Song, G. T. Palmore, *J. Phys. Chem. B*, **109**, 19278 (2005).
64. X. Cui, C. M. Li, J. Zang, Q. Zhou, Y. Gan, H. Bao, J. Guo, P. V. Lee, S. M. Moochhala, *J. Phys. Chem. C*, **111**, 2025 (2007).
65. A. Ramanavicius, A. Kausaite, A. Ramanaviciene, J. Acaite, A. Malinauskas, *Synth. Met.*, **156**, 409 (2006).
66. A. Ramanaviciene, A. Kausaite-Minkstimiene, Y. Oztekin, G. Carac, J. Voronovic, N. German, A. Ramanavicius, *Microchim. Acta*, **175**, 79 (2011).
67. R. Cruz-Silva, E. Amaro, A. Escamilla, M. E. Nicho, S. Sepulveda-Guzman, L. Arizmendi, J. Romero-Garcia, F. F. Castillon-Barraza, M. H. Farias, *J. Colloid Interface Sci.*, **328**, 263 (2008).
68. Y. N. Kupriyanovich, B. G. Sukhov, S. A. Medvedeva, A. I. Mikhaleva, T. I. Vakul'skaya, G. F. Myachina, B. A. Trofimov, *Mendeleev Commun.*, **18**, 56 (2008).
69. M. Mazur, A. Krywko-Cendrowska, P. Kryski, J. Rogalski, *Synth. Met.*, **159**, 1731 (2009).
70. R. Bouldin, S. Ravichandran, A. Kokil, R. Garhwal, S. Nagarajan, J. Kumar, F. F. Bruno, L. A. Samuelson, R. Nagarajan, *Synth. Met.*, **161**, 1611 (2011).
71. K. Junker, G. Zandomenighi, L. D. Schuler, R. Kissner, P. Walde, *Synth. Met.*, **200**, 123 (2015).

1

2

1\*

1

2

RO-800008,

47,

47, RO-800008,

15 2016 .;

10 2017 .

( )

(PPY),

PPY PPY

## Hydrogen Economy: the future for a sustainable and green society

M. Pandev<sup>1\*</sup>, P. Lucchese<sup>2</sup>, C. Mansilla<sup>3</sup>, A. Le Duigou<sup>3</sup>, B. Abrashev<sup>1</sup>, D. Vladikova<sup>1</sup>

<sup>1</sup> Acad. Evgeni Budevski Institute of Electrochemistry and Energy Systems, Bulgarian Academy of Sciences  
Acad. Georgi Bonchev Str., bl. 10, 1113 Sofia, Bulgaria

<sup>2</sup> Commissariat à l'énergie atomique et aux énergies alternatives (CEA), Université Paris- Saclay, F-91191 Gif-sur-  
Yvette, France

<sup>3</sup> Institut de Technico-Economie des Systèmes Energétiques, Commissariat à l'énergie atomique et aux énergies  
alternatives (CEA), Université Paris- Saclay, F-91191 Gif-sur-Yvette, France

Received March 7, 2017      Revised April 10, 2017

The increasing demand for sustainable energy efficiency and industrial decarbonisation leads researchers from different areas to seek alternative and more effective ways for attaining these goals. A hydrogen economy based on fuel cell and hydrogen technologies is a plausible and promising way to reach the European energy targets and improve the quality of life of society, providing independence and security of the energy supply across Europe. The need for rapid deployment of environment-friendly technologies implies for integrated policy measures and joint efforts of all Member States. This paper gives an overview of hydrogen and fuel cell technologies considering intensively their place in the European policy for decarbonisation and smart growth. The paper also discusses international initiatives in the field and suggests a pathway for greener society.

**Key words:** hydrogen, fuel cells and hydrogen, hydrogen technologies, hydrogen economy, sustainable development; long-term scenario, legal and administrative barriers removal, market deployment

### INTRODUCTION

The hydrogen-based economy is a long-term dream of society and scientists for meeting the increasing demand for energy by using hydrogen as fuel in a clean energy system. The term “hydrogen economy” was introduced by the world-renown scientist John Bockris in 70s of the 20th century [1] evolving from the concept introduced by the British scientist J. B. S. Haldane [2].

The element hydrogen is the most abundant and lightest chemical element in the universe, as on Earth it is most commonly linked to molecules of water or organic compounds. The hydrogen gas is colourless, odourless and tasteless. It has a boiling point of -252.9 degrees Celsius and a melting point of -259.2 degrees Celsius. It is dissolved slightly in water, but occludes in significant amounts in certain metals as, for instance, palladium which may dissolve up to 3000 volume parts of hydrogen (occlusion is a term related to particular type of absorption of gases by metals).

In addition to its vast industrial applications in the chemical industry, metallurgy, glass industry and others, hydrogen is taking one of the leading positions in the energy sector as an energy carrier for both transport and stationary applications: as a

fuel for motive power (including vehicles and waterborne vessels) and on-board auxiliary power, stationary power generation (for the energy demands involving household and industrial applications), as an energy carrier for storage applications medium, related to excess electric power generated off-peak, load levelling and balancing of the energy system, long-term energy storage [3]. Hydrogen does not exist naturally in convenient reservoirs with an exception regarding the actively investigated onshore natural hydrogen (H<sub>2</sub>) emissions [4] but nonetheless, it may be generated by water electrolysis, steam reforming of hydrocarbons, thermal decomposition of water or by other methods [5]. Some algae and bacteria, using sunlight as their main source of energy in certain circumstances also release hydrogen naturally.

Currently, the technologies with highest potential for producing hydrogen are divided in four categories: electrochemical, photo-electrochemical, thermochemical and photo-biological [6]. Some authors claim that one of the problems related to the production of hydrogen is that in the process a large amount of energy is consumed in comparison to the gained energy when using it as a fuel [7].

Fuel cell technologies are essential for attaining a carbon free hydrogen based economy. The fuel cell converts chemical energy from a fuel into

---

To whom all correspondence should be sent:  
E-mail: pandeff@gmail.com

electricity by an electrochemical reaction between hydrogen and oxygen from the air which brings to the production of electricity and heat, while the by-product is water [8]. Fuel cells need a source of fuel (hydrogen) and oxidizer to sustain the electrochemical reaction producing electricity continuously which is their significant advantage in comparison to batteries that need recharging. In similarity to batteries, the main active components of the fuel cells are two electrodes sandwiching the electrolyte. There are several different technologies for fuel cell such as: solid-oxide fuel cells (SOFCs), proton exchange membrane fuel cells (PEMFCs), alkaline fuel cells (AFCs), phosphoric acid fuel cell (PAFCs), solid acid fuel cell (SAFCs) and others.

The most promising technologies which are under intensive development are SOFCs and PEMFCs. SOFCs components are ceramics which have significant conductivity at elevated temperatures, thus having a high temperature operating mode which makes them suitable mainly for stationary applications. PEMFCs have no alternative for mobility applications. They are successfully used also for stationary applications. One of the serious problems faced is the large consumption of platinum. It should be marked that extensive research and development is conducted for the diverse application of all types of fuel cell. In general, the main hurdles for the large-scale market introduction of fuel cells and hydrogen technologies presently are their yet insufficient durability and high costs: two directions where common research and industrial efforts are concentrated.

Fuel cell and hydrogen technologies have already started to play a key EU role in contributing to the targeted reductions in greenhouse gas emissions together with the improvements in air quality and increased energy independence needs of the Community. Europe is facing serious challenges related to the production of energy which has key impact on its economy, environment, society and security. In the new package of measures "Clean Energy for all Europeans" [9], intended to support all European citizens and businesses with the means to maximize the benefits of the clean energy transition [10], an emphasis is given to the development of affordable and integrated energy storage solutions from renewable energy and fuel cells and hydrogen are foreseen as one of viable and sustainable problem solving solutions.

## OVERVIEW

Advanced energy technologies are identified as an essential element for coping with climate change

and securing energy supply. Europe's ambitious climate and energy targets are foreseen in the Strategic Energy Technology Plan (SET-Plan) which has been the technology pillar of the EU Energy and Climate policy since its adoption in 2008 [11] but these targets cannot be met without deploying more efficient energy technologies. The plan was designed as a tool for supporting decision making in the energy policy field having several main goals [12]:

- to accelerate knowledge development, technology transfer and up-take;
- to maintain EU industrial leadership on low-carbon energy technologies;
- to foster science for transforming energy technologies to achieve the 2020 Energy and Climate Change goals;
- to contribute to the worldwide transition to a low carbon economy by 2050.

The implementation of the SET-Plan began with the establishment of the European Industrial Initiatives (EIIs) which bring together industry, the research community, the Member States and the Commission in risk-sharing, public-private partnerships aimed at the rapid development of key energy technologies at European level. In parallel, the European Energy Research Alliance (EERA) has been working since 2008 to align the R&D activities of individual research organisations to the needs of the SET-Plan priorities, and to establish a joint programming framework at EU level. The projected budget for the SET-Plan has been estimated at up to €1.5 billion [12]. The SET-Plan has two major timelines. For 2020, the SET-Plan provides a framework to accelerate the development and deployment of cost-effective low carbon technologies aiming to reach the 20-20-20 goals of a 20 % reduction of greenhouse gases (GHG) emissions, a 20 % share of energy from low-carbon energy sources and 20 % reduction in the use of primary energy in order to improve energy efficiency. For 2050, the SET-Plan is aimed at limiting climate change to a global temperature rise of no more than 2°C (by the end of the century) and more specifically to reduce EU's GHG emissions by 80-95 % depending on the sector [12]. The SET-Plan objective in this regard is to establish a low-carbon energy technology and industry sectors by lowering the cost of low-carbon energy hence, providing energy security, environmental preservation and better quality of life.

Currently, the European energy system relies 80 % on fossil fuels which produce 80 % of all the Union's GHG emissions thus, highlighting the importance of decarbonisation of the energy system. In line with the common objective of a

competitive European economy and the accepted long term GHG emission reduction of 80-95% by 2050 compared to 1990 levels, the European Council agreed on a domestic greenhouse gas reduction target of at least 40% by 2030 compared to 1990 and set a target of at least 27% for renewable energy, binding at EU level, as well as an indicative target of energy savings [13].

The qualities of the energy system are very much linked to its energy supply. The Union and its Member States have set as a matter of high priority the development of a diverse, reliable and cost-effective portfolio of energy supply technologies to meet the EU climate and energy policy goals. Transforming the present system needs adequate and serious changes to the energy system in the medium and long term into an economic and industrial prospect for Europe. That cannot happen without extensive further research, development and deployment of new solutions and innovations to reduce the energy demand further, diversify and consolidate supply options (both external and local) attuned with Member States energy mix choices, and to develop a flexible and integrated energy system. Moreover, innovative business models and financial schemes that guarantee a diverse approach are also needed in order to do so.

The energy system is essential for every economy. Thus, the European Commission has set the energy sector as one of its main priorities. In accordance with the plan for modernisation of the current energy system, where two thirds of the greenhouse emissions result from energy production and use, an accelerated transition to a clean and efficient energy system is needed. That will have an impact on all Member States and will support the implementation of the developed the Energy

package: “Clean Energy for all Europeans” with additional regulatory proposals and facilitating measures. The three principal objectives are [14]:

- energy efficiency first;
- Europe as the global leader in renewable;
- a fair deal to consumers.

The achievement of these 3 goals is strongly related to activities in 3 general directions [15]:

- investment in energy efficiency and renewable technologies;
- development of clean energy business models;
- embracing the new opportunities and consumer empowerment brought about by digitisation.

As very clearly implicated in the Energy package the transition to a low-carbon energy-efficient and climate-resilient economy will require a decentralised open system with the involvement of all stakeholders. Traditionally, the energy system is marked by the dominance of large enterprises, incumbents and large-scale, centralised technological projects. Nevertheless, the future requires for the consumer to be in the focus of the energy system. As marked in the SET plan, for putting the active consumers at the centre of the energy system, they should be [13]:

- engaged in better understanding, information and market transformation;
- activated through innovative technologies, products and services – leading to innovative business models.

All these efforts (Fig.1) work hand in hand with other flagship initiatives such as the Digital Single Market, the Capital Markets Union and the Investment Plan for Europe in order to deliver on jobs, growth and investments for Europe [14].

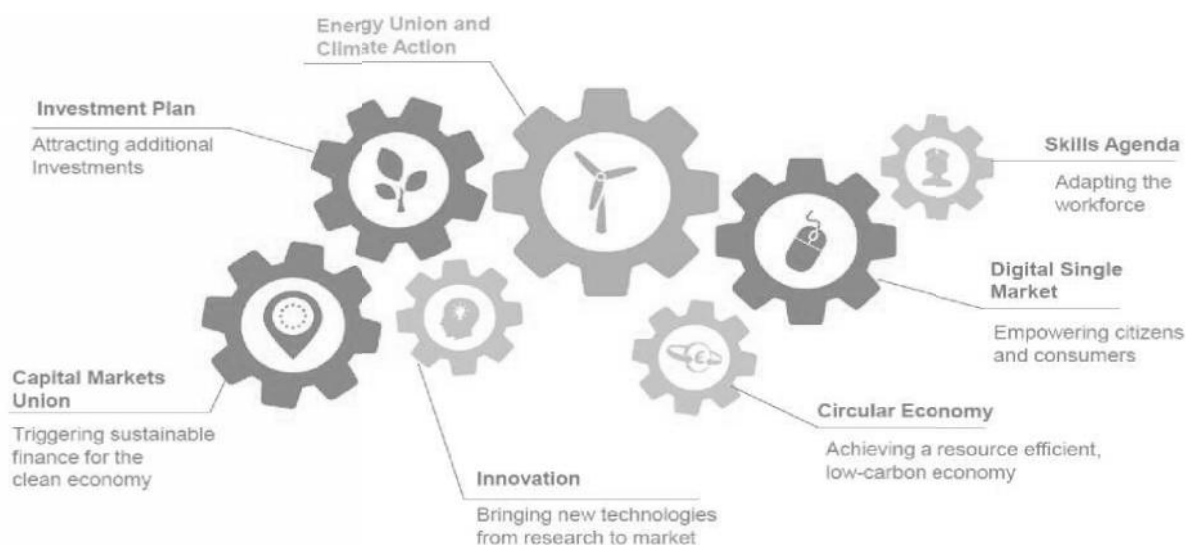


Fig. 1. Modernisation of the economy - role of the Energy Union and Climate Action [14].

Moreover, the package presents an opportunity to speed both the clean energy transition and growth and job creation. By mobilising up to an additional 177 billion euro of public and private investment per year from 2021, this package can generate up to 1% increase in GDP over the next decade and create 900.000 new jobs [16]. It will also mean that on the average the carbon intensity of the EU's economy will be 43% lower in 2030 than now [17], with renewable electricity representing about half of the EU's electricity generation mix [18].

Two complementary activities may also be taken into account for the implementation of the common goals:

- increasing public awareness – also in terms of national policy making, local authorities' activities and penetration of new legislation and educational and demonstration activities;
- integrated knowledge approach – expert knowledge bank focused on networking related to new technologies for overcoming the specifics in the different European countries.

Hydrogen has been accepted as a fuel / energy carrier together with advanced biofuels and other alternative liquid and gaseous fuels, including Liquefied natural gas (LNG), in the portfolio of sustainable means [13], therefore necessary to improve the EU security of energy supply and to achieve the ambitious European goals aiming to reduce the GHG emissions with respect to the overall EU 2020, 2030 and 2050 objectives in energy, transport, climate, economic and social policies. That leads to the need of advanced R&D for gaining advanced novel materials and components for fuel cell and hydrogen technologies accompanied with incentives and analyses of the key processes and mechanisms for hydrogen production and conversion and storage. On EU level there is sustainable collaboration for the acceleration of the market introduction on FCH technologies maintained by the Fuel Cells and Hydrogen Joint Undertaking (FCH JU) which concentrates the efforts of the European Commission, the FCH industries and the research community in the FCH sector in order to reduce dependence on hydrocarbons and to contribute to economic growth.

FCH technologies are expected to deliver economic benefits through job creation, improved balance of payments and long-term return on investments in the European economic area. It is acknowledged that the fuel cell and hydrogen industry sector has moved beyond the R&D stage and large scale investments have been made by the

industry to deliver fuel cell and hydrogen products to end-users, including substantial financial resources allocated to research, development and demonstration by fuel cell and electrolyser suppliers, automotive original equipment manufacturers (OEMs), industrial gas companies, technology system integrators and grid energy network operators. These investments, together with the public sector funding at EU, national and regional levels, has placed the mobility, energy storage and stationary fuel cells sectors on the brink of commercial deployment that will deliver substantial macroeconomic and societal benefits on a Europe wide basis.

During the recent years FCH industry has achieved considerable progress toward meeting market based product performance, functionality, and cost improvement. Deployment for a range of applications such as mobility (including hydrogen refuelling infrastructure), stationary fuel cells (with/without on-site generation) and energy storage (with/without grid integration) in the energy systems of the EU.

A focus is taken to address non-technological aspects to facilitate deployment of FCH technologies, such as demonstration of their socio-economic effect, the environmental and energy benefits throughout the whole life cycle. At the moment there is no unitary regulatory framework in the EU in terms of FCH relevant regulations, codes and standards which represents of the barriers for large scale deployment.

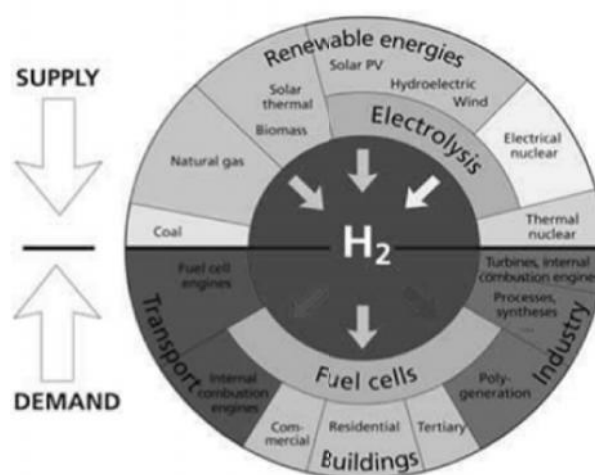


Fig. 2. Hydrogen economy [19].

The potential of hydrogen and FC technologies as an energy carrier is also becoming more and more plausible in economic terms as the need for integrated energy storage solutions grows rapidly and becomes more critical where renewable energy

generation systems such as wind turbines and photo-voltaic that are already generating gigawatt hours (GWh) of electricity, often with a significant mismatch in grid power demand. In that sense, electricity storage becomes a key enabler of the large-scale deployment of fluctuating renewable energy (RE) generation capacity across Europe. Hydrogen as an energy carrier may be considered as a core element of the energy system of today – and will be even more so in the future: through stabilising power generation to make the best use of conventional and RE generation assets (Fig. 2).

From an economic point of view an extensive in-depth analysis of key trends, market drivers, and growth factors in the energy sector in Europe is needed – in order to clarify realistically the quantify of market supply and demand, taking into account relevant storage applications such as hydrogen with focus on regional, national and European specific regulations and standards. That would benefit the industrial and financial players in the energy sector as their return on investment (RoI) is closely related to the right setting and timing of market entry and is dependable on technology costs and low RE generation.

From a technological point of view, joint efforts of research, industry and society are focused and the efficiency of these actions is demonstrated by the activities and achievements of the Fuel Cells and Hydrogen Joint Undertaking – in synergy with the targets and goals implied by SET-Plan (Fig. 3.).

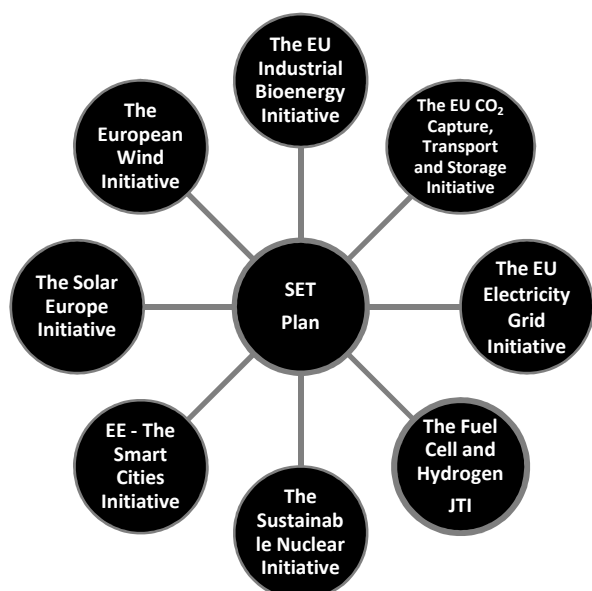


Fig. 3. European Strategic Energy Technology Plan [20].

The Fuel cell and Hydrogen Joint Undertaking (FCH JU) has a Multi-Annual Implementation Plan (MAIP) as primary strategic document which sets

out the scope and details for basic, breakthrough and applied research and demonstration activities according to five main ‘application areas’ [21]:

- Transport and refuelling infrastructure;
- Hydrogen production and distribution;
- Stationary power generation and combined heat and power;
- Early markets;
- Cross-cutting issues.

According to the latest available data from the FCH JU Annual Activity Reports and the H2020 portal 204 projects were supported by the FCH JU to date, of which 155 originated under FP7 and 49 as part of Horizon 2020. They are distributed between the three main pillars of the programme [22]:

- Transport;
- Energy;
- Cross-cutting activities.

The first pillar (Transport) aims to accelerate the commercialisation of FCH technologies in the transport sector (which has an important role in the GHG emissions) through support of demonstration and research (RTD) projects across Europe.

The demo projects’ focus is directed to proving technology readiness and public acceptance while increasing the number of fuel cell electric vehicles (FCEVs) and the hydrogen refuelling network across Europe. There are six targeted segments: cars, buses, material handling vehicles (MHVs), auxiliary power units (APUs) and refuelling infrastructure [23]. The demo activities involving cars concern more than 1,500 vehicles, 250 of which are already in operation while the rest are planned within currently running projects. Also, a network of hydrogen refuelling stations is being created across Europe covering 8 countries and in 2015 it delivered 130,000 kg of hydrogen in 17,500 refuelling operations at 96% availability. Demonstration activating related to buses involve 67 vehicles in 12 European cities as 41 buses in 7 cities are already in operation while demonstrations of material handling vehicles have involved 48 vehicles (covering 6 models) from 3 manufacturers on 10 sites [22].

The research and innovation projects target a cost-efficient increase in the performance of fuel cell systems and hydrogen refuelling station (HRS) system. More specifically, the RTD projects in transportation relate to new materials and components development, improvement of performance levels, optimisation, reduction of costs and novel modelling in 8 technological segments [22]:

- Membrane electrodes assembly (MEA);
- Catalysts;

- Gas diffusion layer (GDL);
- Bipolar plates;
- Manufacturing and process development;
- Methodologies and tools;
- System and balance-of-plant (BoP) components;
- Advanced refuelling developments;

The second pillar (Energy) aims to accelerate the commercialisation of FCH technologies related to stationary fuel cells and the production of “green” hydrogen as an energy carrier. More specifically it targets reduction in costs while increasing the efficiency and the durability of fuel cells for energy production and at the same time also making the best use of the deployed of renewables in the European energy system. The FCH JU programme supports activities in three main areas [24]:

- stationary fuel cells (power and heat) demonstration and proof-of-concept activities related to technology capability and readiness;
- Stationary fuel cells (power and heat) research and innovation for performance, durability and cost improvements;
- Hydrogen production pathways from renewable energy sources, handling, distribution and storage technologies to enable hydrogen as a key energy carrier in the EU.

Until now around 40 projects have been funded by the FCH JU in the Energy pillar. It is notable to mention that the demo projects related to combined heat and power (CHP) are structured in different topic areas:

- Micro-CHP (< 5 kW)
- Mid-size CHP
- Large size CHP (>400 kW)
- Off grid/back up

So far, around 700  $\mu$ -CHP systems for residential applications have been installed in 11 European countries by 10 manufacturers. The generation of own electricity allows home owners to cut energy costs by 800-1,300 € per year [22]. The aim is to reach 3,000 units installed by 2020 and to increase their market competitiveness. As a comparison it may be noted that Japan’s ENE-FARM program has supported the deployment of well over 120,000 residential fuel cell units [25] as plans are to reach 1.4 million units by 2020 and 5.3 million units by 2030 [26].

The third pillar (Cross-cutting activities) is closely related to the first two as it supports the commercialisation efforts in the energy and transport areas through a range of market preparation and readiness support measures. More specifically [22]:

- providing new knowledge to develop and improve regulations, codes and standards (RCS);
- preparing the European workforce;
- increasing public awareness and social acceptance;
- ensuring FCH technologies are environmentally sustainable.

Since 2014, projects addressing portable applications, previously classified within the ‘early markets’ application area, have also been categorised as cross-cutting. Until now more than 30 projects have been undertaken in the third pillar [22]. Efforts have been directed in order to gather knowledge and support the stakeholders in the FCH and energy fields thus, allowing that knowledge to pave the way for further regulations, codes and standards. Identification of economically viable niches for the FCH technologies has also been a priority in the joint efforts of the industry and research stakeholders.

On European level joint activities have also been directed towards support for the market penetration of fuel cells and hydrogen applications through a Horizon 2020 flagship project HyLAW which has already started as of January 2017 and will run until December 2018. HyLAW stands for “Hydrogen Law and Removal of Legal Barriers to the Deployment of Fuel Cells and Hydrogen Applications” [27]. It aims at boosting the market uptake of hydrogen and fuel cell technologies providing market developers with a clear view of the applicable regulations whilst calling the attention of policy makers on legal barriers to be removed. The project brings together 23 partners from Austria, Belgium, Bulgaria, Denmark, Finland, France, Germany, Hungary, Italy, Latvia, Norway, Poland, Romania, Spain, Sweden, Portugal, the Netherlands and United Kingdom (Fig. 4.) and is coordinated by Hydrogen Europe [27].



Fig. 4. HyLAW project partners [27].

The HyLAW partners will first identify the legislation and regulations relevant to fuel cell and hydrogen applications and legal barriers to their

commercialisation. They will then provide public authorities with country specific benchmarks and recommendations on how to remove those barriers.

HyLAW's main outputs will be [27]:

- an online and publicly available database compiling legal and administrative processes applicable to hydrogen and fuel cell technologies in 18 countries across Europe;
- national policy papers describing each legal and administrative process, highlighting best practices, legal barriers and providing policy recommendations;
- a pan-European policy paper targeted towards European decision makers;
- national and European workshops for dissemination of the findings and convincing public authorities to remove barriers.

The database will be maintained by Hydrogen Europe for minimum three years after the end of the project.

The HyLAW project has received funding from the Fuel Cells and Hydrogen 2 Joint Undertaking under grant agreement No 737977.

From a boarder perspective, international efforts have also been directed to support of the deployment of FCH technologies for cleaner and safer future. The International Energy Agency (IEA) Hydrogen Implementing Agreement (HIA), which is a leader in the management of coordinated hydrogen research, development and demonstration activities, has launched a specific task (Task 38) entitled: "Power-to-Hydrogen and Hydrogen-to-X: System Analysis of the techno-economic, legal and regulatory conditions" with aim to examine hydrogen as a key energy carrier for a sustainable and smart energy system [28]. The IEA-HIA has long-term and vast experience in facilitating and managing an inclusive range of Research, Development & Demonstration (R, D&D) and analysis programs (over 40) among its international members – including international organisations, industrial and research partners, non-profit organisations [30]. The "Power-to-hydrogen" concept implies that hydrogen is produced via electrolysis as the electricity supply may be either grid, off-grid or though mixed systems while "Hydrogen-to-X" implies that the hydrogen supply concerns a large portfolio of uses. More specifically [29]:

- Transport (hydrogen for fuel cells, biofuels, synthetic methane for transport etc.);
- Natural gas grid (by mixing hydrogen directly with natural gas or synthesising methane and injecting it into the natural gas grid);
- Re-electrification through hydrogen turbines or fuel cells;

- General business of merchant hydrogen for energy or industry, especially refinery, steel industry, ammonia, etc.
- Ancillary services or grid services for the electricity grid, transport or distribution grid. Hydrogen provides flexible energy storage and carrier options which could defer the need for new lines and would alleviate the transmission difficulties

Task 38 has a lifespan of 4 years (2016-2019) and ambitions goals [31]:

- to provide a comprehensive understanding of the various technical and economic pathways for power-to-hydrogen applications in diverse situations;
- to provide a comprehensive assessment of existing legal frameworks;
- to present business developers and policy makers with general guidelines and recommendations that enhance hydrogen system deployment in energy markets.

The IEA-HIA Task 38 involves more than 50 experts in different fields from 15 countries. It is coordinated by the French Commissariat à l'énergie atomique et aux énergies alternatives / Institut de Technico-Economie des Systèmes Energétiques (CEA/I-tésé) and supported by the French Environment and Energy Management Agency (ADEME). There are also 15 participating IEA HIA ExCo Members: Australia, Belgium, European Commission, France, Germany, Japan, The Netherlands, New Zealand, Norway, Shell, Southern Company, Spain, Sweden, United Kingdom, and the United States [31].

The ongoing work conducted in Task 38 shows that an international joint effort is needed to analyse strategic studies in the FCH field, archive external synergies, and manage existing knowledge in order to identify possible pathways and niches together with all stakeholders for the successful market deployment of FCH technologies leading to a carbon-free and sustainable economy.

## CONCLUSION

The establishment of sustainable European expert knowledge network arises as a necessary component for the further market integration of FCH technologies in the EU, being a specific knowledge niche emerging from a combination of resources from the European Research Area and from the established public private partnerships. Thus, its role in the total package of measures is quite important. Presently, novel technologies are needed in order to ensure energy efficiency and integration of renewables in the energy mix. A



large number of the innovative technologies are in a pre-commercial stage. On EU level serious efforts are devoted for commercialisation of research and innovation above Technology Readiness Level 4 (TRL), and that in fact, somewhat brought to an underestimation of fundamental research in specific areas which were left to be developed on national level. However, in some new Member States that does not happen with the same pace and leads to fragmentation on European level. Fortunately, in the results from the currently performed analysis, introduced in the set of measures “Clean Energy for all Europeans”, all those issues have been taken into account and an updated strategy has been proposed. Thus, it is the right time to start the development of the next generation through breakthrough research with multi-fold benefits.

Currently, the existing regulatory and legal and administrative processes (LAPs) covering areas such as local and national planning, safety, installation and use/operation do not reflect adequately the use of FCH technologies. The limited awareness and coverage of FCH technologies in LAPs creates complications and requires substantial time, incurs additional costs and resources therefore, representing a barrier for rapid deployment. In this way, the financial resources are not directly targeted to the technology deployment leading to relative inefficiency and restricting quick access to the potential market. That hot topic of the European policy in the field will be supported by the planned and on-going activities of European HyLAW project and the International Task 38 of the IEA/HIA. The synergy of those activities would also support the growing necessity for the setting up of a distinct guild of highly-trained technical personnel needed for the newly created FCH infrastructure in Europe and worldwide.

The joint efforts of science, industry and policy-makers on European and international level have shown considerable success during the recent years for the implementation and market penetrations of FCH technologies. FCH technologies in a pre-commercial state have already been developed (above TRL 7). It can be highly been acknowledged that they will not only serve as transitional technologies during the decrease of fossil fuels utilisation but also as end point technologies for the efficient production and utilisation of hydrogen, and more generally in the global energy system as well.

**Acknowledgements:** *This review has received funding from the European Union’ Research and Innovation Framework Programme (Horizon*

*2020/2014-2020) Fuel Cells and Hydrogen Joint Undertaking 2 (FCH-JU-2016-1) under grant agreement 735977.*

## REFERENCES

1. Pirie, N. W. (1966). "John Burdon Sanderson Haldane. 1892–1964". Biographical Memoirs of Fellows of the Royal Society. 12 (0): 218–249. doi:10.1098/rsbm.1966.0010.
2. Turelli, M; Orr, HA (1995). "The dominance theory of Haldane’s rule". Genetics. 140 (1): 389–402. PMC 1206564 . PMID 7635302.
3. A portfolio of power-trains for Europe: a fact-based analysis: The role of Battery Electric Vehicles, Plug-in Hybrids and Fuel Cell Electric Vehicles ([http://www.iphe.net/docs/Resources/Power\\_trains\\_for\\_Europe.pdf](http://www.iphe.net/docs/Resources/Power_trains_for_Europe.pdf))
4. <http://www.ifpenergiesnouvelles.com/News/Press-releases/Natural-hydrogen-a-new-addition-to-the-energy-mix-IFPEN-studies-the-potential-of-onshore-sources-of-natural-hydrogen>
5. Carmo, M; Fritz D; Mergel J; Stolten D (2013). "A comprehensive review on PEM water electrolysis". Journal of Hydrogen Energy. 38: 4901–4934. doi:10.1016/j.ijhydene.2013.01.151.
6. Jones, J.C. (March 2015) "Energy-return-on-energy-invested for hydrogen fuel from the steam reforming of natural gas" Fuel 143: 631. doi:10.1016/j.fuel.2014.12.027
7. Zehner, Ozzie (2012) “Green Illusions” Lincoln and London: University of Nebraska Press, pp. 1-169, 331–42
8. Khurmi, R. S. Material Science (<http://www.biblio.com/book/materials-science-rs-khurmir-sedha/d/436308472>)
9. <https://ec.europa.eu/energy/en/news/commission-proposes-new-rules-consumer-centred-clean-energy-transition>
10. [http://eurlex.europa.eu/resource.html?uri=cellar:fa6e-a15b-b7b0-11e6-9e3c-01aa75ed71a1.0001.02/DOC\\_2&format=PDF](http://eurlex.europa.eu/resource.html?uri=cellar:fa6e-a15b-b7b0-11e6-9e3c-01aa75ed71a1.0001.02/DOC_2&format=PDF)
11. <https://ec.europa.eu/energy/sites/ener/files/publication/Complete-A4-setplan.pdf>
12. <https://setis.ec.europa.eu/about-setis/set-plan-governance>
13. [https://setis.ec.europa.eu/system/files/Towards\\_an\\_Integrated\\_Roadmap\\_0.pdf](https://setis.ec.europa.eu/system/files/Towards_an_Integrated_Roadmap_0.pdf)
14. <https://ec.europa.eu/transparency/regdoc/rep/1/2016/EN/COM-2016-860-F1-EN-MAIN.PDF>
15. [http://ec.europa.eu/energy/sites/ener/files/documents/1\\_en\\_act\\_part1\\_v6\\_0.pdf](http://ec.europa.eu/energy/sites/ener/files/documents/1_en_act_part1_v6_0.pdf)
16. Impact Assessment for the amendment of the Energy Efficiency Directive, SWD(2016) 405
17. Underlying results of the Impact Assessment for the amendment of the Energy Efficiency Directive, SWD(2016) 405.
18. Impact Assessment for the recast of the Renewables Directive, SWD(2016) 418
19. <http://www.engineersjournal.ie/2016/07/12/electrochemical-water-splitting-hydrogen-economy/>



# Contributions



# Influence of light intensity on the kinetics of light-driven hydrogen evolution using Rh-doped SrTiO<sub>3</sub>: a study by photoelectrochemical impedance spectroscopy

M. Antuch<sup>1</sup>, A. Kudo<sup>2</sup>, P. Millet<sup>1\*</sup>

<sup>1</sup> ICMMO-ERIEE (UMR CNRS 8182), Université Paris Sud, 91405 Orsay, France

<sup>2</sup> Department of Applied Chemistry, Tokyo University of Science, 1-3 Kagurazaka, Shinjuku-ku, Tokyo 162-8601, Japan

Received November 28, 2016      Revised March 6, 2017

Interest in the visible-light-driven hydrogen evolution reaction (HER) is nowadays determined by the urgent need for clean energy carriers. The mechanism of HER is known to be multistep, and is generally a bottleneck displaying kinetic hindrance. In this work, we report on the kinetics of the HER using a rhodium-doped strontium titanate (Rh:SrTiO<sub>3</sub>) as photoactive material. In particular, we have been interested in determining the influence of light intensity (68-529 mW/cm<sup>2</sup> at 450 nm) on the kinetic parameters of the system. We observed that increasing light intensity yielded a slight increase in electron-hole recombination rate, because of the increasing amount of photo-generated electrons at the surface of the photo-electrode. We also found that the rate constant of the charge transfer process was independent of light intensity. The increase of electron-hole recombination determined the efficiency loss of the system when light was intensified. This work provides insights into the kinetics of charge transfer at photo-excited Rh:SrTiO<sub>3</sub>/electrolyte interfaces, and also provides guidance for photoelectrochemical kinetic studies performed with photoelectrochemical impedance spectroscopy (PEIS).

**Key words:** hydrogen evolution, photoelectrochemical impedance spectroscopy, kinetics, doped strontium titanate.

## INTRODUCTION

Increasing energetic demands of modern society, along with the exhaustion of carbon based fuels, has turned the attention of the scientific community to develop alternative, sustainable and low cost energetic sources [1]. In this context, the use of semiconductors, photoactive upon visible-light excitation, is a promising route [2-6]. Among all possible energetic applications of semiconducting electrodes, the study of the hydrogen evolution reaction (HER) is still a hot-spot [7-12] because of its possibilities of changing the planet energetic dependence for a fully clean source.

These facts prompted us to study the kinetics of the novel advanced semiconducting material (Rh doped SrTiO<sub>3</sub>) that absorbs visible light, and has recently been shown to act as a potentially interesting hydrogen evolving photo-catalyst [13-16]. However, multistep charge transfer reactions, such as the HER, display poor kinetics, which determines the importance of unraveling the kinetic parameters behind the performance of this photoelectrocatalytic material.

Herein we present a kinetic study of the surface reactivity of Rh:SrTiO<sub>3</sub> ( $E_g = 2.4$  eV, [13]) by photoelectrochemical impedance spectroscopy (PEIS), a technique originally developed by Ponomarev and Peter [17]. We were interested in particular at measuring the effect of light intensity on the kinetic parameters at constant applied potential. A theoretical background and the appropriate references to the models we employed in this work for data analysis are provided.

## METHODS

SrTiO<sub>3</sub> powder doped with 1 mol % Rh at Ti sites was prepared by a solid-state reaction. The starting materials, SrCO<sub>3</sub> (Kanto Chemical; 99.9%), TiO<sub>2</sub> (Soekawa Chemical; 99.9%), and Rh<sub>2</sub>O<sub>3</sub> (Wako Pure Chemical), were mixed in a Sr:Ti:Rh ratio of 1.07:(1-x):x. The mixture was calcined in air at 1173 K for 1 h and then at 1373 K for 10 h in an alumina crucible [13]. The chemical composition of the samples was determined using SEM-EDS Cambridge equipment and electron microprobe measurements (EPMA) (microprobe SX 100 CAMECA).

Photoelectrodes were prepared by drop-casting 10  $\mu$ L of an isopropanol suspension containing Rh:SrTiO<sub>3</sub> (30 mg in 0.5 mL) on top of an ITO surface. Next, 10  $\mu$ L of Nafion (50  $\mu$ L to a final volume of 1 mL in isopropanol) were put on top of

To whom all correspondence should be sent:  
E-mail: pierre.millet@u-psud.fr

the surface through the same methodology, and let dry for three hours. In all cases, the solvent was let to evaporate at room temperature. Before measurements, photoelectrodes were put into Na<sub>2</sub>SO<sub>4</sub> (0.1 M) solution and allowed to wet overnight. All electrochemical measurements were performed in aqueous Na<sub>2</sub>SO<sub>4</sub> (0.1 M) in a three electrode cell configuration employing ITO-Rh:SrTiO<sub>3</sub>-Nafion, saturated calomel electrode (SCE) and a carbon plaque, as working, reference and counter electrodes, respectively. MilliQ water was employed for all tests, and was obtained from a Merck Millipore device.

Photoelectrochemical impedance (PEIS) determinations were performed in a quartz photoelectrochemical cell from Pine Research Instrument Company. Measurements were performed in a Modulab Solartron Analytical potentiostat, model 2100A. The light source was controlled with a calibrated optical bench (Thorlabs Inc. DC2100), equipped with a LED giving light of 450 nm. PEIS spectra were recorded under potentiostatic control in the frequency range of 300 kHz to 50.2 mHz, the amplitude of the sinusoidal potential perturbation was 10 mV in all cases. Fitting of experimental PEIS spectra was performed in Matlab R2014b, with home-made code.

### THEORETICAL BACKGROUND

The interface between a semiconducting electrode and a solution is special since for a p-type semiconductor there is an accumulation of electrons at the interface associated with an electron exchange between the electrolyte and the material, whose driving force originates in equating the Fermi levels of the solution and the semiconductor. Such electron accumulation causes a downward bending of the valence and conduction band edges, when the electrode is biased at a potential negative to the flat-band potential (Figure 1a). As a consequence, when an electric potential (V) is applied, a part of V drops inside the solid material and the other part drops in the solution side. This fact contrasts with metallic electrodes in which all the applied potential drops within the solution. In general, the part of the solution where the electric potential drops, called the Helmholtz layer, has an associated capacitance ( $C_H$ ). In an analogous manner, the space located inside the semiconducting material in which the potential drops, has an associated capacitance as well, the so-called space charge capacitance ( $C_{sc}$ ). Excepting heavily doped semiconductors,  $C_H$  is much higher than  $C_{sc}$ . This fact determines that most of the overall potential drops inside the material (i.e., in

the space charge region) and not in the solution side of the interphase, i.e.  $\phi_{sc} \gg \phi_H$ , where  $\phi_{sc}$  stands for the potential drop within the space charge, and  $\phi_H$  represents the potential drop in the Helmholtz layer. Naturally  $V = \phi_{sc} + \phi_H$ . When a semiconducting electrode is illuminated by light with an energy  $h\nu$  higher than its band gap, charge separation occurs and an electron-hole pair is consequently generated (Figure 1 a) [2-4,18]. Because of band bending, the electrons move towards the surface with a flux represented here as  $I_0$ . At the surface, electrons can be transferred to the solution to reduce species in the nearby (in this work we aim at the reduction of water according to  $H_2O + 2e^- = 1/2H_2 + OH^-$  with a phenomenological rate constant  $k_t$ ). Additionally, the electrons can recombine at the surface with photogenerated holes with a rate constant  $k_r$ .

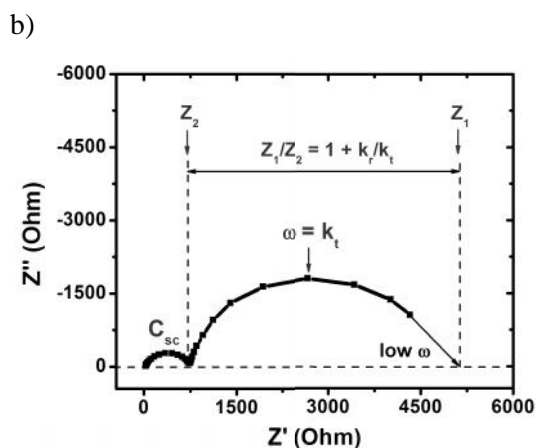
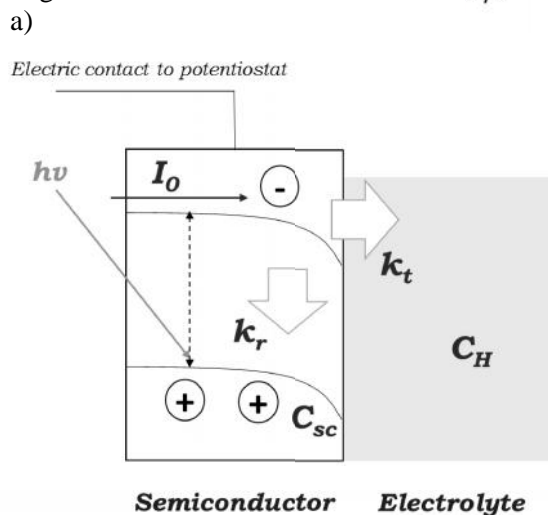


**Fig. 1.** a) Scheme of an illuminated p-type semiconductor under reverse bias. Main kinetic and photoelectrochemical parameters discussed in the text are presented; b) typical photoelectrochemical impedance spectrum (PEIS) of an illuminated semiconductor. The figure highlights how to determine the kinetics of light-driven reactions from PEIS (see text for explanations).

Understanding the kinetics of charge transfer and recombination in semiconducting electrodes is of paramount importance to continually improve their performance. In order to study the kinetics of charge transfer at Rh:SrTiO<sub>3</sub>/electrolyte interfaces, we employed photoelectrochemical impedance spectroscopy (PEIS). PEIS consists in recording a usual EIS spectrum at a constant level of illumination. The space charge capacitance and the Helmholtz capacitance can be viewed as a part of two RC circuits in series, thus, the interfacial capacitance is  $\frac{1}{C} = \frac{1}{C_{sc}} + \frac{1}{C_H}$ . When  $C_{sc} \ll C_H$ , the overall capacitance is mostly due to the space charge and in such conditions experimental data may be fitted using Eq. (1). This permits to obtain a semi-quantitative evaluation of relevant transfer and recombination kinetic parameters (Figure 1) [19-20].

$$Z(\omega) = R + \frac{1}{i\omega C_{sc} + \left(\frac{q}{k_B T}\right) I_0 \left(\frac{k_r}{k_r + k_t}\right) \left(\frac{k_t + i\omega}{k_r + k_t}\right)} \quad (1)$$

In Eq. (1),  $\omega$  is the angular frequency of the ac perturbation,  $Z(\omega)$  represents the  $\omega$ -dependent impedance of the interface in  $\Omega$ ,  $R$  corresponds to the ionic resistance of the solution in  $\Omega$ ,  $i$  is the imaginary unit,  $C_{sc}$  is the space-charge capacitance in F,  $q$  is the elemental charge,  $k_B$  stands for Boltzman's constant,  $T$  is the absolute temperature,  $I_0$  is the photogenerated current of minority carriers (electrons in the case of a p-type semiconductor),  $k_r$  and  $k_t$  are the pseudo first order rate constants for recombination and charge transfer, respectively Eq. (1) describes two semicircles in the Nyquist plot.

For the case where the charge transfer rate constant does not depend on  $\phi_H$ , the interface impedance  $Z(\omega)$  tends to  $Z_1$  at low frequencies (eq. 2).

$$\lim_{\omega \rightarrow 0} Z(\omega) = Z_1 = R + \frac{k_t + k_r}{\left(\frac{q}{k_B T}\right) I_0 k_r \left(1 + \frac{k_r}{k_t}\right)}, \quad (2)$$

where  $R$  is the resistance associated to the solution and the electric wiring.

The low frequency semicircle passes through a maximum from which the charge transfer rate constant  $k_t$  may be directly determined using Eq. 3:

$$\omega_1 = k_t \quad (3)$$

The high frequency limit of the low frequency semicircle is  $Z_2$  given by Eq. (4):

$$Z_2 = R + \frac{k_r + k_t}{\left(\frac{q}{k_B T}\right) I_0 k_r} \quad (4)$$

Therefore, the ratio  $Z_1/Z_2$  (Eq. 5) provides an estimation of  $k_r$  once  $k_t$  is known

$$\frac{Z_1 - R}{Z_2 - R} = 1 + \frac{k_r}{k_t} \quad (5)$$

Since the space charge capacitance and the Helmholtz capacitance are connected in series, the overall interface capacitance shall be determined by the lowest of both (i.e.  $C_{sc}$ ). Thus, the high-frequency semicircle will provide an estimate of  $C_{sc}$ . The way PEIS may be used to extract all the above-mentioned kinetic parameters is summarized in Figure 1b.

Consequently, PEIS is a powerful technique to assess the kinetics at illuminated semiconducting electrodes, and getting information of the interfacial capacitances associated to the system.

## RESULTS AND DISCUSSION

The first step we undertook was the characterization of the Rh:SrTiO<sub>3</sub> semiconducting material by means of Scanning Electron Microscopy (SEM) and Energy Dispersive Spectroscopy (EDS). Figure 2-a shows a SEM micrograph of the electrode surface. This is a microporous material in which the width of the space charge region is smaller than the particle size. Roughness effects have been disregarded in the analysis of PEIS spectra. In Figure 2 a, the Nafion film is not visible, indicating that it forms a very thin layer on top of the semiconducting powder. Additionally, the polycrystalline nature of the Rh:SrTiO<sub>3</sub> surface may be appreciated, as has been reported before [13]. Figure 2-b displays the EDS spectra of the ITO support compared to the semiconductor. The signals of the L-shells of In and Sn coming from ITO are well defined, and the Si K-shell is observed as well, which originates from the glass substrate on top of which ITO is deposited. In the case of the photoelectrode assembly, EDS revealed the presence of F at the surface, coming from Nafion. Additionally, the Sr and Rh L-shells, and Ti K-shell confirmed the identity of the semiconducting material.

Subsequently, the photoelectrochemical characterization was undertaken. The first interesting issue to note is that the PEIS spectra changed upon cycling. In particular, the spectra evolved from a broad semicircle (Figure 3 black) until the response stabilized providing two well defined semicircles (Figure 3-a, red). Such change indicates that the interface is changing with the electrochemical treatment. It could be caused either by the binding and accumulation of charged intermediates in surface states, or by chemical modification of the surface, as has been reported before [21]. Further photoelectrode surface characterization is required to deepen into the real

causes of the observed evolution of PEIS. These two facts would redistribute  $\phi_{SC}$  and  $\phi_H$ , thus changing  $C_{SC}$  and  $C_H$ , and hence modifying the appearance of PEIS diagrams. When a stable and reproducible PEIS spectrum was obtained, we proceeded to perform subsequent measurements at different light intensities, in order to unravel its effect upon the displayed kinetics.

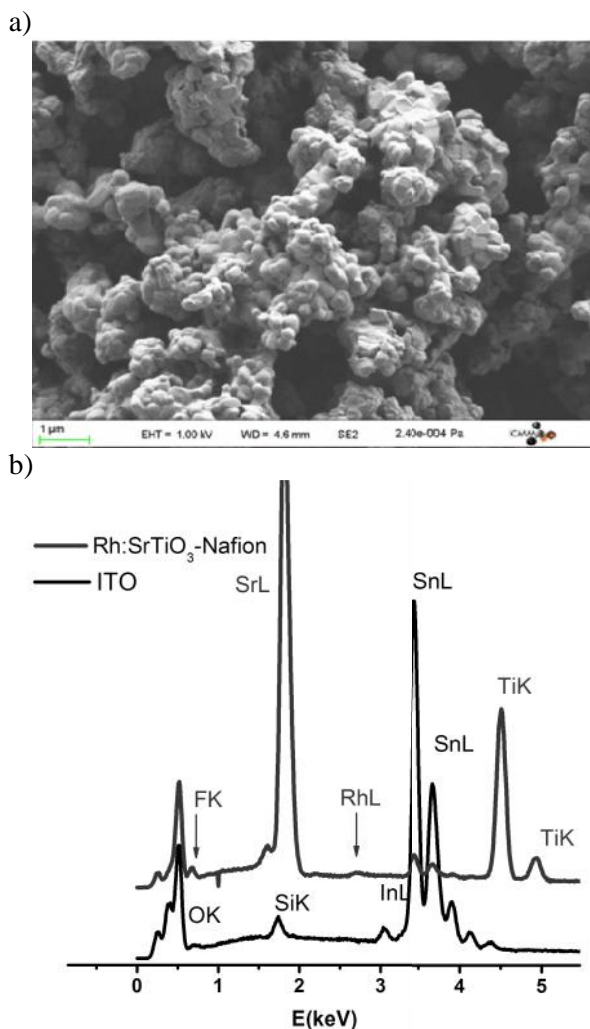


**Fig. 2.** a) SEM image of the electrode surface corresponding to Rh: SrTiO<sub>3</sub>; b) EDS spectrum of the surface.

Figure 3-b shows the effect of light intensity upon the PEIS response of the photoelectrode. It may be perceived in Figure 3-b that the effect of light intensity on PEIS diagrams is small, but measurable, reproducible and reversible. No heat effect under illumination was identified. It follows a tendency in which an increase in light intensity provokes a shrinking of the high frequency semicircle and an expansion of the low frequency semicircle.

Before analyzing the PEIS results in the framework of the formalism exposed above in the theoretical section, it should be verified that

$C_H C_{SC} \ll C_H$ . The space charge capacitance was estimated initially by a fit of the high frequency semicircle (in the 300 kHz to 30 Hz frequency domain) to a RC circuit, yielding a value of  $\sim 2.7 \cdot 10^{-7}$  F. Such value is small enough to ensure neglecting  $1/C_H$  in front of  $1/C_{SC}$ .

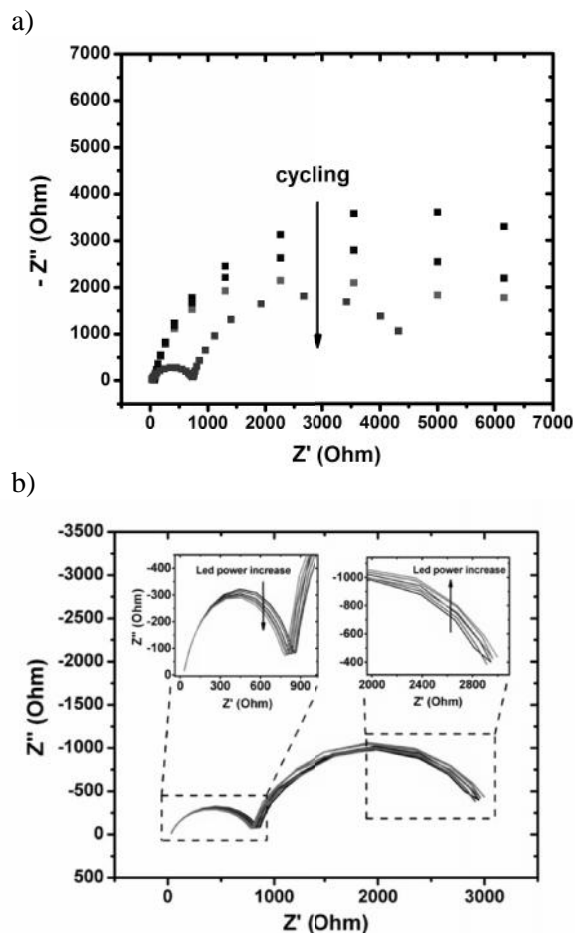


**Fig. 3.** a) Evolution of PEIS spectra of Rh: SrTiO<sub>3</sub> upon potential cycling at constant illumination. The red curve was found to be the stable response; b) Evolution of PEIS spectra at different light intensities. The sense of light increase is depicted in the insets. PEIS spectra were taken in the range of 300 kHz to 50.2 mHz at a constant applied potential of -1.25 V vs SCE. Light intensities were 67.9, 185.92, 294.13, 393.52, 485.34, 529.03 mW/cm<sup>2</sup>.

To get detailed information, PEIS spectra were fitted to Eq. (1) with  $I_0$ ,  $C_{SC}$ ,  $k_r$  and  $k_t$  as adjustable parameters. Fitting results are shown in Figure 4, where dashed lines have been put as a guide to the eye. For example, it may be appreciated that  $I_0$  increases with increasing light intensity. This is a logical result since the flux of photogenerated electrons should become higher when light is made more intense. In the same way, the recombination rate constant showed a slight tendency to increase with light intensity (observed as a slight expansion of the low frequency semicircle in Figure 3-b).



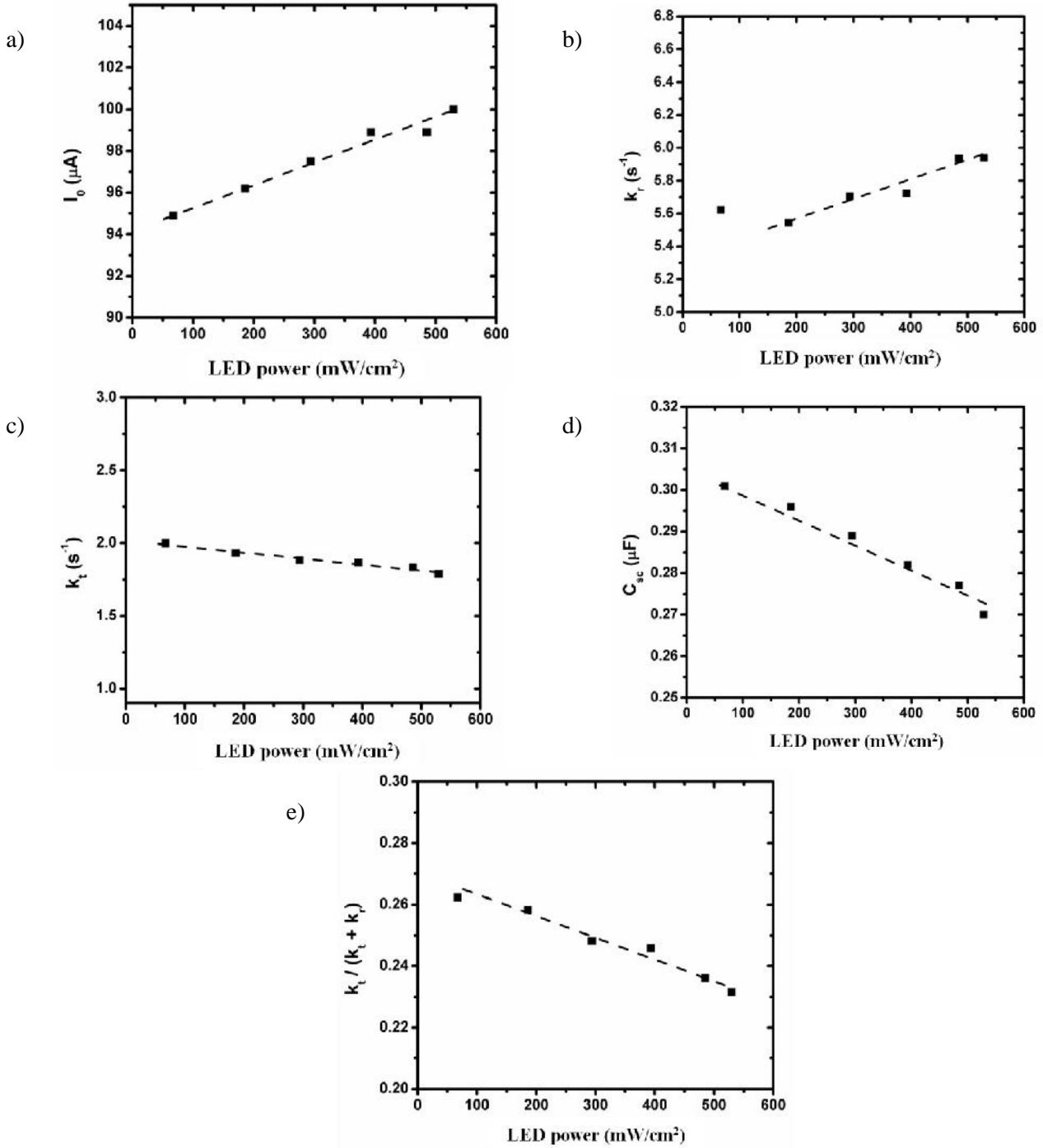


**Fig. 4.** Fitting results of PEIS spectra shown in Figure 3 b, to equation 1; Dependence with light intensity of: a) the flux of photogenerated minority carriers ( $I_0$ ); b) the recombination rate constant ( $k_{rec}$ ); c) the charge transfer rate constant; d) the space charge capacitance ( $C_{sc}$ ) and e) the efficiency of the photoelectrode.

Considering that  $k_r$  is proportional to the electron surface concentration as shown in Eq. (6) [20],

$$k_r = k'_r n_{surf} = k_r^0 \exp\left(\frac{-q\phi_{sc}}{kT}\right), \quad (6)$$

where  $n_{surf}$  is the electron concentration at the surface of the electrode,  $k$  represents the Boltzmann's constant,  $T$  is the absolute temperature and  $q$  is the elemental charge.

It follows directly from Eq. (6) that further light power will increase the electron concentration at the surface of the semiconductor and hence the value of  $k_r$ , thus decreasing band bending ( $\phi_{sc}$ ). At a constant applied potential  $V$ , a decrease in  $\phi_{sc}$  should be compensated by an increase in  $\phi_H$ , which should be translated into an increase in  $k_t$  (Eq. 7)

$$k_t = k_t^0 \exp\left(\frac{q\phi_H}{kT}\right). \quad (7)$$

However, such an increase in  $k_t$  is not well defined and  $k_t$  appears to keep the same value in the whole range of light intensities tested here, suggesting that the electron concentration at the surface does not change much over the entire range of light intensities under consideration. Such behavior is characteristic of Fermi level pinning associated with the presence of surface states in the photoelectrode [19].

On the other hand,  $C_{sc}$  displays a decrease with LED power augmentation (Figure 4-d), a behavior observed before in semiconducting photoelectrodes [19]. This can be interpreted as follows: as light increases, more electrons go to the surface while the holes remaining inside the material create an opposing electric field that continually diminishes the band bending ( $\phi_{sc}$ ). According to Eq. (8), such fact would increase  $C_{sc}$ . Though, the rise in light intensity makes the electrons to be located at the surface and the holes migrate to the bulk (where no electric field exists), the net charge in the space charge region ( $Q_{sc}$ ) diminishes as well, which appears to be the dominating factor to explain the observed trend in  $C_{sc}$  with increasing light intensity

$$C_{sc} = \frac{dQ_{sc}}{d\phi_{sc}}. \quad (8)$$

Finally, the fraction of photogenerated electrons that are indeed transferred to the electrolyte to evolve H<sub>2</sub> is given by Eq. (9), and provides a measure of the efficiency of the photoelectrode

$$\eta = \frac{k_t}{k_t + k_r}. \quad (9)$$

Figure 4-e shows a loss in photoelectrode efficiency as light becomes stronger, which is a cause of increased recombination upon intensification of incoming light.

## CONCLUSIONS

In this work, we have studied the influence of light intensity on the kinetics of light-driven hydrogen evolution at Rh doped SrTiO<sub>3</sub> photoelectrode in sodium sulfate electrolyte. Photoelectrochemical impedance spectroscopy proved to be a powerful technique to determine the kinetic parameters of the system under different light intensities. As expected, the flux of photogenerated minority carriers ( $I_0$ ) (i.e. the flux of electrons in p-type semiconductors under reversed bias) increased with light strengthening. Furthermore, we observed that the recombination rate constant ( $k_r$ ) displayed a slight tendency to rise as light became more intense, which was interpreted to be related to the increasing concentration of electrons at the interface.

Conversely, the charge transfer rate constant  $k_r$  proved to be independent of light intensity, a characteristic known as light-induced Fermi level pinning. Stronger illumination caused a decrease in band bending ( $\phi_{sc}$ ) and in the charge within the space charge region ( $Q_{sc}$ ), which determined a decrease in the space charge capacitance. Overall, the efficiency of the photoelectrode regarding the transformation of visible light into H<sub>2</sub> decreased as light became more intense, due to increased recombination rate.

## REFERENCES

1. S. Chu, A. Majumdar, Opportunities and challenges for a sustainable energy future, *Nature*, 488, 294 (2012), doi:10.1038/nature11475.
2. D. Fabian, S. Hu, N. Singh, F. Houle, T. Hisatomi, K. Domen, F. Osterloh, S. Ardo, Particle Suspension Reactors and Materials for Solar-Driven Water Splitting, *Energy Environ. Sci.*, 8, 2825 (2015), doi:10.1039/C5EE01434D.
3. T. Hisatomi, J. Kubota, K. Domen, Recent advances in semiconductors for photocatalytic and photoelectrochemical water splitting., *Chem. Soc. Rev.*, 43, 7520 (2014), doi:10.1039/c3cs60378d.
4. J. Ran, J. Zhang, J. Yu, M. Jaroniec, S.Z. Qiao, Earth-abundant cocatalysts for semiconductor-based photocatalytic water splitting, *Chem. Soc. Rev.*, 43, 7787 (2014), doi:10.1039/c3cs60425j.
5. M. Schreier, J. Luo, P. Gao, T. Moehl, M.T. Mayer, M. Grätzel, Coordinative immobilization of a molecular catalyst on Cu<sub>2</sub>O photocathodes for CO<sub>2</sub> reduction, *J. Am. Chem. Soc.*, 138, 1938 (2016), doi:10.1021/jacs.5b12157.
6. J. Swierk, T. Mallouk, Design and development of photoanodes for water-splitting dye-sensitized photoelectrochemical cells., *Chem. Soc. Rev.*, 42, 2357 (2013), doi:10.1039/c2cs35246j.
7. J. Saioa Cobo, P. Jacques, J. Fize, V. Fourmond, L. Guetaz, B. Jusselme, V. Ivanova, H. Dau, S. Palacin, M. Fontecave, V. Artero, A Janus, Cobalt-based catalytic material for electro-splitting of water, *Nat. Mater.*, 11, 802 (2012), doi:10.1038/nmat3385.
8. B. Rausch, M. Symes, G. Chisholm, L. Cronin, Decoupled catalytic hydrogen evolution from a molecular metal oxide redox mediator in water splitting, *Science*, 345, 1326 (2014).
9. E. Andreiadis, P. Jacques, P. Tran, A. Leyris, M. Chavarot-Kerlidou, B. Jusselme, M. Matheron, J. Pécaut, S. Palacin, M. Fontecave, V. Artero, Molecular engineering of a cobalt-based electrocatalytic nanomaterial for H<sub>2</sub> evolution under fully aqueous conditions, *Nat. Chem.*, 5, 48 (2013), doi:10.1038/nchem.1481.
10. R. Subbaraman, D. Tripkovic, D. Strmcnik, K. Chang, M. Uchimura, A. Paulikas, V. Stamenkovic, N. Markovic, Enhancing Hydrogen Evolution Activity in Water Splitting by Tailoring Li<sup>+</sup>-Ni(OH)<sub>2</sub>-Pt Interfaces, *Science*, 334, 1256 (2011).



## Chebyshev's noise spectroscopy for testing electrochemical systems

B. Grafov\*, A. Klyuev, A. Davydov\*\*, V. Lukovtsev

A. N. Frumkin Institute of Physical Chemistry and Electrochemistry of Russian Academy of Sciences, Moscow, Russia

Received December 7, 2016      Revised January 11, 2017

The electrochemical noise spectroscopy based on the orthonormal Chebyshev's polynomials of discrete variable is presented. Chebyshev's noise spectroscopy has an important advantage. The majority of Chebyshev's spectral lines is stable with respect to a drift of electrochemical noise. This property of Chebyshev's noise spectroscopy is demonstrated by the examples of electrochemical corrosion noise and the noise of lithium primary power source. Chebyshev's noise spectroscopy can be used as a technique for non-destructive testing in various field of pure and applied electrochemistry including electrochemical energetics and electrochemical corrosion.

**Key words:** electrochemical noise, Chebyshev's test spectroscopy.

### INTRODUCTION

The electrochemical noise spectroscopy has great advantages [1-14]. Under the conditions of electrochemical noise spectroscopy, an electrochemical system is not subjected to any external electric impact. The internal state of electrochemical system does not change in the course of noise testing. The electrochemical noise spectroscopy has many areas of application, including the electrochemical corrosion processes and electrochemical energetics.

In many cases, the analysis of noise data is complicated by a drift of electrochemical noise, which can considerably distort the noise spectra [15-20].

The aim of this work is to present the electrochemical noise spectroscopy based on orthonormal Chebyshev's polynomials of discrete variable [21, 22]. Chebyshev's spectroscopy has an important advantage. The majority of discrete lines of Chebyshev's noise spectrum are stable with respect to a drift of electrochemical noise [23, 24]. The stability of discrete lines of Chebyshev's noise spectrum is demonstrated by the examples of electrochemical corrosion noise and the noise of lithium primary power source at the open circuit.

### ALGORITHM OF DISCRETE CHEBYSHEV'S NOISE SPECTROSCOPY

Let us consider a random time series  $y(t)$  containing  $N \cdot M$  samples. A period of discretization

of electrochemical noise signal is taken as a unit time. A random series  $y(t)$  can be formed, for example, by using discrete measurements of open-circuit voltage of primary power source. A random time series  $y(t)$  is divided into  $M$  segments  $\{y_t^{(m)}\}$ . The number of segment  $m$  takes all integer numbers from 0 to  $M - 1$  inclusive. Each segment contains  $N$  samples. Index  $t$  (the sample number inside a segment) takes all integer numbers from 0 to  $N - 1$ .

Let matrix  $P_{kt}$  be a square  $N \times N$  matrix based on the system of orthonormal Chebyshev's polynomials of discrete variable  $t$  ( $t = 0, 1, \dots, N - 1$ ). The subscript  $k$  of matrix  $P_{kt}$  indicates a degree of Chebyshev's discrete polynomial ( $k = 0, 1, \dots, N - 1$ ). The information on the properties of Chebyshev's polynomials of discrete variable is available from [21, 22].

The matrix product of the matrix  $P_{kt}$  by a random vector  $y_t^{(m)}$  forms a set of random vectors  $\{P_{kt}y_t^{(m)}\}$ :

$$P_{kt}y_t^{(m)} = \sum_{t=0}^{N-1} P_{kt}y_t^{(m)} \quad (1)$$

To each segment with number  $m$ , its own random vector  $P_{kt}y_t^{(m)}$  corresponds. To obtain a discrete Chebyshev's spectrum  $Y_k^{(2)}$ , a square of random vector (1) should be averaged over the entire set of segments:

$$Y_k^{(2)} = \frac{1}{M} \sum_{m=0}^{M-1} [P_{kt}y_t^{(m)}]^2 \quad (2)$$

The sample intensity  $Y_k^{(2)}$  of any spectral line  $k$  of Chebyshev's spectrum was calculated by equation (2). In our experiments, the total number

To whom all correspondence should be sent:  
E-mail: \*grafov.boris@yandex.ru, \*\*alexandavydov@yandex.ru

of samples  $M \cdot N$  did not exceed  $2^{18}$  and the segment length  $N$  did not exceed 16. The choice of relatively small values of  $N$  enabled us to obtain discrete Chebyshev's spectra (2),  $Y_k^{(2)}$ , with a high degree of averaging.

Fig. 1 shows the discrete Chebyshev's polynomial of the 15<sup>th</sup> degree, when  $N = 16$ . It is seen that the discrete Chebyshev's polynomials serve as a window [25, 26]. A modulus of the Chebyshev's polynomial in the center of segment has the largest value.

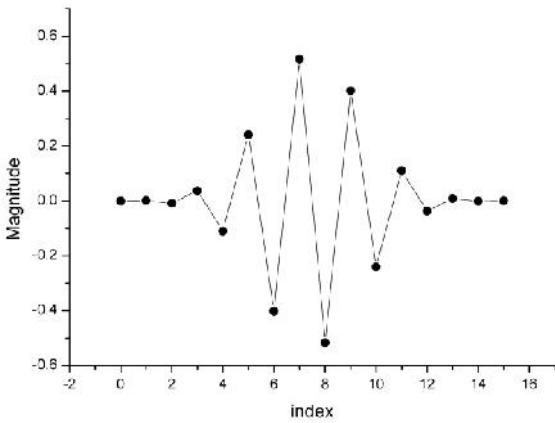


Fig. 1. Discrete Chebyshev's polynomial of 15<sup>th</sup> degree ( $N = 16$ ).

### STABILITY OF DISCRETE CHEBYSHEV'S SPECTRUM WITH RESPECT TO A DRIFT OF CORROSION NOISE

Figure 2 (curve A) shows a discrete realization of electrochemical corrosion noise. The discretization frequency was 45.5 Hz. The noise signal was measured with an IPC-Pro MF potentiostat (Russia). The realization  $y_c(t)$  of electrochemical corrosion noise contained  $2^{15}$  samples.

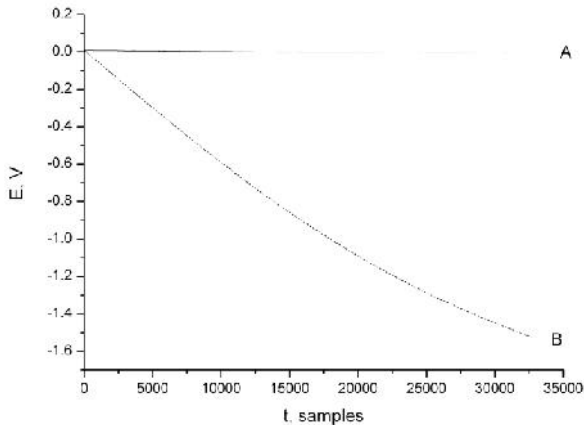


Fig. 2. (A) Electrochemical corrosion noise of a couple of identical NiMo16Cr15W electrodes  $y_c(t)$  and (B) the same noise with added artificial drift  $y_c(t) + y_c^{(d)}(t)$ .

To check the stability of intensity of Chebyshev's spectral lines with respect to a drift of electrochemical noise, an artificial drift signal  $y_c^{(d)}(t)$  was added to the realization  $y_c(t)$ :

$$y_c^{(d)}(t) = b_c \cdot \tanh(t / \tau_c), \quad (3)$$

where  $b_c = -2$  V and  $\tau_c = 2^{15}$ . Figure 2 (curve B) shows the total signal  $y_c(t) + y_c^{(d)}(t)$ , (the realization plus an artificial drift).

Figure 3 (A) shows the discrete Chebyshev's spectrum  $Y_k^{(2)}$  of corrosion noise signal  $y_c(t)$  calculated by equation (2) ( $N = 8$ ). Curve B (Fig. 3) shows the discrete Chebyshev's spectrum of the total signal  $y_c(t) + y_c^{(d)}(t)$ . It is seen that the dependences A and B (Fig. 3) almost coincide at all spectral lines except for lines  $k = 0$  and  $k = 1$ . When an artificial trend (3) is added, the intensity of the first spectral line of Chebyshev's spectrum increased by 35 times. It is seen that the intensity of high spectral lines starting from the line  $k = 2$  of Chebyshev's spectrum is stable with respect to a drift of electrochemical corrosion noise.

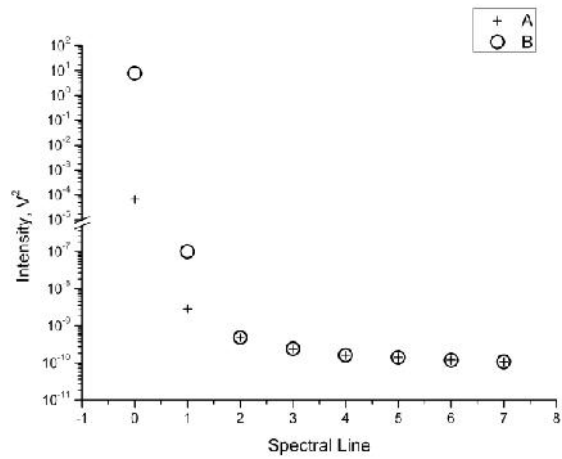


Fig. 3. Discrete Chebyshev's spectra of (A) electrochemical corrosion noise of a couple of identical NiMo16Cr15W electrodes  $y_c(t)$  and (B) the same noise with added artificial drift  $y_c(t) + y_c^{(d)}(t)$ .

### STABILITY OF DISCRETE CHEBYSHEV'S SPECTRUM WITH RESPECT TO A DRIFT OF CORROSION NOISE OF LITHIUM PRIMARY POWER SOURCE

The fluctuating voltage  $y_L(t)$  (Fig. 4, curve ) of uncharged lithium primary power source LS-33600 (Saft) (17 A h) was recorded with a

spectrometer of electrochemical noises (Frumkin Institute of Physical Chemistry and Electrochemistry, RAS). The discretization frequency of noise signal was 25 Hz. The noise signal realization contained  $2^{13}$  samples. To demonstrate the stability of Chebyshev's spectrum with respect to a drift of electrochemical noise, an artificial drift signal  $y_L^{(d)}(t)$  was added to the curve A (Fig. 4):

$$y_L^{(d)}(t) = b_L \cdot \tanh(t / \tau_L) \quad (4)$$

where  $b_L = 0.2$  V and  $\tau_L = 2^{13}$ .

The total signal  $y_L(t) + y_L^{(d)}(t)$  is shown on Fig. 4, curve B.

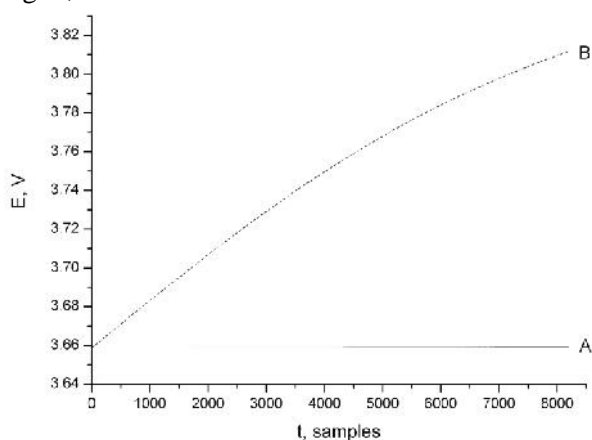


**Fig. 4.** (A) Noise of lithium primary power source LS-33600  $y_L(t)$  and (B) the same noise with added artificial drift  $y_L(t) + y_L^{(d)}(t)$ .

Figure 5 gives the Chebyshev's spectra ( $N = 8$ ) for noise signal  $y_L(t)$  of lithium primary power source (A) and for the total noise signal  $y_L(t) + y_L^{(d)}(t)$  (B). The Chebyshev's spectra were calculated by equation (2).

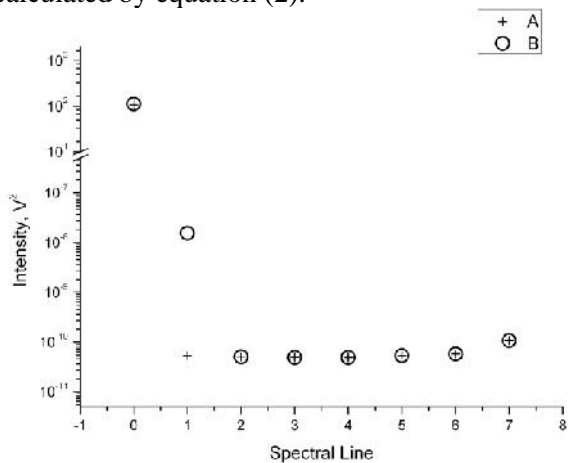


**Fig. 5.** Discrete Chebyshev's spectra of (A) noise of lithium primary power source LS-33600  $y_L(t)$  and (B) the same noise with added artificial drift  $y_L(t) + y_L^{(d)}(t)$ .

Figure 5 shows that the intensities of spectral lines  $k = 2,3,4,5,6,7$  for dependences A and B virtually coincide. The Chebyshev's spectra are stable to a drift of electrochemical noise. The exceptions are the spectral lines  $k = 0$  and  $k = 1$ . The intensities of these lines are rather sensitive to the drift of electrochemical noise. When an artificial trend (4) was added, the intensity of the first spectral line ( $k = 1$ ) of Chebyshev's spectrum increased by 291 times.

## CONCLUSIONS

The electrochemical Chebyshev's noise spectroscopy is a powerful tool for gaining the information on the internal state of electrochemical systems without imposing an external electrical signal. The intensities of spectral lines, starting from the second spectral line of Chebyshev's spectrum, are stable against a drift of electrochemical noise.

Sustainability of discrete Chebyshev spectrum to a strong drift of electrochemical noise is the basis for reliable noise monitoring of electrochemical systems. Moreover, the sustainability of discrete Chebyshev spectrum allows one to investigate the structure of electrochemical noise. The structural description of noise of electrochemical systems can be used for their monitoring.

We can perform the discrete spectrum analysis of electrochemical noise with a strong drift by using the transformations of other type. The transformations include the discrete wavelet transformation [9] and the discrete Fourier transformation with special windows [25-26]. We believe that the Stoyanov rotating transformation [27] can be useful for spectral analysis of electrochemical noise with a strong drift. A comparison between the spectral properties of discrete Chebyshev transformation and the spectral properties of the discrete transformations outlined above is outside the scope of the present paper. The authors hope to discuss this topic elsewhere.

The Chebyshev's noise spectroscopy is appropriate for soft testing of electrochemical systems. The soft testing, i.e. testing without imposing an external electrical signal, is especially important for the devices and systems of electrochemical energetics and the electrochemical corrosion systems.

**Acknowledgements.** We are grateful to Daria Vladikova, Visnja Horvat-Radosevic, and Tamas Pajkossy for their kind invitation to present a paper for a special issue of the journal *Bulgarian Chemical Communications* devised by the

Bulgarian Electrochemical Society to honor Prof. Zdravko Stoynov.

This work was supported by the Russian Foundation for Basic Research, project no. 16-29-09375.

#### REFERENCES

1. V. A. Tyagai, *Elektrokhimiya*, **3**, 1331 (1967).
2. W. P. Iverson, *J. Electrochem. Soc.*, **58**, 617 (1968).
3. B. M. Grafov, V. G. Levich, *Soviet Journal of Experimental and Theoretical Physics*, **27**, 507 (1968).
4. M. Fleischmann, J. W. Oldfield, *J. Electroanalyt. Chem.*, **27**, 207 (1970).
5. G. C. Barker, *J. Electroanalyt. Chem.*, **39**, 484 (1972).
6. I. Epelboin, C. Gabrielli, M. Keddam, L. Raillon, *J. Electroanalyt. Chem.*, **105**, 389 (1979).
7. P. C. Searson, J. L. Dawson, *J. Electrochem. Soc.*, **135**, 1908 (1988).
8. S. Martinet, R. Durand, P. Ozil, P. Leblanc, P. Blanchard, *J. Power Sources*, **83**, 93 (1999).
9. A. Aballe, M. Bethencourt, F. J. Botana, M. Marcos, *Electrochim. Acta*, **44**, 4805 (1999).
10. A. Hassibi, R. Navid, R. W. Dutton, T. H. Lee, *J. Appl. Phys.*, **96**, 1074 (2004).
11. R. A. Cottis, *Russ. J. Electrochem.*, **42**, 497 (2006).
12. S. F. Timashev, Y. S. Polyakov, *Fluct. Noise Lett.*, **7**, R15 (2007).
13. C. A. Loto, *Int. J. Electrochem. Sci.*, **7**, 9248 (2012).
14. P. S. Singh, S. G. Lemay, *Anal. Chem.*, **88**, 5017 (2016).
15. F. Mansfeld, Z. Sun, C. H. Hsu, A. Nagiub, *Corr. Sci.*, **43**, 341 (2001).
16. U. Bertocci, R. P. Nogueira, P. Rousseau, *Corrosion*, **58**, 337 (2002).
17. H. Ashassi-Sorkhabi, D. Seifzadeh, *J. Appl. Electrochem.*, **38**, 1545 (2008).
18. M. Ohanian, V. Martinez-Luaces, V. Diaz, *J. Corros. Sci. Eng.*, **13**, 52 (2010).
19. A. M. Homborg, T. Tinga, X. Zhang, E. P. M. van Westing, P. J. Oonincx, J. H. W. de Wit, *Electrochim. Acta*, **70**, 199 (2012).
20. S. S. Jamali, D. J. Mills, *Prog. Org. Coat.*, **95**, 25 (2016).
21. A. V. Nikiforov, S. K. Suslov, V. B. Uvarov, *Classical Orthogonal Polynomials of a Discrete Variable*, Springer-Verlag, Berlin, Heidelberg, 1991.
22. N. Gogin, M. Hirvensalo, *On the Generating Function of Discrete Chebyshev Polynomials*, TUCS Technical Report No.819, TUCS, Turku, 2007.
23. M. G. Astaf'ev, L. S. Kanevskii, B. M. Grafov, *Russ. J. Electrochem.*, **43**, 17 (2007).
24. B. M. Grafov, Yu. A. Dobrovol'skii, A. D. Davydov, A. E. Ukshe, A. L. Klyuev, E. A. Astaf'ev, *Russ. J. Electrochem.*, **51**, 503 (2015).
25. J. Harris, *Proc. IEEE*, **66**, 172 (1978).
26. D. J. Thomson, *Proc. IEEE*, **70**, 1055 (1982).
27. Z. Stoynov, *Fourier analysis in the presence of nonstationary aperiodic noise*, Diss. Techn. Wiss. ETH Zürich, Nr. 7839, 1985.

\* , . \*\* , .

7 2016 .; 11 2017 .  
( )

## Electrochemical impedance measurements in non-stationary systems – application of the 4-dimensional analysis method for the impedance analysis of overoxidized poly(3,4-ethylenedioxythiophene)-modified electrodes

M. Ujvári<sup>1</sup>, D. Zalka<sup>1</sup>, S. Vesztergom<sup>1</sup>, S. Eliseeva<sup>2</sup>, V. Kondratiev<sup>2</sup>, G. G. Láng<sup>1\*</sup>

<sup>1</sup> Institute of Chemistry, Laboratory of Electrochemistry and Electroanalytical Chemistry, Eötvös Loránd University, Pázmány P. s. 1/A, H-1117 Budapest, Hungary

<sup>2</sup> Chemical Department, St. Petersburg State University, Universitetskii pr. 26, 198504, Russia

Received March 10, 2017      Revised March 26, 2017

In this study it has been shown that the 4-dimensional analysis method, originally proposed by Stoynov, can not only be used for the correction of existing (experimentally measured) impedance data, but it also opens up the possibility of the estimation of impedance spectra outside the time interval of the measurements. As an illustrative example the method is applied for the determination of the charge transfer resistance of a polymer modified electrode corresponding to the time instant just after overoxidation of the poly(3,4-ethylenedioxythiophene) (PEDOT) film.

**Key words:** non - stationary system, instantaneous impedance, overoxidation of poly(3, 4 - ethylenedioxythiophene) (PEDOT), 3D complex interpolation method, charge transfer resistance..

### INTRODUCTION

The single sine excitation method is by far the most commonly used technique for measuring impedance in electrochemical systems. In a single sine excitation measurement, the excitation signal is time-invariant and deterministic. When this method is employed the system under investigation is sequentially excited by applying small sinusoidal waves of a quantity, such as current or voltage. This is done within a given frequency range (e.g. from some mHz to some MHz). If the condition of linearity is fulfilled, the response of the system is an alternating voltage or current signal with the same frequency as that of the input signal. The frequency dependence of the response can be attributed to specific processes occurring either at the interfaces (electrodes) or inside the phases in contact. The impedance at a given frequency is the complex ratio of the Fourier transforms of the voltage and the current signals (sinusoids of the same frequency). A frequency spectrum can be obtained by sweeping the excitation frequency. Unfortunately single sine impedance spectroscopy measurements suffer from increasing time consumption if the frequency range is extended toward lower frequencies. When data recording occurs at low frequencies a complete measurement sequence can take significant time (at least several minutes).

However, many electrochemical systems are intrinsically nonstationary and are affected by time-dependent phenomena. According to the usual interpretation of the concept of impedance, impedance is not defined as time-dependent and, therefore, there should not exist impedance out of stationary conditions. On the other hand, it is possible to show that under some suitable conditions time dependence can be conciliated into the concept of impedance.

Stoynov pointed out that there are two general cases in the impedance measurements related to the non-stationary errors [1]:

(i) measurements in a stationary system under non-steady state conditions;

(ii) investigation of non-stationary systems.

The error of the first type increases sharply with decrease of the frequency (see ref. [2]). In the second case, an additional error appears, related to the measurement delay due to the classical “frequency by frequency” mode of impedance measurements.

Different methods to deal with a non-stationary behavior can be found in literature. Stoynov proposed a method of determining instantaneous impedance diagrams for non-stationary systems based on a four-dimensional approach [1, 3]. Darowicki et al. developed a dynamic EIS method to trace the dynamics of the degradation process by the calculation of an instantaneous impedance [4]. The possibility to analyze non-stationary impedance spectra by employing standard equivalent circuits was discussed in [5]. In [6] a procedure was proposed to quantify and correct

---

To whom all correspondence should be sent:  
E-mail: langgyg@chem.elte.hu



for the time-evolution by means of the calculation of an instantaneous impedance. (The instantaneous impedance is defined as an instantaneous projection of the non-stationary state of the system into the frequency domain [1].)

The method of Stoynov (the 4-dimensional analysis) provides for correction of the systematic errors arising during the measurements of time-evolving impedance, i.e. when the consecutive impedance measurements are performed at different system states, but each of the measured impedance values can be accepted as “valid” in the classical sense. In this case the measured data are corrupted by typical errors caused by the system evolution during the experiment [7]. (If the problem is related to the mathematical basis of the transfer function analysis [2, 8], the so called rotating Fourier transform can be used [7, 9].)

As discussed before, the four-dimensional analysis method is based on the assumption for the continuum of the object’s state and parameters space. It requires a number of impedance spectra recorded subsequently at the same set of frequencies. Every measured data at a given frequency should additionally contain the time of measurement. Thus, the experimental data form a set of 4-dimensional arrays, containing frequency, real and imaginary components of the impedance and the time of measurement. The post-experimental analytical procedure previews the reconstruction of calculated instantaneous impedances. For every measured frequency two one dimensional functions of “iso-frequency dependencies” (e.g. for the real and for the imaginary components) are constructed. Then, each iso-frequency dependence is modeled by an approximating formal model. On the basis of the continuity of the evolution, interpolation (and extrapolation) is performed resulting in instantaneous projections of the full impedance-time space and “reconstructed” instantaneous impedances related to a selected instant of the time (i.e. the beginning of each frequency scan). Thus a set of impedance diagrams is obtained, containing instantaneous impedances, virtually measured simultaneously. Each of these diagrams can be regarded as a stationary one, free of non-steady-state errors.

On the basis of the above, one could conclude that the four-dimensional analysis method can be most effective in the correction of low-frequency impedance data. However, as it will be shown in the present study, this technique can also be used for solving other problems. For instance, it is known that the impedance spectra of overoxidized poly(3,4-ethylenedioxythiophene) (PEDOT) films

on gold recorded in aqueous sulphuric acid solutions differ from those measured for freshly prepared films. The most interesting feature is the appearance of an arc (or a “depressed semicircle”) at high frequencies in the complex plane impedance plot. The decreasing capacitance and the increasing charge transfer resistance suggest that during overoxidation the electrochemical activity of the film decreases and the charge transfer process at the metal/film interface becomes more hindered than in the case of pristine films. The published results support the mechanistic picture, according to which the originally compact and strongly adherent polymer films undergo structural changes during the overoxidation (degradation) process [10-16]. Overoxidation results in the partial delamination of the polymer layer and leads to the exposure of some parts of the underlying metal substrate to the electrolyte solution.

Nevertheless, it should be emphasized here that the polymer film still present on the substrate after overoxidation remains electroactive, and its internal structure may be an interesting subject for further studies, since according to literature reports conducting polymers in different overoxidation states show unique features useful for analytical, sensing and biomedical applications [17-22].

The time evolution of the impedance spectra is a remarkable feature of the electrodes with overoxidized PEDOT films. To our knowledge, this phenomenon was first reported in ref. [23]. According to this observation, the charge transfer resistance at the (electronically conductive) substrate/polymer film interface decreases continuously over several hours when the potential is held in the “stability region” after overoxidation of the film. This means that the impedance spectra recorded using the consecutive frequency sweep mode (typical of EIS) are corrupted by typical errors caused by the system evolution during the experiment. On the other hand, for reasons of measuring technology, we are not able to record an impedance spectrum immediately after the overoxidation process. But even if we would be able to do so it wouldn’t solve the problems related to the nonstationarity of the system. It is beyond doubt that the knowledge of the “initial” charge transfer resistance is essential for the better understanding of the degradation process and it may also have an impact on practical applications.

In the present study, an attempt was made to solve both problems simultaneously by using a method very similar to that proposed by Stoynov.

## EXPERIMENTAL

*Electrodeposition of PEDOT*

Poly(3,4-ethylenedioxythiophene) films were prepared by galvanostatic deposition on both sides of thin gold plates from 0.01 mol·dm<sup>-3</sup> ethylenedioxythiophene (EDOT) solution containing 0.1 mol·dm<sup>-3</sup> Na<sub>2</sub>SO<sub>4</sub> supporting electrolyte. Analytical grade 3,4-ethylenedioxythiophene (Aldrich), p.a. Na<sub>2</sub>SO<sub>4</sub> (Fluka), and ultra-pure water (specific resistance 18.3 MΩ·cm) were used for solution preparation. All solutions were purged with oxygen-free argon (Linde 5.0) before use and an inert gas blanket was maintained throughout the experiments.

The deposition was performed in a standard three electrode cell in which the gold plate in contact with the solution served as the working electrode (WE). A spiral shaped gold wire immersed in the same solution served as the counter electrode (CE), and a KCl-saturated calomel electrode (SCE), as the reference electrode (RE). A constant current density of  $j = 0.2 \text{ mA}\cdot\text{cm}^{-2}$  ( $I = 0.2 \text{ mA}$ ) was applied for 1000 s (the geometric surface area of the working electrode was 1 cm<sup>2</sup>). The film thickness was estimated from the polymerization charge by using the charge/film volume ratio determined earlier by direct thickness measurements [24-26]. The average thickness of the PEDOT film was about 0.8 μm, the structure of the PEDOT film was globular, cauliflower-like.

*Cyclic voltammetry and impedance measurements*

Solutions used for cyclic voltammetric and impedance measurements were prepared with ultra-pure water and p.a. H<sub>2</sub>SO<sub>4</sub> (Merck). The solutions were purged with oxygen-free argon (Linde 5.0) before use and an inert gas blanket was maintained throughout the experiments. In the conventional three-electrode cell configuration the PEDOT-modified gold substrate in contact with the solution was used as the working electrode (WE), a spiral shaped gold wire immersed in the same solution as the counter electrode (CE), and a NaCl-saturated calomel electrode (SSCE) as the reference electrode (RE). The counter electrode was arranged cylindrically around the working electrode to maintain a uniform electric field.

The overoxidation of the PEDOT film was carried out in 0.1 mol·dm<sup>-3</sup> H<sub>2</sub>SO<sub>4</sub> solution a day after the deposition.

A Zahner IM6 electrochemical workstation was used in all electrochemical experiments.

## RESULTS AND DISCUSSION

*Cyclic voltammetry and overoxidation of the PEDOT-film*

The potential program applied to the PEDOT-modified electrode used in the impedance measurements (geometric surface area: 1.0 cm<sup>2</sup>) is given in Fig.1a, and the corresponding cyclic voltammograms in Fig.1b. The cyclic voltammograms recorded before and after overoxidation of the gold|PEDOT|0.1 mol·dm<sup>-3</sup> sulfuric acid (aq.) electrodes were very similar to those reported in the literature (see e.g. [13, 27]).

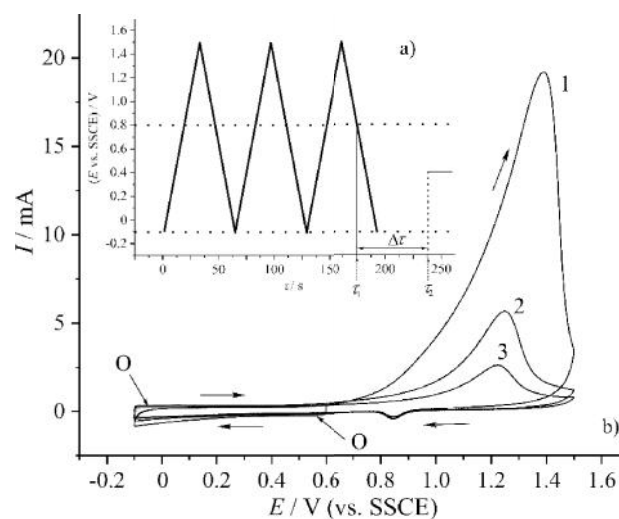


**Fig. 1.** a) The potential program applied to the PEDOT-modified electrode. The impedance measurements started at  $t_{2-1}$  is the estimated end of the overoxidation process.  $t_{2-1} = 66.4 \text{ s}$ . b) O: Cyclic voltammogram recorded before overoxidation in the potential range between - 0.1 V and 0.6 V vs. SSCE, sweep rate:  $v=50 \text{ mV/s}$ . 1-3: Successive cyclic voltammograms („overoxidation cycles”) recorded in the potential range from - 0.1 V to 1.50 V vs. SSCE, sweep rate:  $v=50 \text{ mV/s}$ .

In the 3 overoxidation cycles, the positive potential limit has been set to 1.5 V vs. SSCE (Fig. 1a). It is known [11-15] that between - 0.3 and 0.8 V vs. SSCE the oxidation-reduction process of the PEDOT films is reversible. However, at more positive potentials irreversible degradation of the polymer layer occurs. As it can be seen in Fig. 1b (curve O), the cyclic voltammograms of PEDOT-modified electrodes show almost pure capacitive behavior in the potential range between -0.1 V and +0.6 V, i.e. if the positive potential limit is kept below 0.8 V vs. SSCE. If the polarization potential exceeds this critical value, an oxidation peak without corresponding reduction peak appears (see Fig. 1b). The voltammograms recorded before

and after overoxidation are similar in shape and show typical (pseudo-)capacitive behavior, but the redox capacity of the (over)oxidized polymer film is considerably smaller than that of the freshly prepared film.

### Impedance measurements

After overoxidation, subsequent impedance measurements were performed at 0.4 V vs. SSCE over a frequency range from 100 mHz to 100 kHz (starting at  $t_2$  in Fig. 1a).

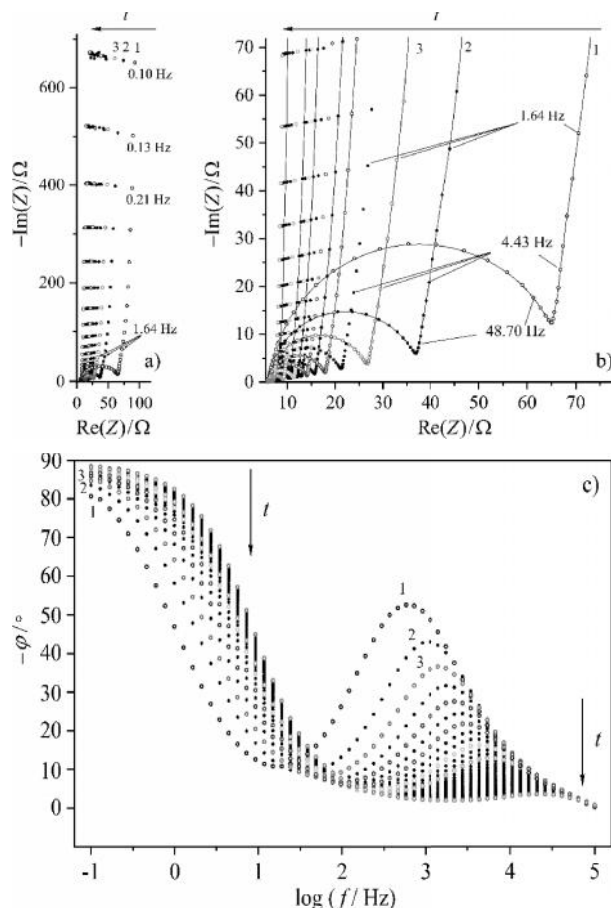


**Fig. 2.** a) Successive impedance diagrams of the Au | PEDOT | 0.1 M H<sub>2</sub>SO<sub>4</sub> at  $E = 0.4$  V vs. SSCE recorded after overoxidation; b) High frequency part of the Argand diagrams; c) Phase angles corresponding to a); The solid lines are to guide the eye only: not curve fits.

The data points were measured at 60 discrete frequencies in the frequency region investigated during each scan at an amplitude of 5 mV.

In Fig. 2 the results are presented in the complex plane. The 3D representation of the data is shown in Fig. 3. The curves in Figs. 2 and 3 are similar to those reported for other polymer modified electrodes [28, 29], all the complex plane diagrams contain a capacitive semicircle and a Warburg-like region (quite narrow) followed by a CPE-like domain at low frequencies

[30]. However, since the successive impedance diagrams are continuously changing with time (see Figs. 2 and 3), it is obvious that the system is still in a transient state rather than in a stationary (or equilibrium) state.

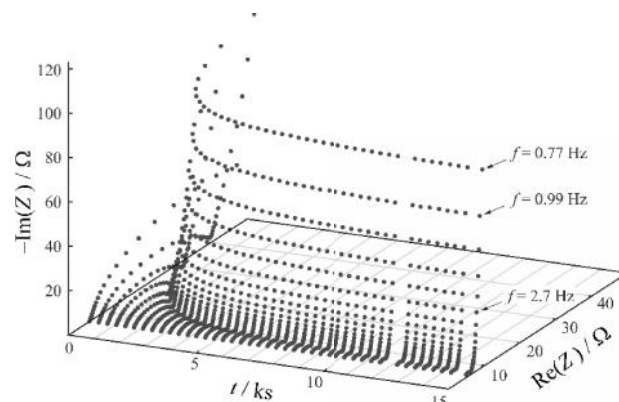


**Fig. 3.** Time dependence of the locus curves of recorded impedance spectra in the Argand-representation.

As already discussed in the introduction, in such cases a post-experimental analytical procedure is necessary for the reconstruction of “instantaneous impedances” [2, 3, 7, 9, 31-33].

For this purpose a 3D complex interpolation method using a three-dimensional bicubic spline interpolation algorithm implemented in LabVIEW [34] has been adopted. Mathematically, this corresponds to the 4-dimensional analysis proposed by Stoyanov [1-3, 7].

Two different approaches were applied for the calculation of the corrected (synthetic) impedance diagrams. In the first, the measured magnitudes and phase angles were used in the interpolation/extrapolation process (Fig. 4), and the interpolated/extrapolated magnitude and phase angle values corresponding to the same time moments were converted into real and imaginary parts of the complex impedance. In the second, the interpolation/extrapolation was carried out using real and imaginary parts of impedances measured at identical frequencies („isofrequential components”) [1] (see Fig. 5). This means that for every measured frequency two one-dimensional functions of iso-frequency dependencies (for the real and for the imaginary components) have been constructed, and on the basis of the continuity of the evolution, interpolation (and extrapolation) has been performed. As a result a set of instantaneous impedances related to a selected instant of time (i.e. the beginning of each frequency scan) has been obtained.) As it can be seen by comparing Figs 4 and 5, the corrected impedances obtained by the two methods practically coincide.

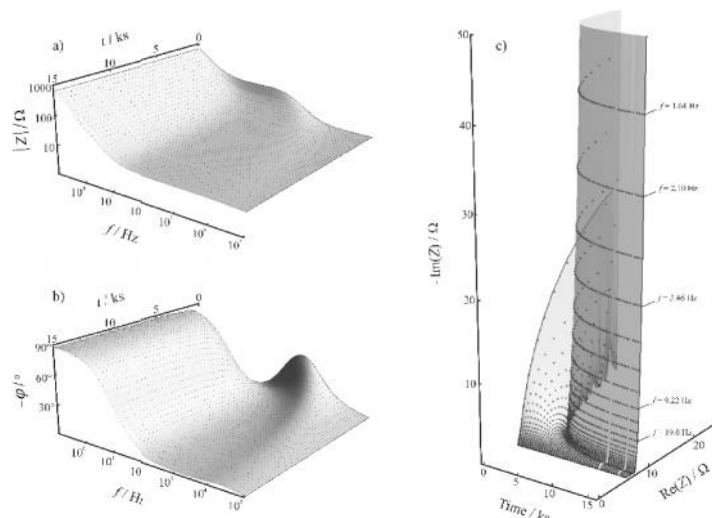


**Fig. 4.** Results of a 3D complex interpolation. The absolute values (a) and phase angles (b) of measured impedances are shown as a function of time and frequency (discrete points). The continuous surface is created by a three-dimensional bicubic spline interpolation algorithm implemented in LabVIEW [1]. In (c) both the measured data (discrete points) and the interpolated surface are transformed to a time-dependent complex plane representation.

According to the above considerations, extrapolation allows the reconstruction of spectra that can be regarded as “original” (undistorted) from a series of time-dependent spectra. By extrapolation to  $t = 0$  (2 in Fig. 1) the impedance diagram corresponding to the starting time of the measurement series could be constructed (Fig. 6, plots designated by S2)

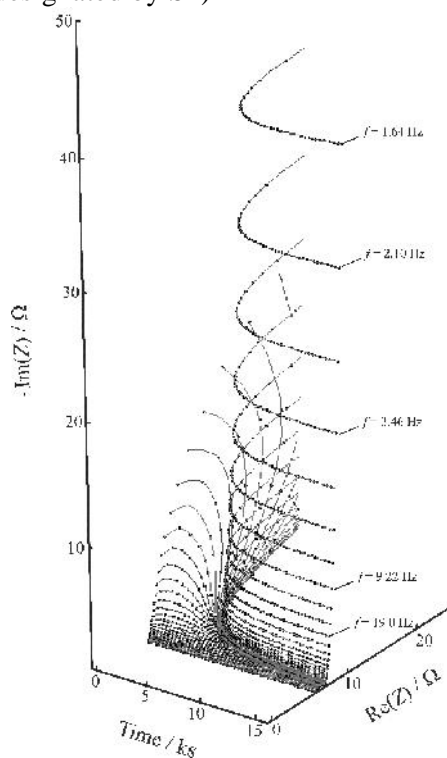


**Fig. 5.** The measured impedance spectra and some isofrequent space curves created by spline interpolation shown in a three-dimensional (time dependent) complex plane representation.

The differences between the diagrams S1 (directly measured data points) and S2 (calculated values for  $t = 0$  s) in Fig. 6 are assumed to a first approximation to be entirely due to time evolution of the charge transfer resistance ( $R_{ct}$ ) at the gold substrate/polymer interface. The value of the charge transfer resistance at  $t = 0$  s was estimated by fitting the high-frequency impedance data (frequency range 38.57 Hz – 10.65 kHz) to an equivalent-circuit analog, shown in the inset of Fig. 7. The equivalent-circuit analog is based on the impedance model proposed in [29], wherein the double layer capacitance at the substrate/polymer interface has been replaced by a constant-phase element (CPE), which more accurately imitates the behavior of the double layer ( $Z_{CPE} = \frac{1}{B}(i)^{-a}$ , where  $i$  is the imaginary unit,  $B$  and  $a$  are the CPE parameters, and  $\omega$  is the angular frequency, respectively).

The estimated values of the parameters (obtained by complex non-linear least squares (CNLS) fitting based on the Levenberg–Marquardt algorithm [35, 36]) are shown in the first column of Table. 1. Curve F1 in Fig. 7 is the complex plane diagram (Argand plot) simulated by using these parameters.

All the above results imply that the extrapolation method can not only be used for the correction of experimental data (i.e. the measured impedances), but it opens up the possibility of the estimation of the impedance spectra outside the time interval of the impedance measurements.

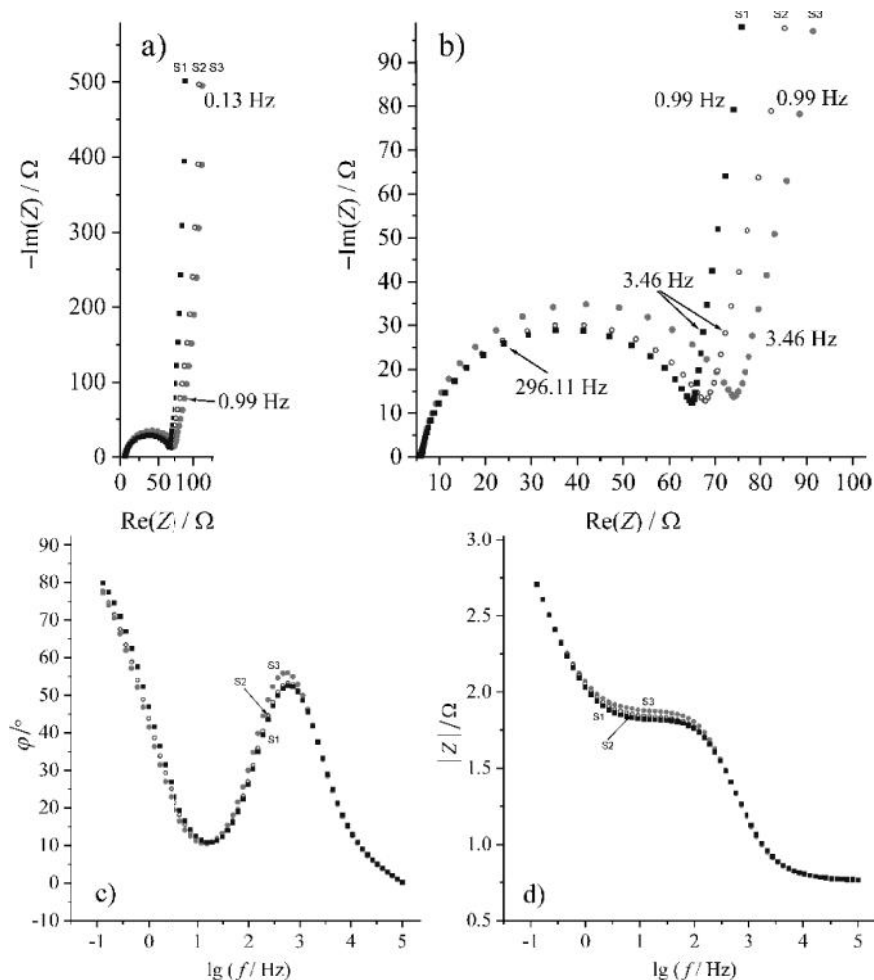


**Fig. 6.** S1 (■): Data measured during the frequency sweep starting at  $t_2$  in Fig. 1.  $t = 0$  is the starting time of the impedance measurement series. S1 is the first set of data measured in the series and contains inherent time dependence; S2 (○): corrected impedance diagram obtained by extrapolation to  $t = 0$  (the „instantaneous” spectrum corresponding to the starting time of the impedance measurement series); S3 (□): calculated spectrum corresponding to the presumed end of the overoxidation process,  $t = -66.4$  s ( $t_1$  in Fig. 1). The data are shown in complex plane (a,b) and in Bode (b,c) representations.

Complex plane and Bode plots of the calculated impedance corresponding to the presumed end of the overoxidation process are shown in Fig. 6 (plots marked by S3). Similarly to the charge transfer resistance at  $t = 0$  s, the  $R_{ct}$  at  $t = -66.4$  s was obtained by CNLS fitting of the extrapolated data (frequency range 38.57 Hz – 10.65 kHz) [29, 36,37]. The best-fit values of the parameters are shown in the 2nd column of Table. 1, while F2 in Fig. 7 is the impedance spectrum calculated by using the estimated parameters.

As it can be seen from Fig. 7, the model function fits the extrapolated impedance data for  $t = 0$  s quite well, for  $t = -66.4$  s the goodness of the fit is poorer. This is most probably the consequence of the very rapid time evolution of the impedance response immediately after overoxidation of the PEDOT film.

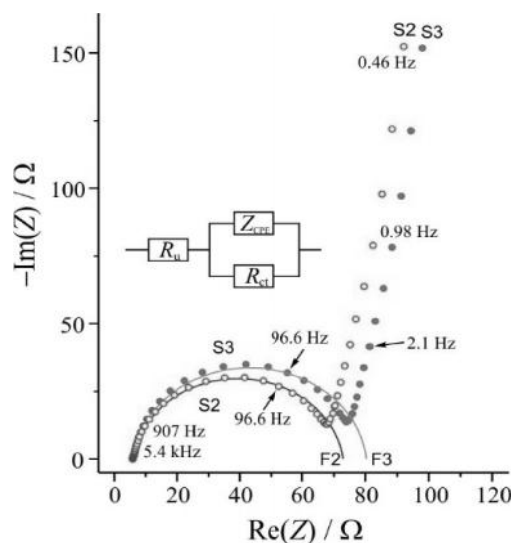


**Fig. 7.** S2 and S3: Impedance diagrams containing the „instantaneous impedances”, virtually measured simultaneously at  $t = 0$  s (S2) and at  $t = -66.4$  s (S3). F2 and F3: Impedance spectra calculated by using the estimated („best-fit”) parameters.

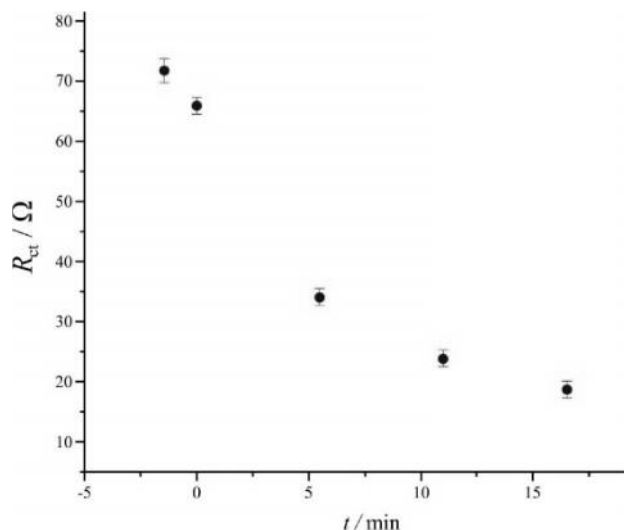


**Fig. 8.** Time evolution of the charge transfer resistance at the beginning of the experiment. The  $R_{ct}$  values are determined from the calculated impedance spectra.

**Table 1.** EDS surface composition of BCY15 and BCY15/Ni.

	$t = 0$ s	$t = -66,4$ s
	Estimated mean values with confidence intervals at 95% confidence level	Estimated mean values with confidence intervals at 95% confidence level
$R_u/\Omega$	$5.97 \pm 0.27$	$5.97 \pm 0.41$
$R_{ct}/\Omega$	$67.0 \pm 1.1$	$74.4 \pm 1.6$
$B/Fs^{a-1}$	$(1.064 \pm 0.063) \cdot 10^{-5}$	$(1.141 \pm 0.093) \cdot 10^{-5}$
$a$	$0.925 \pm 0.012$	$0.939 \pm 0.017$

Some of the charge transfer resistance values determined by using the “instantaneous” impedances are shown in Fig. 8. It can be seen from Table 1 (and from Fig. 8), that the highest value of  $R_{ct}$  is about 75  $\Omega$ . This value corresponds to the time instant just after overoxidation of the film. Starting from this value,  $R_{ct}$  decreases continuously with experimental time to a value somewhat higher than the charge transfer resistance of the pristine electrode.

## CONCLUSIONS

The 4-dimensional analysis method, originally proposed by Stoynev, can serve as an efficient tool for the study of non-stationary systems. It can not only be used for the correction of the existing (experimentally measured) impedance data, but it opens up the possibility for the estimation of the impedance spectra outside the time interval of the

impedance measurements. The method was successfully applied for the determination of the charge transfer resistance of a gold|PEDOT|0.1 mol·dm<sup>-3</sup> sulfuric acid (aq.) electrode corresponding to the time instant just after overoxidation of the PEDOT film. In the experiment presented in this study, the “starting” (calculated)  $R_{ct}$  value was approximately 75  $\Omega$ ·cm<sup>2</sup>. After 66.4 seconds this value fell to about 67  $\Omega$ ·cm<sup>2</sup>, i.e. it decreased by ~10 % in the first minute after the overoxidation procedure.

On the other hand, we acknowledge that criticism may arise from the choice of the method used to overoxidize the polymer film before the impedance measurements, since between the end of the last CV and the start of the first impedance measurement ( $t_2$  in Fig. 1a) the electrode was held at the open circuit potential. Nevertheless the extrapolation procedure may be justified by the fact that according to experimental observations the impedance parameters of the Au|PEDOT|0.1 mol·dm<sup>-3</sup> sulfuric acid (aq.) electrode are practically independent of the electrode potential within a wide potential range (here between -0.1 and -0.8 V vs. SSCE). It should also be noted that in most practical cases no or only little information is available about the past history of the system involved. Therefore, because the measured data are from a time series experiment carried out within a given time period, any extrapolation beyond this time period is somewhat arbitrary.

**Acknowledgements:** Financial support from the Hungarian Scientific Research Fund (grants No. K 109036) and from the Russian Foundation for Basic Research (grant N-16-03-00457) are gratefully acknowledged.

## REFERENCES

1. Z. Stoynev, B. Savova-Stoynev, *J. Electroanal. Chem.*, **183**, 133 (1985).
2. Z. Stoynev, B. Savova, *J. Electroanal. Chem.*, **112**, 157 (1980).
3. B. Savova-Stoynev, Z. Stoynev, *Electrochim. Acta*, **37**, 2353 (1992).
4. K. Darowicki, *J. Electroanal. Chem.* **486**, 101 (2000).
5. A. Battistel, G. Du, F. La Mantia, *Electroanalysis*, **28**, 2346 (2016).
6. T. Breugelmans, J. Lataire, Th. Muselle, E. Tourwé, R. Pintelon, A. Hubin, *Electrochim. Acta*, **76**, 375 (2012).
7. Z. Stoynev, *Electrochim. Acta*, **38**, 1919 (1993).
8. M. Keddám, Chr. Rakotomavo, H. Takenouti, *J. Appl. Electrochem.*, **14**, 437 (1984).
9. Z. Stoynev, *Electrochim. Acta*, **37**, 2357 (1992).

10. A. Zykwincka, W. Domagala, B. Pilawa, M. Lapkowski, *Electrochim. Acta*, **50**, 1625 (2005).
11. M. Ujvári, M. Takács, S. Vesztergom, F. Bazsó, F. Ujhelyi, G.G. Láng, *J. Solid. State. Electrochem.*, **15**, 2341 (2011).
12. G. Láng, M. Ujvári, F. Bazsó, S. Vesztergom, F. Ujhelyi, *Electrochim. Acta*, **73**, 59 (2012).
13. M. Ujvári, J. Gubicza, V. Kondratiev, K.J. Szekeres, G.G. Láng, *J. Solid. State. Electrochem.*, **19**, 1247 (2015).
14. M. Ujvári, G.G. Láng, S. Vesztergom, K.J. Szekeres, N. Kovács, J. Gubicza, *J. Electrochem. Sci. Eng.*, **6**, 77 (2015).
15. G. Láng, M. Ujvári, S. Vesztergom, V. Kondratiev, J. Gubicza, K. Szekeres, *Z. Phys. Chem.*, **230**, 1281 (2016).
16. G. Láng, C. Barbero, Laser techniques for the study of electrode processes, in: Monographs in electrochemistry, F. Scholz (Ed.), Springer, Berlin Heidelberg, 2012.
17. N. Kovács, M. Ujvári, G.G. Láng, P. Broekmann, S. Vesztergom, *Instrum. Sci. Technol.* **43**, 633 (2015).
18. J. Li, X-Q. Lin, *Sens. Actuators B*, **124**, 486 (2007).
19. D.C. Martin, J. Wu, C.M. Shaw, Z. King, S. Spanninga, S. Richardson-Burns, *J. Hendricks, J. Yang, Polym. Rev.* **50**, 340 (2010).
20. Z. Zhuang, J. Li, R. Xu, D. Xiao, *Int. J. Electrochem. Sci.*, **6**, 2149 (2011).
21. Y. Hui, C. Bian, J. Wang, J. Tong, S. Xia, *Sensors*, **17**, 628 (2017).
22. M. Irimia-Vladu, *Chem. Soc. Rev.*, **43**, 588 (2014).
23. G.G. Láng, M. Ujvári, Z. Dankházi, S. Vesztergom, K.J. Szekeres: Analysis of impedance spectra of electrochemically deposited PEDOT films recorded before and after overoxidation, 10th International Symposium on Electrochemical Impedance Spectroscopy, A Toxa, Spain, June 19 - 24, 2016, Book of Abstracts, p.16 (0720).
24. J. Bobacka, A. Lewenstam, A. Ivaska, *J. Electroanal. Chem.*, **17**, 489 (2000).
25. A. Stoyanova, V. Tsakova, *J. Solid State Electrochem.* **14**, 1947 (2010).
26. W. Poppendieck, K.P. Hoffmann, in: J. Vander Sloten, P. Verdonck, M. Nyssen, J. Haueisen (Eds.), ECIFMBE 2008, IFCMBE Proceedings 22, Springer-Verlag, Berlin, Heidelberg, 2009, p. 2409.
27. D. Zalka, N. Kovács, K. Szekeres, M. Ujvári, S. Vesztergom, S. Eliseeva, V. Kondratiev, G.G. Láng, *Electrochim. Acta*, submitted.
28. G. Inzelt, G. Láng, *Electrochim. Acta*, **36**, 1355 (1991).
29. G. Inzelt, G. G. Láng, Electrochemical Impedance Spectroscopy (EIS) for Polymer Characterization, Ch. 3, in: Electropolymerization: Concepts, Materials and Applications, S. Cosnier, A. Karyakin (Eds.), Wiley-VCH Verlag GmbH & Co. KGaA, Weinheim, 2010.
30. G. Láng, K.E. Heusler, *J. Electroanal. Chem.*, **481**, 227 (2000).
31. Z. Stoynov, in Materials for Lithium-Ion Batteries 1999, C. Julien and Z Stoynov, Eds, 85, p. 359, NATO Science Series, Kluwer Academic Publishers, Dordrecht, Boston, London, 2000.
32. Z. Stoynov, B. Savova-Stoynov, T. Kossev, *J. Power Sources*, **30**, 275 (1990).
33. B. Savova-Stoynov, Z. Stoynov, *Key Eng. Mater.*, **59-60**, 273 (1991).
34. W.H. Press, S.A. Teukolsky, W.T. Vetterling, B.P. Flannery (Eds) *Numerical Recipes in C++: The Art of Scientific Computing*. 2nd ed. Cambridge: Cambridge University Press, 2002.
35. D. Marquardt, *SIAM J. Appl. Math.*, **11**, 431 (1963).
36. P. Valkó, S. Vajda, Advanced scientific computing in BASIC with applications in chemistry, biology and pharmacology, Data handling in science and technology, Vol. 4, Elsevier, Amsterdam, 1989.
37. G. Inzelt, G. Láng, *J. Electroanal. Chem.*, **378**, 39 (1994).

4-D  
 (3,4- )-  
 1, 1, 1, 2, 2, 1  
 1, , , . . 1 / , -1117 ,  
 2, " , " , 26, 198504,  
 10 2017 .; 26 2017 .  
 ( )  
 4- , ,  
 ( ) ,  
 ethylen ) (PEDOT) . (3,4-

## A multisine perturbation EIS system for characterization of carbon nanotube layers

T. Pajkossy\*, G. Mészáros, I. Felhősi, T. Marek, L. Nyikos

Institute of Materials and Environmental Chemistry, Research Centre for Natural Sciences, Hungarian Academy of Sciences, Magyar tudósok körútja 2, Budapest, Hungary, H-1117

Received December 29, 2016    Revised January 26, 2017

*Dedicated to Professor Zdravko Stoyanov on the occasion of his 80th birthday to honour his contributions to electrochemistry in general and impedance spectroscopy in particular*

With the purpose of fast characterization of supercapacitors' electrode materials, an impedance measurement system has been constructed which employs multisine perturbation. The properties of this system are described.

**Key words:** impedance, capacitance, interface, double layer

### INTRODUCTION

In the past decades much effort has been done to develop high surface area carbon electrodes with a view to use them in electrochemical capacitors (in “supercaps”, [1]). A possible candidate for high power applications is the electrode with vertically aligned carbon nanotubes (VACNT or shortly: CNT) [2]. In a project done mainly in the Fraunhofer Institute for Material and Beam Technology, IWS, Dresden, Germany, a device – actually an atmospheric pressure CVD furnace is being developed by which a layer of CNT can be grown onto a nickel substrate („CNT-on-Ni”) in a continuous, i.e. a „roll-to-roll” process. As a quality control step, the CNT-on-Ni layer is characterized by the measurement of surface area as if it were a supercapacitor's electrode; specific capacitances were determined from measured impedance spectra.

In general, impedance spectra of supercaps look like the ones shown in Fig.1. One of the spectra is of the traditional ones with activated carbon electrodes, the other is the one with CNT-on-Ni electrodes. At low frequency both spectra are capacitive, the higher frequency parts of the spectra are characteristic to the pore structure. To obtain a good estimate of pore-structure related parameters and of surface area, it is sufficient to measure impedance spectra in the audio frequency range, and somewhat below.

For an on-line characterization – that is, on the slowly moving Ni band leaving the CVD furnace, we need (i) an appropriate electrochemical cell

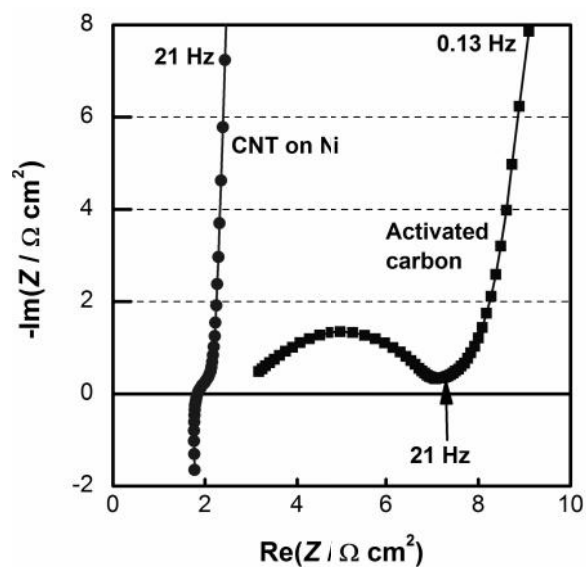


**Fig. 1.** Complex plane impedance spectrum (circles, highest frequency 66 kHz) of a supercap, realised as two CNT-on-Ni electrodes separated by a 50 $\mu$ m paper spacer. Electrolyte: 1 M Et<sub>4</sub>NBF<sub>4</sub> in acetonitrile. For comparison the impedance spectrum of a supercap made with activated carbon electrodes is also shown (squares).

which can be easily attached to, or pressed to, or snapped on the metal sheet already covered by the CNT layer and (ii) an impedance measurement system which performs very fast measurements, within seconds.

The first item is under development and hence will be shortly discussed only. The second item is the subject of the present communication: fast impedance measurement system which directly yields parameters of a simple three to five elements equivalent circuit within two to three seconds. The properties of this measurement system are demonstrated with two-electrodes symmetrical cells.

To whom all correspondence should be sent:  
E-mail: \*pajkossy.tamas@tk.mta.hu



## THE IMPEDANCE MEASUREMENT AND ANALYSIS

Usually impedance measurements are performed by sinusoidal perturbation of one of the quantities of potential or current and the resulting sinusoidal signal of the other quantity is related to the perturbing signal. The spectra are compiled from frequency-by-frequency measurements. The devices needed for this method are commercially available and precise, though somewhat time-consuming in particular at low frequencies. An alternative method employs steady state multi-frequency perturbation in the form of a sum of harmonics. The potential and current signals are Fourier-transformed and impedances are calculated for each frequency. It is worth to be noted that this method has been elaborated almost half a century ago [3,4]; also employing other forms of multi-frequency perturbation like white noise [3], pulse sequences [5] or wavelets [6]. Though multi-frequency impedance methods were sometimes used in studies of electrode kinetics [7] and of corrosion [8], these have been much scarce than those with frequency-scan, mostly because the frequency response analyzers apparently proved to be superior over the spectrum analyzers. The multi-frequency variants of EIS are much faster than the conventional one (on the expense of lower precision for a thorough analysis see [9]) and thus can be used to track temporal changes at constant potential or when the potential is scanned. In the latter case, obviously, certain conditions must be held regarding the relation of minimum frequency and scan rate. With this method called dynamic EIS (DEIS) the advantages of CV and EIS can be coupled; for details see a recent review [10]. In the present case, the short time available was the reason for applying multifrequency voltage perturbation.

The perturbation signal contained certain odd prime number harmonics of a base frequency only; all harmonics are of equal amplitudes and of random phases. The base frequency was chosen by adhering to the sampling rate  $f_s$  (or sampling time  $t = 1/f_s$ ) of the signal digitizer. In our first experiments a „laboratory version” of the setup was developed based on a Tektronix MSO-2014 oscilloscope with  $f_s=62.5$  kHz.

1) Apart portability, the idea of using the ADC rather than the oscilloscope can be traced back to the fact, that the contribution-to-impedance of a capacitance is larger at lower frequencies, hence it is advisable to shift down the frequency range as much as possible within the allowable time frame of a spectrum measurement. The ADC's data can be read out continuously while the measurement is still running, thereby much time is gained.

Later on, to provide portability for the system, we replaced the oscilloscope with a laboratory-built USB-interfaced 12-bit analog-to-digital converter (ADC), the sampling rate of which with almost simultaneous sampling on its two inputs, was  $f_s = 5$  kHz<sup>1)</sup>.

The fast Fourier transform (FFT) algorithm [11], requires  $2N$  data-point array (we employed  $N=13$ , i.e. 8192 data points were sampled); to get sharp spectrum lines, the period length of the base harmonic of frequency  $f_0$  must match the time of the  $2N$  data-points. The frequency limit of impedance determination is  $f_s/2$ , according to the Nyquist criterion. Keeping these in mind, the frequency range of the measurement is  $k_{\min}:f_s/2^N$  to the upper limit  $f_s/2$  where the factor  $k_{\min}=11$  stands for the first used harmonic included in the perturbing signal. Hence the frequency range is about two-and-a-half orders of magnitude broad. The frequencies of the used harmonics are approximately equidistant in the logarithmic scale. Actually, with  $N=13$ ,  $f_0=0.6103$  Hz, and  $f_s=5$  kHz; the signal consists of altogether 38 harmonics in the 6.71-1786 Hz frequency range. This frequency range more-or-less fits to that of the sound cards of the personal computers (PCs), therefore the audio output of the PC can be used as a function generator as follows: the perturbing signal has been generated once as an array of  $2^N$  data points; from this array of points - simply by repeating it - a 100 seconds record-length audio-file of .wav format has been generated. This audio file is played back by an audio player program of the computer, yielding a noise-like voltage of approximately 0.3V rms amplitude<sup>2)</sup>.

Data acquisition, i.e. digitization of the two voltages proportional to the perturbation voltage and current is performed by the ADC. Its full control and data readout are carried out by a PC via its USB interface by a program written in C++. Some parts of the data processing (conversion of the binary readout of the digitizer and the FFT) are done also by C++ subprograms called from a VBA program ("Excel macro"). This macro performs the subsequent calculations including the curve fitting (nonlinear least means squares minimization using modulus weighting [12]), the plotting and documenting. The impedance spectra of the supercaps exhibit typical characteristics of porous electrodes.

2) Obviously, an arbitrary function generator would have done the same task with giving us more flexibility in setting amplitudes and frequency range. As the next step of the development, a dedicated function generator working simultaneously with a two-channel ADC is under construction

The different shapes of the spectra – like those in Fig. 1, can be attributed to the differences of the pore-size distributions. The CNT-covered electrode's spectrum corresponds to the limiting case of a pore system with uniform pores. Accordingly, its spectrum can be well fitted with the equivalent circuit model containing the impedance element of the porous layer of finite thickness [13], having a frequency dependence of  $Z_{\text{pore}} = \frac{k_1 \coth[k_2 / (j \omega)]}{j \omega}$ , where  $k_1$  and  $k_2$  are constants,  $\omega$  is the angular frequency, and  $j$  is the imaginary unit. However, replacing this element by a serial W-C circuit (W is a pseudo-Warburg element and C represents the double layer capacitance of the complete surface) yields just as good fits as with  $Z_{\text{pore}}$ . The complete equivalent circuit is usually an R-W-C one, where the R resistance represents the internal resistance or the supercap electrode. In addition, at the high frequency end an inductive term also appears, which is of instrumental origin; it is easy to correct its effect, and it is irrelevant in the present context. We note that the spectrum of the activated carbon-covered electrode in Fig.1. represents another limiting case of the pore systems: when the micropores' orifices are within macropores. Impedance spectra of electrodes of such complicated geometries can be modelled by a recent theory [14].

The measurement time plus data processing time - including FFTs, impedance calculations and curve fitting to extract the capacitance and Warburg parameter, is about two seconds; measurement accuracy is sufficient to the actual purpose. The whole measurement and the subsequent analysis are carried out upon a single mouseclick.

### THE CELL AND ELECTRONICS

The basic idea is that there is an electrochemical cell mounted just above the slowly moving Ni sheet - close to the edge of the sheet - in such a way that it can be pressed against the sheet and after the two-seconds measurement it can be lifted up. The cell comprises parallel layers of metal electrodes and separators: in up-to-down direction a metal disk as a counter electrode (CE), a separator, a stainless steel mesh serving as a quasi-reference electrode (RE), and finally a separator as the terminating element. These four layers are disks of 9 mm diameter, surrounded by and held together by a silicon tube acting as sealing ring. Measurement is done in such a way that the cell is lowered, and the second separator is pressed against the Ni sheet. All parts of the cell must be kept wet by the electrolyte, which is slowly injected in the interelectrode space

from an electrolyte reservoir. The whole cell is built into an Al cylinder serving as a Faraday cage.

The electronics belonging to the cell is simple and self-explanatory (Fig. 2). Since the working electrode (WE), i.e. the Ni sheet is in metallic contact with various parts of the furnace, the working electrode is grounded. Hence current is to be measured in the counter electrode's circuit, as a voltage across the  $R_m = 10$  ohm resistor. The measurement is done at open circuit potential, thus there is no need to apply a potentiostatic feedback. The perturbation from DAC is attenuated to 10 mV amplitude by an input amplifier. The two instrumentation amplifiers are designed to be very similar to each other. They are constructed using Texas Instruments TL 082C operational amplifiers. Their AC and DC amplifications are 100 and 1, respectively.

The three-electrodes cell is still under development; for testing the impedance setup (electronics of Fig. 1, the digitizers and the programs) a two-electrodes simplified version is used: this comprises two stainless-steel disks of 8 mm diameter within a plastic cylinder.

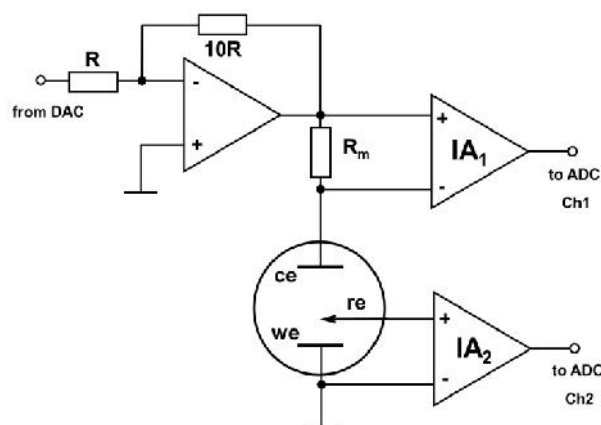


**Fig. 2.** Connection scheme of the cell, without the DAC and the two-inputs ADC. Note that the two instrumental amplifiers (the IAs) are of identical characteristics. For the two-electrode cell CE and RE are shorted.

The „supercap” is a sandwich of two electrode sheets (disks of 7 mm diameter) separated by two 25  $\mu\text{m}$  thick ethyl-cellulose sheets (Nippon Kodoshi Corp.), wetted by the electrolyte and pressed together with the stainless steel disks by a force of 75N. In the audio-frequency range the capacitive interfacial impedance of the CNT-on-Ni is as low as 1-10  $\text{ohm}\cdot\text{cm}^2$ , hence the solution resistance must be also small - i.e. thin separators and high conductivity electrolyte are to be used (this latter is 34 wt% 1-ethyl-3-methylimidazo-liumtetrafluoroborate

(EMImBF<sub>4</sub>) in acetonitrile with about 45 mS/cm specific conductivity at room temperature).

The presence of water and oxygen – as impurities in the organic electrolyte – affects somewhat the low frequency impedances; a parallel charge transfer resistance appears in the equivalent circuit. However, it does not affect the interfacial capacitance. In addition its effect is negligible in the frequency range of the multisine measurement. Therefore, the experiment can be done in the ambient atmosphere.

## RESULTS

The accuracy of the multisine setup was tested by comparing the obtained impedance spectra with

those obtained with a Solartron impedance measurement setup (1286 potentiostat +1250 frequency response analyzer); the results are shown in Fig.3. The first is a test with a dummy cell whose impedance is similar to those of supercap cells in the audio-frequency range (a 7 ohm + nominally 4700  $\mu$ F electrolytic condenser serial RC). Apart the couple of outlier points, the spectra measured with the two setups are practically the same (Fig. 3a). Fitting the parameters of a serial RC circuit to the spectra within the 5Hz-2kHz frequency yield fairly good fits are obtained (the fitting residuals are within the 1% absolute value and 1 degree margins, see Fig.3c); the fitted capacitance values are 5.4 mF (for the Solartron setup data) and 5.1 mF (for the portable multisine setup data).

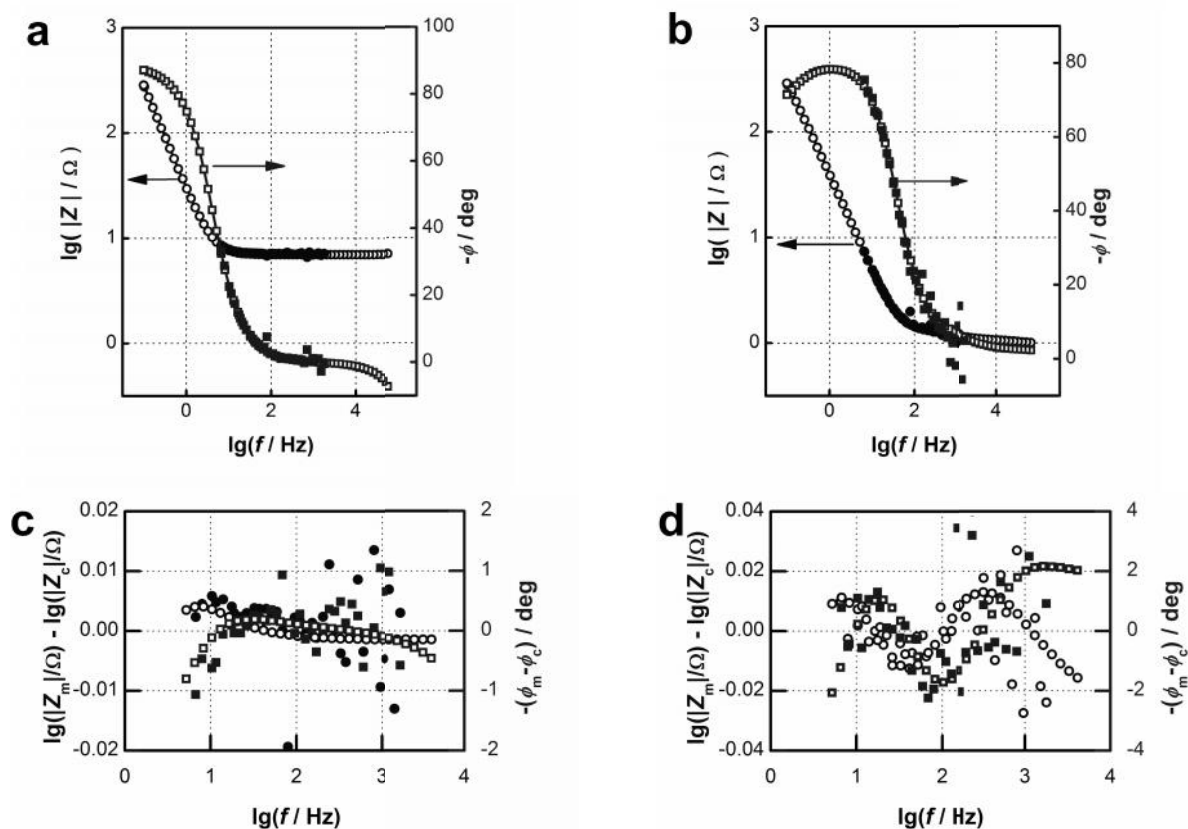


**Fig. 3.** Impedance spectra of: (a) a serial-RC dummy cell (7 ohm+4700  $\mu$ F); (b) a CNT-on-Ni supercap (see the text), measured with a Solartron 1250+1286 setup (open symbols) and with the setup of multisine perturbation (full symbols); (c) and (d) are the fitting residuals for the two spectra. For all figures circles and squares are magnitudes and phase angles, respectively.

Thus the multisine setup yields approximately the same capacitance (in two seconds) as the precise Solartron setup (in about one minute). The other test was performed on a “real supercapacitor cell”, that is, with CNT covered Ni sheets electrodes. The impedance spectra are shown in Fig. 3b. Just as in the case of the dummy cell, disregarding the noise around 1 kHz, the spectra measured with the two setups are practically the same. Fitting the

parameters of a serial RWC circuit to the spectra within the 5Hz-2kHz frequency range resulted in sufficiently good fits (the fitting residuals are within the 2% absolute value and 2 degrees margins, see Fig. 3d); the fitted capacitance values are 23.6 mF/cm<sup>2</sup> (for the Solartron setup data) and 21.6 mF/cm<sup>2</sup> (for the multisine setup data). The difference is around 10% which is still an acceptable error limit for the given purpose.

### SUMMARY

We have constructed a simple instrument (for the simplest and inexpensive version the required components are a two-channel ADC, some operational/instrumentation amplifiers, and a PC with appropriate programs) to measure and analyze audio-frequency impedance spectra in a short time (seconds) following a single mouseclick. Due to the use of the multi-sine perturbing signal, the measurement system is fast – on the expense of accuracy.

However, its accuracy might be sufficient for certain purposes, like in the present case of characterizing CNT layers produced in a continuous process.

**Acknowledgements:** *The atmospheric pressure CVD process line was developed by Benjamin Schumm, Althues Holger and Stefan Kaskel at the Fraunhofer Institute for Material and Beam Technology, IWS, Dresden, Germany. Financial assistance of the PLIANT (Process Line Implementation for Applied Surface Nanotechnologies) FP7 project, and of the National Research, Technology and Innovation Office of the Hungarian government through the project OTKA-K-112034 is acknowledged.*

### REFERENCES

1. B.E. Conway: *Electrochemical Supercapacitors: Scientific Fundamentals and Technological Applications*, Springer, 1999
2. S. Dörfler, I. Felhösi, T. Marek, S. Thieme, H. Althues, L. Nyikos, S. Kaskel: High power supercap electrodes based on vertical aligned CNTs on aluminum, *J. Power Sources*, **227**, 218 (2013).
3. S.C. Creason, D.E. Smith: Fourier transform Faradaic admittance measurements: I. Demonstration of the applicability of random and pseudo-random noise as applied potential signals, *J. Electroanal. Chem. Interf. Electrochem.*, **36**, A1 (1972).
4. G. Blanc, I. Epelboin, C. Gabrielli, M. Keddam: Measurement of the electrode impedance in a wide frequency range using a pseudo-random noise, *Electrochim. Acta*, **20**, 599 (1975).
5. L. Pospíšil, N. Fanelli: Application of the fast Walsh-Hadamard transform and the fast Haar transform for electrochemical impedance measurements based on a periodic square-wave perturbation signal derived from Walsh-functions, *J. Electroanal. Chem.*, **222**, 367 (1987).
6. G.A. Ragoisha, A.S. Bondarenko: Potentiodynamic electrochemical impedance spectroscopy, *Electrochim. Acta*, **50**, 1553 (2005).
7. L. Pospíšil, M. Štefl: The application of microprocessors in electrochemistry, *Collect. Czech. Chem. Commun.*, **48**, 1241 (1983).
8. L. Nyikos, T. Pajkossy: Electrochemical impedance measurements using Fourier transform (Elektrokémiai impedanciámérés Fourier transzformációval), Magyar Kémikusok Lapja XL (1986) 550 (in Hungarian)
9. C. Gabrielli, F. Huet, M. Keddam, J.F. Lizee: Measurement time versus accuracy trade-off analyzed for electrochemical impedance measurements by means of sine, white noise and step signals, *J. Electroanal. Chem.*, **138**, 201 (1982).
10. A.S. Bandarenka: Exploring the interfaces between metal electrodes and aqueous electrolytes with electrochemical impedance spectroscopy, *Analyst*, **138**, 5540 (2013).
11. J.W. Cooley, J.W. Tukey, An algorithm for the machine calculation of complex Fourier series, *Math. Comp.*, **19**, 297 (1965).
12. B.A. Boukamp: A Nonlinear Least Squares Fit procedure for analysis of immittance data of electrochemical systems, *Solid St. Ionics*, **20**, 31 (1986).
13. R. de Levie, Electrochemical response of porous and rough electrodes, in: P. Delahay and C.W. Tobias, (Eds.), *Advances in Electrochemistry and Electrochemical Engineering*, Vol. 6, Wiley-Interscience, New York, pp. 329 (1967).
14. J. Huang, J. Zhang: Theory of Impedance Response of Porous Electrodes: Simplifications, Inhomogeneities, Non-Stationarities and Applications, *J. Electrochem. Soc.*, **163**, A1983 (2016).

## Application of Stoynov's 4-D analysis for nonstationary impedance spectra corrections of thin poly(*o*-ethoxyaniline) modified Pt electrode

V. Horvat-Radošević \*, K. Kvastek, K. Magdi Košićek

Division for Marine and Environmental Research, Rudjer Bošković Institute, Bijenikac c. 54, 10000 Zagreb, Croatia

Received November 18, 2016      Revised January 02, 2017

Stoynov's 4-D analysis has been applied for corrections of nonstationary impedance spectra of poly(*o*-ethoxyaniline) POEA modified Pt electrode measured using conventional EIS technique at the potential of conducting to insulating conversion of polymer. The series of nine sequentially measured impedance spectra of Pt/POEA electrode showed significant increase with operating time of experiment, implying not only time-varying system but also nonstationarity, *i.e.* time changes within time interval of the single impedance spectrum measurement. Correction procedure for nonstationarity, comprising three mathematical steps, was applied to each of sequentially measured impedance spectrum. In the first step of the procedure, central times of data acquisition at each frequency point were determined, referred to the operating time of experiment and as the fourth variable included into impedance data sets of all experimentally measured IS. In the second step of the procedure, the operating time function of measured real and imaginary impedance parts at iso-frequency points was built up and "frozen" at starting times of each impedance spectrum measurement. In the last step of the procedure, nine instantaneous impedance spectra were calculated using extrapolation/interpolation method. Comparison between measured and instantaneous impedance spectra showed differences that indicate overestimation of all charge transfer and charge transport resistances and underestimation of charge pseudocapacitance values for not corrected *vs.* corrected IS of Pt/POEA electrode.

**Key words:** electrochemical impedance spectroscopy, Stoynov's 4-D analysis, nonstationarity, poly(*o*-ethoxyaniline) modified electrode.

### INTRODUCTION

Electrochemical impedance spectroscopy (EIS) is a frequency domain technique based on the transfer function concept defining the input-output relation for a linear, time invariant, casual and stable system [1–6]. For a small signal sinusoidal current fluctuation  $i(t)$  as the system input and the resulting small signal sinusoidal voltage fluctuation  $v(t)$  as the output, the impedance  $Z$  is defined in the complex frequency,  $i\tilde{\omega}$  domain as the system transfer function relating Fourier-transformed  $F$  forms of  $i(t)$  and  $v(t)$ :

$$Z(i\tilde{\omega}) = F[v(t)]/F[i(t)] = V(i\tilde{\omega})/I(i\tilde{\omega}) = |Z| \exp^{i\varphi} = Z' + iZ'' \quad (1)$$

Impedance spectra of electrochemical systems in steady-state have conventionally been measured by the frequency response analysis (FRA) technique, carried out frequency by frequency at  $n$  points, covering wide range of time ( $10^{-5}$  –  $10^3$  s). At each frequency  $\tilde{\omega}$ , vector properties of impedance have been defined according to eq. (1) by impedance modulus  $|Z|$  and phase angle  $\varphi$ , or real  $Z'$  and imaginary  $Z''$  impedance components, respectively.

The collected three-dimensional (3-D) measured data set ( $Z'_{(n)}$ ,  $Z''_{(n)}$ ,  $\tilde{\omega}_{(n)}$ ) contains all the information of the system properties, which in the form of impedance parameter values might be extracted by impedance modeling procedure [1–6]. In practice, however, measured electrochemical systems are usually nonlinear, noisy and nonstationary, what prevents proper evaluation of impedance values and thus properties of the measured system. There have been several procedures already proposed for avoiding these problems, including application of selected input signal amplitude, measurements and analysis of non-linear and higher order voltage harmonics, pulse, multisinusoidal or pseudo-white noise excitations, etc. [7–11].

The present paper is focused to the problem of nonstationarity that is common for many electrochemical systems in either two-electrode or three-electrode configurations [8,10,12–17]. In conventional, FRA measured impedance spectra, nonstationarity is usually manifested as drifts of experimental impedance spectra measured sequentially. Drifts can be found on different time scales, most usually at low frequencies, altering thus effective characteristics of the system between two subsequent experiments. Reasons for drifts are different, ranging from departure from the causality condition to time changes inherent to a system

To whom all correspondence should be sent:  
E-mail: vhorvat@irb.hr

under investigation. Time changes of a system are usually generated by changes of electrode surfaces caused by different phenomena such as erosion-corrosion, various structural relaxations or load changes as in batteries and fuel cells during operation [18–21]. Several numerical procedures for correction of conventionally measured EIS data upon nonstationary conditions and elimination of drifts have already been proposed, resulting in highly relevant impedance data for system characterization [20,21]. Almost all these procedures are actually based on the simple and powerful method developed by Stoynov [12–14] and known as the four-dimensional, 4-D impedance analysis. According to Stoynov's 4-D impedance analysis, duration of measurement, including time of data acquisition at every  $\tilde{S}$  point, generates additional variable which makes the measured data set for a time evolving system determined by four variables. Thus, the standard 3-D data set ( $Z'_{(n)}$ ,  $Z''_{(n)}$ ,  $\tilde{S}_{(n)}$ ) is enhanced to 4-D by the fourth variable  $t_{(n)}$ , defined as central time of measurement at each  $\tilde{S}_{(n)}$ . By realizing a series of impedance measurements at distinct time intervals giving 4-D experimental data sets ( $Z'_{(n)}$ ,  $Z''_{(n)}$ ,  $\tilde{S}_{(n)}$ ,  $t_{(n)}$ ), impedance spectra can be numerically reconstructed for some strictly defined moment of time, than turned back to standard 3-D data sets and parametrized by standard procedures. In combination with differential impedance analysis, DIA [22], 4-D impedance analysis defined a new technique, known as nonstationary differential impedance spectroscopy NODIS [23]. 4-D analysis and/or NODIS have already been applied to impedance analyses of hydrogen underpotential deposition and battery cycling [23,24].

In the present study, Stoynov's 4-D analysis will be applied for correction of time evolved impedance spectra of poly-*o*-ethoxyaniline (POEA) film modified Pt electrode, measured at the potential of polymer redox transition. POEA is the ring-substituted polyaniline (PANI) derivative with  $-\text{OC}_2\text{H}_5$  groups [25] that together with PANI belongs to the class of intrinsic conducting organic polymers (ICPs) [26]. ICPs are materials of high potential and actual applications, mostly due to ability of fast switching from insulating to conducting state and *vice versa*. Electrochemical switching of ICPs, including PANI and its derivatives, is basically electrochemical oxidation/reduction coupled by ionic (proton or counterion) egress/ingress. Switching reaction involves a number of underlying processes which were found to be different in time scale and dependent on the switching direction [27–29]. This, together with the

irreversible degradation of PANI found prominent at some circumstances [30,31], have implied that for PANI based electrodes time invariant impedance spectra can hardly be assured. Although some adapted EIS techniques giving instantaneous impedance spectra have already been applied to PANI electrodes [32,33], the conventional EIS has been used for a long time [34–42] and still proposed [43,44] for assessment of charge storage and charge transfer/transport processes in PANI based polymer films. Conventional EIS, however, has primarily been explored for characterization of PANI and its derivatives in their conducting state [34–39] where all relaxations are generally fast, diminishing thus a probability for nonstationarity. Even for the conducting state of PANI in some conditions [40,41] and particularly at potentials of conductor to insulator or inverse conversions [42], nonstationary impedance spectra have actually been measured, needing necessary corrections for obtaining real impedance parameter values. In this work, corrections of nonstationary impedance spectra measured for the POEA modified Pt electrode at the specific potential of conducting to insulating conversion in the sulphuric acid solution will be performed using the mathematical treatment of Stoynov's 4-D analysis [12–14,24]. It must be stressed here, that such a type of correction has not been performed to impedance spectra of PANI based electrodes heretofore.

## EXPERIMENTAL

### *Electrochemical cell and solutions*

In the present measurements, three-electrode cell filled with  $0.5 \text{ mol dm}^{-3} \text{ H}_2\text{SO}_4$  (Kemika, 96%) electrolyte solution (pH = 0.5) was explored. Pt wire of  $0.09 \text{ cm}^2$  geometric area served as the working electrode. High surface Pt-spiral in the separate compartment and Luggin capillary ended saturated calomel electrode (SCE) were used as the counter and reference electrodes, respectively. The pseudo-reference electrode in the form of Pt-probe put across Luggin capillary served for diminishing contributions of experimental artefacts to high frequency parts of impedance spectra [45]. All here mentioned potentials  $E$  are referred to the SCE. Electrochemical measurements were performed at room temperature with solution being deoxygenated by purging high purity  $\text{N}_2$  for at least 15 minutes before the start of every experiment.

### *Preparation of Pt/POEA electrode*

Pt/POEA electrode was prepared by potentiodynamic growth of POEA at the Pt wire

substrate from the monomer solution containing  $0.5 \text{ mol dm}^{-3}$  o-ethoxyaniline (Aldrich, p.a.) (previously distilled under reduced pressure) and  $0.5 \text{ mol dm}^{-3} \text{ H}_2\text{SO}_4$  [38,46]. Potential was cycled continuously at the scan rate of  $50 \text{ mV s}^{-1}$  between  $-0.20$  and  $1.00 \text{ V}$  using Solartron 1287 Electrochemical Interface (ECI) under CorrWare (Scribner Assoc.) software control. After passing of three potential cycles, the synthesis procedure was stopped at  $-0.20 \text{ V}$ , Pt/POEA electrode was extracted from the cell, rinsed in  $0.5 \text{ mol dm}^{-3} \text{ H}_2\text{SO}_4$  and transferred to newly prepared deaerated and o-ethoxyaniline free  $0.5 \text{ mol dm}^{-3} \text{ H}_2\text{SO}_4$ . The electrode was then submitted to four cyclic voltammetry scans between  $-0.15$  and  $0.40 \text{ V}$  at scan rate of  $50 \text{ mV s}^{-1}$ , where the polymer was switched from insulating leucoemeraldine (LE) to conducting emeraldine (EM) form and vice versa [38,46]. Charge density,  $q_a = 30 \text{ mC cm}^{-2}$  necessary for switching LE to EM was calculated by integrating the area under anodic current peak [38,46,47] indicating formation of thin polymer film ( $q_a < 150 \text{ mC cm}^{-2}$ ) [47]. CV scanning was finished at  $-0.15 \text{ V}$  and Pt/POEA electrode was held at this potential overnight prior to its transformation to EM state performed by the potential step oxidation at  $0.30 \text{ V}$ .

#### Impedance spectra measurements

Impedance spectra (IS) measurements were carried out using the Solartron equipment with 1287 ECI and 1255B FRA under  $Z_{\text{plot}}$  (Scribner Assoc.) software control. At selected voltage, a sine wave ac signal of  $10 \text{ mV}$  amplitude was imposed between  $10^5 \text{ Hz}$  and  $0.01 \text{ Hz}$  and 10 impedance points were measured per decade, resulting in 71 frequency points  $f_{(1-71)} = \omega_{(1-71)}/2\pi$ . Integration time  $t_{\text{in}} = 10 \text{ s}$  at each frequency point and time delay  $t_d = 1 \text{ s}$  before start of every consecutive frequency measurement were pre-selected.

Fig. 1 displays the duration  $t_m$  of data acquisition for each of the 71 frequency points of a single IS measured in the above given conditions.

As can be seen in the inset of Fig. 1 where  $t_m$  of the first three frequency points are enlarged, the measurement at each frequency point has its beginning ( $t_s$ ), central ( $t_c$ ) and ending ( $t_e$ ) time, all referred to the starting time of the corresponding IS measurement at  $f_{(1)} = 10^5 \text{ Hz}$ . Although  $t_m$  is generally defined as the sum of pre-selected  $t_{\text{in}}$  and  $t_d$ , Fig. 1 shows that at  $f < 0.1 \text{ Hz}$ ,  $t_m$  becomes longer than  $11 \text{ s}$ . The measurement time of one IS ( $T_m$ ) took  $1182 \text{ s}$  ( $19.7 \text{ min}$ ) to complete, with about half of  $T_m$  spent for measurements at  $f < 0.1 \text{ Hz}$ .

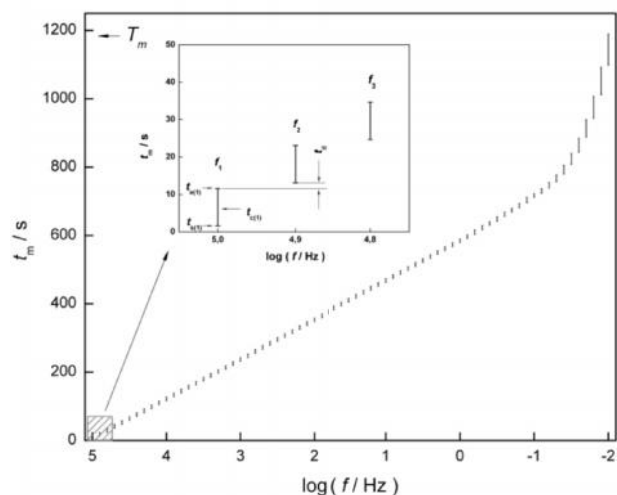


**Fig. 1.** Duration of the single frequency measurement time  $t_m$  under the given conditions of IS measurements at each of the 71 frequency points explored.

In the present experiment, IS of the Pt/POEA electrodes were measured as the series of 9 sequential measurements after the potential was stepped in the negative direction from  $0.30 \text{ V}$  (EM state) to  $0.05 \text{ V}$  (EM→LE conversion state). Principle time program of sequential IS measurements is presented in Fig. 2.

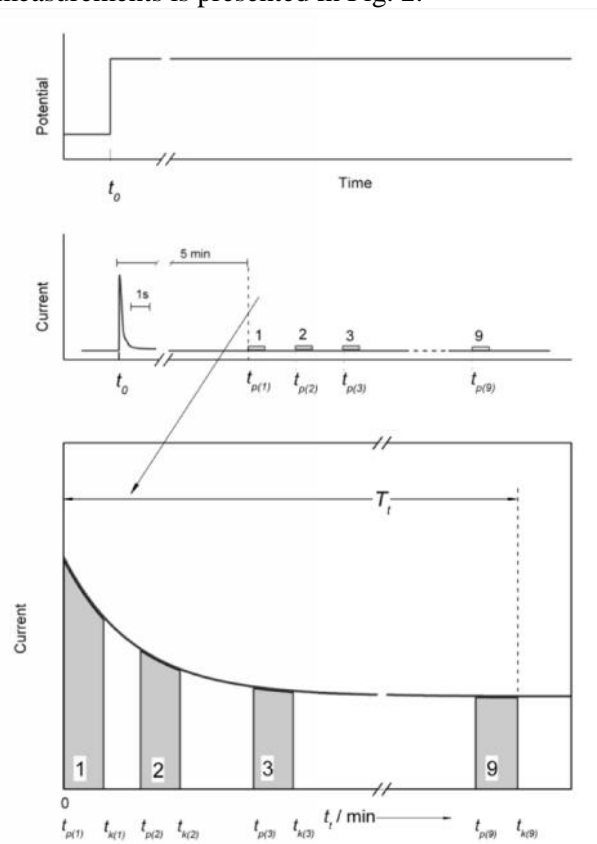


**Fig. 2.** Principle time program of 9 sequential IS measurements in the performed experiment.

As designated by small rectangles in the medium part of Fig. 2, the series of 9 sequential IS measurements commenced after the impose of potential step (upper part of Fig. 2), defining  $t_0$  as the moment when measurement of current transient has started. The first IS measurement started 5 min later (when current transient fully vanished) at time  $t_{p(1)}$ , while subsequent IS measurements started at  $t_{p(2)}$  to  $t_{p(9)}$  with some time left between them. By referring operative time of the impedance experiment  $t_i$  to  $t_{p(1)}=0$ , the undermost part of Fig. 2 is obtained. Here, the starting  $t_p$  and ending  $t_k$  time of IS measurements are denoted and  $T_m$  of each IS is shadowed. At the end of the full experiment after total operating time  $T_t = 540$  min, 9 impedance spectra were totally obtained, each composed from 71 4-D data sets ( $Z_m'$ ,  $Z_m''$ ,  $\tilde{S}$ ,  $t_e$ ). According to Fig. 1 and Table 1 that summarizes definitions and abbreviations of all time symbols used here,  $t_{e(1-71)}$  denotes ending time of measurement at each one of the 71 frequency points. Since  $t_e$  at each frequency is referred to the start of the corresponding IS measurement ( $t_{p(1)}$  to  $t_{p(9)}$ ), the values of  $t_e$  are equal for each of the sequentially measured IS.

**Table 1.** Time definitions and abbreviations.

$t_0$	Starting time of current transient measurement after potential step
SINGLE IS	
$t_{s(1-71)}$	Starting time of data acquisition at each frequency point (1–71)
$t_{e(1-71)}$	Ending time of data acquisition at each frequency point (1–71)
$t_{c(1-71)}$	Central time of data acquisition at each frequency point (1–71)
$t_{in}$	Integration time of data acquisition at each frequency point (1–71)
$t_d$	Time delay before start of data acquisition at consecutive frequency point
$t_m$	Time of data acquisition at each frequency point
$T_m$	Time of data acquisition at all frequency points of single IS spectra
SERIES OF SEQUENTIAL IS	
$t_{p(1-9)}$	Starting time of each IS measurement
$t_{k(1-9)}$	Ending time of each IS measurement
$t_t$	Operating time of the experiment referred to $t_{p(1)}=0$
$T_t$	Total operating time of the experiment
$t^*$	„Frozen“ time (at $t_{p(1-9)}=0$ )

### Calculations and fittings

All calculations related to the non-linear (NNL) data fittings of the built-in function for time dependence of impedance (ExpAssoc), determination of corresponding parameters and subsequent extrapolation/interpolations were made by the Origin (Origin Lab. Incorp.) software. Statistical criteria for reasonable fits were set as acceptable chi-square  $\chi^2$  test for goodness of the overall fit and low values of relative standard deviation for each parameter value.

## RESULTS AND DISCUSSION

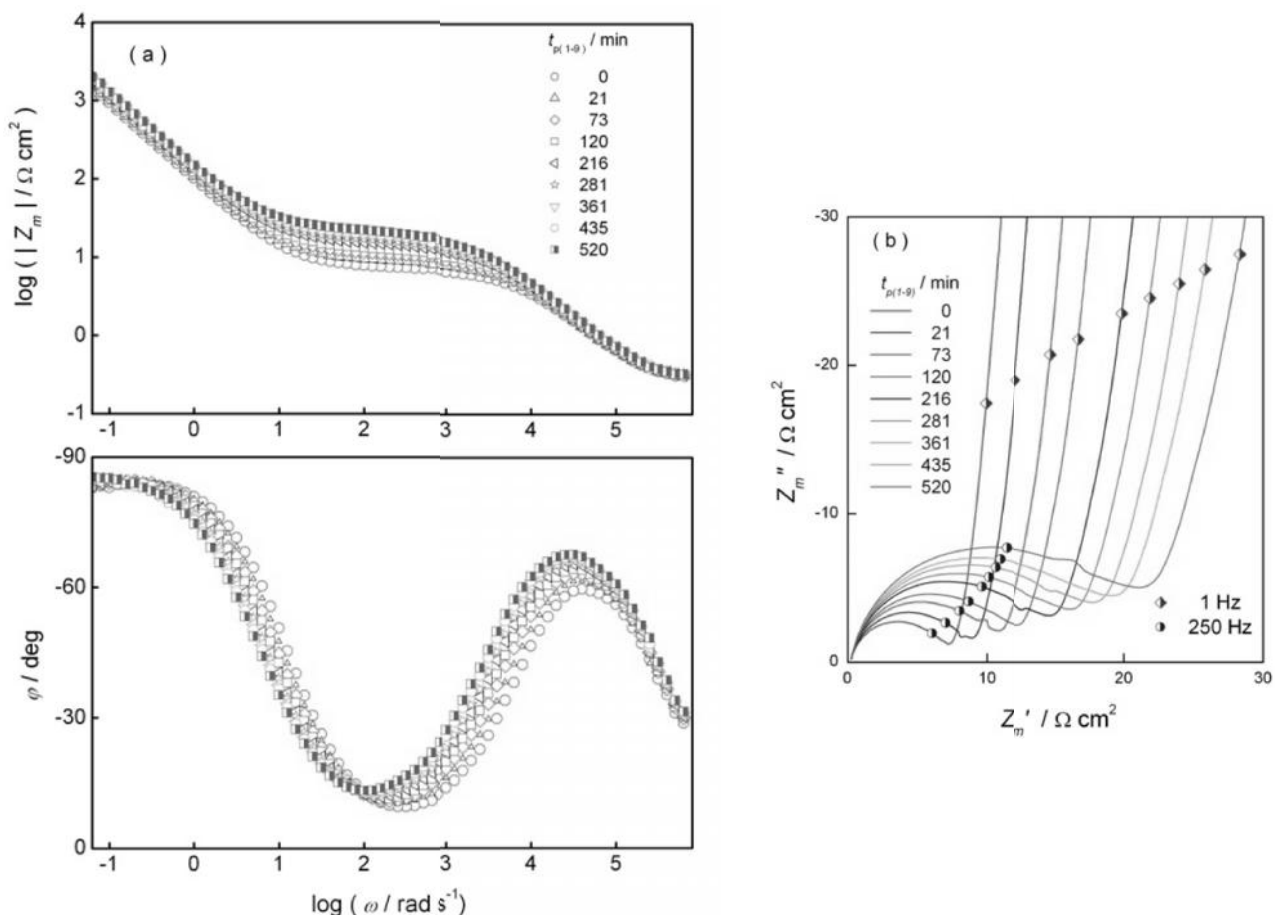
### Experimental impedance spectra

Experimental IS of Pt/POEA electrode measured sequentially at 0.05 V are depicted in Fig. 3 as Bode ( $\log |Z_m|$  and  $\{ \text{ vs. } \log \tilde{S} \}$ ) and Nyquist ( $Z_m''$  vs.  $Z_m'$ ) plots.

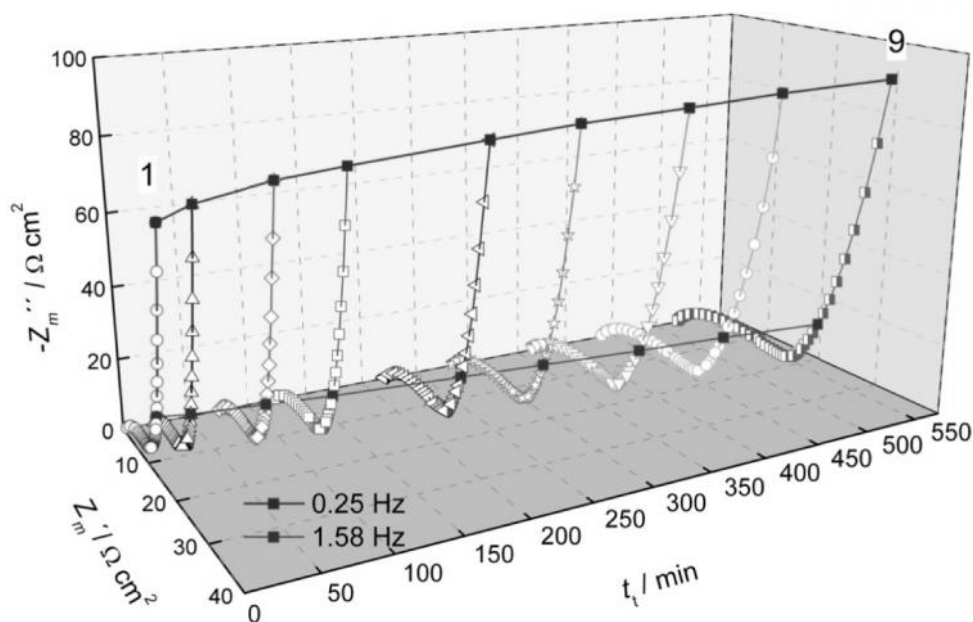
IS shown in Fig. 3 exhibit impedance/frequency responses typical for polyaniline based polymer films in transition oxidation states [34–37, 42–44]. Impedance increases in sequential measurements suggest significant time evolution of the system within operating time  $t_i$  of the impedance experiment [40–42]. The same is shown in Fig. 4, presenting  $t_i$  dependence of sequentially measured Nyquist plots in the form of 3-D plotting [16, 21].

Fig. 4 illustrates changes of sequentially measured IS with  $t_i$  referred to the beginning of the first IS measurement  $t_{p(1)} = 0$  (cf. Fig. 2). Each of the sequentially measured IS presented in Fig. 4 is seen as usual 2-D Nyquist plot (cf. Fig. 3b) presenting here for convenience data measured down to 0.25 Hz only, i.e. 56 frequency points between and  $10^5$  and 0.25 Hz. In agreement with the already shown Nyquist plots at EM→LE transition potentials of PANI [34–37], depressed semicircles at high to medium frequencies and capacitive lines at lower frequencies can clearly be recognized in Fig. 4. Obvious increase of circle diameters and capacitive lines with  $t_i$  suggests increased impedances in sequential measurements. This is also supported by bold lines drawn in Fig. 4 that connect impedances of each IS measured at the same  $f$  (1.58 Hz and 0.25 Hz) (iso-frequency points) and show continuously increased values with the operating time of the experiment. As in other cases of time changes of measured impedance [20,21], one might presume that time changes did not appear between measurements only, but also during recording of each single IS that lasts for 19.7 minutes (cf. Fig. 1). This suggests that all experimental IS presented in Figs. 3 and 4 are nonstationary and should be corrected.





**Fig. 3.** (a) Bode and (b) Nyquist plots of sequentially measured IS of Pt/POEA electrode in  $0.5 \text{ mol dm}^{-3} \text{ H}_2\text{SO}_4$  at  $E = 0.05 \text{ V}$ .  $t_{p(1-9)}$  denote starts of 9 sequential IS measurements (*cf.* Fig. 2).



**Fig. 4.** 3-D presentation of Nyquist plots for sequentially measured IS (1–9) of Pt/POEA electrode in  $0.5 \text{ mol dm}^{-3} \text{ H}_2\text{SO}_4$  at  $E = 0.05 \text{ V}$ . Iso-frequency points (1.58 Hz and 0.25 Hz) of 9 sequential IS are connected by bold lines

Implementation of Stoynov's 4-D analysis

Generation of instantaneous impedance spectra:

According to Stoynov's 4-D analysis for correction of nonstationarity [12–14,24], each of the experimentally obtained data sets in a sequential series of conventionally measured IS has to be "frozen" in some well defined time. This procedure would give instantaneous IS, i.e. IS measured virtually for all frequencies at some strictly defined moment of time, e.g. starting time of IS measurement. The whole correction procedure is based on the assumption of continual impedance time change and is comprised from three steps of impedance data refinement.

In the first step of the correction procedure, each measured 4-D data set has to be transformed for the operating time  $t_t$  of sequential measurements, i.e. time elapsed from the start of the first IS measurement  $t_{p(1)} = 0$ . It is clear from Fig. 2 that each IS of the sequential series is actually measured at different time when referred to  $t_{p(1)}$ . This also implies different starting ( $t_{s(1-71)}$ ), central ( $t_{c(1-71)}$ ) and ending ( $t_{e(1-71)}$ ) times of measurement at each frequency point (cf. Figs. 1

and 2). Selection of  $t_{c(1-71)}$  values for further transformation is mostly justified, but needs additional calculations. According to Fig. 1 the central time of measurement at a given frequency  $t_{c(n)}$  is defined as  $t_{c(n)} = [t_{s(n)} + t_{e(n)}] / 2$ , or in the terms of  $t_{e(n)}$  values that are available in experimentally obtained data sets,  $t_{c(n)} = [t_{e(n-1)} + t_{e(n)} + t_d] / 2$ . Transformation for operating time  $t_t$  is made using calculated  $t_{c(1-71)}$  and replacing  $t_{e(1-71)}$  in experimentally obtained data sets by  $t_{t(1-71)} = t_{p(1-9)} + t_{c(1-71)}$ . In such a way the series of new 4-D data sets ( $Z_m'_{(1-71)}$ ,  $Z_m''_{(1-71)}$ ,  $\tilde{S}_{(1-71)}$ ,  $t_{t(1-71)}$ ) are formed for all 9 IS measured sequentially. Since  $t_t$  is referred to  $t_{p(1)} = 0$  at each frequency, the values of  $t_{t(1-71)}$  are different for each of the sequentially measured IS.

In the second step of the correction procedure the mathematical function that properly describes the  $t_t$  changes of the measured impedance at all iso-frequency points has to be built up. The example presented in Fig. 5 shows  $Z_m'(t_t)$  and  $Z_m''(t_t)$  of sequentially measured IS at some frequencies chosen between 71 measured frequency points (iso-frequency dependences).

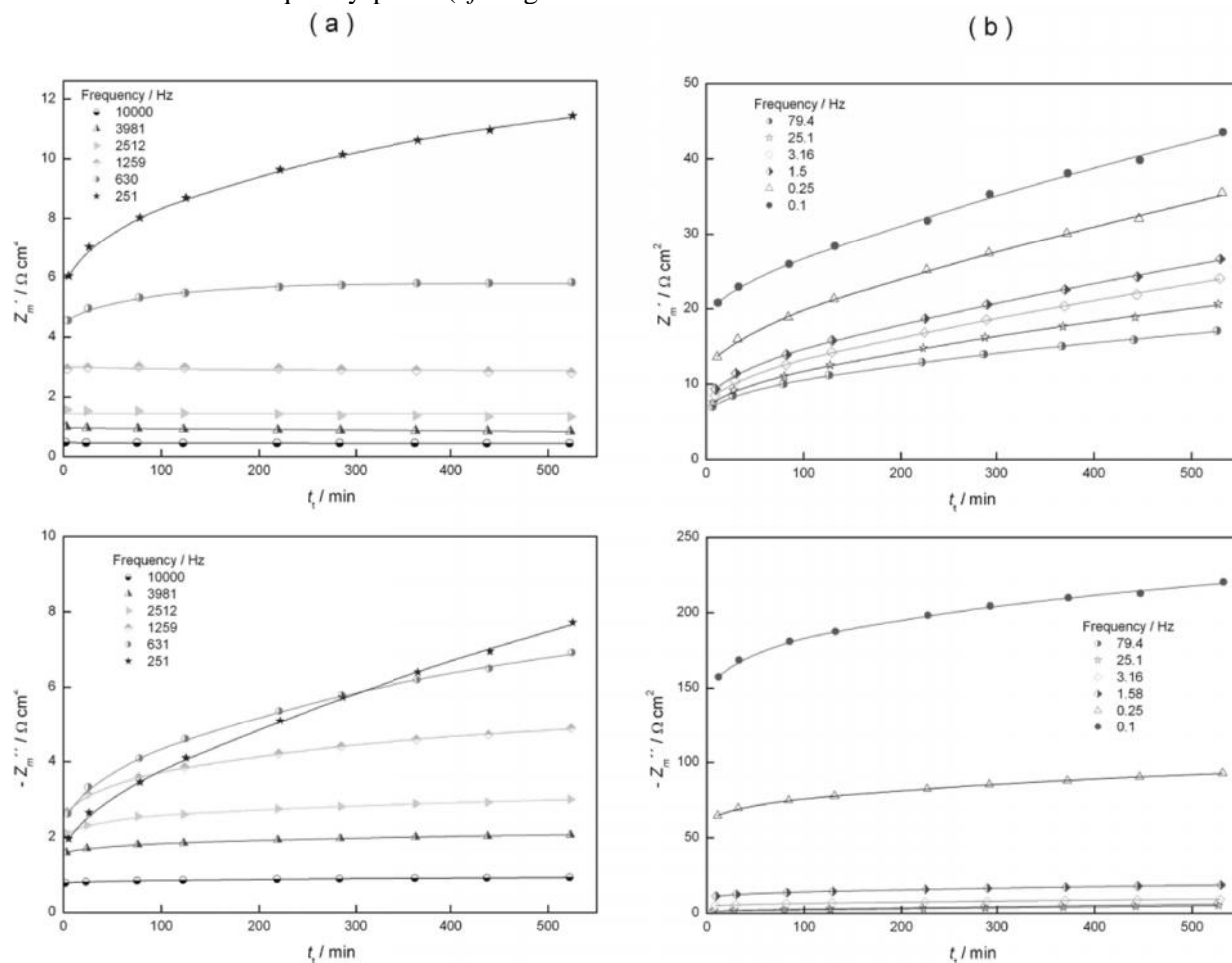


Fig. 5. Iso-frequency time dependences of  $Z_m'$  and  $Z_m''$  of sequentially measured IS of Pt/POEA electrode in  $0.5 \text{ mol dm}^{-3} \text{ H}_2\text{SO}_4$  at  $E = 0.05 \text{ V}$ . The chosen frequencies are divided to (a) high and (b) low range.

According to Fig. 5 the values of  $Z_m'$  and  $Z_m''$  increased with  $t_i$  and the changes are obviously higher between the first few IS than afterward. Taking into account different ordinate scales, Fig. 5 also shows more prominent changes at lower frequencies and higher changes in  $Z_m'$  than in  $Z_m''$  values. It has already been shown that just the time dependence of measured impedance at iso-frequency points makes the basis for calculations of IS at any desired time [12–14,21,22,24,41]. For further impedance data refinement, the proper impedance/time function has to be defined first. According to Stoynov [12–14,24] the piecewise polynomial function known as the complex spline, has proved to be appropriate. Here, temporal functions of  $Z_m'$  and  $Z_m''$  at each frequency in the time interval given in Fig. 5 were found well described (cf. full lines in Fig. 5) by the following combination of two exponential functions:

$$Z_m'(t_i) \text{ and } Z_m''(t_i) = A_0 + A_1(1 - \exp^{-t/T_1}) + A_2(1 - \exp^{-t/T_2}) \quad (2)$$

Eq. (2) is the multiparameter exponential function described by five constant parameters ( $A_0, A_1, A_2, T_1, T_2$ ) that were for each of the 9 IS estimated separately for  $Z_m'$  and  $Z_m''$  at every second among the 71 frequency points. In such a way new data sets were obtained, containing numerical values of all five constant parameters

( $A_0, A_1, A_2, T_1, T_2$ ) simulating  $Z_m'(t_i)$  and  $Z_m''(t_i)$  at 35 frequency points for each of the 9 IS.

In the third step of the correction procedure calculation of  $Z_c(i\check{S})$  in some “frozen“ time  $t^*$  has to be performed using these new data sets. Here the values of  $Z_c'$  and  $Z_c''$  for each IS were estimated for  $t^* = t_{p(1-9)} = 0$  by extrapolation/interpolation method and repeated for each frequency of the 35 frequency points. This step resulted in the usual 3-D data sets ( $Z_c'(1-35), Z_c''(1-35), \check{S}(1-35)$ ) determining now 9 instantaneous IS, or in other words, 9 IS measured virtually at all frequencies just in the starting moments of the impedance measurements.

Comparison of measured and corrected impedance spectra: Nyquist plots of corrected impedances „frozen“ at  $t^* = t_{p(1-9)} = 0$  are presented in Fig. 6 together with the 1<sup>st</sup>, 2<sup>nd</sup> and 9<sup>th</sup> measured IS. In difference to Figs. 3 and 4, the measured IS in Fig. 6 are presented for every second of the 71 experimentally explored frequencies, i.e. for the same 35 frequency points for which calculations were performed.

The comparison between instantaneous, i.e. corrected for  $t^* = t_{p(1-9)} = 0$  and measured IS in Fig. 6 shows differences that are higher for the first two than the last measured IS. Differences are primarily seen as different impedance values and are particularly obvious at medium and low frequency regions.

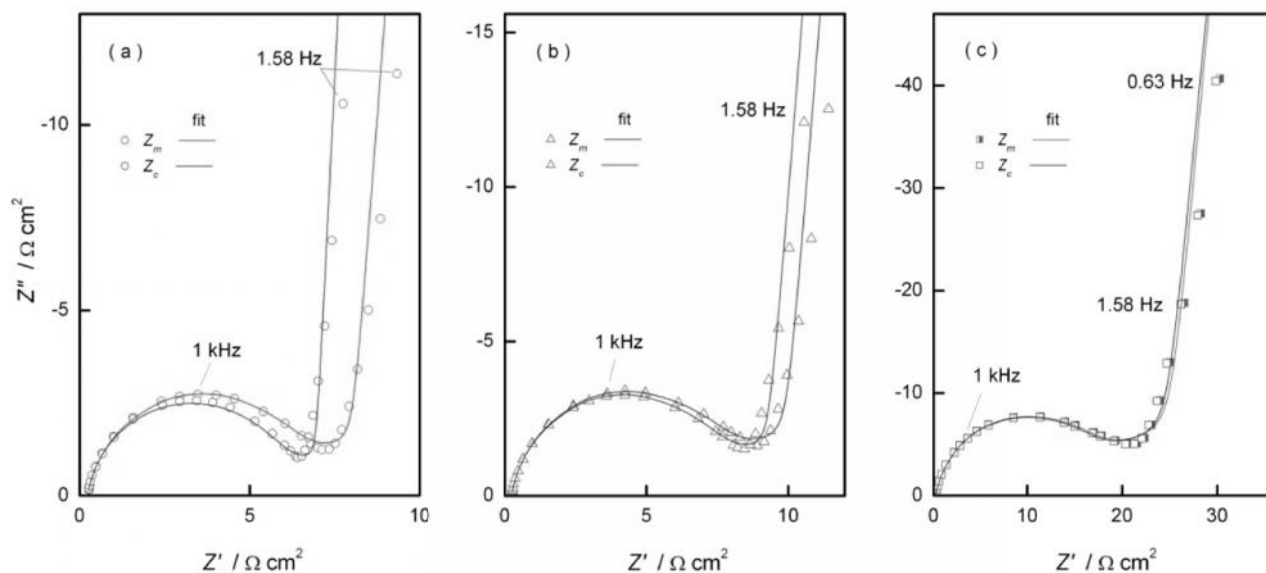


**Fig. 6.** Measured and corrected ( $t^* = t_{p(1-9)} = 0$ ) Nyquist plots of (a) 1<sup>st</sup>, (b) 2<sup>nd</sup> and (c) 9<sup>th</sup> IS of Pt/POEA electrode in 0.5 mol dm<sup>-3</sup> H<sub>2</sub>SO<sub>4</sub> at  $E = 0.05$  V.

Instantaneous IS showed generally lower semicircle diameters and lower capacitive lines (cf.  $Z''$  values at the same  $f = 1.58$  Hz), indicating different quantitative impedance parameter values

describing characteristic Pt/POEA electrode properties. In terms of the usual model for metal/PANI/solution electrode arrangement comprising interfacial double-layer capacitance,

interfacial charge transfer resistance and charge transport within polymer film [38,40,42–44], overestimation of all charge transfer and charge transport resistances and underestimation of charge pseudocapacitance values for not corrected IS of Pt/POEA electrode have strongly been indicated.

Not only measured, but also instantaneous IS change with time suggests that Pt/POEA electrode is inherently time-varying system. These time variations can be related to electrochemical aging, the phenomenon generated by polymer volume decrease at EM→LE conversion, what has already been found characteristic for PANI and PANI based derivatives [41,47].

## CONCLUSIONS

Stoynov's 4-D model was successfully applied for corrections of nonstationary impedance spectra of the Pt/POEA electrode measured in acid sulphate solution at the potential of transition between the conducting and insulating state of the polymer. The conventional FRA based EIS technique was used and the experiment was performed as series of 9 sequentially measured impedance spectra in the total operating time of 540 min. Measured impedance spectra of Pt/POEA electrode showed continuous increase with operating time, including changes within time interval of one single impedance spectrum measurement of 19.7 min, indicating nonstationarity.

To account for nonstationarity, experimental data sets of the series of sequentially measured impedance spectra must be obtained in 4-D form. In comparison with ordinary 3-D data set ( $Z'_{(n)}$ ,  $Z''_{(n)}$ ,  $\tilde{S}_{(n)}$ ), 4-D form must involve some specific time variable. Here, a specific time moment, defined as the central time of data acquisition at each measured frequency point  $t_{c(n)}$  is calculated and involved as the fourth variable in experimental 4-D data sets ( $Z'_{(n)}$ ,  $Z''_{(n)}$ ,  $\tilde{S}_{(n)}$ ,  $t_{c(n)}$ ) of each measured impedance spectrum.

Correction procedure has to be applied in several steps. As a first step  $t_{c(n)}$  values of each impedance spectrum must be referred to the operating time of the experiment. After that, iso-frequency dependences of measured real and imaginary impedance parts of all measured impedance spectra must be extracted and their changes with operating time simulated by implementing of proper mathematical function. Here combination of two exponentials providing five constant parameters for each frequency point was found satisfactory. Thus, the obtained constant parameter values and the extrapolation/interpolation method were in turn

used for calculations of 3-D data sets ( $\tilde{S}_{(n)}$ ,  $Z'_{(n)}$ ,  $Z''_{(n)}$ ) of instantaneous IS, i.e. IS "frozen" to the starting time of each impedance spectrum measurement.

Comparison between experimentally measured and instantaneous impedance spectra pointed to overestimation of all charge transfer and charge transport resistance values and underestimation of charge pseudocapacitance values for IS of Pt/POEA electrode not corrected for nonstationarity.

**Acknowledgements:** This work is supported by the Croatian Science Foundation under the project ESUP-CAP (IP-11-2013-8825).

## REFERENCES

1. M. Sluyters-Rehbach, J.H. Sluyters, Sine wave methods in the study of electrode processes, in: A.J. Bard (ed), Analytical Chemistry, M. Dekker, New York, 1970, p. 1.
2. A. Lasia, Electrochemical impedance spectroscopy and its application, in: R.E. White, B.E. Conway and J. O Bockris (eds), Modern aspects of electrochemistry, Kluwer Acad. Publ., New York, 1999.
3. E. Barsoukov and J. R. Macdonald (eds), Impedance spectroscopy: Theory, experiment and applications, J. Wiley & Sons, 2005.
4. M.E. Orazem, B. Tribollet, Electrochemical impedance spectroscopy, J. Wiley & Sons, 2008.
5. B.-Y. Chang, S.-M. Park, *Annu. Rev. Anal. Chem.*, **3**, 207 (2010).
6. P. Zoltowski, *Bulg. Chem. Commun.*, **44**, 383 (2012).
7. K. Darowicki, *Electrochim. Acta*, **40**, 439 (1995).
8. G.S. Popkirov, *Electrochim. Acta*, **41**, 1023 (1996).
9. E. Barsoukov, S.-H. Ryu, H. Lee, *J. Electroanal. Chem.*, **536**, 109 (2002).
10. E. Van Gheem, R. Pintelon, J. Vereecken, J. Schoukens, A. Hubin, P. Verboven, O. Blajiev, *Electrochim. Acta*, **49**, 4753 (2004).
11. J. R. Wilson, D.T Schwartz, S.B. Adler, *Electrochim. Acta*, **51**, 1389 (2006).
12. Z. B. Stoynov, B. Savova-Stoynov, *J. Electroanal. Chem.*, **183**, 133 (1985).
13. B. Savova-Stoynov, Z. B. Stoynov, *Electrochim. Acta*, **37**, 2353 (1992).
14. Z. Stoynov, *Electrochim. Acta*, **38**, 1919 (1993).
15. K. Darowicki, P. Iepski, *Electrochim. Acta*, **49**, 763 (2004).
16. P. Iepski, K. Darowicki, E. Janicka, G. Lentka, *J. Solid State Electrochem.*, **16**, 3539 (2012).
17. T. Breugelmans, J. Lataire, T. Muselle, E. Tourwé, R. Pintelon, A. Hubin, *Electrochim. Acta*, **76**, 375 (2012).
18. F. Berthier, J.-P. Diard, A. Jussiaume, J.-J. Rameau, *Corr. Sci.*, **30**, 239 (1990).
19. M. A. Vorotyntsev, M. D. Levi, A. Schechter, D. Aurbach, *J. Phys. Chem. B*, **105**, 188 (2001).
20. C.A. Schiller, F. Richter, E. Gülzow, N. Wagner, *Phys. Chem. Chem. Phys.*, **3**, 374 (2001).

21. N. Wagner, E. Gülzow, *J. Power Sourc.*, **127**, 341 (2004).
22. Z. Stoynov, D. Vladikova, Differential impedance analysis, Marin Drinov Acad. Publ. House, Sofia, 2005.
23. G. Raikova, Z. Stoynov, D. Vladikova, in: Advanced Techniques for Energy Sources Investigation and Testing, Proc. Int. Workshop, P18-1 (2004).
24. Z. Stoynov, B. Savova-Stoynov, T. Kossev, *J. Power Sourc.*, **30**, 275 (1990).
25. J. Pouget, S.LZhao, Z.HWang, Z. Oblakowski, A. Epstein, S. Manobar, J. Wiesinger, A. Macdiarmid, C. Hsu, *Synth. Met.*, **55**, 341 (1993).
26. A. MacDiarmid, *Angew. Chem. Int. Ed.*, **40**, 2581 (2001).
27. G. Inzelt, M. Pineri, J.W. Schultze, M.A.Vorotyntsev, *Electrochim. Acta* **45**, 2403 (2000).
28. M. Grzeszczuk, P. Poks, *Synth. Met.*, **98**, 25 (1998).
29. E. Csahók, E. Vieil, G. Inzelt, *J. Electroanal. Chem.*, **482**, 168 (2000).
30. R. Mažeikienė, A. Malinauskas, *Synth. Met.*, **123**, 349 (2001).
31. X. Yang, Q. Xie, S. Yao, *Synth. Met.*, **143**, 119 (2004).
32. J. Yoo, I. Song, J. Lee, S. Park, *Anal. Chem.*, **75**, 2962 (2003).
33. K. Darowicki, J. Kawula, *Russ. J. Electrochem.*, **41**, 1055 (2007).
34. I. Rubinstein, E. Sabatani, J. Rishpon, *J. Electrochem. Soc.*, **134**, 3078 (1987).
35. H. Dinh, P. Vanysek, V. Birss, *J. Electrochem. Soc.*, **146**, 3324 (1999).
36. C.-C. Hu, C.-H. Chu, *J. Electroanal. Chem.*, **503**, 105 (2001).
37. S. Mondal, K. Prasad, N. Munichandraiah, *Synth. Met.*, **148**, 275 (2005).
38. V. Horvat-Radoševi, K. Kvastek, M. Kralji Rokovi, *Electrochim. Acta*, **51**, 3417 (2006).
39. M.C.E. Bandeira, R. Holze, *Microchim. Acta*, **156**, 125 (2007).
40. M. Žic, *J. Electroanal. Chem.*, **610**, 57 (2007).
41. W.A. Marmisollé, M. I. Florit, D. Posadas, *J. Electroanal. Chem.*, **673**, 65 (2012).
42. V. Horvat-Radoševi, K. Kvastek, *J. Electroanal. Chem.*, **631**, 10 (2009).
43. V. Lvovich, *Electrochem. Soc. Interface*, 62 (2009).
44. J. Rubinson, Y. Kayinamura, *Chem. Soc. Rev.* **38**, 3339 (2009).
45. V. Horvat-Radoševi, K. Kvastek, *J. Electroanal. Chem.*, **591**, 217 (2006).
46. M. Kralji Rokovi, L. Dui, *Electrochim. Acta*, **51**, 6045 (2006).
47. W. Marmisollé, D. Posadas, M. Florit, *J. Phys. Chem. B*, **112**, 10800 (2008).

4-D

Pt

( - )

10000

18

2016

;

2

2017

( )

4-D

) POEA

Pt

( -

( )

Pt / POEA

Pt / POEA

## Formation of zirconium dioxide layers on microelectrode of zirconium. Inhibition of the hydrogen evolution reaction

L. Pospíšil<sup>1\*</sup>, N. Fanelli<sup>2</sup>, M. Hromadová<sup>1</sup>

<sup>1</sup> J. Heyrovský Institute of Physical Chemistry, CAS v.v.i., Dolejškova 3, Prague, Czech Rep.

<sup>2</sup> Institute of Chemistry of Organometallic Compounds, CNR Pisa, via Moruzzi 1, Pisa, Italy

Received September 30, 2016      Revised October 29, 2016

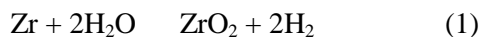
Electron transfer reactions on high purity grade Zr microelectrode were investigated in borate buffer. Oxidation producing a surface layer of ZrO<sub>2</sub> occurs at potentials more positive than -0.5 V (against Ag|AgCl|1M-LiCl). Surface layer effectively retards the hydrogen evolution reaction. Mechanistic information was obtained by the application of cyclic voltammetry and electrochemical impedance spectroscopy.

**Key words:** zirconium, ZrO<sub>2</sub>, corrosion, impedance, hydrogen evolution.

### INTRODUCTION

Pioneering work of professor Zdravko Stoynev was devoted to the development of innovative methods of electrochemical impedance analysis for various aspects of the power sources development [1]. Our contribution to a special issue celebrating his anniversary deals with impedance characteristics of zirconium used in the nuclear power plants.

Zirconium and its alloys are materials essential for the nuclear power plants, where they find use as cladding of the active fuel. The choice of Zr is due to its very low thermal neutron-capture cross-section, high hardness and resistance to corrosion. Nuclear-grade zirconium alloys contain about 95 % of zirconium and less than 2% of tin, niobium, iron, chromium, nickel and other metals, which are added to improve its mechanical properties. One disadvantage of zirconium alloys is that zirconium reacts with water at high temperatures, producing hydrogen gas and accelerated degradation.



Oxidative reaction of zirconium with water releases hydrogen gas, which partly diffuses into the alloy and forms zirconium hydrides. The hydrides are less dense and are weaker mechanically than the alloy. Formation of hydrides leads to blistering and cracking which is called hydrogen embrittlement. The redox reaction is causing the instability of fuel supports at high temperatures though it is slow at low temperatures. This reaction was responsible for a small hydrogen

explosion at the Three Mile Island nuclear power plant and in Fukushima I nuclear power plant disaster initiated by the earthquake. Hence the mechanism of the hydrogen evolution reaction (HER) on zirconium and zirconium dioxide layers is an issue.

Oxidation of zirconium occurs at the same rate in air or in water and proceeds in the ambient condition or in high vacuum. The rate of oxidation was measured at various temperatures and pressures [2]. A sub-micrometer thin layer of zirconium dioxide is rapidly formed at the surface and stops further diffusion of oxygen to the bulk and the subsequent oxidation. ZrO<sub>2</sub> adopts a monoclinic crystal structure at room temperature, which transforms to tetragonal and cubic at higher temperatures. The volume expansion caused by the cubic to tetragonal to monoclinic transformation induces large stresses upon cooling, and these stresses cause ZrO<sub>2</sub> to crack. The oxide layer is a semiconductor. The ZrO<sub>2</sub> band gap is dependent on the phase (cubic, tetragonal, monoclinic, or amorphous) and preparation methods, with typical estimates from 5–7 eV [3]. Numerous studies were devoted to Zr corrosion [4]; nevertheless operating conditions require a continuous improvement of protection techniques. Electrochemical impedance was investigated under high temperature and the open circuit potential with the aim to identify the layer thickness [5, 6]. Conditions were selected to those of various types of nuclear reactors [7-9].

This communication summarizes our results aimed at characterization of possibly oxide free Zr surface and the kinetics of growth of ZrO<sub>2</sub> layer at early stages of its formation. In difference to experiments at the open circuit potential and operating conditions we explored the characteristics of HER at controlled applied potential and at

To whom all correspondence should be sent:  
E-mail: pospasil@jh-inst.cas.cz

ambient conditions using zirconium without the presence of additional metals.

## EXPERIMENTAL

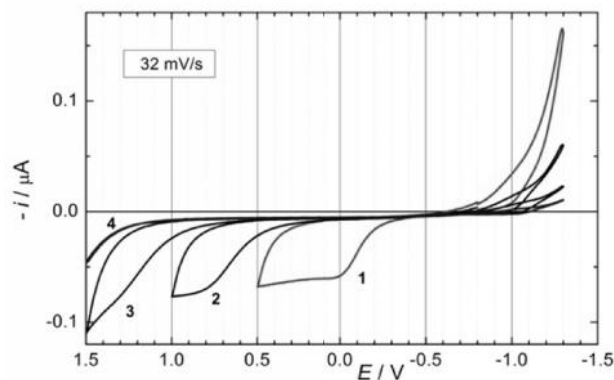
Zirconium wire of 0.25 mm diameter was purchased from Alfa Aesar of 99.95% purity grade containing metallic impurity of 29 ppm Hf, 190 ppm Fe, 1.8 ppm Cu, 8.4 ppm Cr and 4.1 ppm Ni. Wire was soldered to a support copper wire, inserted in a thick walled tight glass capillary and fixed with a TorrSeal™ resin. The exposed part of the wire was polished with the emery paper Schmirgelpapier 6/0 (SIA, Switzerland). Only the small polished disc was in contact with the solution. This served as the working electrode. The auxiliary electrode was a Pt wire of approximately 100-times larger area compared to Zr electrode. The reference electrode was Ag|AgCl|1M-LiCl electrode separated from the sample by a salt bridge. Borate buffer pH 8.25 contained 0.2 M boric acid and 0.05 M sodium tetraborate. Sample was degassed by a stream of argon. Electrochemical measurements were made using potentiostat/galvanostat PGSTAT30 with frequency analyzer option (Metrohm, Switzerland). Data were analyzed by means of ZView software, version 3.2b (Scribner Associate, Inc., North Carolina, USA).

## RESULTS AND DISCUSSION

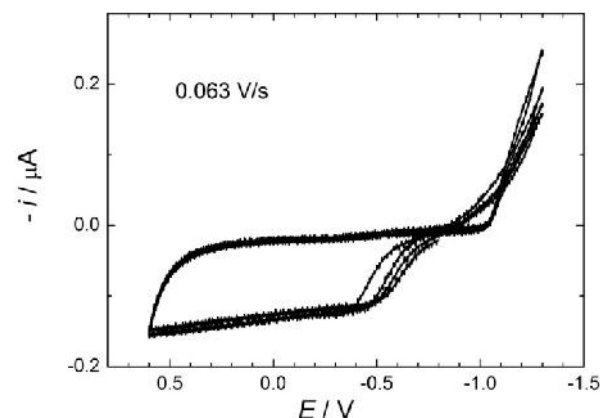
Cyclic voltammetry was used for identification of the potential ranges, where the zirconium surface remains relatively free of oxide and where the  $ZrO_2$  layer is formed. The initial and vortex potentials of experiments were optimized together with the surface treatment. We found that only dry polishing leads to reproducible voltammograms. Wet polishing with alumina slurry or contact of a polished surface with rinsing water immediately produced certain oxide formation.

Figure 1 shows subsequent voltage scans without polishing between scans. Anodic waves at -0.2, +0.7 and +1.2 V correspond to the oxidation of Zr to its dioxide. Each subsequent scan displaces the wave toward more positive potentials. The shift indicates that the originally formed layer may still contain vacancies, which can be filled with  $ZrO_2$ . The cathodic current at the most negative potentials (< -1.0V) corresponds to the hydrogen evolution reaction. Evidently, the oxide layer of different compactness inhibits the hydrogen reaction to a different extent. When the polished electrode was inserted into the solution with an immediate potential control at -0.7 V the oxidation wave occurred at -0.5 V. Repeated polishing and the resulting limited reproducibility is shown in Figure

2. For the rest of our experiments we used this procedure. Anodic oxidation yields a wave-shaped curve instead of typical voltammetric peak-shaped current-voltage dependence. This signifies that the mass transport is absent and the redox step indeed involves metallic zirconium.



**Fig. 1.** Cyclic voltammogram of Zr disc of 250  $\mu\text{m}$  diameter fitted in glass. Solution was the borate buffer 0.2 M boric acid and 0.05 M sodium tetraborate. The scan rate was 32 mV/s initiated at -0.7 V toward positive potentials. Three subsequent scanning cycles without polishing the surface: 1<sup>st</sup> cycle (red), 2<sup>nd</sup> and 3<sup>rd</sup> cycles in black. The blue curve corresponds to a covered surface.



**Fig. 2.** Cyclic voltammogram of Zr in the same solution as in Figure 1. The surface was polished by the emery paper prior to each scan. The contact of the electrode with the solution was made under application of -0.8 V.

The dependence of the anodic wave height on the voltage scan rate from 0.032 V/s to 1 V/s is linear confirming thus a surface-bound redox reaction.

Further characterization was performed by application of AC techniques, firstly by the phase sensitive AC voltammetry (Figure 3). Scanning the freshly polished electrode from negative to positive potentials causes a gradual decrease of the imaginary admittance component  $Y''$ , which is proportional to the double layer capacitance  $C$ . At positive potentials  $Y'' \sim C$  is about one half of the original value. The second scan yields only a low value of  $Y''$ . Observed picture confirms an

irreversible formation of a surface layer. AC voltammetry does not yield a detectable faradaic maximum at 160 Hz of the superimposed sine voltage. However, by lowering the frequency of the applied signal to 16 Hz, one can distinguish a peak on the real admittance component located at potentials, where the cyclic voltammograms show the anodic wave (Fig. 4).

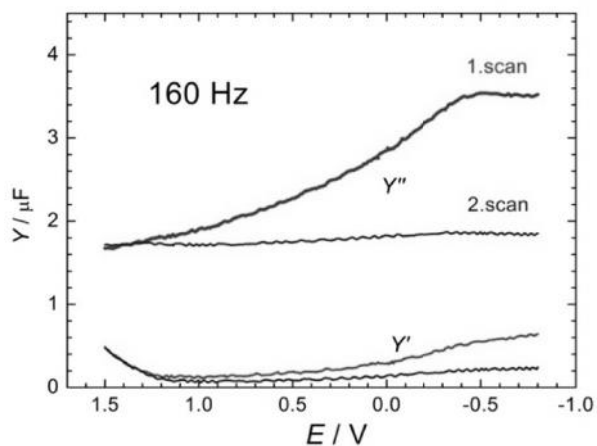


**Fig. 3.** The phase-sensitive AC voltammetry of Zr microelectrode in the same solution as in Figure 1. Upper curves are the imaginary admittance components, the lower curves correspond to the real admittance vector component. Curve labels distinguish the first and the second subsequent scan. The initial potential was  $-0.8$  V and the DC applied voltage was scanned at  $10$  mV/s.

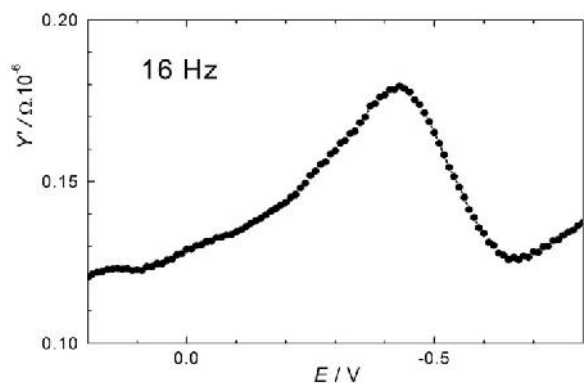


**Fig. 4.** The real admittance vector component of the phase-sensitive AC voltammetry of Zr microelectrode in the same solution as in Figure 3. The applied frequency was  $16$  Hz and the amplitude was  $10$  mV. The initial DC potential was  $-0.8$  V and the DC applied voltage was scanned at  $10$  mV/s. The imaginary component showed no faradaic maximum.

Since there was no faradaic maximum at the imaginary admittance component, we can conclude that the electron transfer producing the oxide layer is very slow. We examined the time dependence of the double layer capacitance, which yields an estimate of conditions to get a final complete oxide layer.

A potentiostatic step pulse was applied, after which the  $Y''$  values were recorded (Figure 5). For

the step to  $+0.3$  V the final low double layer capacitance value is not reached even after  $300$  sec, whereas a step to  $+0.6$  V produced a stable layer within less than a second. Information collected from these experiments was used for exploration of the hydrogen evolution reaction (HER).

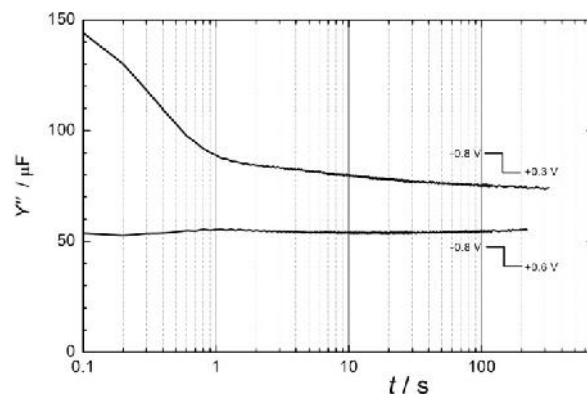


**Fig. 5.** The time dependence of the imaginary admittance component of Zr electrode in borate buffer measured at  $160$  Hz. The DC potential was stepped as indicated for respective curves.

Firstly, we applied electrochemical impedance spectroscopy (EIS) for control of the polishing quality. Irreversible electron transfer like HER, is very sensitive to the surface coverage. Hence, the lower the charge transfer resistance the less oxide is on the zirconium surface. The electrode, which was dry polished, was immediately inserted in the cell against a stream of argon. Electrical connections have been already made and hence the electrode was polarized to  $-0.8$  V upon contact with the solution. The electrode potential was stepped to  $-1.50$  V and the EIS data were collected. Figure 6 shows three successive polishing (full points) leading to a minimum  $R_{ct}$  and two EIS spectra of deliberately oxidized surface at  $0.00$  V (hollow points).

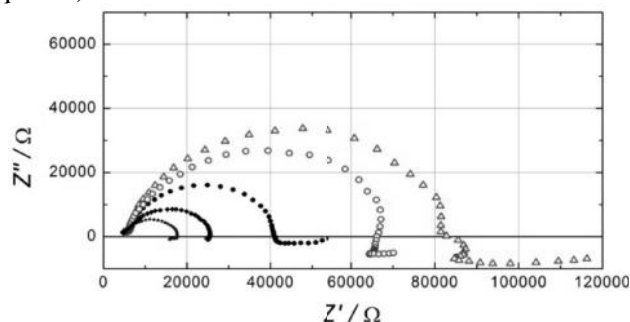


**Fig. 6.** The complex impedance plot of Zr electrode in borate buffer and polarized to  $-1.50$  V. Three curves plotted with full points show subsequent polishing leading to the lowest observed value  $R_{ct} = 12.4$  k $\Omega$ . Two large semicircles (hollow points) correspond to the deliberately oxidized surface kept at  $0$  V for  $30$  and  $60$  seconds.



Partial oxidation of Zr surface causes also low frequency loops with negative imaginary impedance. Data at the lowest frequencies are not suitable for interpretation because they are influenced by time changes of the surface during EIS measurements. This was confirmed by the application of the Kramers–Kronig relations, which often failed to confirm causality below 1 Hz. Low frequency loops are better developed at less negative potentials.

Performing EIS at different potentials using meticulously polished Zr electrode yields the dependence of the charge transfer resistance of hydrogen evolution on the applied potential (Figure 7). Measurements were repeated at each potential and only data with the lowest circle diameter of the Nyquist plot were accepted. Values of  $R_{ct}$  were obtained by two methods, fitting data to a circle and fitting to an equivalent circuit of ladder type (Chart 1).

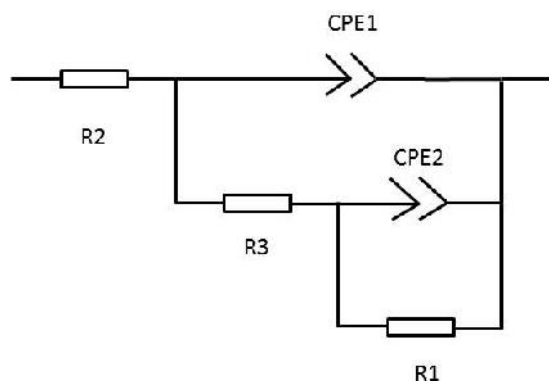


Chart 1. Ladder type equivalent circuit used to estimate  $R_{ct}$  and CPE1 by Z-view software.

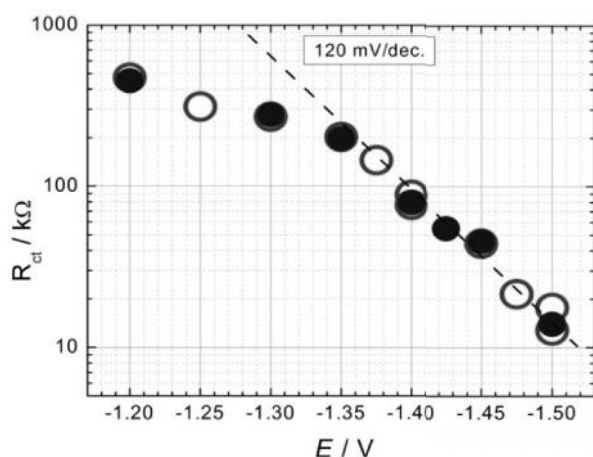


Fig. 7. The dependence of the charge transfer resistance of HER on polished Zr in borate buffer. Data fitting to a circle are hollow points. Fitting to a ladder circuit is shown as filled points.

The dependence  $R_{ct}$  vs  $E$  yields an asymptote with the slope of 120 mV/decade, which corresponds to the one-electron irreversible reduction and the transfer coefficient  $\alpha = 0.5$ . The CPE1 element at different potentials is shown in

Figure 8. Decreasing values toward less negative potentials may reflect accentuated adsorption effects.

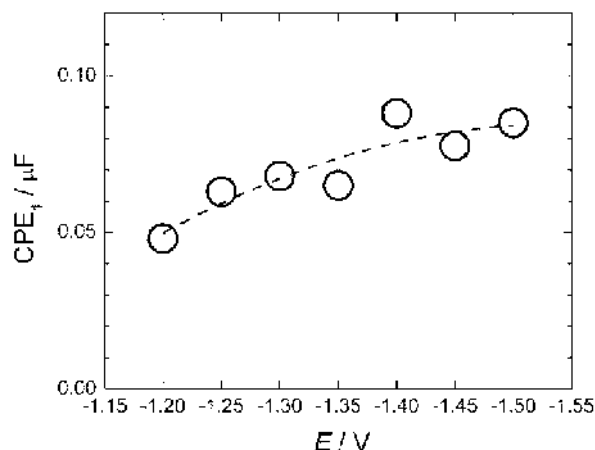


Fig. 8. The dependence of the constant phase element CPE1 on the applied potential. Data were obtained by the same fitting as those given in Figure 7.

Small low frequency loops, which were already noticeable on polished electrode at -1.5 V (see Figure 6) become quite large when the Zr surface is oxidized. Appearance of two large circles in EIS spectra of oxidized electrodes led us to use the ladder circuit for data analysis. An example is given in Figure 9 and the corresponding data in Table 1.

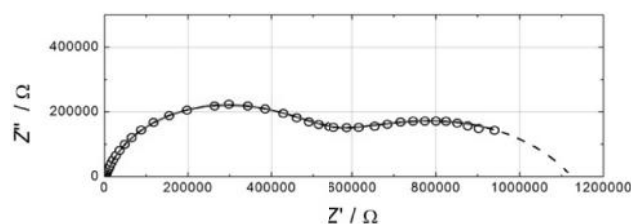


Fig. 9. The complex impedance plot of Zr electrode in borate buffer. The surface was oxidized for 60 seconds at the potential +0.5 V and data were measured at -1.20 V. Data are shown as circles, the solid line shows fitted data and the dashed line represents the simulation to 1 MHz using fitted parameters.

Table 1. Results of fitting EIS data in Figure 9 using the ladder circuit given in Chart 1

Element	Value	Error %
R2	3761	0.12
R3	533930	0.033
R1	586610	0.074
CPE1-T	15.1 nF	0.10
CPE1-P	0.85	0.018
CPE2-T	1.05 μF	0.047
CPE2-P	0.62	0.06

The reproducibility of the second CPE2 element and the corresponding R1 resistance were not sufficient for suggesting a quantitative interpretation.

The low frequency loops with positive or negative elements indicate the electron transfer coupled with the adsorption of one or two species [10]. Adsorption of hydrogen in metals and alloys is of importance in the field of fuel cells. Therefore a large amount of reports is focused on this phenomenon. The direct (one-step) insertion reaction mechanism was introduced by Bagotskaya and Frumkin [11]. Indirect (two-step) insertion of hydrogen in metals and alloys was thoroughly treated in several studies of Montella's group [12]. Nyquist plots presented here qualitatively resemble systems, where HER proceeds in the presence of a deposited surface layer (see for example report of Castro et al. [13]). EIS for those cases was analyzed using the equivalent circuit related to the HER according to the Volmer-Heyrovský-Tafel mechanism. The model used here (Chart 1) follows the same line. The properties of low frequency loop(s) are determined by rather complicated combination of adsorption and kinetic parameters reflecting the influence of the coverage of redox active species on the electron transfer rate and vice versa [10]. The present case is still more complicated because the adsorption of hydrogen may involve Zr and/or ZrO<sub>2</sub> surfaces. Indeed the negative loops in Figure 6 can be simulated (Figure 10) though the data fitting is still not sufficiently accurate.

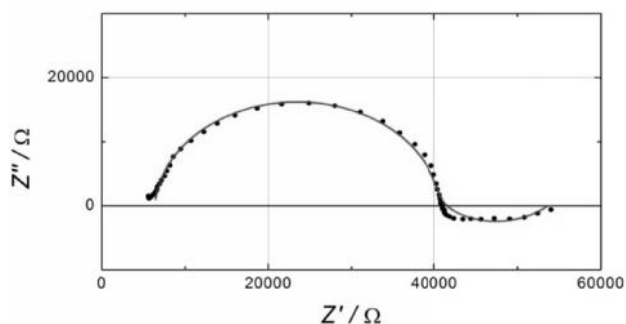


Fig. 10. Nyquist plot of experimental (points) and simulated (solid line) data for HER at -1.5 V and partially polished Zr in borate buffer. Simulation used the following values of Chart 1 circuit: R1=13kΩ , R2=6.4kΩ , R3=34kΩ, CPE1T=23.4 nF, CPE1P=0.96 , CPE2T=-3.53 μF , CPE2P=1.5.

We suppose to explore low frequency features in the future examining their dependence on time, deposition potential and pH of the medium.

## CONCLUSIONS

Zirconium microelectrode in a form of a disc fitted in glass enables controllable polishing and reproducibility of the voltammetric and impedance data. Freshly polished electrode has to be inserted in the sample solution with an immediate application of a potential at which the oxidation of

Zr is prevented. The formation of ZrO<sub>2</sub> surface layer begins at -0.5 V. The hydrogen evolution reaction (HER) was investigated in the range of potentials -1.2 to -1.5 V and a single-electron transfer with transfer coefficient = 0.5 was confirmed. The presence of surface oxide layer effectively retards the HER and yields additional low frequency impedance loops attributed to the adsorption effects.

**Acknowledgements:** This research was supported by the Grant Agency of the Czech Republic (16-03085S).

## REFERENCES

1. Z. Stoynov, D. Vladikova, D. Differential Impedance Analysis, Marin Drinov Publ. House, Sofia, 2005.
2. R. Causey, D. Cowgill, B. Nilson, Review of the Oxidation Rate of Zirconium Alloys. 2006, Report of Sandia National Lab., Livermore, CA, USA.
3. J. Chang, L. You-Sheng, L.; Karen, C. Rapid thermal chemical vapor deposition of zirconium oxide for metal-oxide-semiconductor field effect transistor application, *J. Vacuum Sci. Technol. B*, **19**, 1782 (2001).
4. Y. Chen, M. Urquidi-Macdonald, D. Macdonald, The electrochemistry of zirconium in aqueous solutions at elevated temperatures and pressures, *J. Nucl. Mater.*, **348**, 133 (2006).
5. G. Nagy, Z. Kerner, G. Battistig, A. Pintér-Czordás, J. Balogh, T. Pajkossy, Oxide layers of Zr-1% Nb under PWR primary circuit conditions, *J. Nucl. Mater.*, **297**, 62 (2001).
6. G. Nagy, Z. Kerner, T. Pajkossy, In situ electrochemical impedance spectroscopy of Zr-1% Nb under VVER primary circuit conditions. *J. Nucl. Mater.*, **300**, 230 (2002).
7. J. Macák, R. Novotný, P. Sajdl, V. Ren iuková, V. Vrtílková, Electrochemical study of pre- and post-transition corrosion of Zr alloys in PWR coolant, Proc. of 15th Int. Conf. on Environmental Degradation of Materials in Nuclear Power Systems – Water Reactors, Wiley Inc., 621 (2011).
8. A. Krausová, J. Macák, P. Sajdl, R. Novotný, V. Ren iuková, V. Vrtílková, In-situ electrochemical study of Zr-Nb alloy corrosion in high temperature Li<sup>+</sup> containing water. *J. Nucl. Mater.*, **467**, 302 (2015).
9. A. Krausová, J. Macák, P. Sajdl, V. Ren iuková, R. Novotný, Corrosion of Zr-Nb and Zr-Sn alloys under simulated condition of VVER reactor. *Corrosion and Material Protection* (in Czech), **59**, 99 (2015).
10. A. Lasia, Electrochemical Impedance Spectroscopy and its Applications. Springer, New York, 2014, Chapter 5.
11. A. Frumkin in: P. Delahay (Ed.), Advances in Electrochemistry and Electrochemical Engineering, vol. 3, Interscience, New York, 1963.
12. C. Montella, EIS study of hydrogen insertion under restricted diffusion conditions. I. Two-step insertion reaction. *J. Electroanal. Chem.*, **497**, 3 (2001).
13. E. Castro, M. de Giz, E. Gonzalez, J. Vilche, *Electrochim. Acta*, **42**, 951 (1997).

1\* , 2 , 1  
2 1 - ” “ 3 ,  
I ,  
30 2016 .; 29 2016 .  
( )  
(Zr)  
0.5 V ( Ag|AgCl|1M-LiCl )  
ZrO<sub>2</sub>.

## Electrochemical bond cleavage in pesticide ioxynil. Kinetic analysis by voltammetry and impedance spectroscopy

R. Sokolová<sup>1\*</sup>, S. Giannarelli<sup>2</sup>, N. Fanelli<sup>3</sup>, L. Pospíšil<sup>1,4</sup>

<sup>1</sup> J. Heyrovský Institute of Physical Chemistry of the CAS, v.v.i., Dolejškova 3, 18223 Prague, Czech Republic

<sup>2</sup> University of Pisa, Department of Chemistry and Industrial Chemistry, via Moruzzi 13, 56124 Pisa, Italy

<sup>3</sup> Institute of Chemistry of Organometallic Compounds, CNR Pisa, via Moruzzi 1, 56124 Pisa, Italy

<sup>4</sup> Institute of Organic Chemistry and Biochemistry of the CAS, v.v.i., Flemingovo n. 2, 16610 Prague, Czech Republic

Received October 29, 2016

Revised December 20, 2016

The cleavage of carbon-halogen bond is a common process in electrochemistry of halogenated aromatic compounds. We describe such a cleavage for the reduction of pesticide ioxynil, 4-hydroxy-3,5-diiodobenzonitrile. The reaction mechanism is complicated by the presence of two iodine substituents and by self-protonation equilibrium. We compare three methods for the determination of the rate-determining step. The electrochemical impedance spectroscopy is rarely used for the determination of coupled fast chemical reactions of organic compounds. Our procedure involves simulation of cyclic voltammograms, search for parameters of Gerischer impedance and simulation of the faradaic phase angle as a function of the applied frequency. The last procedure is considerably more sensitive for the detection of chemical reaction compared to fitting the entire electrode impedance spectrum.

**Key words:** electrochemical impedance spectroscopy, rate constant, self-protonation, faradaic phase angle, halogen cleavage, EC processes fitting

### INTRODUCTION

Electron transfer in organic redox systems is often coupled with fast chemical reactions like halogen cleavage. Cyclic voltammetry is usually applied for the determination of the reaction mechanism and corresponding kinetic parameters. The solution of complicated reaction pathways includes several unknown parameters often originating from protonation equilibria. The presence of proton donors influences the number of electrons consumed during the reductive cleavage of halide anions from halogenated aromatic compounds [1-7]. Increased number of "adjustable" parameters leads to ambiguity. The same fitting or simulation results may be achieved with quite different set of kinetic and equilibrium constants.

Ioxynil (Fig. 1) belongs to the group of benzonitrile herbicides which are used in agriculture, because it inhibits the electron transfer in the Photosystem II [8].

The role of self-protonation in the reduction mechanism of ioxynil was studied in dimethylsulfoxide by electrochemical methods (Fig. 2) [9-11]. Final products were identified by GC/MS. The cleavage of the carbon-halogen bond was confirmed also by the detection of iodide anions

during electrolysis.

Resulting monohalogenated intermediates are further reduced in the second redox step at more negative potentials.

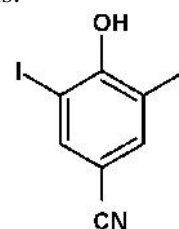


**Fig. 1.** The chemical structure of ioxynil, 4-hydroxy-3,5-diiodobenzonitrile.

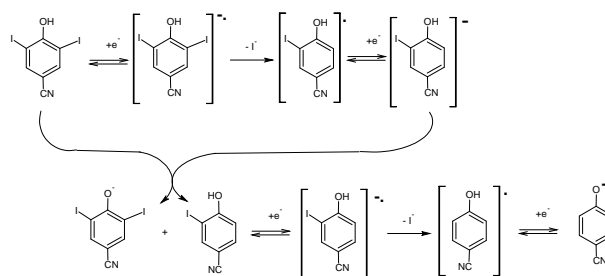


**Fig. 2.** Mechanism of ioxynil reduction.

Electrochemical impedance spectroscopy (EIS) is a suitable tool for studies of fast processes. However, EIS was rarely applied for analysis of coupled chemical reactions. In this communication we combine established research tools with the application of EIS for the determination of kinetic parameters.

To whom all correspondence should be sent:  
E-mail: sokolova@jh-inst.cas.cz

## EXPERIMENTAL

## Reagents

Ioxynil (3,5-diiodo-4-hydroxybenzotrile) was purchased as a pesticide reference material from Dr. Ehrenstorfer, GmbH (Augsburg, Germany). Tetrabutylammonium hexafluorophosphate (Sigma) was used as a supporting electrolyte and dried before use. Dimethylsulfoxide (DMSO, content of  $\text{H}_2\text{O} < 0.005\%$ , Aldrich) was used as received. All reagents and chemicals were used without any further purification.

## Methods

Electrochemical measurements were done using potentiostat Autolab PG STAT 30 equipped with FRA2 module (ECO Chemie, The Netherlands). A three-electrode electrochemical cell was used with an  $\text{Ag}|\text{AgCl}||1\text{M LiCl}$  reference electrode (with potential 0.210 V vs. SHE) separated from the test solution by a salt bridge. The working electrode (WE) was a static mercury drop electrode 663 VA Stand (Metrohm) with an area  $3.4 \times 10^{-3} \text{ cm}^2$ . The Stand was interfaced to the potentiostat through controller Autolab IME 663 (ECO Chemie, The Netherlands). The auxiliary electrode was cylindrical platinum net with area ca. 200 times higher than the area of WE. Oxygen was removed from the solution by passing a stream of argon. The electrochemical data from cyclic voltammetry and electrochemical impedance were analyzed and fitted using Autolab software (GPES, FRA). Data were collected in the frequency-scanned mode in the range 0.1 Hz to 100 kHz in both directions. The EIS data were measured on a single mercury drop electrode, which was freshly formed by a trigger pulse and equilibrated for 150 s at a given measurement potential under conditions of stationary state. The prolongation of the equilibration time yielded the same EIS data. Experimental voltammetric data were fitted by DigiSim software (Version 3.03b, Bioanalytical systems, Inc., USA). Analysis of EIS data used ZView software, version 3.2b (Scribner Associate, Inc., North Carolina, USA). Calculations of the Faradaic phase angle according to Moreira and de Levie [12] treatment were programmed in Mathematica version 8.0 (Wolfram Research, Inc., USA).

## RESULTS AND DISCUSSION

## Cyclic voltammetry

The cyclic voltammetry of ioxynil shows two reduction peaks at peak potentials -1.0 and -1.4 V (Fig. 3).

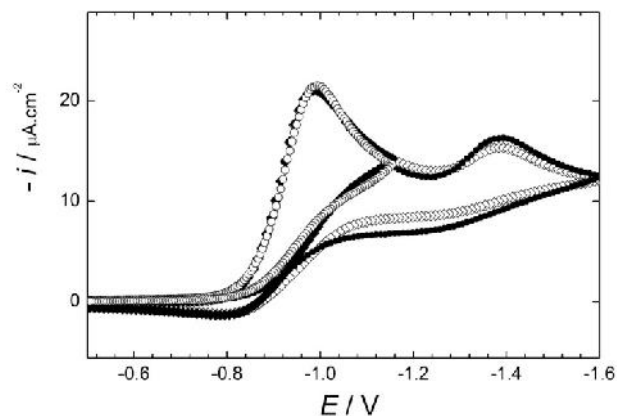


**Fig. 3.** Cyclic voltammogram of  $2.5 \times 10^{-4} \text{ M}$  ioxynil in dimethylsulfoxide with 0.1 M  $\text{TBAPF}_6$  supporting electrolyte at  $0.2 \text{ V} \cdot \text{s}^{-1}$ . Experimental data are circles and diamonds are results of the numerical fitting.

Mono-iodinated intermediate is the product of the first reduction peak, in which the reaction mechanism is of ECEC type (E stays for the electron transfer and C for a chemical reaction) [11]. The second reduction peak corresponds to the reduction of mono-iodinated product and the cleavage of the second iodide atom in a sequence of ECE-type process (Fig. 2) [11]. Numerical fitting of voltammograms at scan rates in the range 0.05 to  $0.5 \text{ V} \cdot \text{s}^{-1}$  yielded for the rate determining step  $k_1 = 3.0 \times 10^5 \text{ s}^{-1}$  and  $K = 22$ . The rate constant of the first iodide atom cleavage is quite high:  $k_2 = 7.1 \times 10^8 \text{ s}^{-1}$ . This is in the range of values found for a *single* halogen-carbon bond cleavage in other aromatic systems. Savéant reported the value  $1 \times 10^9 \text{ s}^{-1}$  for cleavage of C-halogen bond [13]. M'Halla et al. [7] found rate constants of halogen cleavage  $5 \times 10^8 \text{ s}^{-1}$  for 4-chlorobenzotrile and values  $3 \times 10^8 \text{ s}^{-1}$  and  $5 \times 10^7 \text{ s}^{-1}$  for 1-bromonaphthalene and 1-chloronaphthalene, respectively.

## Electrochemical impedance spectroscopy

The electrochemical impedance data were measured at potentials of the first reduction peak of ioxynil in 50 mV intervals. The measured impedance at the rise of the reduction peak is shown in Figure 4. All data were measured at stationary state and frequencies were scanned in both directions in the interval 0.1 Hz to 100 kHz. No differences were noticed. Data comply with the test based on the Kramers-Kronig transformation [14,15]. An example of EIS data at -0.950 V is shown in Figure 5.

Chemical reactions participating in an overall electron transfer mechanism are known from early studies by DC polarography and later by cyclic voltammetry. The application of AC methods, like EIS, offers measurements on much shorter effective time period. This allows detection of kinetic effects,

which in slower techniques would exhibit only thermodynamic influence. Electron transfer reactions coupled with chemical reactions yield the Gerischer-type impedance element (G) [16]. The Gerischer impedance is characterized by an admittance  $Y_0$  and a kinetic parameter  $k$  ( $s^{-1}$ ). The kinetic parameter  $k$  is related to the rate constants  $k_n$ ,  $k_{-n}$  and the equilibrium constants  $K_n = k_n / k_{-n}$  of the  $n$ -th's chemical reaction by rather complicated functions [12,17,18]. Due to its complexity, the experimental evidence of the Gerischer-type impedance element was for a long time lacking. First reports were given for systems differing from the present one [19-21]. Hence we explored also a possibility to search for G in electrochemically initiated carbon-halogen bond cleavage.

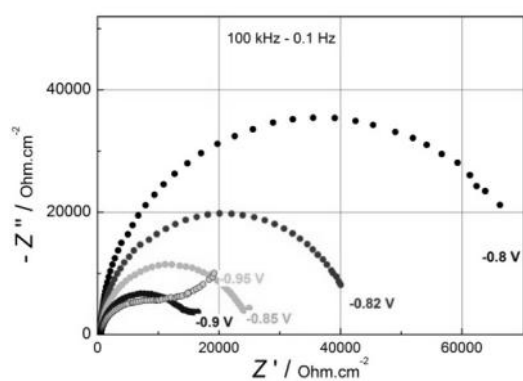


Fig. 4. EIS of  $2.5 \times 10^{-4}$  M ioxynil in dimethylsulfoxide with 0.1 M TBAPF6 supporting electrolyte at potentials indicated at each curve.

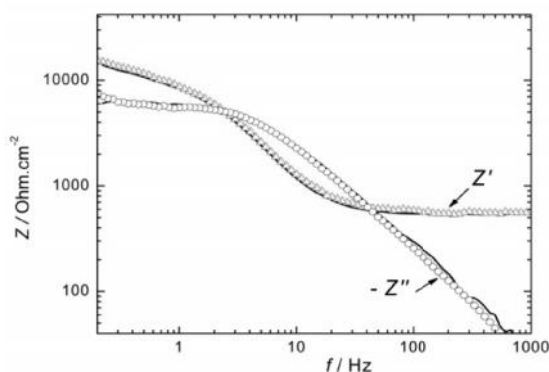


Fig. 5. Experimental impedance data measured at the potential -0.950 V ( $Z'$  red points,  $-Z''$  black points). The application of the Kramers-Kronig transform yields lines overlapping with experimental points.

The impedance data were fitted using the Randles equivalent circuit and by a similar circuit containing G in place of the Warburg element. Unfortunately the fitting of experimental data could not distinguish which circuit fitted better. The heterogeneous rate constants  $k(E)$  of the first electron transfer as a function of  $E$  were estimated

from values of the charge transfer resistance [22] and are given in Figure 6.

Knowing from other experiments (cyclic voltammetry, exhaustive electrolysis and product analysis) that chemical steps are indeed involved in the mechanism, heterogeneous rates  $k(E)$  estimated from the charge transfer resistance  $R_{ct}$  are not correct because the Gerischer impedance  $Z_0$  contributes to the overall complex impedance diagram. We estimated Gerischer parameters as  $Y_0 = 9.79 \times 10^{-5} \text{ S}\cdot\text{cm}^{-2}$  and  $k \sim 0.195 \text{ s}^{-1}$ . It is known that  $Z_0 (=1/Y_0)$  can be detected only for the time-scale of EIS and hence for  $10^{-4} < k < 10^{-2}$ . Much faster chemical reactions contribute to the overall impedance by  $Z_0$  in the frequency range, where  $R_{ct}$  and non-faradaic components prevail. Since experimental data could not be measured for frequencies lower than 0.2 Hz the estimated parameters of the Gerischer impedance are not very reliable. Simulation using the fitted parameters  $Y_0$  and  $k$  for much lower frequencies outside the measured range is shown in Figure 7. It is evident that data should be measured to much lower frequencies, which is technically impossible for the present system.

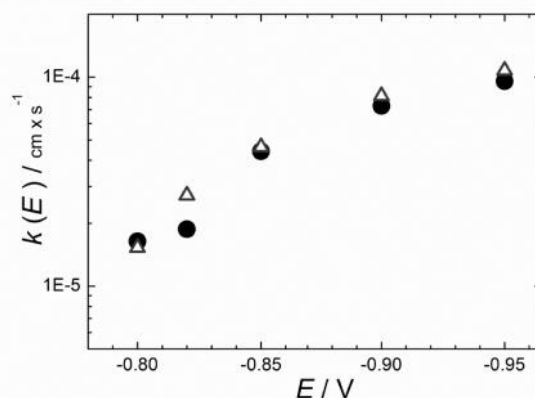


Fig. 6. The heterogeneous rate constant  $k(E)$  estimated from the charge transfer resistance for two concentrations of ioxynil: (  $\circ$  )  $1.9 \times 10^{-4}$  M and (  $\Delta$  )  $2.5 \times 10^{-4}$  M.

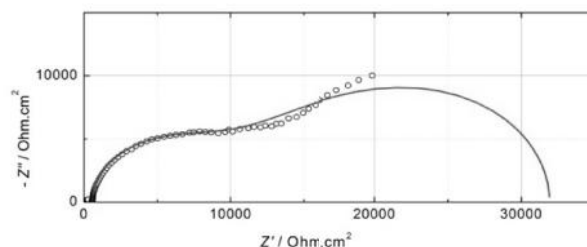
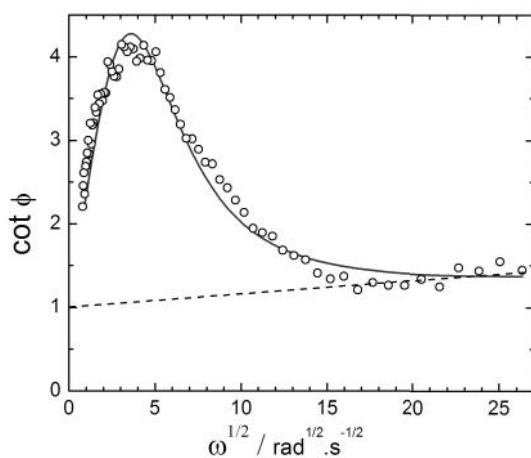


Fig. 7. Diagram of the experimental complex electrode impedance at -0.950 V (circles). Data were fitted with the Gerischer-type circuit resulting in the solution resistance  $568 \text{ Ohm}\cdot\text{cm}^{-2}$ ,  $R_{ct}=8057 \text{ Ohm}\cdot\text{cm}^{-2}$ , the double layer capacitance  $6.23 \mu\text{F}\cdot\text{cm}^{-2}$ ,  $Y_0=9.79 \times 10^{-5} \text{ S}\cdot\text{cm}^{-2}$  and  $k = 0.195 \text{ s}^{-1}$ . Simulation using these

parameters and the frequency range from 1 mHz to 30 kHz is shown as the red curve.

It was recognized [17] that predicted influence of a chemical reaction is readily apparent from a *qualitative* inspection of the faradaic phase-angle  $\phi$  data, whereas similar examination of impedance vectors diagrams may show no definitive indication of the presence of chemical kinetics. The dependence of the faradaic phase angle on the square root of frequency ( $\cot \phi$  vs.  $\omega^{1/2}$ ) in such cases shows a hump with low- and high-frequency asymptotes. Our experimental data indeed show such humps of various heights for different DC potentials. An example is given in Figure 8.



**Fig. 8.** The experimental dependence of the faradaic phase angle on the applied frequency. The DC potential was  $-0.95$  V. Simulation (full red curve) according to Moreira-De Levie equations used the following values:  $k(E)=0.157$  estimated from the dashed asymptote,  $k_1=76$ ,  $k_{-1}=3.8$ ,  $K_1=20.0$  and  $\alpha=0.5$ .

Simulation of the  $\cot \phi$  vs.  $\omega^{1/2}$  plot yields the rate constants of the chemical rate determining step coupled with the first electron transfer step  $k_1=3.62 \times 10^5$  s $^{-1}$  and  $K_1=20.0$ . These data remarkably agree with the corresponding values  $k_1=3.0 \times 10^5$  s $^{-1}$  and  $K_1=22$  obtained by fitting of the cyclic voltammograms.

## CONCLUSIONS

The application of three methods for the estimation of the rate determining coupled chemical reaction in electrochemical iodine-carbon bond cleavage was tested. The overall reaction scheme, elucidated in our previous reports, is rather complicated due to the participation of self-protonation process [10,11]. Simulation of cyclic voltammograms was used as an established method in organic electrochemistry. The electrochemical impedance spectroscopy is an alternative for the evaluation of kinetic parameters. However, its

application to organic redox systems is lacking. Redox properties of ioxynil indicate that the kinetic Gerischer impedance would be observable in the frequency range, in which also the charge transfer resistance dominates. This makes also the determination of the standard heterogeneous rate constant  $k^0$  quite uncertain (see a non-linear dependence of  $k(E)$  vs.  $E$  in Figure 6). We concluded, as already noticed by Smith [17], that the inspection of the faradaic phase angle as a function of the applied frequency is the most reliable method of proving the coupling of a chemical reaction and the electron transfer. Using the formalism of Moreira and de Levie, we obtained the homogeneous and heterogeneous rate parameters in a good agreement with values estimated from voltammetry. Results reported here promote further attempts to apply EIS for more simple cases of organic EC processes.

**Acknowledgements:** This work was supported by the Academy of Sciences of the Czech Republic (RVO: 61388963) and the Grant Agency of the Czech Republic (GACR 14-05180S).

## REFERENCES

1. K. Houser, D. Bartak, M. Hawley, *J. Am. Chem. Soc.*, **95**, 6033 (1973).
2. F. M'Halla, J. Pinson, J. Savéant, *J. Am. Chem. Soc.*, **102**, 4120 (1980).
3. H. Jensen, K. Daasbjerg, *Acta Chemica Scandinavica*, **52**, 1151 (1998).
4. D. Peters in: *Organic Electrochemistry*, Eds. H. Lund, O. Hammerich, M. Dekker, Inc., New York, 2001, p. 341 - 377.
5. M. Prasad, M. Sangaranarayanan, *Chem. Phys. Lett.*, **414**, 55 (2005).
6. J. Jaworski, M. Cembor, B. St pie , G. Häfeling, *Electrochim. Acta*, **51**, 2322 (2006).
7. J. Jaworski, M. Cembor, D. Kuck, *Electrochim. Acta*, **52**, 2196 (2007).
8. Tomlin, C. D. S. *The Pesticide Manual*, 12<sup>th</sup> ed., British Crop Protection Council, Farnham, UK, 2000.
9. R. Sokolová, M. Hromadová, L. Pospíšil in: *New Trends in analytical, environmental and cultural heritage chemistry*, Eds. Colombini, M. P.; Tassi, L. Research Signpost, 2008, p. 43.
10. R. Sokolová, M. Hromadová, J. Fiedler, L. Pospíšil, S. Giannarelli, M. Valášek, *J. Electroanal. Chem.*, **622**, 211 (2008).
11. R. Sokolová, M. Hromadová, J. Ludvík, L. Pospíšil, S. Giannarelli, *Electrochimica Acta*, **55**, 8336 (2010).
12. H. Moreira, R. De Levie, On the coupling of interfacial and diffusional impedances II, *J. Electroanal. Chem.*, **29**, 353 (1971).
13. J. Savéant, *Elements of Molecular and Biomolecular Electrochemistry. An Electrochemical Approach to*

- Electron Transfer Chemistry. 2006, John Wiley and Sons, Inc., New Jersey, Chapter 2.
14. R. Kramers, *Transactions of Volta Centenary Congress*, **2**, 545 (1927).
  15. R. de L. Kronig, *J. Opt. Soc. Am.*, **12**, 547 (1926).
  16. H. Gerischer, *Phys. Chem.*, **198**, 216 (1951).
  17. D. Smith in Bard, A.J. (Ed.), *Electroanalytical Chemistry*, Vol.1, Marcel Dekker, New York, 1970, 42-70.
  18. R. Sluyters in A. Bard (Ed.), *Electroanalytical Chemistry*, Vol.4, Marcel Dekker, New York, 1970, 65-71.
  19. E. Levillain, A. Demortier, J. Lelieur, *J. Electroanal. Chem.*, **394**, 103 (1995).
  20. B. Baukamp, *Solid States Ionic*, **169**, 65 (2004).
  21. B. Boukamp, M. Verbraeken, D. Blank, P. Holtappels, *Solid States Ionic*, **177**, 2539 (2006).
  22. A. Lasia, *Electrochemical Impedance Spectroscopy and Its Application in: Modern Aspects of Electrochemistry*, B. Conway, J. Bockris, R. White (Eds.), Kluwer Academic/Plenum Publishers, New York, 1999, Vol. 32, p. 143-248.2002.

1, 3, 4, 1,2  
 1, 3, 18223  
 2, 13,56124  
 3, I, 2, 16610  
 4, 29 2016 .; 20 2016 .  
 ( )

-3,5-

, 4-



## Anodic oxidation of sulphite in alkaline aqueous solution on graphite electrode

A. Enache, M. Dan, A. Kellenberger, N. Vaszilcsin\*

University Politehnica Timisoara, Faculty of Industrial Chemistry and Environmental Engineering, Laboratory of Electrochemistry, Corrosion and Electrochemical Engineering, 6 Parvan, 300223 Timisoara, Romania

Received November 15, 2016      Revised December 28, 2016

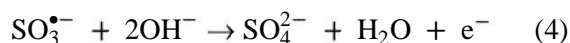
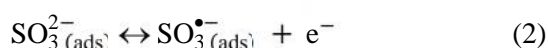
The anodic oxidation of sulphite in alkaline aqueous solution on graphite electrode has been studied by voltammetric methods and electrochemical impedance spectroscopy. The cyclic voltammograms allowed identification of the following processes that take place during anodic polarization of the working electrode: mediated oxidation of sulphite ions with adsorbed atomic oxygen, direct oxidation of sulphite on graphite and oxygen evolution. The kinetic parameters that characterize the charge transfer process have been determined by the Tafel method. The obtained Tafel slope (+0.123 V dec<sup>-1</sup>) is close to the theoretical value (+0.118 V dec<sup>-1</sup>) and therefore the charge transfer coefficient  $\tau$  tends to 0.5. A high value of the exchange current density  $i_0$  (1.9 A m<sup>-2</sup>) has been obtained. Chronoamperometric and chronocoulometric measurements have been performed to evaluate the conversion degree of sulphite to sulphate. The results obtained by voltammetry experiments were confirmed by electrochemical impedance spectroscopy. The morphological changes of graphite electrode surface after a certain time of electrolysis have been highlighted by scanning electron microscopy.

**Key words:** anodic sulphite oxidation, graphite electrode, electrochemical impedance spectroscopy, chronoamperometry, chronocoulometry.

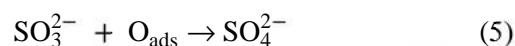
### INTRODUCTION

The favorable results of researches regarding the use of hydrogen sulfide in H<sub>2</sub>S/O<sub>2</sub> fuel cells [1,2] have focused the researchers interest on other sulfur compounds too. As a result, an opportunity to use sulfur compounds originating from recovery plants in refineries as fuel for alkaline fuel cells has been provided [3]. Generally, sulfur is recovered in refineries in the form of liquid volatile or gaseous compounds such as hydrogen sulfide, sulfur dioxide, carbonyl sulfide or carbon disulfide [4], what makes feasible their use in fuel cells. Large amounts of SO<sub>2</sub> from combustion gasses of fossil fuels are recovered as sulphites. One way to exploit residual sulphites is given by their use in the alkaline SO<sub>3</sub><sup>2-</sup>/O<sub>2</sub> fuel cells. Since the composition of fuel cells electrodes is based on carbon materials with various graphitization degrees, it is necessary to carry out a systematic study of the electrochemical behavior of sulphites on graphite. The use of graphitic materials as electrodes for fuel cells has been widely studied due to the influence of their properties on the performance and lifetime of fuel cells [5-13]. Even in its manufacturing, the surface of graphite is modified with oxygenated functional groups, such as hydroxyl, carbonyl and/or carboxyl groups. Anodic polarization in aqueous solution

increases the number of these functional groups [14], but may also lead to degradation of graphite that occurs simultaneously with oxygen evolution reaction and forms either carbon dioxide in acid solutions, or carbonate ions in alkaline solutions [15]. Two mechanisms have been proposed for the alkaline oxidation of sulphites. In the systematic study of sulphite oxidation on graphite rotating disk electrode [16], direct oxidation mechanism carried out in 4 steps has been described as follows:



The second proposed mechanism of sulphite oxidation is described as a mediated oxidation with atomic oxygen adsorbed on the surface of graphite anode [17]:



It should be taken into account that in an aqueous sulphite solution, the chemical species SO<sub>2</sub>, HSO<sub>3</sub><sup>-</sup> and SO<sub>3</sub><sup>2-</sup> are present simultaneously in pH depending rates. In alkaline conditions at pH > 10, the sulphite ions are the predominant chemical species [18].

The aim of this work is to study electrochemical behavior of sulphite ions on graphite electrode, in order to identify the optimal conditions for recovering

To whom all correspondence should be sent:  
E-mail: nicolae.vaszilcsin@upt.ro

sulphites from the by-products of various technological processes. In addition, researches on electrochemical behavior of sulfur dioxide will allow its use in the  $\text{SO}_2/\text{O}_2$  fuel cell, which besides electricity will also produce sulfuric acid.

## EXPERIMENTAL

Electrolyte solutions were prepared using sodium hydroxide NaOH (Merck *p.a.*  $\geq 99\%$ ) and sodium sulphite  $\text{Na}_2\text{SO}_3$  (Merck *p.a.*  $\geq 98\%$ ).

Electrochemical studies were carried out using a Biologic SP 150 potentiostat/galvanostat. The anodic oxidation of sulphite was studied by linear and cyclic voltammetry experiments and electrochemical impedance spectroscopy. The amount of oxidized sulphite as a function of potential was determined by chrono-methods (chronoamperometry and chronocoulometry).

All electrochemical experiments were performed in a glass electrolysis cell equipped with two graphite counter electrodes positioned symmetrically near the working electrode (graphite, geometric surface area of  $0.8 \text{ cm}^2$ ) and a silver-silver chloride Ag/AgCl reference electrode ( $E = +0.197 \text{ V/SHE}$ ). The surface of the working electrode was prepared by the mechanical polishing with SiC grinding paper #2400 and diamond paste  $3 \mu\text{m}$ , washed and ultrasonicated in distilled water for 10 minutes before each measurement. The anodic oxidation of sulphite was studied in  $1 \text{ mol.L}^{-1}$  NaOH solution as the supporting electrolyte with different concentrations of  $\text{Na}_2\text{SO}_3$ :  $10^{-3}$ ,  $10^{-2}$  and  $10^{-1} \text{ mol.L}^{-1}$ , at  $25^\circ\text{C}$ . All measurements were carried out in solutions purged with high purity nitrogen. Cyclic voltammograms were recorded at scan rates of 500 and  $100 \text{ mV s}^{-1}$  and linear polarization curves were obtained at the scan rate of  $1 \text{ mV s}^{-1}$ . Electrochemical impedance spectra were recorded in the frequency range 100 kHz to 10 mHz with alternating voltage signal amplitude of 10 mV. The surface morphology of graphite electrode before and after chronoamperometry measurements was studied by scanning electron microscopy (SEM) using a FEI INSPECT S microscope.

## RESULTS AND DISCUSSION

### Cyclic voltammetry

In order to identify the processes that take place at the electrode/electrolyte interface, cyclic voltammograms were recorded in  $1 \text{ mol L}^{-1}$  NaOH in the absence and presence of various concentrations of sodium sulphite:  $10^{-3}$ ,  $10^{-2}$  and  $10^{-1} \text{ mol.L}^{-1}$ , respectively. The first cycle voltammograms of the working electrode, recorded

after 5 minutes of conditioning at the open circuit potential are drawn in Fig. 1. Voltammograms presented in Fig. 1 indicate that at anodic polarization, the oxidation of sulphites occurs simultaneously with oxygen formation. These processes are accompanied by chemical transformation of the graphite surface, as it has been mentioned before.

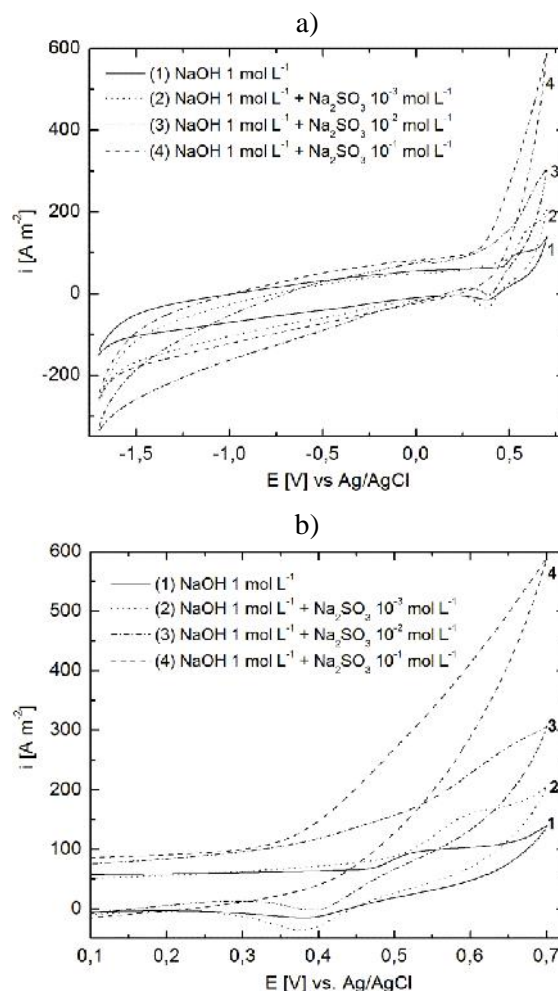
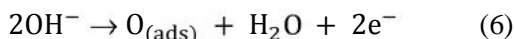


**Fig.1.** Cyclic voltammograms on graphite electrode in  $1 \text{ mol L}^{-1}$  NaOH solution with different concentrations of  $\text{Na}_2\text{SO}_3$  at  $500 \text{ mV s}^{-1}$ : a) voltammograms drawn over entire domain of the potential, b) zoom in the anodic area.

The cathodic peak observed at reverse potential sweep at about  $+0.38$  to  $+0.4 \text{ V}$  in both NaOH and NaOH+ $\text{Na}_2\text{SO}_3$  solutions is assigned to the reduction of oxygenated functional groups at the surface of graphite electrode [14], taking into account that it is not present on platinum [19]. Since in the presence of sulphite this peak does not significantly alter its shape and height, it can be concluded that oxidation of sulphite is an irreversible process. At advanced cathodic polarization, the hydrogen evolution takes place. Details of cyclic voltammogram (Fig. 1b, curve 1)

show that in the absence of sulphite ions, a limiting anodic current appears, which is attributed to formation of adsorbed atomic oxygen, according to the reaction (6) [20]:



By addition of small amounts of sulphite, the limiting current increases proportionally to its concentration (Fig. 1b, curves 2 and 3), what means that sulphite ions react with atomic oxygen adsorbed on the graphite surface. The continuous removal of adsorbed oxygen from the electrode surface enhances its formation reaction, and as a result the limiting current increases. Therefore, it can be concluded that at low concentrations, the anodic oxidation of sulphite ions in alkaline solution is mediated by the adsorbed oxygen, what is contrary to the results obtained by Lu *et al.* [16]. At higher concentrations of sulphite ( $\geq 10^{-1} \text{ mol L}^{-1}$ ), however, the anodic peak corresponding to the formation of adsorbed atomic oxygen is no longer observed. This is due to a facile access of sulphite ions to the electrode surface, where the oxygen mediated oxidation takes place concomitantly with direct oxidation of sulphite according to the mechanism proposed by Lu *et al.* [16]. At higher anodic potentials the oxygen evolution reaction takes place, as is highlighted on the cyclic voltammograms recorded in an extended potential range (Fig. 2).

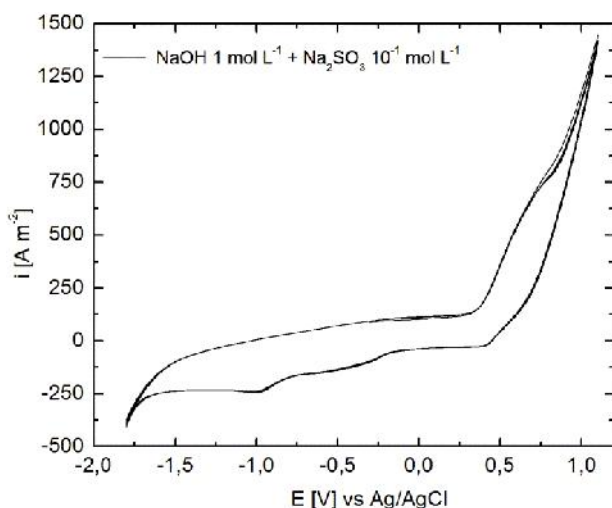


**Fig. 2.** Cyclic voltammograms (5 scans) on graphite electrode in  $1 \text{ mol L}^{-1}$  NaOH solution with  $10^{-1} \text{ mol L}^{-1}$   $\text{Na}_2\text{SO}_3$  at  $500 \text{ mV s}^{-1}$ .

To obtain information on the sulphite anodic oxidation in time, cyclic voltammograms were recorded with a large number of scans (25 scans) at a lower scan rate ( $100 \text{ mV s}^{-1}$ ). By analyzing cyclic voltammograms given in Fig. 3, one can observe significant reduction of limiting current density with increasing number of cycles.

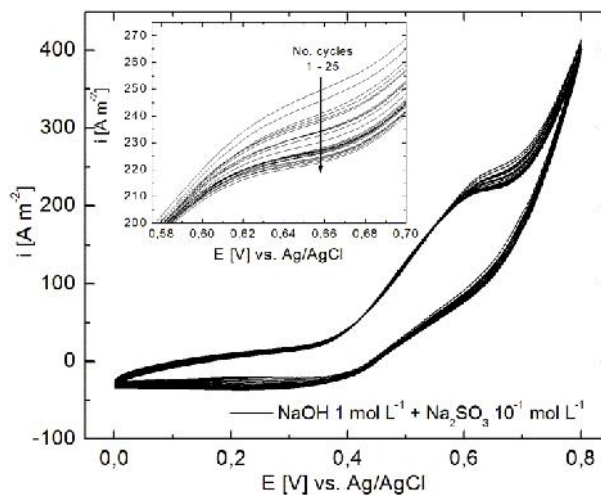


**Fig. 3.** Cyclic voltammograms – anodic branch (25 scans) on graphite electrode in  $1 \text{ mol L}^{-1}$  NaOH solution with  $10^{-1} \text{ mol L}^{-1}$   $\text{Na}_2\text{SO}_3$  at  $100 \text{ mV s}^{-1}$ . Inset: evolution of anodic limiting current density as function of number of cycles.

The inset in Fig. 3 shows decrease of the limiting current density by approximately 13% from about  $245 \text{ A m}^{-2}$  (scan 1) to  $215 \text{ A m}^{-2}$  (scan 25). This fact can be explained by continuous degradation of the graphite surface during cycling and by filling of graphite pores with oxygen leading to reduction of the active surface area of the electrode.

#### Linear voltammetry

Cyclic voltammograms obtained at high scan rates showed that at high sulphite concentrations ( $10^{-1} \text{ mol L}^{-1}$ ) the formation of adsorbed atomic oxygen takes place simultaneously with the direct oxidation of sulphite on the graphite electrode. Since the atomic oxygen formed on graphite is consumed entirely for the oxidation of sulphite, it can be considered that the total anodic current is used only for the oxidation of sulphite to sulphate. Therefore, the kinetic parameters that characterize the oxidation of sulphite, the anodic charge transfer coefficient  $\Gamma$  and exchange current density  $i_0$ , can be determined by the Tafel method for the potential range where the electrode process is controlled by charge transfer. It should, however, be noted that the values obtained in this case for  $\Gamma$  and  $i_0$  are just apparent values because they refer to an undefined process.

Since the kinetic parameters can be calculated for quasi-stationary conditions, linear polarization curves were obtained at low scan rates ( $1 \text{ mV s}^{-1}$ ) and presented in Fig. 4.

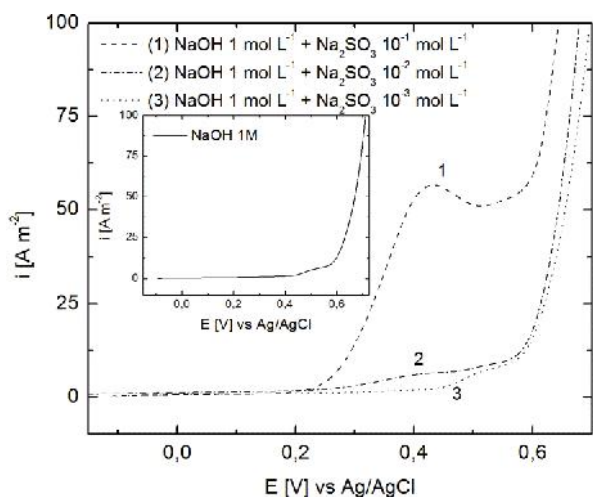


**Fig. 4.** Linear voltammograms on graphite electrode in alkaline solution with different concentrations of  $\text{Na}_2\text{SO}_3$  at  $1 \text{ mV s}^{-1}$ . Inset: linear voltammogram of the supporting electrolyte.

Each anodic overpotential ( $\eta$ ) value was calculated as the difference between the working electrode potential and the equilibrium potential. The equilibrium potential was approximated by extrapolating the linear part of the voltammogram (corresponding to charge transfer) to the abscissa. The dependence of  $\eta$  on the logarithm of current (Tafel plot) for the alkaline solution with  $10^{-1} \text{ mol L}^{-1} \text{ Na}_2\text{SO}_3$  is shown in Fig. 5, while the corresponding kinetic parameters are given in Table 1.

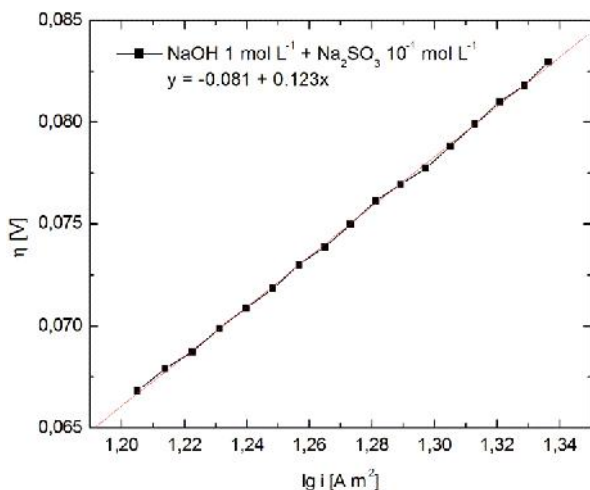


**Fig. 5.** Tafel plot for anodic oxidation of sulphite on graphite electrode in alkaline solution with  $10^{-1} \text{ mol L}^{-1} \text{ Na}_2\text{SO}_3$ .

The calculated value of the Tafel slope ( $+ 0.123 \text{ Vdec}^{-1}$ ) is close to the theoretical value of  $+ 0.118 \text{ Vdec}^{-1}$  for one-electron charge transfer process and the anodic charge transfer coefficient  $\Gamma$  is close to 0.5. A high value of the exchange current density is obtained ( $1.9 \text{ Am}^{-2}$ ), what is characteristic for the fast charge transfer processes and comparable to that obtained by other authors on skeletal nickel [17]. In these circumstances, it can be evaluated

that the rate determining step for formation of atomic oxygen is the charge transfer process that leads to formation of  $\text{HO}\ddot{\text{O}}$  radicals adsorbed on the graphite according to the following reaction [19]:



Similarly, for the direct oxidation of sulphite, the rate determining step is the charge transfer given by equation (2).

**Table 1.** Kinetic parameters for  $10^{-1} \text{ mol L}^{-1}$  sulphite in alkaline solution.

$\text{Na}_2\text{SO}_3$ concentration [mol L <sup>-1</sup> ]	b [mV dec <sup>-1</sup> ]	$\Gamma$	$i_0$ [A m <sup>-2</sup> ]
$10^{-1}$	123	0.48	1.9

#### Chronoamperometry and chronocoulometry

For establishing potential step values applied in the chronoamperometric and chronocoulometric study of the anodic oxidation of sulphite, the linear voltammogram obtained on graphite in  $10^{-1} \text{ mol L}^{-1} \text{ Na}_2\text{SO}_3$  was used. Six potential steps were chosen (0.25, 0.35, 0.45, 0.55, 0.65 and 0.75 V) to highlight the anodic processes that take place. The applied DC potential was maintained for one hour and the corresponding current – time curves were recorded, as shown in Fig. 6.

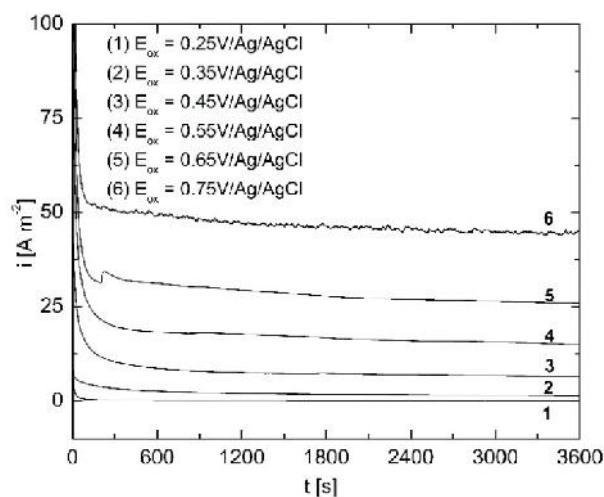


**Fig. 6.** Current-time curves on graphite in  $1 \text{ mol L}^{-1} \text{ NaOH} + 10^{-1} \text{ mol L}^{-1} \text{ Na}_2\text{SO}_3$  solution.

Each of the chronoamperometric curves obtained for the first 5 potential steps is characterized by a decay of the current followed by a plateau of constant and smooth currents, suggesting that the anodic processes (mediated oxidation and direct oxidation of sulphite) are taking place without major variation of the resistance of the solution, *i.e.* without oxygen release. Curve 6, obtained for the applied potential

of +0.75 V shows obvious irregularities, indicating that in parallel to oxidation of sulphite to sulphate, the reaction of oxygen evolution occurs. The significant increase of current density at the electrode potential of +0.75 V is another evidence of the oxygen evolution reaction. Therefore, only for the first five electrode potential step values, one can admit that the entire amount of electricity through the electrode is used exclusively for the oxidation of sulphite to sulphate, *i.e.* the current efficiency for the oxidation of sulphite to sulphate is 100%.

Similar chronoamperometric curves were also obtained for sulphite concentrations of  $10^{-2}$  and  $10^{-3}$  mol L<sup>-1</sup>, indicating that the potential for the oxygen evolution reaction shifts to more negative values as the concentration of sulphite decreases. Thus, for  $10^{-3}$  mol L<sup>-1</sup> sulphite solution, the oxygen release starts at the electrode potential of +0.65 V. It was also noted that the values of quasi-stationary current densities are increased after 1 hour as has been expected for the increasing concentration of sulphite.

Chronoamperometric curves obtained for three different concentrations of sulphite at electrode potentials where oxygen evolution does not take place were integrated to obtain the amount of electricity passing at the anode. Based on the

Faraday's laws, the amount of sulphite oxidized to sulphate (  $\delta$  ) has been calculated, together with the degree of transformation (  $r$  ) of sulphite to sulphate. These two parameters are represented as a function of the electrolysis time in Fig. 7, showing the chronocoulometric curves for the base solution with  $10^{-1}$  mol L<sup>-1</sup> Na<sub>2</sub>SO<sub>3</sub>. Table 2 gives the chronoamperometric and chronocoulometric data for all three concentrations of sulphite.

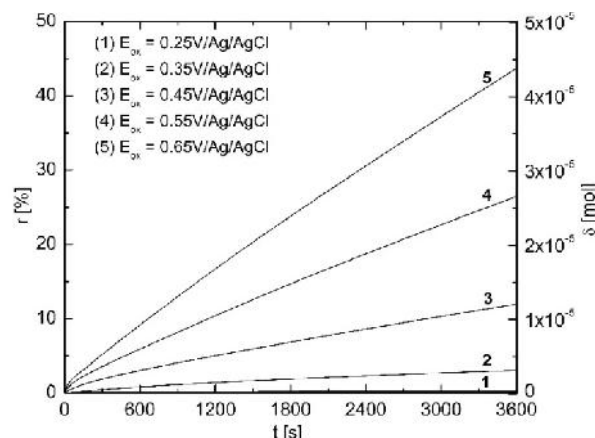


**Fig. 7.** Chronocoulometric curves on graphite in 1 mol L<sup>-1</sup> NaOH +  $10^{-1}$  mol L<sup>-1</sup> Na<sub>2</sub>SO<sub>3</sub> solution.

The linear dependence of  $r$  and  $\delta$  over time is another argument indicating that current efficiency for the oxidation of sulphite to sulphate is 100%.

**Table 2.** Chronoamperometric and chronocoulometric measurements on graphite electrode in 1 molL<sup>-1</sup> NaOH solution with different concentrations of Na<sub>2</sub>SO<sub>3</sub>.

Na <sub>2</sub> SO <sub>3</sub> concentration [mol L <sup>-1</sup> ]	E [V] vs. Ag/AgCl	Chronoamperometric measurements				Chronocoulometric measurements			
		$i_{\text{final}}$ [A m <sup>-2</sup> ]				$r$ [%]			
		$t$ [min]				$t$ [min]			
$10^{-3}$	0.25	0.11	0.07	0.06	0.05	0.15	0.19	0.21	0.23
	0.35	0.17	0.13	0.12	0.11	0.13	0.18	0.23	0.27
	0.45	0.42	0.33	0.28	0.26	0.27	0.40	0.52	0.62
	0.55	2.79	2.46	2.29	2.18	1.52	2.50	3.39	4.22
	0.65	43.09	41.26	40.00	39.04	-	-	-	-
$10^{-2}$	0.25	0.20	0.16	0.14	0.13	0.20	0.30	0.33	0.38
	0.35	0.69	0.61	0.52	0.56	0.40	0.60	0.87	1.07
	0.45	1.20	1.06	1.01	0.94	0.70	1.14	1.52	1.89
	0.55	3.43	3.15	2.95	2.91	1.93	3.16	4.43	5.40
	0.65	47.57	44.00	41.85	40.23	-	-	-	-
$10^{-1}$	0.25	1.20	1.10	1.06	1.01	0.63	0.92	1.03	1.49
	0.35	2.28	1.81	1.59	1.48	1.23	1.98	2.61	3.17
	0.45	7.91	7.36	6.84	6.52	4.16	6.84	9.58	12.06
	0.55	18.03	16.74	15.75	14.87	8.26	14.80	20.81	26.55
	0.65	30.32	27.76	26.64	25.85	13.07	23.91	34.01	43.80
	0.75	48.28	46.60	45.43	44.96	-	-	-	-

*Electrochemical impedance spectroscopy*

Electrochemical impedance spectra were recorded at several electrode potentials in the range +0.35 to +0.50 V, for the base solution in the absence and in the presence of various concentrations of sulphite ions. Typical Nyquist plots are given in Fig. 8.

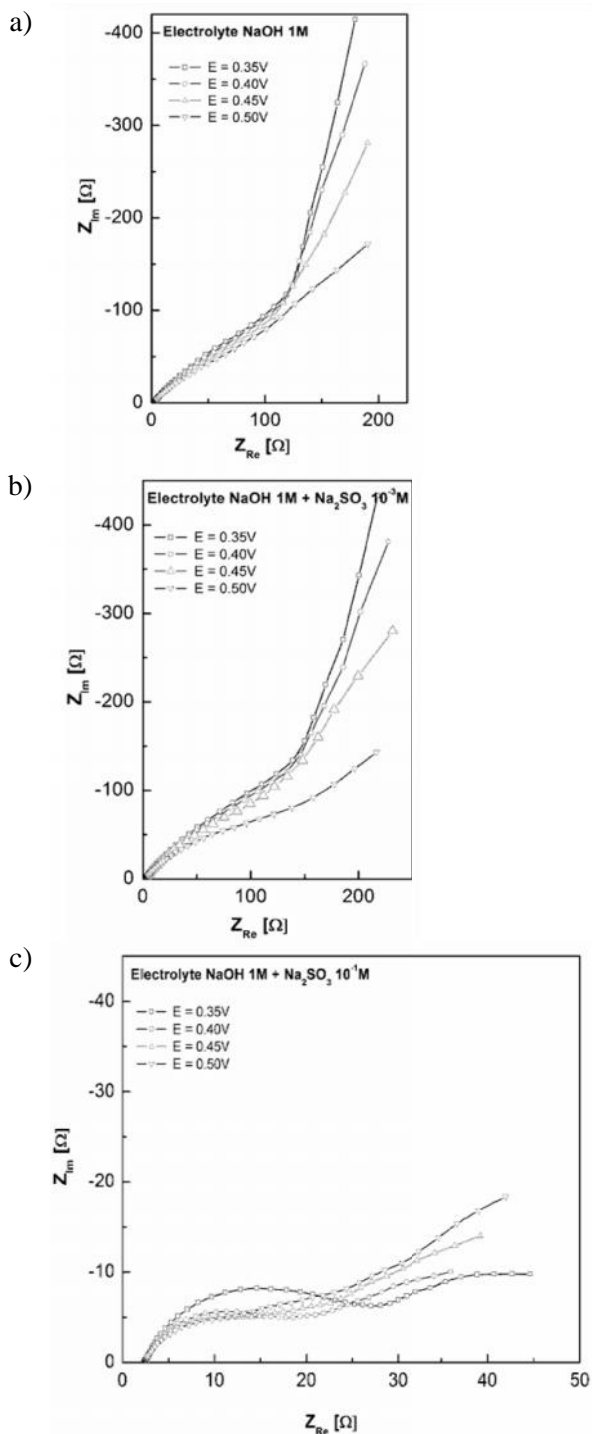


**Fig. 8.** Nyquist plots for sulphite oxidation on graphite in 1 mol L<sup>-1</sup> NaOH solution: (a) without sulphite, (b) with 10<sup>-3</sup> mol L<sup>-1</sup> Na<sub>2</sub>SO<sub>3</sub> and (c) with 10<sup>-1</sup> mol L<sup>-1</sup> Na<sub>2</sub>SO<sub>3</sub>.

In the absence and at low concentrations of sulphite, the shape of the complex plane plots is characterized by the presence of a high frequency semicircle for the charge transfer process followed by diffusion at low frequencies, corresponding to the formation of adsorbed atomic oxygen. In the presence of low concentrations of sulphite (10<sup>-3</sup> mol L<sup>-1</sup>) the diameter of the charge transfer semicircle starts to decrease at higher potentials due to the onset of sulphite oxidation process. At high concentration of sulphite (10<sup>-1</sup> mol L<sup>-1</sup>) the high frequency semicircle is well pronounced and its radius is potential dependent, so it can be attributed to the charge transfer of direct oxidation process. The oxidation of sulphite starts at lower electrode potentials. The Randles equivalent circuit was fitted to measured impedance spectra and the impedance of the faradic reaction was expressed by charge transfer resistance  $R_{ct}$  and Warburg diffusion element. The results of the complex non-linear fittings are given in Table 3.

*Scanning electron microscopy*

The morphology of the graphite electrode surface was studied by scanning electron microscopy. Fig. 9 shows the SEM images of the working electrode before and after chronoamperometric measurements of sulphite oxidation carried out in alkaline solution.

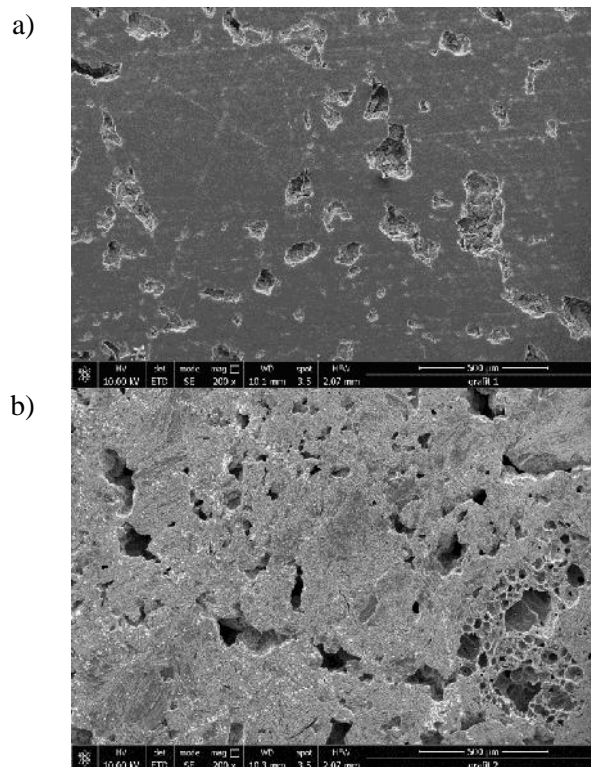


**Fig. 9.** SEM images before (a) and after (b) chronoamperometric studies, magnification 200.

**Table 3.** Fitting results and standard errors for equivalent circuit parameters related to oxidation of sulphite on graphite in 1 mol L<sup>-1</sup> NaOH in the presence of 10<sup>-1</sup> mol L<sup>-1</sup> Na<sub>2</sub>SO<sub>3</sub>.

	$E = 0.35 \text{ V}$	$E = 0.40 \text{ V}$	$E = 0.45 \text{ V}$	$E = 0.50 \text{ V}$
$R_s$ [ $\text{cm}^2$ ]	2.4 (0.2%)	2.4 (0.2%)	2.4 (0.2%)	2.4 (0.2%)
$T$ [F $\text{cm}^{-2} \text{ s}^{n-1}$ ]	0.00305 (1.4%)	0.00311 (2.0%)	0.00350 (3.0%)	0.00384 (3.7%)
$n$	0.78 (0.3%)	0.78 (0.4%)	0.77 (0.6%)	0.75 (0.8%)
$C_{dl}$ [F $\text{cm}^{-2}$ ]	$9.13 \times 10^{-4}$	$8.56 \times 10^{-4}$	$8.26 \times 10^{-4}$	$7.81 \times 10^{-4}$
$R_{ct}$ [ $\text{cm}^2$ ]	20.6 (1.4%)	12.6 (2.1%)	10.0 (3.2%)	8.7 (4.2%)
$R_d$ [ $\text{cm}^2$ ]	34.4 (3.3%)	43.0 (4.4%)	69.8 (7.4%)	118.5 (30.1%)
$\tau_d$ [s]	41.1 (9.6%)	107.7 (15.5%)	246.6 (25.1%)	703.8 (> 30%)
$p$	0.36 (2.2%)	0.32 (2.0%)	0.31 (1.8%)	0.32 (1.6%)

By analyzing the SEM images in Fig. 9, it can be emphasized that the initial surface of the graphite electrode is smooth, showing only slight defects originated from the finishing process. The SEM images after the chronoamperometry experiments show that the electrooxidation of sulphite influences the morphology of the electrode, most likely because in alkaline medium at high anodic potentials, the formation of carbonate ions occurs. Even if the rate of carbonate ions formation is reduced, the effect on the morphology of graphite electrode is significant. In time, the increase of the specific surface is favorable for the oxidation of sulphite to sulphate, but after longer electrolysis time the graphite electrode should be replaced.

## CONCLUSIONS

Cyclic voltammetry studies revealed that at low current densities and low concentrations of sulphite in alkaline solution, the oxidation of sulphite is mediated by atomic oxygen adsorbed on the graphite electrode surface. At high concentrations of sulphite (>10<sup>-1</sup> mol L<sup>-1</sup>), due to a good access of sulphite ions to the electrode surface, the direct oxidation of sulphite takes place together with mediated oxidation. At significantly high current densities, the oxygen evolution reaction occurs in parallel with both above mentioned oxidation processes.

The Tafel method was used to determine the kinetic parameters characterizing the anodic process in the range of charge transfer control. The obtained slope (+0.123 V dec<sup>-1</sup>) is indicative for one-electron transfer process. Consequently, the resulting value of the anodic charge transfer coefficient is close to 0.5. It is noteworthy that the exchange current density has a quite high value, specific for fast electron transfer reactions.

Chronoamperometry curves confirmed that at advanced anodic polarization the oxidation of sulphite to sulphate is accompanied by oxygen evolution reaction. By integrating chronoamperometric curves at potentials where there is no oxygen release, chronocoulometric curves were obtained. Since the chronocoulometric curves, showing the dependence of the amount of transformed sulphite and the degree of transformation of sulphite to sulphate as a function of electrolysis time, are quasi-linear dependencies, it can be stated that the current efficiency for sulphite oxidation is close to 1. As a result, the formation rate of oxygenated functional groups on the graphite surface and of carbon dioxide evolution is reduced.

Different shapes of the electrochemical impedance spectra were obtained for the oxidation of low and high concentrations of sulphite, in accordance with the two different oxidation routes proposed, mediated oxidation and direct oxidation of sulphite.

**Acknowledgements:** This work was partially supported by the University Politehnica Timisoara within the frame of PhD studies.

## REFERENCES

- 1.D. Uzun, E. Razkazova-Velkova, V. Beschkov, *J. Appl. Electrochem.*, **46**, 943 (2016).
- 2.N. Dermendzhieva, E. Razkazova-Velkova, V. Beschkov, *Bulg. Chem. Comm.*, **49**, 793 (2015).
- 3.V. Beschkov, private communication.
- 4.T. Whaley, G. Long, Sulfur and Hydrogen Sulfide Recovery, in *Petroleum Technology*, Wiley Critical Content, 2007, p. 872.
- 5.T.M. Gur, R.A. Huggins, *J. Electrochem. Soc.*, **139**, L95 (1992).
- 6.M. Ihara, K. Matsuda, H. Sato, C. Yokoyama, *Solid State Ion.*, **175**, 51 (2004).

7. X. Cheng, L. Chen, C. Peng, Z. Chen, Y. Zhang, Q. Fanc, *J. Electrochem. Soc.*, **151**, 48 (2004).
8. J. Wang, G. Yin, Y. Shao, S. Zhang, Z. Wang, Y. Gao, *J. Power Sources*, **171**, 331 (2007).
9. C.H. Paik, G.S. Saloka, G.W. Graham, *Electrochem. Solid-State Lett.*, **10**, 39 (2007).
10. K.H. Lim, H-S. Oh, S-E. Jang, Y.-J. Ko, H-J. Kim, H. Kim, *J. Power Sources*, **193**, 575 (2009).
11. C.A. Reiser, L. Bregoli, T. W. Patterson, J. S. Yi, J. D. Yang, M.L. Perry, T. D. Jarvi, *Electrochem. Solid-State Lett.*, **8**, 273 (2005).
12. H.-S. Oh, J.-H. Lee, H. Kim, *Int. J. Hydrogen Energy*, **37**, 10844 (2012).
13. S. Maass, F. Finsterwalder, G. Frank, R. Hartmann, C. Merten, *J. Power Sources*, **176**, 444 (2008).
14. I. Radoi, C. Daminescu, G. Musca, Z. Popa, *Revista de Chimie*, **40**, 202 (1989).
15. A. L. Dicks, *J. Power Sources*, **156**, 128 (2006).
16. J. Lu, D. Dreisinger, W. Cooper, *J. App. Electrochem.* **29**, 1161 (1999).
17. A. Enache, N. Vaszilcsin, M. Dan, *Chem. Bull. Politehnica Univ. (Timisoara)* **61**, 12 (2016).
18. J. O'Brien, J. Hinkley, S. Donne, S-E. Lindquist, *Electrochim. Acta*, **55**, 573 (2010).
19. E. Skavas, T. Hemmingsen, *Int. J. Electrochem. Sci.* **2**, 203 (2007).
20. D. Santos, C.A.C. Sequeira, *Quim. Nova*, **36**, 1176 (2013).

\*

6, 300,223

15 2016 .; 28 2016 .

( )

(+0.123 V dec-1)

(0.118 V dec-1),

io (1.9 Am-2).

0,5.



## Modified glassy carbon electrode based on myoglobin and reduced graphene oxide for hydrogen peroxide detection

A. Szöke, G. Turdean\*, L. Muresan

*"Babe -Bolyai" University, Faculty of Chemistry and Chemical Engineering, Department of Chemical Engineering, Research Center for Electrochemistry and Non-conventional Materials, 11 Arany Janos St., RO-400028, Cluj-Napoca, Romania*

Received November 1, 2016      Revised March 6, 2016

In this work, a novel sensor (GC/Chit/rGO-Chit-Mb) for hydrogen peroxide ( $H_2O_2$ ) detection was developed, based on the immobilization of myoglobin (Mb) and reduced graphene oxide (rGO) on the surface of a glassy carbon electrode in a biopolymer matrix (Chitosan, Chit). The obtained device was characterized by cyclic voltammetry (CV), amperometry and electrochemical impedance spectroscopy (EIS). The Mb modified electrode showed excellent electrocatalytic activity for the reduction of  $H_2O_2$  in the concentration range up to 30  $\mu M$   $H_2O_2$  with a detection limit below 10  $\mu M$   $H_2O_2$  (by both CV and amperometry).

**Key words:** modified electrodes, myoglobin, reduced graphene oxide,  $H_2O_2$  detection.

### INTRODUCTION

Myoglobin (Mb) is a water-soluble single-chain protein of amino acids containing a heme (iron-containing porphyrin) group in the center, and having peroxidase-like activity, extensively used for investigating electron transfer [1]. In this regard, some problems resulted from the fact that direct electron transfer between Mb and bare solid electrode is usually very slow and the electrochemical behavior of the electrode is unstable [2, 3]. Consequently, many efforts have been made to improve the electrodes stability, as well as the electron transfer characteristics of Mb by using polymers, mediators, promoters, or other materials [4, 5].

In order to increase Mb-based electrodes stability, different matrices such as carboxymethyl cellulose (CMC) [6], polytyramine [7], Nafion [8], chitosan [9] etc. were used to immobilize Mb on pyrrolitic graphite, glassy carbon or gold. On the other hand, the electrochemical response of Mb was enhanced by introducing different conducting materials in these matrices such as gold [5] or silver nanoparticles [10], TiC nanoparticles [11], carbon nanotubes [8, 12], etc. In addition to conductivity, the nanomaterials exhibit high biocompatibility, adsorption ability and little harm to the biological activity of redox proteins.

In recent years, graphene, or its derivatives such as reduced graphene oxide (rGO) have been widely

used as modifying agents which, owing to their outstanding electronic properties and large surface area [13,14], could improve the analytical parameters of electrode materials. With its 2D sheet-like structure, graphene may act as a support for the molecular catalysts with large molecules such as Mb and other porphyrin species through cation- and  $\pi$ -interactions [15]. Besides, graphene derivatives have been proven to act as functional polymer reinforcements [16, 17].

Graphene-chitosan modified electrodes were successfully used for selective detection of dopamine [18, 19], nitrophenols [20], glucose [21], catechol, resorcinol and hydroquinone [22], etc. Chitosan is a conductive biopolymer derivative of chitin [23, 24] which can successfully play the role of an electrochemistry promoting polymeric binder as backbone.

In the present work, the preparation of a novel bi-layered composite electrode with large surface area, based on the glassy carbon (GC) modified by drop casting with reduced graphene oxide (rGO), myoglobin (Mb) and chitosan (Chit), GC/Chit/rGO-Chit-Mb, is reported. The intermediate Chit layer was added to improve the adhesion of the Mb containing active layer on glassy carbon and hence, the electrode stability. Detection of  $H_2O_2$  based on direct electrochemistry of myoglobin on different electrode materials such as gold deposited on ITO [25], nanopyramidal gold surface [26], silver nanoparticles decorated oxidized multi-walled carbon nanotubes [27], glassy carbon [28,29,30], has already been reported in the literature. To the best of our knowledge, however, the electrochemical behavior of a modified electrode

---

To whom all correspondence should be sent:  
E-mail: gturdean@chem.ubbcluj.ro

consisting from rGO, chitosan and myoglobin combination deposited on GC for  $\text{H}_2\text{O}_2$  detection has not been the subject of a detailed investigation.

The GC/Chit/rGO-Chit-Mb electrode was characterized by cyclic voltammetry and amperometry techniques. Electrochemical impedance spectroscopy was used to get deeper insight into the modification process of the GC surface. It was found that the bi-layered composite film could provide a favorable microenvironment for Mb to realize a direct electron transfer.

## EXPERIMENTAL

### Reagents

The reduced graphene oxide (rGO) was provided by Chengdu Organic Chemicals Co. Ltd., Chinese Academy of Sciences. As shown in Fig. 1, the TEM image of the reduced graphene oxide sheet (rGO) presents continuous structure with dimension of nanometers.



**Fig. 1.** TEM micrograph of 1 mg/mL rGO dispersion in ethanol.

Myoglobin (Mb) from horse skeletal muscle ( $M = 18800$  Da) was provided by Fluka. The  $\text{Na}_2\text{HPO}_4 \times 2 \text{H}_2\text{O}$ ,  $\text{NaH}_2\text{PO}_4 \times 12 \text{H}_2\text{O}$  and high viscosity chitosan from crab shells were provided by Sigma Aldrich (CAS9012-76-4). A 30%  $\text{H}_2\text{O}_2$  solution and glacial acetic acid were provided by Merck. All chemicals were of analytical grade and used without any purification step.

A 1 mg/mL dispersion of reduced graphene oxide (rGO) was obtained by mixing the appropriate quantity of powder for 30 minutes on a vortex mixer, followed by sonication (2 hours) and mixing (30 minutes) on a vortex mixer. Before every usage, the stored dispersion was further sonicated, and then mixed for 30 minutes. A 0.1 % chitosan solution was prepared by dissolving appropriate amount of powder in 0.1 M acetic acid solution. A 10 mg/mL myoglobin solution was prepared by dissolving myoglobin in distilled water. 0.1 M phosphate buffer solutions of various pH values were prepared by dissolving appropriate amounts of  $\text{Na}_2\text{HPO}_4$  and  $\text{NaH}_2\text{PO}_4$  in distilled

water and adjusting the pH values with 0.1 M  $\text{H}_3\text{PO}_4$  or NaOH solutions, respectively.

### Methods

Transmission electron microscopy (TEM) measurements were performed using a H7650 Hitachi TEM apparatus.

Electrochemical measurements were performed using a PGStat 12 computer controlled potentiostat (Autolab, The Netherlands). An undivided electrochemical cell containing the modified glassy carbon electrode (GC, 3 mm diameter) as the working electrode, a platinum wire as the counter and an Ag/AgCl/KCl<sub>sat</sub> as reference electrode, was connected to the potentiostat. All experiments were carried out at room temperature.

Impedance spectra were recorded in 0.5 M KCl containing 1 mM  $\text{K}_3[\text{Fe}(\text{CN})_6]$  solution at the open circuit potential (OCP). Impedance spectra were analyzed by fitting to equivalent electrical circuits using the ZView (Scribner Assoc.) software.

### Electrode preparation

The cleaning of glassy carbon electrodes (GC) surfaces consisted in polishing with 1200 abrasive paper and alumina powder (0.4  $\mu\text{m}$ ), followed by ultrasonication for 3 minutes. Between each step the electrode surface was rinsed with distilled water and the surface inspected *via* optical microscope.

The modified electrodes were prepared by drop casting technique as reported in a previous paper [19]. Thus, the GC/Chit/rGO-Chit-Mb electrodes were prepared by successive deposition of Chit (2  $\mu\text{L}$ ), and 10–18  $\mu\text{L}$  of a mixture containing rGO dispersion (5  $\mu\text{L}$ ), Chit solution (5  $\mu\text{L}$ ) and various amounts (0, 2, 4, 6, 8  $\mu\text{L}$ ) of 10 mg/ml myoglobin solution. Between each deposition step, the solvent was evaporated by air drying [19]. For electrochemical impedance spectroscopy studies, GC/rGO-Chit-Mb electrodes were prepared by deposition of 12–17  $\mu\text{L}$  from a mixture of Chit solution (7  $\mu\text{L}$ ), Mb solution (5  $\mu\text{L}$ ) and various amounts of rGO dispersion (0, 2.5, 5  $\mu\text{L}$ ) on the GC electrode surface. The solutions were deoxygenated by bubbling nitrogen prior to each experiment.

## RESULTS AND DISCUSSION

### 3. 1. Electrochemical characterization of GC/rGO-Mb/Chit modified electrodes

The direct electron-transfer behavior of Mb at GC/Chit/rGO-Chit-Mb modified electrodes was characterized by cyclic voltammetry (CV). As seen in Fig. 2A, a pair of well-defined peaks ( $I_q/I_c$ ) placed at -0.100 V and -0.350 V vs. Ag/AgCl,

$\text{KCl}_{\text{sat}}$ , respectively, was observed on the voltammograms recorded at the modified electrode. This pair of peaks was attributed to the redox process involving the protein heme Fe(III)/Fe(II) couple, described by the following equation:



The formal potential ( $E^0$ ) calculated as the arithmetic mean of the anodic and cathodic peak potentials was  $-0.225 \text{ V}$  and is typical for the active center of Mb Fe(III)/Fe(II) redox couple [31]. On the other side the value of the peak potential

separation ( $\Delta E_p$ ) of  $0.250 \text{ V}$  confirms the quasi-reversible behavior of the redox process occurring at GC/Chit/rGO-Chit-Mb modified electrode. Having a large surface-to-volume ratio [5] and providing a suitable pathway for protein to exchange electrons with the electrode surface, the biopolymer film of chitosan and the rGO structure constitute an appropriate environment for the immobilization of Mb.

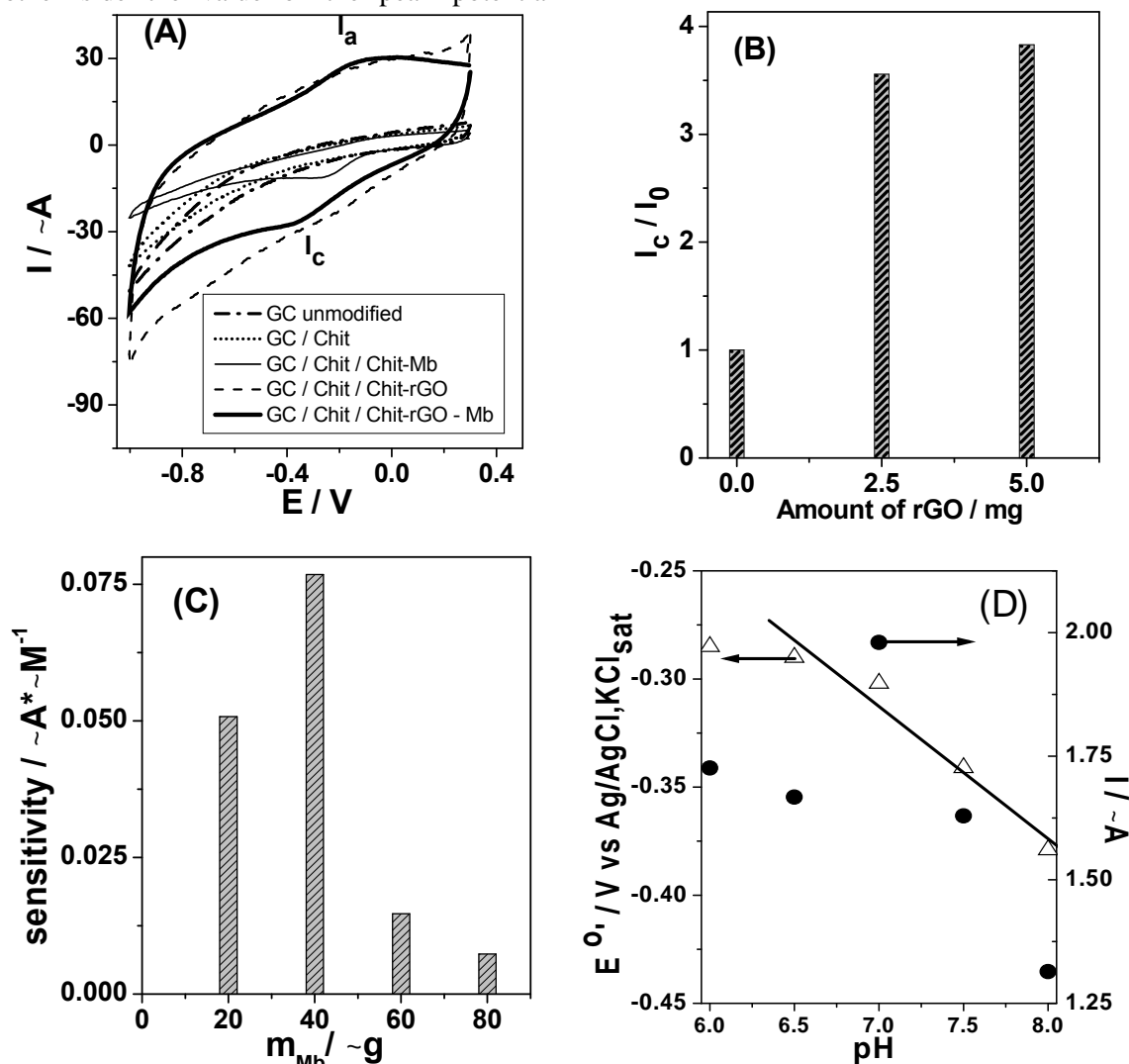


**Fig. 2.** Cyclic voltammograms of bare and GC/Chit/rGO-Chit-Mb modified electrodes (see legend) (A); influence of the rGO amount on the cathodic peak current intensity obtained for the detection of  $10 \mu\text{M H}_2\text{O}_2$  (B); influence of Mb amount on the sensitivity of the calibration curves of GC/Chit/rGO-Chit-Mb modified electrodes for  $\text{H}_2\text{O}_2$  detection (C); influence of the pH on the cathodic peak current and the formal potential (D). Experimental conditions: electrolyte,  $0.1 \text{ M}$  phosphate buffer (pH 7); starting potential  $+0.3 \text{ V}$  vs. Ag/AgCl,  $\text{KCl}_{\text{sat}}$ ; scan rate,  $0.050 \text{ V s}^{-1}$ .

For an immobilized redox species, the surface coverage can be estimated from the slope of the Laviron equation:  $I_p = n^2 F^2 A X \epsilon / (4RT)$ , where  $I_p$  is the peak current value in A,  $n$  is the number of electron transferred in the electrode reaction,  $F$  is Faraday constant,  $A$  is the effective surface area of

the modified electrode in  $\text{cm}^2$ ,  $X$  is the surface coverage of the immobilized Mb in  $\text{mol}/\text{cm}^2$ ,  $\epsilon$  is the scan rate in  $\text{V}/\text{s}$ ,  $R$  is the universal gas constant in  $\text{J}/(\text{mol K})$ , and  $T$  is the absolute temperature ( $298.15 \text{ K}$ ) [32, 33]. Thus, for the GC/Chit/rGO-Chit-Mb modified electrode in the scan rate range

from 0.01–0.1 V s<sup>-1</sup>, the average X value was calculated as 1.89 10<sup>-10</sup> mol/cm<sup>2</sup>. As expected for the present electrode architecture, the value of X is much larger than the reported for a monolayer coverage (1.58 10<sup>-11</sup> mol/cm<sup>2</sup> [34] or 1.89 10<sup>-11</sup> mol/cm<sup>2</sup> [35]). Ten times higher value of X suggests that: (i) a multilayer of Mb participated to the electron transfer pathway within the electrode matrix [36], or (ii) the rGO-Chitosan matrix provides a high surface area for Mb immobilization [37], allowing a proper orientation and homogenous distribution of the Mb active sites on the electrode surface [38].

#### *Influence of rGO amount*

Although the position of the peak potential for the GC/Chit/rGO-Chit-Mb electrode remains almost the same regardless the amount of rGO used for the preparation of the electrode material, the current intensity ratio has changed. As shown in Fig. 2B, the ratio of the cathodic peaks I<sub>c</sub>/I<sub>0</sub> (where I<sub>0</sub> is the current peak in the absence of rGO from the electrode matrix) shows an increase of 3.5–4 times in the presence of rGO, reaching a quasi-stable value at 2.5–5 µg of rGO. Consequently, a value of 5 µg of rGO was considered sufficient and appropriate for modifying the electrode surface.

#### *Influence of Mb amount*

The influence of the Mb amount on the analytical performances of the modified electrodes was expressed by means of the electrode sensitivity, calculated as the slope of the linear domain of the calibration curve for H<sub>2</sub>O<sub>2</sub> detection obtained by cyclic voltammetry. As seen in Fig. 2C, the electrode sensitivity shows a polynomial dependence on the amount of Mb immobilized on the electrode surface having a maximum value for 40 µg Mb.

#### *pH influence*

The redox behavior of Mb is significantly dependent on the pH of solution, because the microstructure of protein undergoes conformational changes. Therefore, the influence of the pH of 0.1 M phosphate buffer solution on the cyclic

voltammetric behavior of GC/Chit/rGO-Chit-Mb modified electrode was investigated in the pH range from 6.0 to 8.0. As shown in Fig 2D, the linear dependence of the formal potential (E<sup>0'</sup>) of the immobilized Mb has a negative slope with the increase of the electrolyte pH. The slope value obtained from the linear fitted equation, E<sup>0'</sup>/V = -(0.061 ± 0.009)pH + (0.116 ± 0.066) (n = 4, R= 0.9785), is found to be close to the theoretical value of 0.059 V/pH at 25<sup>o</sup> C for a reversible 1e<sup>-</sup> transfer. Also, this slope value could indicate that each electron transfer from the Mb to the electrode is accompanied by 1 H<sup>+</sup>, according to the modified equation (1a):



This behavior has usually been explained in the literature either by the influence of protonation states of the trans-ligands to the Heme iron and the amino acids around the Heme, or by protonation of the water molecule coordinated to the central iron [4]. As shown in Fig. 2D, the cathodic peak current intensities have a non-linear dependency on the pH with a maximum value observed at pH 7.0 that was selected as the working pH in further investigations.

#### *Influence of the scan rate*

The influence of the potential scan rate (v) on the voltammetric responses of GC/Chit/rGO-Chit-Mb modified electrode is presented in Fig. 3, where the pair of well-defined redox peaks with almost equal anodic/cathodic peak current intensities can be observed. The redox peak currents increased linearly with the scan rates from 0.01 to 0.25 V s<sup>-1</sup> (results not shown). The values of the slopes, calculated by linear regression of the log I - log v dependencies, were found to be 0.678 and 0.715, respectively (Table 1), indicating a typical thin-layer surface-controlled electrochemical response of the Mb immobilized on the electrode surface [5,40]. Increase of the potential scan rate leads to the shifting of the voltammograms and to a gradual enlargement of the peak-to-peak separation (E<sub>p</sub>), confirming the existence of a quasi-reversible electrode process.

**Table 1.** Parameters of the log-log linear regression corresponding to the peak current - potential scan rate dependence at the GCE/Chit/rGO-Chit-Mb modified electrode. Experimental conditions as in Fig. 3.

Electrode	Slope of the log I <sub>p</sub> – log v dependence			
	reduction	R <sup>2</sup> /n	oxidation	R <sup>2</sup> /n
GCE/Chit/Mb/Chit/rGO	0.715 ± 0.065	0.9602/11	0.678 ± 0.032	0.9891/11

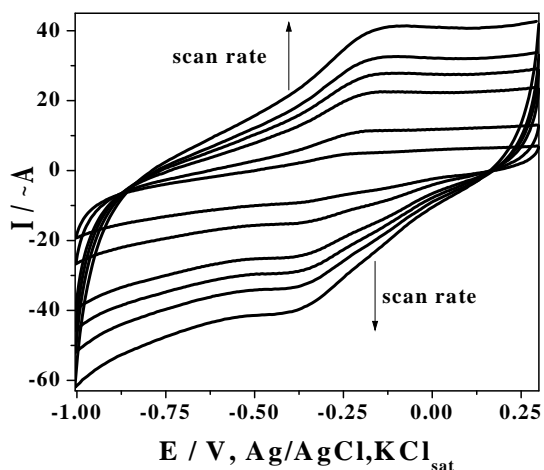


**Fig. 3.** Influence of the scan rate (0.010 – 0.080 V s<sup>-1</sup>) on cyclic voltammograms of the GC/Chit/rGO-Chit-Mb modified electrode. Experimental conditions: electrolyte, 0.1 M phosphate buffer (pH 7); starting potential +0.3 V vs. Ag/AgCl, KCl<sub>sat</sub>.

#### Short time stability

The short time stability of the electrochemical response of the GC/Chit/rGO-Chit-Mb modified electrode was very good. The continuous scanning in a potential window of 1.3 V (from +0.3 V to -1 V) did not affect significantly the cyclic voltammetric signals. As shown in Fig. 4, the time dependencies of anodic and cathodic peak currents follow the first order kinetic in either absence or presence of H<sub>2</sub>O<sub>2</sub>, proving a good stability of the modified electrode (deactivation constants are between 3.05 × 10<sup>-11</sup> and 4.5 × 10<sup>-11</sup> s<sup>-1</sup>).

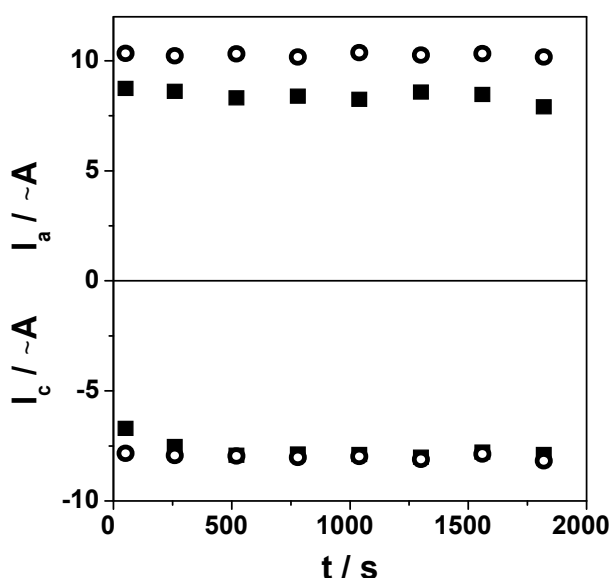


**Fig. 4.** I<sub>c</sub> and I<sub>a</sub> versus time dependencies of the GC/Chit/rGO-Chit-Mb modified electrode recorded by CV before (■) and after addition of 40 μM H<sub>2</sub>O<sub>2</sub> (○). Experimental conditions: electrolyte, 0.1 M phosphate buffer (pH 7); starting potential +0.3 V vs. Ag/AgCl, KCl<sub>sat</sub>; scan rate, 0.050 V s<sup>-1</sup>.

#### EIS measurements

In order to better understand the role of every component of the modifier layer and to get more information regarding the modified GC surface, electrochemical impedance spectroscopy (EIS) was applied. Impedance spectra of GC, GC/Chit-Mb and GC/rGO-Chit-Mb electrodes, measured at the open-circuit potential in 0.5 M KCl containing 1mM K<sub>3</sub>[Fe(CN)<sub>6</sub>] solution, are presented as Nyquist plots (Z'' vs. Z') in Fig. 5.

Usually, the Nyquist representations of EIS spectra for redox reactions include a semicircle portion at higher frequencies, corresponding to the electron transfer limited process and a linear portion at lower frequencies, corresponding to the diffusion process. The diameter of the semicircle part recorded at higher frequencies is equal to the electron transfer resistance (R<sub>ct</sub>) at the electrode interface, which controls the electron transfer kinetics of the redox probe at the electrode interface [39].

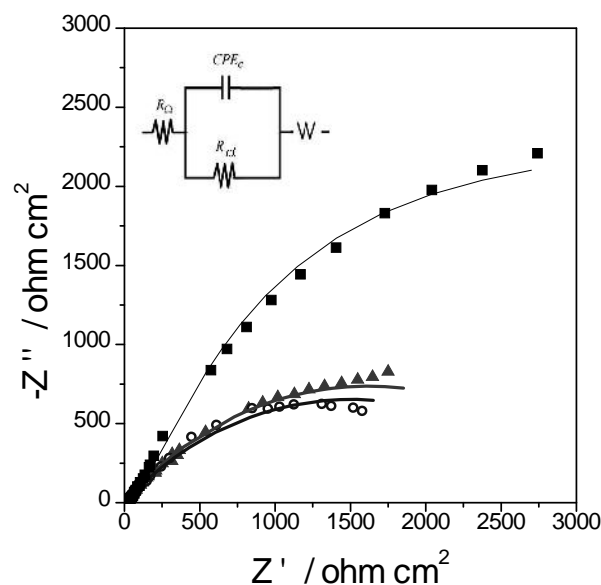


**Fig. 5.** Nyquist plots for different types of modified electrodes: GCE (■), GCE/Chit-Mb (○), GCE/rGO-Chit-Mb (△) at open-circuit potential value. Experimental conditions: electrolyte, 1 mM K<sub>3</sub>[Fe(CN)<sub>6</sub>] solution containing 0.5 M KCl; frequency range, 10<sup>-2</sup> - 10<sup>5</sup> Hz; perturbation amplitude, 5 mV. Inset: schemes of the equivalent circuits used for fitting the experimental data.

In our case, two equivalent circuits, R(QR<sub>ct</sub>) and R(CR<sub>ct</sub>)W (insets in Fig. 5), including electrolyte resistance (R), constant phase element for double-layer capacitance (Q), active charge transfer resistance (R<sub>ct</sub>), and Warburg impedance (W) were used to fit impedance data of GC/Chit-Mb and GC/rGO-Chit-Mb electrodes and GC electrode, respectively.

Using the above-mentioned equivalent circuits, the values of  $R_{ct}$  for the bare GC, GC/Chit-Mb and GC/rGO-Chit-Mb modified electrodes were estimated. The lowest value was noticed for the GC and higher for the two modified electrodes, suggesting that as expected, the chitosan layer hinders the charge transfer of the redox probe  $[\text{Fe}(\text{CN})_6]^{3-/4-}$  at the electrode surface. The capacitance values increased somewhat by addition of rGO (GC/Chit-Mb ( $316.2 \mu\text{F}/\text{cm}^2$ ) < GC/Chit/Chit-rGO-Mb ( $386.8 \mu\text{F}/\text{cm}^2$ )), which is probably due to an increase in the electroactive area of the electrode. The complex architecture of the electrode matrix, containing chitosan and 2D porous structure of rGO provide the expected largely exposed surface area with high activity, which permits the electron transfer from the redox probe  $[\text{Fe}(\text{CN})_6]^{3-/4-}$  to reach the electrode surface [5,39,40]. As expected, the impedance spectra demonstrate that both resistivity and electrode surface structure changed with the modification of the GC surface.

### 3.2. Electrocatalytic effect

The electrocatalytic activity of GC/Chit/rGO-Chit-Mb modified electrode towards  $\text{H}_2\text{O}_2$  was studied by cyclic voltammetry and illustrated in Fig. 6A. When increasing concentrations of  $\text{H}_2\text{O}_2$  were added to the buffer solution, the following typical phenomena, characteristic for electrocatalysis, were observed: (i) shifting and in this case splitting of the Mb peak into two peaks ( $I_c$ ,  $II_c$ ) placed at  $-0.340 \text{ V}$  and  $-0.15 \text{ V}$  vs.  $\text{Ag}/\text{AgCl}$ ,  $\text{KCl}_{\text{sat}}$  respectively and (ii) increase of the  $II_c$  peak current intensity accompanied by simultaneous decrease of the oxidation peak ( $I_a$ ).

Two reduction peaks are attributed to the peroxidase-like electrocatalytic reactions which can be involved in the reduction of Mb Heme Fe(III) to Heme Mb Fe(II), and the reduction of  $\text{H}_2\text{O}_2$  at the Mb modified electrode, according to the following equations [41,42]:

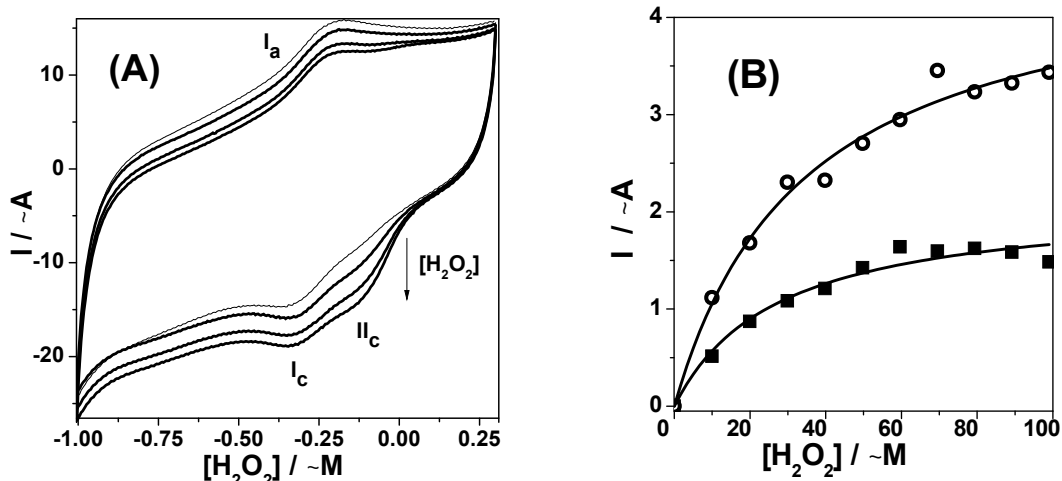
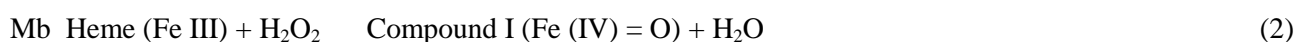


**Fig. 6.** Cyclic voltammograms of GC/Chit/rGO-Chit-Mb modified electrodes before (thin black line) and after addition of various (30, 40, 50  $\mu\text{M}$ )  $\text{H}_2\text{O}_2$  concentrations (thick black lines) (A); calibration curves for  $\text{H}_2\text{O}_2$  electroreduction at GC/Chit/Chit-Mb ( $\blacksquare$ ) and GC/Chit/rGO-Chit-Mb ( $\bullet$ ) modified electrodes (B). Experimental conditions: electrolyte 0.1 M phosphate buffer (pH 7); starting potential  $+0.3 \text{ V}$  vs.  $\text{Ag}/\text{AgCl}$ ,  $\text{KCl}_{\text{sat}}$ ; scan rate  $0.050 \text{ V s}^{-1}$ .

**Table 2.** Analytical parameters of the calibration curves for  $\text{H}_2\text{O}_2$  electroreduction at the GCE/Chit/rGO-Chit-Mb modified electrode.

Amount of rGO [ $\mu\text{g}$ ]	Sensitivity [ $\mu\text{A} / \mu\text{M}$ ]	Limit of detection [ $\mu\text{M}$ ]	Linear domain [ $\mu\text{M}$ ]	R/n
0	$0.076 \pm 0.009$	<b>8.83</b>	10....30	0.9830 / 4
5	$0.152 \pm 0.016$	<b>7.91</b>		0.9863 / 4



A good linear relationship between the current intensity of the reduction peak  $II_c$  and  $H_2O_2$  concentration was obtained in the range 10–30  $\mu M$ , with a sensitivity between 0.076 and 0.152  $\mu A/\mu M$  in the absence and presence of rGO in the modifying matrix of the electrode, respectively (Fig. 6B, Table 2). The detection limit calculated for a signal/noise ratio of 3 was in both cases below 10  $\mu M H_2O_2$ .

When the  $H_2O_2$  concentration was up to 30  $\mu M$ , the current intensity of peak  $II_c$  leveled off, reaching a saturation value and indicating a Michaelis-Menten kinetic for the electrocatalytic reaction of  $H_2O_2$ . The apparent Michaelis-Menten constant ( $K_{M,app}$ ) calculated using Origin 6.5 software fitting facility, was equal to 27.2  $\mu M$  for GC/Chit/Chit-Mb and to 34.2  $\mu M$  for GC/Chit/rGO-Chit-Mb electrodes, respectively. The obtained values for  $K_{M,app}$  are smaller or similar to those reported in the literature [5,36,39], proving that the Mb shows affinity for the studied substrate ( $H_2O_2$ ).

In order to quantitatively investigate the catalytic properties of GC/Chit/rGO-Chit-Mb modified electrodes,  $I$  vs. time dependencies were recorded by amperometry at applied potential of  $-0.3 V$  vs. Ag/AgCl,  $KCl_{sat}$  for successive additions of 5  $\mu M H_2O_2$  solution. The reduction current reaches a stable 95% of steady-state value within 100 s after each addition of  $H_2O_2$ , suggesting that sufficiently fast electrocatalytic response was achieved. The analytical parameters of the GC/Chit/rGO-Chit-Mb modified electrode extracted from the amperometric linear calibration curve presented in Fig. 7 were: sensitivity of  $0.047 \pm 0.003 \mu A/\mu M$ , linear range of 5–30  $\mu M$  and detection limit of 4.99  $\mu M H_2O_2$  ( $R = 0.9929$ ).

Thus, the detection limit recorded at GC/Chit/rGO-Chit-Mb modified electrode is in agreement with other values reported for similar electrode architectures for signal/noise ratio = 3 (i.e.: 1.02  $\mu M H_2O_2$  at Chit-MWNTs/Mb/AgNPs/GCE [36]; 1.5  $\mu M$  at Mb/SGO/Nafion electrode [39]; 6  $\mu M H_2O_2$  at Nafion/Mb/MWCNTs/CILE [40]; 40  $\mu M H_2O_2$  at Mb-DTAB/Ceramic carbon electrode [32]). Even if the analytical parameters of the GC/Chit/rGO-Chit-Mb modified electrode are not high enough, the periodical scanning of the potential did not affect the electrochemical signal (see Fig 4), so that the compromise between the analytical parameters values and the stability of the electrochemical response of the GC/Chit/rGO-Chit-Mb modified electrode can be considered acceptable.

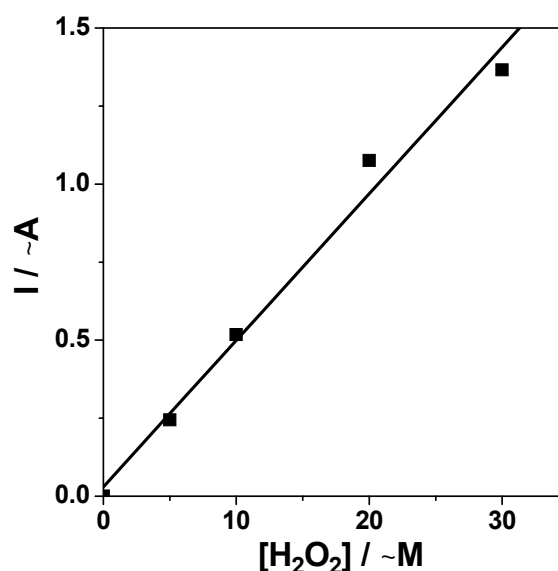


Fig. 7. Linear domain of the amperometric calibration curve for  $H_2O_2$  electroreduction at GCE/rGO-Chit-Mb modified electrodes. Experimental conditions: electrolyte, 0.1 M phosphate buffer (pH 7); potential  $-0.3 V$  vs. Ag/AgCl,  $KCl_{sat}$ ; rotation speed, 250 rpm.

## CONCLUSIONS

Chitosan and rGO can act as an effective support matrix for Mb immobilization in view to prepare a novel GC/Chit/rGO-Chit-Mb modified electrode by drop-casting method. Direct electrochemistry of the immobilized Mb on the modified electrode was carefully investigated by cyclic voltammetry, amperometry and electrochemical impedance spectroscopy. The experimental results showed that the immobilized Mb displayed good enzyme-like catalytic activity for the reduction of  $H_2O_2$ , characterized by good analytical and kinetic parameters.

These results suggest that the modified matrix of the studied electrodes appears to be a promising material for fabricating electrochemical sensors based on the direct electrochemistry of a redox protein.

**Acknowledgements.** The authors thank Dr. Katona Gabriel for the TEM measurements.

## REFERENCES

1. C. U. Carlsen, I. M. Skovgaard, L. H. Skibsted, *J. Agric. Food Chem.*, **51**, 5815 (2003).
2. H. Huang, N. F. Hu, Y. H. Zeng, G. Zhou, *Anal. Biochem.*, **308**, 141 (2002).
3. K. Chattopadhyay, S. Mazumdar, *Bioelectrochem.*, **53**, 17 (2000).
4. C. Ruan, T. Li, Q. Niu, M. Lu, J. Lou, W. Gao, W. Sun, *Electrochim. Acta*, **64**, 183 (2012).
5. F. Shi, J. Xi, F. Hou, L. Han, G. Li, S. Gong, C. Chen, W. Sun, *Mater. Sci. Eng. C*, **58**, 450 (2016).

6. H. Huang, P. He, N. Hu, Y. Zeng, *Bioelectrochem.*, **61**, 29 (2003).
7. A. T. Ezhil Vilian, V. Veeramani, S.-M. Chen, R. Madhu, C. H. Kwak, Y. S. Huh, Y.-K. Han, *Sci. Rep.*, **5**, 18390 (2015), doi:10.1038/srep18390.
8. E. Canbay, B. ahin, M. Kiran, E. Akyilmaz, *Bioelectrochem.*, **101**, 126, (2015).
9. L.-S. Duan, Q. Xu, F. Xie, S.-F. Wang, *Int. J. Electrochem. Sci.*, **3**, 118 (2008).
10. S. Palanisamy, C. Karuppiyah, S.-M. Chen, R. Emmanuel, P. Muthukrishnan, P. Prakash, *Sens. Actuat. B*, **202**, 177 (2014).
11. M. Wang, Q. Sheng, D. Zhang, Y. He, J. Zheng, *Bioelectrochem.*, **86**, 46 (2012).
12. G. L. Turdean, G. Szabo, *Food Chem.*, **179**, 325 (2015).
13. V. B. Mohan, R. Brown, K. Jayaraman, D. Bhattacharyya, *Mater. Sci. Eng. B*, **193**, 49 (2015).
14. M. Cui, B. Xu, C. G. Hu, H. B. Shao, L. Y. Qu, *Electrochim. Acta*, **98**, 48 (2013).
15. T. Xue, S. Jiang, Y. Qu, Q. Q. Su, R. Cheng, S. Dubin, Ch-Y. Chiu, R. Kaner, Y. Huang, X. Duan, *Angewandte Chem. Int. Ed.*, **51**, 3822 (2012).
16. G. Mittal, V. Dhand, K. Y. Rhee, S.-J. Park, W. R. Lee, *J. Ind. Eng. Chem.*, **21**, 11 (2015).
17. K. Hu, D. D. Kulkarni, I. Choi, V. V. Tsukruk, *Prog. Poly. Sci.*, **39**, 1934 (2014).
18. Y. Wang, Y. Li, L. Tang, J. Lu, J. Li, *Electrochem. Commun.*, **11**, 889 (2009).
19. Á. F. Szöke, G. L. Turdean, G. Katona, L. M. Muresan, *Stud. UBB Chem.*, **61(3)**, 135 (2016).
20. J. Tang, L. Zhang, G. Han, Y. Liu, W. Tang, *J. Electrochem. Soc.*, **162(10)**, B269 (2015).
21. X. Kang, J. Wang, H. Wu, I. A. Aksay, J. Liu, Y. Lin, *Biosens. Bioelectron.*, **25(4)**, 901 (2009).
22. H. Yin, Q. Zhang, Y. Zhou, Q. Ma, T. Liu, L. Zhu, S. Ai, *Electrochim. Acta*, **56**, 2748 (2011).
23. J. B. Marroquin, K.Y. Rhee, S.J. Park, *Carbohydrate Polymers*, **92 (2)**, 1783 (2013).
24. M. Rinaudo, *Prog. Poly. Sci.*, **31(7)**, 603 (2006).
25. Dengale S. M., Yagati A. K., Chung Y. H., Min J., Choi J. W., *J. Nanosci. Nanotechnol.*, **13**, 6424 (2013).
26. P. Xia, H. Liu, Y. Tian, *Biosens. Bioelectron.*, **24**, 2470 (2009).
27. B. Liu, M. Wang, *J. Electrochem. Sci.*, **8**, 9801 (2013).
28. A. Safavi, F. Farjami, *Anal. Biochem.*, **402**, 20 (2010).
29. L.-S. Duan, Q. Xu, F. Xie, S.-F. Wang, *Int. J. Electrochem. Sci.*, **3**, 118 (2008).
30. A. Babaei, A. R. Taheri, *Anal. Bioanal. Electrochem.*, **4**, 342, (2012).
31. Y. Z. Zhou, H. Wang, S. Y. Dong, A. X. Tian, Z. X. He, B. Chen, *Chin. Chem. Lett.*, **22**, 465 (2011).
32. E. Laviron, *J. Electroanal. Chem.*, **101**, 19 (1979).
33. A. J. Bard, L. R. Faulkner, *Electrochemical Methods: Fundamentals and applications*, Wiley, New York, 2001.
34. S. F. Wang, T. Chen, Z. L. Zhang, X. C. Shen, Z. X. Lu, D. W. Pang, K. Y. Wong, *Langmuir*, **21(20)**, 9260 (2005).
35. S. F. Wang, T. Chen, Z. L. Zhang, D. W. Pang, K. Y. Wong, *Electrochem. Commun.*, **9**, 1709 (2007).
36. Y. Li, Y. Li, Y. Yang, *Bioelectrochem.*, **82**, 112 (2011).
37. S. Pakapongpan, R. Palangsuntikul, W. Surareungchai, *Electrochim. Acta*, **56**, 6831 (2011).
38. S. Ray, S. Chand, Y. Zhang, S. Nussbaum, K. Rajeshwar, R. Perera, *Electrochim. Acta*, **99**, 85 (2013).
39. G. Chen, H. Sun, S. Hou, *Anal. Biochem.*, **502**, 43 (2016).
40. W. Sun, X. Li, Y. Wang, X. Li, C. Zhao, K. Jiao, *Bioelectrochem.*, **75**, 170 (2009).
41. Y. Zhang, Z. Xia, H. Liu, M. Yang, L. Lin, Q. Li, *Sens. Actuat. B*, **188**, 496 (2013).
42. G. L. Turdean, *Studia UBB Chem.*, **60(3)**, 119 (2015).

-

\* , .

“ , . A 11, RO-400028,

1 2016 .; 6 2017 .

( )

(GC / Chit / RGO-Chit-Mb) ( 2 2 )

(Mb) (RGO)

(Chitosan, Chit).

(CV),

(EIS). (Mb)

2 2 2 2 30 μM 10μM 2 2 ( CV

).



## Application of the differential impedance analysis on the microbiologically induced corrosion of bronze

R. Spotorno\*, G. Ghiara

Department of Chemistry and Industrial Chemistry, University of Genoa, Via Dodecaneso 31, I-16146 Genoa, Italy

Received December 8, 2016    Revised March 6, 2017

In this work, the behavior of a binary Cu-Sn (12wt% Sn) alloy has been studied in presence and absence of bacteria in aqueous solution simulating stagnant fresh water. The corrosion processes have been investigated using the Electrochemical Impedance spectroscopy (EIS) technique. The application of the Differential Impedance Analysis (DIA) allowed identifying three processes attributed to the electrical double layer, electrical properties of the passive film and mass transfer processes at the metal/solution interface. Based on DIA structural analysis, equivalent circuit model was proposed and used for better parametric identification of the impedance data. The formation of a biofilm strongly influenced the passive layer behavior, promoting localized corrosion. Post-experiment characterization performed by Scanning electron microscopy (SEM) supported the electrochemical characterization.

**Key words:** microbiologically induced corrosion, tin-bronze alloys, electrochemical impedance spectroscopy, differential impedance analysis

### INTRODUCTION

Microbiologically Induced Corrosion (MIC) is a phenomenon often considered when non-defined morphologies occur on metallic surfaces. It is linked to microbial activity interacting with the substrate. Bacteria promote the formation of a biofilm which influences the corrosion processes by selective introduction or removal of chemical species at the interface with the metal [1-4].

When MIC occurs an increase of the corrosion potential, associated to biofilm growth, is usually observed. The presence of the biofilm induces local reactions shifting the corrosion potential to a more noble state, therefore increasing the risk of pitting corrosion [4,5]. MIC processes have widely been studied for stainless steel in several environments as a result of interests linked to some applications, focusing on the prevention of failures under operating conditions [6]. Several studies can also be found for copper alloys, when applied as structural or mechanical parts operating in aqueous solutions where they are subject to bacteria colonization [7,8]. Despite the fact that copper is often used as biocide, several types of bacteria are able to become tolerant toward ions and survive in adverse conditions [9,10]. Aerobic bacteria commonly present in fresh water as *Pseudomonas sp.* are known to have a role in copper alloys corrosion [11,12]. They cause the acceleration of the

corrosion processes mainly producing a biofilm capable of creating concentration cells replacing oxygen with CO<sub>2</sub> and acting as chelating agent [12-14]. Among classical electrochemical techniques suitable for the study and evaluation of MIC, electrochemical impedance spectroscopy (EIS) is one of the most powerful tools for monitoring and understanding the corrosion processes. EIS allows obtaining more information related to the system under investigation such as the polarization resistance contributions ( $R_p$ ) that can be used for the calculation of the corrosion rate [1]. The resistive and capacitive contributions related to the processes taking place in the system can also be deconvoluted, however, this operation requires additional and more complicated data analyses. In the classical deconvolution approach, an equivalent circuit model is hypothesized, based on preliminary knowledge of the system under investigation and the recorded spectrum. Then it is parametrically identified by Complex Non-linear Regression Least Squares (CNRLS) fitting procedure [15-18]. Thus the contribution of the model components is evaluated. EIS measurements at different experimental conditions can be additionally acquired in order to evaluate better the influence on the individual contributions and thus to refine the equivalent circuit model. Structural identification is an alternative approach which is very convenient for systems where little or no knowledge is available. This approach consists in the generalized deconvolution of the impedance data using mathematical techniques which do not need *a priori* chosen assumptions.

---

To whom all correspondence should be sent:  
E-mail: roberto.spotorno@edu.unige.it

The Differential Impedance Analysis (DIA) is a technique that applies the structural identification approach [19-22]. It ensures both structural and parametric identification based on the experimental data and thus eliminates the necessity of preliminary working hypothesis. The method applies a local estimator – local operating model (LOM) which is used for the performance of a local parametric analysis by scanning along the analytical coordinate frequency. The LOM describes a simple first order inertial system extended with an additive term [21,22]. The simplest electrical equivalent of its transfer function is a mesh of resistance  $R$  and capacitance  $C$  in parallel, extended with additive term  $Ad$  connected in series, which for electrochemical systems can be additive resistance, most often the resistance of the electrolyte  $R_s$ . The effective time constant  $T = RC$  is also introduced as parameter. The parametric identification of the LOM applies a scanning identification window of one frequency point which makes the use of statistical approach impossible. Thus it is replaced with a deterministic one by extension of the initial set of data (real  $Z'$ , imaginary  $Z''$  components of the impedance and frequency ) with two additional terms – the derivatives of  $Z'$  and  $Z''$  in respect to the frequency. Thus the LOM parameters estimates are determined for every frequency. They form a new experimental set of data (  $i_s, \hat{R}_s, \hat{C}_s, \hat{T}_s, \hat{R}_s$  ). The frequency analysis of the LOM parameters estimates  $\hat{P}_{LOM}$  known as Temporal analysis provides for structural and parametric identification. It identifies the number of time constants (steps) involved in the total process, their distribution, and easily defines the rate limiting ones. In the frequency range where the LOM corresponds to the object's behaviour, the temporal plots exhibit plateaux. Their number corresponds to the number of time constants [21,22]. The temporal analysis can qualitatively estimate frequency distribution which is marked as deviation from the plateau-behavior. However, for quantitative analysis, i.e. for structural and parametric identification, a new algorithm, named Secondary DIA, should be used [21, 22]. In this study only DIA is applied. For more precise parametric evaluation CNRLS is performed based on the results obtained by DIA.

The aim of this study is to define the influence of *Pseudomonas sp.* on the corrosion processes of tin-bronzes and their ability to promote localized phenomena applying electrochemical impedance spectroscopy and DIA, supported by post-experimental observations. The experiments were performed on a binary Cu-Sn (12%wt) alloy in

artificial fresh water containing mixed chlorides, nitrates, sulphates and carbonates, in presence and absence of bacteria.

## MATERIALS AND METHODS

A commercial tin-bronze (12 wt % Sn) alloy was chosen for the corrosion experiments in presence and absence of bacteria. Samples were cut from a sheet in pieces of 1 cm x 1 cm x 0.5 cm and additionally treated in order to obtain a suitable microstructure. Recrystallization was promoted by application of a thermo-mechanical treatment combining cold hammering which creates superficial and bulk defects with heating up to 600°C for 12h. Such treatment was performed twice to ensure homogeneity of the solid solution, avoiding the presence of secondary phases. Figure 1 shows the microstructure of the samples prepared for the corrosion testing. They were embedded in epoxy resin leaving an exposed surface of 1 cm<sup>2</sup>. The samples were immersed in the artificial fresh water solution (AFW) with pH 8.1 containing MgSO<sub>4</sub>\*7H<sub>2</sub>O (100 mg L<sup>-1</sup>); MgCl<sub>2</sub>\*6H<sub>2</sub>O (135 mg L<sup>-1</sup>); NaHCO<sub>3</sub> (185 mg L<sup>-1</sup>); Na<sub>2</sub>CO<sub>3</sub> (230 mg L<sup>-1</sup>); KNO<sub>3</sub> (20 mg L<sup>-1</sup>) [21]. The solution conductivity was 1020±80 μS cm<sup>-1</sup>. For tests in the presence of bacteria (BAFW), a *Pseudomonas Fluorescens N3* strain [23, 24] was added to the AFW with a concentration of 1x10<sup>7</sup> CFU mL<sup>-1</sup> (colony forming unit mL<sup>-1</sup>).

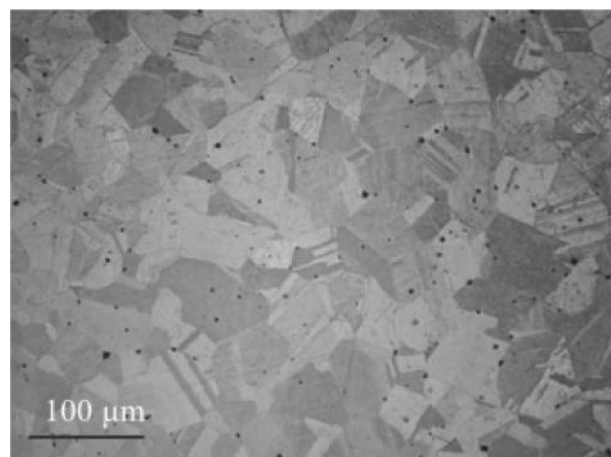


**Fig. 1.** Micrograph of certified material (12 wt% Sn) after thermo-mechanical treatment, 100x, etched with Fe<sub>3</sub>Cl.

The EIS analysis was performed using a three electrode cell with the sample as working electrode (WE), a reference electrode (RE) of Ag/AgCl sat. KCl and a platinum wire as counter electrode (CE) in a volume of 0.3 L in static conditions. The measurements were carried out at the first stabilization of the open circuit potential (OCP) after the immersion of the sample in the solution,

in the frequency range 40kHz-10mHz with an amplitude of the a.c. signal 20mV, using Ivium CompactStat (Ivium Technologies). Structural analysis of the impedance data was carried out applying the DIA technique [21,22]. Based on the DIA, a more precise parametric identification was performed by CNRLS using the software Zview (Schriber Associates Inc.). Post-experiment characterization was carried out by Scanning Electron Microscopy (SEM; Zeiss Evo40, Carl Zeiss, Oberkochen, Germany). Chemical analyses of the surface layers were performed by energy-dispersion x-ray spectroscopy (EDS; Cambridge INCA 300 with PentaFET EDXS detector; Oxford Instruments, Oxfordshire; U.K.) connected to the SEM.

## RESULTS AND DISCUSSION

The recorded impedance spectra are characterized with two arcs (Fig. 2) - a large and incomplete one at low frequencies and a small one at high frequencies. The low frequency arc can be associated to slower processes as mass transfer phenomena which are linked to the dissolution of the metal and the formation of a passive layer on the metal surface [25]. The addition of bacteria to the solution causes a decrease of this arc which indicates increase of the corrosion rate provoked by the microbial activity. The high frequency semicircle corresponds to fast phenomena

which can be attributed to the charge transfer processes [26]. This part of the spectrum is not significantly influenced by the presence of *Pseudomonas* in the solution.

However, a disturbance of the signal at high frequencies limited the measurement, making difficult the identification of its intercept with the real part axis which determines the ohmic resistance.

The performance of the DIA Temporal analysis (Figure 3) shows comparable in shape parametric profiles corresponding to the two impedance spectra. Following the procedure for spectral transformation [20-22], the temporal plots in Fig. 3 are represented in a spectral form (Fig. 4). The intensity of the spectral lines is proportional to the frequency length in which the corresponding parameter's estimate has similar values. Thus every plateau from the Temporal plot is transformed in a spectral peak. The smaller the frequency dispersion, the sharper the spectral maximum.

The temporal plots presented in Fig. 3 can be divided in 3 segments (Fig. 3 - Segments I-III) with different frequency dependence which indicates 3 different steps. The high frequency contribution (segment I) has a plateau-type behavior, thus recognising a process described with a time-constant, which corresponds to the charge transfer. The spectral presentation illustrates in an explicit form the *R*, *C* and *T* spectral peaks.

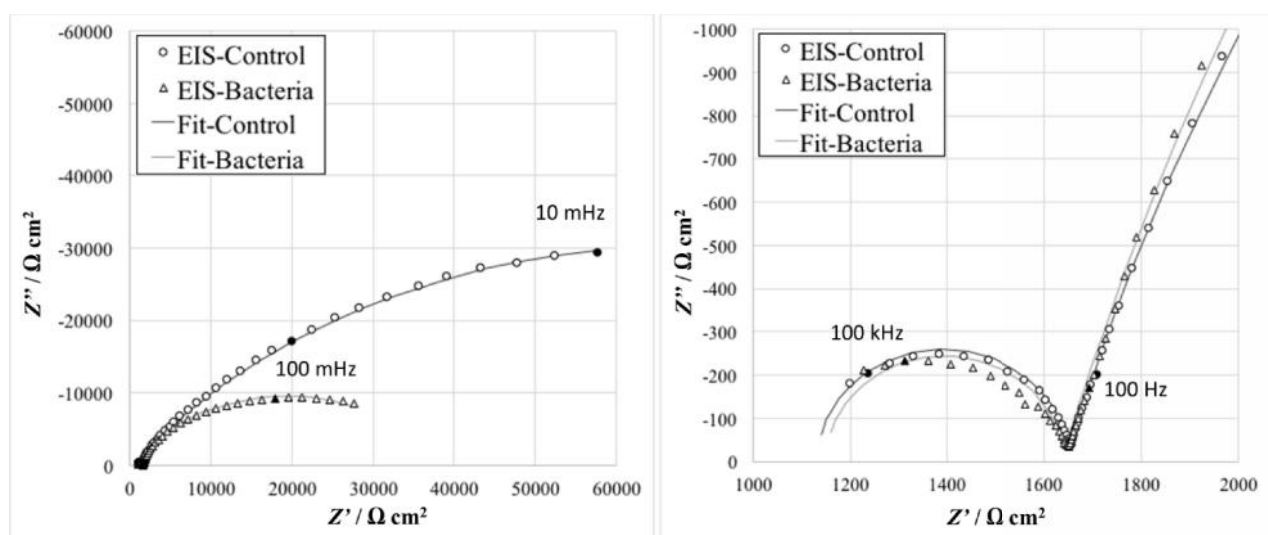


**Fig. 2.** Impedance spectra and fitting results of the two samples in the whole frequency range (left); zoomed high frequency range (right).

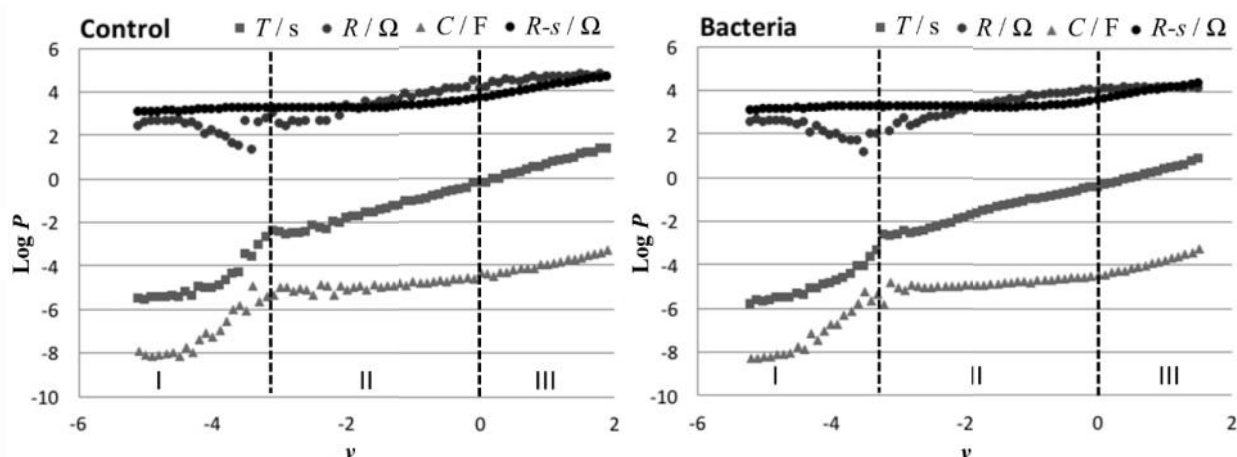


**Fig. 3.** DIA temporal plots of the control sample (left) and the sample with bacteria (right).  $P$  represents the value of the respective effective parameter ( $T, R, C, R_s$ ) and  $\epsilon|| = \lg(\cdot^{-1})$ .

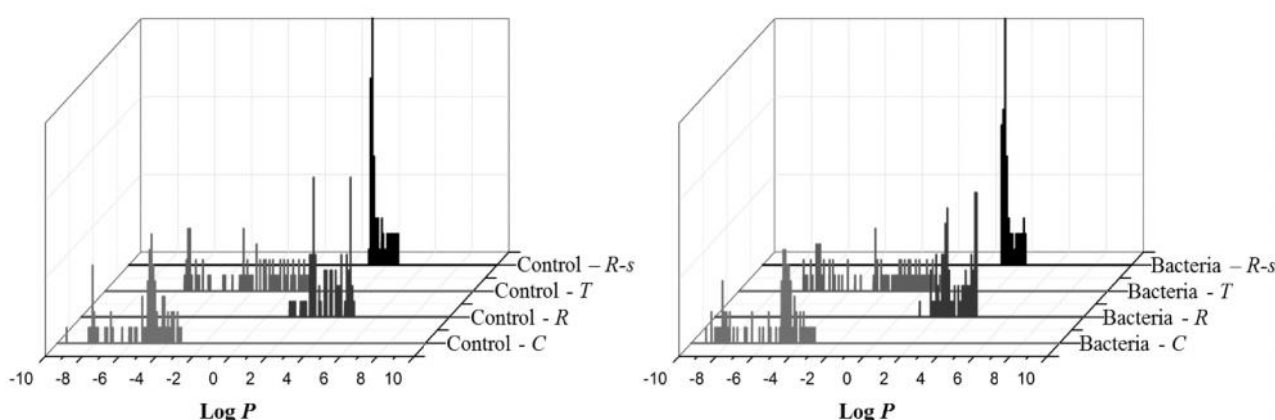


**Fig. 4.** Spectral presentation of the Temporal plots from Fig. 3.

Although the plots are similar for the system with and without bacteria, the presence of bacteria increases the frequency distribution of  $T$ , which is more pronounced for its  $C$  component. At lower frequencies DIA distinguishes two processes (segments II and III) identified by the difference in the frequency dependence of the LOM parameters estimates. For precise structural and parametric identification a Secondary DIA is needed. On this stage those two steps were further modeled with constant phase elements (CPEs) in a proposed equivalent circuit of the system (Fig. 5). The analysis of the  $R$  temporal plot shows that the low frequency step (Segment III) which has the highest level of frequency distribution, is the rate limiting stage, i.e. it gives the biggest contribution in the resistance of the system.

The  $R_s$  spectra allowed identifying the solution resistance of both samples. Even for the bacteria sample, where the first intercept of the real axis was not visible, a peak in the spectral plot was well distinguishable. The solution resistance was estimated to be 1132  $\Omega$  for the control sample and 1150  $\Omega$  when bacteria were present. Such values

are comparable with the results from conductivity measurements of the solution.

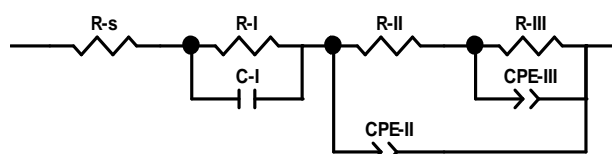


**Fig. 5.** Equivalent circuit used for fitting calculated with measured data.

Although for structural and parametric identification of Segments II and III a procedure of Secondary DIA is needed, the analysis of the corresponding  $R$  and  $C$  spectral peaks pronounced in the Spectral plot gives valuable information. The second  $R$  peak corresponds to segment III and thus it is related to the lowest frequency phenomenon, which was identified as the rate limiting step considering its values, which are one order of magnitude higher than the others. Obviously the resistance of segment II has strongly distributed character and cannot be pronounced on this plot with a spectral maximum. For the capacitance contribution at lower frequencies, a spectral

maximum is pronounced for Segment II. It has more distributed character for the experiment without bacteria.

Based on the structural and parametric information obtained by DIA, an equivalent circuit was proposed (Figure 5) and used for the performance of a fitting procedure on the EIS spectra. The parametric results are summarized in Table I.

**Table I.** CNRLS fitting results.

Sample	Control	Bacteria
Rs /	1132	1150
R-I/	516.8	487.5
C-I (Q)/ F	6.30E-9	4.81E-9
R-II /	6769	15403
CPE-II (Q)/ F	1.92E-5	2.65E-5
CPE-II (n)	0.85	0.84
R-III/	1.31E5	18734
CPE-III (Q)/ F	3.80E-5	1.00E-4
CPE-III (n)	0.49	0.68

The resistance of the solution was identified by the first Rs peak of the DIA spectral analysis. The high-frequency process corresponding to the first semicircle in the EIS spectra was fitted using a resistance in parallel with a capacitor (R-I/C-I), which describes the charge transfer processes at the sample/electrolyte interface. The low-frequency depressed semicircle in Fig. 1 was modelled using a ladder circuit structure with two R//CPE meshes (R-II//CPE-II; R-III//CPE-III) in agreement with the presence of two processes, identified as segments II and III in the temporal plots. Considering the frequency range of the processes and the influence of bacteria, they can be attributed to the electrical properties of the passive film on the sample surface (R-II//CPE-II) and the mass transport at the sample/solution interface (R-III//CPE-III).

Fitting results confirmed the values of the solution resistance calculated by DIA. The high frequency process exhibits lower values for both resistance and capacitance when bacteria are present in the solution. Although the difference in the EIS spectra is small, the correspondent parameters indicate influence of bacteria on the charge transfer phenomena. More significant effect of the bacteria is registered for the processes presented in Segments II and III. The resistance of the second process increases twice (from 6796 to 15403 ) which, related to the electrical properties of the passivation film, signals about the formation of more resistive layer in the presence of

*Pseudomonas*. The increase of the film resistance corresponds to passivation of the sample which could lead to higher risk of pits formation. No significant changes were measured for the associated CPE values. The process which is observed in Segment III was supposed to be related to mass transfer phenomena due to the frequency range and confirmed by the obtained CPE values. In the presence of bacteria the resistance decreased from 1.31E+5 to 18734 indicating higher activity of the localized phenomena. The proposed behavior, associated with the increase of the passivation layer resistance, is consistent with pits formation.

The post-experiment characterization (Figure 6) evidenced the formation of an inner layer constituted by Cu and Sn oxides and areas rich in copper chlorides on the control sample, which is in agreement with other studies on copper alloys in aqueous environment [27].

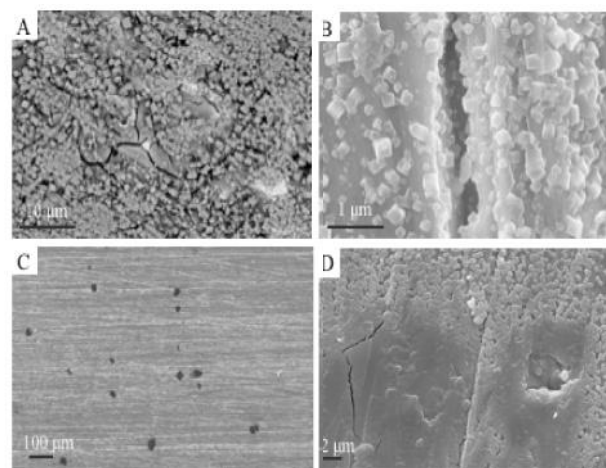


**Fig. 6.** Surface topography of the samples: (a) SEM-BSE 4500x micrograph of a thick passive film of copper and tin oxides and hydroxides under secondary corrosion products identified as CuCl; (b) SEM-SE 15500x micrograph of cracks inside the passive film formed; (c) 100x SEM-SE micrograph of micro-colonies randomly distributed; (d) 4000x SEM-SE micrograph of micro-pits under the removed biofilm.

For samples tested in bacteria rich solution, organic structures were found on the surface. They are formed in the first stage of the biofilm formation (Figure 6c). In several areas, where the biofilm was removed during the sample preparation, localized attacks consisting of micropits were detected (Figure 6d), supporting the electrochemical characterization.

## CONCLUSIONS

The effect of microbiological activity on tin-bronze samples was investigated combining

electrochemical measurements with post-experiment characterization.

The application of a structural approach, based on the DIA technique for EIS data analysis, led to the identification of three corrosion processes for the investigated copper alloy in artificial fresh water. DIA allows studying the distribution of the phenomena in the frequency domain, estimating their resistive and capacitive parameters. It identified the solution resistance despite the disturbance of the signal at high frequencies. The influence of bacteria was visible by changes in the processes distribution using the DIA spectral plots. This information supported the choice of an adequate equivalent circuit to model the corrosion processes for more precise parametric identification. The CNRLS results allowed to estimate quantitatively the changes caused by bacteria in every step of the total process. Minor effects were measured for the charge transfer processes. Microbial activity brought to localized corrosion phenomena. The pit formation, post-experimentally observed, was identified by the decrease of mass transport resistance. For precise structural and parametrical identification of the frequency distributed phenomena which are presented at low frequencies, Secondary DIA will be further applied.

**Acknowledgements:** *The authors would like to thank Prof. Zdravko Stoynov for sharing his knowledge in electrochemistry and teaching on the Differential Impedance Analysis technique.*

## REFERENCES

1. B. Little, J. Lee, Microbiologically Influenced Corrosion, John Wiley and sons, Hoboken, 2007.
2. P. Cristiani, G Perboni A. Debenedetti, Biocorys 2007 International Conference on Biocorrosion and Materials, Paris, 11–14 June 2007, congress acts, 2007.
3. P. Cristiani, Corrosion monitoring in microbial environments, in L. Yang, Techniques for corrosion monitoring, (2008), Woodhead Publishing, Cambridge, p. 347.
4. W. Characklis, K. Marshall, Biofilms, John Wiley and sons, New York, 1990.
5. P. Marcus (Eds), Corrosion Mechanisms in Theory and Practice, Marcel Dekker, Inc., New York, 2002.
6. P. Cristiani (org.), Biofilm and MIC Monitoring: State of the art, Meeting of Task 5 of Microbiologically Induced Corrosion of Industrial Materials, Venezia, 2000.
7. M. Carvalho, J. Doma, M. Sztylek, I. Beech, P. Cristiani, The study of marine corrosion of copper alloys in chlorinated condenser cooling circuits: The role of microbiological components, *Bioelectrochem.*, **97**, 2 (2014).
8. M. Carvalho, P. Cristiani, Experiences of on-line monitoring of microbial corrosion and antifouling on copper alloys condenser tubes, in M. Malayeri, H. Muller-Steinhagen, A. Watkinsons (Eds.) Proceedings of International Conference on Heat Exchangers Fouling and Celaning, Crete Island, Greece, 2011.
9. G. Borkow, J. Gabbay, Copper as a Biocidal tool, Cupron Inc., 2004.
10. S. Kakooei, M. Ismail, B. Ariwahjoedi, Mechanisms of Microbiologically Influenced Corrosion: A Review, *World Appl. Sci. J.*, **17(4)**, 524 (2012).
11. J. Morales, P. Esparza, S. Gonzalez, R. Salvarezza, M. P. Arevalo, The role of *Pseudomonas aeruginosa* on the localized corrosion of 304 stainless steel, *Corros. Sci.*, **34(9)**, 153 (1993).
12. I. Beech, J. Sunner, K. Hiraoka, Microbe–surface interactions in biofouling and biocorrosion processes, *Intern. Microbiol.*, **8**, 157 (2005).
13. J. Busalmen, M. Frontini, S. de Sanchez, Microbial Corrosion: effect of microbial catalase on oxygen reduction, in S. A. Campbell, N. Campbell, F. C. Walsh (eds.), Developments in Marine Corrosion, Royal Society of Chemistry, Cambridge, p. 119(1998).
14. I. Beech, L. Hanjagst, M. Kalaji, A. Neal, V. Zinkevich, Chemical and structural characterization of exopolymers produced by *Pseudomonas* sp. NCIMB 2021 in continuous culture, *Microbiology*, **145**, 1491 (1999).
15. K. Levenberg, A method for the solution of certain non-linear problems in least squares, *Q. Appl. Math.*, **2**, 164 (1944).
16. D. Marquardt, An algorithm for least-squares estimation of nonlinear parameters, *J. Soc. Ind. Appl. Math.*, **11**, 431(1963).
17. B. Boukamp, A nonlinear least squares fit procedure for analysis of immittance data of electrochemical systems, *Solid State Ionics*, **20**, 31 (1986).
18. J. Macdonald, L. Potter, A flexible procedure for analyzing impedance spectroscopy results: Description and illustrations, *Solid State Ionics*, **24**, 61(1987).
19. Z. Stoynov, Differential impedance analysis - an insight into the experimental data, *Polish J. Chem.*, **71**, 1204 (1997).
20. D. Vladikova, P. Zoltowski, E. Makowska, Z. Stoynov, Selectivity study of the differential impedance analysis - comparison with the complex non-linear least squares method, *Electrochim. Acta*, **47**, 2943 (2002).
21. Z. Stoynov, D. Vladikova, “Differential Impedance Analysis“, Marin Drinov Publ. House, Sofia, 2005 (ISBN 954-322-057-3).
22. Z. Stoynov, D. Vladikova, “Impedance Spectroscopy of Electrochemical Power Sources” in: U. Garcke (Ed.) Encyclopedia of Electrochemical Power Sources, Elsevier, 2009, p. 632 – 642 (ISBN-13: 978-0-444-52093-7; ISBN-10: 0-444-52093-7).
23. JDS 3 I. (2015). Joint Danube Survey 3. A Comprehensive Analysis of Danube Water Quality. Vienna: ICPDR – International Commission for the Protection of the Danube River.

24. G. Sello, S. Bernasconi, F. Orsini, P. Mattavelli, P. Di Gennaro, G. Bestetti, Biocatalyst expressing cis-naphthalene dihydrodiol dehydrogenase from *Pseudomonas fluorescens* N3 catalyzes alcohol and 1,2-diol dehydrogenase reactions, *J. Molecul. Catal. B: Enzymatic*, **52**, 67 (2008).
25. S. Yuan, A. Choong, S. Pehkonen, *Corros. Sci.*, **49**, 4352 (2007).
26. E. Barsoukov, J. Macdonald, Impedance Spectroscopy: Theory, Experiment, And Applications, John Wiley And Sons, Hoboken (2005).
27. Cristiani, G. Rocchini, F. Mazza, Microbial Corrosion Proc. 3th International Efc Workshop Portugal 1994, (Estoril) 13-16 March 1994 Ed. A.K. Tiller And C.A.C Sequeira, Estoril, The Institute Of Materials, P. 243 - 260, 1995.

8 2016 ; 6 2017 .  
( )  
Cu-Sn (12wt% Sn)  
( )  
(SEM).

## Structural and electrochemical characterization of yttrium doped barium cerate $\text{BaCe}_{0.85}\text{Y}_{0.15}\text{O}_{3-x}$ for applications in solid oxide fuel cells

G. Raikova<sup>1\*</sup>, K. Krezhov<sup>2</sup>, I. Genov<sup>1</sup>, A. Thorel<sup>3</sup>, A. Chesnaud<sup>3</sup>, T. Malakova<sup>2</sup>, D. Vladikova<sup>1</sup>, Z. Stoynov<sup>1</sup>

<sup>1</sup> Acad. E. Budevski Institute of Electrochemistry and Energy Systems, Bulgarian Academy of Sciences, 10 Acad. G. Bonchev St., Sofia 1113, Bulgaria

<sup>2</sup> Institute for Nuclear Research and Nuclear Energy, Bulgarian Academy of Sciences, 72 bul. Tzarigradsko Shose, Sofia 1784, Bulgaria.

<sup>3</sup> Centre des Matériaux, Mines-ParisTech, BP 87, 91003 Evry Cedex, France

Received January 27, 2017      Revised March 17, 2017

The aim of this work is to achieve a deeper understanding of the conductivity mechanisms in  $\text{BaCe}_{0.85}\text{Y}_{0.15}\text{O}_{3-x}$  (BCY15) material displaying good proton conductivity. The study is directly related to the application of BCY15 in an innovative and competitive concept for a high temperature fuel cell operated in reverse mode in the range of 600-700 °C. New approach for combining the information on atomic level by X-ray and neutron-diffraction (ND) and on macro level by impedance spectroscopy for deeper insight into the origin of its mixed (proton and oxide-ion) conductivity is applied. Single-phase  $\text{BaCe}_{0.85}\text{Y}_{0.15}\text{O}_{3-x}$  samples with different porosity obtained by addition of graphite powders as pore former and changing sintering conditions were characterized in wet and dry atmosphere and their conductivity was measured in air and hydrogen in wide temperature range. The first neutron diffraction data collected at different temperatures show that the crystal structure of the samples adopts orthorhombic symmetry independently of their porosity and preparation technological conditions. Oxygen vacancies remain random at room temperature. Comparison of the proton and oxide-ion conductivity indicates that at operating temperatures (600-700 °C) they are equal. The results obtained from the electrochemical studies show that porosity of about 30-35% ensures an optimal microstructure in respect to conductivity and mechanical stability.

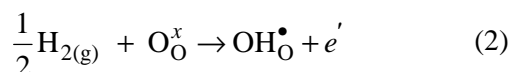
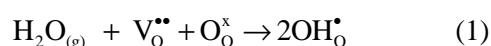
**Key words:** doped perovskite oxides, mixed ionic conductivity, electrochemical impedance spectroscopy, neutron diffraction..

### INTRODUCTION

Defect perovskite oxides are intriguing mixed conducting ceramic materials but there are only a few studies on their mixed ionic conducting properties available. The barium cerate based material under study belongs to the extrinsic systems since the defects which enable the charge carriers' transport are activated in the crystal structure by dissolution of water vapour. The proton transport kinetics in the crystal lattice of these materials is closely related to the oxygen vacancies created by the Y substituent. These vacancies can be filled with the oxygen from adsorbed water molecule and the introduced protons will be bound to the lattice oxygen. Thermal activation acts as the driving force for the protons to overcome an energy barrier of a few hundred eV and to jump to another oxygen site, thus constituting proton mobility.

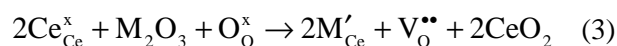
Under humidified hydrogen atmosphere protonic defects are formed by dissociative absorption of

water in the presence of oxygen vacancies (Eq.1). It is believed that protons could migrate by hopping from the OH site to oxide ion site at a normal lattice site nearby causing this material to exhibit proton conductivity (Eq. 2) [1-4].



Water vapour dissociates into a hydroxide ion which fills an oxide-ion vacancy, and a proton that forms a covalent bond with lattice oxygen, i.e. two proton defects are created stoichiometrically [1]. Since the incorporation of water is exothermic [1,4], the protonic transport is dominating at lower temperatures (under 600°C).

The doping with aliovalent rare earth cations brings to the formation of oxygen vacancies and significantly improves the proton conductivity [1-3,5]. In the  $\text{BaCeO}_3$  system, which is considered to be very promising because of the registered high protonic conductivity (0.01 – 0.05 S/cm between 600-800 °C [4,5]), the reaction can be described as:



To whom all correspondence should be sent:  
E-mail: graikova@bas.bg



Proton conductivity in cerates depends on the crystallographic structure, which is a function of temperature and doping concentration. It decreases when transformations to higher symmetry (from orthorhombic to cubic) which bring to equivalent distribution of all oxygen positions and to evenly distributed oxygen ion vacancies take place [1,5]. In addition to the temperature, gas atmosphere and pressure, including water vapor, is detrimental for proton conductivity.

The aim of the present paper is a deeper insight into the conduction mechanism and stability issue for application of BCY15 in a Dual membrane fuel cell (dmFC) which is an innovative SOFC architecture (Fig.1a). Here an oxygen compartment (cathode and oxide ion conducting electrolyte) is combined with a hydrogen compartment (anode

and proton conducting electrolyte) through a porous mixed conducting central membrane (CM) where the two types of ions react and produce water which is evacuated through the pores [6-13]. The new design overcomes a principle construction disadvantage connected with the production of water at the electrodes, which brings to dilution of the fuel or oxidizer and reduction of the electrodes catalytic activity.

The key-point of the dmFC development is the design and fabrication of the porous central membrane [10-14]. The first generation Dual Membrane fuel cell was proved by application of a composite central membrane based on the proton conducting  $\text{BaCe}_{0.85}\text{Y}_{0.15}\text{O}_3$  (BCY15) and oxide ion conducting  $\text{Ce}_{0.85}\text{Y}_{0.15}\text{O}_{1.925}$  (YDC15) electrolyte [10,12,14].

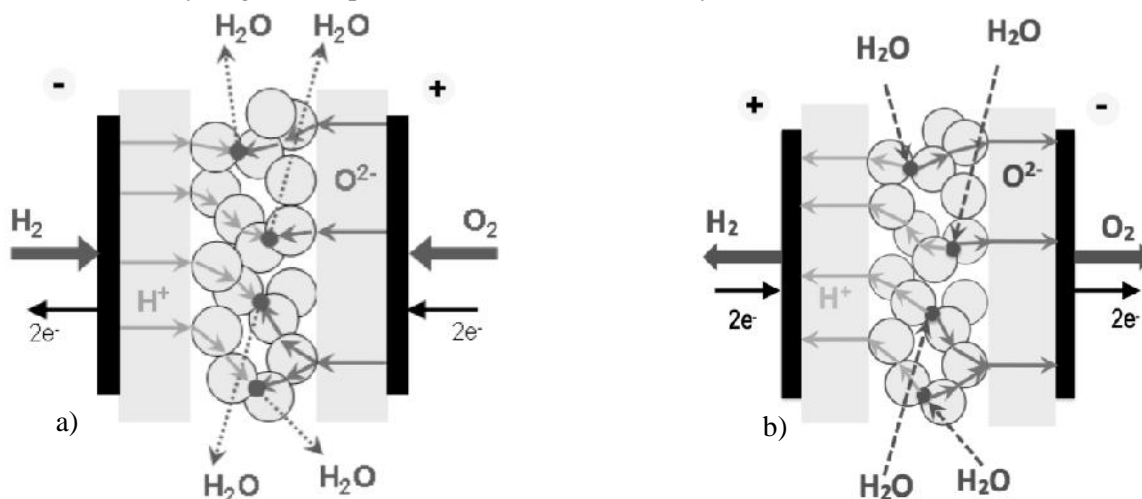


**Fig. 1.** Schematic representation of the reversible dual membrane fuel cell concept based on a single mixed ion conduction material: a) fuel cell mode of operation; b) electrolyzer mode of operation.

Applying dielectric impedance spectroscopy, a new phenomenon connected with the formation of water as a dipole semi-liquid film in the porous BCY15 structure was discovered. It improves the operation of the dmFC design by decreasing its resistance [11]. In addition, a mixed ionic conductivity in the proton conducting electrolyte BCY15 was registered. Based on the new findings, an innovative trend of dmFC design in which the 3-layered electrolyte assembly (oxide-ion conducting dense electrolyte/porous mixed ion conducting CM/dense proton conducting electrolyte) was fabricated from a single BCY15 material [7]. It is expected that this “monolithic” design will improve the conductivity, the mechanical stability and in consequence the durability of the cell, as well as will simplify the technology. The presence of “water chamber” apriori opens a new opportunity for reversible mode of operation (fuel cell/electrolyzer). The disclosed new phenomena, which define an innovative niche for further

improvement of this fuel cell design, need deeper fundamental insight.

The present investigation of the mixed ionic conductivity in the proton conducting electrolyte BCY15 is aimed at obtaining a deeper understanding of the mechanisms which govern this behaviour. Combining the results collected by the techniques based on electrochemical impedance spectroscopy with the advanced methods of the neutron scattering techniques, it is expected to provide reliable information about the transport (diffusion) and hopping in microscopic scale, as well as about the topology of the pores’ volume (internal surface areas, porosity, particle size, void size, fractality) at atomic level.

## EXPERIMENTAL

The BCY15 powders were fabricated by auto-combustion process starting from metal nitrates and applying urea as reducing agent (Marion Technologies SA, Toulouse, France). Calcination

of the precursor at 1100-1150 °C in a carrier gas (helium or argon) for complete CO<sub>2</sub> elimination ensured the production of single phase powder with chemical composition Ba<sub>1.04</sub>Ce<sub>0.82</sub>Y<sub>0.15</sub>O<sub>3-</sub>, determined by ion coupled plasma analysis, with dominating particle size around 200 nm and minor degree of agglomeration.

The BCY15 electrolyte support pellets (diameter/thickness = 20-25/1-1,3mm) were prepared by cold pressing and sintering at heating rate given in Fig. 2. Porous material was obtained by mixing thoroughly the powder BCY15 with graphite powder (2 - 8 wt %) as pore former. The relative porosity (in vol. %) of pellets was evaluated by weighing and measuring the dimensions of the samples which are presented in Table 1. The morphological examinations (Fig. 2) validated that the samples listed in Table 1 have

a relatively homogeneous porous structure with a grain size of about 2 microns. Only for sample 1 the average grain size is bigger than 2 microns.

**Table 1.** Porosity of the samples.

Sample	1	2	3	4	5	6	7
Porosity, %	9	22	27	35	47	47	48

In order to characterise the changes in the microstructure of the materials, a number of analytical techniques was used: X-Ray Diffraction (XRD) with Energy Dispersive X-ray spectroscopy (EDX), Transmission Electron Microscopy (JEM 200 CX, JEOL Japan) in combination with Electron Dispersive Spectrometry (EDS, TRACTOR, USA) and an ASID 3 D TECNAL 20F ST appliance.

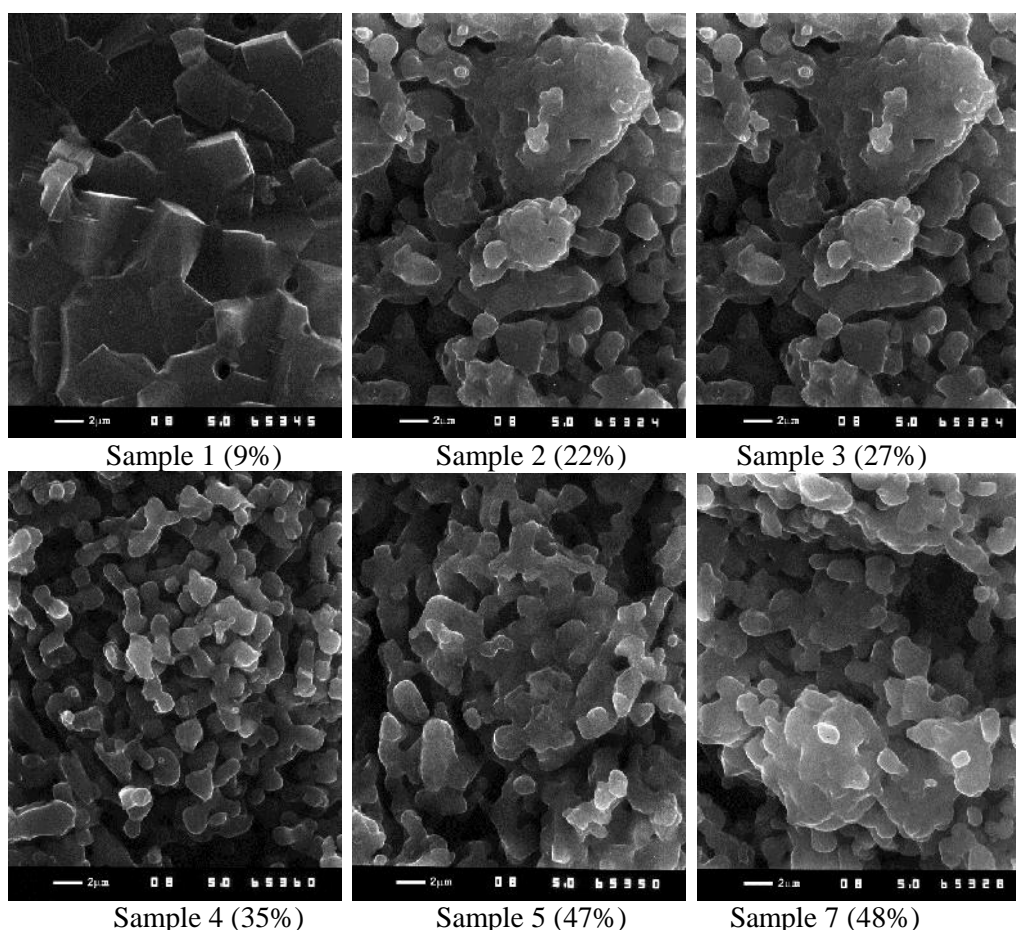


**Fig. 2.** SEM micrographs of BCY15 samples.

The structural characterization of polycrystalline BCY15 was carried out by X-ray diffraction (XRD) and neutron diffraction (ND). Quantitative phase analyses were done on a Bruker D8 Advanced (filtered Cu radiation; 40kV, 30 mA) diffractometer in Bragg-Brentano geometry. The ND studies were conducted by the time of the flight method (TOF)

and the method of constant wavelength (CW). Correspondingly, two instruments were used: the high intensity instrument PSD [15] at the research reactor VVR-M of the Budapest Neutron Centre and the spectrometer DN-12 [16] of JINR, Dubna at the pulsed reactor IBR-2M. The XRD and ND data were analysed using the FULLPROF suite [17] by

applying profile matching mode followed by full profile Rietveld refinement of the structural model. The tabulated coherent scattering lengths  $b_{\text{coh}}$  were used: 5.07, 4.84, 7.75 and 5.803 fm for Ba, Ce, Y and O, respectively.

The electrochemical characterization of the CM in the monolithic design was conducted by impedance measurements of symmetrical half-cells Pt/BCY15porous/Pt and Pt/BCY15dense/Pt in dry and wet hydrogen and oxygen. Platinum (Metalor) electrodes were painted and sintered in air following a procedure recommended by the producer.

The impedance measurements were performed with IVIUM-CompactStat e10030 in a temperature interval of 100 – 700°C at frequency range from 1

Hz down to 0,01Hz and density of 5 points/decade. They were done in two modes: potentiostatic and galvanostatic. The half cell measurements were carried out at OCV in working atmosphere wet (3% H<sub>2</sub>O) hydrogen.

## RESULTS AND DISCUSSION

Some results from the XRD and ND experiments were published previously [18, 19]. Here we supplement the findings with the outcomes from additional experiments aimed to further clarify the structural behaviour of the BCY based materials.

The XRD patterns recorded on samples from fragmented materials after their preparation confirmed that the sintering conditions do not affect in general the single phase structure and the composition of the initial powdered substance BCY15 (Fig. 3). More careful XRD examinations of both sides of BCY15 based pellets showed that the appearance of an additional set of peaks on the upper side of the pellets discloses the presence of a

small quantity of Y<sub>0.1</sub>Ce<sub>0.9</sub>O<sub>2.95</sub> (Fig. 3c). This can be due to loss of BaO on the upper surface because of evaporation during the sintering step.

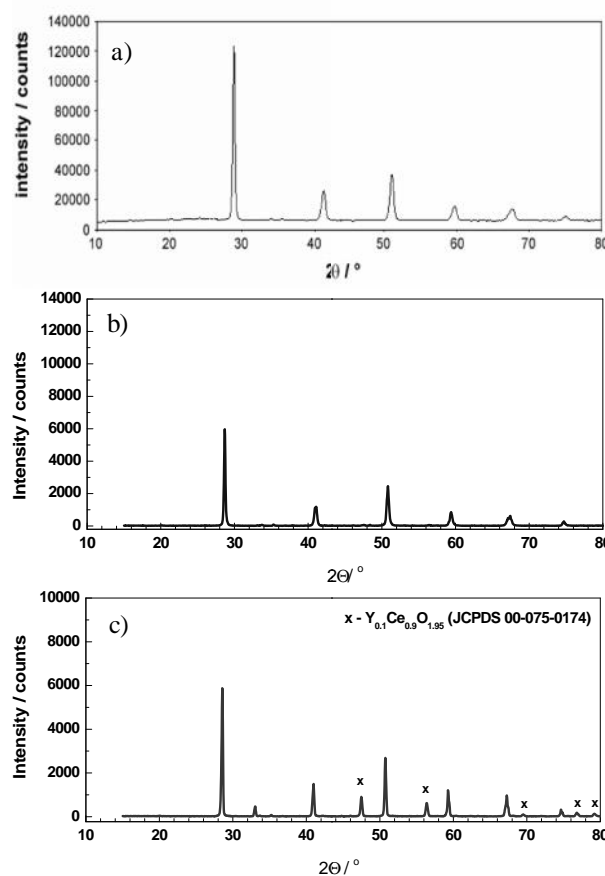


**Fig. 3.** X-ray diffraction patterns of BCY15: powders according to the producer (a); milled material after cold pressing and sintering (b) and pellets' surface (c).

Fig. 4 shows the neutron diffraction (ND) patterns collected on representative powder samples of the three types of BCY15 based material. There are no any indications of difference in crystallographic symmetry of the particular samples.

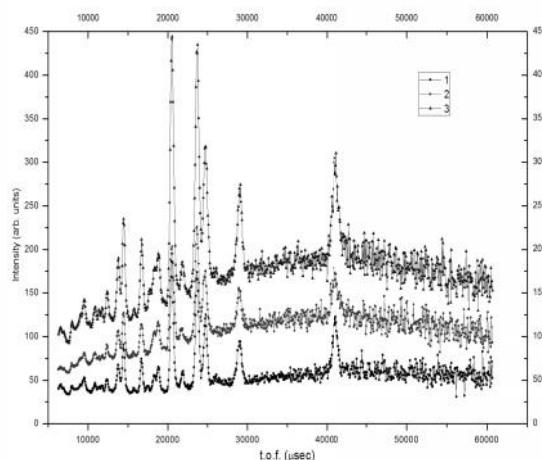
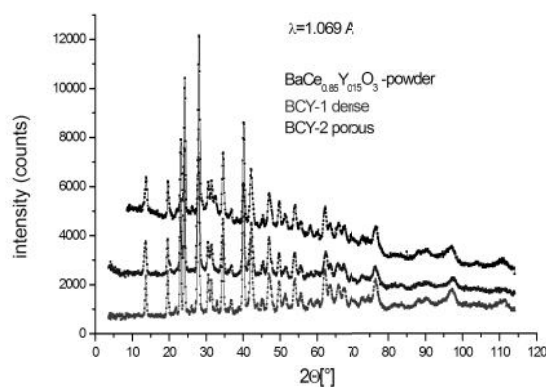


**Fig. 4.** ND patterns of BaCe<sub>0.85</sub>Y<sub>0.15</sub>O<sub>3</sub>- based samples at 295 K: a) constant wavelength ( $\lambda = 1.069 \text{ \AA}$ ) pattern. The sample denoted as powder was kept for three days in moist air; b) TOF patterns: 1 (dense), 2 (porous), 3 (powder). The patterns are vertically shifted to improve visibility.

The patterns could be indexed in rhombohedral space group R-3c and monoclinic symmetry space group I2/m. We have also checked for a mixture of two perovskite phases of R-3c and I2/m symmetry as recommended for compositions with this and higher substitution rates [20-23]. However, in all the cases the structure refinements did not produce better agreement factors than in orthorhombic Pnma.

The multi-pattern mode of the FullProf program for simultaneous treatment of neutron (constant wavelength) and x-ray data sets were used to refine the structure and to determine the lattice parameters, atomic positions and thermal factors. We considered the crystal structure of undoped BaCeO<sub>3</sub> as the starting structural model, with orthorhombic symmetry and space group Pnma; all the Bragg peaks of the diagram could be thus indexed. Because the structure contains two different B-site cations the possibility of ordered and disordered variants was checked. Best refinements were produced by models where Yttrium atoms were introduced at random at 4b positions together with Cerium, and the complementary occupancy factors were refined, constrained to a full occupancy. The formula checked was BaCe<sub>1-x</sub>Y<sub>x</sub>O<sub>3-0.5x</sub>, where x=0.15. In the final refinement, the Ce/Y occupancy factors were unconstrained, indicating a slight deviation from the nominal 0.85:0.15 stoichiometry.

Fig. 5 shows on the example of a powdered “dense” material the agreement between the observed and calculated NPD curves in the final multi pattern Rietveld fit. The structure parameters and the discrepancy factors describing the Rietveld fit quality are presented in Table 2.

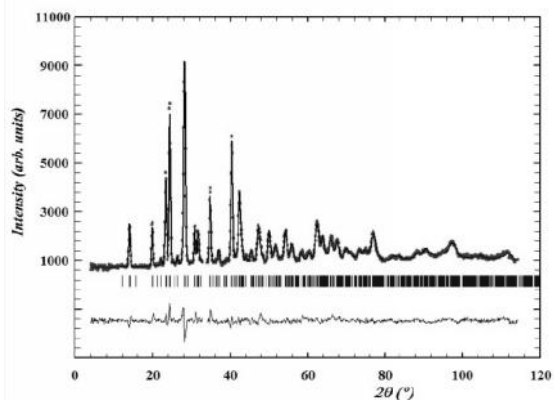


**Fig. 5.** Observed (crosses), calculated (continuous line), and difference (bottom) Rietveld ND profiles of milled material of dense BCY15 pellet at 295 K. The row of tick marks gives the positions of the allowed Bragg reflections.

The unit cell parameters of BaCe<sub>0.85</sub>Y<sub>0.15</sub>O<sub>3-</sub> are close to the values of BaCe<sub>0.9</sub>Y<sub>0.1</sub>O<sub>2.95</sub> given in the references included in the ICDD PDF-4 database.

The relationship between the lattice parameters is typical for O-type perovskites, where the tilting of the oxygen octahedra is the main reason for the deviation from the ideal perovskite structure ABX<sub>3</sub> [24, 25].

**Table 2.** Refined structural parameters of BaCe<sub>0.85</sub>Y<sub>0.15</sub>O<sub>3-</sub> in space group Pnma. Unit cell parameters (Å): a=6.2089(9), b=8.8292 (6), c=6.2066(8), volume (Å<sup>3</sup>) = 340.24(25). Agreement factors (%): R<sub>wp</sub>=5.92, R<sub>B</sub> = 3.66, 2= 1.85. Estimated standard deviations are in parenthesis.

	x	y	z	B, Å <sup>2</sup>
Ba	0.0098(5)	0.25	-0.0028(7)	1.14(5)
Ce	0	0	0.5	0.56(6)
Y	0	0	0.5	0.56(6)
O1	0.5212(5)	0.25	-0.0792(7)	0.86(6)
O2	0.2674(4)	0.0395(7)	0.7249(7)	0.86(6)

Fig. 6 illustrates the agreement between the observed and calculated ND curves after the Rietveld refinement. Table 3 presents the structure parameters of a BCY15 pellet (Left panel).

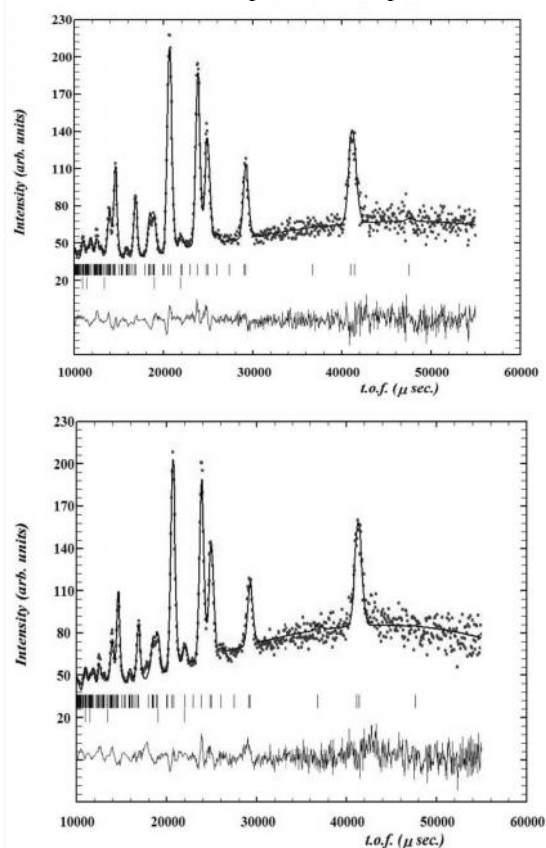


**Fig. 6.** Observed (crosses), calculated (continuous line), and difference (bottom) Rietveld ND profiles at 295 K. Left: BCY15 based pellet; Right: as received BCY15 powder without temperature treatment. The row of tick marks gives the positions of the allowed Bragg reflections.

The pelletized BCY15 material without pore former (graphite) was sintered at 1400 °C for 8 hours in air. The TOF diffraction data were taken for 6 hours at 295 K. The prolonged sintering resulted into a more compact unit cell. Right panel gives the diffraction pattern of BCY15 powder before the usual temperature annealing at 1000°C aiming to reduce possible consequences of sample transportation to JINR. In both panels the lines originating from the aluminium foil of the sample holder are distinctly observable. The quantitative phase analysis yields below 1.2% Al for the second phase.

Here is to recall that the ideal perovskite structure is cubic ( $Pm\bar{3}m$ ) in which the B-cations are surrounded by six anions arranged in corner-sharing octahedral geometry. This arrangement forms cubooctahedral cavity in which the A-cation is placed. Many functional properties observed in perovskite oxides  $ABO_3$  exhibit close couplings to slight structural distortions in the perovskite lattice that consist of this three-dimensional network of corner-sharing  $BO_6$  octahedra. In general the distortion of the ideal perovskite structure of oxides is manifested by (1) cooperative tilting (in-phase and/or antiphase rotations) of the  $BO_6$  octahedra; (2) deformation of the  $BO_6$  octahedra and (3) displacement of the B-cation from the center of the octahedra. The documentation of such distortions and elucidation of their influence on properties have been important issues in fundamental materials science investigations, as well as for the broad range of applications of oxide materials.

Fig.7 and Fig.8 illustrate on the example of a BCY15 pellet of 13% porosity the attempt to understand the structural accommodation to working temperature.

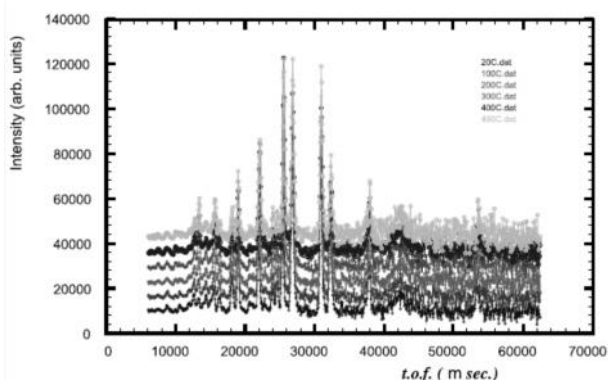


**Fig. 7.** Successive TOF patterns taken at stabilized temperatures in increasing order (in °C): 20, 100, 200,300, 400, 480. The patterns are vertically shifted to improve visibility.

The careful examination of the Rietveld fits to the set of temperature dependent diffraction

patterns (at 480 °C is the one presented) showed that although the unit cell volume is steadily expanding with increasing temperature (see Fig.9) the counting statistics of present experiment was not sufficient to provide outside the error limits sound grounds in deriving irrefutable conclusions regarding the subtle structural changes. Nevertheless the trends in structure development validate that in the investigated materials based on  $BaCe_{0.85}Y_{0.15}O_{3-}$  the tilting of the  $(Y-Ce)O_6$  octahedra is reasoning the orthorhombic symmetry observed.

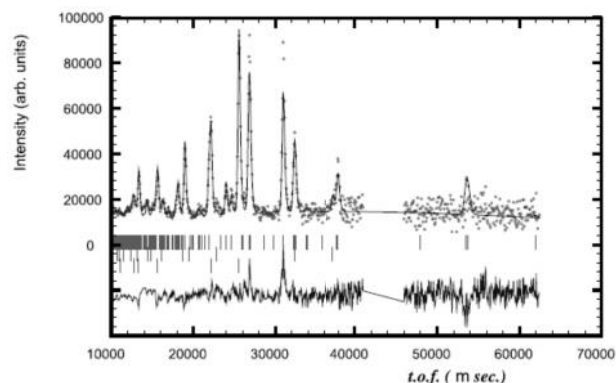


**Fig. 8.** Observed (crosses), calculated (continuous line), and difference (bottom) Rietveld ND profiles at 480 °C. The rows of tick marks give the positions of the allowed in  $Pnma$  space group Bragg reflections for the main phase of BCY15 (upper) and the minor contribution of Al foil (middle) and Cu heater (lower). The affected region of the pattern because of experimental geometry is excluded from the refinement.

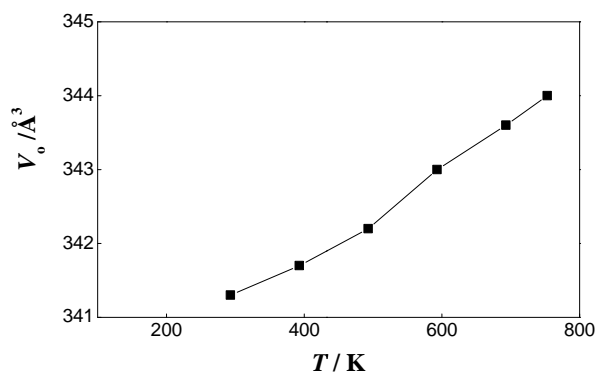


**Fig. 9.** Temperature dependence of unit cell volume  $V_0$  of BCY15 pellet of 13% porosity.

On the other hand, Fig.10 illustrates the attempt to understand the impact of water on the BCY15 structure. In this experiment several drops of water with consecutive stirring were applied to achieve homogeneous humidification of the powder before carrying out the measurement of the so-protonated sample.

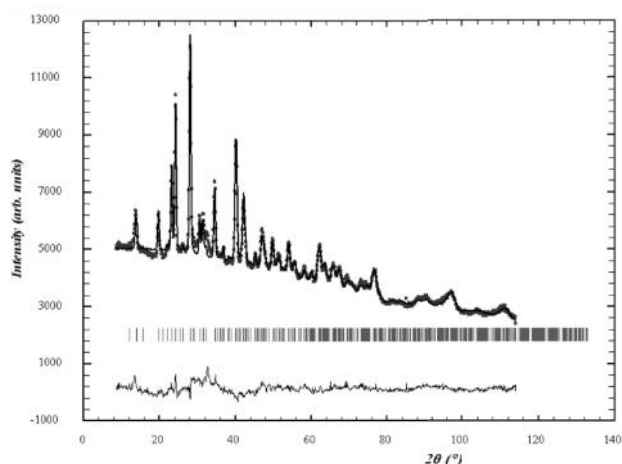


**Fig. 10.** Observed (crosses), calculated (continuous line), and difference (bottom) NPD Rietveld profiles of BCY15 protonated powder at 295 K. The row of tick marks gives the positions of the allowed Bragg reflections.

The extensive incoherent scattering of hydrogen from the hydroxyl groups is reflected by the steadily rising contribution to the background with decreasing to zero scattering angles. The fit is not of the required quality to allow for drawing up unambiguous conclusions for the structural details. By simultaneous treatment of multiple powder diffraction datasets obtained by present constant wavelength X-ray and neutron diffraction experiment the powder overlap problem is partially resolved in a Rietveld refinement. The effect of the multi pattern Rietveld analysis is effectively the deconvolution of overlapping reflections by differing shifts in their relative positions. The medium resolution neutron powder data however have restricted the solution of the peak overlap problem in the structure models with protons.

In summary, the neutron diffraction experiments performed so far have shown that the BCY15 based materials are anion deficient perovskites. The crystal structure of these materials adopts orthorhombic symmetry independently of the technological preparation of the samples (sintering conditions, presence of pore former etc.) and microstructure, including porosity. In their structures oxygen vacancies remain random at room temperature. The actual long range atomic order strongly reflects the storage conditions, annealing temperature and humidity.

In addition to the deeper structural characterization, the investigated BCY micro-samples which present components (electrolyte and central membrane) of the dual membrane cell were investigated in respect to their conductivity in both air and hydrogen, which gives the possibility to register mixed ion conductivity and to compare it.

Characteristic impedance diagrams for one and the same sample measured in the two selected atmospheres are presented in Fig. 11.

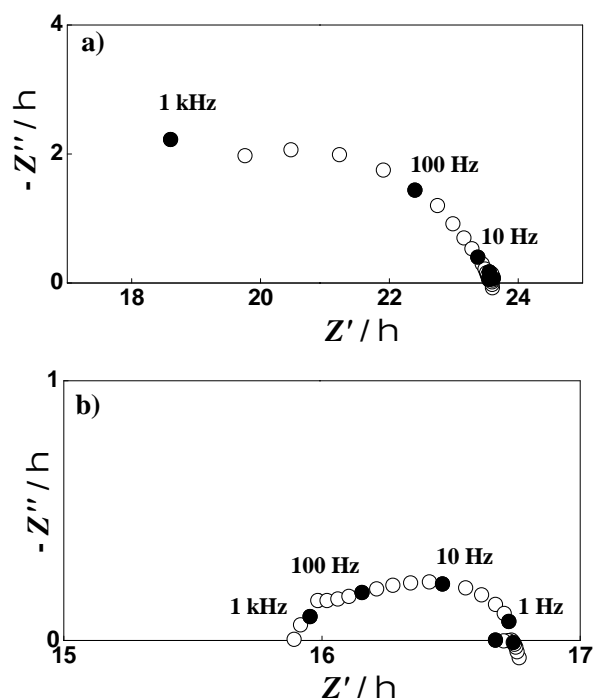


**Fig. 11.** Complex plane impedance diagrams of sample 3 (27% porosity) measured in dry air (a) and wet hydrogen (b) at 700°C.

The resistance values obtained from the impedance measurements at different temperatures were used for the construction of the Arrhenius plots (Figs. 12, 13):

$$\dots = A/T \exp(-E_a / kT) \quad (4)$$

where ... is the resistivity,  $A$  is the pre-exponential term,  $k$  is the Boltzmann constant,  $E_a$  is the activation energy and  $T$  is the temperature in K.

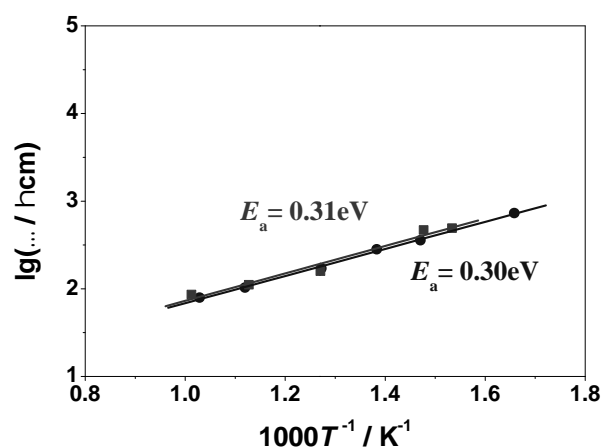


**Fig. 12.** Arrhenius plots of sample 4 (35% porosity) measured in dry air ( ) and wet hydrogen ( ).

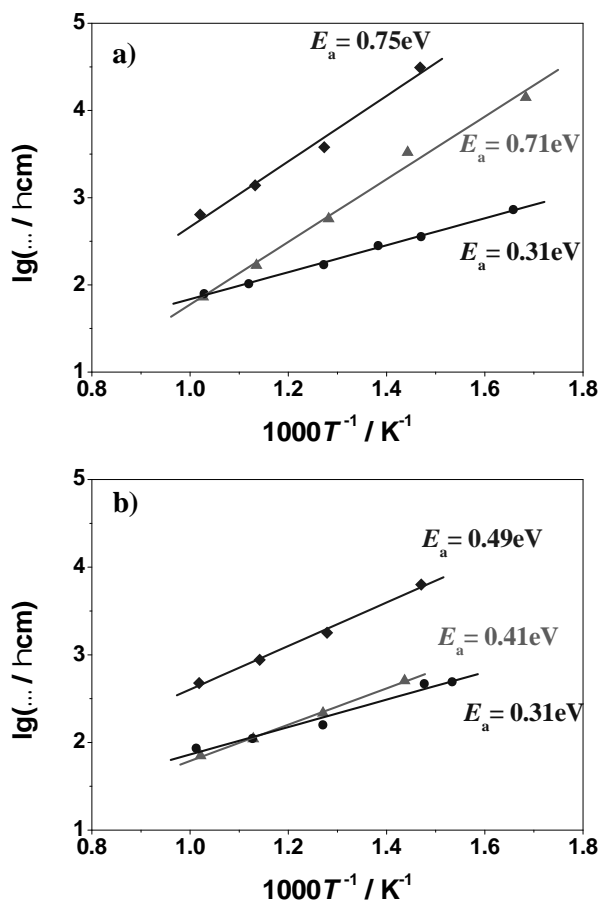


**Fig. 13.** Arrhenius plots of BCY15 samples with different porosity measured in dry air (a) and wet hydrogen (b): (◆) - sample 5 (47% porosity), (▲) - sample 4 (35% porosity), (●) - sample 3 (27% porosity).

The results show that oxide ion conductivity is more sensitive to samples microstructure (25-35% porosity) at low temperatures, whereas at operating temperatures the effect of porosity decreases, while proton conductivity is less sensitive to porosity in the whole temperature range. At operating temperatures 650-700 °C the proton and oxide ion conductivities of BCY15 electrolyte are equal. It is interesting to note that the change of the porosity in the limits 25-35% does not influence the mixed conductivity. This result is important for the optimization of the CM which has to combine high conductivity with sufficient porosity.

## CONCLUSIONS

Mixed proton and oxide-ion conductivity of ceramic BCY15 is an attractive property for its application as an electrolyte in a new design of a fuel cell which eliminates the formation/evacuation of the water produced during operation from the electrodes. New approach for combining the information on atomic level by ND and on macro level by impedance for deeper insight into the

conductivity mechanisms is applied. It needs further development. The results obtained from the combined electrochemical and structural studies of BCY15 in addition to its natural property to split water reinforce a new emerging niche for development of other materials with similar structure and mixed conductivity which will further stimulate the development of the dual membrane fuel cell concept for operation in both fuel cell and electrolyzer mode.

**Acknowledgements:** The research leading to these results has received funding from Bulgarian NSF under grant No E02/3/2014. The authors express their gratitude to Prof. E.Svab and Dr. M. Fabian from the Budapest Neutron Centre and Prof. D. Kozenko and his team (Dr. S. Kichanov and Dr. E. Lukin) from the FLNP laboratory of JINR - Dubna for constructive discussions and help in execution of neutron beam experiments.

## REFERENCES

1. L. Malavasi, C. Fisher, M. Islam, *Chem. Soc. Rev.*, **39**, 4370 (2010).
2. T. Ishihara, N. Sammes, O. Yamamoto in *High Temperature Solid Oxide Fuel Cells: Fundamentals, Design and Applications*, edited by S.C. Singhal and K. Kendall, (Elsevier, 2003) pp. 83-117.
3. H. Iwahara, *Solid State Ionics*, **86-88**, 9 (1996).
4. A. Bassano, V. Buscaglia, M. Viviani, M. Bassoli, M-T. Buscaglia, M. Sennour, A. Thorel, Nanni, *Solid State Ionics*, **180**, 168 (2009).
5. N. Bonanos, K. Knight, B. Ellis, *Solid State Ionics*, **79**, 161 (1995).
6. Patent N°0550696000 March 17th, 2005 "Cellule de Pile a Combustible Haute Temperature a Conduction Mixte Anionique et Protonique" extended internationally in 2007, invented by the Centre des Materiaux d'Evry, common research center to ARMINES and MINES ParisTech.
7. A. Thorel, Z. Stoyanov, D. Vladikova, A. Chesnaud, M. Viviani, S. Presto, "Fuel Cell with Monolithic Electrolytes Membrane Assembly", Patent N° 20120156573, 21.06.2012.
8. A. S. Thorel, A. Chesnaud, M. Viviani, A. Barbucci, S. Presto, P. Piccardo, Z. Ilhan, D. Vladikova, Z. Stoyanov, "IDEAL-CeII, a high temperature Innovative Dual mEmbrAne fueL-CeI/" in: *Solid Oxide Fuel Cells (SOFC XI)*, The Electrochemical Society Proceedings Series, Pennington, NJ (2009) 753.
9. D. Vladikova, Z. Stoyanov, G. Raikova, A. Thorel, A. Chesnaud, J. Abreu, M. Viviani, A. Barbucci, S. Presto, P. Carpanese "Impedance Spectroscopy Studies of Dual Membrane Fuel Cell", *Electrochimica Acta*, **56**, 7955 (2011).
10. M. Viviani, S. Presto, A. Barbucci, M. Carpanese, R. Amendol, A. Thorel, A. Chesnaud, J. Abreu, R. Costa, Z. Ilhan, S. Ansar, D. Vladikova, Z. Stoyanov, "Proton and Mixed Conductors for Dual Membrane Fuel





## Ni incorporation in pSOFC anode ceramic matrix: Part I. Wet chemical reduction in an aqueous medium

M. Gabrovska<sup>1\*</sup>, D. Nikolova<sup>1</sup>, E. Mladenova<sup>2</sup>, D. Vladikova<sup>2</sup>, S. Rakovsky<sup>1</sup>, Z. Stoynov<sup>2</sup>

<sup>1</sup>*Institute of Catalysis, Bulgarian Academy of Sciences, Acad. G. Bonchev Str., bl. 11, Sofia 1113, Bulgaria*

<sup>2</sup>*Acad. Evgeni Budevski Institute of Electrochemistry and Energy Systems, Bulgarian Academy of Sciences, Acad. G. Bonchev str., bl. 10, Sofia 1113, Bulgaria*

Received February 2, 2017      Revised March 11, 2017

Yttrium-doped barium cerate  $\text{BaCe}_{0.85}\text{Y}_{0.15}\text{O}_{2.925}$  (BCY15) with  $\text{ABO}_3$  perovskite-type structure was used as an anode ceramic matrix for the preparation of Ni-based BCY15 cermet anode for proton conducting solid oxide fuel cell (pSOFC). The possibility of metal nickel incorporation in BCY15 by wet-chemical reduction route in an aqueous medium with hydrazine was examined. Powder X-ray diffraction,  $\text{N}_2$ -physisorption and SEM techniques were used for characterization of the synthesized BCY15/Ni powder. The electrochemical properties of Ni-based BCY15 anode cermet were determined by impedance spectroscopy after high-temperature sintering followed by reduction in hydrogen atmosphere. It was found that BCY15/Ni anode cermet demonstrated electrochemical performance similar to that of commercial NiO-based anode cermets in respect to the electronic conductivity of the Ni net. This makes the BCY15/Ni anode cermet suitable for application in BCY-based pSOFC. It may be concluded that the wet-chemical reduction route using hydrazine in an aqueous medium is a promising approach for incorporation of the metal nickel in the BCY15 anode ceramic matrix. This method provides better conditions for nickel introduction in the anode ceramic matrix in comparison with the classical solid state ceramic approach.

**Key words:** BCY15/Ni cermet anode, wet-chemical reduction by hydrazine, PXRD, electrochemical impedance spectroscopy.

### INTRODUCTION

Solid oxide fuel cells (SOFCs) are one of the most efficient and environmental-friendly technologies available for generating power from hydrogen, natural gas, and other renewable fuels. SOFC is an all-ceramic device (two electrodes in contact with a dense ceramic electrolyte) that usually operates at elevated temperatures (800–1000°C) where it has sufficient conductivity, thus allowing internal reforming. It promotes rapid electro catalysis with non-precious metals and produces high quality heat by product for co-generation. Major drawbacks are connected to degradation phenomena occurring at high temperatures [1-3]. In this regard, fuel cells based on proton conductor electrolytes (pSOFC) are of great interest for their potential to operate at intermediate temperatures (400–600°C) thus alleviating the technological problems of SOFCs. Proton conductors are practicable electrolytes at intermediate temperatures because protons migrate more easily than oxygen ions at 400–600°C, thus conductivities are high enough for technical applications [4].

The oxygen-deficient ceramic oxides, in particular with perovskite type structure  $\text{ABO}_3$ , are recognized as the most efficient materials that can be used as electrolytes or electrodes (metal-ceramic electrode structures) in pSOFCs, where the A site is occupied by an alkaline earth element, such as Ba, Sr, and Ca, while the B site is occupied by a tetravalent element, usually Ce or Zr. To promote protonic conductivity, it is paramount to dope the B-site with suitable trivalent elements, such as Y, Nd, Sm, Yb, In, Eu, Gd, etc. Doping with a trivalent element via the dissolution of hydroxyl ions at vacant oxygen sites induces the formation of oxygen vacancies, which play a crucial role in the formation of mobile protons [5, 6].  $\text{ABO}_3$  perovskite structured materials like Y-doped barium cerate ( $\text{BaCe}_{1-x}\text{Y}_x\text{O}_{3-}$ ), commonly noted BCY, are of particular interest because they exhibit high proton conductivity, high electronic conductivity, and excellent chemical stability under reduced fuel cell environment over a wide temperature range. Thus, it could be considered as a promising proton conducting electrolyte for pSOFCs [3, 7-13]. BCY is a classical proton conducting electrolyte which may be exploited in two different functional layers of pSOFC: as proton conducting electrolyte and metal-cermet anode.

An inspection of the literature prompts that some metals can be used in SOFC anodes as

To whom all correspondence should be sent:  
E-mail: margo@ic.bas.bg

catalysts for the fuel oxidation, as well as for ensuring electron conductivity, due to the reducing conditions of the fuel during fuel cell operation. The state-of-the-art metal for incorporation in the anode ceramic matrix is nickel. In pSOFC it is coupled with a protonic conducting ceramic to form the so called cermet. The selection of Ni is due to its excellent catalytic activity for hydrogen oxidation in the intermediate temperature range and high electrical conductivity. Ni has performance similar to that of the precious metal-based catalysts, thus, offering significant cost savings [14, 15]. To ensure sufficient current collection, the nickel content is usually over 35 vol. % to form a percolation path for electron transport [16]. The presence of proton conducting ceramic matrix in the anode composite improves the electrode performance, providing a conductivity network for  $H^+$  ions, thus extending the triple-phase boundary (TPB) length [15].

It is well known that the preparative route plays a critical role on the physical and chemical properties of the reaction products, controlling the structure, morphology, grain size and surface area of the obtained materials. Traditionally, anode cermets are prepared by the standard ceramic technology from mixture of their constituent oxides in the so called solid state reaction or “shake and bake”. High temperature is a must in order to accelerate the slow solid–solid diffusion [17]. As a result of the low kinetics and high temperature, this costly method yields solids with low homogeneity, often presence of undesired secondary phases and uncontrolled (and typically large) particle size of low surface area [18].

Alternative approaches are wet chemical synthetic methods which permit mixing of the elements in liquid media at the atomic level resulting in lower firing temperatures, controlled particle size, morphology and improved surface area. Hydrazine is attractive reducing agent for the preparation of fine nickel powder due to its strong reduction properties in low temperature range and high pH values [19]. The temperature and pH dependence of hydrazine reducing ability makes the synthesis easily controllable [19, 20].

In this study, a wet chemical approach for Ni introduction in the anode ceramic matrix of  $BaCe_{0.85}Y_{0.15}O_{2.925}$  (BCY15) is presented aiming to eliminate the problems associated with applying the traditional ceramic route for Ni/BCY cermet anode materials preparation. BCY15/Ni sample was synthesized by wet chemical reduction of  $Ni^{2+}$  ions with hydrazine hydrate ( $N_2H_4 \cdot H_2O$ ) in an aqueous medium.

## EXPERIMENTAL

### Sample preparation

Nickel chloride hexahydrate ( $NiCl_2 \cdot 6H_2O$ ), hydrazine monohydrate (99+%  $N_2H_4 \cdot H_2O$ ), sodium hydroxide (NaOH) and anhydrous sodium carbonate ( $Na_2CO_3$ ) of analytical grade procured by Alfa Aesar USA were used as received without further purification.

BCY15 powder (Marion Technology) was fabricated by auto-combustion process starting from metal nitrates and applying urea as reducing agent. Sintering of the precursor at 1100–1150°C in a carrier gas (helium or argon) for complete  $CO_2$  elimination ensured the production of single phase powder with 48 % porosity, dominating particle size round 200 nm and minor degree of agglomeration. The powder was thermally pre-sintered at 1100°C for 2h before the anode cermet synthesis. The pre-sintering was associated with mass losses of about 0.7 wt. %.

BCY15/Ni sample with a composition of  $NiO/BCY15 = 44.4/55.6$  (volume ratio) was synthesized in a five-necked glass reactor equipped with a steam jacket, stirrer, pH electrode, thermocouple and reflux condenser. An appropriate amount of  $NiCl_2 \cdot 6H_2O$  was dissolved in deionized water, introduced in a reaction vessel and mixed with BCY15 powder in a quantity sufficient to satisfy the desired composition of the final compound. After stirring for a certain time, a suitable volume of 0.3M  $N_2H_4 \cdot H_2O$  solution was slowly drop-wise introduced to the reactor by usage of peristaltic pump under vigorous stirring followed by addition of alkaline solution (3M NaOH/3M  $Na_2CO_3 = 1/1$ ) in the same manner. The suspension was controlled heated up to 95°C at pH=12–13 under vigorous stirring. As the reduction reaction proceeded, green, blue, blue–violet or cyan colored Ni– $N_2H_4$  complexes  $[Ni(N_2H_4)_n]Cl_2$  were initially generated, followed by transition to black, which indicated the formation of metal nickel. The reduction was accompanied by gaseous nitrogen evolution, followed by growth of  $Ni^0$  particles on the BCY15 surface. After the reduction, the resulting mixture was stirred for 1 h at the selected pH and temperature. The obtained black material was filtrated and washed thoroughly with deionized water to remove the by-products of the filtrate which was indicated by decrease of pH down to 6.0. The absence of  $Cl^-$  ions was tested with aqueous solution of 1.5 %  $AgNO_3$ . The sample was further dried at 100°C for 20 h.

To get reference sample for the characterization of BCY15/Ni, unsupported nickel denoted as Ni, was prepared according to the preparation

procedure described above, however in the absence of the anode ceramic matrix BCY15.

### Sample characterization

Powder X-ray diffraction (PXRD) data were collected on an APD 15 Philips 2134 diffractometer employing CuK radiation ( $\lambda = 0.15418$  nm) operated at  $U = 40$  kV and  $I = 30$  mA. The crystalline phases were identified using Joint Committee on Powder Diffraction Standards (JCPDS) files. Electron microscope JEOL 6390 with INCA Oxford EDS detector was used for morphology observations.

The texture characteristics were determined by low-temperature (77.4 K) nitrogen adsorption in a Quantachrome Instruments NOVA 1200e (USA) apparatus. The nitrogen adsorption-desorption isotherms were analyzed to evaluate the specific surface area, determined on the basis of the BET equation. The pore-size distribution (PSD) was made by the adsorption branch of the isotherm using the method of Barrett-Joyner-Halenda. The samples were outgassed for 16 h in vacuum at 80°C before the measurements.

The electrochemical impedance measurements were performed on IVIUM - CompactStat e10030 in the temperature interval 100–750°C and frequency range 1 Hz–0.01Hz with density of 5 points/decade and amplitude of the AC signal 1 mA in reduction atmosphere.

## RESULTS AND DISCUSSION

The PXRD patterns of BCY15 (Fig. 1a) show the presence of a single phase that can be attributed to orthorhombic perovskite, isostructural with BaCeO<sub>3</sub> (JCPDS file 00-022-0074) and yttrium doped analogue, BaCe<sub>0.9</sub>Y<sub>0.1</sub>O<sub>2.95</sub> (JCPDS file 01-081-1386). The recorded well-formed reflections of BaCeO<sub>3</sub> are in agreement with the calculated mean crystallite size ( $L$ ) of 150.0(52) Å. No diffraction peaks due to Y<sub>2</sub>O<sub>3</sub> phase are registered indicating that yttrium ions are incorporated into the perovskite lattice.

Applying PXRD data processing, the lattice parameters of BCY15 were evaluated and compared with those of standard JCPDS files for BaCeO<sub>3</sub> and BaCe<sub>0.9</sub>Y<sub>0.1</sub>O<sub>2.95</sub> (Table 1). The results obtained evidence similar values which are typical for O-type distorted perovskites. The deviation from the ideal perovskite structure can be ascribed to the distortion of the octahedra of the structure.

In general, the distortion of the ideal perovskite structure is manifested by sloping of the BO<sub>6</sub> octahedra, deformation of the BO<sub>6</sub> octahedra and displacement of the B-cation from the center of the

octahedra [21]. In the Y-doped BaCeO<sub>3</sub> the tilting of the octahedra decreases the ideal cubic symmetry to the orthorhombic O-type one.

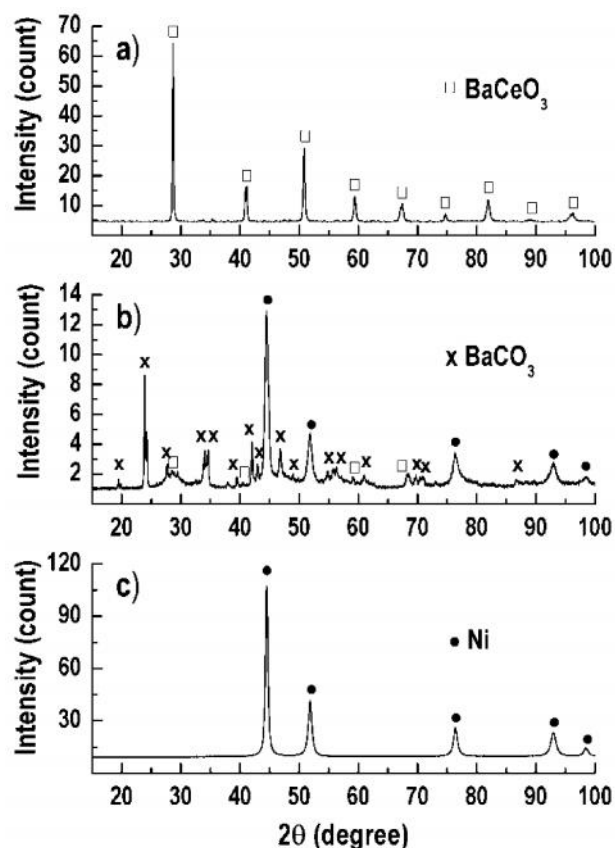


Fig. 1. XRD patterns of: (a) BCY15, (b) BCY15/Ni and (c) Ni samples.

The typical reflections of the metal Ni with cubic lattice symmetry (fcc) according to standard (JCPDS file 00-004-0085) and reference patterns of sample Ni (Fig. 1c) are clearly demonstrated in BCY15/Ni (Fig. 1b). The metal Ni lattice parameter ( $a$ ) and the metal Ni cell volume ( $V_{\text{cell}}$ ) of BCY15/Ni are presented in Table 2 showing values similar to those of standard metal Ni (JCPDS file 00-004-0850). A difference in the intensity of the metal Ni reflections going from BCY15/Ni to unsupported reference Ni sample is observed, indicating a different degree of crystallinity. This can be proved by estimating the mean metal Ni crystallite sizes ( $L$ ) from the full-width at half-maximum values of the (111) diffraction lines (Table 2). Results display that the metal Ni crystallites created in BCY15/Ni (157 Å) are smaller than those in the unsupported reference sample Ni (190 Å), specifying the positive role of the BCY15 presence in the anode composite on the metal Ni dispersion.

**Table 1.** Iridium content in the test samples determined by EDX analysis and kinetic data assessing their catalytic activity.

Compound	JCPDS file	Unit cell parameters			
		a (Å)	b (Å)	c (Å)	V <sub>cell</sub> (Å <sup>3</sup> )
BCY15	-	8.7735(63)	6.2152(36)	6.2164(69)	338.97(38)
BaCeO <sub>3</sub>	00-022-0074	8.7790	6.2140	6.2360	340.19
BaCe <sub>0.9</sub> Y <sub>0.1</sub> O <sub>2.95</sub>	01-081-1386	8.7705	6.2233	6.2393	340.55

Very well organized and intensive reflections of BaCO<sub>3</sub> phase with orthorhombic lattice symmetry (JCPDS file 00-045-1471) are also registered. The observed phenomenon proves that during the synthesis of BCY15/Ni, an interaction occurs between BCY15 and deionized water resulting in partial reorganization of the initial BCY15 structure as it can be expected due to the hydrophilic

properties of the ceramic matrix. The formation of BaCO<sub>3</sub> phase is related to the chemical instability of the BaCeO<sub>3</sub>-based materials in a humid environment and the presence of CO<sub>2</sub>, according to the reaction: BaCeO<sub>3</sub> + CO<sub>2</sub> → BaCO<sub>3</sub> + CeO<sub>2</sub>. PXRD analysis discloses a small number of low intensity reflections of BaCeO<sub>3</sub> perovskite, most probably “covered” by the BaCO<sub>3</sub> phase.

**Table 2.** Lattice parameters of metal Ni and NiO obtained after treatment of Ni/BCY15 in different atmospheres.

Parameter	BCY15/Ni			Reference JCPDS files	
	as-prepared <sup>a</sup>	sintered <sup>b</sup>	reduced <sup>a</sup>	<sup>a</sup> Ni <sup>0</sup> (00-004-0850)	<sup>b</sup> NiO (00-047-1049)
a (Å)	3.5245(10)	4.1786(10)	3.5270(11)	3.5238	4.1771
V <sub>cell</sub> (Å <sup>3</sup> )	43.78(34)	72.96(55)	43.87(43)	43.76	72.88
L (Å)	157.0(41)	124.2(39)	231.0(22)	-	-

N<sub>2</sub>-physisorption analysis reveals that BCY15 anode matrix represents typical macroporous material with Type II isotherm (Fig. 2a) that is characteristic of aggregated powders as clays, cements, etc. [22]. The observed very narrow hysteresis loop shows presence of some mesopores on the surface which are termed as Type IIb exhibiting Type H3 hysteresis. The character of the isotherm type is preserved after incorporation of Ni<sup>2+</sup> ions subsequent by reduction to the metallic state (BCY15/Ni) with clearly outline hysteresis H3 Type, generated from the new mesopore system formation. Type H3 loop is given by aggregates of platy particles or adsorbents containing slit-shaped pores. The increase of surface area from 3 m<sup>2</sup>/g (BCY15) to 8 m<sup>2</sup>/g in BCY15/Ni confirms the creation of the new mesopore system. The pore size distribution (PSD) (Fig. 2b) illustrates uniform pore system for BCY15 powder and presence of macropores (above 50 nm). After the incorporation of Ni in BCY15, the PSD curve of BCY15/Ni takes a poly-dispersed character in the 3–20 nm area. The comparison with BCY15 matrix signifies a creation of new mesopores.

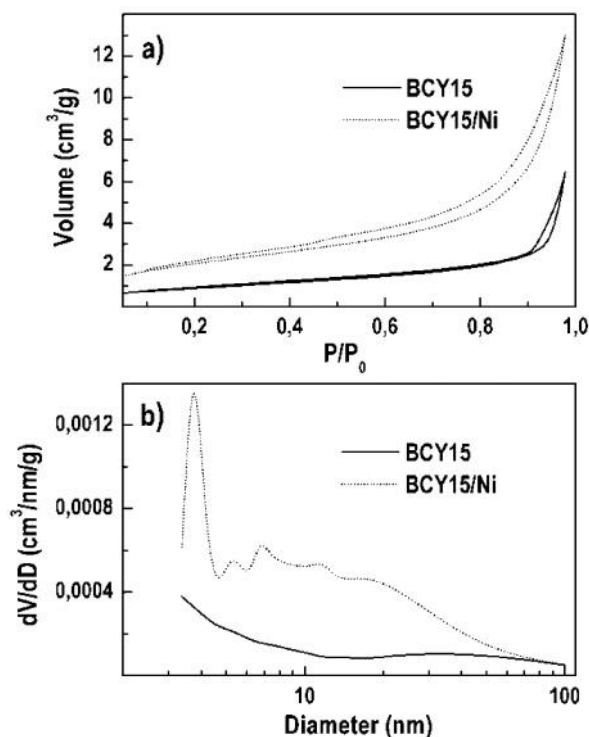


**Fig. 2.** N<sub>2</sub> sorption analysis of BCY15 and BCY15/Ni: (a) adsorption–desorption isotherms and (b) pore size distribution.

The value of BET parameter **C** increases from 90 for BCY15 to 97 for BCY15/Ni indicating an increase of adsorbent–adsorbate interaction in BCY15/Ni that may be assigned to the changes in the polarity of the surface as a result of the formation of mesoporous Ni-containing phase. Constant **C** is related to the interaction force of adsorbent–adsorbate [23].

SEM image of BCY15 powder reveals relatively homogeneous porous structure consisting of particles similar in kind and shape, randomly distributed on the surface (Fig. 3a).

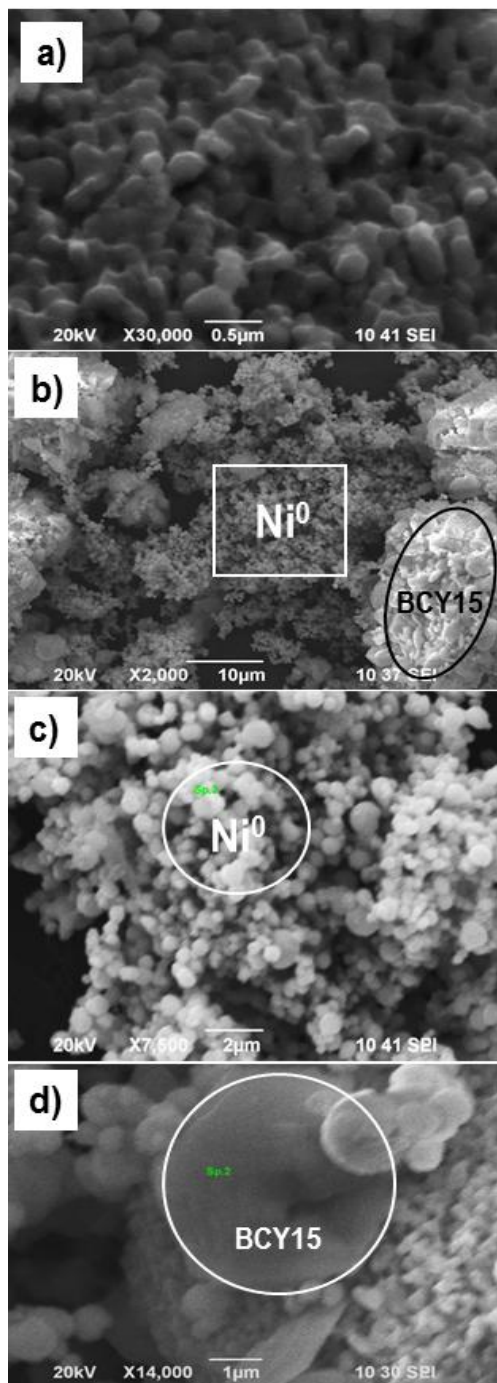


**Fig. 3.** Micrographs of BCY15 (a) and BCY15/Ni (b, c, d) solids.

The presented images of BCY15/Ni (Fig. 3b-d) illustrate change in the morphology of BCY15 ceramic matrix after nickel deposition. Fine mono-dispersed spherical metal nickel particles (Fig. 3b and c) along with fragments of BCY15 mixed or covered with angulated particles different in size can be easily identified on the surface of BCY15/Ni (Fig. 3b,d).

EDS surface composition analyses of BCY15 and BCY15/Ni are collected in Table 3. As it can be observed the composition of anode matrix is changed in a considerable extent after incorporation of metal nickel BCY15/Ni. The data testifies domains for metal nickel (Fig. 3c) and anode matrix (Fig. 3d) respectively, and confirms the results from PXRD analyses.

**Table 3.** EDS surface composition of BCY15 and BCY15/Ni.

Element (wt. %)	O	Ni	Ba	Ce	Y
BCY15	16.54	-	42.34	36.95	4.17
BCY15/ Ni*	14.83	76.38	5.93	2.86	0
BCY15/ Ni**	15.69	6.27	74.01	4.04	0

\*from Fig. 3c; \*\*from Fig. 3d

For analysis of the Ni network quality in a real anode, the standard ceramic technology was used for the preparation of pressed tablets from BCY15/Ni (cold pressing, 3t/5 min), followed by their sintering in air at 1200°C for 5 h. The volumetric shrinkage of the tablet was about 6%.

The thermal treatment of BCY15/Ni in air provokes an oxidation of the metal nickel phase to NiO. PXRD patterns (Fig. 4a) display reflections of well-organized NiO phase with lattice parameters ( $a$  and  $V_{\text{cell}}$ ) close to the standard NiO (JCPDS file 00-047-1049) (Table 2). Well-defined reflections of BaCeO<sub>3</sub> phase can be detected, signifying partial recovery of the perovskite structure. Furthermore, an appearance of two poorly crystallized new phases is found, namely BaNiO<sub>2.36</sub> with hexagonal crystal symmetry (JCPDS file 00-047-0089) and cubic Y<sub>0.10</sub>Ce<sub>0.90</sub>O<sub>1.95</sub> (JCPDS file 01-075-0174). Consequently, the sintered product is a rather complex phase mixture.

After sintering, a step-wise standard reduction procedure was performed at 750°C for 5 h with a H<sub>2</sub>/N<sub>2</sub> gaseous mixture to reduce NiO in the anode material to form BCY15/Ni composite. The first reduction step was accomplished with gaseous

mixture of  $N_2$  (flow rate of  $35 \text{ nml/min} \cdot \text{m}^{-2}$ ) and  $H_2$  (flow rate of  $10 \text{ nml/min} \cdot \text{m}^{-2}$ ) for 60 min. The second reduction step concerns treatment only with  $H_2$  (flow rate of  $35 \text{ nml/min} \cdot \text{m}^{-2}$ ) for 60 min.

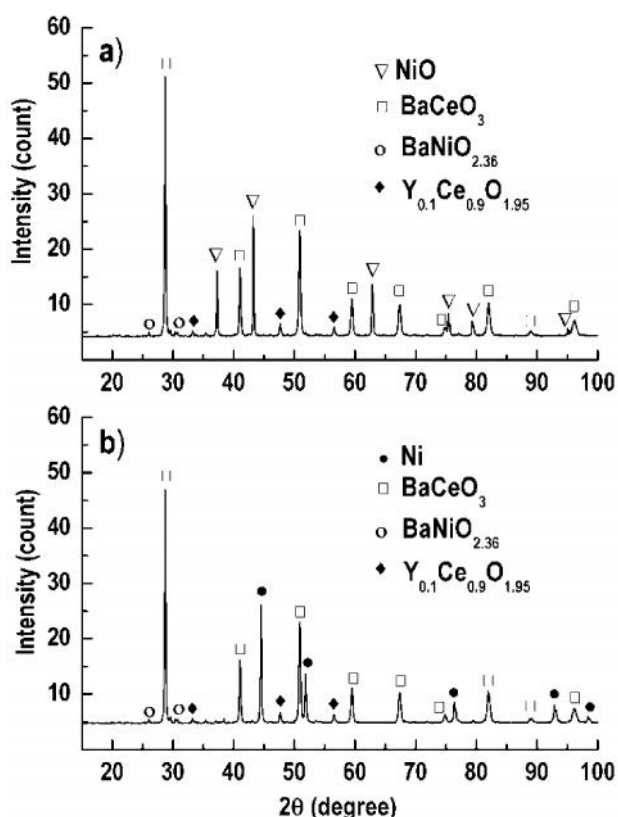


Fig. 4. XRD patterns of BCY15/Ni: (a) sintered and (b) reduced.

The PXRD analyses show that the reduction of sintered BCY15/Ni solid leads only to full conversion of NiO in the metal Ni state. Well organized reflections of metal Ni with cubic lattice symmetry are recorded (Fig. 4b) along with the  $BaCeO_3$ ,  $BaNiO_{2.36}$  and  $Y_{0.10}Ce_{0.90}O_{1.95}$  phases. It may be summarized that the activation of the BCY15/Ni cermet by reduction with  $H_2$  does not cause additional structural changes. The calculated metal Ni lattice parameters values (Table 2) are also comparable to those of the standard metal Ni (JCPDS file 00-004-0850). In addition, the reduction procedure causes growth of the metal Ni crystallites.

For *in situ* analysis of the Ni network performance a recently developed impedance approach for direct measurements of the Ni cermet electronic conductivity in the classical Ni-YSZ was applied [24]. The measurements are carried out directly on “bare” anodes sandwiched between two Ni contact nets. The direct analysis starts in the beginning of the reduction stage which was performed at  $750^\circ\text{C}$ . In this way, the electronic conductivity is directly measured giving

information about for the nickel network formation in the bulk anode structure.

The results obtained from the impedance measurements of BCY15/Ni anode cermet show that prior to the reduction, the cermet BCY15/Ni demonstrates a fairly low resistance of  $31.5 \Omega$  (Fig. 5a), which suggests the presence of some percolation and indicates that the sintering procedure induces only partial oxidation of the metal Ni. The reduction proceeds quickly as the resistance of Ni net decreases down to  $70 \text{ m}\Omega$  for about 20 min and this value remains unchanged until the end of the reduction cycle (Fig. 5b).

Similar phenomenon was observed in experiments with commercial YSZ/Ni cermet, namely Ni/YSZ produced by SOLIDpower (Fig. 5c).

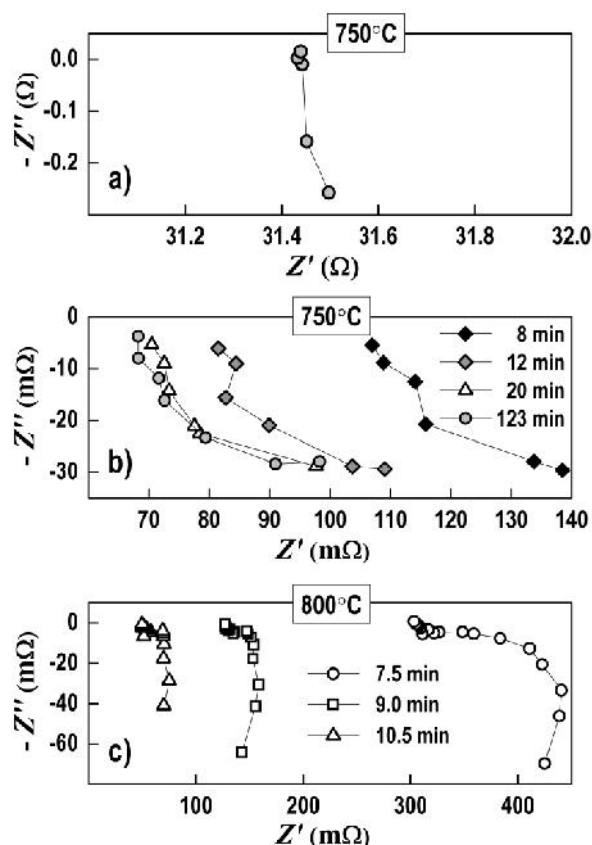


Fig. 5. Impedance diagrams of: ( ) BCY15/Ni before the beginning of the reduction, (b) BCY15/Ni after 8, 12, 20 and 123 min reduction and ( ) Ni/YSZ anode cermet (SOLIDpower) after 7.5, 9.0 and 10.5 min of reduction.

## CONCLUSIONS

The results obtained in this study show that BCY15/Ni anode cermet demonstrated electrochemical performance similar to that of the commercial NiO-based anode cermets in respect to the electronic conductivity of the Ni net. The registered characteristics of BCY15/Ni anode

cermet make it suitable for application in BCY-based pSOFC.

The wet-chemical reduction route using hydrazine in an aqueous medium is a promising approach providing better conditions for nickel introduction in the anode ceramic matrix in comparison with the classical solid state ceramic approach.

The preparation of Ni/BCY15 in aqueous medium results in partial reorganization of the initial BCY15 structure due to the hydrophilic properties of the ceramic matrix. A fully preservation of the anode ceramic matrix in the Ni/BCY15 cermet may be achieved if the synthesis is performed in an anhydrous environment, which is the subject of our future investigations.

**Acknowledgements:** The research leading to these results has received funding from Bulgarian NSF under grant No E02/3/2014.

#### REFERENCES

1. A. Stambouli and E. Traversa, *Renew. Sust. Energ. Rev.*, **6**, 433 (2002).
2. R. Ormerod, *Chem. Soc. Rev.*, **32**, 17 (2003).
3. P. Frontera, V. Modafferi, F. Frusteri, G. Bonura, M. Bottari, S. Siracusano, P. Antonucci, *Int. J. Hydrogen Energy*, **35**, 11661 (2010).
4. A. Lapina, C. Chatzichristodoulou, P. Holtappels, M. Mogensen, *J. Electrochem. Soc.*, **161**, F833 (2014).
5. K. Knight, *Solid State Ionics*, **145**, 275 (2001).
6. E. Fabbri, D. Pergolesi, E. Traversa, *Chem. Soc. Rev.*, **39**, 4355 (2010).
7. H. Iwahara, *Solid State Ionics*, **77**, 289 (1995).
8. N. Ito, M. Iijima, K. Kimura, S. Iguchi, *J. Power Sources*, **152**, 200 (2005).
9. A. Essoumhi, G. Taillades, M. Taillades-Jacquín, D. Jones, J. Rozière, *Solid State Ionics*, **179**, 2155 (2008).
10. L. Chevallier, M. Zunic, V. Esposito, E. Di Bartolomeo, E. Traversa, *Solid State Ionics*, **180**, 715 (2009).
11. J. Dailly, M. Marrony, *J. Power Sources*, **240**, 323 (2013).
12. J. Dailly, M. Marrony, G. Taillades, M. Taillades-Jacquín, A. Grimaud, F. Mauvy, E. Louradour, J. Salmi, *J. Power Sources*, **255**, 302 (2014).
13. T. Higuchi, T. Owaku, Y. Iida, E. Sakai, M. Kobayashi, H. Kumigashira, *Solid State Ionics*, **270**, 1 (2015).
14. Y. Matsuzaki, I. Yasuda, *Solid State Ionics*, **152–153**, 463 (2002).
15. E. Fabbri, D. Pergolesi, E. Traversa, *Sci. Technol. Adv. Mater.*, **11** (2010) article 044301.
16. Q. Fu, F. Tietz, D. Sebold, S. Tao, J. Irvine, *J. Power Sources*, **171**, 663 (2007).
17. A. Safari, R. K. Panda, V. F. Janas, *Ferroelectricity. Materials, Characteristics, and Applications, Key Engineering Materials*, **122–124**, 35 (1996).
18. R.J. Bell, G.J. Millar, J. Drennan, *Solid State Ionics*, **131**, 211 (2000).
19. J. Park, E. Chae, S. Kim, J. Lee, J. Kim, S. Yoon, J.-Y. Choi, *Mater. Chem. Phys.*, **97**, 371 (2006).
20. G.-Y. Huang, S.-M. Xu, G. Xu, L.-Y. Li, L.-F. Zhang, *Trans. Nonferrous Met. Soc. China*, **19**, 389 (2009).
21. Budapest Neutron Centre, Progress report 2008–2009, Edited by R. Baranyai, M. Makai, L. Rosta, Budapest, September 2011; <http://www.bnc.hu>.
22. F. Rouquerol, J. Rouquerol, K. Sing, In *Adsorption by Powders and Porous Solids, Principle, Methodology and Applications*, Academic Press, New York, 1999.
23. A. Lecloux, J. Pirard, *J. Colloid Interf. Sci.*, **70**, 265 (1979).
24. D. E. Vladikova, Z. B. Stoyanov, Z. Wuillemin, D. Montinaro, P. Piccardo, I. Genov, M. Rolland, *ECS Transactions*, **68 (1)**, 1161 (2015).

Ni

I.

A

1\*, 1, 2, 2, 1, 2

1, 11, 1113

10, 1113

2017 ; 11 2017 .

( )

BaCe<sub>0.85</sub>Y<sub>0.15</sub>O<sub>2.925</sub> (BCY15) ABO<sub>3</sub>

BCY15/Ni

BCY15

BCY15/Ni

BCY15/Ni

Ni

NiO. BCY15/Ni BCY-

BCY15,



## Effect of sintering temperature on performance and durability of HT-PEFC cathodes

G. Borisov<sup>1\*</sup>, S. Avramov<sup>1</sup>, E. Petkucheva<sup>1</sup>, E. Lefterova<sup>1</sup>, E. Slavcheva<sup>1</sup>, W. Lehnert<sup>2</sup>

<sup>1</sup> Acad. E. Budevski Institute of Electrochemistry and Energy Systems, Bulgarian Academy of Sciences, 10 Acad. G. Bonchev St., Sofia 1113, Bulgaria

<sup>2</sup> Institute of Energy and Climate Research (IEK-3), Forschungszentrum Jülich GmbH, Germany

Received March 10, 2017      Revised March 30, 2017

The design of the electrodes applicable for high temperature PEM fuel cells (HTPEFC) is a delicate balancing of the transport media. The conductivity of gases, electrons, and protons must be optimized in order to provide efficient transport to and from the electrochemical active area. This article presents the effects of heat treatment on the properties of the anode gas diffusion electrode integrated in a membrane electrode assembly (MEA) with phosphoric acid doped poly-benzimidazol membrane. The sintering procedure reflects on the catalyst activity as well as on the stability and durability of the electrode. The electrochemical performance of the cell was investigated by steady state polarization curves, potential-dynamic curves and electrochemical impedance spectroscopy. It was found, that the different pore size distribution in the active catalytic layer treated at different temperatures affects the transport limitations of the reaction. The optimal cell performance is established for the electrode sintered at 340°C. The measured degradation rate is close to 0.001 $\mu$ V/h.

**Key words:** PEM fuel cell, degradation, catalysts, HT-PEFC cathodes.

### INTRODUCTION

The high-temperature polymer electrolyte fuel cell (HT-PEFC) is a chemical to electrical energy converting electrochemical system operating in the temperature range 160 - 200°C. It offers a number of advantages compared to the low temperature Nafion®-based PEMFC operating at 80-90 °C [1-3]. First of all, the higher operating temperature improves the kinetics and increases the exchange current density of both hydrogen oxidation (HOR) and oxygen reduction (ORR) reactions. Secondly, there is no need for complex water management which makes the electrochemical system much simpler. Furthermore, HT-PEFC has a much higher CO tolerance and can work with reformat gas, particularly when middle distillates (kerosene, diesel, heating oil) are used to provide the necessary hydrogen. Therefore, HT-PEFC is considered as the next generation alternative power supply in ships, trains, buses, and other transport and stationary applications [4-6]. The electrolytes used in HT-PEMFC are mainly PBI-based (poly-benzimidazol) or hydride PBI-based polymers, which are capable to withstand the high operative temperatures [7]. In addition to the thermal stability, the PBI membranes exhibit excellent oxidative stability and mechanical flexibility. However, to achieve high proton conductivity,

these membranes have to be doped with concentrated phosphoric acid. The level of membrane doping and the MEA assembling procedure are of key importance for the efficient functioning of the whole fuel cell system [8-10]. Until now, the achieved level of phosphoric acid inside the membrane is around 400 wt. % which provides excellent proton conductivity (0.05S.cm<sup>-1</sup>) and low crossover of the reactant gases. Nevertheless, the HT-PEFC performance is still lower compared with the LT PEMFC. The main reason is that the liquid phosphoric acid impedes the transport of the gaseous reagents and thus, the electrochemical reactions, due to the low solubility of oxygen in phosphoric acid and adsorption of the phosphate anions on the catalyst (Pt) surface. Another major problem in HT-PEFC is the leakage of the phosphoric acid out of the membrane which increases the resistance of the polymer electrolyte, causes corrosion problems, and decreases the cell energy efficiency [11-13]. In order to prevent these detrimental phenomena, a delicate balance between the gas delivery management, electron flow, and proton conductivity must be achieved, providing an efficient transport to and from the electrochemical reaction zone without degradation of the electrodes. This is accomplished through careful consideration of the gas diffusion electrode (GDE) architecture - catalytic layer, gas diffusion layer, and the distribution of the respective conducting network.

The HT-PEFC gas diffusion electrodes have a rather complex structure. The mechanical stability, electrical conductivity and gas delivery are

---

To whom all correspondence should be sent:  
E-mail: gal.rusev@iees.bas.bg

provided by the gas diffusion layer (GDL), usually water proved carbon paper, while the gas distribution is controlled mainly by the top microporous layer (MPL) built from electro-conductive carbon material with high surface area and a hydrophobic polymer. On the top of MPL layer a catalytic layer (CL) is spread out which beside the carbon supported catalyst contains also a proper binding material. An optimal catalyst to binder ratio is required to ensure the integrity of the CL and achieve large triple phase boundary for the proceeding of the partial electrode reactions which in turn, improves both performance and catalyst utilization during the fuel cell operation [14-18]. The size and distribution of the pores in the catalytic layer also play a role for stability and durability of the electrodes and thus, for the service life of the HT-PEFC [11]. To keep the phosphoric acid inside the polymer membrane and far away from the produced water, the binders usually are highly hydrophilic polymers such as polybenzimidazol (PBI) [18-20], polytetrafluoroethylene (PTFE) [21-22], polyvinylidene difluoride (PVDF) [23-25]. In order to obtain catalytic layer with homogeneous pore distribution, excellent mass transport and increased area of the reactive zone (the triple-phase boundary), the GDEs before assembling have to be treated thermally (sintered) at temperatures close to the melting point of the used binding material. The exact temperature and the time of the sintering affect strongly the pore distribution and hydrophobicity of the electrode. In the literature there are only few papers dealing with the dependence of HT-PEFC performance durability on the parameters of the electrode thermal pretreatment. Some authors (MinJoong and Ai Suzuki), [24] reported that a benign thermal pretreatment of GDE electrodes at 150°C, aiming only at evaporation of the organic solvent used for the preparation of the catalytic ink, improves the cell performance. Kim et al. [26] showed that the GDL sintering in the temperature range 300-350°C improves the cell performance, while at more elevated temperatures it drops back down.

The objective of this work is to study in details the influence of the sintering temperature on the micro-pores size and distribution in HT-PEFC cathode containing polytetrafluoroethylene binder in the catalytic layer, and to elucidate the resulting effects on the electrode active surface area, cell efficiency and durability.

## EXPERIMENTAL

The GDEs under study consisted of commercial gas diffusion layer with microspores layer on top

(H2315, Freudenberg) and a laboratory prepared catalytic layer with  $1\text{mg}_{\text{Pt}}\cdot\text{cm}^{-2}$  loading, spread on the GDL using a "Doctor Blade" technique. The measured thickness of the as-prepared GDEs was about 40  $\mu\text{m}$  and the geometric area - 14,44 $\text{cm}^2$ . The catalytic ink was prepared by ultrasonic horn and contained a mixture of carbon supported Pt (HiSpectm Fuel cell catalysts - 2000) and PTFE binder (commercial polymer suspension, Daneontm TFM 1700 PTFE). The prepared electrodes were sintered for 30 min at different ramp temperature (320, 340, 360°C), reached gradually with increment of 5 °C per min. The phase composition, surface structure, and morphology of the catalytic layers were investigated post mortem by X-ray diffraction (XRD, X-ray diffractometer Philips APD15). The diffraction data were collected at a constant rate of  $0.02^{\circ}\text{s}^{-1}$  over an angle range of  $2\theta = 10 - 90$  degrees. The size of Pt crystallites was determined by Scherrer equation [27]. The thermal behavior was investigated by TG\_DTA and DSC methods using TA Instruments SDT 2960 Simultaneous DTA-TGA/DSC-TGA and DSC Q1000 (V9.9 Build 303). The measurements were carried out in the temperature range 0 – 400°C with Nitrogen as purge gas. In TG/DTA experiments a heating rate of 2 K/min was used, while in DSC measurements 10 fold higher (20K/min) heating/cooling rate was applied in order to increase the sensitivity.

The sintered electrodes were integrated in membrane electrode assemblies (MEA) using AB-PBI membrane (FuMA-Tech) and commercial cathodes (Pt/XC72). The AB-PBI membrane was doped with phosphoric acid following the procedure described in [25]. The doping level was 400 wt. % and the membrane thickness - 100  $\mu\text{m}$ . The performance of thus prepared MEA was investigated in a HT-PEFC single cell at 160°C. The reagent gasses feeding the anode and cathode compartments were pure hydrogen and air at ambient pressure and flow rates corresponding to the stoichiometric factor cathode/anode 2/2. The MEA was run at  $j=200\text{ mA}\cdot\text{cm}^{-2}$ . The galvanostatic experiments were interrupted once at every 24 hours (break-in procedure) to record a control cathode polarization curve (again in galvanostatic mode with current increment of  $50\text{ mA}\cdot\text{cm}^{-2}$ ) and an impedance spectrum in the frequency range of 100 MHz–100 kHz applying an AC voltage with amplitude of 5 mV. In order to evaluate the anode stability, the method of cyclic voltammetry was used as the cathode side of the cell was shunted, replacing the hydrogen by inert gas in order to prevent degradation of the catalytic layer. The CV

curves were recorded at potential scan rate of 50 mV.s<sup>-1</sup> in the range (50mV to 500 mV).

## RESULTS AND DISCUSSION

Figure 1 presents DSC curves of gas diffusion electrode (GDE) consisting of commercial gas diffusion layer (GDL) H2315 and a top laboratory prepared catalytic layer (CL) in which a carbon-dispersed Pt catalyst (0.2 mg.cm<sup>-2</sup>) is mixed with 40% PTFE binder to obtain a catalytic ink spread on the GDL using a “Doctor Blade” technique. During DSC analysis the temperature is scanned in the range 0-400°C.

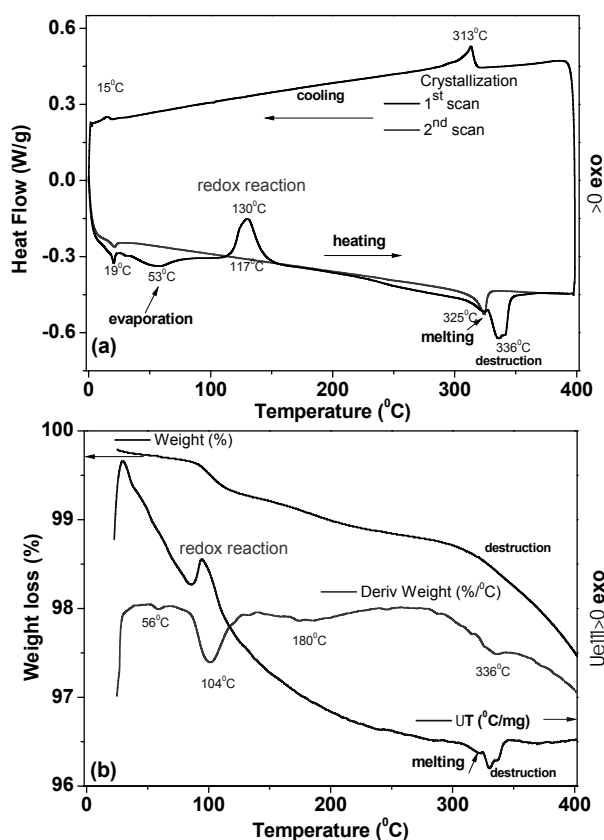


**Fig. 1.** DSCs: (a) and TG/DTG/DTA; (b) curves of the GDE under study.

In the first heating scan three endothermic and one endothermic peaks are registered (at 19, 53, 325-336, and 130°C, respectively). During the cooling scan only two exothermic peaks appeared (at 313 and 15 °C) corresponding to the first and last exothermic peaks (at 19 and 325-336°C). These two peaks are reversible since they appear also during the second heating scan (in red). The first reversible peak (that at 19 °C) is due to the PTFE polymorphous transition, while the one with doublet shape (at 325-336 °C) is related to the phase transformations of PTFE. According to some

authors the observed doublet shape is due to the non-homogeneity of the PTFE in the CL [28]. Another reason could be consecutive processes of PTFE melting and destruction. The endothermic peak at 54 °C is connected with evaporation of the alcohol remains in the microspores of CL. The irreversible exothermic peak observed at 130°C most probably is due to oxidative destruction since it proceeds with loss of weight. Such a process is also registered on TG/DTG/DTA curves (Fig. 1b), although there the peak appears at somehow lower temperature, which is due to the applied tenfold lower heating rate. The weight lost registered on the TG curve in the range 320-340°C implies a superposition of PTFE melting and destruction processes, which might lead to changes in the porosity of CL and MPL of the GDE.

In order to check this assumption, the porosity of the catalytic layer before and after sintering at different temperatures (320, 340, and 360°C) is studied by standard porosimetry (Fig.2).

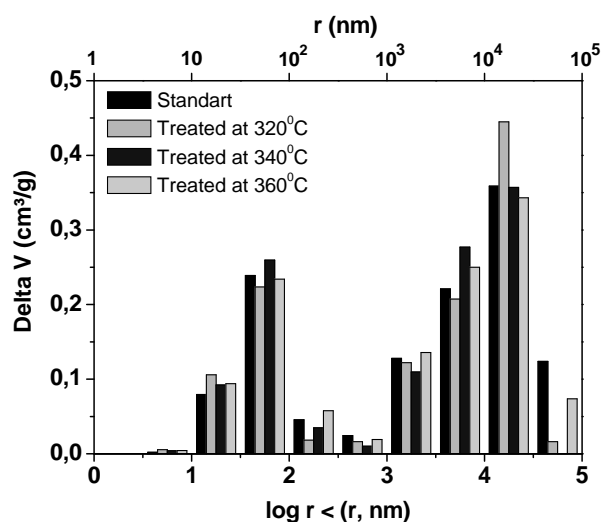


**Fig. 2.** Pore size distribution in CL of GDEs under study.

It is found that the sample treated at 320 °C has a prevailing number of pores with size around 10-50 μm, in similarity to the non-treated electrode. In contrast, for the samples treated at higher temperature than the PTFE melting point, the size of the pores varies in a very broad range – from 10 nm to 100 μm, although the majority of the pores are grouped in two main groups – nanopores with size in the range 10-100 nm and micropores with size 1-5 μm. It can be assumed that the formation of the non-sized group of pores is related to destruction of the PTFE at higher temperatures.

The surface area of the as prepared and sintered electrodes was measured by BET analysis. The results obtained are presented in Table 1. They show a clear trend for decrease of the surface area

with increasing the sintering temperature. The difference between the nontreated electrode and that sintered at 320 °C (21.0 and 17.9 m<sup>2</sup>.g<sup>-1</sup>, respectively) is the biggest one.

**Table 1.** Influence of sintering temperature on the GDE surface area.

Temperature, °C	Surface area, m <sup>2</sup> .g <sup>-1</sup>
as prepared	21.0
320	17.9
340	16.1
360	15.7

The GDE sintered at different temperatures were integrated as cathodes in MEA with a phosphoric acid doped PBI membrane against a self-made anode (Pt/XC72R) and tested in HT-PEFC single cell. The measured open circuit voltages were similar for all investigated samples - approximately 0.95V at 160 °C.

The performance tests were carried out in a galvanostatic mode at constant load of 0.2 A.cm<sup>-2</sup>. In order to follow the occurring degradation phenomena, every 24 hours the performance tests were interrupted to record a control polarization curve and an impedance spectrum. Figure 4 presents the *E/j* curves recorded on the as-prepared MEA (3a) and on MEA worked for 460 h (3b). The results show that the long term operation leads to changes in MEA performance. Initially, the highest current densities were obtained on MEA with a standard (not sintered) cathode. The performance of MEA with cathode sintered at 320 °C was very similar, while for those treated at higher temperatures the obtained current densities were much lower. The worse performed MEA was the one with the cathode sintered at 360 °C.

However, after 460 hours of operation under constant current, the order in which the MEA performed changed. The standard electrode showed worse performance with degradation rate of 54.3μV. h<sup>-1</sup>. The MEAs with the cathodes sintered at 320 °C and 340 °C reached current density of about 0.5 A cm<sup>-2</sup> at 0.5 V, while the calculated degradation rates (Table 1) showed much higher stability for the 340°C sintered cathode. The lowest performing MEA again was the one with the cathode sintered at 360 °C with degradation rate of 86.5 μV.h<sup>-1</sup>. Obviously, the sintering at temperatures quite above the melting point of the binder, leads to decrease in the cell efficiency.

Figure 4 presents the evolution of *E/j* curves with service time of the best performing MEA (cathode sintered at 340 °C).

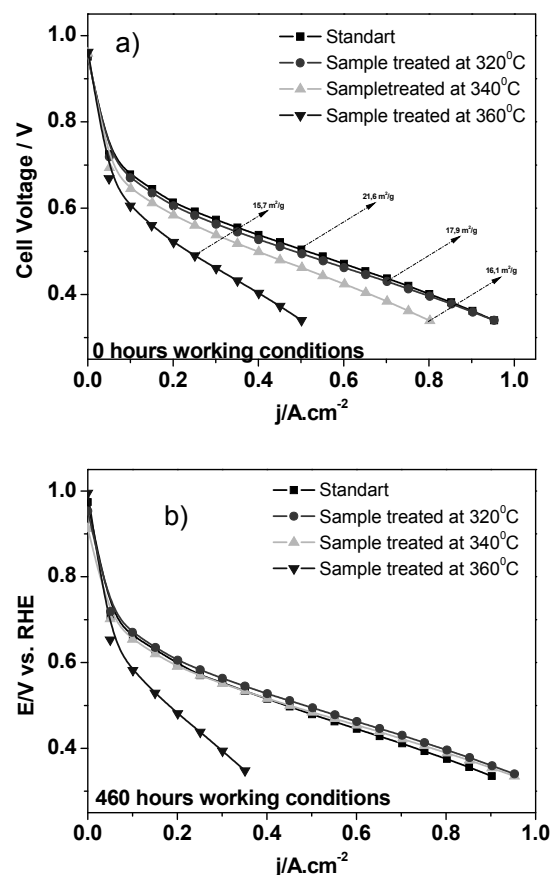


**Fig. 3.** *E/j* curves of MEA with cathodes sintered at varying temperatures; a) before durability tests; b) after 460 h of operation; scan rate 1 mVs<sup>-1</sup>; cell temperature 160 °C.

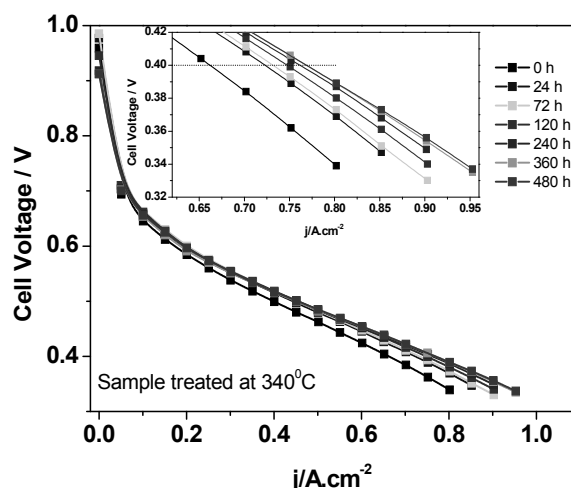


**Fig. 4.** *E/j* curves after different time of operation at 0.2 Acm<sup>-2</sup> at 160 °C of MEA with cathode sintered at 340 °C.

The performance is high without visible degradation. After the low drop of the current density observed in the low overpotential range during the first 72 h of operation, there was stabilization and even a slight improvement in the cell performance. The current density measured at

0.4V changed from 0.66A.cm<sup>-2</sup> in the beginning of the durability tests to 0.75 A.cm<sup>-2</sup> and 0.77 A.cm<sup>-2</sup> after 120 h and 480 h, respectively.

The break-in procedure used to characterize durability of the prepared MEA included also impedance measurements.

The Nyquist plots shown in Fig. 6 are typical for a PEMFC and contain three overlapped impedance semicircles corresponding to different electrochemical electrode processes. The diameter of the distinct loop is a measure for the respective

resistance [29]. Since the charge transfer resistance of the HOR is typically much smaller than the ORR one, the anode reaction HOR is only hinted at high frequencies (~10 kHz), while the cathode reaction (ORR) at middle frequency range (1kHz-1Hz), as well as mass transport at the lowest frequencies are well distinguished. The high-frequency intercept of the impedance with the real axis represents the total cell ohmic resistance,  $R_{el}$ , including resistances of the cables, electrodes and the electrolyte membrane (Fig. 5).

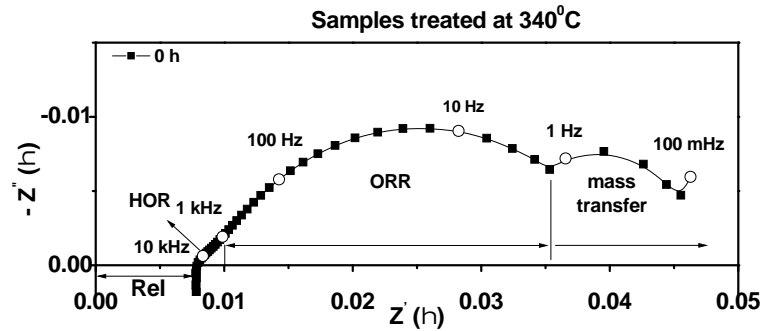


**Fig. 5.** Impedance curve of ORR in HT-PEFC single cell. Cell temperature 160 °C, stoichiometric factors Cathode/Anode = 2/2, gas temperature on both cameras 160 °C, current density 0.2A.cm<sup>-2</sup>.

To analyze the possible changes on the anode side of the MEA, which could affect the cell performance, cyclic voltammetry was applied. The cathode compartment of the cell was shunted letting in an inert gas and the potential was scanned in the range -0.5V and 0.5V with scan rate of 50 mV s<sup>-1</sup>. The results obtained are presented in Fig. 6. The CV curves do not change with time both in shape and current density, which is a proof for the anode stability and durability.

The Nyquist plots presented in Fig. 7 confirm the lack of MEA degradation. They show a reduction of  $R_{el}$  over the time (inset in Fig. 7) and facilitation of the mass transfer process. After the initial reduction of the ORR charge transfer resistance in the first 24 hours, it increases slightly, which could be explained with the Pt crystallites growth.

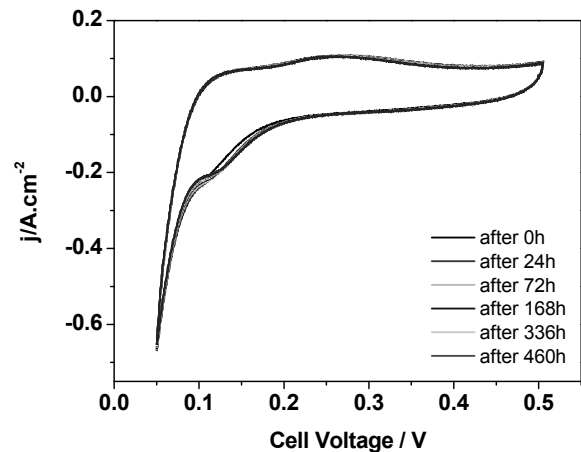


**Fig. 6.** CV curves on the anode side of the cell. Scan rate 50mV.s<sup>-1</sup>, cell temperature 160 °C, stoichiometric factors Cathode/Anode = 2/2, range from 50mV to 500mV.

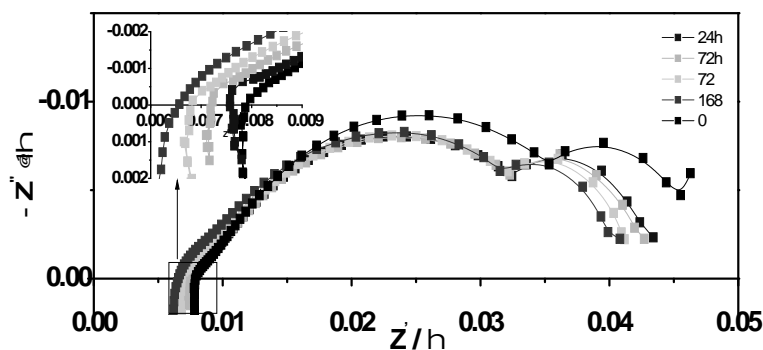


**Fig. 7.** Impedance curves of ORR in HT-PEFC single cell. Cell temperature 160 °C, stoichiometric factors Cathode/Anode = 2/2, gas temperature on both cameras 160 °C, current density 0.2 A.cm<sup>-2</sup>.

In order to investigate the assumed Pt particle agglomeration in dependence of the treatment temperature and working time, the electrodes were analyzed by XRD. Fig 8(a) presents XRD patterns of all electrodes under study before the performed long term galvanostatic tests. The calculated values of the Pt particle size summarized in Table 2 show some increase of the crystallites size for the electrodes treated at 340 and 360 °C. This is not in accordance with the obtained data for the surface area of the electrodes (Table 1) and suggests that the registered decrease in the electrode specific surface area with the time of sintering is not only due to agglomeration of Pt crystallites, but is also related to the melting and degradation of the PTFE which lead to changes in the pores size and distribution and thus, to governing the transport phenomena of the cathode.

stronger the agglomeration of the Pt crystallites than the sintering temperature of electrode.

**Table 2.** Crystallite size calculated from XRD spectra by Scherer equation.

Sample	Temp. [°C]	time [h]	Cryst.size nm [111]
TT	standard	-	2.4
TT	320	-	2.4
TT	340	-	2.8
TT	360	-	2.8
cathode	standard	480	6.5
anode	standard	480	3.8
cathode	340	480	6.4
anode	340	480	3.6

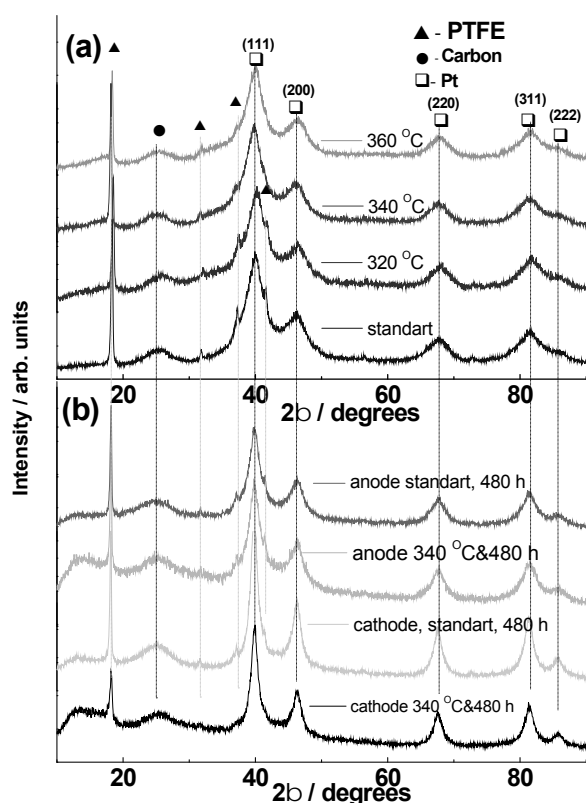


**Fig.8.** XRD patterns of the (a) as prepared electrodes and (b) after 480 h of operation in a MEA (as cathode or anode) at constant current of 0.5 A cm<sup>-2</sup>.

In Figure 8(b) are presented XRD patterns of two electrodes (untreated and treated at 340°C) after 480 hours “in operando” mode. After the end of the long term test both investigated samples have similar particle size of about 6.4nm.

These results prove that the prolonged galvanostatic operation of the cathode affects much

## CONCLUSIONS

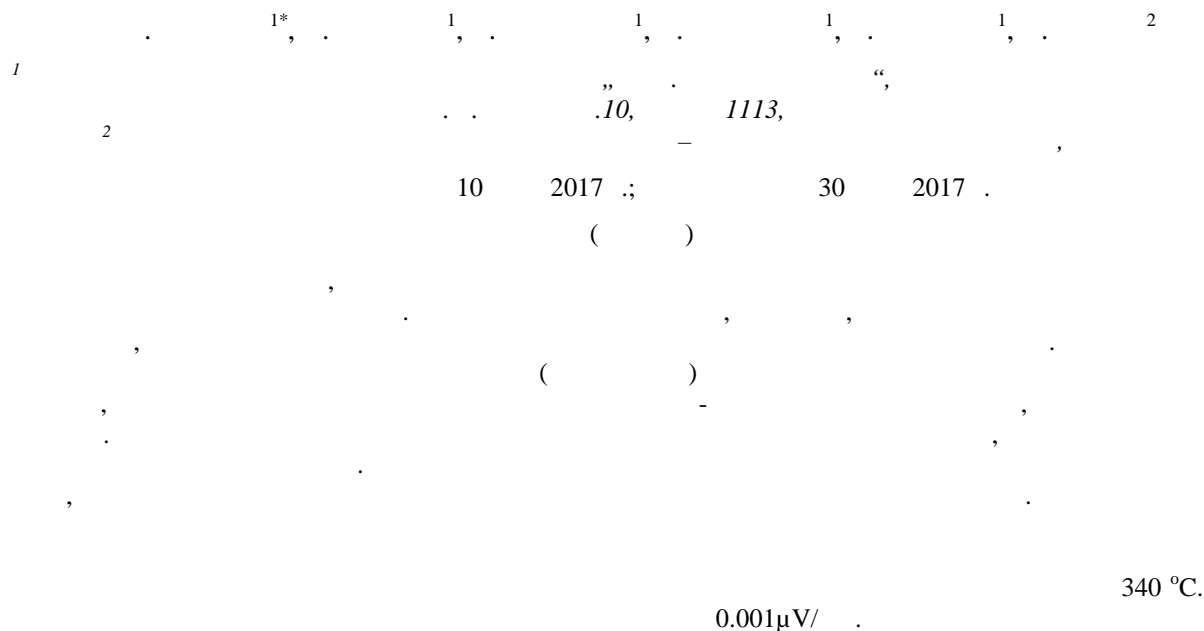
The results obtained proved that the sintering procedure improves essentially the MEA durability. It is necessary only for the anode side where the produced water steam carry out partly phosphoric acid, which leads to degradation on the MEA performance. The registered changes in the GDE structure, porosity, as well as the established redistribution of the pores in the catalyst layer, prevent the leakage of the phosphoric acid from the membrane, thus avoiding loss of proton conductivity and degradation of the catalytic layer. It was found that the optimal temperatures for anode sintering is in the range 320 - 340 °C. Further increase of the sintering temperature leads to loses of electrochemical active surface area and decrease of the cell efficiency. The agglomeration process is influenced much more by working time rather than thermal treatment.

**Acknowledgements:** This research was supported by National Science Fund, Bulgaria, Contr. No. DTK – 02/02 and the German Academic Exchange Service (DAAD).

## REFERENCES

1. Q. Li, J. Jensen, R. Savinell, N. Bjerrum, *Prog. Polym. Sci.*, **34**, 449, (2009).
2. Q. Li, R. He, J. Jensen, N. Bjerrum, *Fuel Cells*, **4**, 47, (2004).
3. L. Zhang, S. Chae, Z. Hendren, J. Park, M. Wiesner, *Chem. Eng. J.*, **204**, 87, (2012).
4. D. Boettner, M. Moran, *Energy*, **110**, 255, (2004).
5. P. Ghosh, U. Vasudeva, *Hydrogen Energy*, **36**, 3138, (2011).
6. A. Arsalis, A. Nielsen, S. Kær, *Hydrogen Energy*, **36**, 9815, (2011).

7. Q. Li, J. Jensen, R. Savinell, N. Bjerrum, *Polymer Science*, **34**, 449, (2009).
8. H. Tang, S. Wang, S. Jiang, M. Pan, *J. Power Sources*, **170**, 85, (2007).
9. T. Suzuki, S. Tsushima, S. Hirai, *Hydrogen Energy*, **36**, 12079 (2011).
10. S. Thanasilp, M. Hunsom, *Fuel cell*, **89**, 379 (2010).
11. J. Asensio, E. Sanchez, P. Gomez-Romero, *Chemical Society Reviews*, **39**, 3210, (2010).
12. S. Neophytidis, S. Zaafairatos, G. Papakonstantinou, J. Jaksic, F. Paloukis, *Int. J. Hydrogen Energy*, **30**, 393, (2005).
13. M. Min, J. Cho, K. Cho, H. Kim, *Electrochimica Acta*, **45**, 4211, (2000).
14. L. Xiong, A. Kannan, A. Manthiram, *Electrochemistry Communications*, **4**, 898 (2002).
15. S. Kraemer, M. Puchner, P. Jannasch, A. Lundblad, G. Lindbergh., Gas diffusion electrodes and membrane, **63**, 1856 (2008).
16. J. Lobato, P. Cañizares, M. Rodrigo, J. Linares, F. Pinar, *Journal of Hydrogen Energy*, **32**, 418 (2010).
17. C. Pan, Q. Li, J. Jensen, R. He, L. Cleemann, M. Nilsson, N. Bjerrum, Q. Zeng, *Journal of Power Sources*, **161**, 622 (2010).
18. A. Ong, G. Jung, C. Wu, W. M. Yan, *International Journal of Hydrogen Energy*, **18**, 249, (2010).
19. C. Wannek, W. Lehnert, J. Mergel, *Journal of Power Sources*, **192**, 258, (2009).
20. M. Mamlouk, K. Scott, *International Journal of Energy Research*, **35**, 507, (2011).
21. Y. Oono, A. Sounai, M. Hori, *Journal of Power Sources*, **210**, 366, (2012).
22. Y. Oono, T. Fukuda, A. Sounai, M. Hori, *Journal of Power Sources*, **1/5**, 95, (2009).
23. B. Tripathi, M. Kumar, V. Shahi, *Journal of Membrane Science*, **340**, 52, (2009).
24. A. Modestov, M. Tarasevich, V. Filimonov, N. Zagudaeva, M. Kim, G. Jeong, K. Eom, E. Cho, J. Ryu, H. Kim, H. Kwon, *Journal of Advanced Functional Materials*, **9**, 367, (2006).
25. A. Majerus, F. Conti, C. Korte, W. Lehnert, D. Stoltena, *Electrochimica Acta*, **52/2**, 1155, (2012).
26. J. Lanford, A. Wilson, *Appl. Crystallogr.*, **33**, 964, (1978).
27. J. Lanford, A. Wilson, *Applied Crystallography*, **11**, 102, (1978).
28. P. Rae, D. Dattelbaum, *Polymer*, **45**, 7367, (2004).
29. X. Yuan, H. Wang, J. Sun, J. Zhang, *International Journal of Hydrogen Energy*, **34**, 1108, (2007).



## Optimization of the electrochemical synthesis of silver nanoparticles in poly(vinyl alcohol) colloid solutions

R. Surudži<sup>1</sup>, A. Jankovi<sup>1</sup>, M. Vukašinovi -Sekuli<sup>1</sup>, A. Peri -Gruji<sup>1</sup>, K. Y. Rhee<sup>2</sup>, V. Miškovi - Stankovi<sup>1,2\*</sup>

<sup>1</sup>Faculty of Technology and Metallurgy, University of Belgrade, Karnegijeva 4, 11 000 Belgrade, Serbia,

<sup>2</sup>Department of Mechanical Engineering, College of Engineering, Kyung Hee University, Yongin, 446-701, Korea

Received November 4, 2016      Revised March 6, 2017

This work focuses on the optimization of electrochemical synthesis of silver nanoparticles in poly(vinyl alcohol) colloid solutions, films and hydrogel discs with the ability for immobilization of silver nanoparticles and their progressive release, as a new, prospective generation of medical wound dressings. Incorporation of silver nanoparticles into polyvinyl alcohol and polyvinyl alcohol/graphene matrices, with the aim to determine the effect of silver and graphene, was achieved by the electrochemical synthesis at different values of constant current density between 10 and 40 mA cm<sup>-2</sup> and for different time between 10 and 75 min, followed by drying (to obtain films) or freezing-thawing method (to obtain hydrogels). Synthesized nanocomposites were characterized by UV-Visible spectroscopy (UV-Vis), transmission electron microscopy (TEM), cyclic voltammetry (CV), Fourier transform infrared spectroscopy (FT-IR), Raman spectroscopy and atomic absorption spectroscopy (AAS). Additionally, antibacterial activity of thus prepared samples was evaluated against pathogenic bacteria strains *Staphylococcus aureus* and *Escherichia coli* using agar diffusion test. The results indicated that both silver/polyvinyl alcohol and silver polyvinyl alcohol/graphene nanocomposites are excellent candidates for soft tissue implants and wound dressings.

**Key words:** electrochemical synthesis, silver nanoparticles, graphene, poly(vinyl alcohol).

### INTRODUCTION

Poly(vinyl alcohol) (PVA) is widely used in biomedical field [1-4] due to its excellent mechanical strength, low toxicity and high biocompatibility [5,6]. PVA hydrogels are three-dimensional network structures generated through crosslinking of linear polymer materials that do not dissolve in water at a physiological temperature or pH, but swell considerably in an aqueous medium [3,7,8]. PVA hydrogels have a wide range of applications in the medical and pharmaceutical areas since they can absorb exudates from wounds and consequently promote the wound healing [3,8,9].

Graphene (Gr), a single layered two-dimensional atomic carbon sheet, has drawn much attention for scientific interests and industrial applications because it has outstanding mechanical, thermal and electrical properties [10-13]. Therefore, it has great potential for use in a wide range of possible applications such as sensors, for energy storage, in nanoelectronics and polymer nanocomposites [10,14]. Due to its high mechanical strength and Young's modulus, graphene is considered as one of the most promising candidates

for the reinforcement and functionalization of polymers. The incorporation of very small amounts of graphene could significantly improve the mechanical properties [15-20].

Silver as a metal and in its ionic form, exhibits strong cytotoxicity towards a broad range of microorganisms and its use as an antibacterial agent is well known [21]. Silver nanoparticles (AgNPs) are well established antibacterial agents against the bacteria commonly present in the burn wound. Due to the excellent bactericidal property, numerous silver containing materials have been used for the treatment of burn wounds [22-24]. The stabilization of silver nanoparticles using polymer is a method of steric stabilization in solution achieved by binding the polymer molecules with long alkyl chains to the particle surface [25,26]. PVA exhibits capping ability with AgNPs [27,28]. Loading silver nanoparticles into the PVA matrix could enhance the wound healing property of the hydrogel by keeping the environment moisturized as well as by killing the bacteria on site, and thus, avoiding infection of the wound [27].

In this work silver nanoparticles were electrochemically synthesized in PVA solution at different values of constant current density between 10 and 40 mA cm<sup>-2</sup> and for different time periods between 10 and 75 min, in order to determine the

---

To whom all correspondence should be sent:  
E-mail: vesna@tmf.bg.ac.rs



optimal synthesis parameters, and to compare Ag/PVA colloid dispersion obtained at optimal parameters with previously synthesized Ag/PVA/Gr colloid dispersion at constant current density of 40 mA cm<sup>-2</sup> and time of 30 min. The goal of our research was a thorough analysis of the effect of the current density and time of electrochemical synthesis on the amount and size of AgNPs, as well as the interaction between silver nanoparticles, PVA and graphene. UV-Vis, FT-IR and cyclic voltammetry were used for verification of the optimized parameters. Prepared Ag/PVA and Ag/PVA/Gr colloid solutions, films and hydrogel discs are intended for future medical applications as wound dressings, soft tissue implants or could serve as drug carriers.

## EXPERIMENTAL

### *Materials and methods*

The following chemicals were utilized in this work: fully hydrolyzed PVA powder ("hot soluble", Mw = 70000-100000 g mol<sup>-1</sup> Sigma, St. Louis, MO, USA), AgNO<sub>3</sub> (M. P. Hemija, Belgrade, Serbia), KNO<sub>3</sub> (Centrohem, Stara Pazova, Serbia), and graphene powders (Graphene Supermarket, Calverton, NY, USA). In all experiments ultra-pure water from a Milli-Q system (Millipore, Billerica, MA, USA) was used, as well as N<sub>2</sub> gas of high purity (99.5%, Messer Tehnogas a.d., Belgrade, Serbia).

### *Electrochemical synthesis of silver nanoparticles in PVA and PVA/Gr matrices*

In order to prepare Ag/PVA and Ag/PVA/Gr colloid dispersions, films and hydrogel discs, the following procedure was applied [18,19]. PVA powder was first dissolved in hot water (90°C), and after cooling of the solution at room temperature, it was mixed with KNO<sub>3</sub> and AgNO<sub>3</sub> to obtain a solution with a final concentration of 10 wt.% PVA, 0.1 M KNO<sub>3</sub>, and 3.9 mM AgNO<sub>3</sub>. To prepare Ag/PVA/Gr, graphene was added to dissolved PVA under vigorous stirring. After the solution was cooled to room temperature and sonicated, KNO<sub>3</sub> and AgNO<sub>3</sub> were added to obtain a final concentration of 10 wt.% PVA, 0.01 wt.% Gr, 0.1 M KNO<sub>3</sub>, and 3.9 mM AgNO<sub>3</sub>. Electrochemical reduction of silver ions was performed galvanostatically using a Reference 600 potentiostat/galvanostat/ZRA (Gamry Instruments, Warminster, PA, USA) in an electrochemical cell containing 50 cm<sup>3</sup> of PVA solution or PVA/Gr dispersion. Two platinum electrodes were employed as working and counter electrodes, and a saturated calomel electrode (SCE) was used as a

reference electrode. The applied current density was varied from 10 to 40 mA cm<sup>-2</sup>, while reaction time was between 10 and 75 min. Synthesis was performed in N<sub>2</sub> atmosphere under continuous stirring.

PVA solution, PVA/Gr, Ag/PVA and Ag/PVA/Gr colloid dispersions were then poured slowly into a Teflon dish. The solvent was then allowed to evaporate at room temperature for 3 days, and the samples were further dried at 60°C for 2 days to completely remove the remaining water to yield PVA, PVA/Gr, Ag/PVA and Ag/PVA/Gr films by casting. Films with an average thickness of approximately 70 μm were peeled off the substrate for testing.

In order to obtain hydrogel discs (diameter, d=10 mm) the PVA solution, PVA/Gr, Ag/PVA and Ag/PVA/Gr colloid dispersions were subjected to five cycles of successive freezing and thawing (one cycle involved freezing for 16 h at -18°C and thawing for 8 h at 4°C).

### *Methods of characterization*

*UV-Visible spectroscopy (UV-Vis).* UV-Vis spectra of Ag/PVA and Ag/PVA/Gr colloid dispersions were recorded by a UV-3100 spectrophotometer (MAPADA, Japan) in the wavelength range between 200 and 1000 nm.

*Transmission electron microscopy (TEM).* Transmission electron microscopy of Ag/PVA and Ag/PVA/Gr colloid dispersions was performed by 100 CX Electron Microscope (JEOL Ltd., Tokyo, Japan) operated at 100 kV, in order to examine the size and shape of Ag nanoparticles. Samples for TEM analysis were prepared by deposition of diluted Ag/PVA colloid dispersions (1:4) on C-coated Cu grids (SPI Supplies/Structure Probe Inc., West Chester, PA, USA).

*Cyclic voltammetry (CV).* CV measurements of the Pt electrode in Ag/PVA and Ag/PVA/Gr colloid dispersions were performed using two platinum electrodes as working and counter electrodes, and saturated calomel electrode (SCE) as a reference electrode, using a Reference 600 potentiostat/galvanostat ZRA (Gamry Instruments) at a scan rate of 50 mV s<sup>-1</sup> in the potential region from -1 to 1 V vs. SCE, starting from the open circuit potential, E<sub>ocp</sub>. All potentials are reported versus the SCE, and stationary voltammograms are shown.

*Fourier transform infrared spectroscopy (FT-IR).* The IR spectra were recorded on PVA, Ag/PVA and Ag/PVA/Gr thin films obtained by evaporating the solvent from PVA solution, Ag/PVA and Ag/PVA/Gr colloid dispersions. The instrument used was ThermoFisher corporation

Nicolet 380 FT-IR spectrophotometer, operating in ATR mode.

**Antibacterial activity test.** The antibacterial activity of the PVA, PVA/Gr, Ag/PVA and Ag/PVA/Gr hydrogel discs containing a maximum of 1 mM AgNPs was tested against the Gram-positive pathogenic bacterium *Staphylococcus aureus* TL (culture collection-FTM, University of Belgrade, Serbia) and the Gram-negative bacterium *Escherichia coli* (ATCC 25922) by the agar diffusion method. Inoculums of the two microorganisms were prepared from fresh overnight LB broth (Lennox) (10 g/L tryptone, 5 g/L yeast extract, 5 g/L NaCl) cultures incubated at 37°C. The agar diffusion test was performed in LB broth containing 0.7 wt% agar. The diffusion technique was conducted by pouring media into Petri dishes to form 4 mm thick layers and adding a dense inoculum of the targeted bacteria to obtain semiconfluent growth. Petri plates were left for 15 min to dry in air and subsequently Ag/PVA or Ag/PVA/Gr hydrogels discs were placed on the agar surface and the plates were incubated for 24 h at 37°C. The width of the zone of inhibition (mm) was then measured.

**Silver release monitoring.** Release of silver from the Ag/PVA and Ag/PVA/Gr hydrogel discs was investigated at  $37 \pm 1^\circ\text{C}$  in simulated body fluid (SBF, pH 7.4) containing 0.39 mM  $\text{KH}_2\text{PO}_4$  + 0.61 mM  $\text{K}_2\text{HPO}_4$ . The SBF was Cl-ion free to avoid eventual  $\text{AgCl}_2$  precipitation. Ag/PVA and Ag/PVA/Gr hydrogel discs ( $d \approx 10$  mm,  $\approx 5$  mm) were placed in 10 ml of SBF, which was changed periodically: every day for the first 7 days, and after that on days 10, 14, 24, and 28. Atomic absorption spectrometer (PYU UNICAM SP9, Philips, Amsterdam, Netherlands) was used to measure the silver content in the solution. Total content of silver inside the hydrogels was determined by treatment with  $\text{HNO}_3$  (1:1 v/v), which induced oxidation of all AgNPs into  $\text{Ag}^+$ . Experiments were performed in triplicate.

## RESULTS AND DISCUSSION

### *UV-vis spectroscopy*

UV-Vis spectroscopy was employed to monitor the silver nanoparticles formation. Nano-sized silver exhibits a strong absorption due to the collective oscillation of the conduction electrons, after appropriate excitement by suitable radiation. This phenomenon is known as a localized surface plasmon resonance (LSPR), highly dependent on the size and shape of nanoparticles [28].

Fig. 1 (a) shows the absorption spectra of pure 10 wt. % PVA solution and Ag/PVA colloid dispersions obtained at different values of current density 10, 15, 25, 40  $\text{mA cm}^{-2}$ , and the duration of synthesis set for 10 min. PVA spectrum did not exhibit the absorbance peak in the examined wavelength range. All Ag/PVA colloid dispersions exhibited absorption spectra with two bands peaking at approximately 400 nm and 650 nm. The absorption peaks at 423, 422, 427, 423 nm for 10, 15, 25, 40  $\text{mA cm}^{-2}$  current density, respectively, confirmed the formation of silver nanoparticles [26,28]. As the current density increased, the maximum of the absorption peak also increased, suggesting that a higher concentration of silver nanoparticles was achieved at higher current densities, since the silver nanoparticle concentration is proportional to the absorbance intensity [29, 30].

The absorption band peaking at nearly 650 nm can be explained by aggregation or agglomeration of silver nanoparticles present in the colloid solution [29, 31].

Fig. 1 (b) shows the absorption spectra of pure 10 wt. % PVA solution and Ag/PVA colloid dispersions for different time periods of synthesis 10, 30, 45, 75 min, respectively, at current density of 40  $\text{mA cm}^{-2}$ . The increase in time of synthesis (10, 30, 45 min) increased the maximum of absorption peak at approx. 420 nm, indicating the higher concentration of silver nanoparticles, up to 75 min of synthesis time, when maximum of absorption peak decreased. In addition, the maximum of absorption peak at around 650 nm also increased, so it can be concluded that aggregation or agglomeration of silver nanoparticles is more pronounced for longer time of the synthesis. Based on these data, optimal synthesis parameters are set at current density of 40  $\text{mA cm}^{-2}$  and time of 30 min. Ag/PVA/Gr colloid dispersion was obtained under the same conditions [18]. Since the concentration of AgNPs is proportional to the absorbance intensity, we concluded that the presence of graphene slightly decreased the amount of AgNPs in the Ag/PVA/Gr colloid dispersion (absorbance peak for Ag/PVA was 0.48 a.u., compared to the peak for Ag/PVA/Gr of 0.39 a.u.).

### *Transmission electron microscopy*

From TEM micrographs depicted in Fig. 2 (a), (b) and (c) it is obvious that the AgNPs assume sphere-like morphologies in appearance at nanoscale levels of approximately 10-40 nm in diameter for both Ag/PVA (Fig. 2a,b) and Ag/PVA/Gr (Fig. 2c). However, at lower current

density of  $15 \text{ mA cm}^{-2}$  (Fig. 2a) silver nanoparticles exhibit greater tendency for aggregation and agglomeration than at higher current density,  $40 \text{ mA cm}^{-2}$  (Fig. 2b), confirming the optimal value of current density of  $40 \text{ mA cm}^{-2}$ . Fig. 2c shows TEM micrograph of Ag/PVA/Gr colloid dispersion at  $40 \text{ mA cm}^{-2}$  ( $t_{\text{synt.}} = 30 \text{ min}$ ), proving also that presence of graphene slightly decreased the amount of AgNPs in respect to Ag/PVA dispersion.

and time of synthesis 10 min, and (b) variable time of synthesis at current density of  $40 \text{ mA cm}^{-2}$ .

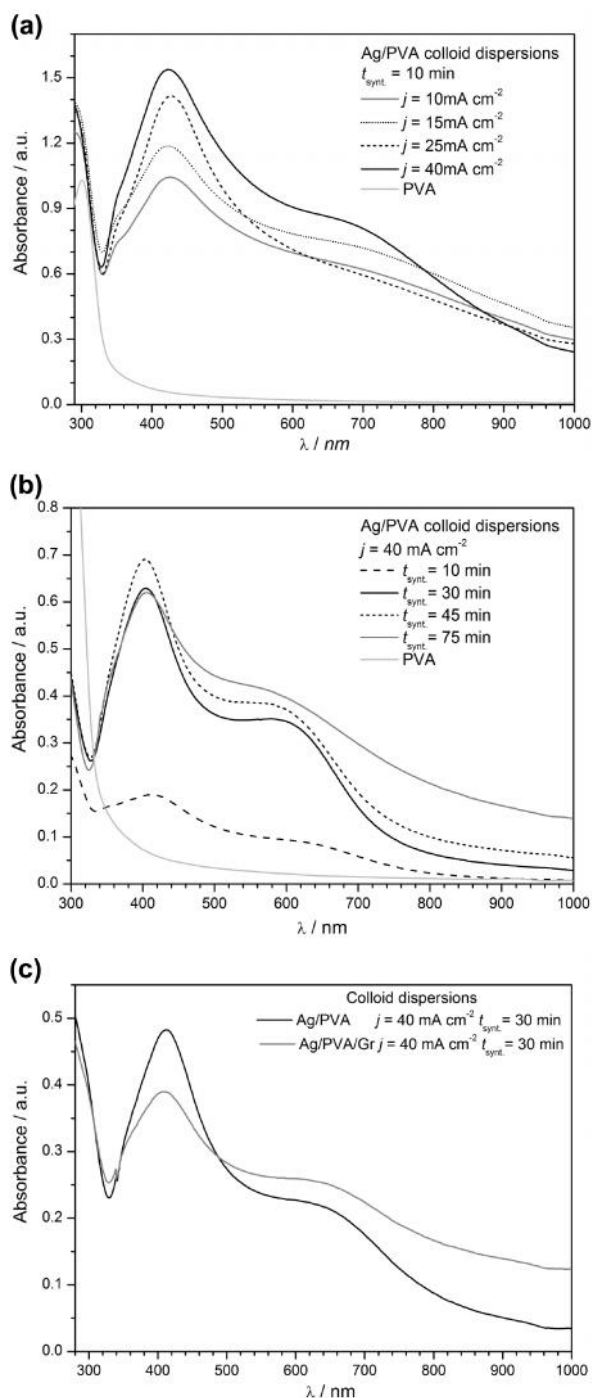


**Fig. 1.** UV-Vis spectra of PVA solution and electrochemically synthesized silver nanoparticles in Ag/PVA colloid dispersions: (a) variable current density

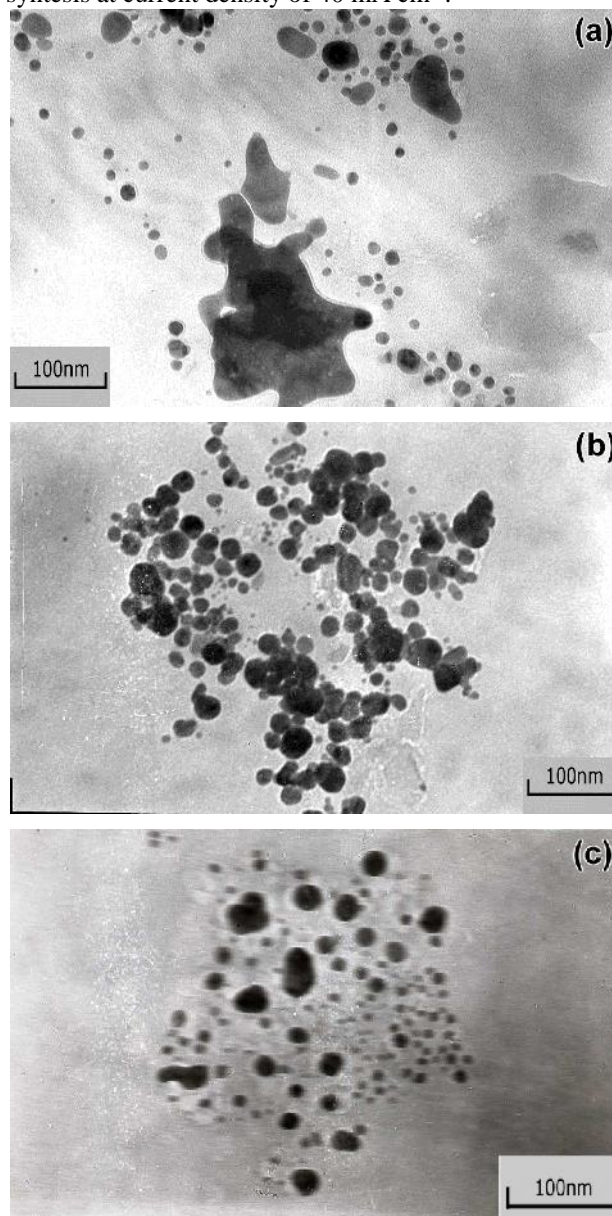


**Fig. 2.** TEM micrographs of electrochemically synthesized silver nanoparticles in Ag/PVA colloid dispersion ( $t_{\text{synt.}} = 10 \text{ min}$ ) at different values of current density: (a)  $15 \text{ mA cm}^{-2}$ , (b)  $40 \text{ mA cm}^{-2}$  and (c) Ag/PVA/Gr colloid dispersion at  $40 \text{ mA cm}^{-2}$  ( $t_{\text{synt.}} = 30 \text{ min}$ ).

### Cyclic voltammetry

The cyclic voltammetry of Pt electrode analysis was performed in 10 wt% PVA solution and in colloid dispersion of Ag/PVA (Fig. 3) obtained at different values of current density, 25 and  $40 \text{ mA cm}^{-2}$ , for 10 min of synthesis time. A better insight into the oxidation/reduction processes occurring in aqueous solutions of silver was obtained by the comparison with cyclic voltammograms of Pt electrode in solutions containing  $3.9 \text{ mM AgNO}_3$  and  $0.1 \text{ M KNO}_3$ .

Cyclic voltammogram of Pt electrode in 10 wt% PVA solution (Fig. 3) exhibited a broad cathodic peak at -100 mV, originating from Pt oxide reduction formed during the anodic sweep. The anodic counterpart of this peak is not seen due to the overlapping with the oxidation current at potentials more positive than 400 mV.

Stationary cyclic voltammograms of Pt electrode in both Ag/PVA colloid dispersions exhibited three anodic peaks at around 595 mV, 665 mV, 875 mV for current density of 25 mA cm<sup>-2</sup> and 560 mV, 700 mV, 880 mV for current density of 40 mA cm<sup>-2</sup> (Fig. 3) The first two can be related to the different oxidation processes of silver nanoparticles in the Ag/PVA colloid solutions, while the peaks at around 875 and 880 mV are related to the Pt oxide. Only one cathodic peak was observed at around 165 mV and 135 mV, for 25 mA cm<sup>-2</sup> and 40 mA cm<sup>-2</sup>, respectively. Two anodic peaks suggest there is a difference between silver species; one is even less susceptible for oxidation. This could be explained by the entrapment of silver nanoparticles by PVA molecules, which implies that enhanced stability of silver nanoparticles was obtained. The results indicated two types of AgNPs in Ag/PVA colloid solution coexisted; the relatively free ones that are susceptible to the oxidation, and those already bonded to PVA molecules, and hence less reactive.

The cyclic voltammogram of Pt electrode in Ag/PVA/Gr colloid dispersion [18] revealed two anodic peaks, one at around 650 mV due to AgNPs oxidation, and the second at around 950 mV due to oxidation of free Pt surfaces and Pt oxide formation. Two cathodic counterparts were observed: a peak at around 130 mV corresponding to AgNP reduction and a peak at around -370 mV due to reduction of the Pt oxide.

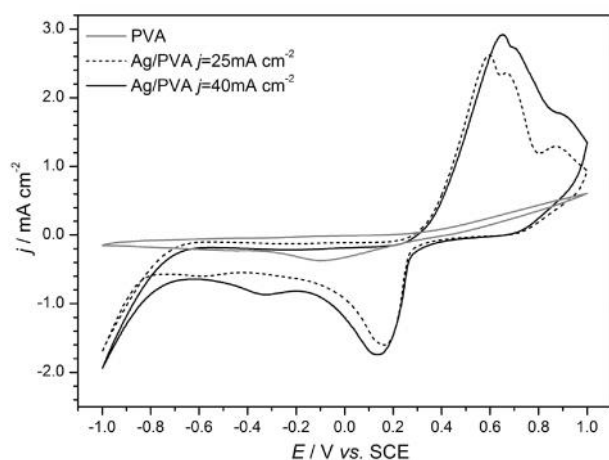


**Fig. 3.** Stationary cyclic voltammograms for Pt electrode in PVA solution and Ag/PVA colloid dispersions ( $j = 25 \text{ mA cm}^{-2}$  and  $j = 40 \text{ mA cm}^{-2}$ ,  $t_{\text{synt.}} = 10 \text{ min}$ ).

#### Fourier transform infrared (FT-IR) and Raman spectroscopy

FT-IR measurements were performed on pure PVA, Ag/PVA and Ag/PVA/Gr thin films in order to determine the type of interactions between PVA molecules, silver nanoparticles and graphene. Thin films were obtained by solvent evaporation from PVA solution and Ag/PVA colloid dispersion (Fig. 4, Table 1) and Ag/PVA/Gr colloid dispersions [18]. The spectrum of the pure PVA film exhibited characteristic peaks associated with poly(vinyl alcohol). A typical strong hydroxyl band for -OH stretching vibration was observed at 3252 cm<sup>-1</sup> [32]; absorption peak originating from carboxyl stretching band (C=O) was verified at a wavenumber of 1715 cm<sup>-1</sup>. Vibration band in the region between 1090 and 1150 cm<sup>-1</sup> is attributed to the crystallinity of the PVA [33], considering that the PVA is a semi-crystalline synthetic polymer [34].

The FT-IR spectrum of Ag/PVA film (Fig. 4) and Ag/PVA/Gr film [18] exhibited few differences in comparison to the spectrum of the pure PVA. Important changes were observed for the band peaking at 1413 cm<sup>-1</sup> (PVA spectrum) compared to 1367 cm<sup>-1</sup>, 1371 cm<sup>-1</sup> and 1353 cm<sup>-1</sup> (Ag/PVA spectrum for current density 15 mA cm<sup>-2</sup> and 40 mA cm<sup>-2</sup> at  $t_{\text{synt.}} = 10 \text{ min}$ , and Ag/PVA/Gr spectrum for current density 40 mA cm<sup>-2</sup> at  $t_{\text{synt.}} = 30 \text{ min}$ , respectively). The band peaking at 1325 cm<sup>-1</sup> disappeared upon incorporation of Ag nanoparticles, which suggested interaction between AgNPs and -OH groups originating from PVA molecules and graphene through the decoupling between the corresponding vibrations.

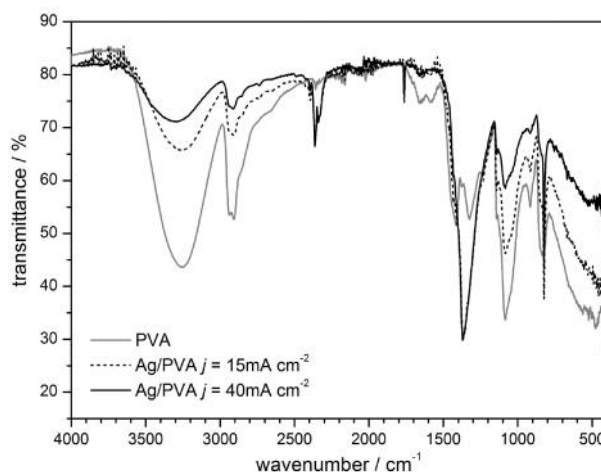


**Fig. 4.** FT-IR spectra of PVA and Ag/PVA thin films obtained by solvent evaporation from PVA solution and Ag/PVA colloid dispersions ( $j = 15 \text{ mA cm}^{-2}$  and  $40 \text{ mA cm}^{-2}$ ,  $t_{\text{synt.}} = 10 \text{ min}$ ).

**Table 1.** Wavenumbers of the characteristic bands and corresponding assignments for PVA, Ag/PVA and Ag/PVA/Gr films.

PVA	Wavenumber/cm <sup>-1</sup>			Assignment [32-35]
	Ag/PVA 15 mA cm <sup>-2</sup>	Ag/PVA 40 mA cm <sup>-2</sup>	Ag/PVA/Gr 40 mA cm <sup>-2</sup> [18]	
3252	3249	3288	3231	–OH stretching vibration
2908	2910	2940	2908	asymmetric CH <sub>2</sub> stretching and aliphatic C–H stretching vibrations
1581			1578	C=C vibration stretching
1413 1325	1367	1371	1353	–OH in plane coupling with C–H wagging
1141	1142	1142	1139	symmetric C–C stretching
1082	1084	1084	1084	C–O stretching vibration of secondary alcohols
916	916	916	916	symmetric C–C stretching
833	823	823	833	C–H rocking vibration

In order to verify the incorporation of graphene in Ag/PVA/Gr composite hydrogel, Raman analysis was performed [18,19]. The presence of exfoliated graphene sheets embedded in the hydrogel matrix was confirmed by the broad spectral bands at 1379 cm<sup>-1</sup> (D-peak) and 1618 cm<sup>-1</sup> (G-peak) supporting our previously published results. The G-peak appears in the spectrum due to the graphitic structure of the material, whereas the D-peak reveals disordered structure of the carbon. Raman analysis confirmed graphene structure in its pure form [36-38].

#### Antibacterial agar diffusion test and silver release monitoring

Antibacterial activity of the samples was tested for microorganisms that are responsible for most of the inter-hospital infections, *S. aureus* and *E. coli*. The results of qualitative antimicrobial agar diffusion tests showed that both Ag/PVA and Ag/PVA/Gr successfully affect both microorganisms. The average inhibition zone was 0.4 mm for *S. aureus* and it can be easily observed around the sample disc of Ag/PVA/Gr and a bit less pronounced zone of 0.2 mm around the disc of Ag/PVA (Fig. 5). In the case of *E. coli* the average inhibition zone is much less pronounced, only 0.1 mm for both discs, Ag/PVA and Ag/PVA/Gr.

Quantitative results of antibacterial activity were obtained from test in suspension (phosphate buffer (PB)) using the spread plate method [18]. Both Ag/PVA and Ag/PVA/Gr hydrogels significantly reduced bacterial cell viability after just 1 h of incubation when compared to the initial number of

cells in suspension. Ag/PVA killed all the *S. aureus* colonies after 24 h and all the *E. coli* colonies after 3 h. In contrast, Ag/PVA/Gr completely destroyed all *S. aureus* TL and *E. coli* colonies after 3 h and 24 h, respectively. The greater antibacterial activity of Ag/PVA/Gr than Ag/PVA could be a consequence of the smaller dimensions of the AgNPs embedded in the hydrogel matrix, as discussed earlier.

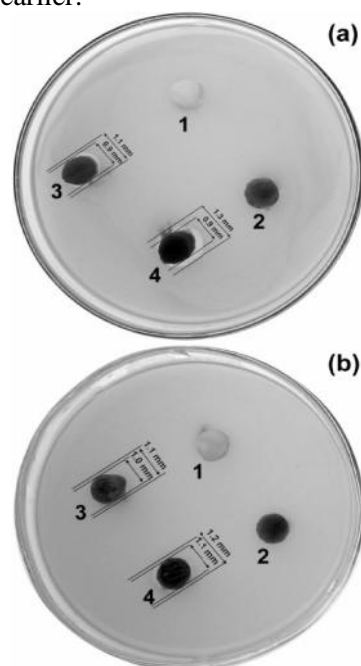


**Fig. 5.** Antibacterial activity of PVA (1), PVA/Gr (2), Ag/PVA (3) and Ag/PVA/Gr (4) hydrogels against strain (a) *S. aureus* and (b) *E. coli* by agar diffusion tests.

Also, antibacterial activity of graphene [39-41] contributes to better activity of Ag/PVA/Gr than

Ag/PVA hydrogel. Based on our results, it can be considered that both composites, Ag/PVA and Ag/PVA/Gr prevent biofilm formation [18].

The silver release kinetics from Ag/PVA and Ag/PVA/Gr hydrogel discs during time of exposure to SBF at 37 °C is depicted in Table 2.

**Table 2.** Time dependence of the concentration of silver released from Ag/PVA and Ag/PVA/Gr hydrogel discs (data represent average of three measurements).

Time/ days	Released silver from Ag/PVA hydrogel disc (wt. %)	Released silver from Ag/PVA/Gr hydrogel disc (wt.%)
1	14.1	17.1
2	15.7	18.5
3	16.3	19.1
4	17.0	19.7
5	17.6	20.2
6	18.1	20.7
7	18.6	21.1
10	19.4	21.7
14	20.6	22.5
24	22.4	23.2
28	23.5	23.9

The amount of silver released from a hydrogel was monitored as a function of time. It can be observed that the silver concentration released from Ag/PVA and Ag/PVA/Gr hydrogels initially increased swiftly with time, and after 3 days of silver release (16 wt. % and 19 wt. % of the initial silver content, respectively) a plateau was observed, indicating the significant lowering of the silver release rate. However, it can also be seen that even after 28 days, both Ag/PVA and Ag/PVA/Gr had released ~24 wt. % of the initial silver content, as a consequence of stability of AgNPs inside the highly crosslinked PVA hydrogel network [18]. This is very important since the remaining silver can preserve the sterility of the samples over time. As a result, these hydrogels could be used for a prolongation the sterility of a soft tissue implant for example.

## CONCLUSIONS

In this work, Ag/PVA colloid dispersions were successfully obtained at different values of current density 10, 15, 25, 40 mA cm<sup>-2</sup> and different times of synthesis 10, 30, 45, 75 min. UV-Vis spectroscopy demonstrated that optimal synthesis parameters were- current density of 40 mA cm<sup>-2</sup> and time of 30 min. Comparison between Ag/PVA colloid dispersion synthesized at optimal conditions

with the Ag/PVA/Gr colloid dispersion synthesized at the same conditions, demonstrated that AgNPs in Ag/PVA/Gr nanocomposite had smaller dimensions than those in Ag/PVA nanocomposite due to the presence of graphene sheets between PVA chains. In addition, the interactions between AgNPs and hydroxyl groups in PVA, as well as between PVA and graphene sheets, were confirmed. Slow silver release (~24 wt. %) after 28 days in simulated body fluid confirmed that both Ag/PVA/Gr and Ag/PVA hydrogels can preserve sterility over time. This characteristic, combined with their strong antibacterial activity indicates that Ag/PVA/Gr and Ag/PVA hydrogels are excellent candidates for soft tissue implants and wound dressings.

**Acknowledgements.** This work was supported by the Basic Science Research Program through the National Research Foundation of Korea (NRF) funded by the Ministry of Education, Science and Technology (project number: 2016R1A2B4016034). The authors would like to express their gratitude to the Ministry of Education, Science and Technological Development, Republic of Serbia (Grant No. III 45019) for the financial support.

## REFERENCES

1. S. Sasaki, T. Murakami, A. Suzuki, *Biosurf. Biotribol.*, **2**, 11 (2016).
2. J. H. Kim, H. Lee, A. W. Jatoi, S. S. Im, J. S. Lee, I.-S. Kim, *Mater. Lett.*, **181**, 367 (2016).
3. L. Fan, H. Yang, J. Yang, M. Peng, J. Hu, *Carbohydr. Polym.*, **146**, 427 (2016).
4. N. Georgieva, R. Bryaskova, R. Tzoneva, *Mater. Lett.*, **88**, 19 (2012).
5. J. Shen, D. J. Burgess, *Int. J. Pharm.*, **422**, 341 (2012).
6. J. L. Drury, D. J. Mooney, *Biomaterials*, **24**, 4337 (2003).
7. R. Ma, D. Xiong, F. Miao, J. Zhang, Y. Peng, *Mater. Sci. Eng., C*, **29**, 1979 (2009).
8. B. Bolto, T. Tran, M. Hoang, Z. Xie, *Prog. Polym. Sci.*, **34**, 969 (2009).
9. C. Cencetti, D. Bellini, A. Pavesio, D. Senigaglia, C. Passariello, A. Virga, P. Matricardi, *Carbohydr. Polym.*, **90**, 1362 (2012).
10. M.-Y. Lim, H. Shin, D. M. Shin, S.-S. Lee, J.-C. Lee, *Polymer*, **84**, 89 (2016).
11. A. Jankovi, S. Erakovi, M. Vukašinovi -Sekuli, V. Miškovi -Stankovi, S. J. Park, K. Y. Rhee, *Prog. Org. Coat.*, **83**, 1 (2015).
12. T. Zhou, F. Chen, C. Tang, H. Bai, Q. Zhang, H. Deng, Q. Fu, *Compos. Sci. Technol.*, **71**, 1266 (2011).
13. A. Jankovi, S. Erakovi, M. Mitri, I. Z. Mati, Z. D. Jurani, G. C. P. Tsui, C.-y. Tang, V. Miškovi -Stankovi, K. Y. Rhee, S. J. Park, *J. Alloys Compd.*, **624**, 148 (2015).
14. S. Bai, X. Shen, *RSC Advances*, **2**, 64 (2012).
15. X. Liu, W. Kuang, B. Guo, *Polymer*, **56**, 553 (2015).



## Electrochemical preparation of Ag nanoparticles involving choline chloride – glycerol deep eutectic solvents

A. Cojocaru<sup>1,2</sup>, O. Brincoveanu<sup>2</sup>, A. Pantazi<sup>2</sup>, D. Balan<sup>2</sup>, M. Enachescu<sup>2</sup>, T. Visan<sup>1,2</sup>, L. Anicai<sup>2\*</sup>

<sup>1</sup>Depart. Inorganic Chemistry, Physical Chemistry and Electrochemistry, POLITEHNICA University of Bucharest, Calea Grivitei 132, Bucharest, Romania

<sup>2</sup>Center of Surface Science and Nanotechnology, University POLITEHNICA of Bucharest, Splaiul Independentei 313, Bucharest, Romania

Received November 4, 2016      Revised March 6, 2017

The paper reports studies about electrochemical synthesis of silver nanoparticles (Ag NPs) at 25°C involving choline chloride – glycerol deep eutectic solvent and pulse reversed current. It was demonstrated that cyclic voltammetry proves to be useful tool to evaluate the optimum content of stabilizer polyvinylpyrrolidone through analysis of the anode current peak values against the cycle's number, as an indicator of the colloidal nano-Ag amount formed into the solution. It is shown that the Ag<sup>+</sup>/Ag couple on glassy carbon electrode exhibits almost reversible behavior with diffusion control of cathodic process and a stripping anodic process. Based on Dynamic Light Scattering measurements and scanning electron micrographs it has been found out that through a proper selection of the pulse regime, the nanoparticles size may be controlled. The obtained Ag NPs showed sizes in the range of 60-200 nm, depending on the electrochemical synthesis conditions.

**Key words:** Ag nanoparticles, electrochemical synthesis, deep eutectic solvents, choline chloride, glycerol.

### INTRODUCTION

Recently, a special attention has been paid to the synthesis of nanomaterials based on silver nanoparticles (Ag NPs) that may be applied in antimicrobial and antibacterial coatings [1-3], medicine, pharmacy and cosmetology [4-6], electronics and energy sources [7-9], or sensing [10-14], due to their respective biological, physical, chemical, electronic properties and catalytic activity, distinctly different from those of the bulk metal. It is also known that the collective oscillation of conduction electrons in Ag nanostructures results in surface plasmon resonance, enabling their extensive use in plasmonics, optical sensing, and surface-enhanced Raman scattering (SERS) detection [15,16].

The synthesis of silver nanoparticles may be carried out by different methods, but the most usual ones are chemical reduction methods involving the reduction of silver salt by a reducing agent in the presence of suitable stabilizer. Thus, silver nanoparticles can be prepared via a simple technique (i.e., the 'silver mirror reaction') [17]. However, the electrochemical deposition [18-22] used for the synthesis of Ag NPs in various aqueous or non-aqueous media is an inexpensive, effective,

simple and versatile route toward shape-controlled synthesis of metal nanocrystals. The electrolysis parameters like the electrode potential or current density can be tuned continuously and reversibly. The method has however its limitations, because the deposition of silver on the cathode diminishes the current efficiency. Better control may be achieved using sonoelectrochemistry to prepare monodisperse silver NPs [23]; ultrasounds include the cleaning of electrodes and the acceleration of mass transport and reaction rates. Electrochemical deposition of Ag NPs was also successfully applied in ionic liquids as dispersing media [24-32].

In general, controlling the size, shape, and structure of metal nanoparticles during both the synthesis and the usage is technologically important because of correlation with their properties. This may be performed by using capping agents which preferentially stabilize a specific set of crystal facets and thus guide the nanocrystals to grow into different shapes with very narrow size distribution. Historically, quaternary ammonium salts were among the most common classes of stabilizing agents for metal nanoparticles [33]. Li et al. [32] have achieved the controllable electrochemical synthesis of Ag nanoparticles of diameters 2–13 nm from a quaternary ionic liquid (1-butyl-3-methylimidazolium chloride) microemulsion. Ahmadi et al. [5] have synthesized Ag NPs on the surface of a glassy carbon electrode modified with *p*-tert-butylcalix[4]arene and *p*-tert-butylcalix[6]arene by

---

To whom all correspondence should be sent:  
E-mail: lanicai@itenet.ro



the reduction of  $\text{Ag}^+$  at an open circuit potential, followed by the electrochemical reduction of the  $\text{Ag}^+$ .

Among the other additives as capping and steric stabilizing agents preventing agglomeration, there have been reports of silver nanoparticle shape-selective synthesis using poly(N-vinyl pyrrolidone) PVP [34–37], because it manipulates the growth by selectively adhering to certain crystallographic planes. This capping agent prevents uncontrolled particle growth and agglomeration like particle clusters. PVP as capping agent surrounds the nucleated particle and naturally restricts the particle from growing. PVP is a homopolymer with a polyvinyl backbone and its repeating units contain a highly polar amide group that confers hydrophilic and polar-attracting properties. The non-polar methylene groups both in the backbone and in the ring confer hydrophobic properties [36]. The PVP content in the electrolyte had a significant influence on silver nanoparticles morphology and optical properties. Tang et al. [23] demonstrated the controllability of the distance of reaction conditions away from equilibrium over a wide range for the synthesis of silver NSs with the assistance of PVP. Not only dendritic rods, dendritic sheets, and flower-like dendrites, but also Ag NPs with spherical or oval shapes and surface structure including snow flake-like and nanothorns were prepared in this way.

In this work we present some preliminary results on the electrochemical synthesis of silver nanoparticles (Ag NPs) using choline chloride (2-hydroxy-ethyl-trimethyl ammonium chloride) - glycerol mixture as electrolyte and pulse reversed current. Recently the possibility of forming ionic liquids as an eutectic of a quaternary ammonium salt (most used being choline chloride) with amides, glycols (such as glycerol) or carboxylic acids, named ‘hydrogen-bond donors’ has been demonstrated [38–40]. These media are known as ‘deep eutectic solvents’ (DESs) being also called ‘ionic liquid analogues’. DESs are used as sustainable media for the creation of well-defined nanoscale and functional materials involving shape-controlled nanoparticles. Compared to ionic liquids, DESs are cheaper, much less toxic and mostly biodegradable. Other advantages of DESs are their non-volatility, non-inflammability and good air and water stability. DESs have been regarded as the most promising environmentally benign and cost-effective alternatives to conventional ionic liquids and volatile organic solvents. Although they share many characteristics and properties with ionic liquids, they represent a different type of solvent, because in contrast to ionic liquids, which are

composed of one type of discrete anion and cation, DESs are formed from a eutectic mixture of Lewis and Brønsted acids and bases. The preparation of DESs is simple, just by mixing the components and heating them up under stirring. The method is safe and cost effective because it may be carried out with 100% atom economy, without purification being required, which would favor large-scale applications of DESs.

DESs have a large depression in their freezing points compared to the pure substances. For example, the DES mixture formed from choline chloride (ChCl, m.p. = 302°C) and glycerol (m.p. = 18°C) at 1:2 molar ratio has a melting point of –40°C [41]. This ionic liquid, denoted here as ILG, trade name Glyceline, is stable and transparent at room temperature. The mixture can even be prepared from food-grade components. The physical–chemical properties of ILG are similar to properties of other DESs and of traditional ionic liquids, namely density, viscosity, electrical conductivity, potential window, and their temperature dependence. However, only few reports were published until now regarding the ILG deep eutectic solvent [42–49]. Leron et al. [44] showed that this DES has poor conductivity (lower than 2 mS  $\text{cm}^{-1}$  at room temperature) due to its high viscosity. The successive addition of ChCl to glycerol lowers the viscosity and increases the conductivity of the mixture (from 0.74 mS  $\text{cm}^{-1}$  for 1:4 molar ratio of ChCl glycerol to 1.30 mS  $\text{cm}^{-1}$  for 1:2 molar ratio of ChCl glycerol), due to more available charge carriers in an increasingly less viscous solvent.

We studied here the formation of silver nanoparticles based on the use of two-electrode cell in which the  $\text{Ag}^+$  ions are produced either by anodic dissolution of bulk Ag metal, or by dissolution of a silver salt. To our knowledge, the choline chloride – glycerol deep eutectic solvent has not been employed as an electrolysis medium for preparing large amounts of metal nanoparticles.

## EXPERIMENTAL

### *Chemicals and materials*

Choline chloride (denoted as ChCl, 2-hydroxy-N,N,N-trimethyl-ethyl-ammonium chloride, 99%), glycerol (denoted as G, 99%), silver chloride (AgCl) and poly(N-vinyl pyrrolidone) (PVP, average molecular weight 55,000  $\text{g mol}^{-1}$ , 99.9%) were purchased from Sigma-Aldrich. All chemicals were of analytical grade and used without further purification.

The eutectic mixture (symbolized ILG) has been prepared by mixing and heating with gentle stirring

ChCl with G in 1:2 molar ratio at a temperature in the range 80–100°C, until a homogeneous, clear liquid was formed. AgCl and PVP were then introduced to prepare the electrolytes, as shown in Table 1.

**Table 1.** ILG based electrolytes involved in Ag nanoparticles electrochemical synthesis.

System type	Electrolyte composition
ILG	Choline chloride : glycerol (1:2 molar ratio)
ILG-PVP	ILG + 1-5 gL <sup>-1</sup> PVP
ILG-Ag	ILG + 2-10 mM AgCl
ILG-PVP-Ag	ILG + 1-5 gL <sup>-1</sup> PVP + 2-10 mM AgCl

#### *Electrochemical investigation of Ag/Ag<sup>+</sup> couple*

To get more information on the electrochemical behaviour of Ag/Ag<sup>+</sup> couple in the ILG based electrolytes during Ag NPs electrochemical synthesis, cyclic voltammetry measurements were carried out using a three-electrode cell with a glassy carbon (GC) disk as working electrode having a geometrical surface of 0.196 cm<sup>2</sup> and a Pt mesh as auxiliary electrode. All electrode potentials were measured against Ag wire immersed in DES electrolyte as quasi-reference electrode; the half-cell equilibrium reaction is due to the AgCl film formed onto Ag surface in contact with the ionic liquid with certain content in chloride ions. This Ag quasi-reference electrode has the advantage of achieving the equilibrium potential in short time. It is reproducible and maintains electrode potential within long time, making it particularly well suited for comparison [50,51]. All voltammetric studies were performed at 25°C using an Autolab PGSTAT 12 potentiostat controlled with GPES software. The applied scan rates were in the range 5-100 mVs<sup>-1</sup>. Before each CV measurement, the surface of GC working electrode was cleaned to remove reductive substances by polishing with 50 µm alumina paste and washing with bidistilled water.

#### *Electrochemical synthesis of Ag nanoparticles (Ag NPs)*

The electrochemical synthesis experiments were performed under mild stirring and in an open system using a pulse reverse power supply (pe86CB 3HE, Plating Electronic GmbH, Germany). The cell has a two-electrode configuration, as illustrated in Fig. 1 and contains 300 mL ionic liquid as electrolyte.

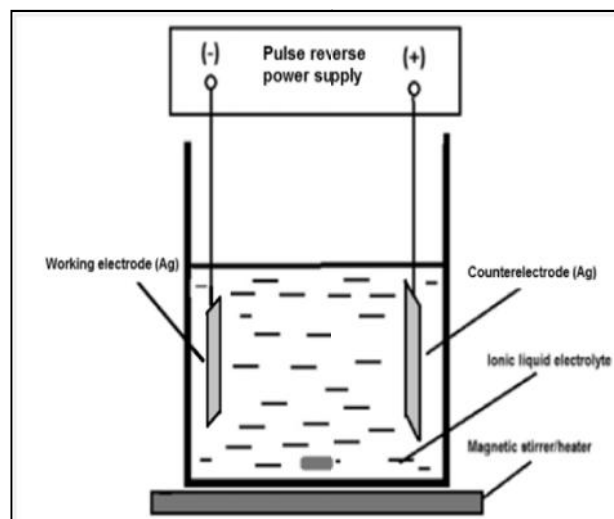


**Fig. 1.** Experimental set-up for Ag nanoparticles electrochemical synthesis.

Both electrodes consisted of Ag plates with 99.999% purity (30 x 20 x 0.5 mm) and exposed surface area of 6 cm<sup>2</sup>. In other series of experiments the electrochemical synthesis was carried out involving Pt plate electrodes having the same surface area.

The electrochemical synthesis experiments have been performed at room temperature (25°C) with duration between 10-30 min. Before each experiment, the silver electrodes were hand polished by fine grade emery paper and washed with bidistilled water and a small amount of acetone and dried. Two regimes of the applied pulse reversed current have been used, as shown in Fig. 2.

After synthesis, the electrolyte containing Ag NPs was subjected to centrifugation at 4000 rpm for 15 min., with intermediary washing steps using ethanol. This sequence has been repeated for 4 times.

#### *Characterization*

The morphology and composition of the electrochemically prepared Ag NPs have been analyzed by scanning electron microscopy (SEM) associated with energy-dispersive X-ray (EDX) analysis (SU8230, HITACHI High-Technologies Corporation, Japan). Particle size distribution of the prepared Ag NPs in ILG based systems was determined by DLS (Dynamic Light Scattering) technique using a Zetasizer Nanoequipment. UV-VIS absorption spectra were recorded from 300 to 800 nm for Ag NPs dispersed in ILG medium involving a JASCO V 500 spectrophotometer.

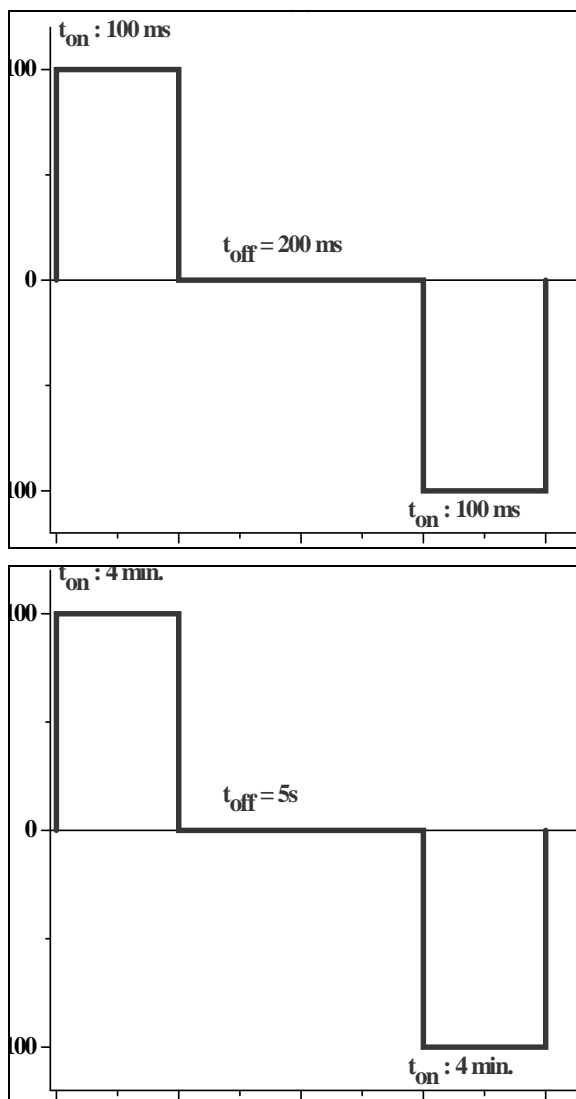


Fig. 2. Programmed electrical parameters for the pulse current electrodeposition of Ag NPs.

## RESULTS AND DISCUSSION

### Investigation of electrode processes by cyclic voltammetry

During the AgNPs formation there is a competition between two different cathode surface processes: (1) particles formation by electroreduction of  $\text{Ag}^+$  ions under protection of PVP, and (2) metal deposition at the cathode surface. This second process limits the synthesis efficiency and must be minimized. We expect for PVP on the one hand to promote the nucleation of Ag NPs and on the other hand to effectively stabilize the dispersed silver nanoparticles.

Cyclic voltammetry experiments were carried out firstly in supporting electrolytes at constant temperature of  $25^\circ\text{C}$  (Fig. 3) to study the potential window and potentially electrochemical reactions occurring on inert glassy carbon electrode. An example of typical CV curve recorded in ILG is

shown in Fig. 3a, indicating a potential window on GC electrode from about +1 V to -1 V (electrode potential vs. Ag quasi reference). This value of more than 2 V presents a good electrochemical stability of ILG, in agreement with CV curves recorded by Figueiredo et al. on GC, Pt and Au electrodes [42].

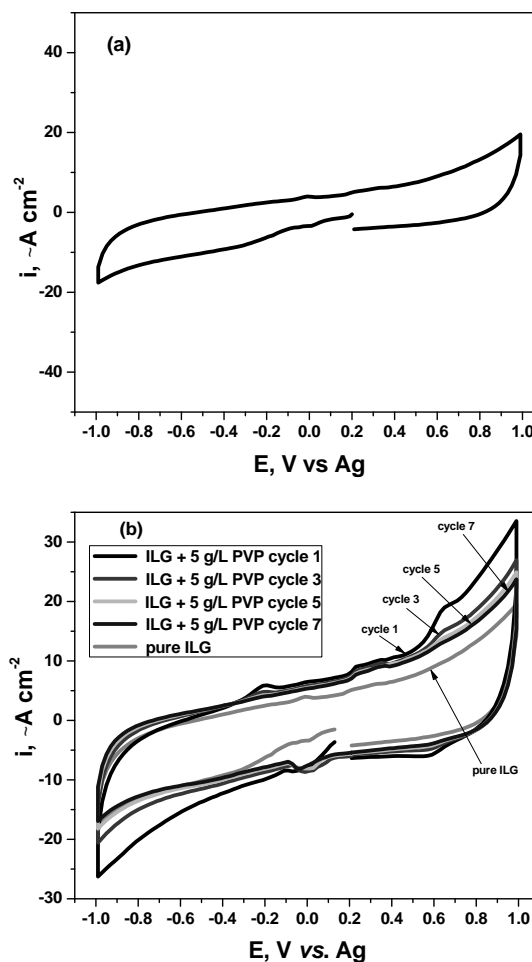


Fig. 3. CVs on GC electrode,  $20 \text{ mV s}^{-1}$  scan rate for supporting electrolytes: ILG (a); comparison of ILG with repetitive cycles of ILG +  $5 \text{ g L}^{-1}$  PVP (b).

Within this interval no peaks are observed which may suggest for the absence of processes related to any electroactive species. The increase of the cathodic current by extending the scan to negative potentials is attributed to the reduction of cholinium cation (this cation is essentially in ILG solvent), while the final increase of the anodic current is attributed to the oxidation of  $\text{Cl}^-$  ions (existing also in this solvent, although they are partially complexed with glycerol) or oxidation of glycerol. Fig. 3b shows that the dissolution of PVP in ILG seems to add a small current contribution as compared to pure ILG. As a whole, the current density in ILG-PVP after 7 cycles is lower than  $20 \mu\text{A/cm}^2$ , very close to the pure ILG solvent. The PVP molecules, having large molecular weight, do

not allow a significant electrochemical modification.

It is worth mentioning that there is lack of information in the literature regarding Ag electrochemistry in choline chloride - glycerol based ionic liquids. Therefore, several cyclic voltammetry experiments were performed and discussed here to confirm the electrochemical reversibility of Ag/Ag<sup>+</sup> couple, as in the case of choline chloride - urea DES [50,51]. Fig. 4 shows CVs for ILG + AgCl (ILG-Ag) systems indicating the influence of Ag<sup>+</sup> concentration at constant scan rate 20 mVs<sup>-1</sup> (Fig. 4a) and at various scan rates for systems with AgCl concentrations of 2, 5 and 10 mM (Figs. 4 b-d). In all the curves presented in Figure 4 a characteristic shape of the Ag<sup>+</sup>/Ag couple voltammograms can be seen. It has a broad cathodic peak for Ag<sup>+</sup> reduction followed by a high limiting diffusion current and a sharp anodic peak assigned to the stripping of Ag metal from GC surface.

As shown in Fig. 4a, both cathodic and anodic peak currents increase with AgCl concentration

from 5 to 16 μA, and from 23 to 54 μA, respectively. When AgCl content is higher, the cathodic peak potential shifts towards positive values (from -0.630 V to -0.470 V). The potential of the anodic peak remains constant at 0.05 V. These trends were also observed for CVs recorded at other scan rates. Moreover, the increase of the scan rate entails the increase of both cathodic and anodic peak currents for each AgCl concentration (Figs. 4 b-d). However, for ILG + 2 mM AgCl system (Fig. 4b) the shape of the cathodic curves is rather a plateau of limiting current and for the other ILG-Ag systems (with 5 and 10 mM AgCl, Figs. 4c,d) the shifting of the cathodic peak is significantly amplified with scan rate, leading to large E<sub>p</sub> differences. The high IR ohmic drop through the electrolyte due to the low electrical conductivity of ILG at room temperature could be an explanation. Therefore, we suppose that the Ag<sup>+</sup>/Ag couple is electrochemically reversible, especially because a shift of the anodic peak potential with AgCl concentration or scan rate was not observed.

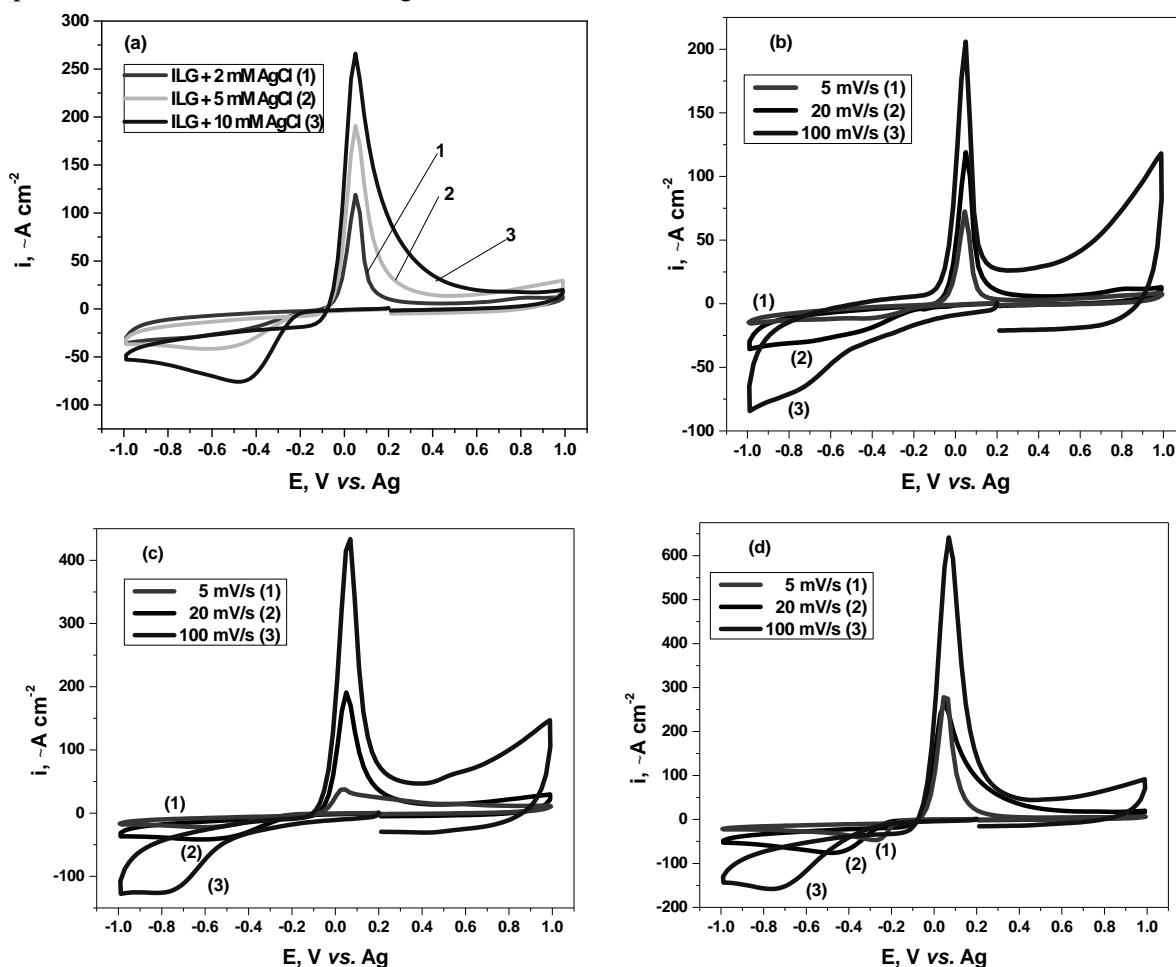


**Fig. 4.** CVs on GC electrode for ILG + x mM AgCl systems, showing the influence of Ag<sup>+</sup> concentration at constant scan rate 20 mVs<sup>-1</sup> (a) and at various scan rates for 2 mM AgCl (b), 5 mM AgCl (c) and 10 mM AgCl (d).

Fig. 5 shows comparatively the families of CVs recorded during 7 repetitive cycles in ILG + 5 mM AgCl and ILG + 10 mM AgCl electrolytes. For both systems the CV curve of the first cycle is very different from the next scans, when a tendency to reach a stationary state is observed for both peak potential and peak current. The maximum value of peak currents (in both cathodic and anodic processes) is recorded in the second cycle. In addition, we suppose that supplementary waves evidenced in the first cycle may be due to the Ag nuclei formed by the underpotential deposition (UPD of Ag, at -0.015 V) and respectively to their anodic dissolution (at 0.55 V).

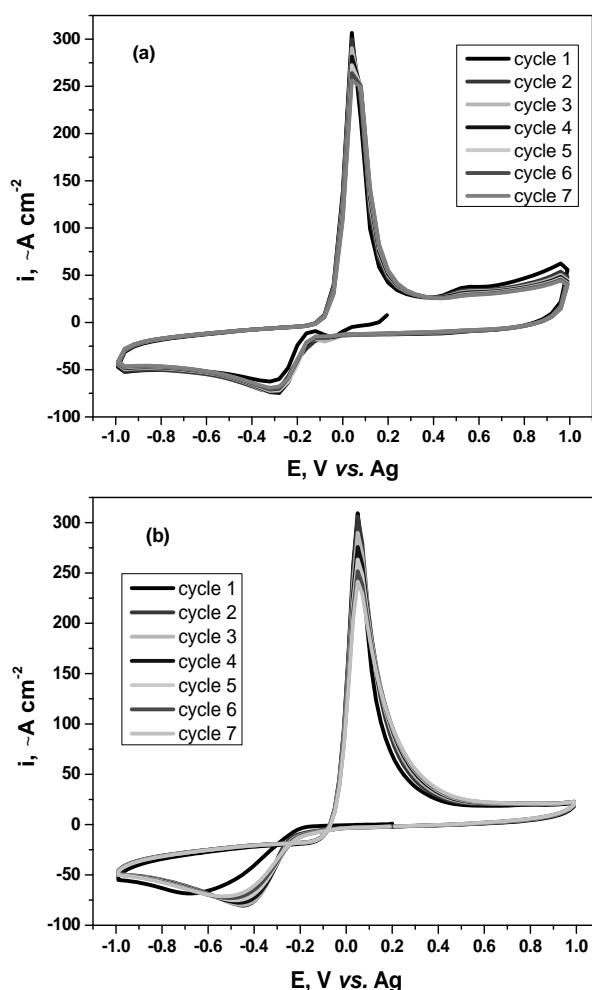


**Fig. 5.** Repetitive seven CV cycles on GC electrode,  $20 \text{ mVs}^{-1}$ , for ILG + 5 mM AgCl (a) and ILG + 10 mM AgCl (b).

A quantitative analysis of CVs for ILG-Ag electrolytes should take into consideration the mass-transport control (diffusion control) of a reversible cathodic process. We obtained plots (not shown here) with the cathodic peak current ( $I_p$ ) almost linearly proportional to square root of the scan rate ( $v^{1/2}$ ); the relative invariance of current function  $I_p/(c \times v^{1/2})$  with  $\text{Ag}^+$  concentration ( $c$ ) allowed us to estimate the diffusion coefficient of

silver ion in ILG systems, using the equation proposed by Schiffrin et al. [52,53]. Values of  $(0.2-1) \times 10^{-7} \text{ cm}^2\text{s}^{-1}$  at room temperature for diffusion coefficient of  $\text{Ag}^+$  using glassy carbon electrode and choline chloride – glycerol electrolyte are much lower than usual values in aqueous electrolytes or in traditional ionic liquids ( $10^{-5} \text{ cm}^2\text{s}^{-1}$ ). However, they are reasonable, taking into account the high viscosity of ILG and a partial complexation of  $\text{Ag}^+$  ions with glycerol.

Cyclic voltammetry studies for systems containing PVP as capping and stabilizer agent are very important to establish its optimum content in the electrolyte.

Fig. 6 presents an example of the recorded CV in the absence and in the presence of PVP for ILG + AgCl system at a constant scan rate. It can be observed for  $\text{Ag}^+$  electroreduction that the cathodic peak potential shifted to more negative values whereas the peak current remains almost similar. The anodic peak corresponding to Ag dissolution as stripping appears at potentials around 0.06 V in the PVP free solution with a displacement towards 0.04 V in the presence of PVP.

The anodic peak current in the absence of PVP is significantly higher than that evidenced in the presence of PVP; this significantly decrease on PVP addition was also observed for all other ILG-PVP-Ag systems (with 0.6; 1 and 5  $\text{gL}^{-1}$  PVP and 2, 5 and 10 mM AgCl, respectively).

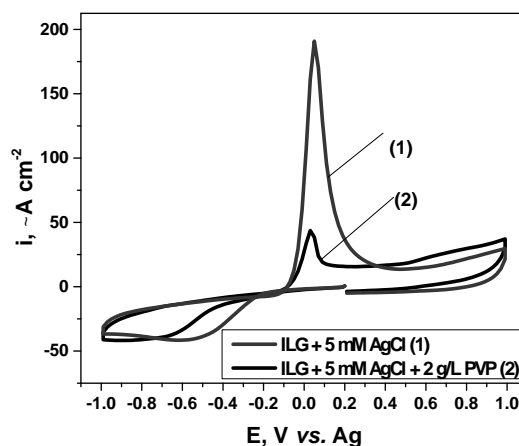


**Fig. 6.** Comparative CVs on GC for ILG + 5 mM AgCl system in the absence and in the presence of  $2 \text{ gL}^{-1}$  PVP (scan rate:  $20 \text{ mVs}^{-1}$ ).

It can be assumed that in the PVP free solution the entire electroreduced silver has been completely dissolved anodically forming  $\text{Ag}^+$  species, while in the PVP containing ones, just the electrodeposited silver has been again dissolved during anodic scan. In the presence of PVP, the anodic dissolution current is lower, thus suggesting that a part of

metallic silver remains into the solution as nanoparticles protected by the stabilizer. This behavior is in a good agreement with previous researches [21 and included references].

To get more information on the influence of PVP content in the electrolyte to maximize the silver nanoparticles electrosynthesis yield, cyclic voltammograms have been recorded for 7 repetitive cycles in systems with constant  $\text{Ag}^+$  concentration and different PVP concentrations (1; 2 and 5  $\text{gL}^{-1}$ ), as exemplified in Fig. 7. For systems diluted in PVP, the evolution of the cathodic peak current with the number of cycles was not significantly influenced by PVP; this current is diminishing only at high PVP concentration (5  $\text{gL}^{-1}$  PVP) as Figure 7a shows. The cathodic peak potential shifts to more negative values with the number of cycles.

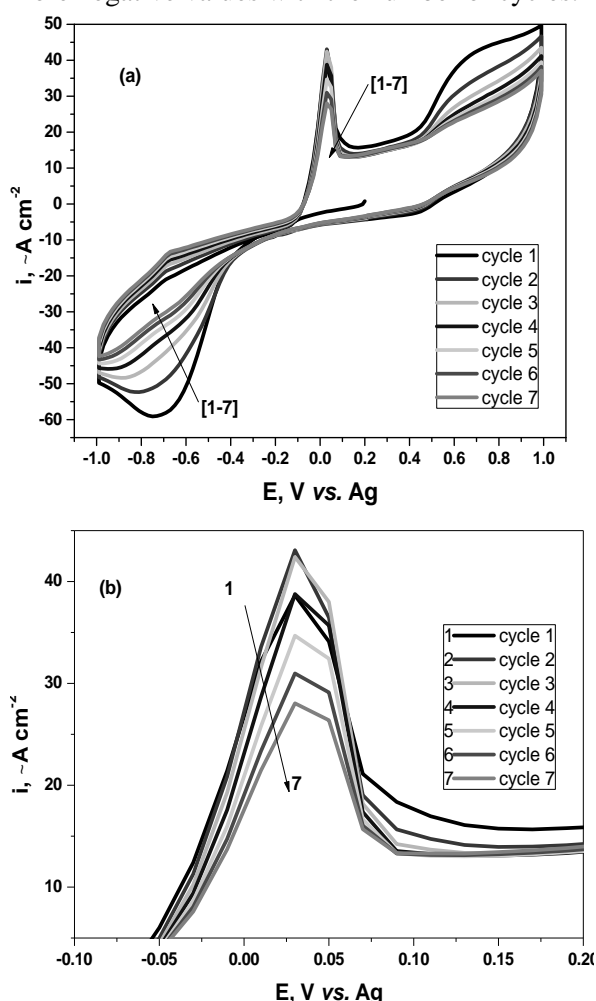


**Fig. 7.** Repetitive seven CV cycles on GC electrode, for ILG + 5 mM AgCl + 5  $\text{gL}^{-1}$  PVP system (a) and details of the anodic peak for Ag stripping (b), for scan rate of 20  $\text{mVs}^{-1}$ .

The most obvious changes are observed on the anodic branch of the voltammograms. Except for the first cycle, the anodic peak current of Ag stripping in systems with 1 and 2  $\text{gL}^{-1}$  PVP decreases slightly with the number of cycles.

However, the decrease was found to be bigger for higher PVP concentrations (of 5  $\text{gL}^{-1}$ ), although the anodic peak potential has not been shifted by cycling (Fig. 7b).

Considering the decrease of the anodic peak current as an evidence for the Ag NPs electrosynthesis rate increase, one may thus suggest that the optimum content of PVP allowing a suitable formation of Ag nanoparticles should be around 5  $\text{gL}^{-1}$ , a slightly lower value as compared to that proposed for water based electrolytes [21].

#### Electrochemical synthesis of Ag NPs and characterization

Following the electrochemical synthesis process, Ag NPs of various size between 60 and 200 nm were obtained, depending on the used ILG based electrolyte, pulse reversed current regime and electrodes type. Fig. 8 comparatively presents examples of the recorded particles size distribution for Ag NPs electrosynthesized under the two regimes of the applied pulse reversed current, using Ag electrodes in the presence and in the absence of PVP. As expected, the PVP addition associated with the use of shorter pulses facilitates the decrease of the average NPs size from around 140-165 nm towards 47-63 nm. It is known that this capping agent may surround the nucleated particle restricting its further growing [34-37].

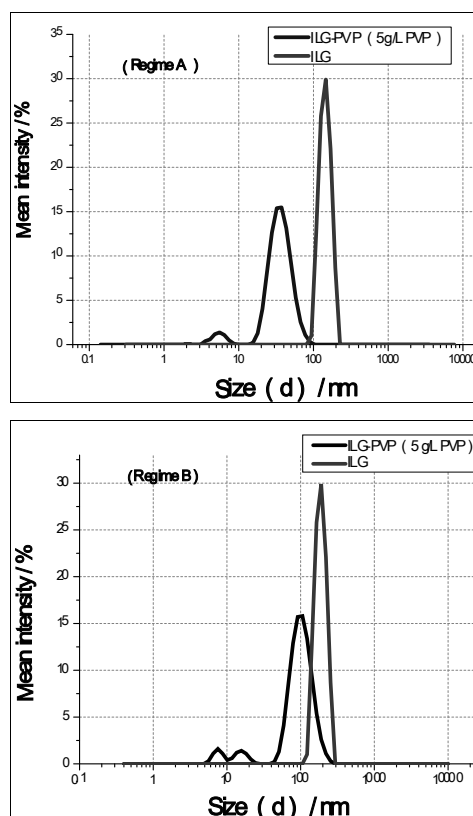


**Fig. 8.** DLS plots for Ag NPs electrosynthesized under regime (A) and (B) from Fig. 2 using Ag electrodes and 30 min. electrolysis time.

The particles size distribution for Ag NPs electrosynthesized under regime (B) of the applied pulse reversed current using Pt electrodes and ILG-Ag and ILG-PVP-Ag electrolytes is presented in Fig. 9. As shown, when Ag<sup>+</sup> ions are already present in the electrolyte, the PVP addition does not act any more as a stabilizer for nanoparticles. Therefore Ag NPs of about 100-200 nm were obtained in the presence of PVP, while for ILG-Ag electrolyte their size was in the range of 70-90 nm.

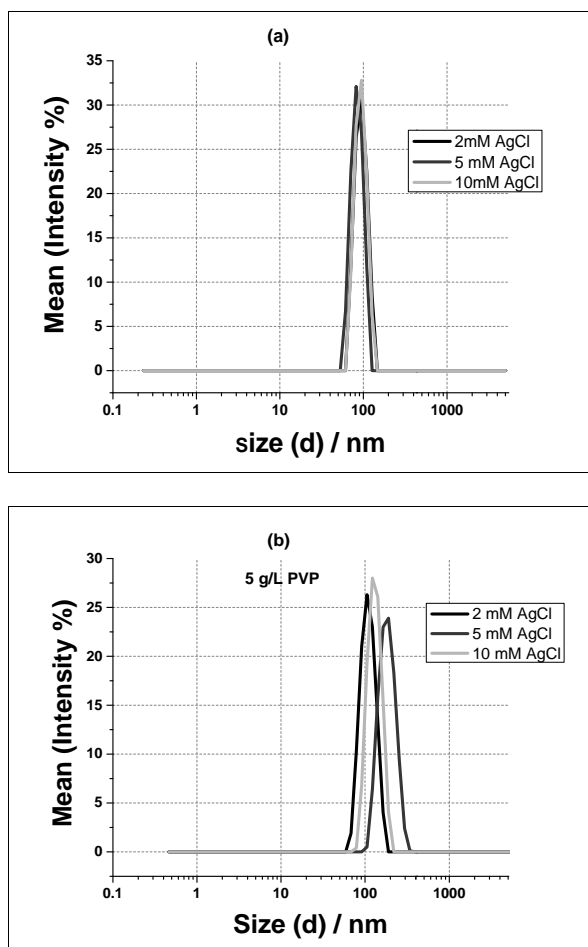


**Fig. 9.** DLS plots for Ag NPs electrosynthesized under regime (B), 30 min., using Pt electrodes in the absence (a) and in the presence of 5 gL<sup>-1</sup> PVP (b).

In this case the role of the ionic liquid itself, which also may act in a similar manner, should be taken into consideration. Thus, the organic cations (cholinium) of the ionic liquid may surround the Ag nuclei produced from Ag<sup>+</sup> electrochemical reduction during the negative pulse, in this way stabilizing the particles size and their dispersion in the ionic liquid. Quite similar behavior has been reported by Fukui et al. [29] in the case of Ag NPs preparation using BMPTFSA, BMITFSA, TMHATFSA, BMIOTf and EMITFSA ionic liquids containing Ag<sup>+</sup> ions.

SEM micrographs of Ag NPs electrochemically synthesized using different pulse reversed current regimes are shown in Figs. 10 and 11.

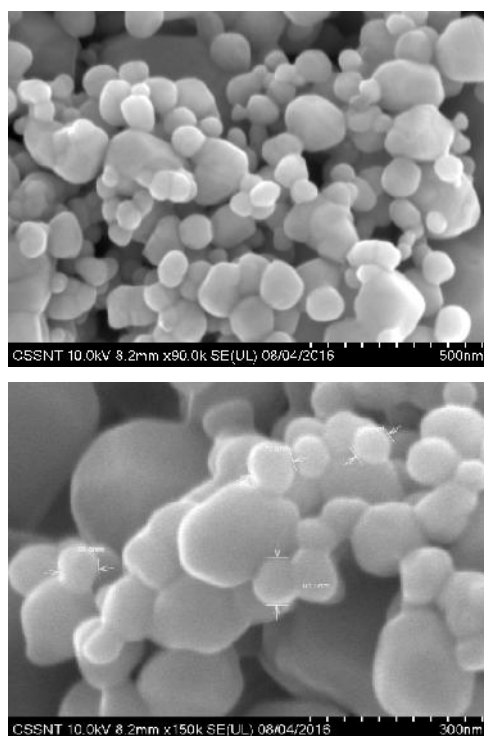


**Fig. 10.** SEM micrographs at different magnifications for Ag NPs electro-synthesized in ILG-PVP under regime (A) of applied pulse reversed current using Ag electrodes.

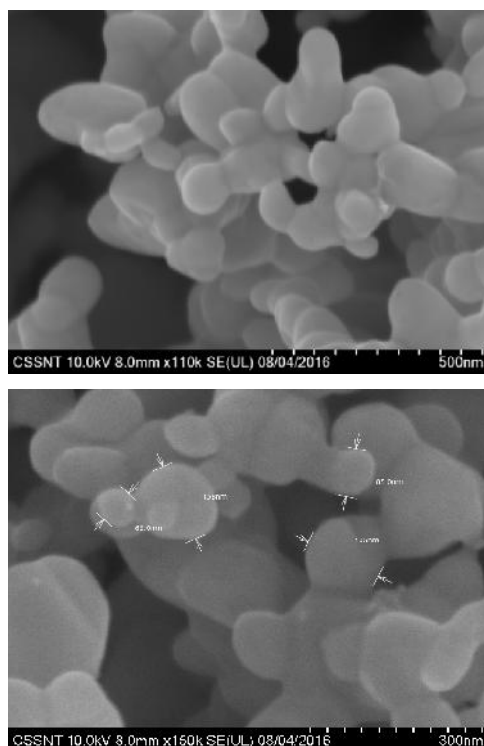


**Fig. 11.** SEM micrographs at different magnifications for Ag NPs electro-synthesized in ILG-PVP under regime (B) of applied pulse reversed current using Ag electrodes.

As it can be seen, the samples consist of quite spherical particles with size between 60-85 nm when regime (A) is applied, while for regime (B) larger particles of about 80-135 nm are observed.

This evidence may suggest for shorter pulses that are more appropriate to obtain smaller Ag NPs; in this way the growth step is limited, mostly facilitating the nucleation one. In addition a slight agglomeration of the nanoparticles in the SEM images may be noticed, due to their small size.

UV/VIS absorption spectra for the electrosynthesized AgNPs involving ILG have been also recorded, as exemplified in Fig. 12.

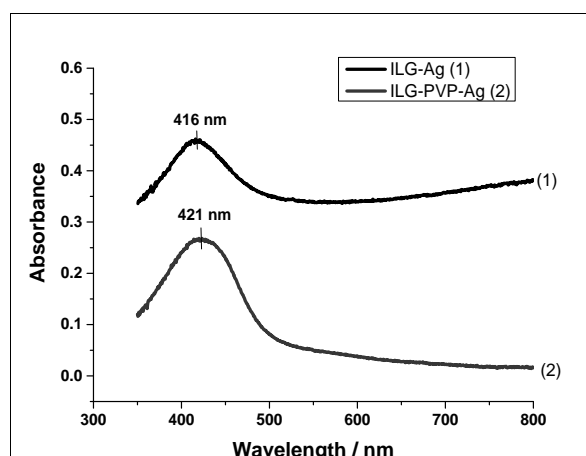


**Fig. 12.** UV/Vis absorption spectra of AgNPs electrosynthesized in ILG-Ag and ILG-PVP-Ag electrolytes using Pt electrodes (5 mM AgCl, 5 gL<sup>-1</sup> PVP).

The absorption spectra from Fig. 12 show one distinct absorption band centered at around 416 - 420 nm, which is characteristic for the presence of metallic silver [54]. This is usually assigned to the surface plasmon excitation of silver nanoparticles with a certain distortion with respect to the spherical shape [3]. Usually, a decrease in the particle size induces a decrease in the plasmon band intensity, as it can be noticed in the case of PVP addition [55,56].

## CONCLUSIONS

Based on the obtained experimental results, a novel electrochemical synthesis procedure for preparing Ag nanoparticles involving pulse reversed current and choline chloride-glycerol eutectic mixture as electrolyte, has been proposed. Voltammetric measurements showed quite reversible and diffusion controlled process of silver deposition in the electrolyte based on choline chloride –glycerol deep eutectic solvent. Through a proper selection of the applied current and of the pulse regime, the nanoparticles size may be

controlled. The obtained Ag NPs showed size in the range of 60-200 nm, depending on the electrochemical synthesis conditions.

Some other important aspects such as a better understanding of the electrochemical process occurring in the choline chloride based ionic liquid electrolyte and their influence on the Ag NPs size and morphology are suggested for further investigation.

**Acknowledgements:** The present work was financially supported by the Romanian Ministry of Education and Research, PNCDI II-PARTENERIATE, under research contract No.167/2012 – SELFPROPIEL and NOVINAL-BEST project (Contract 38/2016) under M ERA Net Program.

## REFERENCES

1. A. Petica, S. Gavrilu, M. Lungu, N. Buruntea, C. Panzaru, *Mater. Sci. Eng. B*, **152(1-3)**, 22 (2008).
2. O. Akhavan, M. Abdolohad, Y. Abdi, S. Mohajerzadeh, *J. Mater. Chem.*, **21(2)**, 387 (2011).
3. L. Blandon, M. V. Vázquez, D. M. Benjumea, G. Ciro, *Portug. Electrochim. Acta*, **30(2)**, 135 (2012).
4. A. Castle, E. Gracia-Espino, C. Nieto-Delgado, H. Terrones, M. Terrones, S. Hussain, *ACS Nano*, **5(4)**, 2458 (2011).
5. F. Ahmadi, J. B. Raoof, R. Ojani, M. Baghayeri, M. M. Lakouraj, H. Tashakkorian, *Chinese J. Catalysis*, **36(3)**, 439 (2015).
6. C. Xie, X. Lu, K. Wang, *Particle Particle Syst. Characteriz.*, **32(6)**, 630 (2015).
7. A. Ivanovic, S. Dimitrijevic, S. Dimitrijevic, B. Trumic, V. Marianovic, J. Petrovic, N. Vukovic, *Optoelectr. Adv. Mater. Rapid Commun.*, **6(3-4)**, 465 (2012).
8. G. Guo, *Chinese J. Rare Metals*, **37(6)**, 922 (2013).
9. J. Tian, D. Peng, X. Wu, W. Li, H. Deng, S. Liu, *Carbohydr. Polym.*, **156**, 19 (2017).
10. S. Sahoo, S. Husale, S. Karna, S. Nayak, P. Ajayan, *J. Am. Chem. Soc.*, **133(11)**, 4005 (2011).
11. J. B. Raoof, R. Ojani, E. Hasheminejad, S. Rashid-Nadimi, *Appl. Surf. Sci.*, **258**, 2788 (2012).
12. R. Sivasubramanian, M. Sangaranarayanan, *Sensors Actuators B*, **213**, 92 (2015).
13. M. Amiri, S. Nouhi, Y. Azizian-Kalandaragh, *Mater. Chem. Phys.*, **155**, 129 (2015).
14. M. Baghayeri, M. B. Tehrani, A. Amiri, B. Maleki, S. Farhadi, *Mater. Sci. Eng. C*, **66**, 77 (2016).
15. J. Bian, Q. Li, C. Huang, Y. Guo, M. Zaw, R.-Q. Zhang, *Phys. Chem. Chem. Phys.*, **17(22)**, 14849 (2015).
16. N. Dar, K.-Y. Chen, Y.-T. Nien, I.-G. Chen, *Analyt. Lett.*, **49(8)**, 1198 (2016).
17. L. Qu, L. Dai, *J. Phys. Chem. B*, **109(29)**, 13985 (2005).
18. S. Djoki, N. Nikoli, P. Zivkovi, K. Popov, N. Djoki, *ECS Trans.*, **33(18)**, 7 (2011).



19. U. Mohanty, *J. Appl. Electrochem.*, **41(3)**, 257 (2012).
20. K. Ignatova, *Bulgarian Chem. Commun.*, **45(3)**, 357 (2013).
21. N. Dobre, A. Petica, M. Buda, L. Anicai, T. Visan, *UPB Sci. Bull. Series B*, **76(4)**, 127(2014).
22. C. Bosch-Navarro, J. Rourke, N. Wilson, *RSC Adv.*, **6(77)**, 73790 (2016).
23. S. Tang, X. Meng, H. Lu, S. Zhu, *Mater. Chem. Phys.*, **116**, 464 (2009).
24. W. Dobbs, J.-M. Suisse, L. Douce, R. Welter, *Angew. Chem. Int. Ed.*, **45(25)**, 4179 (2006).
25. R. Bomparola, S. Caporali, A. Lavacchi, U. Bardi, *Surf. Coat. Technol.*, **201(24)**, 9485 (2007).
26. N. Li, X. Bai, S. Zhang, Y. Gao, L. Zheng, J. Zhang, H. Ma, *J. Dispers. Sci. Technol.*, **29**, 1059 (2008).
27. A. Bhatt, A. Bond, *J. Electroanal. Chem.*, **619**, 1 (2008).
28. T.-H. Tsai, S. Thiagarajan, S.-M. Chen, *Electroanalysis*, **22(6)**, 680 (2010).
29. R. Fukui, Y. Katayama, T. Miura, *J. Electrochem. Soc.*, **158(9)**, D567 (2011).
30. B. H. R. Suryanto, C. A. Gunawan, X. Lu, C. Zhao, *Electrochim. Acta*, **81**, 98 (2012).
31. Y. Li, Q. Qiang, X. Zheng, Z. Wang, *Electrochem. Commun.*, **58**, 41 (2015).
32. Y. Li, Z. Wang, C. Zhao, *J. Electrochem. Soc.*, **163(8)**, D442 (2016).
33. J. Zhu, X. Zhu, Y. Wang, *Microelectron. Eng.*, **77**, 58 (2005).
34. B. Yin, H. Ma, S. Wang, S. Chen, *J. Phys. Chem. B*, **107(34)**, 8898 (2003).
35. H. Ma, B. Yin, S. Wang, Y. Jiao, W. Pan, S. Huang, S. Chen, F. Meng, *Chem. Phys. Chem.*, **5(1)**, 68 (2004).
36. D. Malina, A. Sobczak-Kupiec, Z. Wzorek, Z. Kowalski, *Digest J. Nanomater. Biostruct.*, **7(4)**, 1527 (2012).
37. K. M. Koczur, S. Mourdikoudis, L. Polavarapu, S. E. Skrabalak, *Dalton Trans.* **44(41)**, 17883 (2015).
38. E. Smith, A. Abbott, K. Ryder, *Chem. Rev.*, **114**, 11060 (2014).
39. A. Abo-Hamad, M. Hayyan, M. A. H. Al Saadi, M. A. Hashim, *Chem. Eng. J.*, **273**, 551 (2015).
40. G. García, S. Aparicio, R. Ullah, M. Atilhan, *Energ. Fuels*, **29**, 2616 (2015).
41. A. Abbott, R. Harris, K. Ryder, C. D'Agostino, L. Gladden, M. Mantle, *Green Chem.*, **13**, 82 (2011).
42. M. Figueiredo, C. Gomes, R. Costa, A. Martins, C. M. Pereira, F. Silva, *Electrochim. Acta*, **54**, 2630 (2009).
43. Q. Abbas, L. Binder, *ECS Trans.*, **33(7)**, 49 (2010).
44. R. Leron, D. S. H. Wong, M.-H. Li, *Fluid Phase Equil.*, **335**, 32 (2012).
45. Y. Y. Zhang, X. Y. Ji, X. H. Lu, *Scientia Sinica Chimica*, **44(6)**, 927 (2014).
46. A. Yadav, S. Trivedi, R. Rai, S. K. Pandey, *Fluid Phase Equil.*, **367**, 135 (2014).
47. A. M. P. Sakita, R. Della Noce, C. S. Fugivara, A. V. Benedetti, *Phys. Chem. Chem. Phys.*, **18**, 25048 (2016).
48. F.S.Mjalli, O.U.Ahmed, *Korean J. Chem. Eng.*, **33(1)**, 337 (2016).
49. G. H. Abdullah, M. A. Kadhom, *Int. J. Eng. Res. Develop.*, **12(9)**, 73 (2016).
50. L. Anicai, A. Cojocararu, A. Florea, T. Visan, *Studia Univ. Babeş-Bolyai, Chemia*, **53(1)**, 119 (2008).
51. A. Florea, A. Petica, L. Anicai, T. Visan, *UPB Sci. Bull. Series B*, **72(2)**, 115 (2010).
52. D. J. Schiffrin, *J. Electroanal. Chem.*, **201**, 199 (1986).
53. L. Avaca, S. Kaufmann, K. Kontturi, L. Murtomaki, D. Schiffrin, *Berichte Bunsenges. Physik. Chemie*, **97(1)**, 70 (1993).
54. Z. Zhang, B. Zhao, L. Hu, *J. Solid State Chem.*, **121**, 105 (1996).
55. C. Petiy, P. Lixon, M. Pileni, *J. Phys. Chem.*, **97**, 12974 (1993).
56. A. Taleb, C. Petit, M. Pileni, *J. Phys. Chem. B*, **102**, 2214 (1998).

Ag

1,2, 2, 2, 2, 2, 1,2, 2\*

1, 2

132, 313,

4 2016 ; 6 2017 .

( ) 25 ° , -

Ag+/Ag -Ag

Ag 60-200 ,

## New azulene modified electrodes for heavy metal ions recognition

G.-L. Arnold<sup>1</sup>, I.G. Lazar<sup>1</sup>, E.-M. Ungureanu<sup>1\*</sup>, G.-O. Buica<sup>1\*\*</sup>, L. Birzan<sup>2</sup>

<sup>1</sup>University "Politehnica" of Bucharest, Faculty of Applied Chemistry and Material Sciences, 1-7 Polizu Street, 011061, Bucharest, Romania

<sup>2</sup>Romanian Academy, Organic Chemistry Center "C.D. Nenitzescu", Splaiul Independentei 202B, 71141 Bucharest, Romania

Received November 14, 2016      Revised December 27, 2016

(E)-2-thioxo-5-((4,6,8-trimethylazulen-1-yl)methylene)thiazolidin-4-one (**L**) was electrochemically characterized by cyclic voltammetry, differential pulse voltammetry and rotating disk electrode voltammetry. Poly**L** modified electrode obtained by the controlled potential electrolysis was tested in solutions containing different metal ions (Cd, Pb, Cu, Hg) at increased concentrations. The best response was found for Pb ( $10^{-7}$  M).

**Key words:** (E)-2-thioxo-5-((4,6,8-trimethylazulen-1-yl)methylene)thiazolidin-4-one, cyclic voltammetry, differential pulse voltammetry, rotating disk electrode voltammetry, heavy metal ions detection

### INTRODUCTION

Benzylidene rhodanines, especially those containing electron rich groups as dimethylamino groups, have been used for amperometric [1] and spectrophotometric determination of metal ions such as Cu (II), Fe (II), Ni (II) and Zn (II) [2]. They give good results in preconcentration of silver by quantitative complexation during the samples analysis by flame atomic absorption spectrometry (FAAS) [3]. Due to high affinity to silver, benzylidene rhodanines can be used for indirect titration of anions that form precipitates with silver nitrate, such as cyanide [4]. Other metals that can be dosed quantitatively using these compounds are Hg, Cu, Au, Pt and Pd, according to the Merck index. Here, azulenylynyl rhodanines that are similar to benzylidene rhodanines, were synthesized and tested as good complexants for toxic cations like Cu (II), Pb (II) and Hg (II). Azulenes are polar organic compounds characterized by two condensed cyclic moieties; one cycle moiety containing seven carbon atoms (electron-poor) and the other one containing five carbon atoms (electron-rich) [5]. These properties have been exploited for—preparation of polymer films which have been used for heavy metal ions detection [6], applications in optoelectronics [7] and medicine (antiretroviral activity) [8]. This article presents the electrochemical characterization of the azulene derivative (E)-2-thioxo-5-((4,6,8-trimethylazulen-1-yl)methylene)thiazolidin-4-one

(**L**) (Fig. 1). A new modified electrode based on the poly**L** has been prepared and used for detection of heavy metals Cu (II), Pb (II), Hg (II) and Cd (II) in different concentrations

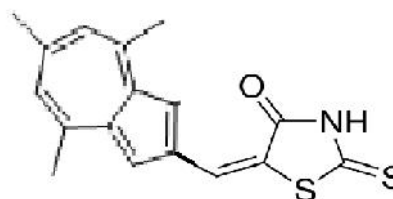


Fig. 1. Structure of azulene derivative **L**.

### EXPERIMENTAL

The ligand **L** was synthesized according to the previously published procedure [9]. Electrochemical characterization of the ligand **L** and preparation of modified electrodes were performed in acetonitrile (CH<sub>3</sub>CN) containing 0.1M tetrabutylammonium perchlorate (TBAP), both from Fluka, and used as solvent and supporting electrolyte. Stock solutions of Cd, Pb, Cu and Hg ( $10^{-2}$ M) have been freshly prepared before each experiment, using Cd (II) nitrate tetra hydrate, Pb(II) nitrate and Hg(II) acetate (all Sigma Aldrich) and Cu(II) acetate monohydrate (Fluka). 0.1 M buffer acetate (pH = 5.5) solution was prepared from 0.2 M acetic acid solution and 0.2 M sodium acetate solution.

Electrochemical experiments have been performed using the PGSTAT 12 AUTOLAB

To whom all correspondence should be sent:

E-mail: \*em\_ungureanu2000@yahoo.com, \*\*buica\_george@yahoo.com

connected to a three-electrode cell. As working electrodes, a glassy carbon disk (with 3 mm diameter) (Metrohm) and polyL glassy carbon modified electrodes were explored in characterization and recognition experiments, respectively.

The auxiliary electrode was a platinum wire, while the reference electrode was either Ag/10 mM AgNO<sub>3</sub> in 0.1 M TBAP/CH<sub>3</sub>CN (in electrochemical experiments performed in acetonitrile solutions), or Ag/AgCl, 3 M KCl (in electrochemical experiments performed in water solutions). The glassy carbon electrode was polished with diamond (2 μm) paste before each experiment and cleaned with the solvent.

Cyclic voltammetry (CV), rotating disk electrode voltammetry (RDE) and differential pulse voltammetry (DPV) methods have been used for electrochemical characterization. CV curves have usually been recorded at the scan rate of 0.1 V/s. DPV curves have been recorded at 0.01 V/s, with a pulse height of 0.025 V and step time of 0.2 s, while RDE curves were recorded at 0.01 V/s. All curves have been recorded at 25°C, under argon atmosphere. In experiments performed in acetonitrile solutions, the potentials were finally referred to the potential of the ferrocene/ferricinium redox couple (Fc/Fc<sup>+</sup>) equal to +0.07 V.

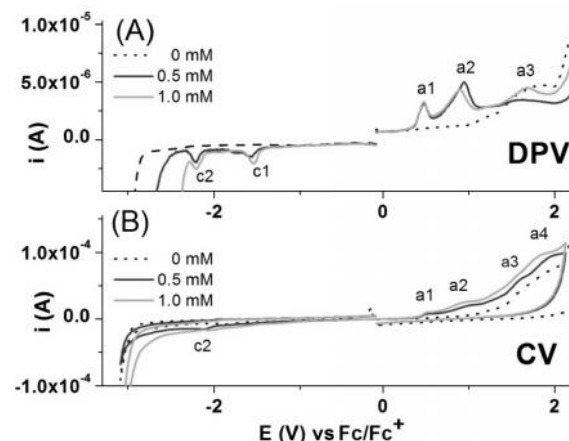
Electrochemical experiments of heavy metal ions detection have been performed in 0.1 M buffer acetate (pH = 5.5) solution as the supporting electrolyte, at 25°C under argon atmosphere. Heavy metal ion solutions of different concentration (10<sup>-4</sup> M – 10<sup>-7</sup> M) were prepared by successive dilution from their stock solutions (10<sup>-2</sup> M) in water.

## RESULTS AND DISCUSSION

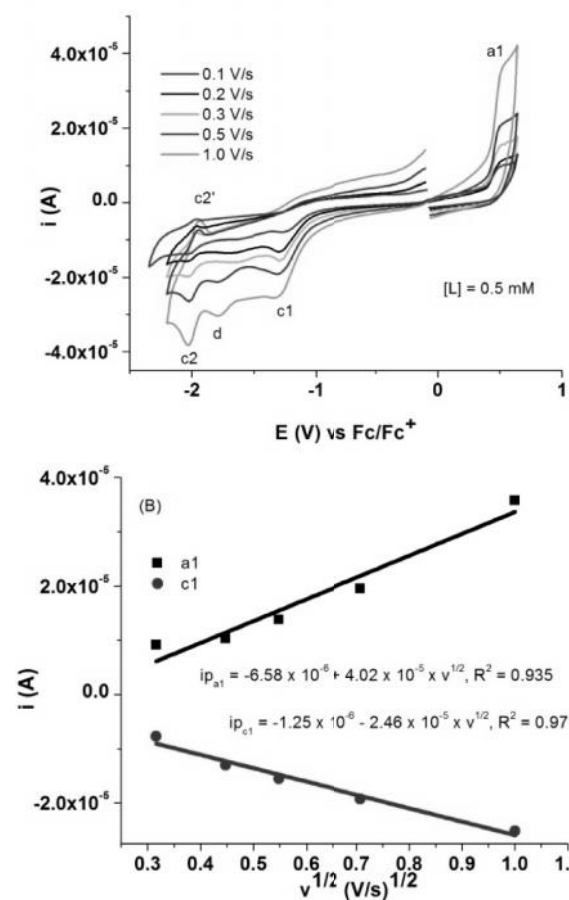
Electrochemical characterization of the azulene derivative **L** has been done by CV, DPV and RDE experiments on the glassy carbon electrode. The CV and DPV oxidation and reduction curves have been recorded at different concentrations of **L** (0 – 1 mM) in 0.1 M TBAP/CH<sub>3</sub>CN, starting from the stationary potential (Fig. 2). DPV curves in Fig. 2A show three oxidation peaks (a1 – a3) and two reduction peaks (c1 and c2). DPV peak currents for a1, c1, and c2 peaks are increasing with the concentration of **L**. For a2 and a3 peaks, however, there is an inversion, which will be explained further on. CV curves in Fig. 2B show 4 anodic peaks (a1 – a4) and one cathodic peak (c2), respecting the notation from DPV curves.

Fig. 3A presents the CV curves obtained at different scan rates (0.1 – 1 V/s) within potential domains of the anodic peak a1 and cathodic peaks

c1 and c2 for 0.5 mM solution of **L**. A new cathodic peak (d) can be clearly seen with increase of the scan rate. Also, all current values increase with the scan rate. Linear dependences for the peak currents on the square root of the scan rate are obtained for a1 and c1 (Fig. 3B).



**Fig. 2.** DPV (0.01 V/s) curves (A) and CV (0.1 V/s) curves (B) of glassy carbon electrode for different concentrations of **L** in 0.1M TBAP/CH<sub>3</sub>CN.



**Fig. 3.** CV curves in the short potential domain at different scan rates of glassy carbon electrode for 0.5 mM of **L** in 0.1M TBAP/CH<sub>3</sub>CN (A) and linear dependences of peak currents on the square root of scan rate (B).

The diffusion coefficient of **L** was calculated from the slope of the a1 peak current using the Randles-Sevcik equation for one electron transfer, giving the value of  $1.77 \times 10^{-5} \text{ cm}^2/\text{s}$ .

Fig. 4 shows the CV curves (0.1 V/s) obtained in different scan potential domains for 0.5 mM solution of **L**, while Table 1 presents the character of processes and potential of each peak, all estimated from CV and DPV curves measured for 0.5 mM solution of **L**. It seems that all processes in the anodic domain are irreversible, while in the cathodic domain, the peak c1 is irreversible, while c2 is reversible, having a corresponding peak in the reverse scan (c2') situated at 89 mV in respect to c2.

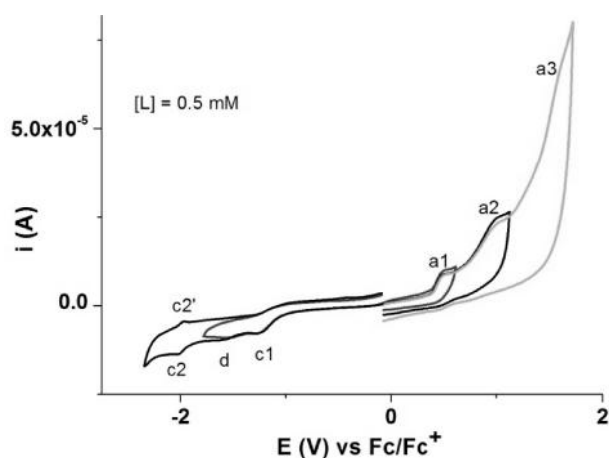


**Fig. 4.** CV curves at different potential scan domains of glassy carbon electrode for 0.5 mM of **L** in 0.1M TBAP/CH<sub>3</sub>CN

Assigning of peaks appearing in voltammetric curves to specific reactions is difficult in the absence of laborious studies of the electrolysis products obtained at each potential. A documentary survey on the reduction of benzylidene rhodanine (which is similar to azulene rhodanine) shows that it is reduced at very negative potentials (this fact can be explained by the bulkiness of the trimethylazulene moiety that hinders electron transfer on the electrode). However, several peaks can be attributed, what is mostly due to different electron densities of the main components of the molecule. Therefore, the peak a1 represents formation of the radical cation, with positive charge being stabilized on the azulene seven-membered cycle as tropylium ion. The second peak a2 represents formation of higher reactive rhodanine radicals which marks the beginning of the polymerization process. In the cathodic domain it is expected that the vinylic double bond is reduced first at the potential of c1, and some desulfuration processes become active at the potential of c2. The reversible peak appearing at higher scan rates (d) at

the potential of -1.8 V at 0.5 V/s (Fig. 3A) could represent reduction of the C=O bond.

**Table 1.** Peak potential (V) values (vs. Fc/Fc<sup>+</sup>) and process types for [**L**] = 0.5 mM in 0.1M TBAP/CH<sub>3</sub>CN

Peak	Method		Process type
	DPV	CV	
a1	0.473	0.49	(i)*
a2	0.94	0.98	(i)*
a3	1.61	1.57	(i)*
c1	-1.54	-	(i)*
d	-	-1.62	(i)*
c2	-2.21	-2.11	(r)*
c2'	-	-1.93	

\* r - reversible process; i - irreversible process

Fig. 5 presents RDE curves of glassy carbon electrode obtained at different rotation rates (500 – 1500 rpm) and DPV curve for 0.5mM of **L** in 0.1 M TBAP/CH<sub>3</sub>CN. Three processes showing peaks in the anodic domain (a1, a2, a4) and two waves in the cathodic domain (c1 and c2) can be observed in Fig. 5A. They are denoted according to the notation given for the peaks of DPV curve shown in Fig.5B. The peculiar shape of RDE curves in the anodic scans is due to the formation of insulating polymer films that cover the electrode surface and lead to drop of the current to the baseline value. The peak a4 (seen in Fig. 2 on CV curves at different concentrations) could not be explained yet.

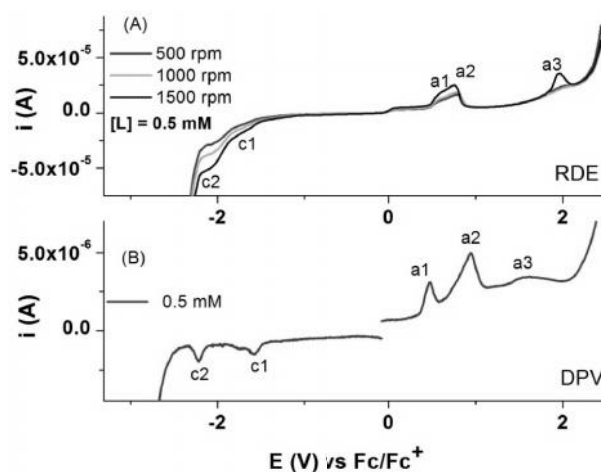


**Fig. 5.** (A) RDE curves (0.01 V/s) at different rotation rates (500 – 1500 rpm) and (B) DPV curves of glassy carbon electrode for 0.5 mM of **L** in 0.1 M TBAP/CH<sub>3</sub>CN.

The current values from RDE curves increase with the rotation rate, more for the cathodic waves and less for the anodic processes. This behavior is also in agreement with the formation of insulating films in the anodic region of potentials.

## Modified electrodes

PolyL modified electrodes have been prepared from 0.5 mM L in 0.1 M TBAP/CH<sub>3</sub>CN by either successive potential scans, or by controlled potential electrolysis (CPE). The prepared modified electrodes were transferred into the ferrocene solution (1 mM) in 0.1M TBAP/CH<sub>3</sub>CN. The

ferrocene signal in CV curves of modified electrodes has been compared with the ferrocene signal on the bare electrode. CVs of two polyL modified electrodes obtained by 20 successive potential scans performed between  $-0.3$  V and two anodic limits of 0.6 V and 1.12 V, respectively, are shown in Figs. 6A and 6B.

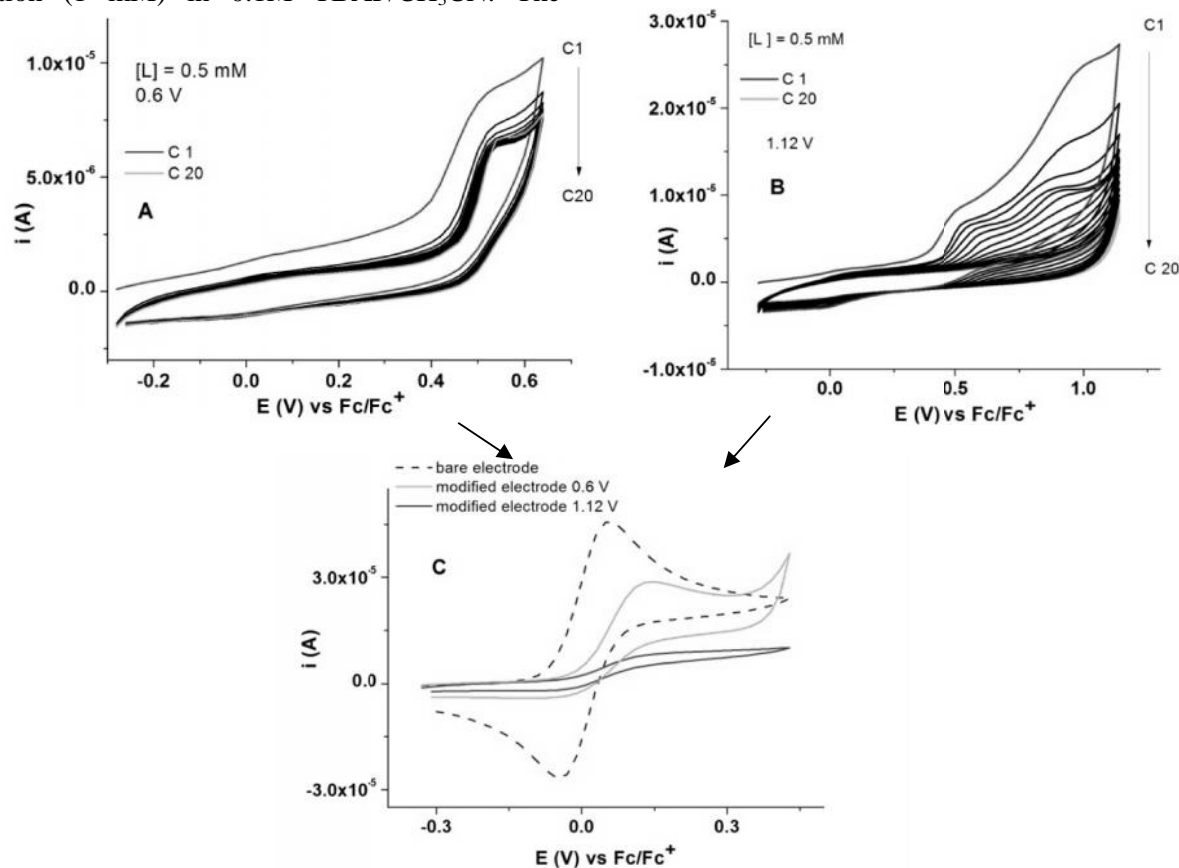


**Fig. 6.** CV curves (0.1 V/s) of polyL modified electrodes obtained by successive potential scanning between  $-0.3$  V and different anodic limits, 0.6 V (A) and 1.12 V (B) and the corresponding CV curves (0.1V/s) measured in 1mM ferrocene solution (C).

CV curves of these two modified electrodes in the ferrocene transfer solution are shown in Fig. 6C. It can be seen that the ferrocene signal is much more distorted for the polyL modified electrode prepared with the anodic limit of 1.12V. That is why this anodic limit of the potential was chosen to prepare modified electrodes by the potential cycling procedure, because the electrode is more covered with the polymeric film. This fact ensures a bigger amount of complexing units in view of complexation and leads to a better detection of heavy metals in our experiments.

The potential of 1.12 V has also been selected for polyL modified electrodes prepared by CPE (Fig. 7). At this potential value, different electropolymerization charges (0.5 and 1 mC) were used, and the CVs of CPE prepared modified electrodes are compared in Fig. 7.

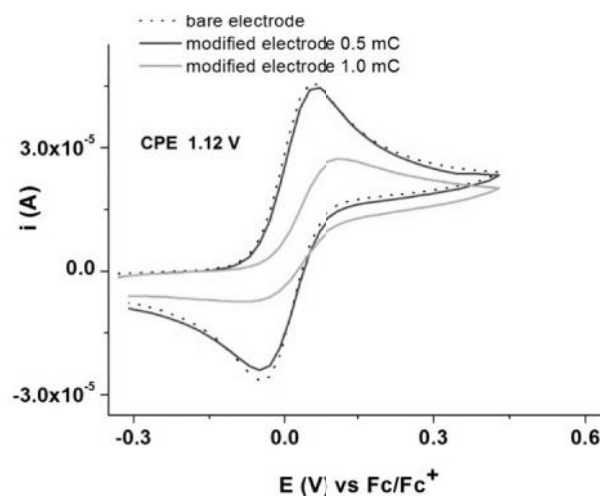


**Fig. 7.** CV (0.1 V/s) curves of polyL modified electrodes prepared by CPE at 1.12 V in 0.5 mM solution of L in 0.1M TBAP/CH<sub>3</sub>CN using different electropolymerization charges (0.5 and 1 mC) and measured in 1 mM ferrocene solutions in 0.1M TBAP/CH<sub>3</sub>CN.

The ferrocene signal for the modified electrode obtained at 1 mC is more flattened than that at 0.5 mC (which is close to that of the bare electrode). Since better coverage of the electrode occurs at higher charge, the polyL modified electrode obtained at 1 mC was chosen for the recognition experiments.

#### Evaluation of recognition properties

During the transition metals amperometric titration using p-dimethylaminobenzylidene rhodanine as titrant in 30% (vol) alcoholic dimethylformamide, the applied potential was varied with respect to the detected metal ions. The potential values were -0.50, -1.10, and -1.3V vs. SCE for Cu(II), Ni (II), Fe (II) and Zn(II), at pH 5.00 for Cu (II), 5.70 for Ni (II), 5.30 for Fe (II) and 5.05 for Zn (II), respectively. The end-point of the ligand titration indicated formation of complexes Me:L = 1:2. The error is under 1% and the detection is till  $2 \times 10^{-4}$  M [1].

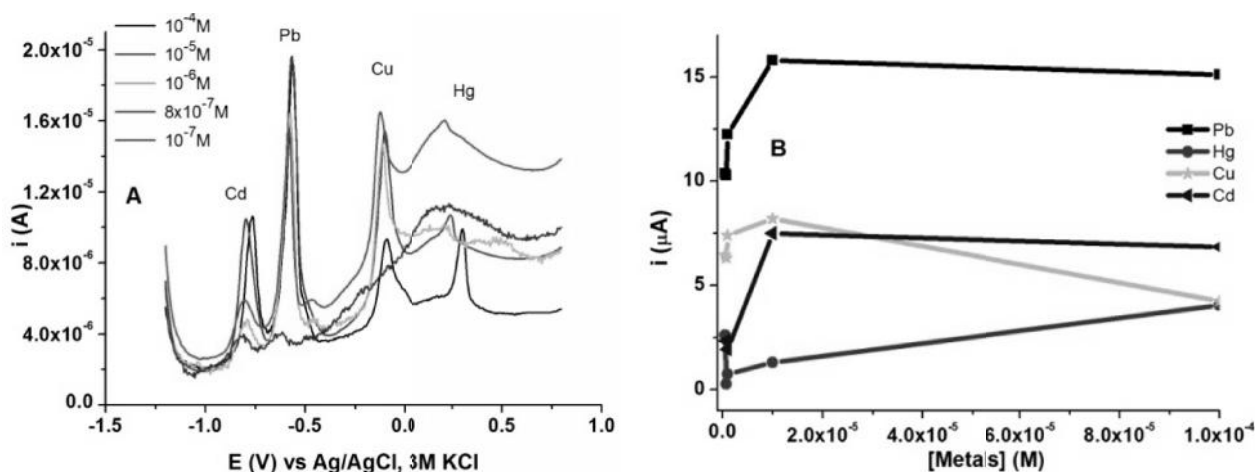


**Fig. 8.** DPV stripping currents for the polyL modified electrode obtained by CPE (1.12V,1mC) in 0.5 mM solution of L in 0.1M TBAP/CH<sub>3</sub>CN, measured at different concentrations of heavy metals in acetate buffer at pH 5.5 (A) and DPV stripping currents in dependence on heavy metals concentration (B).

The calibration curves have been obtained for each heavy metal. The dependences of the DPV stripping currents on the heavy metals concentration are shown in Fig. 8, suggesting that the best analytical signals have been obtained for Pb.

#### CONCLUSIONS

(E)-2-thioxo-5-((4,6,8-trimethylazulen-1-yl)methylene)thiazolidin-4-one (L) has been studied by electrochemical methods. The study led to the finding of the best potential at which this azulene could be polymerized. PolyL modified electrodes were characterized by cyclic voltammetry in ferrocene solutions. The modified electrodes were used for heavy metals recognition

We tried to find another method for heavy metal determination that could monitor these metals at lower concentrations. For heavy metals recognition, polyL modified electrodes obtained by CPE (1.2V, 1mC) from the solution of L (1 mM) in 0.1M TBAP/CH<sub>3</sub>CN have been used. After cleaning with acetonitrile, the modified electrodes were immersed in the transfer solution containing 0.1 M acetate buffer at pH 5.5. After 15 cycles of equilibration (by CV with a scan rate of 0.1 V/s between -0.9 V and +0.6 V) and overoxidation (by CV with a scan rate of 0.1 V/s between -0.2 V and +2.5 V), the modified electrodes were extracted from the cell, washed with water, and put in solutions containing heavy metals ions of different concentrations, under magnetic stirring for 15 minutes. Then, the modified electrodes were polarized at -1.2V, where all cations were reduced, and their DPV stripping currents were recorded between -1.2 V and 0.5V (Fig. 8A).

through preconcentration and anodic stripping. The best response has been obtained for Pb (detection limit of  $10^{-7}$ M).

**Acknowledgements.** The authors are grateful for the financial support from: Executive Unit for Financing Education Higher, Research Development and Innovation (UEFISCDI) project ID PN-II-RU-TE-2014-4-0594 contract no. 10/2015, PN-II-PT-PCCA-2013-4-2151 contract no. 236/2014, and Romania–China bilateral project 68BM/2016.

#### REFERENCES

1. V. Kshirsagar, S. Gandhe, M. D. Gautam, *Rasayan J Chem.*, **3**, 772 (2010).

2. R. Solmaz, G. Kardas, B. Yazici and M. Erbil, *Transition Met. Chem.*, **2**, 207 (1977).
3. E. Yavuz, S. Tokalioglu, S. Sahan, *J. Braz. Chem. Soc.*, **24**, 736 (2013).
4. Casassas E, R. Rubio, G. Rauret, *Analyst*, **109**, 1159 (1984).
5. E.-M. Ungureanu, A.C. Razus, L. Birzan, M.-S. Cretu, G.-O. Buica, *Electrochim. Acta*, **53**, 7089 (2008).
6. G.-O. Buica, E.-M. Ungureanu, L. Birzan, A.C. Razus, L.-R. Mandoc (Popescu), *J. Electroanal. Chem.*, **693**, 67 (2013).
7. J.-X. Dong, H.-L. Zhang, *Chinese Chem. Lett.*, **27**, 1097 (2016).
8. J. Peet, A. Selyutina, A. Bredihhin, *Bioorg. Med. Chem.*, **24**, 1653 (2016).
9. L. Birzan, M. Cristea, C. C. Draghici, V. Tecuceanu, M. Maganu, A. Hanganu, A. C. Razus, G. O. Buica, E. M. Ungureanu, *Dyes Pigm.*, **131**, 246 (2016).

1, . . . 1, . . . 1\*, . . . 1\*, . . . 2  
 1 " " , . . . 1-7,  
 2 , " . . . " , 202B, 71141  
 14 2016 .; 27 2016 .  
 ( )

(E)-2-thioxo-5-((4,6,8-trimethylazulen-1-yl)methylene)thiazolidin-4-one (**L**)

**L**

(Cd, Pb, Cu, Hg)

Pb ( $10^{-7}$  ).



## Application of electrochemical methods in the physicochemical characterization of atmospheric precipitation

P. Orlovi -Leko<sup>1\*</sup>, D. Omanovi<sup>2</sup>, I. Ciglene ki<sup>2</sup>, K. Vidovi<sup>3</sup>, T. Brenko<sup>1</sup>

<sup>1</sup>University of Zagreb, Faculty of Mining, Geology and Petroleum Engineering, Pierottijeva 6, Zagreb, Croatia,

<sup>2</sup>Division for Marine and Environmental Research, Ruđer Boškovi Institute, Bijenička c. 54, 10000 Zagreb, Croatia,

<sup>3</sup>National Institute of Chemistry, Hajdrihova 19, p.p. 660, 1001 Ljubljana, Slovenia

Received November 16, 2016      Revised January 18, 2017

Electrochemical methods play an important role in the environmental analysis. This study demonstrates that electrochemical (voltammetric) methods are a valuable tool with good selectivity and sensitivity for physicochemical analysis of atmospheric precipitation. Studies have been done with daily bulk samples collected in the city of Zagreb (Croatia) in the period of 2009/2010. Heavy metal (HM) content and reduced sulfur species (RSS) were investigated in the precipitation samples by using cathodic stripping voltammetry (CSV) and differential pulse stripping voltammetry in anodic, DPASV (Zn, Cd, Pb and Cu) and adsorptive cathodic modes, DPAdCSV (Ni), respectively, at the hanging mercury drop electrode. In average, the highest concentrations were found for Zn and the lowest for Cd ( $Cd < Ni < Pb < Cu < Zn$ ).

Although generally, low correlation between concentrations of these metals was found (statistical significance only between Zn and Cu), the same pattern of concentration changes relative to precipitation events was observed for Zn, Cd, Pb, Cu and dissolved organic carbon (DOC), whereas an opposite pattern was noticed for Ni and pH. Analyses of bulk samples by CSV technique revealed an existence of different sulfur species, providing an excellent tool for study of organic and inorganic RSS in the atmospheric precipitation at nano-levels.

**Key words:** voltammetric techniques, atmospheric precipitation, heavy metals, reduced sulfur species.

### INTRODUCTION

Atmospheric concentrations of many trace metals have been significantly affected by anthropogenic activities, which have changed the biogeochemical cycles and balance of some metals. In an urban environment, metals can be emitted from numerous anthropogenic sources which include traffic-related activities (fossil fuel combustion, wear production from tires, brake lining, leakage of metal-containing motor oils and corrosion in general of vehicle components), industry activities, the disposal of municipal waste, and the corrosion of building materials [1]. In recent study, Gunarwardena et al. [2] found that concentration of Zn is correlated with traffic volume, whereas Pb, Cd, Ni and Cu are correlated with traffic congestion. Metals are removed from the atmosphere by both, dry and wet deposition processes. Quantifying the total trace metal concentrations in atmospheric deposition is important for understanding their geochemical cycling and their impact on ecosystems, especially on the water ecosystem.

This is due to the possible post-solubilisation in the water body, having different organic ligands and different pH value [3]. Environmental science is benefiting more and more from the development of sensitive, selective and innovative techniques for the determination of metals in environmental matrices, as well as for the identification and quantification of various elemental forms under which an element may occur [4]. Concentration of heavy metals (HM) in atmospheric aerosols is at the trace level [5] and thus sensitive and selective analytical techniques should be used for their analysis.

Electrochemical techniques, particularly anodic (ASV) and adsorptive cathodic (AdCSV) voltammetry feature both characteristics, while in addition they have a potential to provide speciation information. Detection limits for HM by using stripping voltammetry are in the range down to  $10^{-12}$  M [6]. Metals that could be determined by ASV are those that are soluble in liquid Hg (forming amalgams). In contrast, AdCSV does not require the metal solubility in Hg, so it could be used for the analysis of numerous trace metals [7]. Metal-organic complexation is significant in the atmospheric precipitates.

---

To whom all correspondence should be sent:  
E-mail: palma.orlovic-leko@obla.k.rgn.hr

Complexation enhances the solubility of metals in aerosols and atmospheric water [8-10]. Beside organic ligands, sulfur species could play important role in speciation of heavy metals. The major reduced sulfur species (RSS) usually found in the atmosphere are carbon disulfide (CS<sub>2</sub>), dimethyl sulfide (CH<sub>3</sub>SCH<sub>3</sub>, DMS), hydrogen sulfide (H<sub>2</sub>S), carbonyl sulfide (COS) and ethyl mercaptan (CH<sub>3</sub>SH) [11-14]. Some of these compounds have already been electrochemically investigated [15]. Dimethyl sulfide is the dominant biogenic sulfur gas emitted to the atmosphere from the seawater [16]. In the atmospheric aerosols, all these compounds are normally present at very low concentration levels (below ppb levels) [17]. The chemistry of RSS in the atmosphere has significant implications for global climate change, ozone layer depletion and the acidity of precipitation [18 and references therein].

It has already been shown that voltammetry has great potential for detection and characterization of dissolved and particulate sulphur species in water samples without pretreatment [19-22]. For this reason and following our work on model and natural sea- and fresh-water systems [15,23,24], here we have applied for the first time the cyclic voltammetry on mercury electrode in order to study the reduced sulfur species (RSS) in the precipitation samples. The method is based on measurements of inorganic and organic RSS that deposit HgS layer during an accumulation step at the deposition potential, followed by scanning potentials from positive to more negative values at the hanging mercury drop electrode (HMDE). In solutions containing sulfide anions, insoluble HgS layer at the Hg electrode surface can be formed by the reversible process of two-electron-transfer oxidation of Hg at potentials more positive than -0.5 V vs. Ag|AgCl. Organic sulfur compounds are also found to deposit HgS layer by anodic oxidation of Hg at sufficiently positive potentials, around 0 V [20].

In this work, we report results of measurements of the total HM (Cu, Pb, Zn, Cd and Ni), pH, dissolved organic carbon (DOC) and RSS in the atmospheric precipitation. The goal of this study was to demonstrate that electrochemical methods are selective, sensitive and essential for fast and direct qualitative and quantitative characterization of atmospheric deposition. The study has been done with bulk samples collected in the city center of Zagreb (Croatia) in the period of 2009/2010.

## EXPERIMENTAL

### *Samples collection*

Samples were collected in the city center (Zagreb, Croatia) near a cross-road characterized by heavy traffic. Sampling was carried out manually on the roof

of Faculty building (20 m above ground level) in the period from January 2009 until May 2010. A simple bulk sampler consisting of opaque bottle and a glass funnel were used to collect daily precipitation samples.

### *Analysis of heavy metals*

Concentrations of heavy metals were measured in unfiltered samples by differential pulse ASV, DPASV (Zn, Cd, Pb and Cu) and differential pulse AdCSV, DPAdCSV (Ni). An AUTOLAB potentiostat PGSTAT128N (Eco Chemie, Utrecht, The Netherlands), coupled with a hanging mercury drop working electrode (VA Stand 663, Metrohm, Herissau, Suisse) and CAVRO burette system XL-3000 (Tecan, Männedorf, Suisse) were used for automatic determination of, Cd, Pb, Cu and Zn by the standard addition method. A platinum wire was used as a counter electrode and Ag|AgCl with saturated NaCl as a reference electrode. Prior to the measurements, samples were digested by acidification (pH < 2) with suprapur, Merck, Darmstadt, Germany) and irradiated by UV-light with a mercury lamp 150 W (Hanau, Germany) for at least 24 h. Prepared acidified samples were analyzed without further modifications, except for Zn, for which sodium acetate buffer was added in order to adjust pH to 4. Concentrations of metals in unfiltered samples are referred as total metal concentrations in this study.

The following experimental conditions were applied: equilibration time 10 s; modulation time 0.04 s; interval time 0.1 s; modulation amplitude 20 mV and step potential 2 mV. Specific parameters for DPASV and DPAdCSV technique are presented in Table 1.

**Table 1.** Specific parameters used for the determination of heavy metals in precipitation samples by DPASV and DPAdCSV.

Parameter	DPASV Pb, Cd, Cu	Zn	DPAdCSV Ni
Accumulation potential (V)	-0.8	-1.3	-0.7
Accumulation time (s)	600	60	180
Initial potential (V)	-0.75	-1.15	-0.7
Final potential (V)	0.24	-0.75	-1.2

### *Analysis of reduced sulfur species (RSS)*

Electrochemical measurements of reduced sulfur species (RSS) were performed with  $\mu$ -Autolab voltammeter controlled by GPES (General Purpose Electrochemical System) 4.6 software (Eco Chemie

B.V., The Netherlands) in a three-electrode cell (663 VA Stand, Metrohm). The RSS were investigated by using cyclic and/or linear sweep voltammetry (CV/LSV) on the HMDE in fresh nonfiltered samples upon addition of NaCl (final concentration 0.55 M) as a supporting electrolyte. In CV and LSV, the accumulation ( $t_a = 0 - 120$  s) of RSS on the Hg electrode surface with stirring was performed at the deposition potential of  $E = -0.20$  and  $-0.10$  V (vs. Ag|AgCl). After accumulation, the potential was shifted in the negative direction (down to  $E = -1.5$  V vs. Ag|AgCl) with a scan rate of 100 mV/s and HgS reduction peak at around  $-0.6$  V, characteristic of many RSS, was recorded [19-22]. Next, the solution was acidified with 30  $\mu$ L of concentrated HCl (Kemika, Croatia) to pH  $\sim 2$  and purged for 3 min. After restoring the original pH with NaOH (Kemika, Croatia) the accumulation and scan steps were repeated. The result of the first measurement prior to acidification is assigned as total reduced sulfur species,  $RSS_T = H_2S/HS^- + S^0$ , while the result of the second measurement is assigned to elemental sulfur,  $S^0$ , as the model representative for non-volatile reduced sulfur species,  $RSS_{NV}$  [19,23].

#### *Other parameters*

The pH values of the samples were measured using a digital pH meter, Model Metrohm 691. Calibration was always carried out before measurement using standard buffer solutions of pH 4.00 and 7.00.

Dissolved organic carbon (DOC) was determined in the filtered samples (Whatman GF/F filters, pore size 0.7  $\mu$ m) using a sensitive, high temperature catalytic oxidation (HTCO) technique. A Model TOC-5000 System (Shimadzu) with high sensitive Pt catalyst and non-dispersive infrared (NDIR) detector for  $CO_2$  measurement was used.

## RESULTS AND DISCUSSION

Results of determination of HM and RSS in bulk precipitation samples using electrochemical methods are presented in Table 2, together with pH and DOC values. DOC was selected as the characteristic parameter due to likely association of metals with organic carbon.

Metals in the bulk depositions are derived from both, wet and dry components and therefore the total concentration in the bulk precipitation is controlled by their relative amounts and concentrations. Mean concentrations of heavy metals determined by electrochemical methods are comparable to those measured by HR ICPMS (Table 2).

In the current study, the most abundant HM was Zn, followed by Cu, Pb, Ni and Cd. Similar trend has also been found for atmospheric bulk deposition of metals in other studies, where the highest concentration of Zn in rainwater was mostly observed, while Cd concentration was generally reported as the lowest one [25-28]. This order follows also a common pattern of heavy metals concentrations in natural waters [29,30]. Relationships between elements often provide information about the sources of the particles [31]. On the other hand, according to Kaya and Tuncel [32], these correlations are influenced by physical properties of particles that carry elements. Gunawardena et al. [2] have found that wet deposition mostly contributes by heavy metals associated with fine particles ( $< 10 \mu$ m) such as Pb, Cd, Ni and Cu. In contrast, Zn is mostly associated with relatively large particles ( $> 10 \mu$ m) and dry deposition appears to be the main source of this element. Furthermore, it is important to note that trace elements may be transported over long distances by very small particles and be deposited far from emission sources [33]. According to Azimi et al. [34], HM source investigation appears to be more difficult than that of organics, because for inorganic elements, specific ratios are less developed. As some heavy metals (Cd and Cu) did not pass normality test, the Spearman rank correlation analysis is applied. Statistically significant correlation factors ( $r = 0.87$ ;  $p < 0.05$ ) were found only between Zn and Cu. The absence of more correlations among metals is most probably due to the specificity of the sampling location, insufficient number of samples and differences in metal concentrations in different samples. However, despite the absence of statistical correlation which would reflect not only the observed trends, but consider also absolute concentrations of each metal, there are obvious common patterns for heavy metal concentrations in here analyzed precipitation (rain) events. This is clearly visible in Fig. 1, where normalized "trends" of metal concentrations, pH and DOC are plotted. Normalization was performed using the last sampling date as the reference point (symbols denote normalized values for each sample). Note that the x-axis technically corresponds to date/time, but dates are not equally distributed (this is why the numbers (dates) are omitted in order to avoid confusion). The concentrations of most of the metals showed two or more maxima, but the relative increase was not the same for each metal and the maxima were not occurring at the same day(s) (Table 2).

**Table 2.** Concentrations of HM, RSS, pH and DOC in bulk precipitation samples.

No	Date	DPASV				DPAdCSV		DOC (mg/L)	RSS nM
		Zn (µg/L)	Cd (µg/L)	Pb (µg/L)	Cu (µg/L)	Ni (µg/L)	pH		
1	22/01/2009	3.75±0.23	0.060±0.002	1.96±0.08	1.65±0.04		5.28	1.44	
2	28/01/2009	7.72±0.42	0.092±0.005	1.43±0.08	1.71±0.05		5.28	1.18	
3	02/02/2009	18.74±0.87	0.077±0.004	3.45±0.18	9.04±0.28	1.16±0.08	5.28	2.71	
4	10/02/2009	9.75±0.45	0.046±0.002	1.42±0.05	5.52±0.20	2.19±0.15	6.21	1.08	5.0
5	03/03/2009	12.85±0.82	0.102±0.006	5.98±0.13	9.20±0.36	0.72±0.05	4.38	3.64	
6	05/03/2009	9.89±0.61	0.055±0.003	1.39±0.05	1.81±0.06	0.73±0.11	6.30	1.26	
7	20/04/2009	5.97±0.42	0.030±0.003	1.47±0.07	1.75±0.03	0.32±0.09	5.91	2.17	7.0
8	21/04/2009	11.88±0.99	0.467±0.023	2.44±0.14	2.08±0.04	0.57±0.07	5.40	1.72	4.0
9	24/04/2009	25.22±1.87	0.415±0.008	6.65±0.13	7.56±0.19	1.28±0.08	6.76	4.86	
Mean		11.75	0.149	2.91	4.48	0.99	5.64	2.23	
STD		6.64	0.167	2.05	3.35	0.62	0.72	1.29	
Min.		3.75	0.030	1.39	1.65	0.32	4.38	1.08	
Max.		25.22	0.467	6.65	9.20	2.19	6.76	4.86	
Median		9.89	0.077	1.96	2.08	0.73	5.40	1.72	
HRICPMS*		7.56	0.060	1.17	3.37	0.63	5.46	1.59	

Among studied metals, Zn, Cd, Pb and Cu followed the same trend, which is also consistent with the trend of DOC, while Ni and pH showed the opposite trends. Similar patterns without statistical correlation point on general common physicochemical processes related to pre-rainy and rainy periods. It is obvious that there are differences between the amounts of metals deposited and “washed-out” during separate precipitation events, but in general this process is similarly reflected in the “drift” of heavy metal levels (increase/decrease) in water samples collected among different events. The pH values are one of the most important factors controlling the dissolution of trace metals in deposition samples [35, 36]. In the current study, pH values were in the range between 4.38 and 6.76. Generally, metals are more soluble at low pH conditions. However, in our case, no correlation between pH and HM concentration was observed for each compound. Similar result has been obtained in another bulk deposition study [37].

In the bulk deposition, DOC concentrations were strongly correlated only with Pb (Spearman’s correlation coefficient  $r = 0.90$ ). This suggests that the sources of organic ligands and HM in the

samples could be multiple. Copper did not correlate with DOC ( $r = 0.58$ ), but it is known that Cu forms very stable organic complexes.

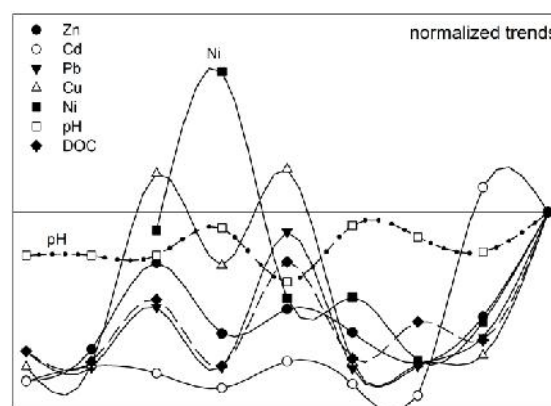


**Fig. 1.** Normalized values of heavy metal concentrations, pH and DOC concentrations. Symbols represent normalized values for each sampling event, while lines are plotted in order to highlight the observed common patterns.

In the second set of precipitation samples analyzed by HR ICPMS, investigation of organic matter content was performed by DPASV [38, 39, and unpublished results]. In comparison with the unfiltered sample, the filtered sample of bulk precipitation showed much lower concentration of binding ligands (up to 33%) evaluated by electrochemical measurements of the complexing capacity value for Cu ions. This pointed to the fact that significant part of Cu could be bound to particles and/or ligands present in the particulate organic fraction, POC. In the same samples, the POC values were in the range between 0.042 and 2.522 mg/L, *i.e.* it represents up to 39% of the total content of organic carbon.

#### Reduced sulfur species

Typical voltammograms of RSS studied in precipitation samples are presented in Fig. 2. From the presented voltammograms, the presence of two peaks is clearly visible at around -0.75 V (Figs. 2A, B) and -0.55 V (Fig. 2B, and as a shoulder in Fig. 2A), indicating two different sulfur species. The more negative peak, usually in our papers designated as C2, represents the well-known dissolution/reduction of HgS layer on the Hg electrode surface [19-23]:



This peak is usually taken as a measure for “free” and labile sulfur species content ( $\text{H}_2\text{S}/\text{HS}^-/\text{S}^{2-}$ ,  $\text{S}^0$ ,  $\text{S}_n$ ,  $\text{S}^{2-}$ , thiols, labile metal sulfide complexes and nanoparticles). The more positive peak can be ascribed to the presence of different organosulfur species (DMS, 3-mercaptopropionat, thio-compounds) [15, 23]. So far, in oxic seawater, in addition to C2, a peak around -0.5 V (vs. Ag|AgCl) can frequently be revealed. This peak is usually ascribed to organosulfur species (DMS) which at applied experimental conditions oxidize the Hg electrode, but do not deposit HgS layer on its surface [15,40]. Therefore, this peak is revealed more positively than the HgS reduction peak.

In Fig. 3, the voltammetric response obtained in natural anoxic seawater sample, where presence of free sulfide (in concentration of 50 nM) was determined by revealing of HgS reduction peak, is shown together with the responses of the same sample after additions of dissolved elemental sulfur ( $\text{S}^0$ ) and DMS. With addition of DMS, new and more positive peak with respect to HgS reduction peak was revealed, similarly as was obtained in some of the precipitation samples represented here in Fig. 2B. As expected, addition of dissolved  $\text{S}^0$  caused an increase of the HgS reduction peak [15, 23].

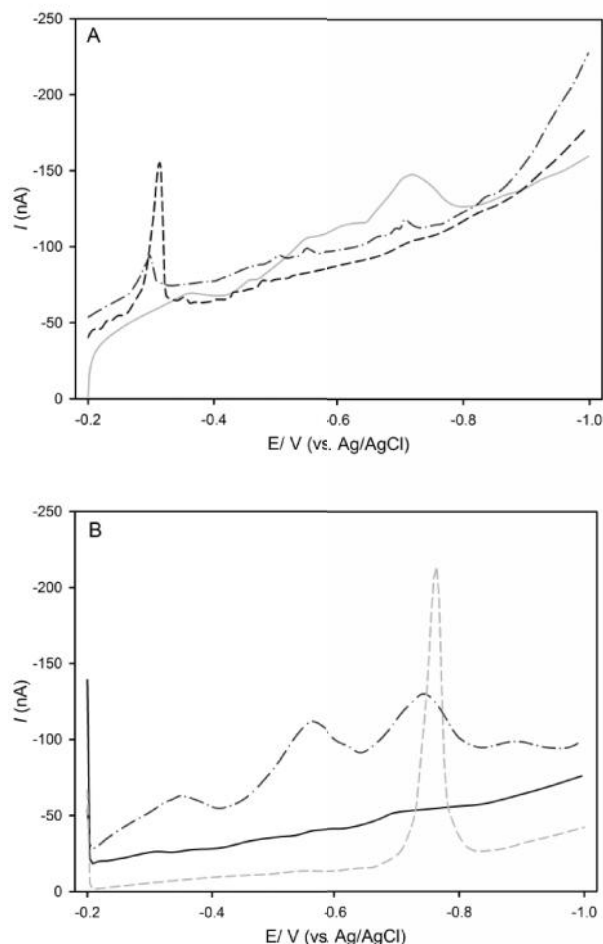


**Fig. 2.** Voltammetric curves obtained in precipitation samples: A) original sample taken in April 2009 (solid), after addition of HCl (pH ~ 2) (dotted-dash), and after addition of  $\text{Na}_2\text{S}$  (dashed) when increase of the voltammetric peak proving presence of RSS was observed; B) sample taken in February 2009 measured without (solid) and with accumulation step of 120 s with stirring (dotted-dash) at the starting potential  $E = -0.2$  V vs. Ag|AgCl; the same sample after addition of  $\text{Na}_2\text{S}$  (dashed).

To confirm that the more negative peak in precipitation samples belongs to RSS which deposit HgS at the starting deposition potential, the same sample was measured without and with accumulation step at the starting potential, as well as in acidic conditions and after addition of standard  $\text{Na}_2\text{S}$ . Accumulation step caused increase of both peaks, as well as their movement to more positive potentials in acidic conditions. After addition of  $\text{Na}_2\text{S}$  and/or  $\text{S}^0$ , increase of more negative peak was recorded. These observations present typical behavior of the RSS at the Hg electrode [15,19 and references therein]. The first RSS peak at -0.55 V was removed by acidification and purging of samples, while the second one, corresponding to nonvolatile RSS, remained [23].

Concentration of volatile and nonvolatile RSS in all studied precipitation samples ranged between 2-5 nM, equivalent to sulfide. Usually the same concentration range of nonvolatile RSS can be found in oxic seawater layers [15, 23 and references therein] and freshwaters [41]. Owing to the relatively small number of samples, it is very difficult to talk about a serious correlation with DOC values measured in the same samples, but it is interesting, however, that the highest RSS were found in the sample with higher DOC concentration. Similar correlation between RSS and DOC in the oxic seawater has already been reported in the literature [23].

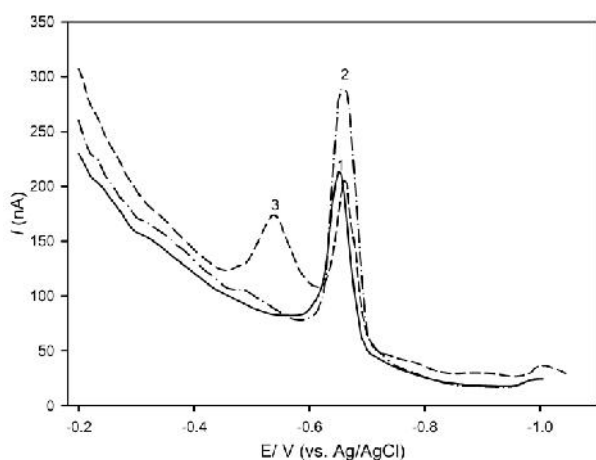


**Fig. 3.** Natural anoxic water sample with detected free sulfide (curve 1), the same sample after addition of dissolved  $S^0$  (curve 2) and DMS (curve 3).

### CONCLUSIONS

Electrochemical techniques, CSV, ASV and AdCSV used in this paper are shown to be important tool for determination of heavy metals and reduced sulfur species content in atmospheric deposition (bulk samples). These methods do not require complex sample pre-treatment and show good selectivity and high sensitivity. The average concentrations of elements followed the order:  $Cd < Ni < Pb < Cu < Zn$ . The DOC concentrations were significantly correlated with Pb, while for heavy metals the correlation was found only between Zn and Pb. Despite weak correlations (in general) between metals and the relatively small number of samples ( $N=9$ ), it was observed that heavy metals (Zn, Cd, Pb and Cu) and DOC followed the same pattern of concentration changes related to precipitation events, while the opposite pattern was found for Ni and pH. Cyclic sweep voltammetry at the HMDE show interesting possibilities for study of nano-levels of organic and inorganic RSS in the atmospheric precipitation.

**Acknowledgements.** This work is supported by the Croatian Science Foundation projects: “The Sulphur and Carbon Dynamics in the Sea and Fresh-Water Environment” (IP-11-2013-1205 SPHERE) and “New methodological approach to biogeochemical studies of trace metal speciation in coastal aquatic ecosystems” (IP-2014-09-7530 MEBTRACE). The authors thank Zdeslav Zovko for the DOC measurements.

### REFERENCES

1. C. Wong, X. LI, I. Thornton, *Environ. Poll.*, **142**, 1 (2006).
2. J. Gunawardena, P. Egodawatta, G.A. Ayoko, A. Goonetilleke, *Atmos. Environ.*, **68**, 235 (2013).
3. A. Baker, P. Croot, *Mar. Chem.*, **120**, 4 (2010).
4. P. Smichowski, D. Gómez, *Comprehensive Anal. Chem.*, **70**, 239 (2015).
5. A. Allen, E Nemitz, J. Shi, R. Harrison, J. Greenwood, *Atmos. Environ.*, **35(27)**, 4581(2001).
6. D. Omanovi, C. Garnier, K. Gibbon-Walsh, I. Pižeta, *Electrochem. Commun.*, **61**, 78 (2015).
7. C. van den Berg, *Analyst.*, **114**, 1527 (1989).
8. H. Okochi, P. Brimblecombe, *Sci. World J.*, **2**, 767 (2002).
9. M. Witt, S. A. Skrabal, R. Kieber, J. Willey, *Atmos. Environ.*, **41**, 3619 (2007).
10. M. Plavši, P. Orlovi -Leko, Z. Kozarac, E. Bura-Naki, S. Strme ki, B. osovi, *Atmos Res.*, **87(1)**, 80 (2008).
11. S. Watts, *Atmos. Environ.*, **34**, 761, 2000.
12. L. Nunes, T.M. Tavares, J. Dippel, W. Jaeschke, *J. Atmos. Chem.*, **50**, 79 (2005).
13. Z-H. Shon, K-H. Kim, E.-C. Jeon, M-Y. Kim, Y-K. Kim, S-K. Song, *Atmos. Environ.*, **39**, 4803 (2005).
14. Z-H. Shon, K-H. Kim, *Chemosp.*, **63**, 1859 (2006).
15. I. Ciglenc ki, B. osovi, *Mar.Chem.*, **52**, 87 (1996).
16. K-H. Kima, L. Gangwoong, Y. P. Kim, *Environ. Poll.*, **110**, 147 (2000).
17. S.K. Pandey, K.H. Kim, *Air Environ. Sci. Technol.*, **43**, 3020, (2009).
18. H. Guo, I.J. Simpson, A.J. Ding, T. Wanga, S.M. Saunders, T.J. Wang, H.R. Cheng, B. Barletta, S. Meinardi, D.R. Blake, F.S. Rowland, *Atmos. Environ.*, **44**, 3805 (2010).
19. I. Ciglenc ki, B. osovi, *Electroanal.*, **9**, 775 (1997).
20. D. Krznari, I. Ciglenc ki, B. osovi, *Anal. Chim. Acta*, **431**, 269 (2001).
21. I. Ciglenc ki, D. Krznari, G. R. Helz., *Environ. Sci. Technol.*, **39**, 7492 (2005).
22. E. Bura-Naki, D. Krznari, D. Jurašin, G. Helz, I. Ciglenc ki, *Anal. Chim. Acta*, **594**, 44 (2007).
23. E. Bura-Naki, G. Helz, I. Ciglenc ki, B. osovi, *Geochim. Cosmochim. Acta*, **73**, 3738 (2009).
24. P. Orlovi -Leko, K. Vidovi, M. Plavši, I. Ciglenc ki, I. Šimuni, T. Minkina, *J. Solid State Electrochem.*, **20(11)**, 3097 (2016).



## Electrocatalysts for sulphur ions oxidation based on DWCNTs, MWCNTs, higher fullerenes and manganese

G. Pchelarov\*<sup>1</sup>, D. Uzun<sup>1</sup>, E. Razkazova-Velkova<sup>2</sup>, O. Dimitrov<sup>1</sup>, S. Vassilev<sup>1</sup>, K. Petrov<sup>1</sup>

<sup>1</sup>Acad. Evgeni Budevski Institute of Electrochemistry and Energy Systems Bulgarian Academy of Sciences, Acad. G. Bonchev Str., bl.10, Sofia 1113, Bulgaria

<sup>2</sup>Institute of Chemical Engineering, Bulgarian Academy of Sciences, Acad. G. Bonchev Str., bl. 103, Sofia 1113, Bulgaria

Received December 14, 2016      Revised March 29, 2017

The possibility of utilizing electrocatalysts such as manganese deposited on fullerenes and carbon nanotubes is considered. These have been studied for oxidation of SO<sub>3</sub> to SO<sub>4</sub> and reduction of NO<sub>3</sub> to NO<sub>2</sub> and N<sub>2</sub>, thus creating a SO<sub>x</sub>/NO<sub>x</sub> fuel cell suitable for cleaning the environment while generating electrical energy. Mn has been deposited on Double Wall Carbon Nanotubes (DWCNTs) and Higher Fullerenes (HFs) from manganese acetate by thermal treatment and/or freeze drying. The electrocatalysts were characterized by scanning electron microscopy (SEM) and X-ray diffraction (XRD). Electrochemical testing has been done by cyclic voltammetry and E/V polarization curve plotting. The freeze dried electrodes comprised of Mn/HFs are found to yield the lowest overpotentials at sulfite oxidation, while the electrodes comprised of Mn/HFs/DWCNTs yield the highest activity at nitrite reduction. The results presented clearly show, that electrodes containing HFs, DWCNTs and manganese oxides are effective catalysts in SO<sub>x</sub>/NO<sub>x</sub> fuel cells.

**Key words:** electrocatalyst, DWCNTs, MWCNTs, C<sub>60</sub>/C<sub>70</sub>, higher fullerenes, manganese acetate.

### INTRODUCTION

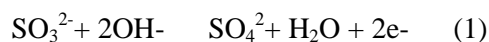
The current work considers the possibility of utilizing electrocatalysts such as fullerenes and carbon nanotubes. The possibility of utilizing fullerenes as catalysts in fuel cells has been discussed in the past [1]. Multiwall Carbon Nanotubes (MWCNTs) are comprised of many graphene layers decreasing in diameter while curved in successive layers. Double Wall Carbon Nano Tubes (DWCNTs) on the other hand are comprised of only a few layers, but larger in diameter. It has been argued in the past that the inner tube formation of the structure of open end DWCNTs can be very defective, containing pentagons, heptagons and octagons [2].

Higher fullerenes include the fairly stable species C<sub>74</sub>, C<sub>78</sub>, C<sub>80</sub>, C<sub>82</sub>, C<sub>84</sub>, C<sub>86</sub>, C<sub>88</sub>, C<sub>90</sub>, C<sub>92</sub>, C<sub>94</sub>, C<sub>96</sub>, C<sub>98</sub>, C<sub>100</sub>. The electro catalytic properties of higher fullerenes have been studied and were deemed more promising than C<sub>60</sub> as catalysts, though their catalytic rate constants were found to be smaller [3]. An interesting new development characteristic for fullerenes and nanotubes is their ability to reversibly modify specific chemical

reactions [4]. Applied in this study is a method to fabricate the electro-catalyst for the electrodes using a lyophilization process [5]. Via the process of lyophilization nitrogen atoms are introduced into the catalyst and these appear to play a key role as active sites in oxygen reduction [6]. Fuel cells driven by sulfides that oxidize sulfides to sulfates removing the toxic pollutant, while recovering the energy stored, have been fabricated in the past [7].

In our work we make use of the electro-catalytic reduction capability of fullerenes to aid the oxidation process in the conversion of sulfites to sulfates as described in [8]. The aim of the current study is to develop a fuel cell for the simultaneous purification of sulfates and nitrites. We study novel catalysts incorporated in the electrode material and use half cells to oxidize SO<sub>3</sub> to SO<sub>4</sub>.

In an oxygen saturated water suspension, SO<sub>3</sub><sup>2-</sup> ions, in the presence of TiO<sub>2</sub>, ZnO and Fe<sub>2</sub>O<sub>3</sub> together with hydrogen peroxide, have been shown to convert to SO<sub>4</sub><sup>2-</sup> ions [9, 10]:



The desulfurization reaction via Mn is:



An intermediate reaction of sulfites to sulphates is:



To whom all correspondence should be sent:  
E-mail: g.pchelarov@iees.bas.bg



The current work is part of a project entitled "New fuel cells based on chemical and microbial processes" that considers the possibility to decontaminate compounds containing sulphur and nitrogen.

## EXPERIMENTAL

### *Catalyst synthesis*

In this study we have used 'Higher Fullerenes' as fabricated by Diener & Alford by applying the carbon arc method, also termed 'Small-bandgap fullerenes' [11]. These were purchased together with manganese acetate from the Sigma Aldrich company. The fullerenes C<sub>60</sub>/C<sub>70</sub>, DWCNTs and Multi Wall Carbon Nanotubes (MWCNTs) were bought from SES Research, Huston, Texas. Vulcan XC-72 has been utilized as an electrocatalyst support in the past, this was acquired from the Cabot Corporation [12].

Manganese has been deposited on fullerenes C<sub>60</sub>/C<sub>70</sub>, HFs, DWCNTs and MWCNTs by two methods, by thermal treatment and by lyophilization. The catalyst fabricated via thermal treatment was prepared as follows: A small quantity of DWCNTs, then MWCNTs, C<sub>60</sub>/C<sub>70</sub> and HFs were dispersed in 6 ml of distilled water in a sonic bath for 15 minutes. Next, 40 mg of manganese acetate and 60 mg of polypyrrole were slowly added to the aqueous suspension. These ternary components were then baked at 180°C for 12h in a Teflon autoclave. Thus, MnO<sub>2</sub> is deposited on the carbon nanotube lattice structures with polypyrrole binding.

The process of lyophilization was applied in order to overcome catalyst agglomeration, but also helps bond nitrogen atoms to the fullerenes and nanotubes. A small quantity of HFs was dispersed in 6 ml of distilled water in a sonic bath for 15 minutes. Next, (20-40) mg of manganese acetate and (20-100) mg of polypyrrole were slowly added to the aqueous suspension. These ternary components were then baked at 180°C for 12h in a Teflon autoclave. Thus, MnO<sub>2</sub> was deposited on the higher fullerene lattice structures with polypyrrole binding. The suspension was finally dehydrated by freeze-drying in a lyophilizer yielding a complex structure. Lyophilization works by freezing the processed material, in this case by pouring liquid nitrogen on the sample thinly spread out on aluminum bowls, specially made for this purpose. Then, after reducing the pressure in the work chamber of the lyophilizer and heating the frozen water, the material sublimates and hence the samples are freeze-dried. Material cooling below its triple point ensures that sublimation occurs, thus

preserving the physical characteristics of the processed material.

The catalyst building up electrode No. 1 was synthesized as follows: 3 mg of higher fullerenes were added to 6 ml of distilled water and processed in an ultrasonic bath for 15 minutes. Between 20 and 40 mg of manganese acetate and 20 to 100 mg of polypyrrole were then slowly added to the water suspension. The catalyst was then processed by lyophilization. The catalyst building up electrode 2 was synthesized as follows: 8 mg of C<sub>60</sub>/C<sub>70</sub> fullerenes were dispersed in distilled water and processed in an ultrasonic bath for 30 minutes. 40mg of manganese acetate and 60 mg of polypyrrole were then slowly added to the suspension. In consequence the mixture was baked at 180°C for 23 hours in a Teflon autoclave. The catalyst was then processed by lyophilization.

### *Electrode preparation*

Different electrodes were prepared with the aid of the immersed type method by deposition of the sample catalyst on both sides of the electrode followed by pressing and heating. The electrodes studied have a geometrical area of 1 cm<sup>2</sup>. All the electrodes were prepared from a mixture of the catalyst and teflonized carbon blacks [60 mg/cm<sup>2</sup> Vulcan XC-72 (35% Teflon)] as a binder [13]. The mixture was pressed on to both sides of a stainless steel current collector at 150°C and pressed at 300kg/cm<sup>2</sup>. Different catalysts were studied: NORIT & manganese oxide; HFs, DWCNTs & manganese oxide; HFs & manganese oxide. We used HFs and DWCNTs to maximize the electro-active surface area of the catalyst.

In the course of the experiment several electrodes from each catalytic mass were prepared. The volt/ampere characteristic of each electrode was measured multiple times and the average values evaluated.

The electrodes incorporate the following catalysts:

- 1 (lyophilized) [content: 7 mg of (37 mg of manganese acetate, 57 mg of polypyrrole, 1.7 mg of HFs), pressed at 150 atm.);
- 2 (lyophilized) [content: 7 mg of (40 mg of manganese acetate, 60mg of polypyrrole, 8 mg of fullerenes C<sub>60</sub>/C<sub>70</sub>), pressed at 150 atm.];
- 3 (lyophilized) [content: 7 mg of (40 mg of manganese acetate, 60 mg of polypyrrole, 8 mg of NORIT), pressed at 150 atm.];
- 4 (non-lyophilized) [content: 100 mg of DWCNTs, pressed at 300°C and 300 kg/cm<sup>2</sup>];
- 5 (non-lyophilized) [content: 100 mg of MWCNTs, pressed at 300°C and 300 kg/cm<sup>2</sup>];

- 6 (non-lyophilized) [content: 120 mg of fullerenes C<sub>60</sub>/C<sub>70</sub>, pressed at 300 kg/cm<sup>2</sup>];
- 7 (non-lyophilized) [content: 100 mg of higher fullerenes, pressed at 300 kg/cm<sup>2</sup>];
- 8 (non-lyophilized) [content: 3 mg DWCNTs + 37 mg manganese acetate + 57 mg polypyrrole];
- 9 (non-lyophilized) [content: 3 mg MWCNTs + 37 mg manganese acetate + 57 mg polypyrrole];
- 10 (non-lyophilized): [20 mg][content: C<sub>60</sub>/C<sub>70</sub> [3 mg] + 37 mg manganese acetate + 57 mg polypyrrole];
- 11 (non-lyophilized): [15 mg][content: C<sub>60</sub>/C<sub>70</sub> [3 mg] + 37 mg manganese acetate + 57 mg polypyrrole];
- 12 (lyophilized) [content: 7 mg of (40 mg of manganese acetate, 60 mg of polypyrrole, 11 mg of HFs, 11 mg of DWCNTs), pressed at 150°C and 300 atm., for 5 minutes].

*Electrochemical experimental set up*

The catalytic properties of anode electrodes were determined with the aid of a three electrode cell Fig. 1. The process of oxidation of sulfites to sulfates in solution was studied. The solution was 1M Na<sub>2</sub>SO<sub>3</sub> + 18g/l NaCl. The NaCl is an additive electrolyte. The cell volume was 50 ml. The counter electrode was platinum foil. The reference electrode was a "Gaskatel" hydrogen electrode.

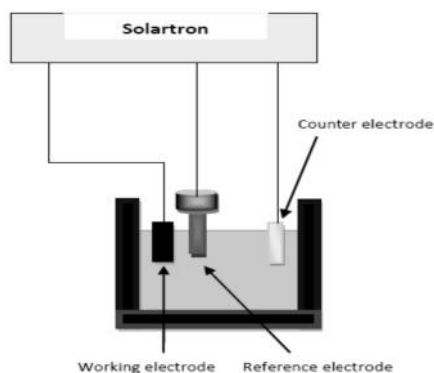


**Fig. 1.** Drawing of the three electrode cell used in the experiments.

The electrochemical testing methods used were cyclic voltammetry and E/V curve plotting.

**RESULTS AND DISCUSSION**

*Physical measurements*

X-ray diffraction (XRD) patterns were recorded utilizing a Philips diffractometer using CuK<sub>α</sub> radiation (λ = 1.54178 Å, 40 kV and 30 mA) with a scanning rate of 2 min<sup>-1</sup>. The intensive diffraction peaks at 36.92, 42.42 and 55.96 should

be assigned to the characteristic peaks for -MnO<sub>2</sub>, while the peaks at 17.94, 28.78, 49.0 and 60.44, respectively, should be ascribed to the peaks for -MnO<sub>2</sub> [14]. The XRD of manganese acetate as purchased from Sigma Aldrich and scanned in our lab is presented in Fig. 2. The XRD of the sample of manganese acetate with added polypyrrole and scanned in our lab is presented in Fig. 3.

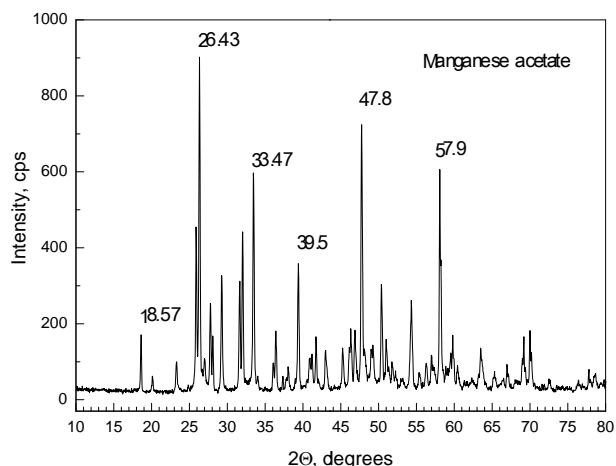


**Fig. 2.** XRD of manganese acetate.

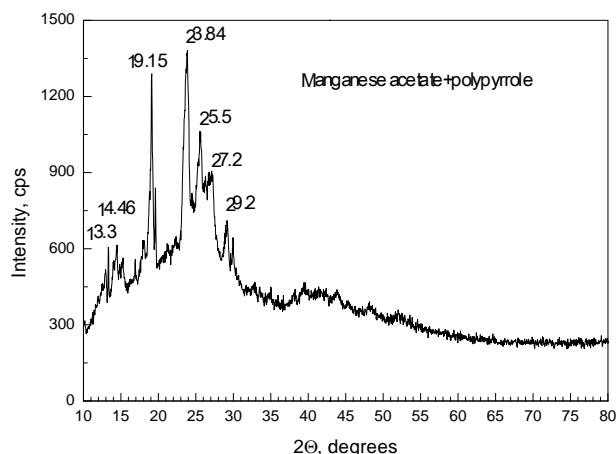


**Fig. 3.** XRD of Manganese acetate and polypyrrole.

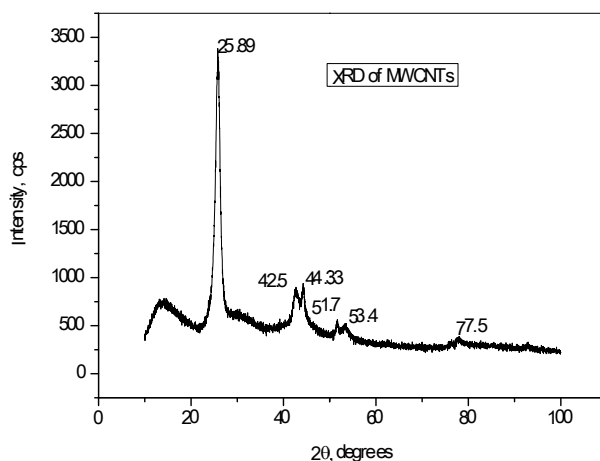


**Fig. 4.** XRD of MWCNTs.

The XRD of MWCNTs as purchased from SES Research and scanned in our lab is presented in Fig. 4. The XRD of DWCNTs as purchased from SES Research and scanned in our lab is presented in Fig. 5. Shown in Fig. 6 is the XRD of HF, DWCNTs and manganese acetate. Shown in Fig. 7 is the XRD of HF and manganese acetate. Presented in Fig. 8 is the XRD of the d space for the sample comprised of HF and manganese acetate.

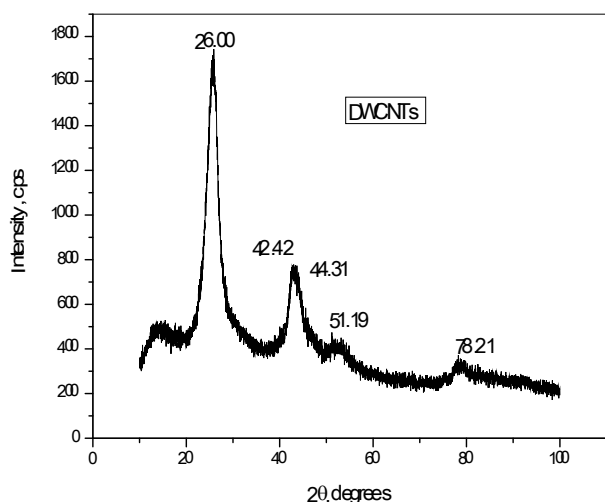


Fig. 5. XRD of DWCNTs.

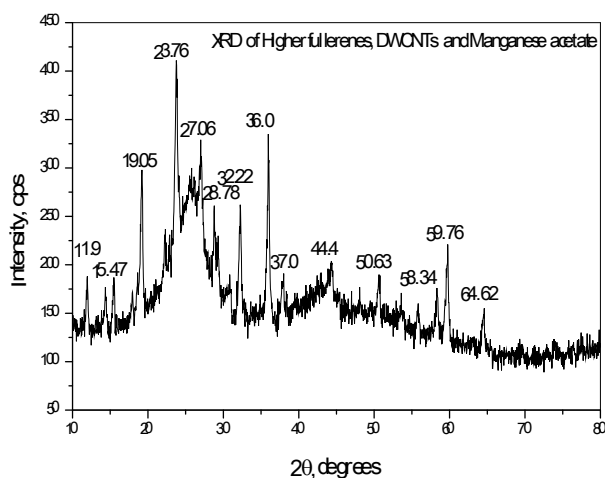


Fig. 6. XRD of HF, DWCNTs and manganese acetate.

Presented in Fig. 9 is the XRD of the HF purchased from Sigma Aldrich and scanned in our lab, numerous broad peaks can be observed characteristic of a wide range of higher fullerene species. The diffraction peak at around 19 degrees on Fig. 3, Fig. 6, Fig. 7 and Fig. 9 is clearly due to carbon especially as it is most intense on Fig. 9 when characterizing HF.

In the photographs made with a SEM presented in Fig. 10 we can observe the freeze dried catalyst containing HF, fullerenes C<sub>60</sub>/C<sub>70</sub> and manganese

oxide, respectively. It is clear that the catalyst with manganese oxide on HF has a higher surface area.

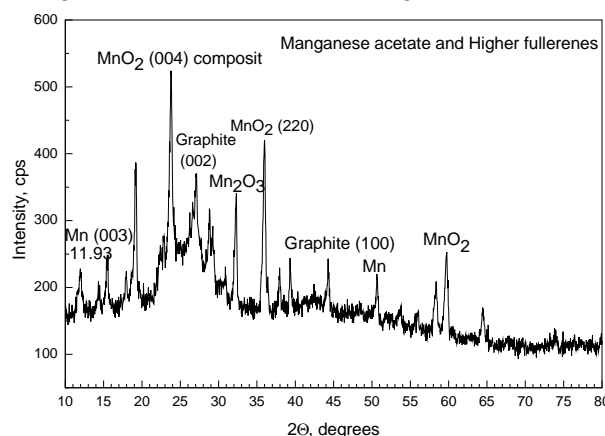


Fig. 7. XRD of HF and manganese acetate.

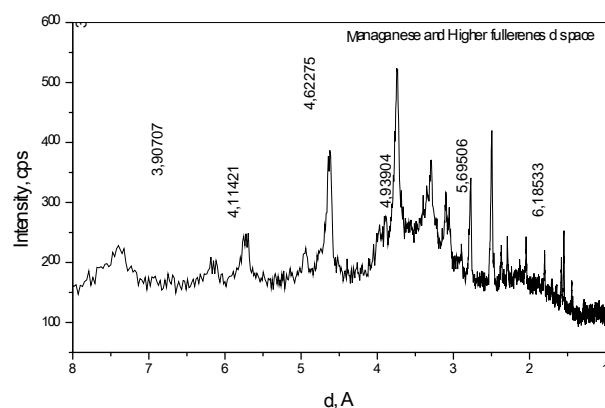


Fig. 8. XRD study of the d space for the sample comprised of HF and manganese acetate.

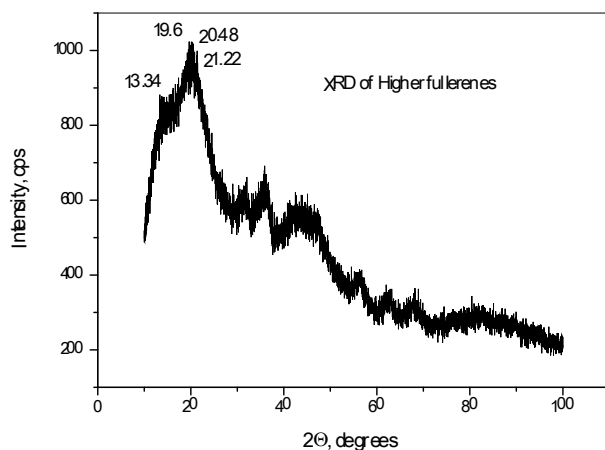
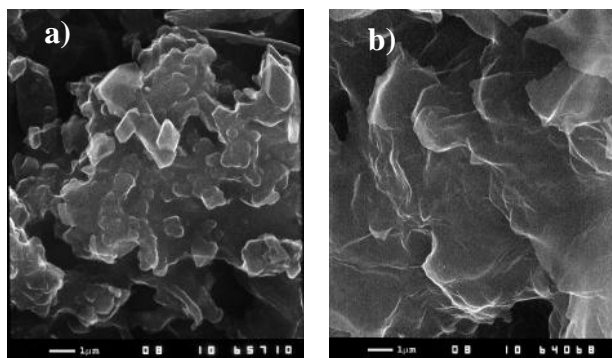


Fig. 9. XRD of HF.

In the photographs made with a SEM presented in Fig. 11 we can observe the thermally treated catalyst containing DWCNTs, MWCNTs and manganese oxide, respectively. The closed cap ends of both MWCNTs and DWCNTs are comprised of numerous pentagons and hence can be termed as macro fullerenes. At the same time as can be observed from the photographs shown in Fig. 11 the DWCNTs are larger in diameter in comparison with the MWCNTs. Some DWCNTs are also open-

ended which allows for the oxidation of sulphite to sulphate to take place within the nanotube structures.



**Fig. 10.** SEM photographs of the catalyst comprised of lyophilized catalyst, polypyrrol and manganese oxide; a) containing HF and b) containing fullerenes C<sub>60</sub>/C<sub>70</sub>.

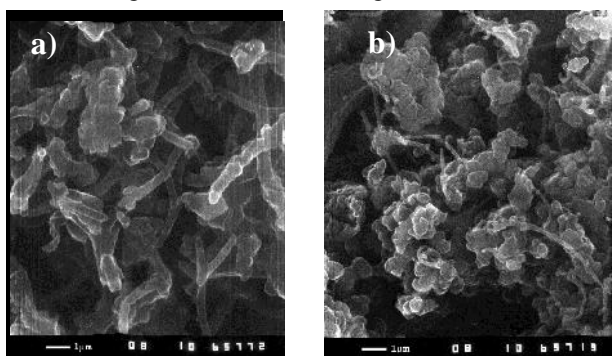


**Fig. 11.** Photographs made with a SEM of non-lyophilized catalyst and manganese acetate comprised of: a) DWCNTs and b) MWCNTs.

### Electrochemical results

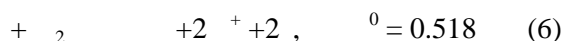
**Cyclic voltammetry:** Cyclic voltammetry plots were made of lyophilized and non-lyophilized catalysts. All the electrodes had a surface area of 1 cm<sup>2</sup> and were fabricated by covering both sides of a stainless steel mesh used as a current collector. The electrodes are compressed at T=300 °C and 300kg/cm<sup>2</sup>.

This curve has been recorded for comparison only. The probable reaction as shown in Fig. 12 is:



with peaks 1 and 2 for the oxidation/reduction of Mn equation (4) at around 500 – 800 mV and potential plateaus for reduction of Mn compounds reaction (5) at 190 mV that correspond (peak 3) to the data as cited in the literature [15].

The fabricated electrodes correspond to number 7 from the catalysts list. A process of carbon oxidation is clearly evident at E=500 mV in Fig. 13 as follows from [16]. These researchers observe that the oxidation of carbons takes place in accordance with equation 6.



The fabricated electrodes correspond to number 1 from the catalysts list. In Fig. 14 we can observe the possible reactions 4 and 5 that are due to manganese.

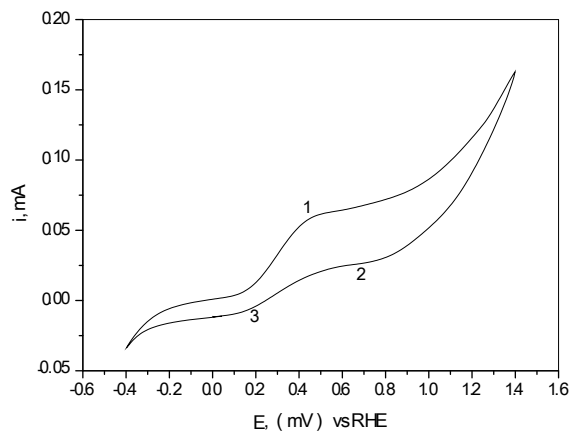


**Fig. 12.** Cyclic voltammogram of the electrode with MnO<sub>2</sub> obtained chemically; 100 mg of MnO<sub>2</sub> onto 35 % teflonized Vulcan XC-72, pressed at 300kg/cm<sup>2</sup>. Electrolyte: 1 Na<sub>2</sub>SO<sub>3</sub> + 18g.l<sup>-1</sup> NaCl, t = 20°. Scan rate 20 mV/s.

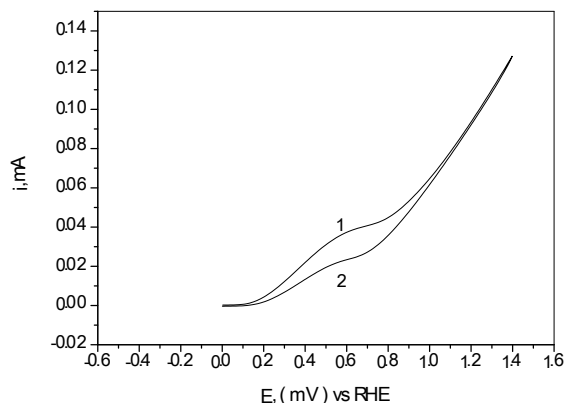


**Fig. 13.** Cyclic voltammogram of the electrode with non-lyophilized catalytic mass content: 100mg HF onto 35 % teflonized Vulcan XC-72. Pressed at 300kg/cm<sup>2</sup>. Electrolyte: 1 Na<sub>2</sub>SO<sub>3</sub> + 18g.l<sup>-1</sup> NaCl, t = 20°C. Scan speed 20mV/s.

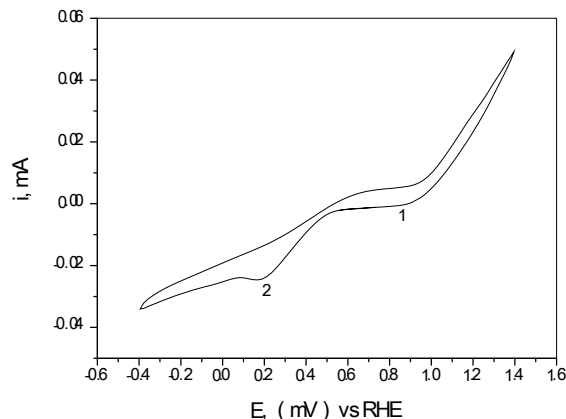


**Fig. 14.** The cyclic voltammogram of the lyophilized catalytic mass content: 7 mg of (37 mg - manganese acetate, 57 mg polypyrrol, 1.7 mg higher fullerenes). Scan rate 50 mV/s at room temperature in 1 M Na<sub>2</sub>SO<sub>3</sub>.

The electrodes fabricated correspond to number 2 from the catalysts list. In Fig. 15 we observe the peaks that correspond to reaction 4 due to the oxidation and reduction of manganese.

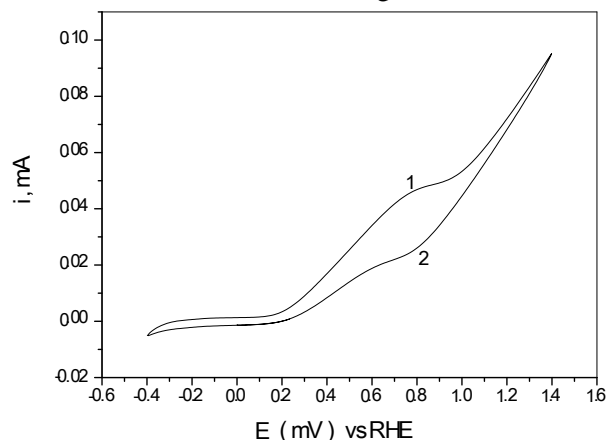


**Fig. 15.** The cyclic voltammogram of the lyophilized catalytic mass content: 7 mg of (40 mg - manganese acetate, 60 mg polypyrrole, 8 mg fullerenes  $C_{60}/C_{70}$  + (60 mg Vulcan  $72$  + 35% Teflon), pressed at 150 atm.]. Scan rate 20 mV/s at room temperature in 1 M  $Na_2SO_3$ .

**Polarization curves analysis:** A number of partial polarization curve measurements were made characterizing the incorporated HF, deposited  $MnO_2$  and polypyrrole binder in different ratios. As observed in Fig. 16 the electrodes 7 with incorporated pristine HF exhibit better characteristics than electrodes 6, incorporating pristine  $C_{60}/C_{70}$ . One likely reason for the better characteristics observed for the electrodes incorporating HF is probably the fact that these have a higher surface area (see, Fig. 10) and a greater number of pentagons within their structure.

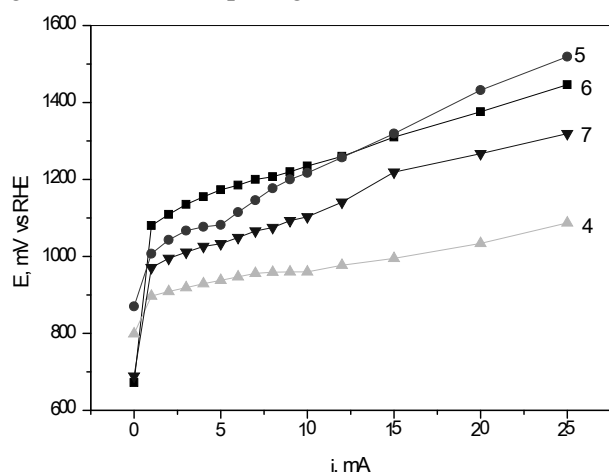


**Fig. 16.** Comparison of the polarization curves of electrodes incorporating non-lyophilized catalysts: 4 - DWCNTs, 7 - HF, 5 - MWCNTs, 6 -  $C_{60}/C_{70}$ .

When comparing the polarization curves of electrodes 4, incorporating pristine DWCNTs and electrodes 5, incorporating MWCNTs it is obvious

that DWCNTs exhibit better characteristics. Judging from the photographs in Fig. 11 it is clear that the DWCNTs are greater in diameter and have a larger surface area.

Straight line Tafel plots were taken of the polarization curves presented in Fig. 16 for the electrodes incorporating DWCNTs and  $C_{60}/C_{70}$ . For  $C_{60}/C_{70}$  fullerenes the value of  $b$  was 81 mV/dec. for DWCNTs  $b = 37$  mV/dec., this confirmed its higher catalytic activity (Fig. 17).

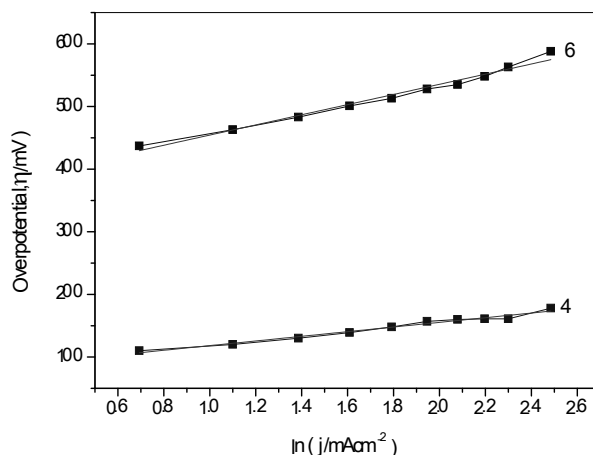


**Fig. 17.** Tafel plots for the electrodes comprised of: 6 - fullerenes  $C_{60}/C_{70}$  - 81 mV/dec and 4 - DWCNTs - 37 mV/dec.

Shown in Fig. 18 are the polarization curves of the electrodes prepared from lyophilized and non-lyophilized catalysts. The lowest overpotential is observed for the electrodes containing a lyophilized catalyst sample + HF (electrodes 1). With slightly higher overpotentials and therefore with inferior characteristics are the electrodes containing the most common fullerenes  $C_{60}/C_{70}$  (electrodes 2). Electrodes (electrodes 3) with a traditional carbon based catalyst, NORIT, were also fabricated using the lyophilization process and manganese acetate included. As shown in Fig. 18 these have inferior characteristics to both electrodes 1 and electrodes 2 incorporating HF and  $C_{60}/C_{70}$ , respectively. The quantity of manganese acetate used to fabricate all three electrodes was the same, therefore, the superior performance of electrodes 1 can only be due to the differences in nature of the respective carbon structures. From the lyophilized catalysts the electrodes incorporating HF and manganese oxide were found to be the most advantageous, yielding the lowest overpotentials at the respective current densities for the polarization curves (electrodes 1 in Fig. 18).

As shown in Fig. 19 electrodes 8 and 9 with incorporated DWCNTs, MWCNTs and manganese acetate have inferior behavior as compared to

electrodes 4, the electrodes incorporating pristine DWCNTs.

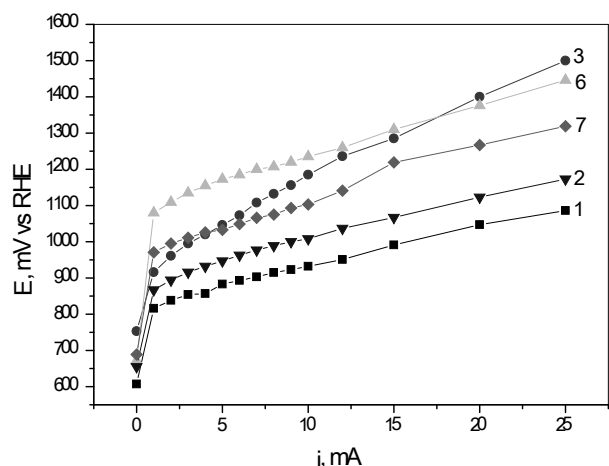


**Fig. 18.** Polarization curves of the electrodes prepared from lyophilized catalysts (at 150° and P = 0.3 mbar) electrodes 1, electrodes 2, electrodes 3 and non-lyophilized catalysts electrodes 6 and electrodes 7. Electrolyte: 1M Na<sub>2</sub>SO<sub>3</sub> + 18g.l<sup>-1</sup>NaCl, t = 20°C.

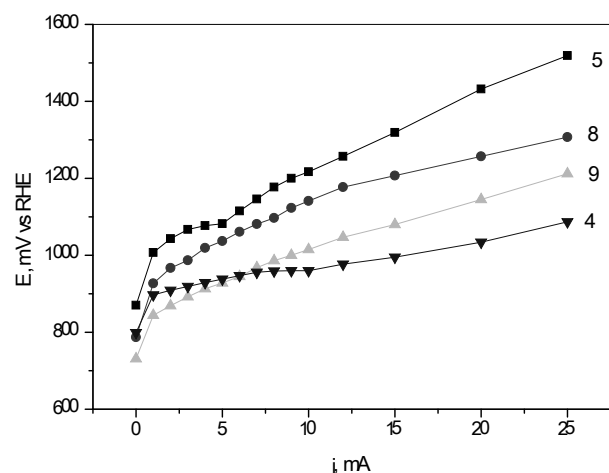


**Fig. 19.** Polarization curves of electrodes containing pristine DWCNTs - 4 and MWCNTs - 5, as well as electrodes incorporating thermally treated manganese acetate: 8 - [DWCNTs + manganese acetate], 9 - [MWCNTs + manganese acetate]. The electrodes were pressed at 300 kg/cm<sup>2</sup>. The electrolyte was 1 M Na<sub>2</sub>SO<sub>3</sub> + 18g.l<sup>-1</sup> NaCl, t = 20°C.

On the other hand the comparison between the electrodes incorporating pristine MWCNTs - 5 and DWCNTs - 4 shows that DWCNTs manifest superior catalytic characteristics. In addition we should note, that the much larger quantity of pristine DWCNTs incorporated in electrodes 4 clearly outweighs in terms of its catalytic activity the presence of manganese in electrodes 8 and 9, thus yielding lower overpotentials.

The catalysts prepared were investigated not only for the oxidation of SO<sub>3</sub> to SO<sub>4</sub>, but also for the reduction of nitrates:



The qualitative analytical measurements show, that reactions (7) yield only NO<sub>2</sub> while N<sub>2</sub> has not been detected [17]. The results presented in Fig. 20 confirm that a reduction is manifest and therefore it is clearly possible to electrochemically purify nitrite polluted aquatic environments.

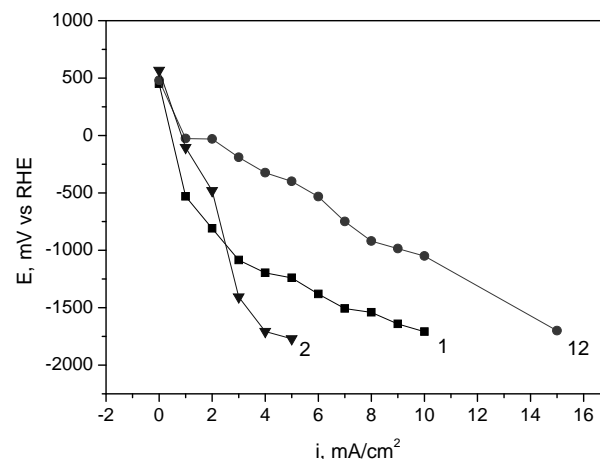


**Fig. 20.** Polarization curves of the electrodes comprised of lyophilized catalysts: 1, 2 and 12. The electrolyte at reduction was 0.1 M KNO<sub>3</sub>, t = 20°C.

A comparison of the reduction and oxidation curves (Fig. 21) shows that the reduction curves are more negative, in other words at this stage it is not possible to build a fuel cell. However, in the future by utilizing microbes to increase the reaction conversion rate it should be possible to build a S/N based fuel cell.

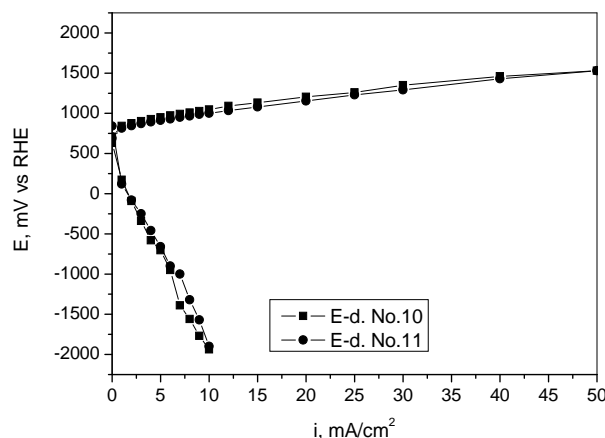


**Fig. 21.** Polarization curves of electrodes with catalysts prepared differently and measured at oxidation and reduction: electrodes 10 [with a pressure of 100 kg applied at room temperature], electrodes 11 [with a pressure of 300 atm. applied, while heated to 150° for 5 minutes]. The electrolyte at oxidation was 1 M Na<sub>2</sub>SO<sub>3</sub> + 18g.l<sup>-1</sup> NaCl, while at reduction it was 0.1 M KNO<sub>3</sub>, t = 20°C.

## CONCLUSIONS

Higher fullerenes, DWCNTs, MWCNTs and C<sub>60</sub>/C<sub>70</sub> appear to play a major role in the synthesis

of more effective catalysts. A diverse catalyst surface with well dispersed manganese particles leads to improved catalyst characteristics. The lyophilized material containing only higher fullerenes and manganese oxide was shown to have the highest activity in the oxidation of  $\text{SO}_3$ . The catalyst with a content combination of DWCNTs, higher fullerenes and manganese oxide yields the highest activity in the reduction of nitrates. The results presented confirm that it is possible to electrochemically purify nitrite polluted aquatic environments utilizing electro-catalysts incorporating fullerenes and nanotubes. At this stage, because the catalytic activity is not high enough and there are very high diffusion limitations of both reactions it is not possible to build a S/N based fuel cell. However, in the future by utilizing microbes to increase the reaction conversion rate of the catalysts studied it should be possible to successfully create a fuel cell such as the one outlined above.

**Acknowledgements:** This work was supported by the project “New fuel cells based on chemical and microbial processes“, through the Ministry of Education and Science and the Bulgarian National Science Research Fund, contract DFNI E02/15. In addition we acknowledge the help of Prof. Momchilov for supplying us with the chemically obtained  $\text{MnO}_2$  utilized as a catalyst in some of the electrodes, Prof. Stoyanova from the Institute of Inorganic Chemistry for the opportunity to utilize the lyophilisation apparatus at the institute and Prof. Ljutzkanov for supplying us with NORIT and helping with the thermal treatment of the samples.

## REFERENCES

1. N. Koprinarov, M. Konstantinova, G. Pchelarov, M. Marinov, Fullerene structures suitable for fuel cells electrodes, in: (Proc. of the NATO Advanced Research Workshop on Fuel Cell Technologies, Kyiv, Ukraine, 6-10 June 2004, p.81), N. Sammers et. al. (eds.), FUEL CELL TECHNOLOGIES: STATE AND PERSPECTIVES, Book Series: NATO Science Series II – Mathematics Physics and Chemistry, 2005, Vol. 202, p. 91.
2. E. Hernández, V. Meunier, B.W. Smith, R. Rurali, H. Terrones, Buongiorno, Fullerene coalescence in nanopeapods: a path to novel tubular carbon, *Nano Lett.*, **3**(8), 1037 (2003).
3. F. D'Souza, J.P. Choi, W. Kutner, *J. Phys. Chem. B*, **103**, 2892 (1999).
4. B. Gebhardt, Z. Syrgiannis, C. Backes, R. Graupner, F. Hauke and A. Hirsch, Carbon Nanotube Sidewall Functionalization with Carbonyl Compounds-Modified Birch Conditions vs the Organometallic Reduction Approach, *J. Am. Chem. Soc.*, **133**, 7985 (2011).
5. J. Wang, G. Wang, S. Miao, J. Liab and X. Bao, Graphene - supported iron-based nanoparticles encapsulated in nitrogen-doped carbon as a synergistic catalyst for hydrogen evolution and oxygen reduction reactions, *Faraday Discuss.*, **176**, 135 (2014)
6. K. P. Gong, F. Du, Z. H. Xia, M. Durstock, L. M. Dai, *Science*, **323**, 760 (2009).
7. K. Kim, J.I. Han, Performance of direct alkaline sulfide fuel cell without sulfur deposition on anode, *International Journal of Hydrogen Energy*, **39**, 7142 (2014).
8. J. W. Wu, W. J. Mei, X.P. Chen, J. C. Liu, H. Li, Fabrication and evaluation of  $[\text{Ru}(\text{bpy})_2(\text{MPyTMPP})\text{Cl}]^+$ -photoelectrocatalyzed  $\text{TiO}_2/\text{ITO}$  anode and  $[\text{Cu}(\text{phen})_2\text{Cl}]^+$ -electrocatalyzed SWCNTs/C cathode for photo-stimulated  $\text{SO}_3^{2-}\text{-H}_2\text{O}_2$  fuel cells, *Electrochimica Acta*, **103**, 1 (2013).
9. S. N. Frank, A. J. Bard, *J. Phys. Chem.*, **81**, 1484 (1977).
10. S. N. Frank, A. J. Bard, *J. Am. Chem. Soc.*, **99**, 4667 (1977).
11. M.D. Diener, J. M. Alford, Isolation and properties of small-gap fullerenes, *Nature*, **393**, 668 (1998).
12. T. R. Ralph, M. P. Hogarth, Catalysis for low-temperature fuel cells – part 1: The cathode challenges, *Plat. Met. Rev.*, **46**(1), 4 (2002).
13. D. Uzun, E. Razkazova-Velkova, K. Petrov, V. Beschkov, Electrochemical method for energy production from hydrogen sulfide in the Black sea waters in sulfide driven fuel cell, *Bull Chem Comm.*, **47**, 929 (2015).
14. J.X. Dai, S.F.Y. Li, K.S. Siow, Z. Gao, *Electrochim. Acta*, **45**, 2211 (2000).
15. V. Nikolova, P. Iliev, K. Petrov, T. Vitanov, E. Zhecheva, R. Stoyanova, I. Valov, D. Stoychev, Electrocatalysts for bifunctional oxygen/air electrodes, *Journal of Power Sources*, **185**, 727 (2008).
16. B. E. Conway, J. O' M Bockris, R. E. White (eds.), Modern Aspects of Electrochemistry, No. 19, Chapter 5, Electrocatalytic Properties of Carbon Materials, M. R. Tarasevich and E. I. Khrushcheva, Plenum Press, New York, 1989, p. 314.
17. Goldman, E., R. Jacobs, “Determination of nitrates by ultraviolet absorption”, *J. Am. Water Works Assoc.*, **53**, 187(1961)..

	MWCNTs,			DWCNTs,
1	*1, 1,	-	2, 1,	1,
2		10, 1113,		103, 1113
	14	2016 ;	29	2017 .
		( )		
SO <sub>x</sub> /NO <sub>x</sub>	SO <sub>3</sub> SO <sub>4</sub>		NO <sub>3</sub> NO <sub>2</sub> N <sub>2</sub> ,	
	(DWCNTs)	n	(HFs)	/ (SEM)
	(XRD).			n/HFs
n/HFs/DWCNTs	E/V			
			SO <sub>x</sub> /NO <sub>x</sub>	



## Synthesis and characterization of poly(azulene-thiophene vinyl pyrylium) salt

I.G. Lazar<sup>1</sup>, E. Diacu<sup>1</sup>, G.-L. Arnold<sup>1</sup>, E.-M. Ungureanu<sup>1\*</sup>, G.-O. Buica<sup>1\*\*</sup>, L. Birzan<sup>2</sup>

<sup>1</sup> University "Politehnica" of Bucharest, Faculty of Applied Chemistry and Material Sciences, 1-7 Polizu Street, 011061, Bucharest, Romania

<sup>2</sup> Romanian Academy, Organic Chemistry Center "C.D. Nenitzescu", Splaiul Independentei 202B, 71141 Bucharest, Romania

Received November 14, 2016      Revised December 20, 2016

This work presents the electrochemical characterization of 2,6-bis((E)-2-(thiophen-2-yl)vinyl)-4-(4,6,8-trimethylazulen-1-yl)pyrylium perchlorate (**L**) by voltammetric techniques such as cyclic voltammetry, differential pulse voltammetry, and rotating disk electrode voltammetry. Poly**L** modified electrodes obtained by controlled potential electrolysis were used to detect the presence of heavy metal ions. Good results have been obtained for Cd(II), Pb(II), Cu(II), Hg(II) ions, but the best limit of detection ( $10^{-7}$  M) has been obtained in the case of Pb(II).

**Key words:** 2,6-bis((E)-2-(thiophen-2-yl)vinyl)-4-(4,6,8-trimethylazulen-1-yl)pyrylium perchlorate, electrochemical characterization, modified electrodes, detection of heavy metals.

### INTRODUCTION

Azulenenes are organic compounds that have a seven carbon atoms ring (electron-poor) connected to a five carbon atoms ring (electron-rich) [1] structure that confers electroactive properties and leads to interesting applications in optoelectronics [2], assessment of antiretroviral activity [3], electrochemical sensors [4]. This paper is related to the last mentioned application and proposes a new azulene based modified electrode which can be used as sensor for heavy metals detection.

The most used methods for the determination of heavy metals are the spectral methods, mainly atomic absorption spectroscopy (AAS) [5], emission spectrometry by inductive coupled plasma (ICP) [6], and lately neutron activation analysis [7, 8]. However, these methods are dedicated especially to very well equipped laboratories. A sensitive and versatile analytical method to detect heavy metals that can be used *on site* is that using electrochemical sensors [9, 10].

This work proposes a new modified electrode based on azulene-thiophene vinyl pyrylium salt, namely 2,6-bis((E)-2-(2-thienyl)vinyl)-4-(4,6,8-trimethylazulen-1-yl)pyrylium perchlorate (**L**) (Fig. 1) which has been tested for the following heavy metal ions detection: Cu(II), Pb(II), Hg(II) and Cd(II).

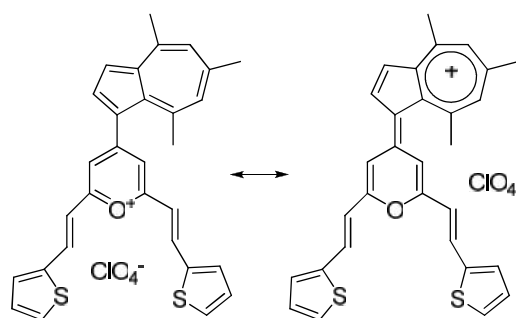


**Fig. 1.** Chemical structure of 2,6-bis((E)-2-(2-thienyl)vinyl)-4-(4,6,8-trimethylazulen-1-yl)pyrylium perchlorate (**L**).

### EXPERIMENTAL

All the reagents used in the electrochemical experiments were of analytical grade. As supporting electrolyte tetra-*n*-butylammonium perchlorate (TBAP, Fluka puriss, electrochemical grade >99%) solved in acetonitrile (CH<sub>3</sub>CN, Sigma Aldrich, electronic grade 99.999% tracetmetals) was used. Metal cation salts were purchased as follows: mercury(II) acetate, cadmium nitrate tetrahydrate, lead(II) nitrate of analytical purity from Sigma Aldrich, and copper(II) acetate monohydrate from Fluka (99.0%). The aqueous solutions were prepared with Millipore Simplicity UV. 0.1M buffer acetate pH = 5.5 was prepared from 0.2M acetic acid and 0.2M sodium acetate.

The electrochemical experiments were carried out in a three-electrode cell connected to a PGSTAT 12 AUTOLAB. The working electrode consisted in a glassy carbon disk from Metrohm (3 mm in diameter), which was polished before each

To whom all correspondence should be sent:  
E-mail: \* em\_ungureanu2000@yahoo.com  
\*\* buica\_george@yahoo.com

experiment with diamond paste (0.25 $\mu$ m) and cleaned with acetonitrile. A platinum wire was used as auxiliary electrode. As reference electrode, Ag/10mM AgNO<sub>3</sub> in 0,1M TBAP/CH<sub>3</sub>CN was used in acetonitrile solvent, and Ag/AgCl, 3M KCl in water solvent.

Cyclic voltammetry (CV) curves were recorded at 0.1 V/s scan rate, the rotating disk electrode voltammetry (RDE) curves were recorded at 0.01 V/s. Differential pulse voltammetry (DPV) curves were recorded at 0.01 V/s with a pulse height of 0.025 V and a step time of 0.2s.

For the curves recorded in acetonitrile, the applied potentials were referred to the potential of the ferrocene/ferricinium redox couple (Fc/Fc<sup>+</sup>), which in the experimental conditions was +0.07 V.

PolyL modified electrodes were prepared by controlled potential electrolysis (CPE) at different potentials and charges. After preparation, the modified electrodes were cleaned with acetonitrile, then transferred in a three electrode transfer cell containing 0.1M buffer acetate pH = 5.5 as supporting electrolyte. 15 cycles (between - 0.9 V and + 0.6 V) and 15 cycles (between -0.2 V and +2.5 V) were applied. Then the electrode was cleaned with water and then introduced in water solutions of heavy metals for 15 minutes, under mechanical stirring. A multielement stock standard solution (10<sup>-2</sup> M) of Cd, Pb, Cu, Hg was prepared and working heavy metals solutions (10<sup>-5</sup> – 10<sup>-8</sup> mol/ L) were prepared daily by successive dilutions.

All electrochemical experiments were performed in standard conditions at 25°C under argon atmosphere.

## RESULTS AND DISCUSSION

The electrochemical behaviour of L has been investigated by CV, DPV, and RDE on glassy carbon electrode. The curves were recorded starting from open circuit voltage potential of around 0 V. The anodic and cathodic CV and DPV curves were recorded at different concentrations (0 – 2 mM) in 0.1M TBAP/CH<sub>3</sub>CN (Fig. 2). CV and DPV curves show 2 oxidation peaks (a1 and a2) and 5 reduction peaks (c1 – c5). The current peaks are increasing with L concentration. The dependences of the significant peak currents ( $\mu$ A) on concentration (mM) for CV and DPV curves are presented in Figure 3. Table 1 presents the equations of the peak current dependencies on L concentration for the main peaks and their correlation coefficients for CV and DPV curves.

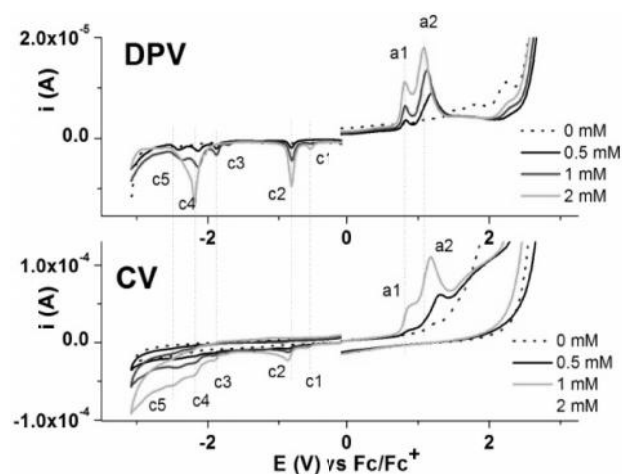


Fig. 2. DPV (0.01 V/s) and CV (0.1 V/s) curves for L at different concentrations on glassy carbon (3mm in diameter) in 0.1M TBAP, CH<sub>3</sub>CN.

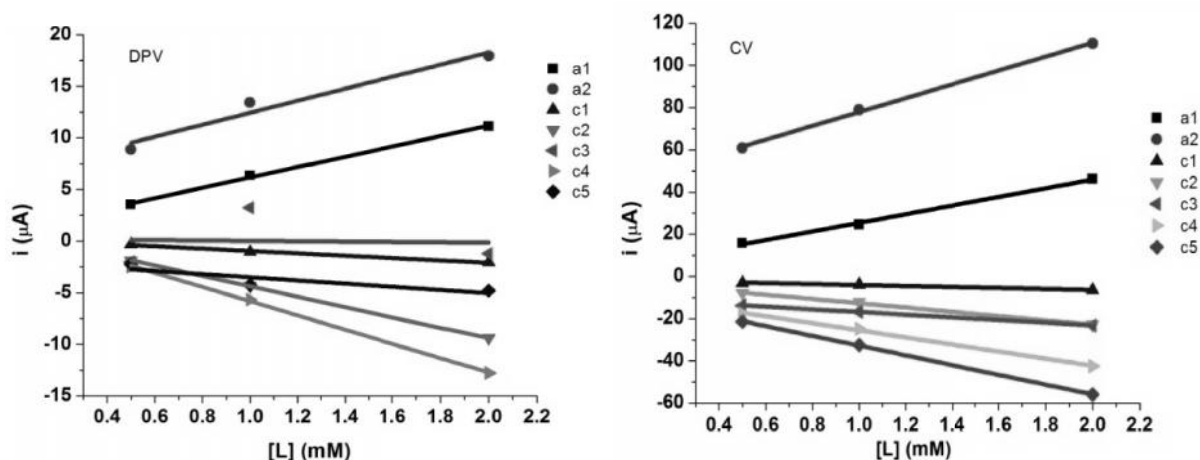


Fig. 3. Dependences of the DPV and CV peak currents on concentration of L.

**Table 1.** CV and DPV equations of significant peak currents ( $i_{\text{peak}}$ )\* on **L** concentration [**L**]

Method	Equation	Correlation coefficient
DPV	$i_{\text{peak a1}} = 1.17 + 5.01 [\text{L}]$	0.9964
	$i_{\text{peak a2}} = 6.63 + 5.82 [\text{L}]$	0.9247
	$i_{\text{peak c1}} = 0.22 - 1.16 [\text{L}]$	0.9764
	$i_{\text{peak c2}} = 0.65 - 5.02 [\text{L}]$	0.9999
	$i_{\text{peak c4}} = 1.09 - 6.90 [\text{L}]$	0.9986
CV	$i_{\text{peak a1}} = 5.03 + 20.42 [\text{L}]$	0.9949
	$i_{\text{peak a2}} = 45.16 + 32.78 [\text{L}]$	0.9975
	$i_{\text{peak c1}} = -1.75 - 2.28 [\text{L}]$	0.9789
	$i_{\text{peak c2}} = -2.51 - 10.15 [\text{L}]$	0.9964
	$i_{\text{peak c3}} = -10.48 - 6.33 [\text{L}]$	0.9995
	$i_{\text{peak c4}} = -8.72 - 16.77 [\text{L}]$	0.9963
	$i_{\text{peak c5}} = -9.65 - 23.09 [\text{L}]$	0.9996

\*  $i_{\text{peak}}$  is given in  $\mu\text{A}$  and [**L**] in mmol/L (mM)

From Table 1, it can be seen that the DPV peaks denoted a1 and c2 have the same slope (of 5) in respect to concentration. The other peaks have higher slopes in absolute value. It can be assumed that these peaks correspond, respectively, to the oxidation of azulene derivative to its radical cation and to its reduction to the corresponding radical anion. They are both one-electron processes. The process c1 has very weak DPV and CV slopes with **L** concentration and could be ascribed to an impurity. Figure 4 presents the CV curves on different scan rates (0.1 – 1 V/s) for a1 and c1 peaks in 1mM solution of **L**, and the linear dependences of the peak currents ( $i$ ) on square root of the scan rate. The peak currents increase with the scan rate in agreement with the Randles-Sevcik equation.

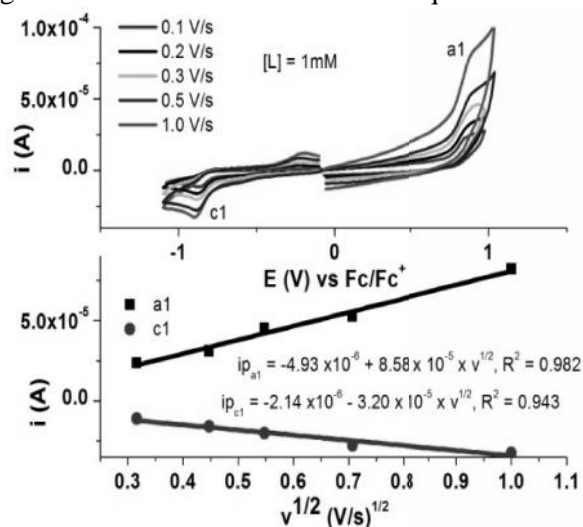


**Fig. 4.** CV curves at different scan rate and dependences of the peak currents (A) on the square root of the scan rate for **L** (1mM) in 0.1M TBAP,  $\text{CH}_3\text{CN}$ .

In figure 5 are presented the CV curves (0.1 V/s) on different scan domains for **L** (1mM), while in Table 2 are given the peak potentials obtained from CV and DPV curves for **L** (1mM). It can be observed that all anodic process (a1 and a2) and c1 are irreversible (as they do not have corresponding peaks in the reverse scans), while the cathodic ones (c2 – c5) are quasi-reversible (having small peaks in the reverse scans).

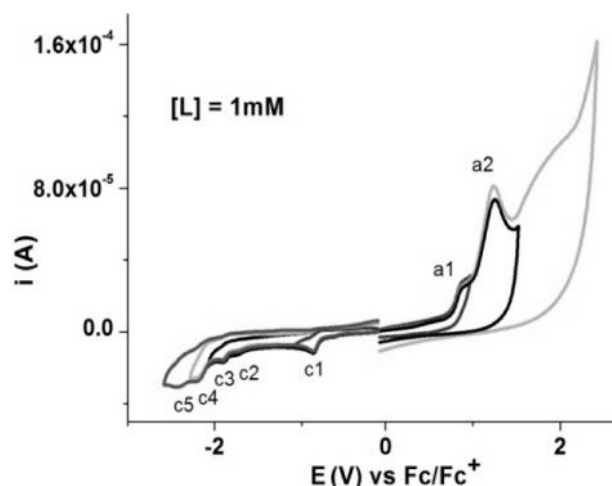


**Fig. 5.** CV curves at different scan domains for **L** (1 mM) in 0.1M TBAP  $\text{CH}_3\text{CN}$ .

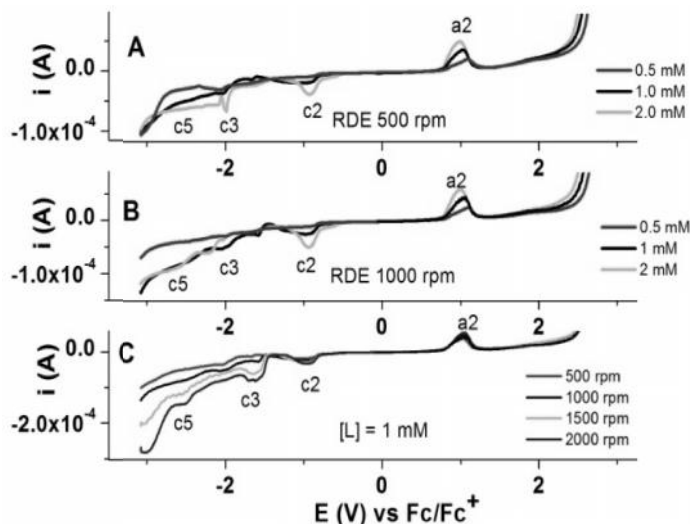
**Table 2.** Values of peak potentials (V) for [**L**] = 1mM

Peak	Method		Process type
	DPV	CV	
a1	0.82	<b>0.86</b>	(i)*
a2	1.12	1.25	(i)*
c1	-0.54	-0.59	(i)*
c2	-0.81	-0.85	(q)*
c3	-1.87	-1.9	(q)*
c4	-2.12	-2.15	(q)*
c5	-2.35	-2.45	(q)*

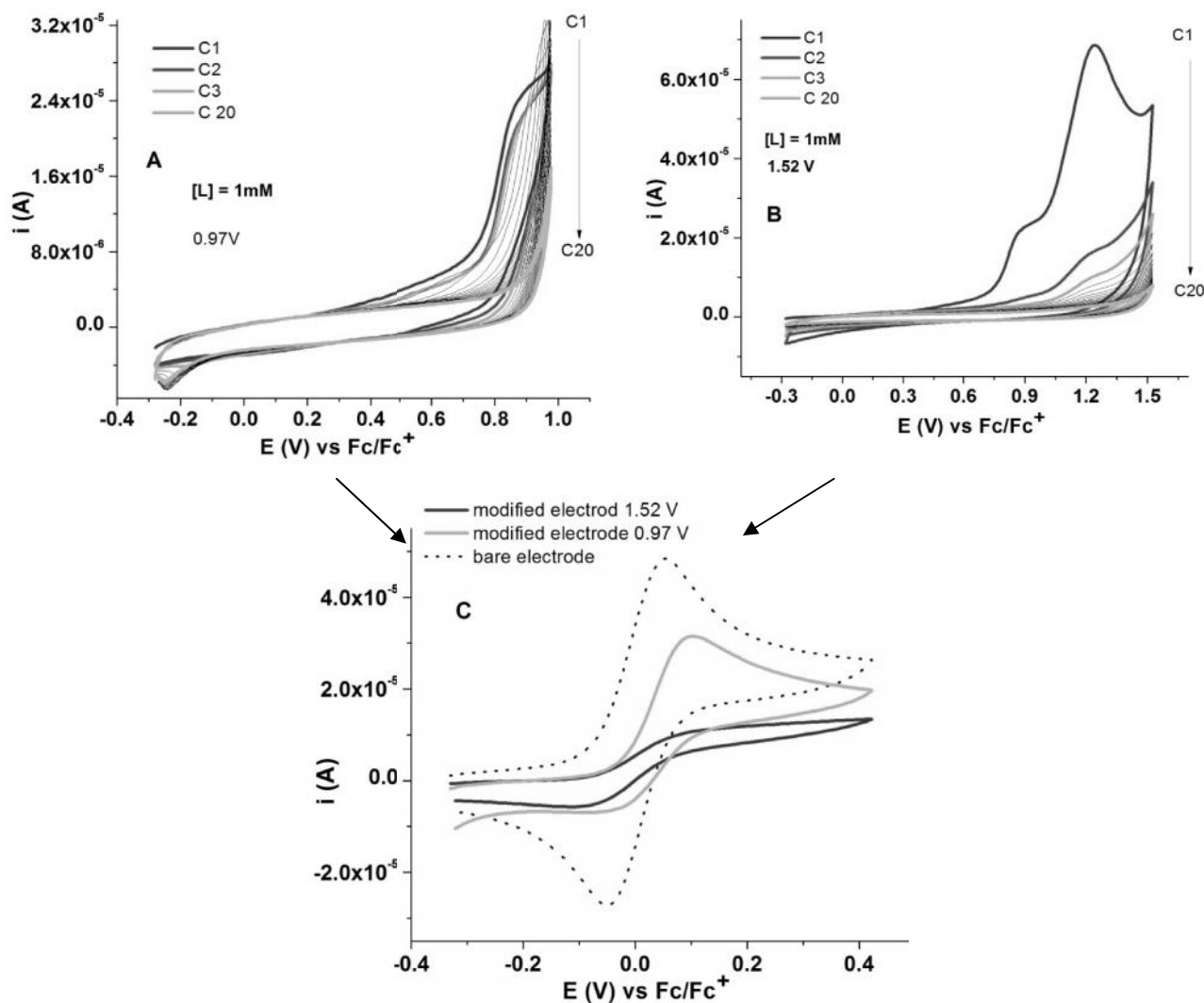
\* q - quasi-reversible process; i - irreversible process

Figure 6 presents the RDE curves at 500 rpm, 1000 rpm and different concentrations (1mM – 3mM). They show one wave as a peak in the anodic domain, and 3 waves (c2, c3, c5) in the cathodic domain, corresponding to the oxidation and reduction peaks seen in DPV curves. RDE currents increase with **L** concentration and with the rotation rate. The form of the anodic waves as peaks indicates the formation of films in the anodic scans.

However, even in cathodic scans there is a form of a peak of the wave, which indicates either the decomposition of **L**, or its cathodic polymerization.



**Fig. 6.** RDE curves (0.01 V/s) on glassy carbon (3mm in diameter) for **L** in 0.1M TPAB,  $CH_3CN$  at different concentrations of **L** at 500 rpm (A) and 1000 rpm (B) and at different rotation rates between 500 and 2000 rpm (C) for  $[L] = 1$  mM.



**Fig. 7.** CV curves (0.1 V/s) during the formation of poly**L** modified electrodes on glassy carbon electrode in 1 mM solution of **L** in 0.1M TBAP,  $CH_3CN$  (A, B) by scanning between -0.3 V and different anodic limits: 0.97V (A) and +1.52V (B), and the corresponding CV curves (0.1V/s) obtained after the transfer of the modified electrodes in 1mM ferrocene solution (C).

### Modified electrodes

PolyL modified electrodes were obtained in L millimolar solutions in 0.1 M TBAP, CH<sub>3</sub>CN by successive scanning (20 cycles) between -0.2V and different anodic potential limits (such as 0.97V, or 1.52V), and by controlled potential electrolysis (CPE) at different potentials and charges.

The modified electrodes were then transferred into a solution of ferrocene (1 mM) in 0.1M TBAP, CH<sub>3</sub>CN and their CV curves were recorded. It can

be seen that, the modified electrode obtained by successive scanning with the anodic limit at the potential of +1.52 V is strongly depressed compared to the bare electrode. As the charge is increased, as the ferrocene signal diminished; the curves for the modified electrodes obtained by CPE at different potentials (for a charge of 1mC) or for different charges (at 0.97V) are shown in Fig. 8. The signal for the modified electrode obtained by EPC at 0.97V 1 mC is different from that on the bare electrode, indicating the electrode coverage by a thin film.

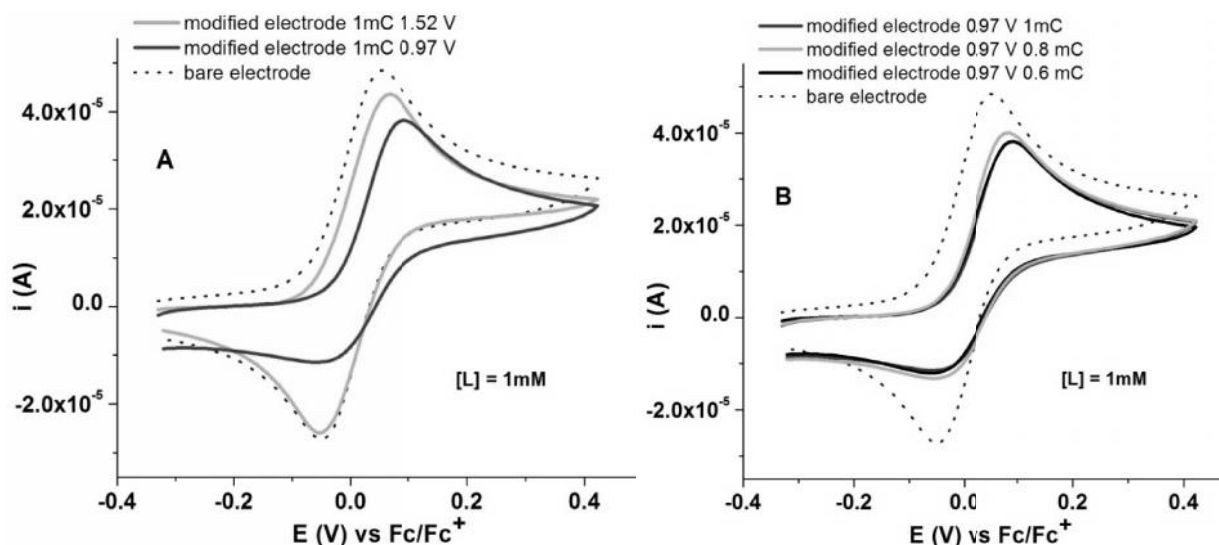


**Fig. 8.** CV curves recorded in 1 mM ferrocene solutions in 0.1M TBAP, CH<sub>3</sub>CN on modified electrodes obtained by CPE in 1 mM solution of L in 0.1M TBAP, CH<sub>3</sub>CN at different electropolymerization potentials and for 1 mC (A) and at 0.97 V using different electropolymerization charges (B).

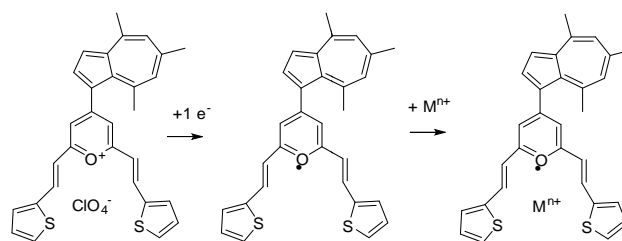
### Evaluation of recognition properties

Modified electrode obtained in solutions of L (1 mM) in 0.1M TBAP, CH<sub>3</sub>CN by CPE (1.62V, 2mC) were placed in a cell with three electrodes containing 0.1 M acetate buffer pH 5.5 for equilibration and overoxidation, then each modified electrode was introduced into a solution containing heavy metal ions at different concentration under magneticstirring for 15 minutes. The metal complexation is facilitated by pyranium salt reduction at around -0.8 V with the formation of a pyranium radical, which does not contain any more a repulsive positive charge.

The responses of the modified electrodes are shown in Figure 9A, and the dependences of the DPV stripping currents on each heavy metal concentration are given in Fig. 9B. The best response was found for Pb (detection

limit lower than 10<sup>-7</sup> M). The polyL modified electrodes can be used for analysis of these heavy metals from water. The work is in progress. It seems that the interaction with Cd<sup>2+</sup> ion is too weak to form strong complexing bonds leading to a failure of its absorption on the electrode surface.

However, in the case of mercury the interaction is too strong, probably forming covalent bonds at 3-position of azulene moiety. Therefore it will be only partially oxidized at its expected potential.





## Quantitative determination of capsaicinoids in ground hot pepper samples using voltammetry of microparticles

L. ižmek<sup>1\*</sup>, I. Novak Jovanovi<sup>2</sup>, Š. Komorsky-Lovri<sup>1</sup>

<sup>1</sup>"Ruđer Bošković" Institute, Bijenička 54, Zagreb, Croatia

<sup>2</sup>Institute for Medical Research and Occupational Health, Ksaverska 2, Zagreb, Croatia

Received November 11, 2016    Revised December 22, 2016

Applicability of standard addition method for determination of pungency in commercially available hot pepper samples using voltammetry of microparticles (VIM) is presented in this work. Analysis was performed on paraffin-impregnated graphite electrode (PIGE) using square-wave voltammetry (SWV) under optimal experimental conditions of pH 11, pulse amplitude of 50 mV, frequency of 150 Hz, and step potential of 2 mV. Concentrations of capsaicinoids in hot pepper samples were determined from internal calibration curves constructed using standard addition method (SAM) and good correlation was obtained between our results and those reported in literature (correlation factor  $r = 0.976$ ). In addition to VIM, applicability of stripping voltammetry microprobe (SPV) method for electrochemical analysis of capsaicinoids was investigated. SWV responses obtained for capsaicin precipitate using SPV method were similar to those obtained using VIM. There was a good dose-response relationship between capsaicin concentrations precipitated on PIGE but in rather narrow concentration range.

**Key words:** capsaicinoids, hot peppers, standard addition method, voltammetry of microparticles, stripping voltammetry microprobe

### INTRODUCTION

Hot peppers (*Capsicum spp.*) are among the oldest cultivated plants that are consumed worldwide mainly because of their unique pungent flavour and aroma. The pungency is caused by capsaicinoids, a group of alkaloids found exclusively in the fruits of hot pepper varieties. The most abundant capsaicinoids in hot peppers are capsaicin (8-methyl-N-vanillyl-*trans*-6-nonenamide) and dihydrocapsaicin (8-methyl-N-vanillylnonanamide), which are responsible for about 90% of the spiciness [1]. In addition to their importance as food additives, capsaicinoids were found to have beneficial effects on human health including chemopreventive and anticancerogenic effects, antioxidative activities, regulation of the energy metabolism, anti-inflammatory, analgesic and antimicrobial properties [2].

An accurate determination of the levels of various capsaicinoids has become important because of the increasing demand by consumers for spicy food and their increasing use in pharmaceuticals. The oldest method for determination of hot pepper pungency is Scoville organoleptic test [3] which is based on the tester's perception of pungency.

Additionally, more accurate and sensitive analytical methods have been developed, including high-performance liquid chromatography (HPLC) which is considered to be the most reliable and accurate method for quantification of individual capsaicinoids in hot peppers as well as for determination of their pungency [4]. However, chromatographic methods are generally complicated, time-consuming and require expensive instruments. Electrochemical techniques, particularly voltammetry, have appeared as a promising alternative due to low cost, miniaturization potential and rapid and simple analysis. There are several published papers dealing with the application of voltammetry for determination of hot pepper's pungency, but all of them describe the solution phase detection of capsaicinoids meaning that extraction of capsaicinoids is required prior to analysis [5-7].

In our latest work we developed a sensor for direct measurement of different pungency levels in hot peppers using voltammetry of immobilized microparticles (VIM) [8]. The proposed method exploits the current intensity of capsaicinoids in pepper samples in order to classify samples according to their pungency. Till date, voltammetry of microparticles has mostly been applied for qualitative electrochemical analysis of various solid compounds, e.g. minerals, alloys, and organic molecules [9, 10]. Also, it was used for the direct

---

To whom all correspondence should be sent:  
E-mail: lcizmek@irb.hr

identification of powders of pharmacological substances [11] and for estimation of antioxidative activity in tea leaves [12].

In this work, we wanted to apply VIM for quantification of capsaicinoids in solid hot pepper samples. However, solid-state voltammetric quantification is not an easy task, mainly because there is no possibility to accurately determine the exact amount of sample attached on the electrode surface. To overcome this problem, a standard addition method (SAM) can be used [13]. Standard addition method in combination with VIM allows the determination of the mass fraction of a depositable analyte in a material on addition of known amounts of a standard material containing analyte of interest to a mixture of that material and a depositable reference compound. The method has been successfully applied for quantification of boron and zirconium in minerals and ceramic materials [13, 14] as well as antidepressant drugs in phytotherapeutic formulations [15]. The main drawback of SAM is the need for relatively high amounts of sample and standard.

Hence, another electroanalytical method, namely stripping voltammetry microprobe (SPV), has received our attention. SPV is a fully new approach in electroanalytical chemistry proposed by Gulppi et al. [16, 17]. This method allows electrochemical trace analysis in micro samples which is a great advantage for such measurements [17]. In this study we wanted to investigate possible application of SPV for electrochemical analysis of capsaicinoids.

## EXPERIMENTAL

### *Reagents and samples*

Capsaicin (95 %, from *Capsicum sp.*), indigo (95%) and sepiolite were purchased from Sigma, Germany.  $\text{KNO}_3$  and buffer solution pH 11 (analytical grade) were from Kemika, Croatia. Ethanol (p. a., 96%) was from Gram-Mol, Croatia. Water was deionised by Millipore Milli-Q system to the resistivity 18 M  $\Omega$  cm. Five ground hot pepper samples (Bhut jolokia, Red savina, Fatalli, Habanero orange and Carolina cayenne) were purchased from local stores in Croatia. The samples were stored at room temperature until the time of analysis. The sources of the tested samples are listed in the footnotes to the Table 1.

### *Instrumentation and procedures*

Voltammetric measurements were carried out using the computer-controlled electrochemical system Autolab PGSTAT 30 (Eco-Chemie, Utrecht, Netherlands). A three-electrode system (Methrom,

Switzerland) with paraffin-impregnated graphite rod (diameter 5 mm, length 50 mm) as the working electrode (PIGE), Ag/AgCl (3 M KCl) electrode as a reference electrode and a platinum wire as a counter electrode were used. All potentials were expressed *versus* Ag/AgCl (3 M KCl) reference electrode. Working electrode was mechanically cleaned before each run. The circular surface of PIGE was rinsed with ethanol and distilled water, polished on a wet polishing cloth, rinsed again, dried with a fine-grade paper tissue (P1200 grade) and carefully polished on a dry, white paper sheet.

Voltammetric measurements were performed in 0.1 mol  $\text{L}^{-1}$   $\text{KNO}_3$  within the potential range from -1.0 to +1.0 V. Optimal experimental conditions for determination of capsaicinoids in hot peppers are pH 11, potential step increment 2 mV, square wave amplitude 50 mV and square wave frequency 150 Hz, as reported in our previous paper [8]. The solutions were degassed with high purity nitrogen prior to all electrochemical measurements. A nitrogen blanket was maintained thereafter. All experiments were performed at room temperature. Unless otherwise stated, each voltammetric measurement was repeated six times.

### *Modified electrodes preparation*

The 15 mg of ground pepper sample, 30 mg of indigo and 30 mg of sepiolite were accurately weighted, powdered in an agate mortar and then ultrasonicated for 5 min. Then, the mixture was spiked with different additions of pure capsaicin, ultrasonicated for 5 min, and powdered again on the agate mortar forming a finely distributed material. The surface of PIGE was contaminated with microparticles of sample by pressing it into a small pile of substance powder on a highly glazed ceramic tile and moving it with circular motion. The working electrode was immersed in the electrolyte only during the voltammetric measurements. Less than 1 mm of the graphite rod was immersed into the electrolyte in order to minimize the capacitive current.

Additional experiments were performed with precipitates of capsaicin (pure and extracted from hot peppers). Namely, a precipitate of capsaicin was formed onto the surface of PIGE by pipetting 5  $\mu\text{L}$  of pure capsaicin solution in ethanol (0.05, 0.07, 0.1, 0.3, 0.4, 0.5 and 1 g  $\text{L}^{-1}$ ) or hot pepper extract, and allowing the solvent to evaporate in air. The precipitate was then analysed by square-wave voltammetry at optimal experimental conditions. The extraction of capsaicinoids from hot pepper samples (200 mg) was performed ultrasonically with ethanol (12.5 mL) as extraction solvent for 20



min. Additional solutions were prepared by pipetting corresponding volume of our original extract and diluting it with ethanol (prepared concentrations were as follows: 8, 4, 2, 1, 0.5 g L<sup>-1</sup>).

#### Description of the standard addition method

For quantification of capsaicinoids in solid hot pepper samples a standard addition method was used, as described by Doménech-Carbó et al. [9]. Briefly, in a standard addition experiment a homogenized mixture of mass  $m$  of sample (ground hot pepper) which contains an unknown mass  $m_X$  of the analyte X (capsaicin), with mass  $m_R$  of the reference compound R (indigo) was spiked with known amounts of standard compound (pure capsaicin),  $m_X^*$ . The calibration curve was constructed by plotting the ratio between the peak currents of the stripping oxidation of pepper sample and indigo [ $\Delta I_p(X)/\Delta I_p(R)$ ] versus mass ratio  $m_X^*/m_R$ :  $I_p(X)/I_p(R) = Km_X^*/m_R + K(m/m_R)(m_X/m)$ . The slope  $K$  of this straight line is the ratio of amperometric constants of capsaicin and indigo. The mass fraction of capsaicin in hot pepper sample ( $m_X/m$ ) is estimated from the ordinate at the origin. Note that  $m/m_R$  is constant and known ( $m/m_R = 15 \text{ mg}/30 \text{ mg}$ ). So, the mass fraction of capsaicin in hot pepper samples was estimated from the intercept multiplied by 2 and divided by the slope.

Calibration was performed by spiking a mixture of indigo + hot pepper + sepiolite (1:0.5:1) with increasing amounts of pure capsaicin. For construction of calibration curves, a minimum of five calibration standards were used.

## RESULTS AND DISCUSSION

### Quantification of capsaicinoids in hot pepper powders

In our previous study [8], the electrochemical behaviour of capsaicin microparticles mechanically attached to a paraffin-impregnated graphite electrode was investigated using square-wave and cyclic voltammetry. It was found that the electrochemical oxidation of capsaicin on PIGE is a complex, pH dependent, irreversible process, and proceeds via the transfer of two electrons. Representative SW voltammogram of capsaicin-modified PIGE recorded under the optimum analytical conditions (pH = 11,  $f = 150 \text{ Hz}$ ,  $dE = 2 \text{ mV}$ ,  $E_{sw} = 50 \text{ mV}$ ) in 0.1 M KNO<sub>3</sub>, consists of a single anodic peak at +0.256 V vs. Ag/AgCl (Fig. 1A). In addition, we have shown that voltammetry of microparticles can be used for estimation of pungency levels of hot peppers. However, quantitative determination of capsaicin in hot

peppers using VIM as such was not possible, because the exact amount of sample deposited on the electrode surface is generally uneasy to control. To overcome this obstacle, Doménech-Carbó et al. [13] developed a methodology for quantification of solids with VIM using mixtures of the test material and an electroactive reference compound. Although the exact amount of each one of the compounds (reference compound and the test sample) deposited on the electrode surface is uncertain, their quotient must be equal to their known mass ratio in the original mixture and proportional to the ratio between their respective peak currents.

Selection of the reference compound is mainly dictated by these two conditions: (i) the stripping of reference compound must occur at potentials clearly separated from those at which the stripping of our analytical objective takes place, and (ii) there should be no effects or reactions between analyte of interest and the reference compound. In this study, indigo was tested as a reference compound, because its voltammetric properties in solid phase are relatively well-known [10]. As can be seen in Fig. 1B the SWV response of indigo at optimum experimental conditions consists of a well-defined peak P2 at -0.639 V and a poorly defined peak P3 at +0.137 V. The SWV of capsaicin gave one peak P1 at +0.258 V if the potential scan was initiated at -1.0 V in the positive direction (Fig. 1A). SWV response of capsaicin + indigo mixture consists of two well-separated peaks P2 at -0.588 V and P1 at +0.288 V corresponding to oxidation of indigo and capsaicin, respectively, as can be seen on Fig. 1C. Capsaicin peak is superimposed on the peak P3 of indigo (see Fig. 1B), and hence this peak was not seen on the SWV response of capsaicin + indigo mixture. The net peak current of the second peak of indigo is very low (order of magnitude 10<sup>-7</sup>  $\mu\text{A}$ ), so it is reasonable to assume that its contribution to peak related to capsaicin oxidation is negligible.

The background signal (a square-wave voltammogram recorded with no compound immobilized on PIGE surface) has been measured before each measurement and peak at ca. -0.1 V was always present which can be attributed to buffer solution. Repeatability tests were performed as a series of independent measurements on six freshly prepared electrodes modified with the mixture of capsaicin and indigo (1/1, w/w).

The peak potential was reproduced with a maximum deviation of ca. 6% and the relative standard deviation of peak current ratio was ca. 26%.

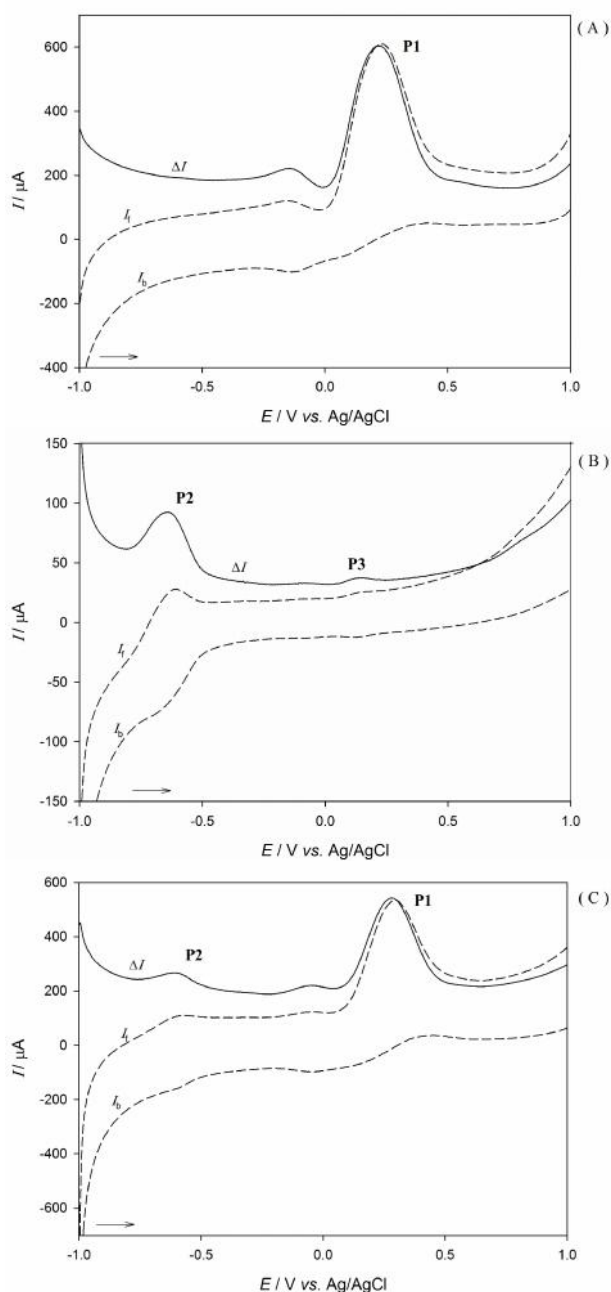


**Fig. 1.** Square-wave voltammetry of capsaicin (A), indigo (B) and mixture of capsaicin and indigo (1/1, w/w) (C) microparticles in 0.1 M KNO<sub>3</sub>, pH 11. The pulse amplitude is 50 mV, the step potential is 2 mV and the frequency is 150 Hz. The net response ( $\Delta I$ ) and its forward ( $I_f$ ) and backward ( $I_b$ ) components are shown.

Relatively high standard deviation of the peak current ratio is due to non-uniformity in deposition of microparticles onto the PIGE surface. In a repeated repeatability test performed with reaction mixture diluted with sepiolite (capsaicin/indigo/sepiolite = 1/1/1), the standard deviation of peak current ratio decreased to 3.4%. Accordingly, further experiments were performed using a mixture of test sample and indigo with sepiolite.

Representative SW voltammograms obtained for a mixture of Habanero orange with indigo and sepiolite spiked with increasing amounts of pure capsaicin, together with the resulting plot of  $[\Delta I_p(X)/\Delta I_p(R)]$  versus  $(m_X^*/m_R)$ , is shown in Fig. 2.

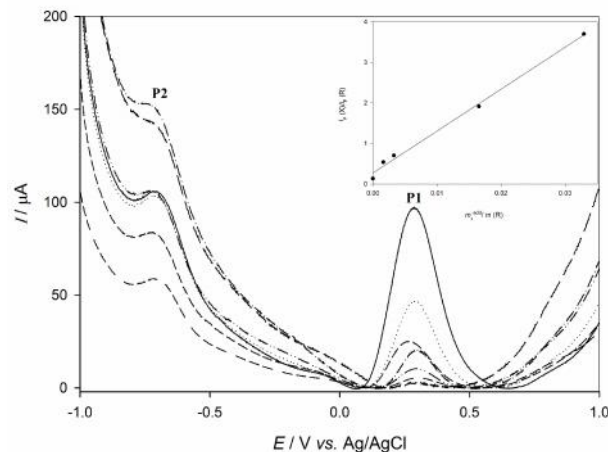


**Fig. 2.** SWV responses for different additions of standard compound in mixture of hot pepper Habanero orange recorded in 0.1 mol L<sup>-1</sup> KNO<sub>3</sub> (pH 11). Additions are as follows: without standard addition (—), 0.05 mg mg<sup>-1</sup> (· · ·), 0.07 mg mg<sup>-1</sup> (— · —), 0.1 mg mg<sup>-1</sup> (· · · ·), 0.3 mg mg<sup>-1</sup> (---), 0.5 mg mg<sup>-1</sup> (····) and 1 mg mg<sup>-1</sup> (— · — · —). The peak P2 can be attributed to indigo, and peak P1 to capsaicinoids. Insert graph in figure: resulting plot of  $[\Delta I_p(X)/\Delta I_p(R)]$  versus  $(m_X^*/m_R)$ .

The SWV response of this mixture is characterised by two anodic peaks, peak P2 at -0.687 V and peak P1 at +0.292 V, corresponding to oxidation of indigo and capsaicin, respectively. Similar voltammetric behaviour was observed for all pepper samples in mixture with indigo and sepiolite. A slight shift of net peak potentials for pepper samples towards more positive values as compared with the peak potential for pure capsaicin ( $E = +0.258$  V) is due to synergistic effects of all naturally occurring capsaicinoids in pepper samples (including dihydrocapsaicin and minor amounts of nordihydrocapsaicin, homocapsaicin, homodihydrocapsaicin, etc.), which have slightly different oxidation potentials. Accordingly, the intensity of peak P1 at +0.290 V is not associated exclusively with capsaicin but involves the record of all capsaicinoids (i.e. total capsaicinoids) in a particular sample. Moreover, in our previous study we have found a strong positive correlation between SWV current responses corresponding to capsaicinoids in pepper samples and the Scoville heat units reported in the literature indicating that SWV peak currents associated with oxidation of capsaicinoids are directly proportional to concentrations of capsaicinoids samples, i.e. the hot pepper's pungency.

**Table 1.** Data from calibration curves for different samples of chilli peppers obtained from SQWVs under the experimental conditions described in Fig. 1.

Chilli pepper	Slope	Origin ordinate	$m_X/m_{-100\%}$	SHU
Bhut jolokia <sup>a</sup>	116.95	0.8233	1.410	$1 \cdot 10^6$
Red savina <sup>b</sup>	124.22	0.3661	0.590	$4.2 \cdot 10^5$
Fatalli <sup>b</sup>	103.71	0.2832	0.546	$3.9 \cdot 10^5$
Habanero orange <sup>b</sup>	103.50	0.2708	0.523	$3.7 \cdot 10^5$
Carolina cayenne <sup>c</sup>	179.19	0.2423	0.270	$1.9 \cdot 10^5$

<sup>a</sup> Harissa; <sup>b</sup> Volim Ljuto; <sup>c</sup> Za ini Buši

Quantification of capsaicinoids in commercially available ground hot pepper samples was performed by means of standard addition method. Calibration curves were obtained for pepper + indigo + sepiolite mixtures with  $m_X^*/m_R$  ratios ranging from 0.0 to 0.03 mg/mg. Linear dependencies of  $[\Delta I_p(X)/\Delta I_p(R)]$  versus  $(m_X^*/m_R)$  were observed in all cases with correlation coefficients in the range from 0.972 to 0.999 (see insert in Fig. 2). The results obtained with SAM for capsaicinoids content in pepper samples are listed in Table 1. Concentrations of capsaicinoids were found in the range from 0.27% to 1.41%, which is in accordance with results obtained with other analytical techniques such as HPLC [18, 19]. If the concentration of capsaicinoids in Bhut jolokia is ascribed to the pungency level of  $1 \cdot 10^6$  SHU [20], the pungency of other peppers can be estimated from linear relationship between the concentration of capsaicinoids and the level of pungency [8,19]. These estimations are reported in the last column of Table 1. The values for Red savina and Fatalli are in agreement with the results from organoleptic method, but for the other two peppers the estimated levels are somewhat higher [20]. Deviations in results can be explained with different environmental conditions, technological processing of peppers in food industry and genetic factors. Environmental factors that could have impact on capsaicinoid content include water deficit [21], addition of mineral supplements [22] and nitrogen supply [23]. Furthermore, capsaicinoid content of peppers can also vary between different fruits within the same plant, even when harvested at the same time. Regarding the technological processing of peppers, drying, grinding and high temperatures

could all have great influence on the capsaicinoid content. They can be a negative factor on the stability of capsaicinoids in certain varieties of chili peppers, so processing could affect the total capsaicinoid content. Also, it is not negligible to mention that capsaicinoids are mostly synthesized and accumulated in the placenta of peppers so total capsaicinoid content in pepper powders can vary because it is not known which part of the dried pepper is dehydrated in technological process [24, 25].

#### Voltammetry of precipitate-modified electrodes

The SW voltammetric response of  $1 \text{ g L}^{-1}$  pure capsaicin precipitate recorded under optimal experimental conditions (aqueous electrolyte of pH 11,  $f = 150 \text{ Hz}$ ) is shown in Fig. 3. The net SW response consists of a single oxidative peak at  $E = +0.254 \text{ V}$ , similar to potential obtained for oxidation of capsaicin microparticles. The forward and backward components of the response indicate totally irreversible oxidation. These results are in accordance with the results for capsaicin microparticles (see Fig. 1A.). It can be concluded that both, capsaicin microparticles and precipitate, undergo the same oxidation mechanism.

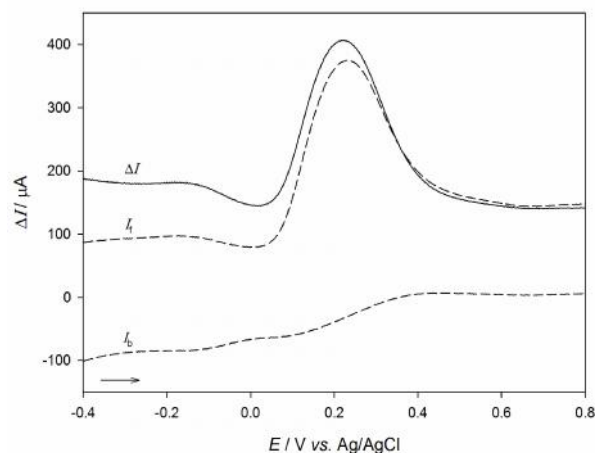


**Fig. 3.** Square-wave voltammograms corresponding to the oxidation of  $1 \text{ g L}^{-1}$  capsaicin precipitate immobilized at a paraffin impregnated graphite electrode (5 mm diameter) in homogeneous buffer solution, pH 11 containing  $0.1 \text{ M KNO}_3$ . The pulse amplitude is 50 mV and the step potential is 2 mV.

The SWV response of capsaicin precipitate attached on PIGE surface depends on the amount of capsaicin. Respective square-wave voltammograms recorded for different amounts of capsaicin attached on PIGE in the form of precipitate are shown in Fig 4. The net peak potential is linearly shifted in the positive direction by increasing the concentration of capsaicin precipitated on electrode surface (see insert plot of Fig. 4) i.e. higher energy is needed for electrooxidation.

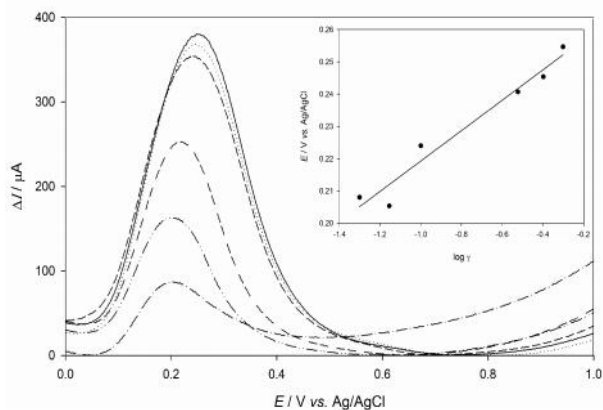


**Fig. 4.** SWV responses for different concentrations of capsaicin dissolved in ethanol, immobilized on electrode surface as a precipitate and recorded in 0.1 mol L<sup>-1</sup> KNO<sub>3</sub> (pH 11). Concentrations are as follows: 0.05 g L<sup>-1</sup> ( · · ), 0.07 g L<sup>-1</sup> ( · · · ), 0.1 g L<sup>-1</sup> ( — ), 0.3 g L<sup>-1</sup> ( — · — ), 0.4 g L<sup>-1</sup> ( — · · — ), 0.5 g L<sup>-1</sup> ( · · · · · ). Insert graph in figure: a plot of the potential against the logarithm of mass concentration of capsaicin.

This phenomenon could be explained on the basis of steric effects due to electroinactive hydrophobic parts of capsaicin molecule causing charge transfer hindrance. SWV current increases with increasing amount of capsaicin precipitated on electrode surface and the relationship between net peak current and concentration is linear with correlation coefficient  $r = 0.935$ . However, for the concentrations higher than 0.3 g L<sup>-1</sup> voltammetric response starts to decline which can be assigned to saturation of electrode surface, respectively the hydrocarbon chain blocks the electron transfer leading to significant decrease in peak current and to the shift of their potential toward more positive values.

SWV responses for different concentrations of pepper Habanero orange are shown in Fig. 5.

If mass concentration of Habanero orange is 16 g L<sup>-1</sup>, the voltammogram consists of a single irreversible oxidative peak at  $E = +0.271$  V which is in accordance with electrochemical behaviour of pure capsaicin. With decreasing of mass concentration of capsaicinoids in pepper extract, a slight shift of potential to more negative values was observed. All net peak currents increase linearly with increasing mass concentration. However, at concentrations above 8 g L<sup>-1</sup> net peak current reaches plateau due to saturation of electrode surface. Similar behaviour was observed for all tested hot pepper samples. These results suggests that net peak current could potentially be used for quantitative determination of capsaicinoids in real pepper samples.

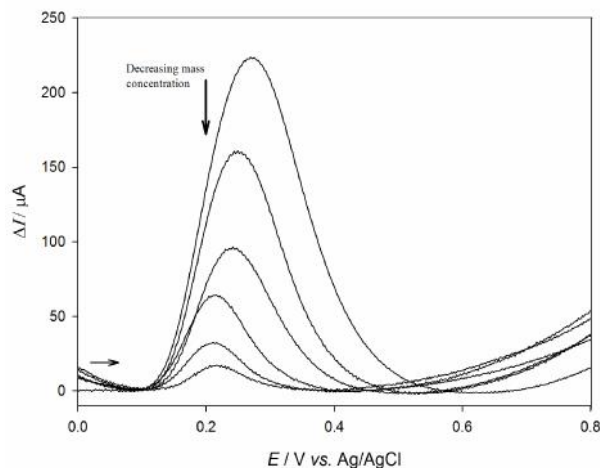


**Fig. 5.** Square-wave voltammograms ( $f = 150$  Hz) for the oxidation of different amounts of pepper Habanero orange deposited in form of precipitates onto a 5.0 mm diameter paraffin impregnated graphite electrode and immersed in an aqueous 0.1 M KNO<sub>3</sub> solution

Fig. 6 shows SW voltammetric responses recorded for precipitates of different pepper samples (16 g L<sup>-1</sup>). The highest signal intensity was observed for Bhut jolokia ( $\Delta I = 266.87$   $\mu$ A), followed by Habanero orange ( $\Delta I = 220.26$   $\mu$ A), Fatalli ( $\Delta I = 165.53$   $\mu$ A), Carolina cayenne ( $\Delta I = 129.96$   $\mu$ A) and Red savina ( $\Delta I = 118.30$   $\mu$ A). It should be emphasized that this trend between samples completely corresponds to that obtained for microparticles of real pepper samples [8].

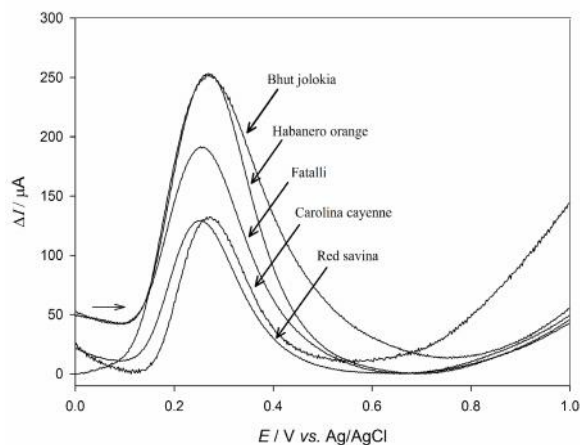


**Fig. 6.** Square-wave voltammograms ( $f = 150$  Hz) for the oxidation of different pepper samples deposited in form of dry precipitate onto a 5.0 mm diameter paraffin impregnated graphite electrode and immersed in an aqueous 0.1 M KNO<sub>3</sub> solution

## CONCLUSIONS

This work has investigated the possibility of application of standard addition method on methodology of voltammetry of immobilized microparticles for the quantification of total

capsaicinoid content in real pepper samples. Also, preliminary investigation was done in context of stripping voltammetry microprobe (SPV), relatively new approach in electrochemical measurements. In each case, we have seen that the results are similar but with some distinct differences between mentioned methodologies. In the first case, with SAM method we successfully quantified pepper samples classified as very highly pungent. Variations in the results can be explained with time and place of the harvest, the stage of maturation, technological process for preservation of dry hot peppers, commercial packaging etc.

Experiments with dry precipitates gave us insight into the electrochemical process that takes place in microsamples, i.e. microvolumes. We have seen that voltammetry is consistent with our previous work [8] with minor differences which can be explained with molecule configuration. Application of stripping voltammetry microprobe showed high sensitivity with microsampling, thus providing a potential for the future determination of low amounts of analytes. However, additional measurements should be performed for complete explanation of mentioned processes.

**Acknowledgements.** *The financial support by the Croatian Foundation in the frame of the project number IP-11-2013-2072 is gratefully acknowledged.*

#### REFERENCES

1. D. Giuffrida, P. Dugo, G. Torre, C. Bignardi, A. Cavazza, C. Corradini, G. Dugo, *Food Chem.*, **140**, 794 (2013).
2. K. Srinivasan, *Crit. Rev. Food Sci. Nutr.*, **56**, 1488 (2016).
3. W. Scoville, *J. Am. Pharm. Assoc.*, **1**, 453 (1912).
4. I. Perucka, W. Oleszek, *Food Chem.*, **71**, 287 (2000).
5. R. T. Kachoosangi, G. G. Wildgoose, R. G. Compton, *Analyst*, **133**, 888 (2008).
6. Y. Yardım, Z. entürk, *Talanta*, **112**, 11 (2013).
7. A. P. Ruas de Souza, M. Bertotti, C. W. Foster, C. E. Banks, *Electroanal.*, **27**, 2295 (2015).
8. I. Novak Jovanovi , L. ižmek, Š. Komorsky-Lovri , *Electrochim. Acta*, **208**, 273 (2016).
9. A. Doménech-Carbó, M. T. Doménech-Carbó, V. Costa, *Electrochemical Methods in Archaeometry, Conservation and Restoration*, Springer, Berlin, 2009.
10. Š. Komorsky-Lovri , V. Mir eski, F. Scholz, *Mikrochim. Acta*, **132**, 67 (1999).
11. Š. Komorsky-Lovri , B. Nigovi , *J. Pharm. Biomed. Anal.*, **36**, 81 (2004).
12. Š. Komorsky-Lovri , I. Novak, *Collect. Czech. Chem. Commun.*, **74**, 1467 (2009).
13. A. Doménech-Carbó, S. Sánchez-Ramos, D. J. Yusá-Marco, M. Moya-Moreno, J. V. Gimeno-Adelantado, F. Bosch-Reig, *Anal. Chim. Acta*, **501**, 103 (2004).
14. A. Doménech-Carbó, M. Moya-Moreno, M. T. Doménech-Carbó, *Anal. Bioanal. Chem.*, **380**, 146 (2004).
15. A. Doménech-Carbó, M. Martini, L. Machado de Carvalho, C. Viana, M. T. Doménech-Carbó, M. Silva, *J. Pharm. Biomed. Anal.*, **80**, 159 (2013).
16. M. A. Gulppi, N. Vejar, L. Tamayo, M. I. Azocar, C. Vera, C. Silva, J. H. Zagal, F. Scholz, M. A. Páez, *Electrochem. Commun.*, **41**, 8 (2014).
17. M. A. Gulppi, J. Pavez, J. H. Zagal, M. Sancy, M. Azocar, F. Scholz, M. A. Páez, *J. Electroanal. Chem.*, **745**, 61 (2015).
18. K. G. Sweat, J. Broatch, C. Borrer, K. Hagan, T. M. Cahill, *Food Chem.*, **210**, 606 (2016).
19. L. Orellana-Escobedo, L. E. Garcia-Amezquita, G. I. Olivias, J. J. Ornelas-Paz, D. R. Sepulveda, *J. Food*, **11**, 179 (2013).
20. [http://www.chillworld.com/FactFile/Scoville\\_Scale.asp](http://www.chillworld.com/FactFile/Scoville_Scale.asp)
21. N. Ruiz-Lau, F. Medina-Lara, Y. Minero-García, E. Zamudio-Moreno, A. Guzmán Antonio, I. Echevarría-Machado, M. Martínez-Estévez, *Hortsci.*, **46**, 487 (2011).
22. B. Estrada, F. Pomar, J. Díaz, F. Merino, M. A. Bernal, *J. Hortic. Sci. Biotechnol.*, **73**, 493 (1998).
23. M. Monforte-González, A. Guzmán-Antonio, F. Uuh-Chim, F. Vázquez-Flota, *J. Sci. Food Agric.*, **90**, 764 (2010).
24. A. González-Zamora, E. Sierra-Campos, J. G. Luna-Ortega, R. Pérez-Morales, J. C. Rodríguez Ortiz, J. L. García-Hernández, *Molecules*, **18**, 13471 (2013).
25. G. F. Barbero, A. G. Ruiz, A. Liazid, M. Palma, J. C. Vera, C. G. Barroso, *Food Chem.*, **153**, 200 (2014).

1\*, . 2, . - 1  
 1 " , 54, , 2, ,  
 2 11 2016 .; 22 2016 .  
 ( )  
 , (VIM).  
 (PIGE), 11, 50 mV, 150 Hz (SWV)  
 2 mV. : (SAM).  
 VIM, ( R = 0.976).  
 (SPV)  
 . SWV  
 VIM.  
 PIGE, .

## Montmorillonite as a catalytic support in water electrolysis

I. Boshnakova \*, E. Lefterova, E. Slavcheva

*Acad. Evgeni Budevski Institute of Electrochemistry and Energy Systems, Bulgarian Academy of Sciences, 10 Acad. G. Bonchev st, Sofia-1113, Bulgaria*

Received February 20, 2017      Revised March 14, 2017

The paper presents a research on the phyllosilicate mineral Montmorillonite (MMT) in regard to its properties as catalytic support for hydrogen generation via electrochemical water splitting. MMT is loaded with noble metal nanoparticles (Ir) having well proven high catalytic activity toward the oxygen evolution reaction (OER). The metal is deposited by the well-established sol gel technique. The catalytic loading is varied in the range 10-30 wt. %. The obtained montmorillonite-supported catalysts (Ir/MMT) are studied using X-ray diffraction (XRD), scanning electron microscopy (SEM), and energy dispersion X-ray (EDX) analysis. Their electrochemical performance and OER catalytic efficiency are investigated by cyclic voltammetry and quasi steady state polarization curves in aqueous acid solution. The performed morphological and electrochemical investigations showed that the Ir/MMT catalysts under study possess superior performance in regard to both activity and durability compared to the previously studied iridium catalysts supported on commercial electrically conductive ceramic support Magnelli phase titania.

**Key words:** hydrogen technologies, water electrolysis, oxygen evolution reaction, electrocatalysts, non-carbon catalytic supports.

### INTRODUCTION

The electrochemical water splitting is a viable method for production of clean hydrogen. The classical alkaline water electrolysis is still the most commonly used production technology for this purpose. In the last decades an intensive research has been carried out on development of acidic polymer electrolyte membrane water electrolysis cells (PEMEC). This new and environmentally friendly method has some advantages over the classical alkaline electrolysis, primarily in regard to the process intensity, efficiency, purity of the generated gases, and compatibility with the renewable energy sources [1-3]. PEMEC is considered as one of the key technologies that can be powered by renewable energy sources and used for the large scale production of clean hydrogen [4]. The partial hydrogen (HER) and oxygen (OER) evolution reactions are of special importance in both fundamental and applied electrochemistry. The OER is fundamentally less studied, as it is much more complex. The efficient oxidation of water is greatly hindered by the OER, which proceeds as a multistep proton-coupled electron transfer process [5]. It is the most critical step severely limiting the overall efficiency of the water splitting due to the intrinsically slow kinetics

requiring considerable overpotential to achieve rational process rate [3, 4]. The rate and mechanism of OER depend strongly on the chemical nature, surface structure, and morphology of the used electrocatalysts, as well as on the process operative conditions (type of the electrolyte, temperature, etc.). The proper combination of these factors is essential to lower the energy barrier and enhance the energy conversion rate.

The major drawback of the PEMEC is the fact that the required electrocatalysts are predominately based on the platinum group metals, their alloys and/or oxides. In 1966 Damjanov et al. studied the kinetics of the OER on Rh, Ir, and Pt-Rh alloys using a liquid electrolyte, showing the increase of activities in the following order: Pt < Pt-Rh < Rh < Ir [6, 7]. Later on, it was proven that iridium (IrO<sub>2</sub>) and ruthenium (RuO<sub>2</sub>) oxides are the most representative and effective OER electrocatalysts [8-10]. However, the large-scale application of these catalysts is strongly hindered by their low abundance and the associated high cost.

The usual approach to decrease the cost of the catalysis and thus, the capital expense of PEMEC, is to deposit the noble metal particles on catalytic support with highly developed surface. The most broadly used catalytic supports are various carbon materials (carbon blacks, nanotubes, nanorods, etc.). OER at the anode takes place at relatively high potentials (1.5–1.8V vs. RHE) which in combination with the intensive gassing, high humidity and elevated temperatures creates critical operative conditions, prohibiting the use of carbon-

---

To whom all correspondence should be sent:  
E-mail: boshnakova.iveta@iees.bas.bg

based materials as catalyst support, since the carbon is oxidized at potential of +0.206 V vs. RHE [11, 12] according the reaction:  $C + 2H_2O \rightarrow CO_2 + 4H^+ + 4e^-$

For this reason, to achieve not only high OER activity but also cost efficiency and durability the IrO<sub>2</sub> particles should be supported on electroconductive material with much higher corrosion stability (titanium nitride, tantalum carbide, doped or reduced forms of titanium, tin oxide etc.). Another approach is to synthesize complex catalytic compositions mixing IrO<sub>2</sub> with inexpensive and electrochemically inert materials such as TiO<sub>2</sub>, SnO<sub>2</sub>, Ta<sub>2</sub>O etc. catalyst layer in order to form Ir-based mixed oxides. In the last decade, a great number of papers using the former approach have been published [13-20]. However, along with the nonsufficient stability of most of those new supports at long term service in oxidizing environment [21], the reported noble metal loadings remained quite high, most often in the range 1.5-5.0 mg cm<sup>-2</sup> [4, 22].

The aim of this work is to explore one natural mineral (Montmorillonite, MMT) as catalytic support and to assess the efficiency of the composite MMT-supported IrO<sub>2</sub> toward OER in acidic electrochemical water splitting. MMT is a phyllosilicate layered clay with 2:1 type sheet structure, high cation exchange capacity, high surface area and low cost [23]. Chemically, it is a complex mixture of hydrated phyllosilicates, having rather complex general chemical formula:  $(Na,Ca)_{0.33}(Al,Mg)_2(Si_4O_{10})(OH)_2 \cdot nH_2O$ .

Clay minerals in general, are layered porous materials which can "trap" significant amount of different fluids (air, water, saline water, etc.) in the pores or/and in the interlayer space. The electrical conductivity of the clay depends on both the type of the fluid and the chemical nature of the matrix. It is attributed to exchange of cations or proton transfer between the dissociated interlayer water and the matrix. The small particle size of the clay minerals (1-2 μm in diameter) results in significantly high surface area per unit volume, where a large number of cations can be adsorbed, thus leading to significant level of electrical conductivity [24].

According to our knowledge, up to now Montmorillonite has not been investigated as catalytic support in water electrolysis.

## EXPERIMENTAL

The catalysts under study are synthesized by sol-gel method from Ir-acetylacetonate  $(Ir((C_5H_7O_2)_n)_m$  precursor, Ir-acac, following the next procedure: (i) pretreatment of the support and the precursor in iso-

propanol using magnetic stirrer and ultrasonic bath, their mixing and heating at temperature 60 °C until a fine gel is obtained; (ii) thermal treatment at temperature 240 °C for 4 h in H<sub>2</sub> gaseous atmosphere.

Five different test samples with iridium loadings of 10, 15, 20, 25, and 30 wt.% Ir supported on MMT are prepared and investigated.

Their structural and phase composition are examined by X-ray diffraction (XRD). The diffraction data are collected using X-ray diffractometer Philips ADP15 with Cu-K radiation ( $\lambda = 1.54178 \text{ \AA}$ ) at a constant rate of 0.02° s<sup>-1</sup> over an angle range  $2\theta = 4^\circ \div 80^\circ$ .

SEM and EDX analysis are obtained using JEOL JSM 6390 electron microscope (images in secondary and back-scattered electrons), equipped with INCA Oxford elemental detector.

The electrochemical performance and catalytic efficiency are studied by cyclovoltammetry and chronoamperometry (potentiodynamic and potentiostatic polarization) methods using a commercial Galvanostat/ Potentiosat POS 2 (Bank Elektronik, Germany). The cyclic voltammograms (CV) are recorded in the "water window" potential range (between the hydrogen and oxygen evolution potentials) at scan rate of 100 mV s<sup>-1</sup>. The quasi steady state polarization tests are carried out in potentiodynamic mode with scan rate of 1 mV s<sup>-1</sup>. To investigate the stability of the catalysts performance with time, chronoamperometric tests at constant potential of 1.8 V are performed.

All electrochemical tests are performed in 0.5 M H<sub>2</sub>SO<sub>4</sub> at room temperature in a conventional 3-electrode electrochemical cell. Pt wire is used as counter electrode and Ag/AgCl as reference electrode. The working area of the test electrode is 0.5 cm<sup>2</sup> and all test samples contain 0.5 mg<sub>Ir</sub>·cm<sup>-2</sup>.

## RESULTS AND DISCUSSION

The XRD patterns of the synthesized Montmorillonite supported catalysts are presented in Fig. 1 together with those of the pure support (MMT clay) and the Ir-acac precursor according Inorganic Crystal Structure Database, ICSD (PDF#23-1711). The phase identification shows presence of MMT and non-destructed Ir-acac in all test samples. Ir or IrO<sub>2</sub> are not registered which does not exclude their presence in amorphous state.

The inset in the Fig. 1 is a zoomed image of XRD patterns in the 5-10° 2θ range. It shows a shift of the (001) diffraction peak corresponding to basal d<sub>(001)</sub> spacing of the catalyzed MMT samples. The shift to lower 2θ angles after deposition of iridium indicates an increase in the interlayer distance



compared to that in the unloaded MMT. In the literature such an increase has been prescribed to intercalation of metal cations (in our case  $\text{Ir}^{+}$  and/or Ir-organometallic cations) into the clay structure [25, 26].

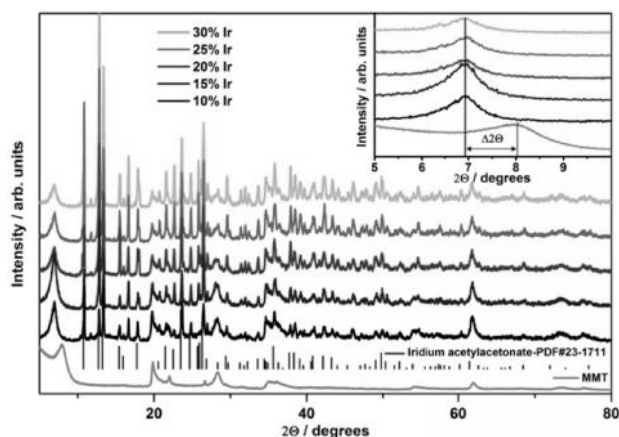


**Fig. 1.** XRD patterns of the synthesized catalysts, pure MMT and Ir-acac.

The synthesized Ir/MMT catalysts with target content of Ir in the range 5 to 30 wt.% are studied by EDX analysis to determine their exact noble metal content. The results obtained (Table 1) demonstrate high efficiency of the applied method of synthesis which ensures close to 100% utilization of the metal precursor. In the same table are shown experimental data from the performed electrochemical tests.

**Table 1.** Iridium content in the test samples determined by EDX analysis and kinetic data assessing their catalytic activity.

Sample	Ir wt. %	OER		
		$E=1.7\text{V}$		Tafel Slopes $mV.dec^{-1}$
	target	obtained	$j/mA.cm^{-2}$	
Ir 10	10	9.85	10.32	180
Ir 15	15	15.03	15.02	200
Ir 20	20	18.84	26.27	160
Ir 25	25	24.96	20.07	170
Ir 30	30	28.73	23.10	170

The morphology of the synthesized catalysts was studied by scanning electron microscopy (SEM). The microscopic images (Figure 2) show highly developed surface and porous structure of the individual clusters (agglomerates), which is an important prerequisite for achieving high utilization of the catalyst.

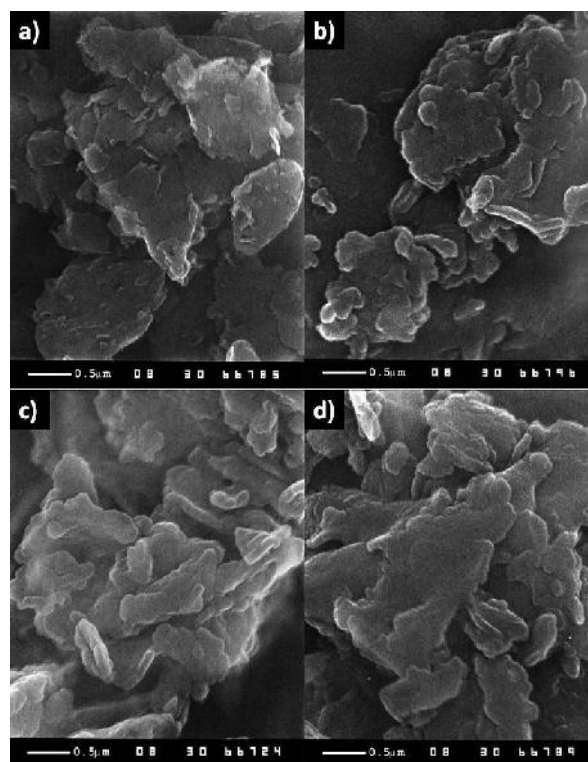


**Fig. 2.** SEM image of a) pure MMT, b) Ir10/MMT, c) Ir25/MMT and d) Ir30/MMT.

#### Electrochemical measurements

In Fig. 3 are shown the obtained cyclic voltammograms of five test electrodes with equal iridium loading ( $0.5\text{mg.cm}^{-2}$ ) and different Ir/MM ratio. The CV curves are recorded in the potential range between  $-0.45$  and  $1.45$  V vs. Ag/AgCl reference electrode at scan rate of  $100\text{ mV s}^{-1}$ .

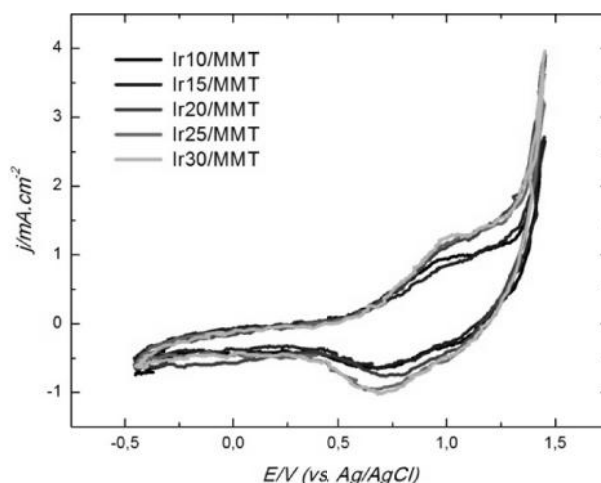
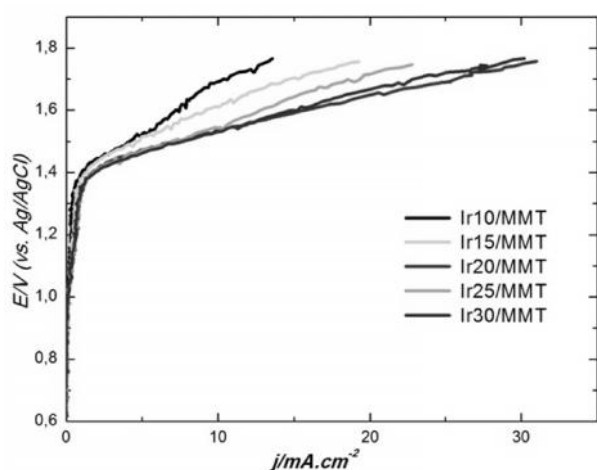


**Fig. 3.** Cyclic voltammograms of Ir/MMT catalysts in  $0.5\text{M H}_2\text{SO}_4$  at room temperature; potential scan rate  $100\text{ mV s}^{-1}$ .

The reversible current peaks typical for transformation of iridium oxidation state in acid media ( $\text{Ir}/\text{Ir}^{2+}$ ,  $\text{Ir}^{2+}/\text{Ir}^{3+}$  and  $\text{Ir}^{3+}/\text{Ir}^{4+}$ ) are well depicted. The peaks on the voltammograms of the

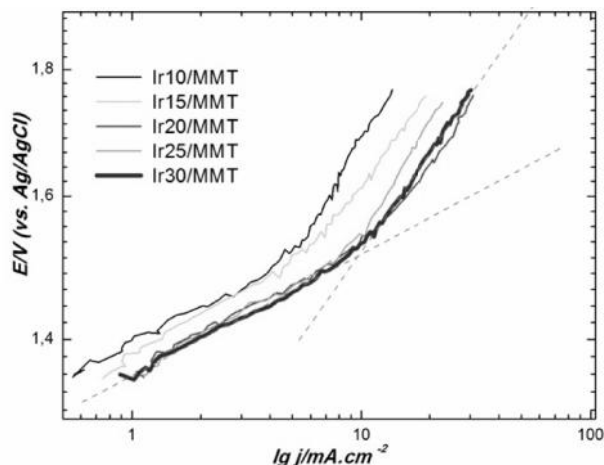
samples Ir20/MMT, Ir25/MMT and Ir30/MMT are visibly broader than those of the electrodes prepared from samples with lower Ir/MMT ratio, indicating higher active surface of these electrodes.

Fig. 4 presents the partial electrode reaction of oxygen evolution for the same electrodes. All polarization curves demonstrate intensive oxygen evolution at potentials above 1.5 V. The reaction proceeds with highest rate on the electrode with Ir20/MMT. The obtained current densities on Ir30/MMT and Ir25/MMT slightly lower, while on Ir10/MMT and Ir15/MMT the oxygen evolution proceeds much slower.



**Fig. 4.** Anodic polarization curves of the Ir/MMT in 0.5M  $\text{H}_2\text{SO}_4$  at room temperature; potential scan rate  $1 \text{ mV s}^{-1}$ .

In order to obtain some data on the electrochemical kinetics and the mechanism of OER in Fig. 5 are presented the semi-logarithmically plotted current–potential curves (Tafel plots). The calculated values of the Tafel plots and the achieved current densities at 1.7 V are summarized in Table 1. They confirm the best efficiency (highest current density) combined with lower Tafel constant  $b$  of the catalyst Ir20/MMT.



**Fig. 5.** ORR Tafel plots of the Ir/MMT in 0.5M  $\text{H}_2\text{SO}_4$  at room temperature; scan rate  $1 \text{ mV.s}^{-1}$ .

Finally, to evaluate the stability of the Ir20/MMT catalytic performance at long service, potentiostatic polarisation tests (chronoamperometry) are carried out at constant potential of 1.8 V where an intensive oxygen evolution takes place. Fig. 6 presents the results obtained in 30-hour experiment. It is seen that after initial slight decrease of the measured current density, the reaction rate stabilizes around  $20 \text{ mA cm}^{-2}$  and does not change for the whole duration of the experiment, indicating both efficiency and durability of the catalyst performance.

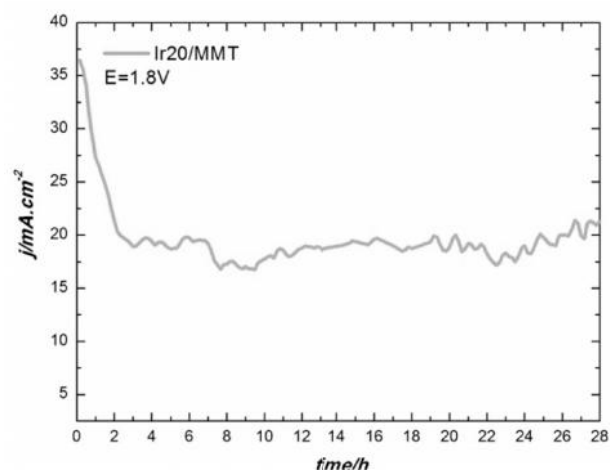


**Fig. 6.** Potentiostatic polarization curves of Ir/MMT in 0.5 M  $\text{H}_2\text{SO}_4$ , at room temperature;  $E=1.8 \text{ V}$ .

In our previous study it was shown that Ir deposited on different commercial ceramic supports also increase essentially the OER. The best efficiency was obtained for Ir supported on Magnelli phase titania (MPT) - a nonstoichiometric mixture of titanium oxides with common formula  $\text{Ti}_n\text{O}_{2n-1}$  that possesses excellent electrical conductivity combined with high corrosion resistance both in acidic and in alkaline media. The research performed with two different commercial products of Magnelli phase titania (Ebonex, Atraverda, UK and MPT, Ti-dynamics, China) proved that the Ebonex-supported iridium has better catalytic efficiency toward oxygen evolution reaction, comparable to the best data published in the literature [27]. It demonstrated enhanced stability during accelerated tests however, the utilization was not satisfactory due to the low surface area of the substrate. The MPT-supported iridium showed even higher efficiency but lower stability at long tests.

In order to evaluate the properties of the herein studied novel catalytic support MMT, in Fig.7 are compared cyclic voltammograms and polarization curves of identical electrodes containing equal loadings of iridium deposited on Ebonex, MPT and MMT, respectively. The results indicate highest

active surface (broadest CV) combined with superior efficiency and stability of the catalyst supported on montmorillonite (Ir/MMT).

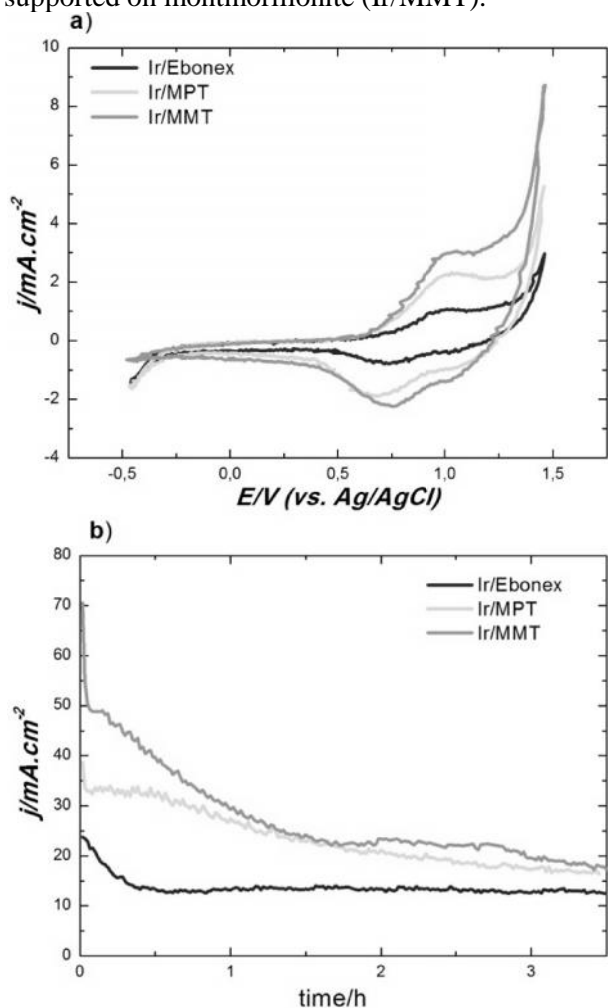


**Fig. 7.** Cyclic voltammograms, scan rate  $100 \text{ mV}\cdot\text{s}^{-1}$  (a) and potentiostatic polarization curves,  $E = 1.8 \text{ V}$  (b) of Ir/Ebonex, Ir/MPT, and Ir/MMT in  $0.5 \text{ M H}_2\text{SO}_4$  at room temperature.

Fig. 8 presents the SEM images of the studied supports. The Ebonex has the largest particles size with smooth surface. The small MPT particles size (100–200 nm) and the rough surface of the MMT particles ensure a higher specific surface area compared to Ebonex and it is a precondition for higher electrochemical activity of the catalysts on MMT and MPT supports.

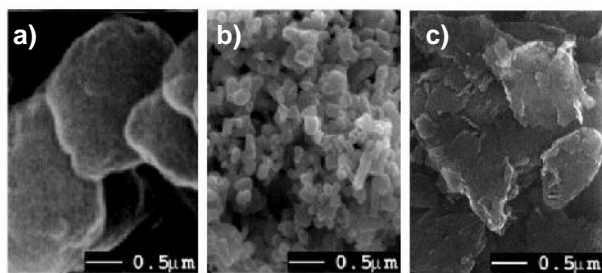


**Fig. 8.** SEM image of a) Ebonex, b) MPT and c) MMT.

In addition, the XRD analysis showed chemical interaction between iridium and the MMT substrate, resulting in structural changes of the clay, namely an increase in the basal spacing between parallel layers. These two effects (the cation intercalation and the increase of surface area) explain the superior catalytic efficiency of the Ir/MMT catalyst.

## CONCLUSIONS

The work demonstrates that the investigated phyllosilicate mineral montmorillonite (MMT) is a promising alternative of the conventional carbon materials for application as anode catalyst support for hydrogen generation via electrochemical water splitting. Ir/MMT showed superior performance in regard to both activity and stability compared to Magnelli phase titania supports (Ebonex, Atraverda and MPT, Ti-Dynamics). The specific morphology and layered structure of the MMT influence the efficiency of the electrode reaction ensuring much higher current densities at equal catalytic loading. The registered Ir intercalation into MMT crystal structure contributes significantly to the catalytic efficiency.

Further research focused on the catalyst-support electronic and/or interionic interactions and their effect on activity is in progress.

**Acknowledgements:** This research has been financially supported by the Bulgarian Academy of Sciences, via " Program for career development of young scientists ", contract: # DFNP-41 /21.04.2016.

## REFERENCES

1. S. Grigorie, V. Porembsky, V. Fateev, *Int. J. Hydrogen Energy*, **31**, 171 (2006).
2. P. Lu, S. Srinivasan, *J Appl Electrochem*, **9**, 269 (1979).
3. J. Polonsky, I. Petrushina, E. Christensen, K. Bouzek, C. B. Prag, J. Andersen, *Int. J. Hydrogen Energy*, **37**, 2173 (2012).
4. C. Rozain, E. Mayousse, N. Guillet, P. Millet, *Appl. Catal. B: Environ*, **182**, 153 (2016).
5. S. Cherevko, S. Geiger, O. Kasian, N. Kulyk, J. Grote, A. Savan, B. Shrestha, S. Merzlikin, B. Breitbach, A. Ludwig, K. Mayrhofer, *Catal. Today*, **262**, 170 (2016).
6. A. Damjanov, A. Dey, J. M Bockris, *J. Electrochem. Soc.*, **113**, 739 (1966)
7. M. Carmo, L. David, *Int. J. Hydrogen Energy*, **38**, 4901 (2013)
8. E. Slavcheva, Magnetron sputtered iridium oxide as anode catalyst for PEM hydrogen generation, *Macedonian Journal of Chemistry and Chemical Engineering*, **30**, 45, (2011).

9. E. Slavcheva, I. Radev, S. Bliznakov, G. Topalov, P. Andreev, E. Budevski, Sputtered iridium oxide films as electrocatalysts for water splitting via PEM electrolysis, *Electrochimica Acta*, **52**, 3889 (2007).
10. P. Paunovic, D. Gogovska, O. Popovski, A. Stoyanova, E. Slavcheva, E. Lefterova, P. Iliev, A. Dimitrov, Preparation and characterization of Co-Ru/TiO<sub>2</sub>/MWCNTs electrocatalysts in PEM hydrogen electrolyzer, *International Journal of Hydrogen Energy*, **36**, 9405 (2011).
11. A. J. Bard, R. Parsons, J. Jordan, *Monographs in Electroanalytical Chemistry and Electrochemist*, Taylor & Francis Inc., New York United States, (1985), ISBN10 0824772911.
12. P. Ross, H. Sokol, *J. Electrochem. Soc.*, **131**, 1742 (1984).
13. L. Ma, S. Sui, Y. Zhai, *Int. J. Hydrogen Energy*, **34**, 678 (2009).
14. J. Polonsky, P. Mazur, M. Paidar, E. Christensen, K. Bouzek, *Int. J. Hydrogen Energy*, **39**, 3072 (2014).
15. S. Siracusano, V. Baglio, C. D'Urso, S. Arico, *Electrochim. Acta.*, **54**, 6292 (2009).
16. A. Stoyanova, G. Borisov, E. Lefterova, E. Slavcheva, *Int. J. Hydrogen Energy*, **37**, 16515 (2012).
17. P. Mazur, J. Polonsky, M. Paidar, K. Bouzek, *Int. J. Hydrogen Energy*, **37**, 12081 (2012).
18. E. Mayousse, F. Maillard, F. Fouda-Onana, O. Sicardy, N. Guillet, *Int. J. Hydrogen Energy*, **36**, 10474 (2011).
19. J. Xu, G. Liu, J. Li, X. Wang, *Electrochim. Acta*, **59**, 105 (2012).
20. S. Marshall, M. Sunde, *Int. J. Hydrogen Energy*, **32**, 2320 (2007).
21. A. Gusev, E.G. Avvakumov, A. Medvedev, A. Masliy, *Sci. Sinter.* **39**, 51(2007).
22. J. Jiang, C. Zhang, L. Ai, *Electrochim. Acta*, **208**, 17 (2016).
23. B. Jiang, B. Dou, K. Wang, C. Zhang, Y. Song, H. Chen, Y. Xu, *Chem. Eng. J.*, **298**, 96 (2016).
24. F. Uddin, *Metall. Mater. Trans. A*, **39A**, 2804 (2008).
25. Yan Li, Xiaojun Wang, Juanfang Wang, Cation exchange, interlayer spacing, and thermal analysis of Na/Ca-montmorillonite modified with alkaline and alkaline earth metal ions, *J Therm Anal Calorim* **110**, 1199 (2012).
26. Y. Fukushima, S. Inagaki, Synthesis of an Intercalated Compound of Montmorillonite and 6-Polyamide, *Journal of Inclusion Phenomena*, **5**, 473 (1987).
27. E. Slavcheva, G. Borisov, E. Lefterova, E. Petkucheva, I. Boshnakova, Ebonex Supported Iridium as Anode Catalyst for PEM Water Electrolysis, *International Journal of Hydrogen Energy*, **40** 11356 (2015).

... , E. ...  
 ... ”, ...  
 ... .10, 1113,  
 20 2017 .; 14 2017 .  
 ( )  
 - ( T)  
 /  
 (Na,Ca)<sub>0.33</sub> (Al,  
 Mg)<sub>2</sub>(Si<sub>4</sub>O<sub>10</sub>)(OH)<sub>2</sub>.nH<sub>2</sub>O  
 / Ir Ir-  
 Ir/  
 (SEM), (XRD) (EDX).  
 (OER) 0.5  
 H<sub>2</sub>SO<sub>4</sub>  
 Ir Ir/MMT -

## Hydrogen sorption and electrochemical properties of Ti-Fe based alloys synthesized by mechanical alloying

B. Abrashev<sup>1\*</sup>, T. Spassov<sup>2</sup>, M. Pandev<sup>1</sup>, S. Vassilev<sup>1</sup>, A. Popov<sup>1</sup>

<sup>1</sup>Acad. Evgeni Budevski Institute of Electrochemistry and Energy Systems, Bulgarian Academy of Sciences, 10, Acad. G. Bonchev St., Sofia 1113, Bulgaria

<sup>2</sup>Faculty of Chemistry and Pharmacy, University of Sofia "St. Kl. Ohridski", 1 James Bourchier str. 1164 Sofia, Bulgaria

Received March 6, 2017      Revised April 4, 2017

The composite nanocrystalline-amorphous TiFe alloys were obtained mechano-chemically by high-energy ball milling in a planetary type mill. The duration of milling was varied with the aim to produce alloys with defined microstructure. The average size of the powders was reduced from 50 μm to <1 μm after 30-40 hours of grinding. The end product of milling consists mainly of nanocrystalline fcc Ti-Fe with CsCl-type structure. Presence of nanocrystalline Fe was also detected. The synthesised composite material showed relatively high thermal stability. The electrochemical hydrogen charge-discharge behaviour of materials with different microstructure was investigated. It was found out that small microstructural changes result in significant discharge capacity and cycling stability differences. The material milled for 40 hours revealed discharge capacity comparable to that of alloy milled for 30 hours, but its stability was greatly improved.

**Key words:** TiFe alloys, discharge capacity, hydrogen storage.

### INTRODUCTION

Hydrogen has attracted a great deal of consideration in the recent years as a feasibly ideal energy carrier. Its application for mobility and portable electronics is to a large extent limited by the difficulty of achieving a capable storage method. AB, AB<sub>2</sub>, AB<sub>5</sub> and A<sub>2</sub>B-type hydrogen storage compounds and related substituted multi-component alloys have been extensively studied in the last 3-4 decades. As a result, the electrodes prepared from AB<sub>5</sub> (LaNi<sub>5</sub>)- and AB<sub>2</sub> (ZrV<sub>2</sub>)-type alloys have already been commercialised in the rechargeable nickel-metal hydride (Ni/MH) batteries. In general, the titanium-based alloys are among the most promising materials for hydrogen storage. The main representative of AB alloys is an intermetallic compound with TiFe composition, which crystallizes in the cubic CsCl-type structure and is lighter and cheaper than the LaNi<sub>5</sub> alloy [1-6]. AB-type alloys require a preliminary activation treatment, being a disadvantage of the TiFe-based alloys. The activation procedure involves heating of TiFe to a high temperature (about 450°C) in vacuum and annealing in H<sub>2</sub> atmosphere at certain pressure (about 7 bar) [7-14]. The AB-type of alloys can be synthesized by using different

laboratory methods. The most commonly used ones are: arc melting and mechano-chemical synthesis. The method of mechanical alloying (MA) by using high-energy ball milling in a planetary mill verified itself to be an effective technique for both synthesis and modification of the intermetallic hydrogen storage compounds [15]. The application of mechanical alloying under inert atmosphere with the use of catalytic elements, as for instance Pd, rapidly improved the activation process and the hydriding kinetics of TiFe. By ball milling under Ar (20-30 hours) of TiFe with small amounts of Ni, easy hydrogen absorption without activation is achieved. The radical improvement of the kinetics is caused by the formation of a fine powder of TiFe covered by nanocrystalline Ni particles, acting as catalytic centres for the decomposition of H<sub>2</sub> molecules [4]. A lot of effort has been devoted to the studying of the kinetics of metal hydrides [16-25]. Currently, the nickel-metal hydride (Ni/MH) battery systems are perceived as one of the most promising for mobility applications. The advantages of the system relate to high energy density, high rate capacity, good overcharge and overdischarge capability, no electrolyte consumption during charge/discharge cycling and lack of poisonous heavy metals [26-32]. Generally speaking, the rechargeable nickel-metal hydride battery has a similar design to that of nickel-cadmium system (Ni/Cd) but with the principal difference that the Ni/MH uses hydrogen absorbed

---

To whom all correspondence should be sent:  
E-mail: babrashev@iees.bas.bg

in a metal alloy for the active negative material in place of cadmium in the Ni/Cd battery design. The active material of the positive electrode of the Ni/MH battery is nickel oxy-hydroxide (NiOOH) in the charged state. The negative active material in the charged state is hydrogen: in the form of a metal hydride. The high-energy density, excellent power density, and long cycle life of Ni/MH batteries make them a leading technology as the battery power source [33]. The aim of the present research is to study the influence of the microstructure on the electrochemical behaviour of the as prepared alloys.

## EXPERIMENTAL

In order to produce TiFe alloys, powders of Fe (99.5%) and Ti (99.7%) in suitable stoichiometric amounts were mixed together in the vial of a high-energy Fritsch planetary equipment (Pulverisette 5). A mass ratio of 10:1 of ball to powder was used. The milling process was executed under a protective argon atmosphere and liquid n-heptane for process control agent. Five different milling times (10, 15, 20, 30 and 40 h) were applied so as to produce powders with different morphology and microstructure.

The mechanically alloyed powders obtained after milling of 10, 15, 20, 30 and 40 hours were microstructurally characterized by X-ray diffraction (XRD) using Philips-APD 15 powder diffractometer with Cu-K $\alpha$  radiation, scanning electron microscopy (SEM, JEOL-5510), differential thermal analysis (DTA – Perkin Elmer), differential scanning calorimetry (Perkin-Elmer DSC 7) and a three-channel software controlled galvanostatic setup (developed in IIES-BAS). The milled powders were used to prepare metal-hydride electrodes by mixing 100 mg alloy with 30 mg Teflonized carbon black (VULKAN 72 with 10 wt% PTFE). Then, 1000 kg cm $^{-2}$  of pressure was applied on the mixture placed on the nickel mesh. The electrode was charged and discharged galvanostatically in a three- electrode cell in 30 wt % water solution of KOH at room temperature. The reference electrode was Hg/HgO and the counter electrode was a high-surface nickel foam sheet. The charge and discharge current density was 100 mA g $^{-1}$  and 20 mA g $^{-1}$ , respectively.

## RESULTS AND DISCUSSION

Five TiFe alloys were obtained by mechanical alloying method (MA) with differing milling duration times (10, 15, 20, 30 and 40 h). The X-ray diffraction patterns of the milled alloys are presented in Fig. 1. Milling for 10 hours leads only

to reduction in the iron and titanium grain size. The average grain size, calculated by the Scherrer equation, for Fe and Ti is 35 nm and 55 nm, respectively. With increased milling time the diffraction peaks of Fe and Ti additionally broaden and partially overlap. That is an indication of a solid-state reaction resulting in the formation of TiFe. The powder milled for 15 hours contains about 25 wt% highly disordered TiFe phase. Milling for 20 hours leads to a substantial increase in the amount of TiFe (~80 wt.%) which has a nanocrystalline microstructure with dimensions of 3–4 nm. During further milling of up to 30 hours we observe that the quantity of TiFe did not change noticeably, although the TiFe nanocrystals become slightly larger – with dimensions of 4–5 nm. When the milling time is increased up to 40 hours we observe an additional widening of the diffraction peaks and an increase of the size of TiFe nanocrystalline up to 5–6nm. The diffraction peak of nanocrystalline Fe is present in all milling times, which probably means that Ti dissolves into TiFe. This is confirmed by the shift of the TiFe main diffraction peak ( $2\theta = 43$ ) to smaller angle (see Fig. 1). The average size of the powders was reduced from 50 $\mu$ m to <1 $\mu$ m after 30–40 hours of grinding. The end product of milling consists mainly of nanocrystalline fcc TiFe with CsCl-type structure. Presence of nanocrystalline Fe was also detected.

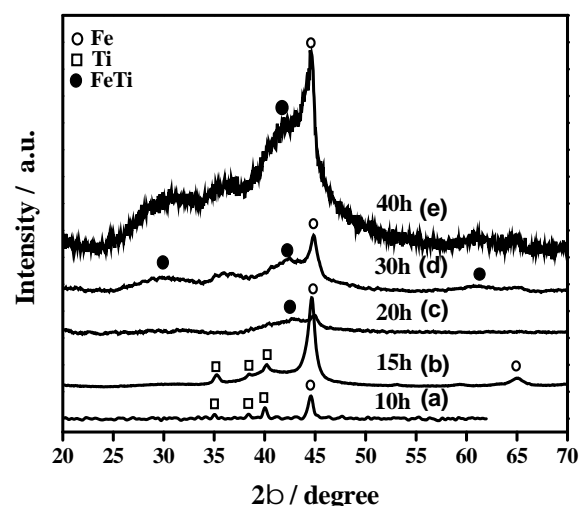


**Fig.1.** X-ray patterns of the TiFe powders milled for different times.

To study the thermal behaviour of the ball-milled alloys a DTA analysis of the as-milled (20 h and 30 h milled) alloys was carried out (Fig. 2). Several exothermic peaks in the range 350–550°C are clearly observed. That is probably a result from processes of crystallisation of amorphous (disordered) phase and/or with growth of existing nanocrystals formed during the mechano-chemical

treatment. The observed processes are in correspondence with the ones previously obtained by Zaluski et al. [34-35]. A high possibility is present that a solid-state reaction resulting in TiFe formation during the annealing of the ball milled material. In the present investigation the enthalpy state deviations related to the exothermic reactions, detected by DTA, are substantially larger for the alloy milled for 30 h in comparison to that milled for 20 h (see Fig. 2). That demonstrates significant differences in the amount of the amorphous (disordered) phase in both alloys. The exothermic effects obtained for the sample milled for 15 h are substantially smaller than those of the 20 and 30 h milled samples. Thus, they are much more difficult to detect via DTA, giving incentives that the amount of the amorphous phase in the samples milled for 10 h and 15 h is negligibly small. In order to analyse thoroughly the origin of the observed exothermic reactions, a XRD analysis of samples annealed after each of the thermal effects has to be carried out. A detailed study on the possibility for producing TiFe alloys with defined microstructures by combining the processes of ball milling with subsequent annealing is in underway.

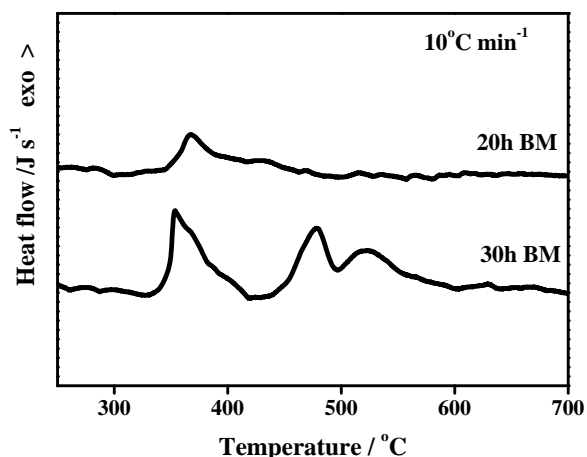


Fig. 2. DTA analysis of as-milled alloys.

For investigation of the hydrogen-sorption properties of the synthesised TiFe alloys from the gas phase a differential scanning calorimetry (High-pressure DSC) under hydrogen pressure was used. That method allows the registration of the processes of hydrogen absorption and desorption in the investigated materials, as well as the determining of the temperature intervals at which the reactions occur. A thermogram of the base TiFe alloy (30 h BM) is shown on Fig. 3 in which it is observed that at 25 atm of hydrogen pressure there is a clearly pronounced low-temperature absorption process in the temperature range of 120-220 and a second absorption process at around 300. The obtained high-temperature exothermic peak is related to the

formation of the hydride phase (TiHx) during interaction with the present in the alloy unbound titanium with hydrogen. For the period of several cycles (absorption / desorption) the exothermic effects resulting from the absorption of hydrogen from the alloy decrease due to partial oxidation of the alloys during the calorimetric analysis.

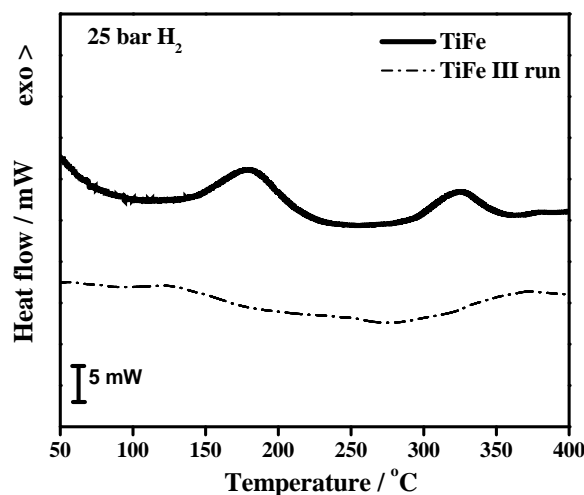


Fig. 3. DSC of 30h milled TiFe alloy.

In Fig. 4 a thermogram at 0.1 bar H<sub>2</sub> of the initially hydrated TiFe alloy is presented. A large and endothermic peak is observed in the temperature range of 150-350 caused by the desorption of the dissolved hydrogen in the fcc TiFe phase. The clearly expressed peak at around 280 corresponds to the decomposition of the formed during hydration hydride. As a result of the enthalpy from decomposition it may be concluded that the formed in these predefined conditions (25 atm H<sub>2</sub>) hydride is in minor quantities (fewer than 10 vol. %).

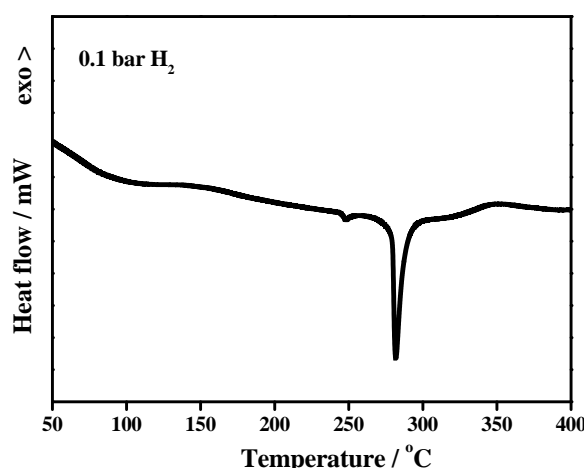
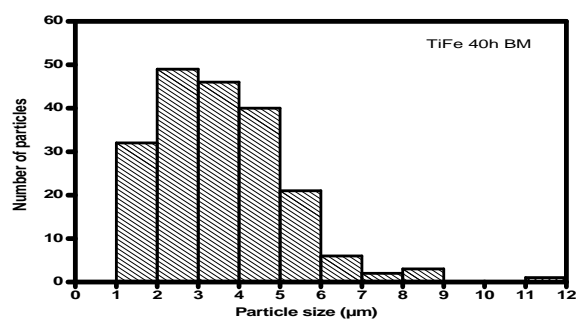
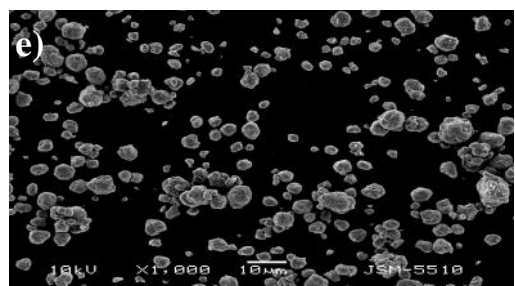
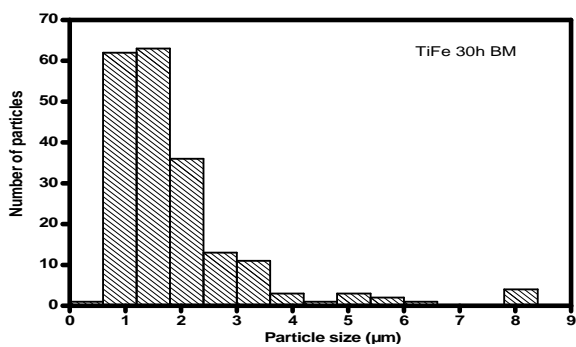
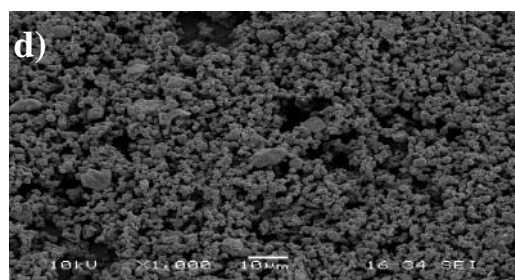
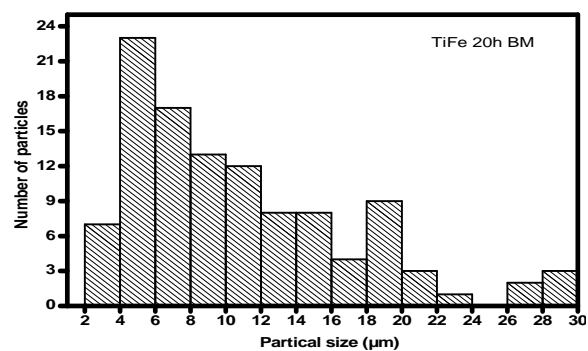
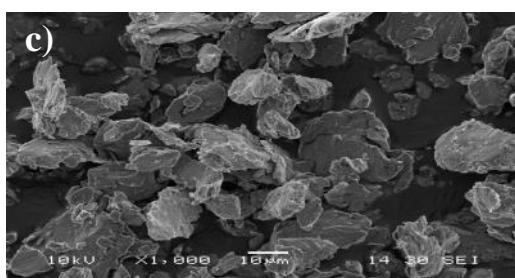
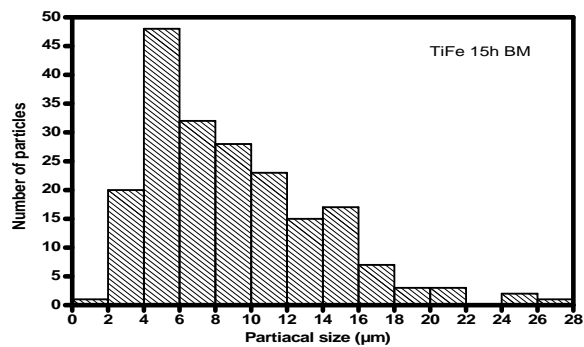
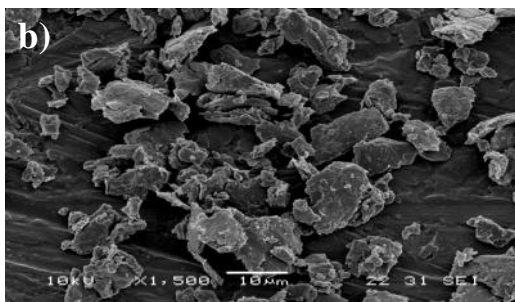
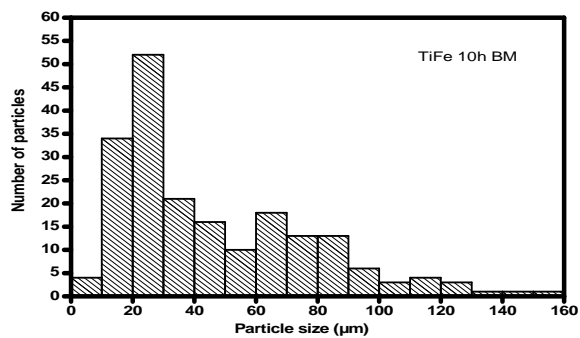
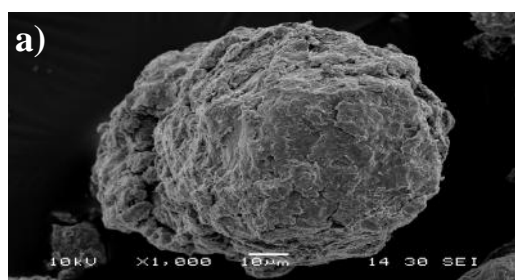


Fig. 4. Thermogram of TiFe alloy.

Scanning electron microscopy (SEM) analysis showed particles size in the range of 10–100 μm with an average particle size of about 50 μm for the sample milled for 10 hours and shown in Fig. 5a.



**Fig. 5.** SEM micrographs and particle size distribution of the TiFe powders milled for (a) 10 h (b) 15 h (c) 20 h, (d) 30 h and 40 h.



On the one hand, the particles are agglomerates of smaller particles with almost spherical (oval) shape. On the other hand the powders milled for 15 and 20 h contain particles with plate-like shape (shown in Fig. 5b,c). The rather dissimilar morphology of the powders milled for a different duration is due to a difference in the mechanical properties (and more specifically: hardness) of the materials, which is most clearly distinct between the samples milled for 10 hours and 15 hours. A spherical shape is also observed in the particles of powder milled for 30 hours, but the average size (1–2  $\mu\text{m}$ ) is significantly reduced in comparison to the particles milled for 10 hours only (Fig. 5d). After continuous milling of up to 40 hours an increase in the average particle size (2–3  $\mu\text{m}$ ) is observed which is possibly due to the agglomerate formation during the further ball milling (Fig. 5e).

During milling the particle size reduces progressively, as the first size reduction (between 10 and 15 h) is larger (Fig. 6).

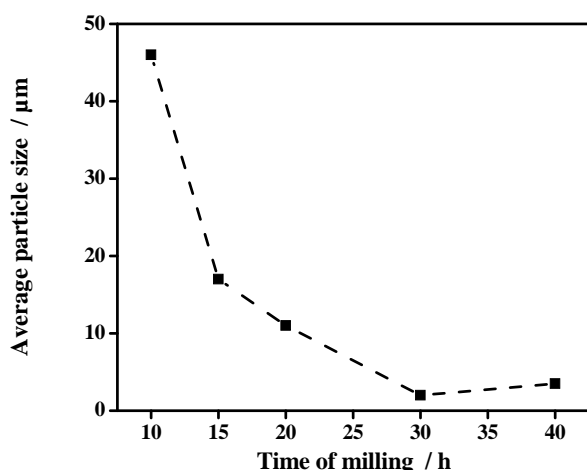


Fig. 6. Particle size vs. milling time.

The electrodes prepared from TiFe alloys with different microstructure were charged for 10 h at current density of  $100 \text{ mA g}^{-1}$  and discharged at  $20 \text{ mA g}^{-1}$  to cut-off potential of  $-400 \text{ mV}$  versus the reference electrode. Two discharge reactions were observed for all four alloys: the first at about  $-880 \text{ mV}$  and the second at about  $-700 \text{ mV}$ . While the first discharge reaction does not show a clear plateau, the second shows a near-horizontal line (Fig. 7). Clearly, the alloys contain two hydriding phases. Most probably these are the nanocrystalline and the amorphous phases, which may also differ slightly in their chemical composition. This result needs further investigation. The total discharge capacity as a function of charge/discharge cycle number is presented in Fig. 8. An initial discharge capacity increase with cycle number followed by a capacity decrease after a certain number of cycles is observed for all alloys. The discharge capacity

maxima appear at different cycle number for the different alloys.

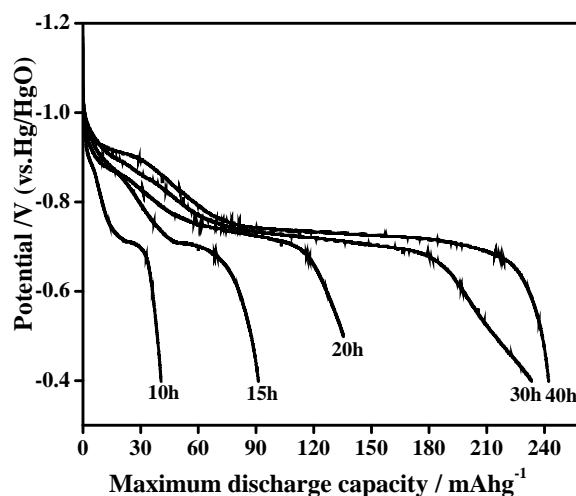


Fig. 7. Discharge curves of TiFe milled for different time 10, 15, 20, 25, 30 and 40 h.

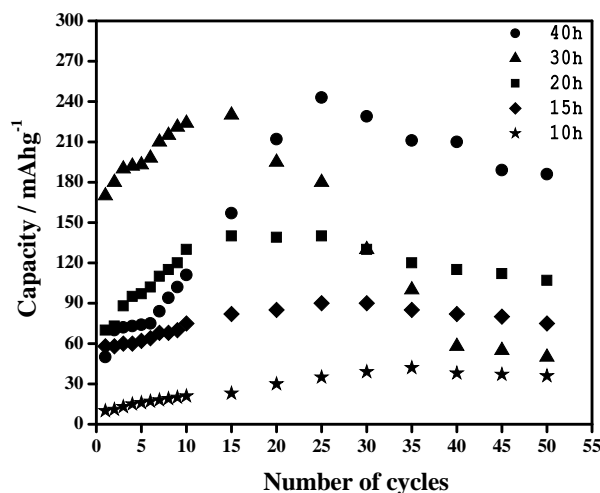


Fig. 8. Capacity as a function of cycle number for different as milled TiFe powders.

For the sample milled for 10 h the activation lasts about 35 charge/discharge cycles and the maximum capacity attained is  $40 \text{ mAh g}^{-1}$ . The alloy milled for 30 h has shorter activation period (15 cycles) and its maximum capacity is  $236 \text{ mAh g}^{-1}$ . The maximum discharge capacity of the alloy obtained at 40 h milling time does not differ substantially ( $240 \text{ mAh g}^{-1}$ ) from the one obtained for 30 h of milling. Nevertheless, it remains relatively stable for a long period of time. For 50 charge-discharge cycles the capacity decay is around 20%. That value is substantially higher than all capacity values published for this alloy composition [11]. As the milling duration increases, a decrease in the activation period is observed, as well as, an increase in the maximum discharge capacity. The large difference between the electrochemical capacity measured in the present work and in previous studies can only be due to the

microstructural difference. In this study we use composite nanocrystalline/amorphous TiFe alloys, which are acknowledged to be suitable for hydrogen storage. Moreover, the presence of nanocrystalline iron in the as-milled material might also be favourable for the hydriding process. The rate of capacity decrease, however, also increases with milling time (Fig. 8).

## CONCLUSIONS

Using the process of high-energy ball milling, nanostructured TiFe alloys with different morphology and microstructure were obtained. The evolution of the particle size was determined. The thermal stability and crystallisation of the as-milled nanocrystalline alloys were investigated and formation of an amorphous phase during milling was found. Strong dependence on the microstructure was observed in relation to the hydrogen capacity of the ball-milled nanostructured alloys. The alloy obtained from 40 hours of milling possesses the maximum discharge capacity which may be related to the increase of the average particle size in comparison to the alloy obtained from 10, 15, 20 and 30 hours of milling. This value of 240 mAh g<sup>-1</sup> is significantly higher than the ones obtained previously [11]. The investigated samples need activation, as the activation time shortens when refining the microstructure. The alloys milled for 20 and 30 hours demonstrate a noticeably poorer cycle life in comparison to those milled for 10 and 15 hours, which have similar stability during continuous charge/discharge cycling. That phenomenon is because of the presence of a larger amount of amorphous phase in the alloys milled for 20 and 30 hours. The material milled for 40 hours revealed discharge capacity comparable to that of alloy milled for 30 hours but its stability was greatly improved. That is most probably due to the formation of agglomerates at continuous milling between 30-40 hours.

## REFERENCES

1. K. Buschow, P. Bouten, A. Miedema, Hydrides formed from intermetallid compounds of two transition metals: a special class of ternary alloys, *Rep. Prog. Phys.*, **45**, 937 (1982).
2. T. Sakai, M. Matsuoka, C. Iwakura, Rare earth intermetallics for metal-hydrogen batteries. In: Gschneider Jr K A, Eyring L, editors. Handbook on the physics and chemistry of rare earth, vol. 21. Elsevier; 1995. p. 142.
3. H. Aoyagi, K. Aoki, T. Masumoto, Effect of ball milling on hydrogen absorption properties of FeTi, Mg<sub>2</sub>Ni and LaNi<sub>5</sub>, *J. Alloys Compd.*, **231**, 804 (1995).

4. M. Bououdina, D. Grant, G. Walker, Review on hydrogen absorbing materials d structure, microstructure, and thermodynamic properties, *Int. J. Hydrogen Energy*, **31**, 177 (2006).
5. H. Hotta, M. Abe, T. Kuji, H. Uchida, Synthesis of TiFe alloys by mechanical alloying, *J. Alloys Compd.*, **439**, 221 (2007).
6. D. Yan, G. Sandrock, S. Suda, Activation of Zr<sub>0.5</sub>Ti<sub>0.5</sub>V<sub>0.75</sub>Ni<sub>1.25</sub> alloy electrodes by hot alkaline solutions, *J. Alloys Compd.*, **216** (1994).
7. J. Kleparis, G. Wojcik, A. Czerwinski, J. Skowronski, M. Kopczyk, M. Beltowska-Brzezinska, Electrochemical behavior of metal hydrides, *J. Solid State Electrochem.*, **5**, 229 (2001).
8. S. Kulkova, D. Valujsky, J. Kim, L. Geunsiik, Y. Koo, Optical properties of TiNi, Ti Co and TiFe thin films, *Physica B*, **304**, 186 (2001).
9. R. Reilly, R. Wiswall, Formation and properties of iron titanium hydride, *Inorg Chem*, **13**, 218 (1974).
10. M. Abe, T. Kuji, Hydrogen absorption of TiFe alloy synthesized by ball milling and post-annealing, *J. Alloys Compd.*, **446-447**, 200 (2007).
11. M. Jurczyk, Nanostructured electrode materials for Ni-MH<sub>x</sub> batteries prepared by mechanical alloying, *J. Mater. Sci.*, **39**, 5271 (2004).
12. R. Wakabayashi R, Sasaki, T. Akiyama, Self-ignition combustion synthesis of oxygen-doped TiFe, *J. Alloys Compd.*, **34**, 5710 (2009).
13. J. Kim, S. Oh, G. Lee, Y. Koo, S. Kulkova, V. Egorushkin, Theoretical study of electronic structure and H adsorption properties in TiFe thin films with Pd coating, *Int. J. Hydrogen Energy*, **29**, 87 (2004).
14. G. Sandrock, P. Goodell, Surface poisoning of LaNi<sub>5</sub>, FeTi and (Fe, Mn) Ti by O<sub>2</sub>, Co and H<sub>2</sub>O, *J. Less-Common Met.*, **73**, 161 (1980).
15. N. Cui, P. He, J. Luo, Magnesium-based hydrogen storage materials modified by mechanical alloying, *Acta Mater.*, **47**, 3737 (1999).
16. T. Bai, S. Han, X. Zh, Y. Zhang, Y. Li, A. Zhang, Effect of duplex surface treatment on electrochemical properties of AB<sub>3</sub>-type La<sub>0.88</sub>Mg<sub>0.12</sub>Ni<sub>2.95</sub>Mn<sub>0.10</sub>Co<sub>0.55</sub>Al<sub>0.10</sub> hydrogen storage alloy, *W. Mater. Chem. Phys.*, **117**, 173 (2009).
17. Y. Li, S. Han, J. Li, X. Zhu, L. Hu, The effect of Nd content on the electrochemical properties of low-Co La-Mg-Ni-based hydrogen storage alloys, *J. Alloys Compd.*, **458**, 357 (2008).
18. J. Ma, H. Pan, Y. Zhu, S. Li, C. Chen, Q. Wang, Electrochemical properties of La<sub>0.9</sub>Sm<sub>0.1</sub>Ni<sub>(5.0-x)</sub>Co<sub>x</sub> (x=2.0, 2.5, 3.0) hydride electrode alloys, *Electrochem. Acta*, **46**, 2427 (2001).
19. H. Ye, Y. Huang, T. Huang, H. Zhang, Influence of the boron additive on the electrochemical properties of the MnNi<sub>3.55</sub>Co<sub>0.75</sub>Mn<sub>0.4</sub>Al<sub>0.3</sub> hydrogen storage alloy, *J. Alloys Compd.*, **330**, 866 (2002).
20. M. Wang, Y. Zhang, L. Zhang, L. Sun, Z. Tan, F. Xu, H. Yuan, T. Zhang, *J. Power Sources*, **159**, 159 (2006).
21. C. Khaldi, H. Mathlouthi, J. Lamloumi, J. Percheron-Guegan, J. Electrochemical study of cobalt-free AB<sub>5</sub>-

- type hydrogen storage alloys, *Int. J. Hydrogen Energy*, **29**, 307 (2004).
22. B. Ratnakumar, C. Withan, R. Bowman, A. Hightower, B. Fultz, Electrochemical Studies on  $\text{LaNi}_{5-x}\text{Sn}_x$  Metal Hydride Alloys, *J. Electrochem. Soc.*, **143**, 2578 (1996).
  23. G. Zheng, B. Popov, R. White, Determination of Transport and Electrochemical Kinetic Parameters of Bare and Copper-Coated  $\text{LaNi}_{4.27}\text{Sn}_{0.24}$  Electrodes in Alkaline Solution, *J. Electrochem. Soc.*, **143** (3), 834 (1996).
  24. M. Ciureanu, D. Moroz, R. Ducharme et al. Electrochemical Studies of Amorphous  $\text{Ni}_{64}\text{Zr}_{36}$  Hydride Electrodes, *Z. Phys. Chem. Bd*, **183**, 365 (1994).
  25. J. Strom-Olsen, Y. Zhao, D. Ryan, Hydrogen diffusion in amorphous  $\text{NiZr}$ , *J. Less-Common Met.*, **172**, 922 (1991).
  26. M. Tliha, H. Mathlouthi, C. Khalid, J. Lamloumi, A. Percheron, Electrochemical properties of the  $\text{LaNi}_{3.55}\text{Mn}_{0.4}\text{Al}_{0.3}\text{Co}_{0.4}\text{Fe}_{0.35}$  hydrogen storage alloy, *J. Power Sources*, **160**, 1391 (2006).
  27. M. Jurczyk, W. Rajewski, W. Majchrzycki, G. Wojcik, Mechanically alloyed  $\text{MmNi}_5$ -type materials for metal hydride electrodes, *J. Alloys Compd.*, **290**, 262 (1999).
  28. J. Willems, K. Buschow, From permanent magnets to rechargeable hydride electrodes, *J. Less-Common Met.*, **129**, 13 (1987).
  29. T. Sakai, H. Miyamura, N. Kuriyama, A. Kato, K. Oguro, H. Ishikawa, Metal Hydride Anodes for Nickel-Hydrogen Secondary Battery, *J. Electrochem. Soc.*, **137**, 795 (1990).
  30. H. Pan, J. Ma, C. Wang, C. Chen, Q. Wang, Effect of Co content on the kinetic properties of the  $\text{MnNi}_{4.3-x}\text{Co}_x\text{Al}_{0.7}$  hydride electrodes, *Electrochim. Acta*, **44**, 3977 (1999).
  31. M. Latroche, Y. Chabre, A. Percheron, O. Isnard, B. Knop, Influence of stoichiometry and composition on the structural and electrochemical properties of  $\text{AB}_{5+y}$ -based alloys used as negative electrode materials in Ni-MH batteries, *J. Alloys Compd.*, **330**, 787 (2002).
  32. A. Anani, A. Visintin, S. Srinivasan, A. Appleby, H. Lim, Microcalorimetry Study of Ni/ $\text{H}_2$  Battery Self-Discharge Mechanism, *J. Electrochem. Soc.*, **139**, 985 (1992).
  33. M. Tliha, C. Khalidi, S. Boussami, N. Fenineche, O. Kedim, H. Mathlouthi, J. Lamloumi, Kinetic and thermodynamic studies of hydrogen storage alloys as negative electrode materials for Ni/MH batteries: a review, *J. Solid State Electrochem.*, **18**, 577 (2014).
  34. L. Zaluski, P. Tessier, D. Ryan, C. Doner, A. Zaluska, J. Strom-Olsen, M. Trudeau, R. Schulz R, *J. Mater. Res.*, **8**, 3059 (1993).
  35. P. Tessier, L. Zaluski, A. Zaluska, J. Strom-Olsen, R. Schulz, *Mater. Sci. Forum*, **225–227**, 869 (1996).

TiFe

1\* , 2 , 1 , 1 , 1

1 “ ” 10, 1113, “ ,

2 “ ” 1164, I,

6 2017 ; 3 2017 .

( )

- TiFe

30-40 50 - 1 Fe.

/

40

30 ,

## Application of permittivity spectroscopy for screening of motor oils lubricating properties

D. Levi\*, Z. Stoynov, D. Vladikova

*Acad. Evgeni Budevski Institute of Electrochemistry and Energy Systems, Bulgarian Academy of Sciences, 10 Acad. G. Bonchev St., 10, 1113 Sofia, Bulgaria*

Received November 4, 2016      Revised January 17, 2017

Motor oils can be regarded as systems of highly dispersed polarizable dielectric in a matrix of non-polarizable or weakly polarizable dielectric. Taking into account that permittivity defines the ability of dielectrics to be polarized under external electric field and thus, to conduct alternative current, Permittivity Spectroscopy (PS) can be one approach for characterization of motor oils lubricating properties determined by their polarization ability. The analysis is based on measurements of the frequency dependence of the real component of the complex capacitance  $C'$ . A sharp increase of  $C'$  at a given frequency is registered. The height of the jump and its starting position in respect to the frequency are accepted as qualitative criterion for the lubricating properties of the oil and used for comparison between different oils in respect to their oiliness. The application of the method is demonstrated and evaluated in testing of technology for production of synthetic motor oil friction modifiers.

**Key words:** permittivity spectroscopy, motor oils and friction modifiers, polarisation, lubricating properties, oiliness.

### INTRODUCTION

The quality of motor oils is essential both for the transport and the economy sectors since high quality oils provide reduced friction and high compression to internal combustion engines. The presence of active additives can significantly increase their lubricating properties. The ability to predict the remaining useful life (RUL) of motor oils could minimise the need for their scheduled changes, providing material saving, labour costs reduction combined with a positive effect on the environmental protection [1].

Motor oils are formulated from base petroleum stocks with about 10-25% additives [2]. The oil forms a film between the surfaces of the adjacent moving parts and thus minimises the direct contact between them, decreasing friction, wear and production of excessive heat. During their use they experience thermal and oxidative stresses which degrade the chemical composition of the base oil and deplete the oil's additive package. Contaminations such as leakage of water, introduction of carbon residues and metal impurities also affect their exploitation life. It is important that motor oils have a high lubricating ability which leads to lower fuel consumption, extended service life of the engine and a direct favourable impact on environment protection

efforts. The methods for testing of oils lubricating properties are slow and require time and significant resources. Accurate full analysis is usually performed in specialised laboratories which additionally increases costs and consumes time. The currently used methods performed by major engine and lubricant manufacturers are in fact frequent, repetitive and time-consuming physical, chemical and mechanical tests. They include determination of oil viscosity, total acid number (TAN), total base number (TBN), insoluble (such as soot) content, fuel and water dilution, glycol contamination and metals content, degree of wear etc. [3-5].

Noticeably, the development of new, more simple, convenient, compact and faster non-destructive methods for complex dynamic characterisation of motor oils quality and assessment of the changes in their lubricating properties during exploitation is strongly needed. One promising approach is the application of physicochemical methods.

What makes them appropriate? The lubricating properties of oils are strongly dependent on viscosity and oiliness. While viscosity as a basic physicomachanical parameter is well formulated in the hydrodynamic theory of lubrication and deeply studied [6], oiliness can be regarded as a "hidden" potential quality parameter of the oil and is hence evaluated with a set of properties which ensure lubricating effect at thickness of the film, small enough to eliminate the viscosity effect [7]. The main characterisation factor is the strength of

---

To whom all correspondence should be sent:  
E-mail: danilevi3@gmail.com

attachment of the thin oil layer towards the two moving parts, which preserves them from direct contact. It depends on the oil's polarisation characteristics which ensure the formation of layers with orientated molecules. The oiliness is superior when polarisation is easier [8]. The addition of compounds with high polarisation activity (oxygen-containing compounds such as naphthene, carbonic acids, asphaltenes, tar and compositions with sulphur in their molecules) improves the strength of the fine polarized oil layer. The oiliness is tested on special traction stands where the degree of wear of the standard moving parts (for instance balls) is evaluated. During exploitation oils progressively deteriorate their functional properties until they entirely lose their lubricating ability. The main degradation process is oxidation which changes the chemical composition [4, 9-11]. There is no universal criterion for determination of the moment at which the oil cannot be used further and should be changed. Since lubricating properties and their deterioration during exploitation are closely related to the presence of highly polarizable components, physicochemical methods that analyse the polarisation properties of molecules are an attractive trend. One path which is under exploitation is the evaluation of the relative permittivity changes of motor oils during exploitation [12-14]. However, the accuracy of the developed devices is still rather low [15-16]. Taking into account that the permittivity defines the ability of dielectrics to be polarised under external electric field and thus, to conduct alternative current, Permittivity Spectroscopy (PS) can be one approach for characterization of motor oils. The classical applications of the Permittivity Spectroscopy are typically related to the dipole properties studies of pure gases and liquids. The applied frequency range is from 1000 MHz down to 1 MHz and requires special measurement instrumentation [17-22].

Motor oils can be regarded as systems of highly dispersed polarisable dielectric in a matrix of non-polarisable or weakly polarisable dielectric. They require measurements in different frequency range. Preliminary experience has shown that important interactions between the two media are well observable in the range of 1 MHz down to 0,1 Hz. [23-24]. For that frequency range it is convenient to apply Permittivity Spectroscopy as a branch of Impedance Spectroscopy especially tuned for studies of dielectrics permittivity. This approach ensures contactless measurements in respect to the object's physical behavior and conductivity without the need of a reference electrode. Preliminary screening experiments confirmed the applicability of PS for motor oils [23, 25]. It should be noted that

in the applied frequency range the penetration depth of the alternative current signal (A.C.) is much larger than the object's thickness [20]. As a result, the electric field strength is practically equal in the total volume of the sample.

When the A.C. signal is applied in the dielectric, the relative permittivity can be expressed as a complex number [20, 26]:

$$\nu = \nu' - j\nu'' \quad (1)$$

where  $\nu'$  and  $\nu''$  denote the real and the imaginary (loss factor) components of the complex value of  $\nu$ . The capacitance  $C$  can be also presented in a complex form:

$$C = C' - jC'' \quad (2)$$

since the capacitive impedance  $Z(j\omega)$  follows the dependence:

$$Z(j\omega) = -j (C')^{-1} \quad (3)$$

where  $\omega$  is the frequency.

The capacitance of a parallel plate capacitor is [17, 26],

$$C = \frac{\epsilon_0 \epsilon S}{d} \quad (4)$$

where  $\epsilon_0$  is the permittivity of vacuum,  $S$  is the surface area of the electrodes and  $d$  is the distance between them.

If the impedance is replaced with admittance:

$$Y(j\omega) = 1/Z(j\omega) \quad (5)$$

then

$$Y(j\omega) = j\omega C = j\omega (C' - jC'') = \omega^2 C'' + j\omega C' \quad (6)$$

The real component  $\omega^2 C''$  in Eqn. 6 can be regarded as dielectric conductivity [26]. It can be expressed also as equivalent resistance  $R = 1/\omega^2 C''$ , which can be directly measured and describes energy dissipative effects as ohmic conductivity, dipole's reorientation losses in electric field and others.  $C'$  is related to the dielectric permittivity, i.e. to the polarisation ability of the system.

The present study aims at applying Permittivity Spectroscopy as a robust and selective method for rapid characterisation of motor oils quality and degradation state. Its application is demonstrated in testing of technology for production of synthetic motor oil and friction modifiers.

## EXPERIMENTAL

The permittivity measurements of motor oils were carried out in a special test cell with two coaxial cylindrical steel electrodes of diameter 49

mm with coplanar working surfaces and added spacer of paper positioned in three places that ensure a constant distance of 0.2 mm between the electrodes spring fixed in the cell. The material (special hardened steel) is identical with the one of the balls used in the traction stands where comparative test of the oiliness are performed. Following a developed oil deposition procedure, all the measured samples had one and the same geometry (surface and thickness). The complex permittivity measurements were performed on Solartron 1260 FRA in the frequency range 1 MHz – 0.1 Hz at room temperature with amplitude of the signal 1 V at density 5 points per decade. The precise determination of the object’s permittivity was ensured by a preliminary calibration procedure, which eliminates the parasitic components coming from the test rig [23]. Following Eqn. 6, the most illustrative form for representing the experimental results was selected [27] - the frequency dependence of  $C'$ , given as  $\log C'(F) / \log f(\text{Hz})$ . More details for the investigated oil samples are given in the next section.

RESULTS AND DISCUSSION

Preliminary measurements have been performed on four different types of motor oils available at the market with preliminary known lubricating quality - oil base, natural, semi-synthetic and synthetic (Table 1). The aim was to define criteria for estimation of the oil quality.

Table 1. Measured oils available at the market.

Sample No	Oil	Type	Status
1	Oil Base SN 500	Base	Fresh
2	Prista M10D	Mineral	Fresh
3	Prista 10W40	Semi-synthetic	Fresh
4	Prista 5W40	Synthetic	Fresh

The results from the permittivity measurements of the fresh samples (Samples 1 - 4 from Table 1) presented as frequency dependence of  $C'$  are shown in Fig. 1.

For the oil base (Sample 1) no frequency dependence of  $C'$  was observed. This composition still has no additives that ensure its lubricating properties. For the rest of the samples at a given characteristic frequency a sharp increase is registered. The increase of  $C'$  is related to the

polarisation ability of the oil components, i.e. to their oiliness. Noticeably, molecules that have higher polarisation ability will react on the external polarisation A.C. signal at higher frequencies and will cause higher increase of  $C'$ . Thus the jump and its starting position in respect to the frequency can be accepted as qualitative criterion for the lubricating properties of the oil and used for comparison between different oils in respect to their oiliness. As seen in Fig. 1, for the mineral oil (Sample 2) the sharp increase of  $C'$  starts at lower frequency in comparison with that of the semi-synthetic (3) and synthetic (4) samples combined with a lower enhancement of this parameter. The increase of  $C'$  for sample 4 is more pronounced than that for sample 3. According to the accepted assumption the quality of the oils increases in the following direction: oil base < mineral < semi-synthetic < synthetic, which correlates with the market evaluation of the 4 samples.

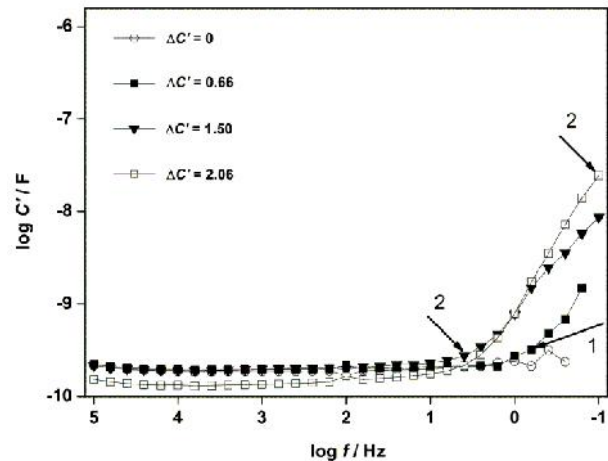


Fig. 1. Frequency dependence of  $C'$  for Sample 1 ( ); Sample 2 ( ); Sample 3 ( ) and Sample 4 ( ).

It should be emphasized that every type of oil exhibits a typical capacitive diagram which ensures an easy distinction between the synthetic and the natural oils.

According to the performed screening measurements, a two-fold semi-quantity criterion for comparative evaluation of oiliness is defined, based on the capacitive impedance measurements: (i) value of the characteristic frequency  $f_{ch}$  of  $C'$  jump; (ii) enhancement/jump defined as  $\Delta C' = \log C'_{max} - \log C'_{f_{ch}}$ . According to this criterion, in oils with better quality,  $\Delta C'$  is larger and occurs at higher frequencies.

The obtained results were applied for evaluation of the quality of modifiers produced in the frames of a technological project [28]. The measurements were performed using mineral oil as an oil base (Table 2).

**Table 2.** Evaluated samples.

Sample No	Oil/modifier	Type	Status
5	Modifier glyceryl monooleate (MGO) with waste glycerine (process catalyst Y zeolite)	Additive	Fresh
6	Modifier MGO with waste glycerine (process catalyst Zn suksinid zeolite)	Additive	Fresh
7	Mineral Oil (sample 2) with 0,5 % modifier (sample 6)	Natural motor oil with additive	Fresh
8	Mineral Oil (sample 2) with 0,5 % with modifier (sample 5)	Natural motor oil with additive	Fresh

Fig. 2 presents results performed with pure modifiers. According to the defined criteria both samples have excellent properties in respect to oiliness ( $C'$  increases more than 4 decades). The comparison of the two modifiers registers a little bit better performance for sample 5, which is marked only in the  $C'$  enhancement and not in the value of the characteristic frequency.

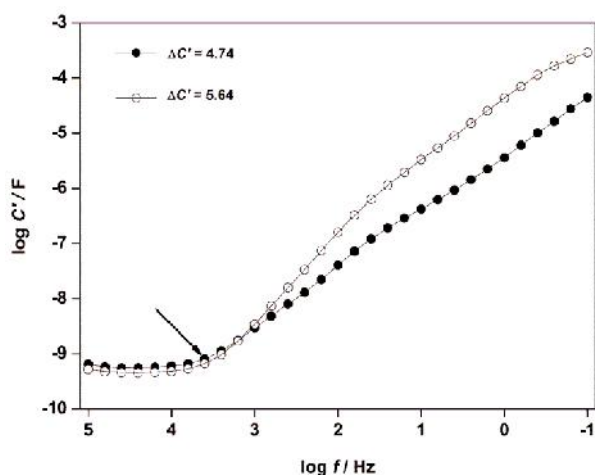


**Fig. 2.** Frequency dependence of  $C'$  for: Sample 6 ( ) and Sample 5 ( ).

The addition of the two modifiers to the base oil shows significant improvement of the motor oil quality (Fig. 3). The additional enhancement of  $C'$  in respect to the base oil is more than 3 decades and the characteristic frequency of  $C'$  jump moves from about 1 Hz to 50 Hz. Obviously the presence of the highly polarizable molecules of the modifier in the

oil matrix accelerates the formation of the organized dipole thin film and the quality of the micelles structure. The comparison of the results for Samples 7 and 8 shows the same difference which has been obtained for the pure modifiers which is logical, since the oil base is one and the same.

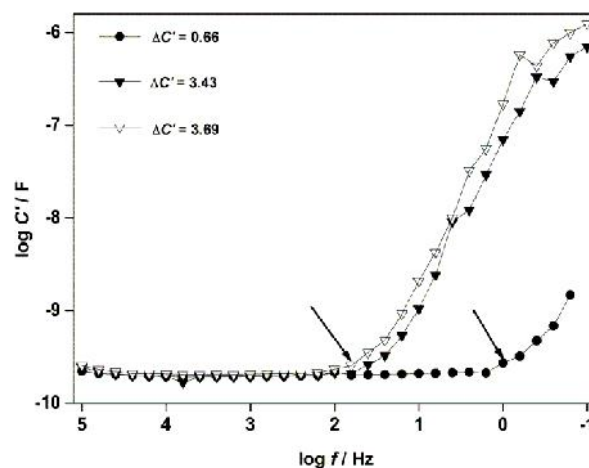


**Fig.3.** Frequency dependence of  $C'$  for: Sample 2 ( ) ; Sample 7 ( ) and Sample 8 ( ).

The obtained results confirm the applicability of the developed technology for production of modifiers, as well as the high quality of the modified oils and their practical applications.

To confirm the selectivity of the method, the results obtained with Permittivity Spectroscopy were compared with those performed by the standardized method based on traction stands, which was carried out in a licensed laboratory (Table 3). It is applied for classification of motor oils according to their level of anti-wear properties. The evaluation of the oils is based on optical measurement of the average diameter of wear  $\bar{d}$  (mm). The smaller the diameter of the spot, the better the anti-wear properties of the tested object. As seen in Table 3, in respect to the quality, the results obtained by the Permittivity Spectroscopy approach are in agreement with those obtained on the traction stand.

For example, the result for Sample 8 obtained by PS shows excellent oiliness properties ( $\epsilon' = 3.69$ ), which is also proven by the standard method ( $\bar{d} = 0.35$  mm).

However, the registered differences for oil base and oil with modifier are of about 0.30 mm (quite difficult for optical registration) in combination with time consuming experiments, while in addition to the quick measurement, the PS approach registers differences of more than 1000 times, which confirms the high sensitivity and robustness of the new approach.

**Table 3.** Comparative analysis.

Name of the sample	Results from the conducted testing with Permittivity Spectroscopy (Frequency dependence of the effective capacity $\epsilon'$ )	Results from the conducted testing with four-ball machine (Average diameter of wear, at time of testing 1 hour) $\bar{d}$ (mm <sub>h</sub> )
1 Oil base SN 500	0	0.70
2 Prista M10D	0.66	0.60
7 Mineral oil M10D Prista Oil with 0,5 % modifier MGO with waste glycerine with catalyst Zn suksinid zeolite	3.43	0.39
8 Mineral oil M10D Prista Oil with 0,5 % modifier MGO with waste glycerine with catalyst Y zeolite	3.69	0.35

### CONCLUSIONS

The performed studies on motor oils analysis confirms the selectivity and sensitivity of Permittivity Spectroscopy, which registers changes in the measurement parameter ( $C'$ ) of several orders, thus ensuring much more reliable and precise classification of oils in terms of their lubricating properties.

The results obtained open a niche for applying the methodology as a quick alternative method for assessing the lubricating properties of oils.

**Acknowledgements:** *The authors acknowledge Operational Programme “Development of the Competitiveness of the Bulgarian Economy” (2007-2013), Contract BG161 003-1.1.06-0102-0001/ 07.12.2012 (2012- 2015) for the financial support that made possible the publication of this paper.*

### REFERENCES

1. R. E. Kauffman, *Lubrication engineering*, **45**, 709 (1989).
2. A. M. Farrington and J. M. Slater, *Analyst*, **122**, 593 (1997).
3. S.S. Wang, H.S. Lee, D.J. Smolenski, *Sens. Actuators B*, **17** (3), 179 (1994).
4. S.S. Wang, H.S. Lee, *Sens. Actuators B*, **40** (2–3), 193 (1997).
5. S. Wang, *Sens. Actuators B*, **73** (2–3), 106 (2001).
6. G. Fukcs, *Viscosity and plasticity of petroleum products*, Gostoptekhizdat in Russian (1951).
7. R. Wilson, D. Barnard, *SAE Technical Paper 220009* (1922).
8. L. Traikov, *Oils, lubricants and liquids*, Sofia, (2007).
9. D. Cipris, A. Walsh, T. Palanisamy in: D. R. Turner (Ed.), *The Electrochemical Society Proceedings Series*, **PV 87-9**, 401 (1990).
10. Shell International Trading Company, Shell lubricants, England, (1991).
11. Agip Petroli, *Lubricants and special products*, Roma (1992).
12. [http://www.google.com/patents/US4646070\(1987\)](http://www.google.com/patents/US4646070(1987)).
13. [http://www.google.com/patents/US4733556\(1988\)](http://www.google.com/patents/US4733556(1988)).
14. [http://www.google.com/patents/US6449580\(2002\)](http://www.google.com/patents/US6449580(2002)).
15. [http://www.skf.com/group/our-company/index.html\(2013\)](http://www.skf.com/group/our-company/index.html(2013)).
16. <http://www.spectrosci.com/product/q1000/>
17. D. Griffiths, *Introduction to Electrodynamics* (Third Edition), Prentice Hall, New Jersey, (1999).
18. R. P. Feynman, R. Leighton, M. Sands, *The Feynman Lectures on Physics, The Definitive Edition 2* (2nd Edition), Addison Welsey, New York, (2005).
19. R. Gorur, *Dielectrics in Electric Fields*, Marcel Dekker, Inc. New York, (2003).
20. V. Komarov, S. Wangand, J. Tang, *Encyclopedia of RF and Microwave Engineering*, John Wiley & Sons (2005).
21. J. Nowotny, M. Rekas, *Key Eng Mat.*, **66&67**, 45 (1992).
22. D. Lide (ed), *CRC Handbook of Chemistry and Physics*, CRC Press, Boca Raton, (2004).
23. Z. B. Stoynov, D. E. Vladikova, Z. H. Xi, *Bulg. Chem. Commun.*, **35** (2), 104 (2003).
24. Z. Stoynov, E. Mladenova, D. Levi, D. Vladikova, *Acta Chim. Slov.*, **61**, 255 (2014).
25. Z. B. Stoynov, Z. H. Xi, D. E. Vladikova, *Bulg. Chem. Commun.*, **35** (3), 162 (2003).
26. R. Coelho, *Physics of Dielectrics for the Engineer*, Elsevier Scientific Publishing Company, (1979).
27. Z.B. Stoynov, D. E. Vladikova, E. A. Mladenova, *J. of Solid State Electrochemistry*, **17** (2), 555 (2013).
28. “Modifiers to reduce the friction and wear of industrial equipment”, Operational Program “Development of the Competitiveness of the Bulgarian Economy”, (2007 - 2013), Contract BG161PO003-1.1.06-0102-C0001 / 07.12.2012 (2012- 2015).



...\*, ... , ...  
... ” .10, 1113, , “,  
4 2016 .; 17 2017 .  
( )  
( )  
C:  
C:



# Letters to the Editor



## Could one achieve a self-recharging double layer capacitor?

N. Vaszilcsin<sup>1</sup>, D.-I. Vaireanu<sup>2\*</sup>

<sup>1</sup> University Politehnica Timi oara, Faculty of Industrial Chemistry and Environmental Engineering, Department of Applied Chemistry and Engineering of Inorganic Compounds and Environment, 2 Pia a Victoriei, 300006, Timi oara, Romania

<sup>2</sup> Politehnica University of Bucharest, Faculty of Applied Chemistry and Materials Science, Department of Inorganic Chemistry, Physical Chemistry and Electrochemistry, 1-7 Gh. Polizu St., sector 1, 011061, Bucharest, Romania

Received November 7, 2016    Revised March 1, 2017

The aim of this short communication is to initiate an open discussion topic, besides the main practical challenge, for electrochemists, electrical engineers or other scientists alike, to investigate and scrutinize whether or not it is possible to obtain, from theoretical point of view, as well as from the practical one, a self-recharging double layer capacitor. This topic has been suggested by the reconditioning in Romania of so-called Karpen's pile, exhibited in the Romanian National Technical Museum "Dimitrie Leonida" in Bucharest. This device provides power continuously (without any external source) to an electric motor, which was the main reason to be considered for a long period of time as a so called, allegedly, "*perpetuum mobile*". Recently, the mechanism of electrical energy generation in Karpen's pile has been elucidated in a paper published in *Revista de Chimie*. Moreover, this paper put forward a well-founded demonstration that Karpen's pile is in fact a self-recharging capacitor and not at all a *perpetuum mobile*.

**Key words:** self-recharging capacitor, Karpen's cells.

### INTRODUCTION

The Romanian National Technical Museum "Dimitrie Leonida" in Bucharest has in possession and displays a device known as "*Karpen's Cell*", which sparked numerous controversies over the last 60 years as it gives the impression that it provides endless energy in the external circuit, apparently in the absence of the characteristic chemical processes or any energy transfer from the surrounding environment. The controversy is even greater in comparison with the *Oxford Electric Bell* or *Clarendon Dry Pile* in operation since 1840 [1,2], as for this type of pile the issue evolves around the fundamental questions "Does it contradict or not the 2<sup>nd</sup> Law of Thermodynamics? Is it or not a 2<sup>nd</sup> degree *Perpetuum mobile*?"

Nicolae Vasilescu-Karpen (1870-1964) was a professor at the Politehnica University of Bucharest and its Chancellor/Rector for more than 20 years (1920-1940). He approached the research of this type of cells that bears his name since the second decade of the twentieth century, patenting the first models in 1924 [3].

From the very beginning, *Karpen's cells* were shrouded in an aura of mystery even by their

author, who said that their operation contradicts the 2<sup>nd</sup> principle of thermodynamics [4], that they are a form of a 2<sup>nd</sup> kind *perpetuum mobile*, fact also advocated until recently by other authors [5].

Despite numerous practical demonstrations made by Karpen with the *Karpen's cells* (Paris, 1922) [6, 7] or theoretical lectures in Bucharest followed by publications [8], the subject had a small audience and received little support in the international scientific community because these devices were associated with the idea of a *perpetuum mobile*. Strictly speaking, *Karpen's cells* are unpartitioned electrochemical systems, tightly sealed, containing two inert metals (gold, platinum) or graphite, immersed into the same electrolyte solution (sulfuric acid solution, pure sulfuric acid) or even in distilled water, containing small amounts of dissolved oxygen (Oxygen *Karpen's Cell* - KOx), or hydrogen (Hydrogen *Karpen's Cell* - KHy). One maintains in both cases, above the solution surface, a layer of air or hydrogen, at a low partial pressure, about 100 Pa [9].

In a number of public lectures (held in Timisoara and Bucharest, 2016) and in two recently published papers [10, 11], we demonstrated that *Karpen's cells* are in fact electrochemical double layer capacitors, which after a discharging process recharge themselves due to a series of endothermic spontaneous processes taking place in the above said systems, leading to a cooling of the electrolyte

---

To whom all correspondence should be sent:  
E-mail: di\_vaireanu@yahoo.co.uk

solution. The occurrence of a temperature gradient between the electrolyte solution and the surrounding external environment determines the generation of a heat flow rate bringing the solution temperature close to the ambient temperature, compensating for the heat loss induced by the spontaneous recharging process. As a result, *Karpen's cells* convert heat supplied from the surrounding environment into electrical energy powering an external resistive circuit made of a micromotor suspended by a torsion wire, thus *Karpen's cells* acting as a heat to electricity (pseudo)converter.

The most significant results achieved by Nicolae Vasilescu-Karpen were in the case of KOx cell, made of a platinized gold electrode (AuPt) of 2000x6x0.4 mm, coiled onto a glass substrate (positive terminal), placed symmetrically between two shiny gold electrodes of an identical geometry, and pure sulfuric acid as electrolyte. KOx cell powers intermittently a micromotor: the electric motor is connected with the cell for a period of time of 0.5 s, followed by a break of 18 s (Fig. 1) [12].

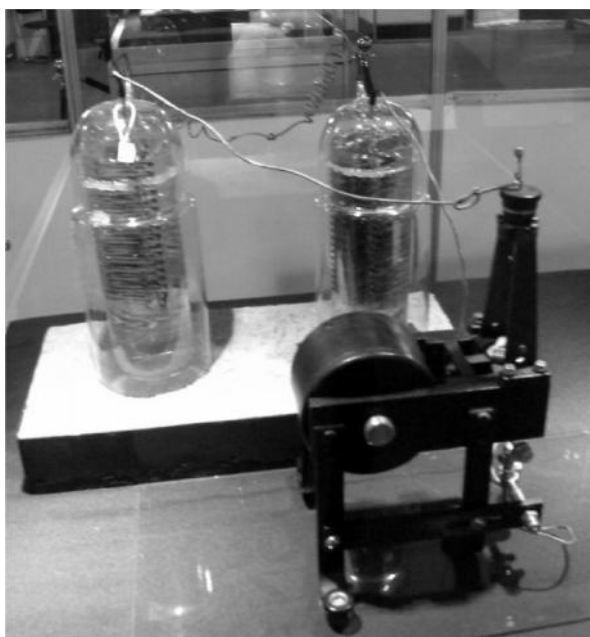


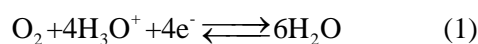
**Fig. 1.** KOx Karpen's cell, (Courtesy of Romanian National Technical Museum *Dimitrie Leonida*, Bucharest).

The maximum current intensity measured during the contact phase is 17.5  $\mu\text{A}$ , the terminal voltage decreasing to 0.02÷0.03 V. After 18 seconds recovering period, the terminal voltage reaches approximately 0.25 V [12].

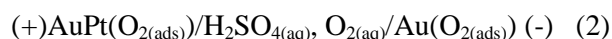
#### THE MECHANISM OF ELECTRICAL ENERGY GENERATION IN KARPEN'S CELLS

Being given the favourable conditions for KOx cell, namely the low partial pressure of oxygen

above the electrolyte solution, the corresponding amount of oxygen dissolved in sulfuric acid solution is very small. Consequently, the AuPt and Au electrodes surface will not be saturated with molecular or atomic oxygen (resulting from the dissociation of  $\text{O}_2$  molecules). We may admit that in this situation, the fractional occupancy of the adsorption sites of electrodes with oxygen is proportional to the strength of metal–oxygen bond. Since Pt–O bond is stronger than the Au–O bond [13], the activity of the adsorbed oxygen on AuPt electrode is higher than the activity of oxygen adsorbed on Au. If the electrolyte solution and the electrode material are of an advanced purity degree, one shall establish an equilibrium at the interface, given by the reversible reaction:



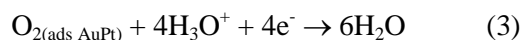
Considering the values of the oxygen activity specifically at the two electrode surfaces, the reversible process equilibrium (1) on AuPt is tilted more towards the right side comparing to that taking place on Au, in accordance with the Châtelier-Braun principle. Therefore, in order to achieve a steady state equilibrium, the AuPt electrode will yield more electrons than the Au electrode, i.e. AuPt will become the positive terminal and Au - the negative terminal of this electrochemical system, so we may write the following:



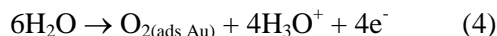
It is well known that the charging process of the above said two metal/solution interfaces is a spontaneous non-faradic process that leads to the formation of an electric double layer [14]. When the electric micromotor is connected to the two cell terminals, a current is passing through the external circuit that determines the micromotor to move in accordance with the above described mechanism. In a matter of fractions of a second (0.5 s), the electrochemical system will discharge its load, the electrochemical potentials of the two electrodes becoming approximately equal. This behaviour allows us to affirm that the considered electrochemical system is, at limit, **a capacitor and not a galvanic cell**, as it was previously believed. During the discharge phase, the electrons pass from the Au electrode through the external resistive motor circuit, reaching finally the AuPt electrode.

When the external circuit is switched off, the AuPt electrode will have an excess of negative electric charges (electrons), while the Au electrode will have an excess of positive electric charges (electrons deficit). This actually means that, in

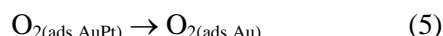
order to restore the chemical equilibrium balance between the two metal - electrolyte solution interfaces, reaction (1) will take place on the AuPt electrode, the equilibrium being shifted towards favouring the reduction process (3):



At the same time, the conjugated oxidation process takes place on the Au electrode:



The overall reaction taking place during the recharge phase of the electrochemical system (2) is obtained by adding up reactions (3) and (4):

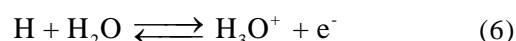


It means that the capacitor charging consists formally by passing the molecular oxygen from AuPt electrode to the Au electrode. As Pt–O bond is stronger than that of Au–O, reaction (5) will be an endothermic one, therefore the capacitor receives during the charging process external thermic energy, which is transformed into electrical energy during the discharge phase. The heat flow rate directed from the outside towards the capacitor has its origin in the very small temperature gradient, taking into account the extremely low electrical current generated during the discharge phase. The electrical energy generated is then converted using the external circuit into a mechanical work using the micromotor and heat, given the passage of a current through the resistive element, known as Joule effect, the energy losses being given not only by the friction between the moving mechanical parts, but also by the frictions with the air; some of the energy is also lost by the heating of the external resistive element by Joule effect, as explained above. Consequently, the electrochemical system is considered a self-charging capacitor whose operation does not contradict the 2<sup>nd</sup> thermodynamics principle, so it is not a 2<sup>nd</sup> kind *perpetuum mobile*. Since the charge is done by non/faradic processes, KOx cell is a double layer electric capacitor and not a galvanic cell. Similar processes take place in hydrogen *Karpen's cell* (KHy). Preliminary attempts to achieve a *Karpen's cell* with hydrogen at normal pressure, close to the atmospheric pressure, were doomed to failure because the electromotive force obtained was close to zero.

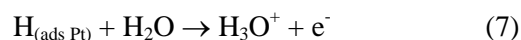
However, changing the conditions leads to a considerable voltage, namely when the cell is fitted with platinum and shiny gold electrodes having the same size (20X30 mm). The basic solution was diluted sulfuric acid (0.30%), and the partial pressure of the hydrogen above the solution was

918 Pa, which means that the dissolved hydrogen concentration in the solution is very low. At temperature of 20°C, the cell terminal voltage of KHy was 0.15 V [9]. Under these conditions, the metals surface will not be saturated with hydrogen and the activity of the adsorbed hydrogen on the metals surface will be proportional to the energy of metal–H bond. According to the available data, Pt–H bond energy is higher than the Au–H bond energy [15].

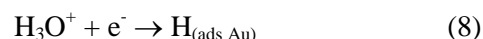
For simplification, let us assume that hydrogen adsorbed on the metals surface, taking into account its reduced concentration, is found in its atomic state [16, 17]. The reversible equilibrium established is given by equation 6:



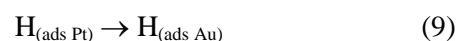
It is obvious that on Pt the equilibrium (6) will be more shifted to the right than on Au. As a result Pt will acquire an excess of electrons, while Au will have a deficit of electrons, which means that Pt will be the negative terminal of KHy cell, and Au, the positive one. Short-cutting the electrodes leads to a flow of the excess electrons from Pt towards Au, performing a mechanical work in the external circuit, while the electrodes terminal voltage will drop quickly. When the external circuit is open, at the Pt electrode will occur reaction (6) shifted towards the oxidation:



and the conjugated one, the reduction reaction, will take place on the Au electrode:



The overall reaction is given by the transport of adsorbed hydrogen from Pt to Au electrode:



As Pt–H bond is stronger than Au–H bond, reaction (9) is an endothermic one, therefore, similarly to the case of KOx cell, KHy cell extracts energy during the recharging process from the surrounding environment.

## RESULTS AND DISCUSSION

### *Development prospects for Karpen's Cells*

KOx and KHy cells are difficult to study because of the practical problems associated with their manufacture: tightly sealed installation, low partial pressure of O<sub>2</sub> and H<sub>2</sub> and difficult to control. This is precisely why we bring forward the proposal of another type of self-charging double-layer capacitor, made of two different electrodes

immersed in a solution of potassium iodide, containing also small amounts of iodine-iodide. The metals used as electrodes have to meet the following condition: the difference between metal-I energy must be as larger as practically possible. If the electrolyte solution is of a high purity and does not contain dissolved gases, at the interface metal-electrolyte solution the following equilibrium will be established:



As the equilibrium constant for the reversible reaction  $I_2 + I^- \rightleftharpoons I_3^-$  is high (698 at 25°C [18]), we may consider that  $I_2$  is found in the solution only as  $I_3^-$ .

If the concentration of  $I_3^-$  ions is reduced and that of  $I^-$  ion is in large excess, then the degree of adsorption on the electrodes surface will depend on the strength of metal- $I_3^-$  bond, meaning that the  $I_3^-$  ions activity at the interface will also be depending on the strength of metal- $I_3^-$  bond. Considering now that the metal- $I_3^-$  bond is noticeably stronger for  $M_1$  than for  $M_2$ , let us examine now the Galvani potential profile alongside the electrochemical system:

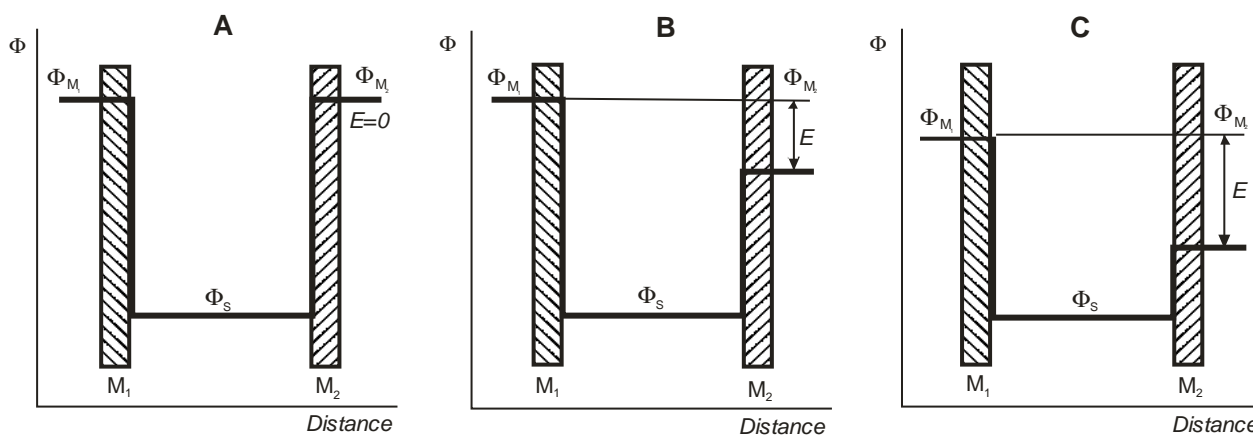
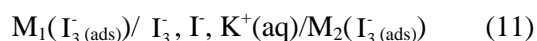


Fig. 2. The profile of the internal Galvani potential alongside the electrochemical system (11).

As one may easily see from Fig. 2, in cases B and C a voltage drop is produced between metals  $M_1$  and  $M_2$  due to the different charge of the electric double layer at the interface  $M_1/S$  and  $M_2/S$ . This is one of the reasons that the above discussed electrochemical system (11) may be considered as being a capacitor, where  $M_1$  is the positive terminal and  $M_2$  is the negative terminal. The absolute potentials may now be expressed using the Nernst relationship:

Depending on the  $I_3^-$  ions concentration, one may have the following cases, presented in Fig. 2:

A -  $I_3^-$  ions concentration is high enough, so that the surfaces of both electrodes are to be saturated with  $I_3^-$  ions, namely the ratio of  $I_3^-$  and  $I^-$  concentrations at the interface is to be equal to the ratio of their concentrations from the electrolyte solution. In this case, the absolute potentials of the two electrodes are equal to each other, and the terminal voltage of the considered electrochemical system is zero (Fig. 2, profile A);

B -  $I_3^-$  ions concentration is high enough, so that the surface of metal  $M_1$  is to be saturated with  $I_3^-$  ions, but, at the same time, the concentration of  $I_3^-$  ions is low enough so that on the surface of metal  $M_2$  there is a deficit of  $I_3^-$  ions. In this situation, the absolute electrode potential of  $M_1/S$  ( $S$  - the electrolyte solution used in the system) is unchanged comparing to the case of A, but the absolute potential electrode  $M_2/S$  will be shifted towards more negative values (Fig. 2, profile B);

C - the concentration is so small that one may not reach the saturation level on both electrode surfaces, which means that the potentials of both electrodes will be shifted towards more negative values, however, of a smaller magnitude in the case of  $M_1/S$  and bigger in the case of  $M_2/S$  (Fig. 2, profile C).

$$\Delta\Phi_{M_1/S} = \Delta\Phi_{I_3^-/I^-}^0 + \frac{RT}{2F} \ln \frac{a_{I_3^-(ads)M_1}}{a_{I^-(S)}} \quad (12)$$

$$\Delta\Phi_{M_2/S} = \Delta\Phi_{I_3^-/I^-}^0 + \frac{RT}{2F} \ln \frac{a_{I_3^-(ads)M_2}}{a_{I^-(S)}} \quad (13)$$

As a result, the electromotive force between the two electrodes is given by:



$$E = \Delta\Phi_{M_2/S} - \Delta\Phi_{M_1/S} = \frac{RT}{2F} \ln \frac{a_{I_3^-(ads M_1)}}{a_{I_3^-(ads M_2)}} \quad (14)$$

From relation (14) one may notice that  $E$  is dependent on the ratio between the energies of the metal- $I_3^-$  bonds; the higher this ratios, the greater the  $E$ .

The equivalent capacitance  $C$  for the electrochemical system (11) shall be given by:

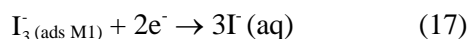
$$\frac{1}{C} = \frac{1}{C_1} + \frac{1}{C_2} \quad (15)$$

and hence:

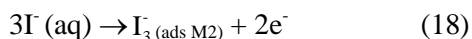
$$C = \frac{C_{M_1/S} \cdot C_{M_2/S}}{C_{M_1/S} + C_{M_2/S}} \quad (16)$$

where  $C_{M_1/S}$  și  $C_{M_2/S}$  are the individual capacitances of the two metal/solution interfaces. By inserting a micromotor connected to the two electrodes, in order to produce a mechanical work in the external circuit, the electrons shall pass from  $M_2$  to  $M_1$ , so that, shortly, the electrodes potentials shall become equal, namely the capacitor will be discharged.

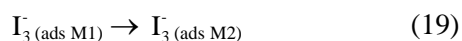
Opening the external micromotor circuit, the equilibrium of reaction (10) will be shifted towards the reduction side, due to an excess of electrons:



At the same time, on metal  $M_2$  the reaction will take place shifted towards the oxidation side:



Equation (19) represents the overall reaction describing the process taking place when the capacitor is charged and it is obtained by adding up reactions (17) and (18):



The charging process of the capacitor depicted in (11) is similar with the above discussed systems  $KOx$  and  $KHy$ , being an endothermic one. As a result the electrochemical system (11) transforms the thermal energy taken from the surrounding environment during the charging phase into a mechanical work and heat using the external circuit during the discharge phase. It is obvious and easy to understand that the electrochemical system (11) will operate intermittently, as the capacitors  $C_{M_1/S}$  and  $C_{M_2/S}$  charging takes place with a limited rate. However, such a capacitor is useful to provide intermittent power/signal in isolated environment,

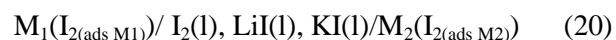
such as the airplane "black box", in electronics for intermittent component excitations (e.g. transistors), in communications systems for blocking the DC signal on the transmission line, or as independent, intermittent signal generator with potential applications in securing a certain perimeter.

A particularly interesting feature of such devices with potential application in evaluating their state of charge/health is linked to the fact that one needs here only straight simple measurements to do this; as the total energy contained in these devices depends only on their capacitance (in fact a constant value) and on the voltage values, one may measure these variables easily and hence the simplicity in determining the total charge or energy stored or left in these devices. With nowadays state of the art electronic gauges, this assessment is easy to be implemented and carried out.

The above presented capacitors operate at room temperature, being limited only by the liquid state of the electrolyte solutions. One may also find suitable similar capacitors of this type, able to operate at low or high temperatures, depending on the nature of electrolytes and solvents used such as: molten salts, ionic liquids, organic solvents.

A novel proposal for a self-charging double-layer capacitor consists of two different metals  $M_1$  and  $M_2$ , immersed in a molten mixture of  $KI$  and  $LiI$ , containing also a small amount of  $I_2$ . The melting temperature of the eutectic system  $LiI-KI$  ( $LiI$  63.2%, 36.8%  $KI$ ) is  $287^\circ C$ , and that of the individual molten salts is  $469^\circ C$  ( $LiI$ ) and  $681^\circ C$  ( $KI$ ) [19]. As a result, such a capacitor is operational in a wide range of temperatures. Triaca *et al.* have shown that in molten salts it is more likely to have the participation of  $I_2$  species in establishing the electrochemical equilibrium in the presence of  $I^-$  ions, rather than that of  $I_3^-$  [20].

Such a capacitor is best represented by the following electrochemical chain:



Metals  $M_1$  and  $M_2$  are selected so that there is a large difference in the energy of metal-iodine interactions for the two metals. As there are no available literature data regarding the metal-iodine energies in molten salts, the selection of  $M_1$  and  $M_2$  is carried out so that there is a significant difference between the electron work function of the two metals. Examples of metal with an appreciable electron work function are:  $Pt$  (5.65 eV),  $Ir$  (5.27 eV),  $Ni$  (5.15 eV),  $Pd$  (5.12 eV),  $Au$  (5.1 eV),  $Co$  (5.0 eV), which may be associated in a self-charging dual-layer capacitor with metals with low electron

work function such as Ta(4.25 eV), Ag(4.26 eV), Nb(4.3 eV), Ti(4.33 eV), Fe(4.5 eV) [21].

Let us consider that the electron work function for the metal  $M_1$  is smaller than that for the metal  $M_2$ . The equilibrium established at the metal-molten salt interface will be given by the equation:



If we have a low concentration of  $I_2$  in the molten salt, the equilibrium established on metal  $M_1$  will be given by (21) and it will be shifted more towards the right side than the similar equilibrium established on metal  $M_2$ , resulting that, for the electrochemical system (20),  $M_1$  will be the positive terminal and  $M_2$  - the negative terminal.

The charge and discharge processes taking place in the capacitor (20) are similar to those occurring in the capacitor (11) made in an aqueous solution.

One of the main characteristics of the above presented mechanism is that the process of storing the electrical charge does not involve alterations of any chemical bonds of the electrode/electrolyte and hence a life-time expressed in charge-discharge cycles limited only by the materials properties. This type of devices may be used for just a fraction of the stored charge or to the full extent, frequently or infrequently, without worrying about the so called „memory effect”, being particularly useful (with adequate capacity considered) for back-up power sources such as UPS (uninterruptible power supplies) systems or in vehicles powered by hybrid systems.

Moreover, as they have an increased tolerance to low, as well as high temperatures, one may envisage potential applications (such as space explorations, volcanic research, deep sea investigations, high or low temperature industrial processes) where such temperatures are unavoidable and unchangeable, and the classical galvanic cells will irreversibly break down in no time (the decrease of the electromotive force with temperature, electrolyte boiling or freezing etc.).

## CONCLUSIONS

The foregoing demonstrations entitle us to state unambiguously that Karpen's, such as KOx and KHy can be considered as self-charging double-layer capacitors, such devices being therefore perfectly achievable from both theoretical and practical point of view. The affirmative answer to the question set in the title raises however some additional issues: what is the capacitance and the efficiency of such electrical power sources?

One of the main advantages of the capacitors in comparison with the classical galvanic cells is the

high stability of the electrical charge stored, as in the case of capacitors we no longer talk about a chemical reaction and hence to the absence not only of the primary reactions, but also of the secondary unwanted reactions which lead to a decreased current efficiency. The drawback here is the reduced time due to the self-discharge phenomenon, so one should pay particular attention when considering such systems for long term energy storage.

Devices as the above presented ones, in existence and operating for more than 50 years, should be looked upon not as a simple scientific curiosity, but as an inspiration source for open-ended novel potential applications.

The necessity for advanced systematic studies in this particular field of such interesting revisited devices calls for interdisciplinary research teams (physicists, electrochemists, electrical and materials engineers), as this issue tends to be more than just a simple theoretical curiosity, overcoming long time ago the theoretical stage.

**Acknowledgements:** Special thanks go to “Dimitrie Leonida” National Technic Museum for the permission to reproduce the picture of Karpen's cells and to Prof. Alexandru Mironov for his invaluable comments.

## REFERENCES

1. A. Croft, *Eur. J. of Phys.*, **5**, 193 (1984).
2. A. Croft, *Eur. J. of Phys.*, **6**, 128 (1985).
3. N. Vasilescu-Karpen, *Brevet d'invention No.577.087*, République Française (1924).
4. N. Vasilescu-Karpen, *Romanian Academy – Sci. Bull., Stiinte matematice si Fizice*, **VIII**, 857(1956).
5. C. Alexandrescu, *J. New Energy*, **1**, 144 (1996).
6. N. Vasilescu-Karpen, *Comptes rendus hebdomadaires des séances de l'Académie des sciences - Paris*, **175**, 96 (1922).
7. N. Vasilescu-Karpen, *Bulletin de la Société Française de Physique – Paris*, **231**, 70 (1926).
8. N. Vasilescu-Karpen, *Bulletin de la Section Scientifique de l'Académie Roumaine*, **VIII**, 27 (1922/1923).
9. N. Vasilescu-Karpen, *Fenomene i teorii noi în electrochimie i chimie fizica*, Editura Academiei RPR, Bucuresti, 1957.
10. N. Vaszilcsin, D.-I. V ireanu, *Rev. Chim.*, **66**, 1293 (2015).
11. N. Vaszilcsin, D.-I. V ireanu, *tiin a i Tehnica*, **58**, 100 (2016).
12. A. Nicolaide, Significance of the scientific research of Nicolae Vasilescu-Karpen, AGIR Publishing House, Bucharest, 2006.
13. I. Katsounaros, S. Cherevko, A. Zeradjanin, K. Mayrhofer, *Angew. Chem., Int. Ed.*, **53**, 102 (2014).
14. J. O'M. Bockris, A. Reddy, M. Gamboa-Aldeco, *Modern Electrochemistry – Fundamentals of*

- Electrodics, Vol. 2A, Kluwer Academic/Plenum Publishers, New York, 2000.
15. S. Trasatti, *J. Electroanal. Chem.*, **39**, 163 (1972).
16. A. Frumkin, in: *Advances in Electrochemistry and Electrochemical Engineering*, Delahay P. (editor), Volume 3, Interscience Publishers, 1963, p.307.
17. C. Hamann, A. Hamnett, W. Vielstich, *Electrochemistry*, 2nd Ed., Wiley-VCH Verlag, Weinheim, 2007.
18. D. Palmer, R.W. Ramette, R.E. Mesmer, *J. Solution Chem.*, **13**, 673 (1984).
19. C. Liu, L. R. Lieto, *J. Chem. Eng. Data*, **14**, 83 (1969).
20. W. Triaca, H. Videla, A. Arvia, *Electrochim. Acta.*, **16**, 1671 (1971).
21. H. Michaelson, *J. Appl. Phys.*, **48**, 4729 (1977).

?

2\*

1

1

2

300006,

“1-7, 011061,

7 2016 .; 1 2017 .

( )

”

“

( )

”

”

”

Chimie“.

“Revista de



CONTENTS

Preface.....	5
<i>D. Vladikova, Zdravko Stoynov</i> - the scientist who turns curiosity into multidisciplinary.....	7
The Fathers	
<i>M. Michailov</i> , Rostislaw Kaischew and his trace in the fundamental science. A brief historical overview.....	23
<i>Z. Stoynov, W. Obretenov</i> , Academician Evgeni Budevski.....	42
Review Papers	
<i>D. Macdonald, S. Sharifi-As, G. Engelhardt</i> , Review of the extraction of electrochemical kinetic data from electrochemical impedance data using genetic algorithm optimization.....	53
<i>Z. Mandi</i> , Electrochemical methods in drug discovery and development .....	65
<i>R.- M. Apetrei, G.-E. Bahrim, G. Cârâc</i> , Spectroelectrochemical characteristics of polypyrrole synthesized by different methods.....	74
<i>M. Pandev, P. Lucchesse, B. Abrashev, D. Vladikova</i> , Hydrogen economy: the future for a sustainable and green society.....	84
Contribution	
<i>M. Antuch, A. Kudo, P. Millet</i> , Influence of light intensity on the kinetics of light-driven hydrogen evolution using Rh-doped SrTiO <sub>3</sub> : a study by photoelectrochemical impedancespectroscopy.....	95
<i>B. Grafov, A. Klyuev, A. Davydov, V. Lukovtsev</i> , Chebyshev's noise spectroscopy for testing electrochemical systems.....	102
<i>M. Ujvári, D. Zalka, S. Vesztergom, S. Eliseeva, V. Kondratiev, G. Láng</i> , Electrochemical impedance measurements in non-stationary systems - application of the 4-dimensional analysis method for the impedance analysis of overoxidized poly(3,4-ethylenedioxythiophene)-modified electrodes.....	106
<i>T. Pajkossy, G. Mészáros, I. Felh si, T. Marek, L. Nyikos</i> , A multisine perturbation EIS system for characterization of carbon nanotube layers.....	114
<i>V. Horvat-Radoševi, K. Kvastek, K. Magdi Košićek</i> , Application of Stoynov's 4-D analysis for nonstationary impedance spectra corrections of thin poly(o-ethoxyaniline) modified Pt electrode.....	119
<i>L. Pospíšil, N. Fanelli, M. Hromadová</i> , Formation of zirconium dioxide layers on microelectrode of zirconium. Inhibition of the hydrogen evolution reaction.....	128
<i>R. Sokolová, S. Giannarelli, N. Fanelli, L. Pospíšil</i> , Electrochemical bond cleavage in pesticide ioxynil. Kinetic analysis by voltammetry and impedance spectroscopy .....	134
<i>A. Enache, M. Dan, A. Kellenberger, N. Vaszilcsin</i> , Anodic oxidation of sulphite in alkaline aqueous solution on graphite electrode.....	139
<i>A. Szöke, G. Turdean, L. Muresan</i> , Modified glassy carbon electrode based on myoglobin and reduced graphene oxide for hydrogen peroxide detection.....	147
<i>R. Spotorno, G. Ghiara</i> , Application of the differential impedance analysis on the microbiologically induced corrosion of bronze.....	155
<i>G. Raikova, K. Krezhov, I. Genov, A. Thorel, A. Chesnaud, T. Malakova, D. Vladikova, Z. Stoynov</i> , Structural and electrochemical characterization of yttrium doped barium cerate BaCe <sub>0.85</sub> Y <sub>0.15</sub> O <sub>3</sub> for applications in solid oxide fuel cells.....	162
<i>M. Gabrovská, D. Nikolova, E. Mladenova, D. Vladikova, S. Rakovsky, Z. Stoynov</i> , Ni incorporation in pSOFC anode ceramic matrix: Part I. Wet chemical reduction in an aqueous medium.....	171
	271

G. Borisov, S. Avramov, E. Petkucheva, E. Lefterova, E. Slavcheva, W. Lehnert, Effect of sintering temperature on performance and durability of HT-PEFC cathodes.....	179
R. Surudži , A. Jankovi , M. Vukašinovi -Sekuli , A. Peri -Gruji , K. Y. Rhee, V. Miškovi -Stankovi , Optimization of the electrochemical synthesis of silver nanoparticles in poly(vinyl alcohol) colloid solutions.....	186
A. Cojocar, O. Brincoveanu, A. Pantazi, D. Balan, M. Enachescu, T. Visan, L. Anicai, Electrochemical preparation of Ag nanoparticles involving choline chloride – glycerol deep eutectic solvents ...	194
G.- L. Arnold, I. Lazar, E.-M. Ungureanu, G.-O. Buica, L. Birzan, New azulene modified electrodes for heavy metal ions recognition.....	205
P. Orlovi -Leko, D. Omanovi , I. Ciglenciki, K. Vidovi , T. Brenko, Application of electrochemical methods in the physico-chemical characterization of atmospheric precipitation.....	211
G. Pchelarov, D. Uzun, E. Razkazova-Velkova, O. Dimitrov, S. Vassilev, K. Petrov, Electrocatalysts for sulphur ions oxidation based on DWCNTs, MWCNTs, higher fullerenes and manganese.....	218
I.G. Lazar, E. Diacu, G.-L. Arnold, E.-M. Ungureanu, G.-O. Buica, L. Birzan, Synthesis and characterization of poly(azulene-thiophene vinyl pyrylium) salt.....	227
L. ižmek, I. Novak Jovanovi , Š. Komorsky-Lovri , Quantitative determination of capsaicinoids in ground hot pepper samples using voltammetry of microparticles .....	233
I. Boshnakova, E. Lefterova, E. Slavcheva, Montmorillonite as a catalytic support in water electrolysis.....	241
B. Abrashev, T. Spassov, M. Pandev, S. Vassilev, A. Popov, Hydrogen sorption and electrochemical properties of TiFe based alloys synthesized by mechanical alloying	247
D. Levi, Z. Stoyanov, D. Vladikova, Application of permittivity spectroscopy for screening of motor oils lubricating properties.....	254
Letter to the Editor	
N. Vaszilcsin, D.- I. Vaireanu, Could one achieve a self-recharging double layer capacitor?.....	263
INSTRUCTIONS TO THE AUTHORS.....	275

.....	5
.....	19
.....	41
.....	50
.....	64
.....	73
.....	83
.....	92
..... Rh- SrTiO <sub>3</sub> :	101
.....	105
..... (3,4- 4-D )-	113
..... 4-D	118
..... Pt ( -	127
.....	133
.....	138
.....	146
.....	154
.....	161
..... ,	170

	o	
BaCe <sub>0.85</sub> Y <sub>0.15</sub> O <sub>3</sub> -		.....
Ni		
: I.	a.....	178
		..... 185
	( ).....	193
Ag		..... 204
		..... 210
		..... 217
	DWCNTs, MWCNTs,	..... 226
	( )	..... 232
		..... 240
	, E.	..... 246
	TiFe	..... 253
		..... 259
	?	..... 269